Lecture Notes in Applied and Computational Mechanics 84

Peter Wriggers
Thomas Lenarz *Editors*

Biomedical Technology

Modeling, Experiments and Simulation

Springer

Lecture Notes in Applied and Computational Mechanics

Volume 84

About this Series

This series aims to report new developments in applied and computational mechanics—quickly, informally and at a high level. This includes the fields of fluid, solid and structural mechanics, dynamics and control, and related disciplines. The applied methods can be of analytical, numerical and computational nature.

More information about this series at http://www.springer.com/series/4623

Peter Wriggers · Thomas Lenarz
Editors

Biomedical Technology

Modeling, Experiments and Simulation

Springer

Editors
Peter Wriggers
Institute of Continuum Mechanics
Leibniz Universität Hannover
Hannover
Germany

Thomas Lenarz
Hals-Nasen-Ohrenklinik
Medical School Hannover
Hannover
Germany

ISSN 1613-7736 ISSN 1860-0816 (electronic)
Lecture Notes in Applied and Computational Mechanics
ISBN 978-3-319-59547-4 ISBN 978-3-319-59548-1 (eBook)
DOI 10.1007/978-3-319-59548-1

Library of Congress Control Number: 2017941488

Printed on acid-free paper

This Springer imprint is published by Springer Nature
The registered company is Springer International Publishing AG
The registered company address is: Gewerbestrasse 11, 6330 Cham, Switzerland

Preface

A major objective of medical research is related to the development of improved medication and implants. Due to the individual anatomy of each human being, the research direction points more and more towards a patient specific medicine. This in turn requires a better understanding of biological systems and of the performance of implants in humans. In engineering disciplines the application of virtual process design has originated many important innovations. Virtual modelling helps understand and control processes. Furthermore, virtual testing is fast and flexible. Hence, many new products can be efficiently designed and verified by numerical approaches.

In recent years these concepts were successfully applied in the field of biomedical technology. Based on the tremendous advances in medical imaging, modern CAD systems, high-performance computing and new experimental test devices, engineering can provide a refinement of implant design and lead to safer products. Computational tools and methods can be applied to predicting the performance of medical devices in virtual patients. Physical and animal testing procedures can be reduced by use of virtual prototyping of medical devices. These advancements enhance medical decision processes in many areas of clinical medicine.

In this book, scientists from different areas of medicine, engineering and natural sciences are contributing to the above research areas and ideas. The book provides a good overview of new mathematical models and computational simulations as well as new experimental tests in the field of biomedical technology.

In the first part of the book the virtual environment is used in studying biological systems at different scales and under multiphysics conditions. Modelling schemes are applied to human brain tissue, blood perfusion and metabolism in the living human, investigation on the effect of mutations on the spectrin molecules in red blood cells and numerical strategies to model transdermal drug delivery systems.

The second part is devoted to modelling and computational approaches in the field of cardiovascular medicine. The contributions start with an overview of current methods and challenges in the field of vascular haemodynamics. This is followed by new methods to accurately predict heart flow with contact between

the leaflets, estimation of a suitable zero stress state in arterial fluid structure interaction, solution strategies for stable partitioned fluid-structure interaction simulations, methods for stable large eddy simulation of turbulence in cardiovascular flow, a demonstration of the importance using non-Newtonian models in specific hemodynamic cases, a multiscale modelling of artificial textile reinforced heart valves, and new strategies to reduce the computational cost in fluid-structure interaction modelling of haemodynamics. The part closes with a method to computationally assess the rupture risk of abdominal aortic aneurysm.

A parameter study of biofilm growth based on experimental observations and numerical test as well as a multiscale modelling approach to dental enamel are contributions that face current challenges in dentistry.

The part related to orthopaedics starts with an overview of challenges in total hip arthroplasty and is followed by a concept for a personalized orthopaedic trauma surgery based on computational simulations.

The last part addresses otology and shows that an off-the-shelf pressure measurement system can be successfully used for intrachochlear sound pressure measurements. The second contribution is a user-specific method for the auditory nerve activity, leading to a better understanding of the electrode nerve interface in the case of cochlear implants.

All contributions highlight the state-of-the-art in biotechnology research and thus provide an extensive overview of this subject.

Hannover, Germany — Peter Wriggers
January 2017 — Thomas Lenarz

Contents

Part V Otology

Part I
Biological Systems

Multiscale Aspects in the Multiphasic Modelling of Human Brain Tissue

Wolfgang Ehlers and Arndt Wagner

Abstract The enormous microscopic complexity of the multicomponent brain-tissue aggregate motivates the application of the well-known Theory of Porous Media (TPM). Basically, a quaternary TPM-model is applied to brain tissue, cf. Ehlers and Wagner, Comput Method Biomech Biomed Eng 18:861–879 (2015), [1]. Besides the model's broad range of application, such as the simulation of brain-tumour treatment, we focus in this article on a specific anatomical property of the brain-tissue aggregate. Namely, its separated pore space which is concurrently perfused by two pore liquids. These are the blood in the blood-vessel system and the interstitial fluid in the interstitial-fluid space. In this regard, the constitutive formulation of evolving liquid saturations under certain loading conditions needs to be found. In order to microscopically underlay and motivate such a macroscopic constitutive relation within a thermodynamically consistent TPM approach, a microscopic study of the interaction between the pore compartments is performed and discussed in terms of scale-bridging aspects.

1 Introduction and Motivation

For various medical purposes regarding brain tissues, it could be of immense benefit to use numerical simulations. The aim to simulate real applications on the length scale of centimetres to metres requests a macroscopic modelling, for example, in case of the simulation of a therapeutic infusion process within brain tissue during brain-tumour treatment as it is shown in Fig. 1. Obviously, processes occurring on the complex microscale have a certain impact on the overall behaviour and need to be included. One example, on which we will focus in the present article, is the stiffness of the blood vessel system in comparison to the surrounding tissue aggregate (under physiological pressure conditions). This issue is still under controversial

W. Ehlers (✉) · A. Wagner
Institute of Applied Mechanics (CE), University of Stuttgart,
Pfaffenwaldring 7, 70569 Stuttgart, Germany
e-mail: Wolfgang.Ehlers@mechbau.uni-stuttgart.de

A. Wagner
e-mail: Arndt.Wagner@mechbau.uni-stuttgart.de

P. Wriggers and T. Lenarz (eds.), *Biomedical Technology*, Lecture Notes in Applied and Computational Mechanics 84, DOI 10.1007/978-3-319-59548-1_1

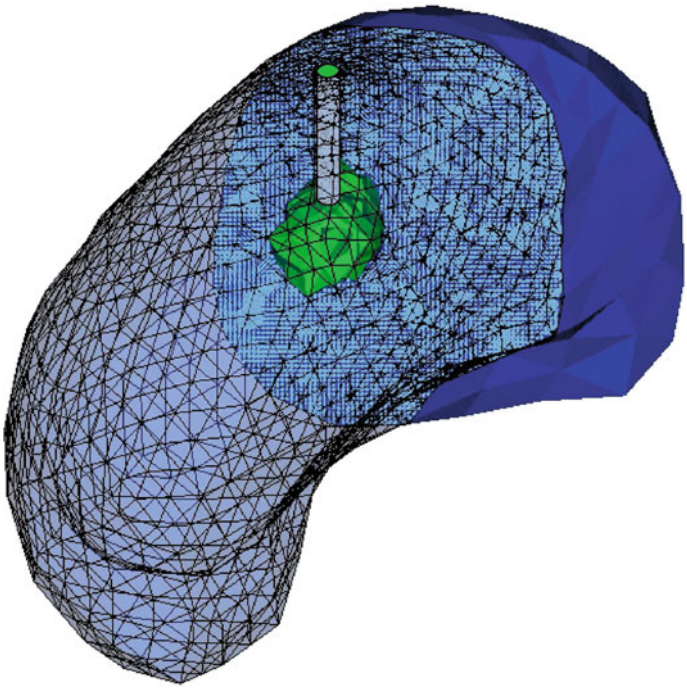

Fig. 1 Simulation of a therapeutic infusion process within brain tissue during brain-tumour treatment. The supplied domain of the brain hemisphere is displayed in *green* and the second-order permeability tensors, governing the patient-specific anisotropic perfusion behaviour, are visualised via ellipsoids in *light blue* on an exemplary cross section, cf. [3] for a comprehensive overview

discussion. Therefore, the purpose of this contribution is to perform within the commercial finite-element (FE) software tool Abaqus® (Dassault Systèmes, Vélizy-Villacoublay, France, cf. http://www.3ds.com) microscopic and locally single-phasic computations of a representative elementary volume of the brain-tissue aggregate. This allows for the assignment of microscopic material parameters for the individual components. In this regard, elastically deformable blood vessels, separating the pore compartments, are assumed. Thus, the liquid with the higher pressure displaces the liquid with the lower pressure. The subsequent geometrical evaluation of certain adjusted pressure situations (applied as boundary conditions) within such a microscopic model allow for a meaningful postulation of a macroscopic constitutive equation. Note in passing that the presented study of scale-bridging aspects differs from a complete two-scale approach using the FE^2-Method (where both the macroscopic as well as the underlying microscopic structure are analysed with the finite-element method, cf. [2] in terms of the TPM). The scale-bridging approach proposed here rather proceeds from an one-time analysis of a specific process on the microstructure and a subsequent transfer to the macroscopic model obtaining a microscopically underlaid constitutive equation.

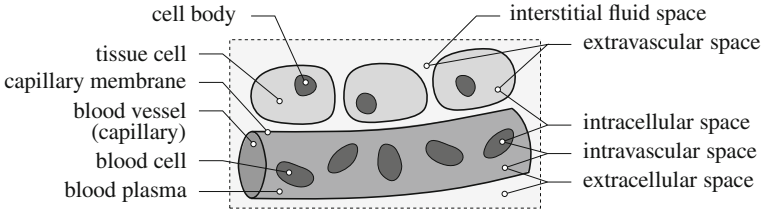

Fig. 2 Exemplary sketch of microscopic fluid spaces in brain tissues, according to [3]

2 Anatomic Elements of Human Brain Tissue

Amongst other things, brain tissue includes the components interstitial fluid and blood, which are mobile in two basically separated pore compartments. In this regard, the interstitial fluid is situated within the interstitial fluid space, whereas the intravascular space contains the blood. Moreover, further tissue spaces are commonly distinguished, such as the intra- and extracellular space or the extravascular space, cf. Fig. 2 for a qualitative sketch. In general, the capillary membrane (wall) is highly selective and governs the passing of molecules from the intravascular to the extravascular space. Thus, the so-called blood-brain barrier separates the individual pore compartments.

The interstitial fluid typically occupies a volume fraction of 20% of the brain's bulk volume, cf. [4]. However, a variation between 15% and 30% is normal and even may fall to 5% during global ischaemia. Typical values of the blood volume fraction are in the range of approximately 3% for healthy tissues, cf. [4] based on, e.g., [5]. In contrast, in tumour-affected domains, the blood amount may vary between 1% and 20%.

3 TPM Model of the Overall Brain-Tissue Aggregate

To provide a framework for the considerations in this paper, the basis of the macroscopic thermodynamically consistent drug-infusion model is briefly described in this section. Using the TPM, a volumetrical averaging procedure (smearing) of the underlying microscopic structure over a representative elementary volume (REV) leads to an idealised macroscopic model of superimposed and mutually interacting constituents. For a detailed discussion of the model, the interested reader is referred to the underlying articles of [1, 6, 7] and citations therein. Basically, the quaternary TPM model includes four constituents. In particular, three immiscible constituents are given by the solid skeleton φ^S, the blood φ^B and the overall interstitial fluid φ^I, where φ^I contains a dissolved miscible therapeutic solute φ^D. To account for the local composition of the aggregate, scalar structure parameters, the volume fractions

$$n^\alpha = \frac{\mathrm{d}v^\alpha}{\mathrm{d}v}\,, \tag{1}$$

are introduced defined as the local ratios of the partial volume elements $\mathrm{d}v^\alpha$ with respect to the volume element $\mathrm{d}v$ of the overall aggregate. Assuming fully saturated conditions (no vacant space within the domain), the well-known saturation condition $\sum_\alpha n^\alpha = n^S + n^B + n^I = 1$ is obtained. As was already mentioned, the pore liquids are mobile in their individual pore compartments. Therefore, the volumetric amount (saturation) of the blood

$$s^B = 1 - s^I = \frac{n^B}{1 - n^S} \tag{2}$$

is specified in relation to the overall pore space (porosity). The set of model equations proceeds from the specific balance relations for multiphasic materials, cf., e.g., [8] or [9], where preliminary assumptions are initially included, i. e. isothermal conditions, materially incompressible constituents, negligible gravitational forces and acceleration terms. Therefore, the governing balance relations are given by the momentum balance $(3)_1$ of the overall aggregate φ, the volume balance $(3)_2$ of φ^B, the volume balance $(3)_3$ of φ^I and the concentration balance $(3)_4$ of φ^D, viz.:

$$\begin{aligned}
&\operatorname{div}\mathbf{T} = \mathbf{0}\,,\\
&(n^B)'_S + \operatorname{div}(n^B\mathbf{w}_B) + n^B \operatorname{div}(\mathbf{u}_S)'_S = 0\,,\\
&(n^I)'_S + \operatorname{div}(n^I\mathbf{w}_I) + n^I \operatorname{div}(\mathbf{u}_S)'_S = 0\,,\\
&n^I(c^D_m)'_S + c^D_m \operatorname{div}(\mathbf{u}_S)'_S + \operatorname{div}(n^I c^D_m \mathbf{w}_D) + c^D_m \operatorname{div}(n^B\mathbf{w}_B) = 0\,.
\end{aligned} \tag{3}$$

Therein, the overall Cauchy stress $\mathbf{T}$ in $(3)_1$ can be derived for, e.g., finite and anisotropic elastic deformation processes of the solid in combination with the overall pore pressure as was described in [1]. The notion $(\,\cdot\,)'_S$ indicates the material time derivative with respect to the solid motion. In terms of the volume fractions and their temporal changes

$$\begin{aligned}
n^S &= n^S_{0S}\,(\det\mathbf{F}_S)^{-1} && \text{and } (n^S)'_S = -n^S \operatorname{div}(\mathbf{u}_S)'_S\,,\\
n^B &= s^B\,(1 - n^S) && \text{and } (n^B)'_S = (s^B)'_S\,(1 - n^S) - s^B (n^S)'_S\,,\\
n^I &= 1 - n^S - n^B && \text{and } (n^I)'_S = -(n^S)'_S - (n^B)'_S\,,
\end{aligned} \tag{4}$$

it turns out that a constitutive relation for the blood's saturation s^B is required, since the saturation condition is not sufficient to determine all volume fractions. Note in passing that the temporal change $(s^B)'_S$ is based on the chosen constitutive ansatz for s^B, cf. Sect. 4.2. In Eq. (4), the quantity n^S_{0S} denotes the initial solid volume fraction and $\det\mathbf{F}_S$ is the determinant of the solid's deformation gradient $\mathbf{F}_S = \mathbf{I} + \operatorname{Grad}_S\mathbf{u}_S$. Therein, the operator Grad_S denotes the material gradient of φ^S with respect to its reference position. Finally, the set of equations in (3) contains the seepage velocities $\mathbf{w}_B$, $\mathbf{w}_I$ and $\mathbf{w}_D$ which are described via

$$
\begin{aligned}
n^B \mathbf{w}_B &= -\frac{\mathbf{K}^{SB}}{\mu^{BR}} \left(\operatorname{grad} p^{BR} + \frac{p_{\text{dif.}}}{s^B} \operatorname{grad} s^B \right), \\
n^I \mathbf{w}_I &= -\frac{\mathbf{K}^{SI}}{\mu^{IR}} \operatorname{grad} p^{IR}, \\
n^I c_m^D \mathbf{w}_D &= -\mathbf{D}^D \operatorname{grad} c_m^D + n^I c_m^D \mathbf{w}_I .
\end{aligned} \tag{5}
$$

The perfusion of the solid skeleton by the mobile but separated pore liquids is considered by the permeability tensors $\mathbf{K}^{SB}$ and $\mathbf{K}^{SI}$, whereas $\mathbf{D}^D$ is the diffusivity of the therapeutic agent. Moreover, μ^{BR} and μ^{IR} are the effective shear viscosities of the liquids. The pressure difference $p_{\text{dif.}} = p^{BR} - p^{IR}$ indicates the difference between the individual pore-liquid pressures. Finally, the TPM model is solved for the primary variables solid displacement $\mathbf{u}_S$, effective pore-liquid pressures p^{BR}, p^{IR} and therapeutic concentration c_m^D after inserting the constitutive relations into the set of equations given in (3). With regard to the corresponding numerical solution of the coupled system of partial differential equations using the research code Pandas (Porous media Adaptive Nonlinear finite element solver based on Differential Algebraic Systems, cf. http://www.get-pandas.com), the Bubnov-Galerkin mixed FEM is applied as shown in [3] for several numerical examples.

4 Microscopically Underlaid Macroscopic Constitutive Relation

As was already mentioned, the TPM model includes two pore liquids. Therefore, a constitutive equation to describe the division for the volume fractions is required, since there is still no general agreement concerning the stiffness of the blood-vessel system in comparison to the surrounding tissue aggregate. Therefore, the purpose of this section is to perform a microscopic and locally singlephasic computation of a representative elementary volume of the brain tissue aggregate. This is realised using Abaqus and consequently allows for the assignment of microscopic material parameters for the individual components. The evaluation of adjusted pressure situations within such a microscopic model allows for a meaningful foundation of the developed macroscopic constitutive equation.

4.1 Microscopic Model Settings

In terms of a microscopic description, a tube-like geometry is considered for the description of a single vascular vessel, cf. Fig. 3. In order to apply a pressure difference between the inside and the outside of a blood vessel, $p_{\text{dif.}} = p^{BR} - p^{IR}$ is subjected at the inside of the blood-vessel wall, cf. Fig. 3a. For the sake of simplicity, a linear elastic material behaviour is chosen. The corresponding parameters are collected in Table 1. Due to the elastically deformable blood vessels, the liquid with

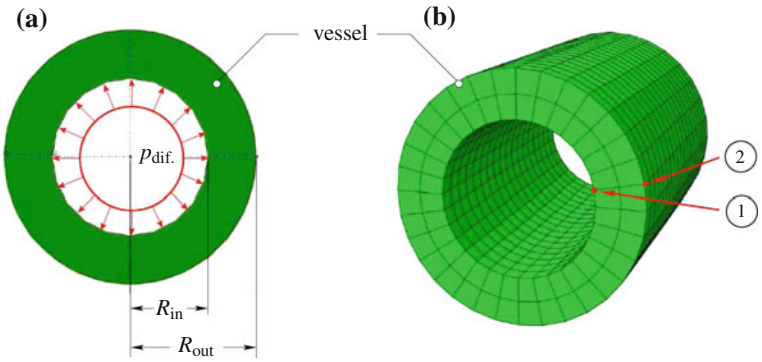

Fig. 3 Boundary conditions on a single blood vessel (**a**) and meshed geometry (**b**) with an exemplary point at the inside (**1**) and the outside (**2**) of the vessel, respectively

Table 1 Collection of parameters for a single blood vessel and a REV

Quantity	Value	Reference/Remark
Blood vessel inner radius R_{in}	1.6×10^{-4} m	[10]
Blood vessel outer radius R_{out}	2.6×10^{-4} m	[10]
Edge length l_{REV} of a single REV	7.3×10^{-4} m	Assumption to satisfy the initial (physiologic) condition $s^B = 0.2$
Poisson's ratio μ	0.48	For the cases $(i) - (iii)$, according to [11]
Young's modulus E	2792 N/m^2	For the cases (i) and (ii), assumption of soft vessel walls
Young's modulus E	1.2×10^5 N/m^2	For case (iii), according to [12]

the higher pressure displaces the liquid with the lower pressure. In particular, three different cases are studied:

- case (i): "soft" vessel walls under unconstrained conditions,
- case (ii): "soft" vessel walls under constrained conditions (cf. Sect. 4.1.1) and
- case (iii): "stiff" vessel walls under unconstrained conditions.

In these microscopic computations, the pressure difference is applied as a boundary condition and the arising volume changes are geometrically evaluated in a subsequent step. To bridge from the microscopic to the macroscopic scale, many single REV are arranged in a regular manner, cf. Fig. 4. In this regard, the edge length of a single REV is chosen such that the initial saturation under zero pressure difference constitutes to $s^B = 0.2$. Physically, a variation of the volume fractions within a single REV requires an inflow (of the blood for a positive pressure difference) and an outflow (of the interstitial fluid for a positive pressure difference) of the liquids. This is provided by free-flow boundary conditions for both liquids in longitudinal direction of the chosen blood-vessel orientation.

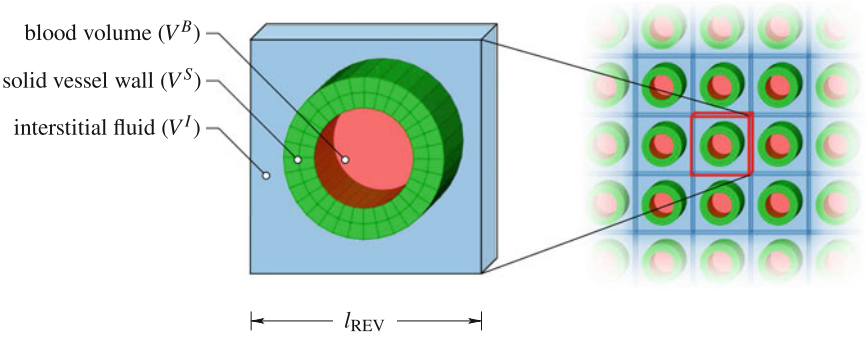

Fig. 4 Exemplary sketch of the macroscopic overall aggregate composed of multiple REVs

4.1.1 Geometrical Evaluation

Within Abaqus, the displacement of each node of the FE grid is obtained by the solution of the considered initial-boundary-value problems. Note in passing that an analytical solution for the widening of a linear-elastic cylindrical shell under constant internal pressure does exist, cf., e.g., [13], and corresponds to an unconstrained microscopic computation. In a geometric evaluation, the deformation of the solid vessel wall can be captured by the displacements of the nodal points under loading conditions. However, the focus of this contribution lies on the evaluation of the liquid's saturations. In this regard, the geometrical evaluation of the arising volume fractions in the unconstrained cases (*i*) and (*iii*), cf. Fig. 5a, is trivial, since the displacements of the nodes ① (located at the inside of the vessel wall) and ② (corresponding point in radial direction at the outside, cf. Fig. 3) are known from the computation and allow for the determination using basic geometrical relations. In addition, the widening of a single vessel is at a certain state somehow constrained by the surrounding vessels, which themselves wide in a similar manner, as it is sketched in Fig. 5b. This is approximated by a linear pathway in the contact domain and a circular shape in the edges. For the sake of simplicity, a constant thickness t of the blood vessel is assumed. Obviously, this represents a simplification, since (at least in the case of mutual contact) a deformation of the vessel wall may occur. However, this assumption allows a relatively simple evaluation of the arising volume fractions. Then, the volume fractions can be computed for the constrained case (*ii*), viz.:

$$\begin{aligned} V^B &= \left[\pi\,(d-t)^2 + 4\,(d-t)\,(l_{\mathrm{REV}} - 2\,d) + (l_{\mathrm{REV}} - 2\,d)^2\right] h_{\mathrm{REV}}\,, \\ V^I &= (4\,d^2 - \pi\,d^2)\,h_{\mathrm{REV}}\,. \end{aligned} \tag{6}$$

Therein, h_{REV} is the height of the REV required to compute a volume. However, h_{REV} vanishes within the determination of the liquid's volume fractions via

$$n^B = \frac{V^B}{V_{\mathrm{REV}}} \qquad \text{and} \qquad n^I = \frac{V^I}{V_{\mathrm{REV}}} \tag{7}$$

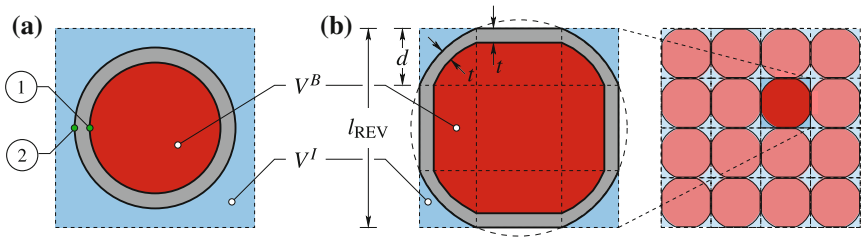

Fig. 5 **a** Unconstrained vessel widening within the REV and **b** constrained vessel deformation caused by interacting vessels

and, thus, has no influence. In conclusion, this allows for the evaluation of the liquid's saturations under applied pressure conditions. In particular, this is carried out for typical pressure states and collected in Sect. 4.3.

4.2 Macroscopic Constitutive Relation

The aim to simulate bio-technical/engineering applications of human brain tissues requires a thermodynamically consistent setting of the blood-saturation function in the context of the TPM model. This is somehow comparable to the procedure within unsaturated soil mechanics. Therein, the capillary pressure, defined as the difference between the pressures of the non-wetting and the wetting fluids in a common pore space is used to evaluate the saturations via capillary-pressure-saturation conditions, cf., e.g., [14]. However, in the specific case of human brain tissue, the blood and the interstitial fluid are not situated in the same pore compartment such that these relations cannot be applied. Instead, further considerations are made here in order to specify the blood saturation, while bearing the microscopic considerations in mind. In general, the macroscopic constitutive equation should provide the flexibility to capture several circumstances. For the case of sufficiently soft elastic arterial walls, a mutually volumetrical interaction is induced by an upcoming pressure difference. Therefore, a constitutively chosen ansatz for the Helmholtz free energy ψ^B of the blood constituent is postulated according to [1], viz.:

$$\psi^B(s^B) = \frac{\tilde{\alpha}^B}{\rho^{BR}} \left((\tilde{\beta}^B + 1) \ln(s^B) + \frac{1}{s^B} - \ln(1 - s^B) \right) + \tilde{\psi}_0^B . \tag{8}$$

Therein, $\tilde{\alpha}^B$ and $\tilde{\beta}^B$ denote material parameters, which allow via $\tilde{\alpha}^B$ for the adaption of the pore-pressure difference to typical pressure values as they exist in the skull and for the initial blood saturation via $\tilde{\beta}^B$. Furthermore, $\tilde{\psi}_0^B$ denotes the constant reference potential (standard state potential). This approach satisfies the thermodynamical restrictions and consequently yields a relation for the pressure difference

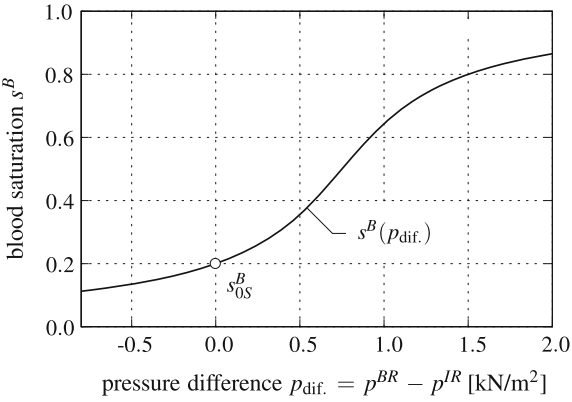

Fig. 6 Thermodynamically consistent constitutive relation for the blood-saturation function s^B

$$p_{\text{dif.}}(s^B) = s^B \rho^{BR} \frac{\partial \psi^B}{\partial s^B} = \tilde{\alpha}^B \left(\frac{1 - 2\,s^B}{s^B\,(s^B - 1)} + \tilde{\beta}^B \right),$$
$$\text{where} \quad \frac{\partial \psi^B}{\partial s^B} = \frac{\tilde{\alpha}^B}{\rho^{BR}} \left(\frac{\tilde{\beta}^B}{s^B} - \frac{1}{s^B\,(s^B - 1)} - \frac{1}{(s^B)^2} \right). \tag{9}$$

The inversion of (9) finally leads to the blood saturation function

$$s^B(p_{\text{dif.}}) = \frac{1}{2\left(\frac{p_{\text{dif.}}}{\tilde{\alpha}^B} - \tilde{\beta}^B\right)} \left(\left(\frac{p_{\text{dif.}}}{\tilde{\alpha}^B} - \tilde{\beta}^B - 2 \right) + \sqrt{4 + \left(\frac{p_{\text{dif.}}}{\tilde{\alpha}^B} - \tilde{\beta}^B \right)^2} \right). \tag{10}$$

It should be noted that Eq. (10) is found by rational investigations of a meaningful inversion of (9), which is a second-order function in s^B. The derived relation for the blood saturation (10) allows for a proper determination of the volume fractions using the relations in (4). To give an example, an equation satisfying typical initial volume fractions of the brain tissue as well as typical pressure values as they exist in the skull is adapted by $\tilde{\beta}^B = 3.75$ and $\tilde{\alpha}^B = 200.0$ N/m^2, cf. Fig. 6. Physically, this leads to a replacement of the interstitial fluid if the pressure difference $p_{\text{dif.}}$ is positive. Note in passing that a constant value of $n^B_{0S} = 0.05$ yields an initial value of $s^B_{0S} = 0.2$ and, as a result, $p_{\text{dif.}} = 0$.

4.3 Results and Discussion

In this section, the evaluated results of the microscopic computation are compared with the macroscopic constitutive approach. For the pressure in the vascular system (cerebral blood pressure depending on its hierarchical position), the range in the capillary bed varies between 10 mm of mercury (mmHg) (corresponds to 1333 N/m^2) at the venous end and 30 mmHg (4000 N/m^2) at the arterial end. Whereas the interstitial-fluid pressure (tissue pressure) has a typical value of 6 mmHg (800

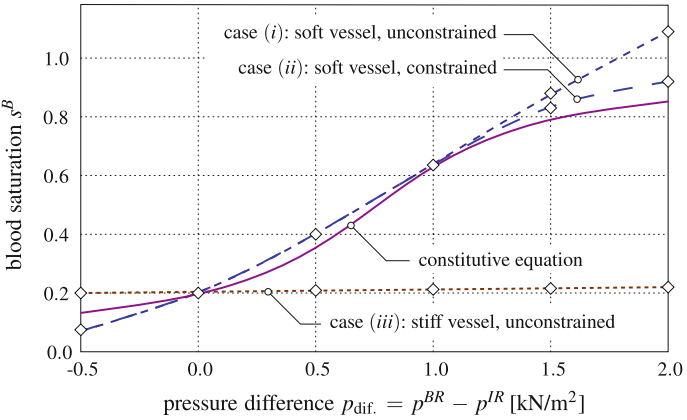

Fig. 7 Comparison of different approaches for the blood-saturation function. Evaluated pressure states from microscopic computations are displayed with *diamonds* which are connected with *dashed lines*

N/m^2). To capture such typical conditions, the adjusting blood saturation is evaluated for pressure differences in the range of -500 N/m^2 $\leq p_{\text{dif.}} \leq 2000$ N/m^2. In particular, the pressure difference is applied in steps of 500 N/m^2 with a subsequent evaluation of the arising volume fractions according to Sect. 4.1.1. The evaluated pressure states from the microscopic computations are then displayed with diamonds and interpolated with dashed lines, cf. Fig. 7. The evaluation of case (*i*) (soft vessel, unconstrained) yields to reasonable results in the pressure range of -500 N/m^2 $\leq p_{\text{dif.}} \leq 1500$ N/m^2. However, for a further increase of the pressure difference, nonphysical results (i. e. a blood saturation greater than one) occur. This is caused by the possibility of an unconstrained widening of the blood vessel. In contrast, in the case (*ii*) (soft vessel, constrained) it is nicely identified that the microstructural computations yield comparable results in relation to the constitutively chosen pressure-saturation relation (Sect. 4.2) in the domain of nearly fully blood saturated conditions. Again, the constitutive formulation of the blood saturation function is not arbitrary but has to fulfil the thermodynamic restrictions discussed in Sect. 4.2. Therefore, the pathway vary slightly from the graph of case (*ii*) obtained by microscopic computations. However, this allows for a scale-bridging in terms of microscopic and macroscopic material parameters. In the specific case (*ii*), the microscopic material parameters, Young's modulus $E = 2792$ N/m^2 and Poisson's ratio $\mu = 0.48$, of the blood vessel wall correspond to the macroscopic material parameters $\tilde{\alpha}^B = 200.0$ N/m^2 and $\tilde{\beta}^B = 3.75$ of the constitutive function. Assuming a higher stiffness of the vessel (corresponding to somehow realistic experimental values of the human intracranial artery) in case (*iii*) yields within the considered pressure regime a nearly constant blood saturation. This would justify to assume a constant blood-volume fraction within macroscopic simulations.

In conclusion, a constitutive approach for the relation between the pressure difference $p_{\text{dif.}}$ of the liquids and the blood saturation s^B was presented which satisfies both

the thermodynamic consistence as well as physical conditions within human brain tissue. Moreover, this macroscopic saturation condition was motivated and studied by a microscopic computation of a representative microstructure using Abaqus and a subsequent geometrical evaluation of the arising saturations under applied liquid pressure conditions. With reliable experimental results, this would provide the possibility to identify the macroscopic material parameter of the constitutive function based on the microscopic material parameter in terms of scale-bridging aspects.

Acknowledgements The authors would like to thank the German Research Foundation (DFG) for the financial support of the project within the Cluster of Excellence in Simulation Technology (EXC 310/2) at the University of Stuttgart.

References

1. W. Ehlers, A. Wagner, Multi-component modelling of human brain tissue: a contribution to the constitutive and computational description of deformation, flow and diffusion processes with application to the invasive drug-delivery problem. Comput. Method Biomech. Biomed. Eng. **18**, 861–879 (2015)
2. F. Bartel, T. Ricken, J. Schröder, J. Bluhm, A twoscale homogenisation approach for fluid saturated porous media based on TPM and FE^2-method. Proc. Appl. Math. Mech.**15**, 447–448 (2015)
3. A. Wagner, Extended modelling of the multiphasic human brain tissue with application to drug-infusion processes. Dissertation, Report No. II-27 of the Institute of Applied Mechanics (CE), University of Stuttgart, 2014
4. E. Syková, C. Nicholson, Diffusion in brain extracellular space. Phys. Rev. **88**, 1277–1340 (2008)
5. R.K. Jain, Determinants of tumor blood flow: a review. Cancer Res. **48**, 2641–2658 (1988)
6. W. Ehlers, A. Wagner, Constitutive and computational aspects in tumor therapies of multiphasic brain tissue, in *Computer Models in Biomechanics*, ed. by G.A. Holzapfel, E. Kuhl (Springer, Netherlands, Dordrecht, 2013), pp. 263–276
7. A. Wagner, W. Ehlers, Continuum-mechanical analysis of human brain tissue. Proc. Appl. Math. Mech. **10**, 99–100 (2010)
8. W. Ehlers, Foundations of multiphasic and porous materials, in *Porous Media: Theory Experiments and Numerical Applications*, ed. by W. Ehlers, J. Bluhm (Springer, Berlin, 2002), pp. 3–86
9. W. Ehlers, Challenges of porous media models in geo- and biomechanical engineering including electro-chemically active polymers and gels. Int. J. Adv. Eng. Sci. Appl. Math. **1**, 1–24 (2009)
10. K.L. Monson, W. Goldsmith, N.M. Barbaro, G.T. Manley, Axial mechanical properties of fresh human cerebral blood vessels. J. Biomech. Eng. **125**, 288–294 (2003)
11. T.E. Carew, N.V. Ramesh, J.P. Dali, Compressibility of the arterial wall. Circ. Res. **23**, 61–68 (1968)
12. K. Hayashi, H. Handa, S. Nagasawa, A. Okumura, K. Moritake, Stiffness and elastic behavior of human intracranial and extracranial arteries. J. Biomech. **13**, 175–184 (1980)
13. Y. Basar, W.B. Krätzig, *Mechanik der Flächentragwerke: Theorie, Berechnungsmethoden* (Anwendungsbeispiele. Springer Fachmedien, Wiesbaden, 2013)
14. T. Ricken, R. de Boer, Multiphase flow in a capillary porous medium. Comput. Mat. Sci. **28**, 704–713 (2003)

Simulation of Steatosis Zonation in Liver Lobule—A Continuummechanical Bi-Scale, Tri-Phasic, Multi-Component Approach

Tim Ricken, Navina Waschinsky and Daniel Werner

Abstract The human liver is an important metabolic organ which regulates metabolism of the body in a complex time depending and non-linear coupled function-perfusion-mechanism. Harmful microstructure failure strongly affects the viability of the organ. The excessive accumulation of fat in the liver tissue, known as a fatty liver, is one of the most common liver micro structure failures, especially in western countries. The growing fat has a high impact on the blood perfusion and thus on the functionality of the organ. This interaction between perfusion, growth of fat and functionality on the hepatic microcirculation is poorly understood and many biological aspects of the liver are still subject of discussion. The presented computational model consists of a bi-scale, tri-phasic, multi-component approach based on the theory of porous media. The model includes the stress and strain state of the liver tissue, the transverse isotropic blood perfusion in the sinusoidal micro perfusion system. Furthermore, we describe the glucose metabolism in a two-scale PDE-ODE approach whereas the fat metabolism is included via phenomenological functions. Different inflow boundary conditions are tested against the influence on fat deposition and zonation in the liver lobules. With this example we can discuss biological assumptions and get a better understanding of the coupled function-perfusion ability of the liver.

1 Introduction

For a realistic simulation of the liver behavior it is important to take into account a detailed description of the biological processes. We present a bi-scale, tri-phasic, continuum multi-component model simulating blood perfusion and metabolism in

T. Ricken (✉) · N. Waschinsky · D. Werner
TU Dortmund, August-Schmidt-Straße 6, Dortmund, Germany
e-mail: tim.ricken@tu-dortmund.de

N. Waschinsky
e-mail: navina.waschinsky@tu-dortmund.de

D. Werner
e-mail: danielq.werner@tu-dortmund.de

P. Wriggers and T. Lenarz (eds.), *Biomedical Technology*, Lecture Notes in Applied and Computational Mechanics 84, DOI 10.1007/978-3-319-59548-1_2

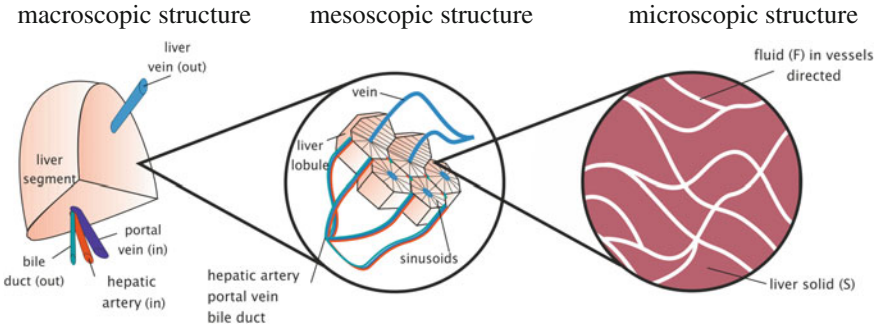

Fig. 1 Bi-scale approach; macroscopic structure: millimeter spatial resolution to observe the vascular system from the in- and outflow of the liver to smaller and smaller branches of the vessels; mesoscopic structure: micrometer spatial resolution to observe the perfusion through the sinusoids; microscopic structure: biochemical description of the metabolism in the liver cells

the human liver based on the two-phasic approach, see Ricken et al. [13]. To get a better understanding of the liver we start with a short physiological outline. For more informations, see Hubscher et al. [8].

The liver is the main metabolic organ in the human body. Roughly, the structure of the organ is segmented into four hepatic lobes of unequal size within the range of centimeters; the main parts are the right lobe (lobus hepatic dexter) and left lobe (lobus hepatis sinister). Each lobe consists of liver lobules which have the size of about a few millimeters. They are hexagonally structured parts of the liver tissue, see Fig. 1. Microscopic sized hepatocytes, the liver cells, are arranged in radial columns embedded in the liver lobules. The hepatic vascular system is important for the blood supply of the hepatocytes. For this, the vascular system consists of branches which supply the organ from the macroscopic to microscopic anatomy of the liver. On the macroscopic level branches of hepatic artery (oxygen rich) and portal vein (nutrient rich) run together and supply the segments of the organ. Intrahepatic bile ducts proceed together with the blood vessels and support the liver during detoxification processes as the bile fluid is excreted with decomposed products. The microcirculation takes place in the liver lobule. In each corner of the liver lobule a portal triad is located which is composed of the three branches of hepatic artery, portal vein and a bile duct in their smallest subdivision. The microcirculation is described by blood vessels connecting the portal triad with the central vein which are called sinusoids. The central vein drains the blood leading to a directed blood flow from the portal triad to the central vein, see Fig. 1.

Under consideration of the physiological background it is unavoidable to classify the liver in different scales to focus on scale depending processes.

We focus on a bi-scale approach; on the mesoscopic level we describe the blood perfusion through the liver lobule and on the microscopic level the metabolism in the cells.

The mesoscopic model is based on an ansatz for transverse isotropic permeability relation describing the perfusion given in Ricken et al. [12]. Due to the complex

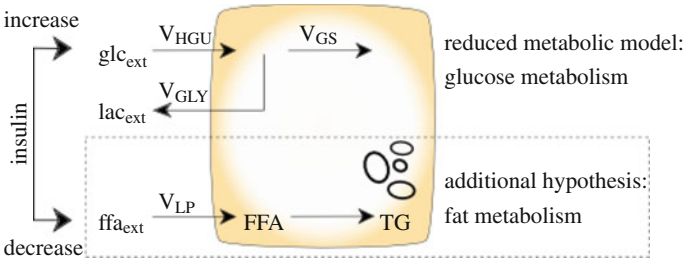

Fig. 2 Metabolism: the biochemical reactions are described with the metabolites of external glucose (glc_{ext}), external lactate (lac_{ext}), external FFA (ffa_{ext}), internal triglyceride (TG) and internal glycogen (glyc). External components are included in the fluid phase whereas internal components are included in the solid tissue of the liver. Triglyceride describes the fat phase in the liver. Reduced metabolic model: the glucose pathways (V_{HGU}), (V_{GS}) and (V_{GLY}) are modeled by sets of ordinary differential equations. With $V_{HGU} < 0$: hepatic glucose production, $V_{HGU} > 0$: hepatic glucose utilization, $V_{GLY} < 0$: gluconeogenesis, $V_{GLY} > 0$: glycolysis, $V_{GS} < 0$: glycogenolysis, $V_{GS} > 0$: glycogenesis. Additional hypothesis: the fatty acid pathway (V_{LP}) is modeled by assumptions concerning the uptake rate of FFA. With $V_{LP} > 0$: lipogenesis and $V_{LP} < 0$: lipolysis

vascular system of sinusoids it is impossible to model the numerous capillaries with an accurate discrete geometrical description. Therefore we apply a homogenized multiphase approach, based on the theory of porous media (TPM) which is a convenient tool in order to describe complex, multi-phasic and porous materials; see de Boer [2, 3] and Ehlers [5]. This approach includes the description of three main phases, namely the liver tissue, fat tissue and blood vessels. Additionally to the main phases, the homogenized liver lobule includes miscible components which are important for the biochemical description of the metabolism. A description of the mesoscopic model is given in the appendix.

We describe the biochemical processes on the microscopic scale of our model as the metabolism takes place in the smallest parts of the liver tissue, the cells. The liver is crucial for metabolites regulation of glucose and free fatty acid (FFA) due to its ability to store glucose in form of internal glycogen and FFA as internal fat deposition. The cells can switch between glucose and FFA deposition and utilization depending on the requirements of the rest of the body. After ingestions, glucose and FFA concentrations coming from the digestive system increase (hyperglycemia). The liver cells start to deposit them as internal metabolites glycogen and triglyceride. Whereas, during fasting times (hypoglycemia) the internal metabolites are served as a backup system and can be used to increase the low concentration of external metabolites. We summarize the metabolism in a set of ordinary differential equations which consider the conditions of hyperglycemia and hypoglycemia and the relations of the internal and external metabolites. The microscopic model approach is derived from a detailed pharmacokinetic model of hepatic glucose metabolism, described in König et al. [10]. We presented a reduced model for glucose metabolism in Ricken et al. [13] and add a phenomenological approach for the fat metabolism (Fig. 2).

2 Glucose and Fat Metabolism

The liver ensures biosynthetic metabolic pathways of immense complexity. In this study we focus on the main metabolic pathway of glucose described by a simplified ordinary differential equation system. Furthermore, we add a phenomenological approach for the fat metabolism.

Figure 2 summarizes the applied pathways for glucose and fat metabolism. The main task of the liver is the maintenance of homeostasis for metabolites which might be necessary for the organism. For this the liver regulates the glucose and fat level in order to offer enough energy for the brain and muscles. The metabolites are stored or utilized depending on hormone concentration levels. We distinguish two conditions: the fed (hyperglycemia) and fasted state (hypoglycemia). During feeding the organism is saturated of glucose and FFA leading to utilization of external metabolites. Glycolysis and glycogenesis are two possible metabolic pathways of glucose. The first metabolic pathway ensures the energy supply for cells and reproduction of lactate. The second describes energy storage in form of internal glycogen. Lipogenesis is the fatty acid pathway describing the ester of FFA and glycerol to triglyceride. The lipid accumulation is reinforced by high carbohydrate diets.

During the fasting state the organism utilizes hepatic glycogen, non-carbohydrate carbon substrates and lipids. Gluconeogenesis is one pathway for the generation of glucose. The utilization of certain non-carbohydrate carbon substrates provides a balanced glucose level. Breaking down hepatic glycogen describes the second mechanism to maintain glucose, namely glycogenolysis. The utilization of lipids is part of the lipolysis pathway and the reverse of lipogenesis. Molecules of lipids are hydrolyzed to glycerol and FFA.

For a realistic depiction of the liver functionalities, we take the above described main metabolic pathways into account. We use a reduced metabolic model, which has been derived from a detailed kinetic model of hepatic glucose metabolism, see König et al. [10]. It fully represents the metabolic behavior of depletion and utilization of glycogen. For further information see Ricken et al. [12, 13].

FFA play an important role in essential functions for the organism. They deliver cells energy and are important constituents for esterifying lipids. For a homeostatic circulation the organism can store, produce and consume FFA. This process is mainly regulated in the liver by fat metabolism. Stored triglyceride in adipocytes and dietary fat are sources, which ensure the availability of FFA in the liver. Beside the external concentration we need to take important enzymes and insulin into account. Insulin is a hormone which is distributed depending on the glucose concentration level in blood. The task of insulin is to regulate glucose and fat metabolism, so the pathways are coupled. Enzymes are responsible for hydrolysis of proteins, which bind FFA for circulation in the blood plasma.

The effects of fatty acid metabolism are not part of the kinetic model. In the following we present the assumptions concerning the FFA pathway. Equally to the glucose metabolism we calculate the rates of changing concentrations for the metabolites $\hat{\rho}^{\alpha\beta}$ contributing in the FFA pathway. We apply the influencing factors

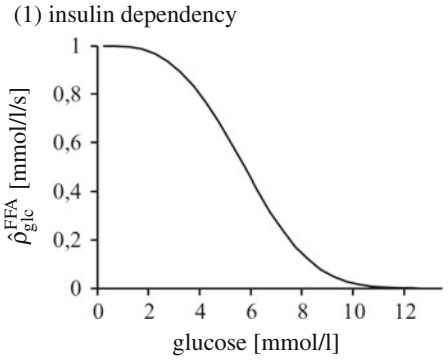

Fig. 3 Insulin dependency $\hat{\rho}^{FFA}_{glc}$: uptake rate of FFA depending on the concentration of glucose

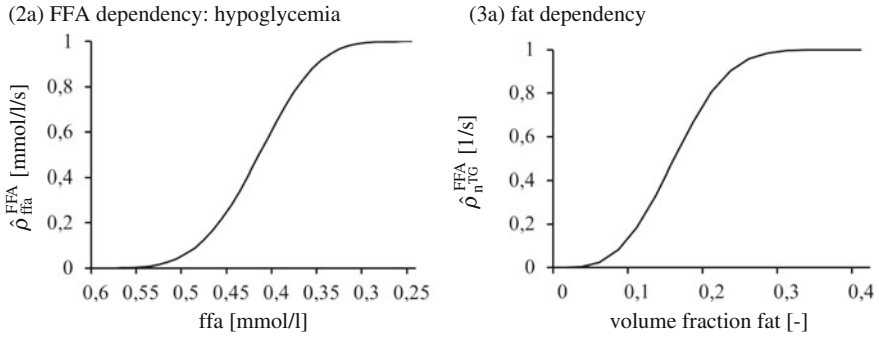

Fig. 4 Threshold of external FFA concentration 0, 6 mmol/l which leads to **a** hypoglycemic condition; **2a** FFA dependency $\hat{\rho}^{FFA}_{ffa}$: uptake rate of FFA depending on the external FFA concentration. **3a** fat dependency $\hat{\rho}^{FFA}_{nTG}$: uptake rate of FFA depending on the volume fraction of fat for a stable computation

$\left\{\hat{\rho}^{FFA}_{glc}; \hat{\rho}^{FFA}_{ffa}; \hat{\rho}^{FFA}_{nL}; \hat{\rho}^{FFA}_{nTG}\right\}$. The terms are postulated via the differential equation of growth function with

$$\begin{aligned}
\hat{\rho}^{FFA}_{glc} &= \exp^{-\log(2)\frac{glc^3}{glc_{TP}{}^3}} \\
\hat{\rho}^{FFA}_{ffa} &= +/-1 + \exp^{-40*((ffa-0{,}6)*2)^4} \\
\hat{\rho}^{FFA}_{nL} &= -1 * \exp^{-\log(2)\frac{(n^L)^3}{0{,}15^3}} + 1 \\
\hat{\rho}^{FFA}_{nTG} &= -1 * \exp^{-\log(2)\frac{(n^{TG})^3}{0{,}2^3}} + 1
\end{aligned} \tag{1}$$

We calculate the maximum uptake rate of FFA considering insulin influence ($\hat{\rho}^{FFA}_{glc}$) which couples the glucose metabolism to the fat metabolism, see Fig. 3. Figure 4 summarizes the effects of hypoglycemic conditions which lead to

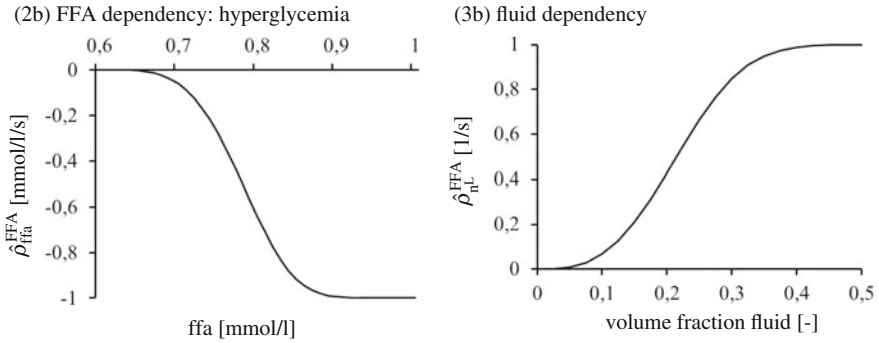

Fig. 5 Threshold of external FFA concentration 0, 6 mmol/l which leads to **b** hyperglycemic condition; **2b** FFA dependency $\hat{\rho}^{FFA}_{ffa}$: uptake rate of FFA depending on the external FFA concentration. **3b** fluid dependency $\hat{\rho}^{FFA}_{n^L}$: uptake rate of FFA depending on the volume fraction of fluid for a stable computation

production of FFA. The uptake rate ($\hat{\rho}^{FFA}_{ffa}$) is positive as the organism needs more FFA for energy supply. The hypoglycemic condition results in phase transition from the fat phase to the fluid phase. To get a stable computation considering the saturation condition we take the influencing factor ($\hat{\rho}^{FFA}_{n^{TG}}$) into account which steers an excessive increase of fluid. However, Fig. 5 shows the impact during hyperglycemic conditions. The uptake rate ($\hat{\rho}^{FFA}_{ffa}$) is negative as the liver stores redundant FFA and synthesizes lipids. In this case the fat phase gets additional mass and we steer an excessive increase of fat with ($\hat{\rho}^{FFA}_{n^L}$).

The mass exchange must fulfill the restrictions of the entropy inequality (24); the exchange can be summarized with

$$\bar{\psi}^{TG\beta} = \bar{\psi}^{TG} := \left[\hat{\rho}^{FFA}_{glc}; \hat{\rho}^{FFA}_{ffa}; \hat{\rho}^{FFA}_{n^L}; \hat{\rho}^{FFA}_{n^{TG}}\right]. \tag{2}$$

3 Numerical Example: Comparison of Different Assumptions for the Perfusion Coupled to the Metabolism

Many aspects of the liver are still subject of discussion. One example is the blood supplying system of the hepatic microcirculation. In this case it is still uncertain how the blood is emanating from the blood vessels into the liver lobule. One assumption, defined by Rappaport in 1954 [11], assumes an idealized hexagonal lobule which regards the portal triad as the 'terminal portal venule'. This case regards the blood supplying system of the microcirculation initiated at the corners of the liver lobule, emanating from the portal triads. In a realistic framework, this point of view is not rational and a different assumption has to be applied. For this case

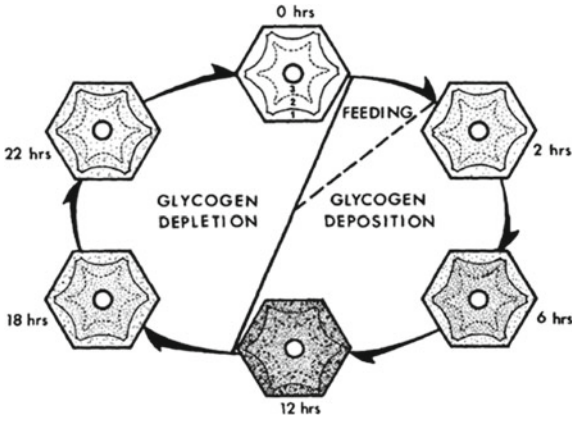

Fig. 6 Schematic sketch of the *feeding cycle* showing duration and typical patterns of glycogen in a single lobule during deposition and depletion. Figure reproduced from Babcock and Cardell [1]

Rappaport described additional portal venules which are derived from the portal vein and deliver the base of the liver lobule with inflowing blood. So the blood supplying system of the microcirculation is located at the surface of the liver lobule.

To get a better understanding of the different approaches and the influence on the metabolism, we simulate both hypotheses for the initial point of the microcirculation:

- Boundary-Model A: Idealized Case—Blood is emanating from the portal triad
- Boundary-Model B: Realistic Case—Blood is emanating from derived portal venules

In the numerical example we compute the microperfusion in one liver lobule coupled to the metabolism similar to Ricken et al. [13]. We evaluate the storage of internal glycogen deposition resulting from glucose metabolism analog to the experiments performed by Babcock and Cardell. In [1], Babcock and Cardell evaluated the glycogen storage during 24 h in one liver lobule after a feeding period (see Fig. 6). Furthermore we analyze the results of the fat metabolism which accrues in the hepatocytes (see Figs. 11–13).

We apply external boundary conditions for the glucose and FFA concentration which are applied in the feeding artery after one meal in 24 h (see Fig. 7). Furthermore we add external conditions for FFA. (cf. Stanhope et al. and Yuen et al. [14, 16])

The boundary conditions focus on the two different assumptions (see Fig. 8) for the initial point of the microcirculation (see Fig. 9). Additionally to the time depending DIRICHLET boundary conditions for the external concentration glucose and FFA, which depend on the food intake (see Fig. 7), we apply constant DIRICHLET boundary conditions for lactate at the inflow. As the blood flow is orientated in the direction of the pressure gradient (transverse isotropic permeability relation, Ricken et al. [13]) we apply a pressure difference between the inflow and the outflow with constant values (see Fig. 10).

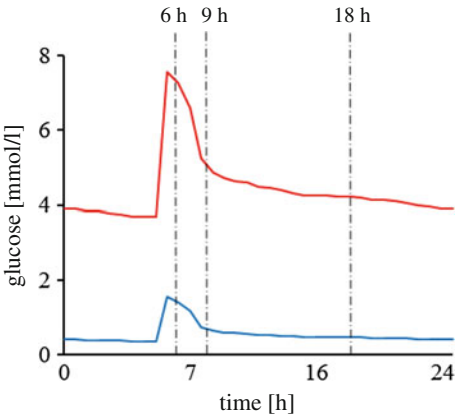

Fig. 7 External boundary conditions: glucose profile corresponding to 2 h food intake and 22 h fasting based on 24 h profiles of plasma glucose (*red*). Analog profile for plasma FFA (*blue*). Experimental data from Stanhope et al. [14] and Yuen et al. [16]. Evaluation for numerical example after 6, 9 and 18 h

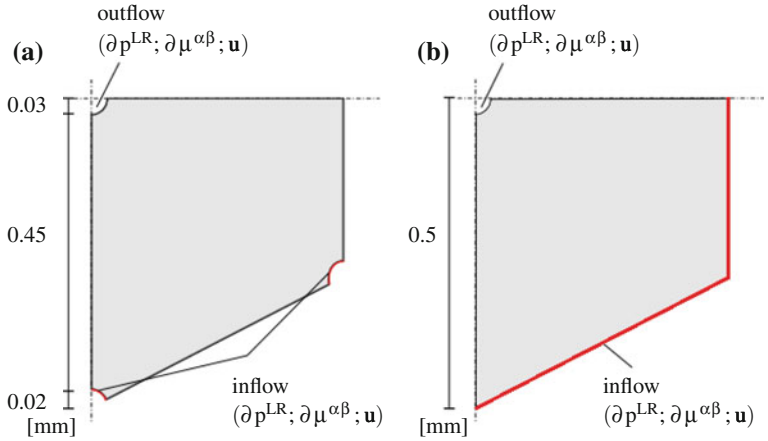

Fig. 8 Depiction of the applied geometry and boundary conditions. **a** Boundary-Model A **b** Boundary-Model B

3.1 Discussion

The simulation provides the evaluation of metabolites (see Figs. 11, 12, 13) resulting from glucose and fat metabolism. On the one hand we focused on the glucose pathway which depends on the external condition of blood glucose concentration. During hyperglycemic conditions the external concentration is high resulting in storage of glycogen. Whereas, a low glucose concentration encourages glycogen depletion. On the other hand we evaluated the phenomenological approach of the fat metabolism which leads to accumulation of fat depending on external blood FFA concentration. Based on the assumption that fat metabolism is inhibited by the presence of insulin we can observe the coupling between glucose and fat metabolism.

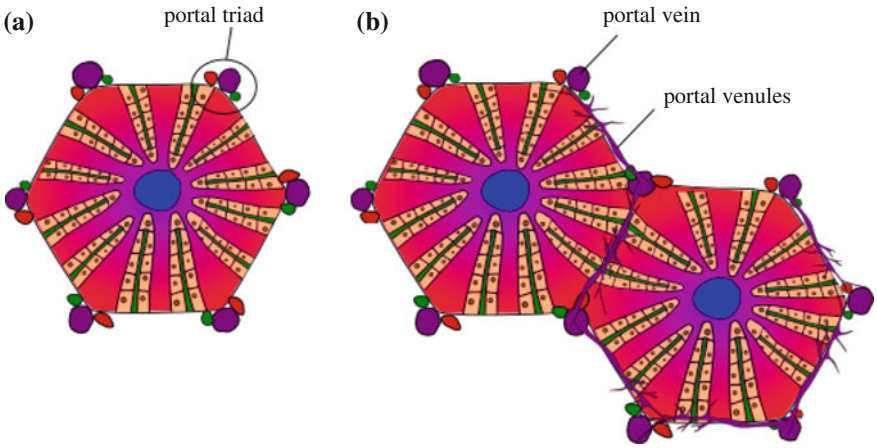

Fig. 9 Different assumptions for the blood supplying system of the microscopic circulation. **a** Boundary-Model A **b** Boundary-Model B

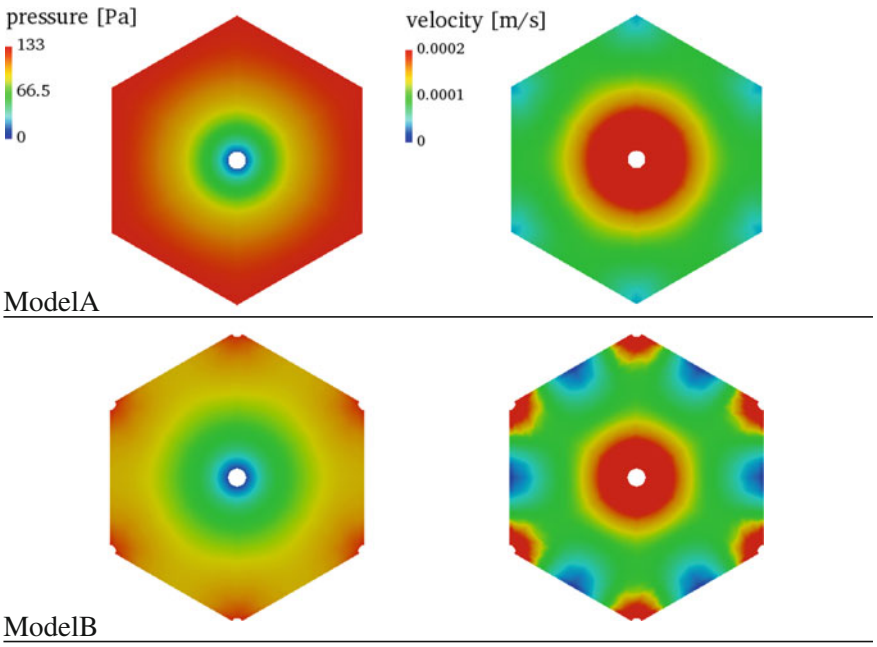

Fig. 10 Contour plot for the pressure distribution on the *left hand side* and velocity distribution on the *right hand side*. Comparison of the two assumptions for the boundaries; Boundary-Model A at top and Boundary-Model B beneath

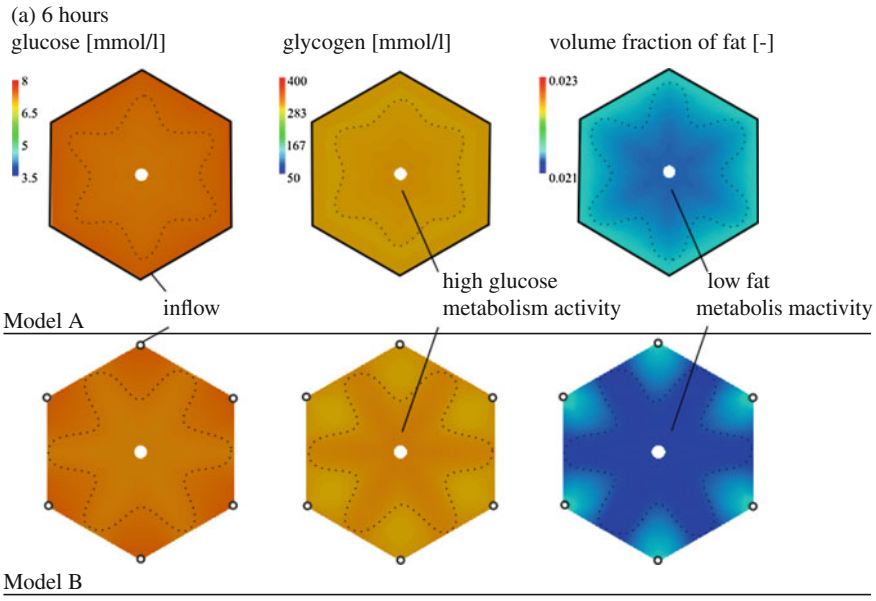

Fig. 11 Contour plot for the partial distribution after 6 h. Comparison of the two assumptions for the boundaries; Boundary-Model A at top and Boundary-Model B beneath

The main objective of this example is the comparison of the different boundary conditions as shown in Fig. 9. Figure 10 shows the influence on the microcirculation which results in a different velocity and pressure distribution. In the first case we assume idealized boundary conditions with an inflow emanating from the portal triad leading to a high pressure at the corners of the lobule. Based on the local pressure-modulated remodeling approach we get a directed blood flow depending on the gradient from the portal triad to the central vein. The velocity in between the portal triads is almost zero. The second assumption results in a high pressure on the lobule surface. The blood flow is directed from the surface to the center of the lobule with continuous values on the surrounding. The superposition at the portal triad leads to increased velocity. In conclusion the patterns of velocity are slightly twisted (see Fig. 10).

The Figs. 11, 12 and 13 evaluate the distribution of external concentration glucose, the deposition of glycogen and volume fraction of fat after 6, 9 and 18 h. The metabolism depends on the availability of metabolites in the lobule. As the motion of the external concentration is controlled by the blood flow, we can observe a higher activity of the glucose metabolism in areas with reduced velocity (more availability of metabolites). Hence, the different boundary conditions lead to slightly reversed depositions of glycogen in the lobule analogue to the microcirculation. The results of the experimental evaluation of the glycogen patterns in Fig. 6 are similar to the

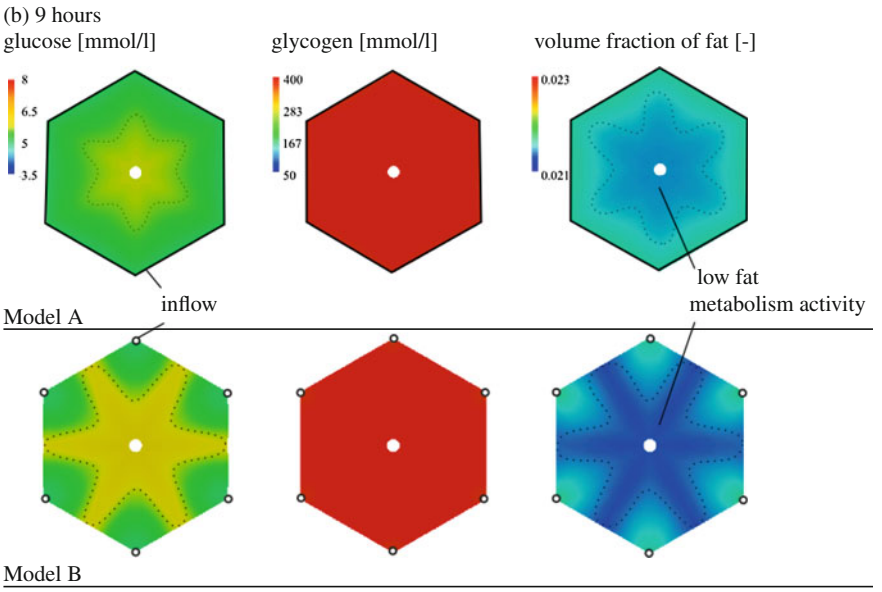

Fig. 12 Contour plot for the partial distribution after 9 h. Comparison of the two assumptions for the boundaries; Boundary-Model A at top and Boundary-Model B beneath

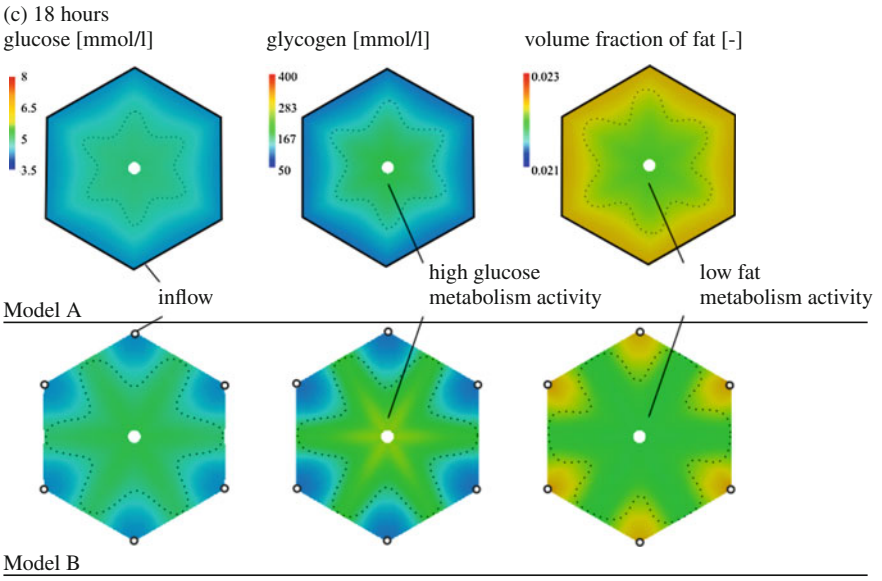

Fig. 13 Contour plot for the partial distribution after 18 h. Comparison of the two assumptions for the boundaries; Boundary-Model A at top and Boundary-Model B beneath

simulation with the boundary-model B and correlate to the hypothesis that additional venules support the microcirculation.

The development of the volume fraction of fat depends on the one hand on the availability of FFA and on the other hand it is controlled by insulin. In conclusion, a high activity of glucose metabolism leads to the release of insulin and the decrease of fat synthesis. Both models result in a higher concentration of lipids at the inflow area, the so called periportal zone of the liver lobule. This outcome is reasonable following the statement of Hubscher et al. who say that the "hepatocytes in the periportal zone have a higher capacity for [...] fatty acid metabolism" (Chap. 1, page 12 [8]).

Although the simulation focuses only on the quantitative evaluation, it approximates the patterns of metabolites in good accordance. Furthermore we could demonstrate that the metabolism including the phenomenological fat metabolism can be modeled via a bi-scale, tri-phasic approach. In this extended example (cf. Ricken et al. [13]) we show the influence of different boundary conditions and the importance of the biological background. But further investigations are needed to validate the fat metabolism and enlarge the applicability of the model to liver disease with growing fat influencing the metabolism.

Appendix

Perfusion-Model with a Multi-phasic Approach

The perfusion of the blood through the liver lobules is an important part to depict realistic descriptions for the viability of the organ. For that we use a homogenized approach on the mesoscopic scale, see Fig. 14. We consider three phases: the liver tissue $\varphi^{\mathbf{S}}$, fat tissue $\varphi^{\mathbf{TG}}$ and fluid phase $\varphi^{\mathbf{L}}$.

The phases are assumed as mutually immiscible materials $\varphi^{\boldsymbol{\alpha}}$ with a heterogeneous arrangement in the overall volume. Each phase consists of a carrier phase φ^{α}, namely a solvent, and small miscible microscopic components $\varphi^{\alpha\beta}$, called solutes in the solvent. The TPM is an approach, which is composed of the mixture theory (Greve [7] and Hutter et al. [9]) and the concept of volume fractions (de Boer [2, 3] and Ehlers [5]). The saturation condition completes the approach.

The overall structure is a mixture of all included components, so the whole body φ can be decomposed by

$$\varphi = \sum_{\boldsymbol{\alpha}=1}^{\kappa} \varphi^{\boldsymbol{\alpha}} := \sum_{\alpha=1}^{\kappa} [\sum_{\beta=1}^{\nu-1} (\varphi^{\alpha\beta}) + \varphi^{\alpha}]. \tag{3}$$

To account the contribution of different phases we use the volume fraction $\mathrm{n}^{\boldsymbol{\alpha}}$ expressed by the ratio of partial volume $\mathrm{dv}^{\boldsymbol{\alpha}}$ to the overall mixture volume dv

$$\mathrm{n}^{\alpha} = \frac{\mathrm{dv}^{\alpha}}{\mathrm{dv}}. \tag{4}$$

In view of the volume fractions, the saturations condition has to be fulfilled with

$$\sum_{\alpha=1}^{\kappa} \mathrm{n}^{\alpha} \text{ mit } \quad \kappa \in \{\mathbf{S}, \mathbf{TG}, \mathbf{L}\}. \tag{5}$$

For an effective connection between the mixture theory and the concept of volume fractions we consider the density ρ^{α} with

$$\mathrm{m} = \sum_{\alpha=1}^{\kappa} \mathrm{m}^{\alpha} = \int_{\mathrm{Bs}} \sum_{\alpha=1}^{\kappa} \rho^{\alpha} \mathrm{dv}. \tag{6}$$

where m is the mass of the mixture and m^{α} is the partial mass. Thereby ρ^{α} describes the partial density, which is derived by the ratio of mass dm^{α} to the volume dv of the structure

$$\rho^{\alpha} = \frac{\mathrm{dm}^{\alpha}}{\mathrm{dv}}. \tag{7}$$

The true density $\rho^{\alpha \mathrm{R}}$ of the phases follows with

$$\rho^{\alpha \mathrm{R}} = \frac{\mathrm{dm}^{\alpha}}{\mathrm{dv}^{\alpha}}. \tag{8}$$

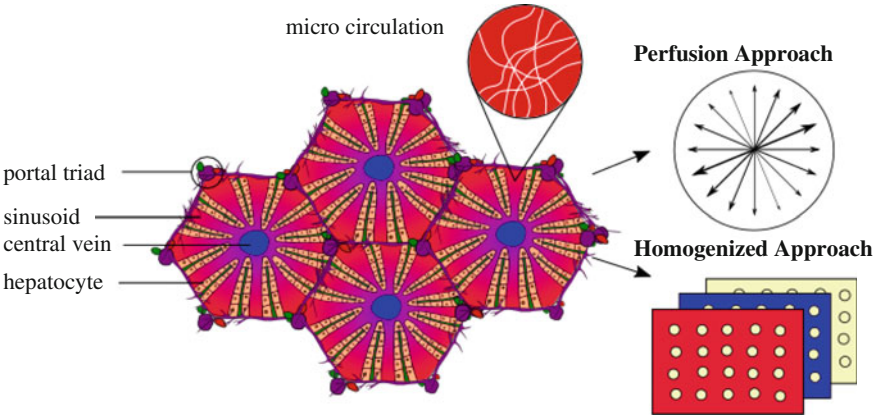

Fig. 14 Numerical implementation: perfusion approach with permeability in dependence of vessel distribution and preferred flow direction. Homogenization of the real structure into a smeared model (TPM)

Including the given Eqs. (3) and (8) we get a connection between the density and the volume fractions with

$$\rho^{\alpha} = \frac{\mathrm{dm}^{\alpha}}{\mathrm{dv}} = \frac{\mathrm{dm}^{\alpha}}{\mathrm{dv}^{\alpha}/\mathrm{n}^{\alpha}} = \mathrm{n}^{\alpha}\,\rho^{\alpha\mathrm{R}}\,. \tag{9}$$

The concentration $\mathrm{c}^{\alpha\beta}$ of the microscopic components which are included in the phases are described by the ratio of the number of moles $\mathrm{dn}^{\beta}_{\mathrm{mol}}$ and the partial volume $\mathrm{dv}^{\boldsymbol{\alpha}}$ with

$$\mathrm{c}^{\alpha\beta} = \frac{\mathrm{dn}^{\beta}_{\mathrm{mol}}}{\mathrm{dv}^{\boldsymbol{\alpha}}}\,. \tag{10}$$

The partial molar density of the microscopic components $\rho^{\alpha\beta}$ is decomposed by the volume fraction $\mathrm{n}^{\boldsymbol{\alpha}}$, the concentration $\mathrm{c}^{\alpha\beta}$ and the molecular weight $\mathrm{M}^{\beta}_{\mathrm{mol}}$ of the constituent

$$\rho^{\alpha\beta} = \mathrm{n}^{\boldsymbol{\alpha}}\mathrm{c}^{\alpha\beta}\mathrm{M}^{\beta}_{\mathrm{mol}}\,. \tag{11}$$

Whereas, the molecular weight of the constituent is calculated by the fraction of the mass dm^{β} of the component and the number of moles $\mathrm{dn}^{\beta}_{\mathrm{mol}}$

$$\mathrm{M}^{\beta}_{\mathrm{mol}} = \frac{\mathrm{dm}^{\beta}}{\mathrm{dn}^{\beta}_{\mathrm{mol}}}\,. \tag{12}$$

Balance Equations in the Framework of TPM

The balance equations for the porous media contain the description for each phase $\varphi^{\boldsymbol{\alpha}}$ analogous to a one phase continuum. The multiphase approach incorporates the chemical and physical interactions of the phases $\varphi^{\boldsymbol{\alpha}}$ with the interaction forces $\hat{\mathbf{p}}^{\boldsymbol{\alpha}}$ and the mass exchange $\hat{\rho}^{\boldsymbol{\alpha}}$ following the metaphysical principles of Truesdell [15]. The local statements of the balance equation of mass, momentum and moment of momentum follow with

$$\begin{aligned}
\sum_{\alpha=1}^{\kappa} \left[\frac{\partial \mathrm{n}^{\boldsymbol{\alpha}}}{\partial \mathrm{t}} + \mathrm{div}(\mathrm{n}^{\boldsymbol{\alpha}}\,\mathbf{x}'_{\boldsymbol{\alpha}}) - \frac{1}{\rho^{\alpha\mathrm{R}}}\,\hat{\rho}^{\alpha}\right] &= 0 \\
\sum_{\alpha=1}^{\kappa} \left[\mathrm{div}\,\mathbf{T}^{\alpha} + \rho^{\boldsymbol{\alpha}}\,(\mathbf{b}^{\alpha} - \mathbf{x}''_{\boldsymbol{\alpha}}) + \hat{\mathbf{p}}^{\alpha} - \hat{\rho}^{\alpha}\,\mathbf{x}'_{\alpha}\right] &= \mathbf{0} \\
\sum_{\alpha=1}^{\kappa} \left[\mathbf{T}^{\alpha} - (\mathbf{T}^{\alpha})^{\mathrm{T}}\right] &= \mathbf{0}
\end{aligned} \tag{13}$$

The balance equation of mass applies the time derivative ∂t of the volume fraction $\mathrm{n}^{\boldsymbol{\alpha}}$. Furthermore, "div" describes the spatial divergence operator, $\mathbf{x}'_{\boldsymbol{\alpha}}$ the velocity of the phases and $\rho^{\alpha\mathrm{R}}$ the true density. $\mathbf{T}^{\boldsymbol{\alpha}}$ is the Cauchy stress tensor, $\mathbf{b}^{\boldsymbol{\alpha}}$ is the specific volume force and $\mathbf{x}''_{\boldsymbol{\alpha}}$ describes acceleration. Truesdell introduced the metaphysical principles in [15] with fundamental formulations for the mixture bodies which lead to the restrictions

$$\begin{aligned} \sum_{\alpha=1}^{\kappa} \hat{\rho}^{\alpha} &= 0 \\ \sum_{\alpha=1}^{\kappa} \hat{\mathbf{p}}^{\alpha} &= \mathbf{0}\,. \end{aligned} \tag{14}$$

Assumptions for the Perfusion Model

In this approach we apply three main phases for the mixture body. Thus, the volume counts the main phases $\varphi^{\boldsymbol{\alpha}}$ with $\boldsymbol{\alpha} \in \mathbf{S}$ (liver tissue), **TG** (fat tissue), **L** (blood). We assume miscible concentrations included in the main phases which are important for the metabolism processes. The liver tissue is described by two components, the hepatocytes which include glycogen $\varphi^{\mathbf{S}\beta} \in \{\mathrm{Gy}\}$ as an internal concentration and fat as the second component which includes triglyceride $\varphi^{\mathbf{TG}\beta} \in \{\mathrm{TG}\}$. Both internal miscible components are results of the metabolism. Furthermore, the blood phase includes external solutes which are important metabolites coming from the intestines. Focusing on the glucose and fat metabolism we apply external concentrations for glucose, FFA and lactate $\varphi^{\mathbf{L}\beta} \in \{\mathrm{Gu}, \mathrm{Lc}, \mathrm{FFA}\}$. Since the overall solutes $\varphi^{\alpha\beta}$ are negligibly small in contrast to the phases $\varphi^{\boldsymbol{\alpha}}$ we do not take the volume fraction of the concentrations into account. So, the volume of the main phases is nearly the same as the volume of the carrier phases and we can simplify $\varphi^{\boldsymbol{\alpha}} \cong \varphi^{\alpha}$. Thus, we summarize the description for the mixture body with $\kappa = 3$

$$\varphi^{\alpha} = \{\mathrm{S}, \mathrm{TG}, \mathrm{L}\} = \alpha_{\mathrm{i}} \,|\mathrm{i} = 1 \ldots 3 \tag{15}$$

and $(\nu - 1)$ the microscopic components

$$\begin{aligned} \varphi^{\mathrm{S}\beta} &= \{\mathrm{Gy}\} &&= \beta_{\mathrm{i}} \,|\mathrm{i} = 1 \\ \varphi^{\mathrm{TG}\beta} &= \{\mathrm{TG}\} &&= \beta_{\mathrm{i}} \,|\mathrm{i} = 1 \\ \varphi^{\mathrm{L}\beta} &= \{\mathrm{Gu}, \mathrm{Lc}, \mathrm{FFA}\} &&= \beta_{\mathrm{i}} \,|\mathrm{i} = 1 \ldots 3 \end{aligned} \tag{16}$$

The overall volume v can be calculated by the volume fractions n^{α} of the phases

$$\mathrm{v} = \sum_{\alpha=1}^{\kappa} \mathrm{dv}^{\alpha} = \int_{\mathrm{Bs}} \sum_{\alpha=1}^{\kappa} \mathrm{dv}^{\alpha} = \int_{\mathrm{Bs}} \sum_{\alpha=1}^{\kappa} \mathrm{n}^{\alpha}\, \mathrm{dv} \text{ mit } \quad \kappa \in \{\mathrm{S}, \mathrm{TG}, \mathrm{L}\} \tag{17}$$

The basis of the TPM applies superimposed continua with interactions and independent motion functions for the included phases. De Boer [4] and Ehlers [5] give

an explanation of the kinematics of TPM. We assume a Lagrange description of the motion for the liver tissue $\chi_S(\boldsymbol{X}_S, t)$ with $\boldsymbol{X}_S$ describing the reference configuration of the liver cells and t describing the time. As the fat tissue is connected to the liver cells we use the same motion function with $\chi_S = \chi_{TG}$. Additionally, the internal concentrations which are exclusively present in the cells of the liver have the same motion function as the liver and fat tissue. So we extend $\chi_S = \chi_{TG} = \chi_{S\beta} = \chi_{TG\beta}$. As a consequence of the identical motion function one velocity follows for the liver tissue, fat tissue and the internal concentration (glycogen, triglyceride) with $\mathbf{x}'_S = \mathbf{x}'_{TG} = \mathbf{x}'_{S\beta} = \mathbf{x}'_{TG\beta}$. Beside the fixed solid fraction the porous body contains the fluid phase which represents the blood flow. For the kinematics of the blood flow we use a modified Eulerian description with respect to the solid phase. We apply independent motion functions for the blood phase $\chi_L(\boldsymbol{X}_L, t)$ and the external concentration: glucose $\chi_{L,Gu}(\boldsymbol{X}_{LGu}, t)$, lactate $\chi_{L,Lc}(\boldsymbol{X}_{LLc}, t)$ and FFA $\chi_{L,FFA}(\boldsymbol{X}_{LFFA}, t)$, which are included in the blood phase. The velocities follow with $\mathbf{x}'_L = \mathbf{x}'_L(\boldsymbol{X}_L, t)$ for the main phase of the fluid and $\mathbf{x}'_{L,Gu} = \mathbf{x}'_{L,Gu}(\boldsymbol{X}_{LGu}, t)$ for glucose, $\mathbf{x}'_{L,Lc} = \mathbf{x}'_{L,Lc}(\boldsymbol{X}_{LLc}, t)$ for lactate and $\mathbf{x}'_{L,FFA} = \mathbf{x}'_{L,FFA}(\boldsymbol{X}_{LFFA}, t)$ for FFA.

The blood flow in the liver lobules mainly depends on the vascular system, which is designed by the sinusoidal arrangement. The sinusoids guide the blood from the portal triads to the central vein and lead to an anisotropic diffusivity. We introduced an approach for the anisotropic perfusion in Ricken et al. [13]. This includes an ansatz for the filter velocity $n^L \mathbf{w}_{LS}$ with the volume fraction of the fluid n^L and the seepage velocity $\mathbf{w}_{LS}$. The seepage velocity defines the difference in velocity of the fluid and solid phase $\mathbf{w}_{LS} = \mathbf{x}'_L - \mathbf{x}'_S$.

$$n^L \mathbf{w}_{LS} = k^S_{0S} \left(\frac{n^L}{1 - n^S_{0S}}\right)^m \mathbf{M}^* \left[-\mathrm{grad}\lambda + \rho^{LR} \mathbf{b}\right] \tag{18}$$

It depends on the deformation $\left(\frac{n^L}{1 - n^S_{0S}}\right)^m$ (see Eipper [6]) which includes a dimensionless material parameter m, controlling the isotropic dependency of the permeability. Furthermore, it depends on the Darcy permeability with $k^S_{0S}\,[\frac{m^4}{Ns}]$ and on the transverse isotropic permeability relation $\mathbf{M}^*$ which includes the alignment of the sinusoids (for further information see Ricken et al. [12, 13]).

Field Equations and Constitutive Modeling

Summarizing, we consider a quasi-static, isothermal, tri-phasic porous model with microscopic substances. The model takes into account an incompressible solid phase φ^S and fat phase φ^{TG} which are derived by the same motion function and an incompressible fluid phase φ^L. We assume mass exchange between the fat and fluid phase. All phases include substances $\varphi^{\alpha\beta}$ which are calculated by the microscopic model and allow phase transition to build up the metabolism. The solid phases φ^S and

fat phase φ^{TG} include the internal concentrations $\varphi^{\mathrm{S}\beta}$ with $\varphi^{\mathrm{S}\beta} \in \{\mathrm{Gy}\}$ and $\varphi^{\mathrm{TG}\beta}$ with $\varphi^{\mathrm{TG}\beta} \in \{\mathrm{TG}\}$. The external concentrations $\varphi^{\mathrm{L}\beta}$ with $\varphi^{\mathrm{L}\beta} \in \{\mathrm{Gu}, \mathrm{Lc}, \mathrm{FFA}\}$ are included in the fluid phase. For the calculation of the presented model we use the following independent relations. On the one hand we use the local form of the balance equation of mass and momentum for each component with

$$\begin{aligned} (\mathrm{n}^{\alpha})'_{\alpha} + \mathrm{n}^{\alpha} \operatorname{div} \mathbf{x}'_{\alpha} &= \frac{1}{\rho^{\alpha \mathrm{R}}} \hat{\rho}^{\alpha} \\ \operatorname{div} \mathbf{T}^{\alpha} + \rho^{\alpha} \mathbf{b}^{\alpha} + \hat{\mathbf{p}}^{\alpha} &= \hat{\rho}^{\alpha} \mathbf{x}'_{\alpha} \end{aligned} \tag{19}$$

for the main phases and

$$\begin{aligned} (\mathrm{n}^{\alpha})'_{\alpha\beta} \mathrm{c}^{\alpha\beta} \mathrm{M}^{\beta}_{\mathrm{mol}} + \mathrm{n}^{\alpha} (\mathrm{c}^{\alpha\beta})'_{\alpha\beta} \mathrm{M}^{\beta}_{\mathrm{mol}} + \mathrm{n}^{\alpha} \mathrm{c}^{\alpha\beta} \mathrm{M}^{\beta}_{\mathrm{mol}} \operatorname{div} \mathbf{x}'_{\alpha\beta} &= \hat{\rho}^{\alpha\beta} \\ \operatorname{div} \mathbf{T}^{\alpha\beta} + \rho^{\alpha\beta} \mathbf{b}^{\alpha} + \hat{\mathbf{p}}^{\alpha\beta} &= \hat{\rho}^{\alpha\beta} \mathbf{x}'_{\alpha} \end{aligned} \tag{20}$$

for the included concentrations. The field equations include the interaction terms between the main phases $\hat{\rho}^{\alpha}$ and the miscible substances $\hat{\rho}^{\alpha\beta}$. On the other hand we consider the physical constraint condition derived by the assumptions of the porous medium with the saturation condition

$$\mathrm{n}^{\mathrm{S}} + \mathrm{n}^{\mathrm{TG}} + \mathrm{n}^{\mathrm{L}} = 1, \tag{21}$$

the conditions for the mass exchange between the components with

$$\hat{\rho}^{\mathrm{S}} + \hat{\rho}^{\mathrm{TG}}, + \hat{\rho}^{\mathrm{L}} + \hat{\rho}^{\alpha\beta} = 0\,, \tag{22}$$

and the interaction forces

$$\hat{\mathbf{p}}^{\mathrm{S}} + \hat{\mathbf{p}}^{\mathrm{TG}} + \hat{\mathbf{p}}^{\mathrm{L}} + \hat{\mathbf{p}}^{\alpha\beta} = \mathbf{0}\,. \tag{23}$$

Beside the field equations we need constitutive relations to complete the calculation concept of the saturated porous body. The constitutive equations are derived by the evaluation of the entropy inequality

$$\sum_{\alpha=1}^{\kappa} [-\rho^{\alpha} (\psi^{\alpha})'_{\alpha} - \hat{\rho}^{\alpha} (\psi^{\alpha} - \frac{1}{2} \mathbf{x}'_{\alpha} \cdot \mathbf{x}'_{\alpha}) + \mathbf{T}^{\alpha} \cdot \mathbf{D}_{\alpha} - \hat{\mathbf{p}}^{\alpha} \cdot \mathbf{x}'_{\alpha}] \geq 0, \tag{24}$$

The constitutive equations follow with

Table 1 Material parameters of liver lobule

Parameter	Value	Unit	Remark
n^{S}_{0S}	0.8	–	Volume fraction solid
n^{TG}_{0S}	0.02	–	Volume fraction fat
n^{L}_{0S}	0.18	–	Volume fraction fluid
μ^{S}, μ^{TG}	4×10^{4}	Pa	Lam constant
λ^{S}, λ^{TG}	3×10^{4}	Pa	Lam constant
θ	280	K	Temperature
R	8.3144	J/molK	Gas constant
k^{L}_{D}	4.5×10^{-10}	m/s	Darcy permeability

$$\begin{aligned} \mathbf{T}^{S} + \mathbf{T}^{S\beta} + \mathbf{T}^{TG} + \mathbf{T}^{TG\beta} &= 2\,\rho^{S}\,\mathbf{F}_{S}\,\frac{\partial \psi^{S}}{\partial \mathbf{C}_{S}}\,\mathbf{F}_{S}^{T} + 2\,\rho^{TG}\,\mathbf{F}_{S}\,\frac{\partial \psi^{TG}}{\partial \mathbf{C}_{S}}\,\mathbf{F}_{S}^{T} \\ &\quad - (n^{S} + n^{TG})\,\lambda\,\mathbf{I} \\ \mathbf{T}^{L} &= -\lambda\, n^{L}\,\mathbf{I} + \rho^{\alpha\beta}\, c^{\alpha\beta}\,\frac{\partial \psi^{\alpha\beta}}{\partial c^{\alpha\beta}}\,\mathbf{I} \\ \mathbf{T}^{L\beta} &= -\rho^{\alpha\beta}\, c^{L\beta}\,\frac{\partial \psi^{\alpha\beta}}{\partial c^{\alpha\beta}}\,\mathbf{I}. \end{aligned} \tag{25}$$

for the description of the stresses.

We postulate a hyperelastic material description of the solid following the Hooke's law with the Neo-Hookean Helmholtz free energy function

$$\begin{aligned} \psi^{S} &= \frac{1}{\rho^{S}_{0S}}\left[\lambda^{S}\,\frac{1}{2}\,(\ln J_{S}) - \mu^{S}\ln J_{S} + \frac{1}{2}\,\mu^{S}\,(\mathrm{tr}\,\mathbf{C}_{S} - 3)\right] \\ \psi^{TG} &= \frac{1}{\rho^{TG}_{0S}}\left[\lambda^{TG}\,\frac{1}{2}\,(\ln J_{S}) - \mu^{TG}\ln J_{S} + \frac{1}{2}\,\mu^{TG}\,(\mathrm{tr}\,\mathbf{C}_{S} - 3)\right] \end{aligned} \tag{26}$$

including the Lamé constants λ^{S} and μ^{S} for the liver solid and λ^{TG} and μ^{TG} for the liver fat (Table 1). Moreover we describe the free energy function for the concentrations $\psi^{\alpha\beta}$ with the general gas constant $R\,[\frac{J}{mol\,K}]$, the temperature of the mixture θ [K], the molecular weight of the constituent $M^{\beta}_{mol}\,[\frac{g}{mol}]$ and the reference chemical potential $\mu_{0}^{\alpha\beta}\,[\frac{J}{mol}]$

$$\psi^{\alpha\beta} = \frac{1}{c^{\alpha\beta}}\left[\frac{R\,\theta}{M^{\beta}_{mol}}\,(\ln(\frac{c^{\alpha\beta}}{c_{0}^{\alpha\beta}}) - 1) + \mu_{0}^{\alpha\beta}\right]. \tag{27}$$

References

1. M.B. Babcock, R.R. Cardell, Hepatic glycogen patterns in fasted and fed rats. Am. J. Anat. **140**(3), 299–337 (1974)

2. R. Boer, *Theory of Porous Media: Highlights in Historical Development and Current State* (Springer, New York, 2000)
3. R. De Boer, Highlights in the historical development of the porous media theory: toward a consistent macroscopic theory. Appl. Mech. Rev. **49**(4), 201–262 (1996)
4. R. De Boer,*Theory of Porous Media: Highlights in Historical Development and Current State*, (Springer Science & Business Media, 2012)
5. W. Ehlers, *Foundations of Multiphasic and Porous Materials*, (Springer, 2002)
6. G. Eipper, *Theorie und Numerik Finiter Elastischer Deformationen in Fluidgesättigten Porösen Festkörpern*. PhD thesis, Inst. für Mechanik, (Bauwesen, 1998)
7. R. Greve, *Kontinuumsmechanik: Ein Grundkurs für Ingenieure und Physiker*, (Springer, 2013)
8. S.G. Hubscher, A.D. Burt, B.C. Portmann, L.D. Ferrell, *MacSween's Pathology of the Liver*, (Elsevier Health Sciences, 2011)
9. K. Hutter, K. Jöhnk, *Continuum Methods of Physical Modeling: Continuum Mechanics, Dimensional Analysis, Turbulence*, (Springer Science & Business Media, 2013)
10. M. König, S. Bulik, H.-G. Holzhütter, Quantifying the contribution of the liver to glucose homeostasis: a detailed kinetic model of human hepatic glucose metabolism. PLoS Comput. Biol. **8**(6), e1002577 (2012)
11. A. Rappaport, Z. Borowy, W. Lougheed, W. Lotto, Subdivision of hexagonal liver lobules into a structural and functional unit. role in hepatic physiology and pathology. Anat. Rec. **119**(1), 11–33 (1954)
12. T. Ricken, U. Dahmen, O. Dirsch, A biphasic model for sinusoidal liver perfusion remodeling after outflow obstruction. Biomech. Model. Mechanobiol. **9**(4), 435–450 (2010)
13. T. Ricken, D. Werner, H. Holzhütter, M. König, U. Dahmen, O. Dirsch, Modeling function-perfusion behavior in liver lobules including tissue, blood, glucose, lactate and glycogen by use of a coupled two-scale pde-ode approach. Biomech. Model. Mechanobiol. **14**(3), 515–536 (2015)
14. K.L. Stanhope, S.C. Griffen, B.R. Bair, M.M. Swarbrick, N.L. Keim, P.J. Havel, Twenty-four-hour endocrine and metabolic profiles following consumption of high-fructose corn syrup-, sucrose-, fructose-, and glucose-sweetened beverages with meals. Am. J. Clin. Nutr. **87**(5), 1194–1203 (2008)
15. C. Truesdell, Thermodynamics of diffusion. In *Rational Thermodynamics*, (Springer, 1984), pp. 219–236
16. K.C. Yuen, P.A. McDaniel, M.C. Riddle, Twenty-four-hour profiles of plasma glucose, insulin, c-peptide and free fatty acid in subjects with varying degrees of glucose tolerance following short-term, medium-dose prednisone (20 mg/day) treatment: evidence for differing effects on insulin secretion and action. Clin. Endocrinol. **77**(2), 224–232 (2012)

Nano-Mechanical Tensile Behavior of the SPTA1 Gene in the Presence of Hereditary Hemolytic Anemia-Related Point Mutations

Melis Hunt

Abstract A skeletal network of spectrin molecules provides shear stiffness to the red blood cell (RBC) membrane maintaining its shape (by providing elasticity) and thus its stability. There are two α and two β subunits of human spectrin; the α1 and β1 spectrin subunits are encoded SPTA1 and SPTB, respectively. Hereditary elliptocytosis (HE), one of the hereditary blood disorders, results in elliptical/oval, elongated RBCs due to the abnormalities that occur mainly at the atomistic level because of the mutations in SPTA1 and SPTB. In HE, the RBC membrane partly loses its elasticity and this results in a reduced overall durability of RBCs. In its severe forms, hereditary blood disorders can lead to hemolytic anemias when the abnormal RBCs start to depreciate. This study aims to observe mechanically how the abnormalities due to the mutations in SPTA1 gene affect single spectrin molecules. The stiffness of the mutated and normal/wild-type molecules are calculated using Steered Molecular Dynamics (SMD) by subjecting the spectrin α chain to displacements up to tens of nanometers and drawing force-extension maps from these computational experiments. The most common HE mutations being SPTA1 gene missense mutations in the dimer-tetramer self-association site makes it interesting to introduce mutations at the binding site and compare the change in the mechanical response of the mutated molecules to that of the wild-type. Overall, the results presented here show that the nano-mechanical tensile behaviour at the chain-level does not change under the presence of the point mutations. This suggests that the local structural disturbances the mutations cause, will affect the spectrin scaffold on the network-level rather than on the on the single chain level implying more complicated molecular interactional disorders. The work presented here is a part of a larger effort to improve understanding the functional implications of the mechanical and structural properties of proteins starting at the atomistic level.

M. Hunt (✉)
Department of Mechanical Engineering, TED University, Ankara, Turkey
e-mail: melis.hunt@tedu.edu.tr

P. Wriggers and T. Lenarz (eds.), *Biomedical Technology*, Lecture Notes in Applied and Computational Mechanics 84, DOI 10.1007/978-3-319-59548-1_3

1 Introduction

Many protein molecules (i.e. spectrin, titin, spider silk…) have multi-domain structures which result in a force-displacement behavior with a characteristic saw-tooth pattern when exposed to mechanical stretching due to the unfolding of their domains along the molecular chains (Fig. 1). Unfolding of molecules provide numerous advantages to proteins. Unfolding of the "hidden length" (when the contour length of a molecule is different than the end-to-end distance of the molecule) along the constituent domains of a molecule, eases the molecule into high levels of strain by keeping low force levels. This enables "softening" of the proteins. "Softening" acts as a manner to first allow for an initially stiff behavior, then to limit the overall force level and to enable large extensions at low forces and low compliance [1–14].

Figure 1 shows schematics for the unfolding of a single molecule with a folded-domain. When a molecule with folded domains is subjected to tensile strain, the force increases until all the domains are aligned with each other, then one of the domains unfolds revealing some hidden length dropping the force. If the tensile strain further increases, force starts increasing but this time with a more resilient response until all the domains are aligned again yet another unfolding event happens dropping the force one more time… This behavior goes on till all the hidden length is revealed as long as the molecule is subjected to higher strain levels. The force-extension map reveals the "saw-tooth" pattern which is bound to have a softer edge/lower plateau force and less peaks as the pulling speed decreases and also as the event numbers increase.

In order to understand the mechanical behaviour of structural proteins, it is useful to study their response to mechanical unfolding. These direct investigations are commonly performed by atomic force microscopy (AFM); the macromolecule is mechanically unfolded by the imposition of elongations at constant strain-rate, and the required force is measured as a function of the elongation. The unfolding patterns and force-extension maps can also be studied using computational

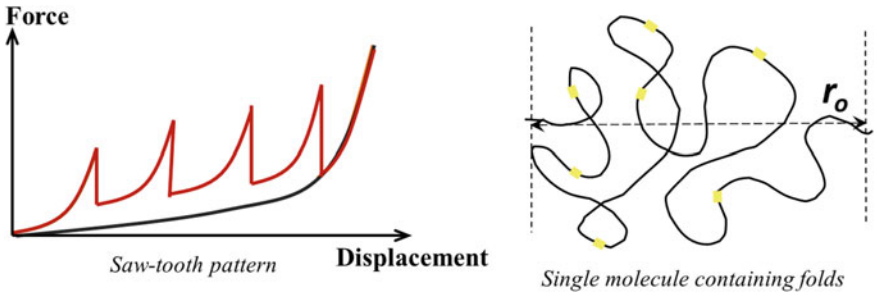

Fig. 1 A schematic of the force-extension behavior yielding a "saw-tooth pattern" eventually resulting in a more compliant behavior for a single molecule containing folded domains along which the end-to-end distance (r_o) is shorter than the contour length of that particular domain

experiments; in particular Steered Molecular Dynamics (SMD); where a harmonic potential (spring) is used to induce motion through constant velocity mimicking the AFM experiments in which a molecule is stretched by a cantilever moving at constant velocity. There are difficulties in directly comparing simulations and AFM experiments as the elongations speeds differ greatly (*i.e.* in the order of 10^{-7} for AFM experiments versus 0.5 m/s for SMD experiments). However the unfolding scenario (*i.e.* position of force peaks) and the order of magnitude in forces enable us to draw consistent conclusions from SMD simulations.

2 Spectrin Structure

A skeletal network of spectrin molecules provides shear stiffness to the red blood cell (RBC) membrane maintaining its shape (by providing elasticity) and thus its stability. The spectrin network is composed of lateral heterodimeric association of α and β subunits which possess 16–20 tandem homologous repeats each. The principal form of the spectrin molecule constitutes of head-to-head interactions between two α/β dimers leading to the formation of a spectrin tetramer; where the tetramerization site is comprised of α-0 and β-17 partial domains (see Fig. 2) [15–17].

Hereditary elliptocytosis (HE) is an inherited RBC membrane disorder associated with defective spectrin due to the mutations in codons 28, 46, 48, and 49 [18]. HE disorders are characterized by visibly elliptical RBCs. HE disorders range from asymptomatic to hemolytic anemia [19]. Although many defects are known to result in HE, cases generally involve disruptions of horizontal cytoskeleton interactions; i.e. mutations in the tetramerization site which influences the function and

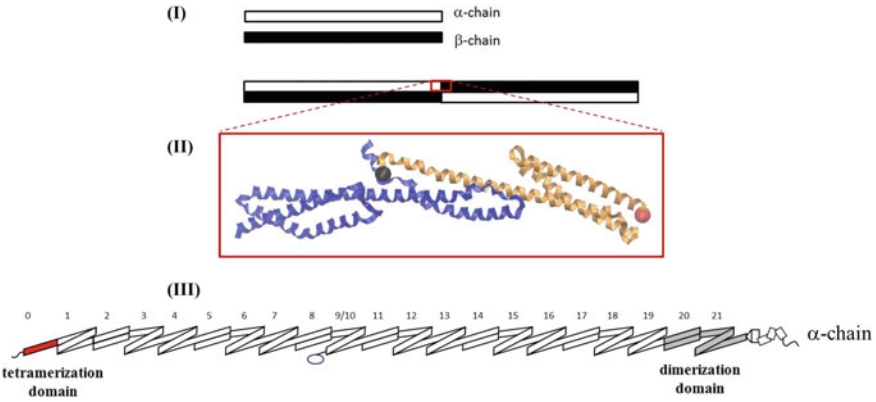

Fig. 2 Spectrin assembly constitutes of a lateral heterodimeric association of α- and β-chains which form the spectrin tetramer by the antiparallel head-to-head interactions between two α/β dimers (**Panel I**). α-chain has 20 full repeats and a partial repeat (**Panel III**). Tetramerization site comprised of α-0 and β-17 partial domains as shown in the ribbon diagram (**Panel II**)

structural integrity of the molecule by reducing the elasticity of the RBCs and thus resulting in mechanical weakness or fragility of the membrane skeleton that leads to a reduced overall durability of RBCs.

Arginine at the 28th residue (ARG28), located in the tetramerization site, is a vital residue for the conformational stability of α-spectrin [20]. There are four major types of replacements at this site: arginine replaced by cysteine, histidine, leucine or serine (ARG28 [CYS/HIS/LEU/SER]) residues [18]. The literature provides excellent structural analyses on the conformations undertaken by the mutated residues of spectrin [21]. However mechanical analysis at the atomistic level is the missing piece in studying the mechanisms that lead to RBC diseases. It has been suggested that the ARG28 mutations lead to abnormality in the folding and the bonding of the tetramerization site; however there is limited knowledge about whether these mutations cause disruptions on the dimer level in the α-chain directly or disrupt the chain-chain inter-bonding in the heterodimer/tetramerization level or even further in the network level. One of the objectives of this work is to elaborate on whether one could observe disturbances due to mutations at the local site when the site is applied external forces. Here, for that reason, the mechanical stiffness of the wild-type (WT)/healthy and the mutated (cysteine (CYS), serine (SER), histidine (HIS) and leucine (LEU) replacements) cases will be calculated using Steered Molecular Dynamics (SMD) by subjecting the spectrin tetramerization complex to displacements up to tens of nanometers drawing force-extension maps from these computational experiments.

The complete tetramer structure illustrating the interactions of the domains (mainly hydrophobic and also electrostatic) was revealed and identified in 2010 [22] providing a guide for designing further computational experiments to explore more details of the HE-related mutations and their effects. This work aims to go beyond the focus on the biochemical structural analysis and characterize tetramerization site mechanical properties and discuss the possible local effect of the ARG 28 point mutations on these properties.

3 Materials and Methods

The α-0 and α-1 domain as well as the β-16 and β-17 domain (encompassing the tetramerization site) data was obtained from the PDB with the identification (ID) 3LBX [22]. Four types of point mutations; cysteine (CYS), histidine (HIS), serine (SER) and leucine (LEU) amino acid residue, were introduced in the ARG 28 location in the α-0 residue in the spectrin tetramerization domain.

The Molecular Dynamics (MD) simulations were carried out using the all-atom CHARMM force field [23] as implemented in the NAMD program [24] and to visually observe the results in 3D, visual molecular dynamics (VMD) [25] is used. Energy minimization is performed using a conjugate gradient (CG) scheme. The equilibration is carried out at a temperature of 310 K (resembling body temperature). The stretching of the proteins is performed via the Steered Molecular

Dynamics (SMD) method [26–28]. This method is based on the concept of pulling the center of mass of a collection of chosen atoms via a spring along the direction of the molecular axis, while keeping the center of mass of another group of atoms fixed through a stiffer spring.

Each SMD simulation is set up in three stages as follows:

1. Energy minimization: Energy minimization is carried out for several thousand steps, ensuring that convergence is achieved. The convergence is determined by confirming that the total energy of the system converges to a steady value.
2. Equilibration: The equilibration process ensures that the molecules start in the most likely in vivo condition at finite temperature. We find that the 20 ns equilibration, limited due to computational constraints, gives a well equilibrated structure with good geometry convergence.
3. Tensile loading: SMD approach is used to pull part of the spectrin tetramerization site to model tensile loading. SMD simulations give valuable insights in the unfolding pathways of a protein. For the SMD simulations, the fixed atoms consist of the C_α (α Carbon) atoms at one end of a chain, and the pulled atom is the C_α atom at the other end of the chain. Different pulling speeds are tested (0.5, 0.05, 0.005, 0.0005 nm/ps). The SMD spring constant used is $k = 400$ kcal mol^{-1}Å^2.

All simulations are performed with a 2 femtosecond time step.

The simulations are carried out using an implicit solvent model [29–34] where the need for explicit water atoms is eliminated by including the effects of solvent in the inter-atomic force calculation. The advantage of implicit solvent models is that the computational cost (*i.e.* the necessary CPU time) of the simulation is used more efficiently to monitor longer and slower simulations as opposed to the necessity for a very large water bath to accommodate the spectrin structure. The Generalized Born model has been demonstrated to provide a good approximation of explicit solvent simulations of proteins [7, 8, 35]. In this work, employing an implicit solvent model will allow faster convergence at lower pulling speeds at a lower computational cost so that enough simulations can be done to obtain statistically meaningful results and at the same time, here, demonstrating an example of the applicability of this approach to large protein systems.

4 Results

We begin with the presentation of the SMD analysis. The C_α atom of codon 19 is fixed while the C_α atom of codon 158 is the SMD atom as shown in Fig. 3I. The figure outlines the three segments of the folded domain.

Force-extension plots of the tensile experiments for the wild type (WT) are shown in Fig. 3II for four different pulling speeds (0.5, 0.05, 0.005, 0.0005 nm/ps).

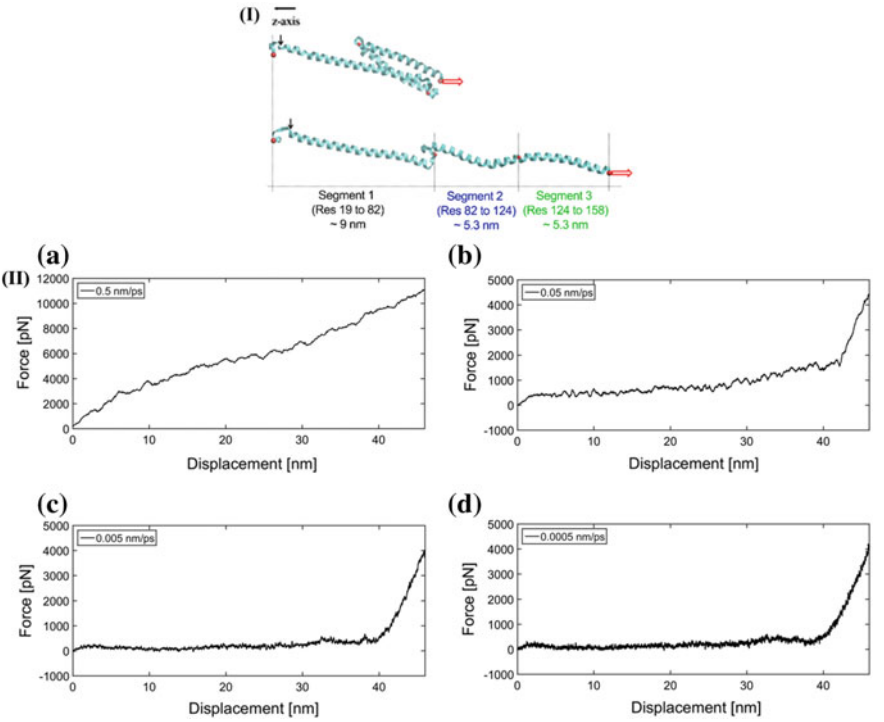

Fig. 3 Panel (**I**) outlines the three segments of the folded domain in the SMD test along with the length of each segment. The C_α atom of codon 19 is fixed while the C_α atom of codon 158 is the SMD atom. Panel (**II**) a–d shows the force-extension plots of tensile experiments for the wild type (WT) for four different pulling speeds; 0.5 nm/ps, 0.05 nm/ps, 0.005 nm/ps, 0.0005 nm/ps; respectively

For all pulling speeds except 0.5 nm/ps, one can observe the typical three regimes;

1. The elastic regime where the force increases linearly with the applied deformation.
2. The plateau regime where the force remains constant with the applied deformation.
3. Final regime where the force increases rapidly with the applied deformation.

It can be observed from the figure that for pulling rates 0.005 and 0.0005 nm/ps; the results are very similar. This shows the convergence of the simulations and that the pulling speed chosen is appropriate. Here, it must also be noted that in total 11 trajectories were calculated and averaged to increase the statistical precision of the results.

Figure 4I shows the force versus applied displacement behavior for the 'wild type (WT)/healthy' structure. The force level required to unravel the hidden length comes out to be ~200 pN. At a displacement of ~5 nm, Segment 3 (see Fig. 4IV)

becomes completely aligned with the pulling direction while Segment 2 is unfolded and the force drops to zero. Figure 4II details how the length of Segment 1 remains unchanged as Segment 2 and 3 re-arrange themselves to accommodate the applied displacement. This confirms that the increase in the force for an applied displacement of ~5 nm manifests itself as stretching of Segment 3 coupled with re-orientation/conformation change of Segment 2. Further examination of Fig. 4I reveals that the force, due to the applied displacement, increases linearly until the tertiary structure changes and the triple helix starts unfolding. This process is a step-wise process and the unfolding is completed at the point "D" as shown in Fig. 4I. We can observe from Fig. 4II that as Segment 3 stretches and Sect. 2 re-orients itself, the end-to-end distance of the former section increases and that of the latter decreases until point "D" where the unfolding of the tertiary structure is completed and Segment 1 and 3 are completely aligned. Following this point, there is no further increase or decrease in the end-to-end distance of either section. Although there is some unfolding in Segment 3, the 10 nm displacement ultimately only results in tertiary re-arrangements of the helices as detailed in Fig. 4IV. Figure 4III shows the applied displacement versus the change in the contour length (here referred to as the addition of subsequent Segments 1; 2 and 3). We can observe here that the overall contour length does not change with the applied displacement of 10 nm since the increase in the end-to-end distance of Segment 3 is cancelled out by the decrease in the end-to-end distance of Segment 2 during the test as detailed in (II).

The tensile test performed here encompasses the unfolding of the protein's tertiary structure as shown in the early experimental studies [1–14] and 10 nm displacement applied results in unraveling the 'hidden' 10 nm in the tertiary structure with no change in the secondary alpha-helical structure of the protein. Once the unfolding of the 'hidden length' is completed at point "D" as denoted in Fig. 4I, the force drops to zero revealing an initial unfolding stiffness of ~0.0125 N/m.[1]

Overall, the 'hidden length' of protein structures gives rise to very compliant materials with high levels of ductility involved not just owing to the secondary structure of the protein (alpha helix) but mainly the tertiary structure is the reason for this very ductile behavior. Despite the gap between the pulling speeds between AFM experiments and SMD simulations where the AFM results are reproduced, the simulations here have been able to capture the peaks observed at similar force levels to those in AFM [1, 3, 6].

Following the basic SMD analysis for the WT, four types of missense mutations are introduced in the codon 28 in the α-0 region in the spectrin tetramerization site. The arginine amino acid (ARG 28) is replaced by cysteine (CYS), histidine (HIS), serine (SER) and leucine (LEU) amino acid residues. As we can see in Fig. 5, the

[1]The stiffness values for protein structures from MD simulations are obtained using averaging approaches (*i.e.* moving average) therefore instead of an exact number, the order of magnitude of the values obtained should be considered.

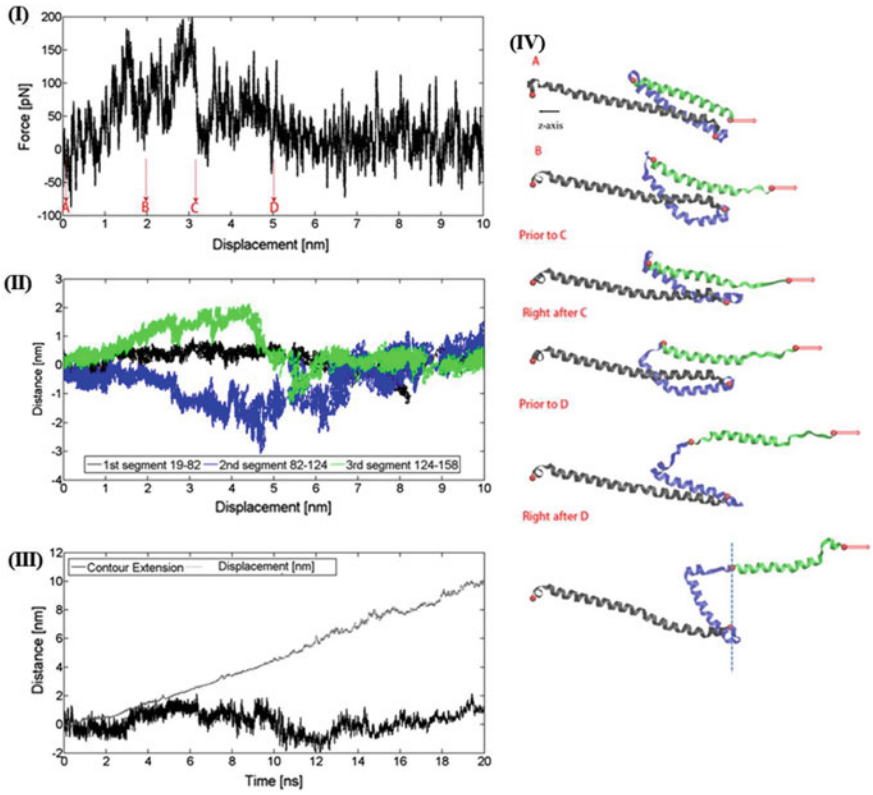

Fig. 4 The characteristic SMD data is detailed from the tensile test on WT (wild type/healthy) case. Panel **I** shows the force-displacement graph with the critical points marked by *A–D* which are also detailed in the ribbon-diagram of α-spectrin. Segment 1 is denoted by *black*, segment 2 is denoted by *blue* and segment 3 is denoted by *green*. The same notation is used in panel **II** where each segment's elongation is plotted with respect to the applied displacement. Panel **III** shows the applied displacement with respect to time together with the contour length fluctuations around -0- for the same applied displacement. Panel **IV** shows the ribbon diagram of the unfolding pattern: tertiary structure unraveling with the applied axial displacement

results for the mutated structures follow a similar trend to that for the WT. The slight tendency toward the more compliant behavior for the mutated structure is possibly from the statistically varying conformations each structure assumes after the equilibration process which would also depend on factors such as the size of the structures' side groups.

Figure 6 shows the force versus displacement graph for all cases for larger displacements up to ~45 nm. The contour length for the α-0 and α-1 combined alpha-helical repeat is 20 nm as shown in the latter analysis (From the fixed C_α atom of codon 19 to the SMD atom/C_α atom of codon 158; the constituent 139

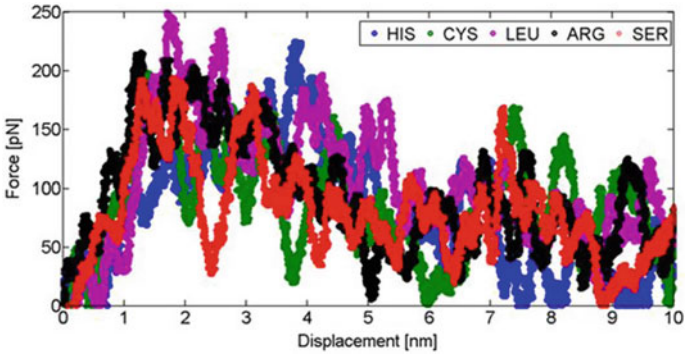

Fig. 5 The characteristic SMD force-displacement data is shown for the WT/arginine (ARG; *black*) together with the cases with the point mutations; histidine (HIS; *blue*), cysteine (CYS; *green*), leucine (LEU; *purple*); serine (SER; *red*)

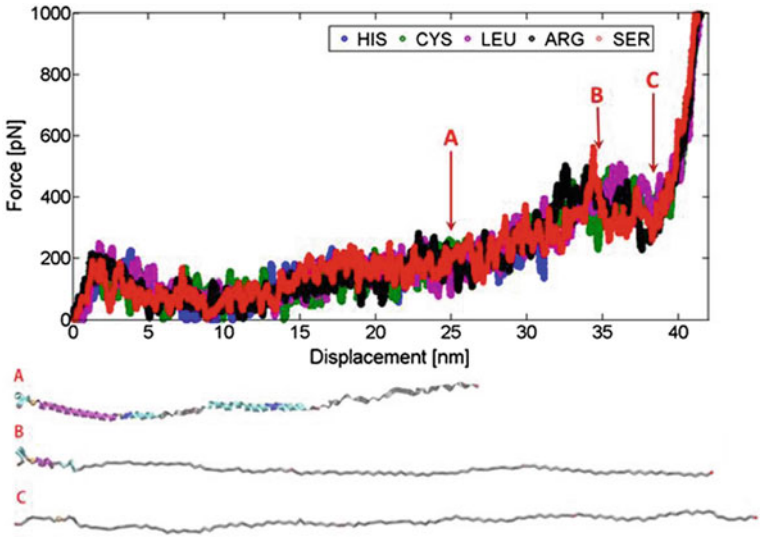

Fig. 6 The characteristic SMD force-displacement data is shown for the WT/arginine (ARG; *black*) together with the cases with the point mutations; histidine (HIS; *blue*), cysteine (CYS; *green*), leucine (LEU; *purple*); serine (SER; *red*) for an applied larger displacement. Snapshots under the graph display the ribbon diagrams for (*A*), (*B*) and (*C*) for the denoted displacement for the WT (ARG 28 for the wild type/healthy case). The *ribbon diagrams* show the 'alpha helix' convolution with *purple*; 'turn's with *blue* and 'coil's with *gray*. ARG 28 C_α atom; the 'hot spot' (the mutation site) is shown with an *orange sphere*. After point C; the secondary structure is 'coil' and the backbone is completely aligned which also corresponds to the H-bonds in the backbone breaking resulting in a stiffer response shown from the force-displacement data for all cases

codons/38 alpha-helical turns-taking into account that each turn in an alpha helix is 0.54 nm long and constitutes of 3.6 residues- are approximately 20 nm long when aligned). Further displacement applied once Segment 1–3 are all aligned will result in the unfolding of the alpha helix convolution; that is the change in the protein's secondary structure. Figure 6 inset shows the configuration the WT structure assumes at different displacement levels. At a displacement of 25 nm (A), the alpha helix in some parts starts transforming into 'turn's. Once 'coil' secondary structure starts appearing in the structure there is a slight increase in the force levels with the applied deformation, although the change from an alpha helix to 'turn' secondary structure happens at a constant force level.

At (B), at a displacement of 35 nm, only the alpha helix around ARG 28 remains in-tact and at a displacement level of ~38 nm at the point (C), the whole secondary structure has turned into 'coil' and the 139 constituent residues have a total end-to-end distance of ~40 nm (meaning each turn almost doubles in length when stretched to completely unfold the alpha helix). After reaching an end-to-end distance of 40 nm; after which the alpha helix structure is no longer maintained, the H-bonds in the backbone start breaking giving a resistant response to the applied displacement. This stiffness is calculated to be ~8 N/m. This stiffness level also shows more clearly why the SMD spring stiffness is chosen to be 400 kcal/molÅ^2 (~300 N/m) instead of the conventional choice of 10 kcal/molÅ^2 (~7 N/m) which would be too low to obtain the correct stiffness. The spring stiffness has to be sufficiently large so that in a series of springs its effect is negligible (*i.e.* $1/\overline{k} = \sum_{i=1}^{n} (1/k_i) + 1/k_{spring}$; where $\overline{k}$ is the equivalent stiffness of n springs in series which is shown to be an acceptable model for the bonding of a protein structure [36]).

In order to further investigate the effect of the mutations on the particular 'hot spot' (codon 28), another analysis is conducted here where the stretching of the alpha helix around the 'hot spot' is investigated by pulling on the C_α atoms equidistant from the codon 28; in particular: C_α atoms of the codon 26 in the axial direction and the C_α atom of the residue 30 in the opposite axial direction. This tensile test is shown step-by-step (A–E) in the inset of Fig. 7.

This segment of the α-chain structure tested here is approximately as long as a 'turn' in the alpha-helical convolution with an initial length of ~0.6 nm. The force versus displacement path initially follows a linear trend (with a slope of ~10 N/m) as it essentially involves breaking the alpha-helical hydrogen bonds (H-bonds) which act as linear springs. Thus in the first stage (A → B) the segment goes from one energy well (folded convolution) to another (unfolded convolution). The slope found for the four residues involved concur with the stiffness derived in the literature (~42 N/m for one residue to break the H-bonding for unfolding an alpha-helical convolution; which would then imply (42/4) N/m for residues which act like harmonic springs in series) [36]. This slope also concurs with the result shown in Fig. 6 beyond point C where the slope is measured to be ~8 N/m.

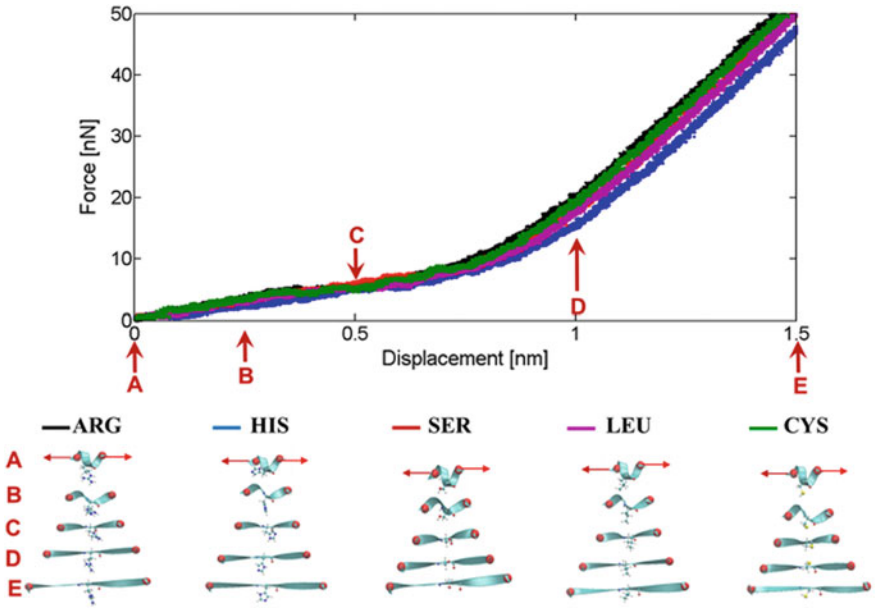

Fig. 7 Total force versus displacement is shown for the WT/arginine (ARG; *black*) together with the cases with the point mutations; histidine (HIS; *blue*), cysteine (CYS; *green*), leucine (LEU; *purple*); serine (SER; *red*) for a tensile test on the local 'hot spot' from the point A; folded configuration to the point E where the backbone is being stretched. Point C, in the middle, marks the complete unfolding of the 'alpha helix'. The ribbon diagrams for each case are shown with the boundary condition: the end C_α atoms applied equal displacement in opposite directions

Once the ~0.6 nm length-segment is stretched another ~0.6 nm, the strain on it being 100%, the secondary structure is completely altered and alpha helix is unfolded followed by the backbone stretching. Interestingly, point (C) is the point where codon 28 secondary structure becomes a 'coil' where from then on the force levels increase nonlinearly in order to displace the atoms until (D) where every backbone residue is completely aligned. The constant slope observed after this point (a displacement amounting to ~1.2 nm) is the stiffness of the bonds of the backbone atoms of the polypeptide and is ~50–70 N/m. This is approximately four orders of magnitude higher than the stiffness obtained while unfolding the tertiary structure (Fig. 4).

Here, it has been presented that the unraveling of the 'hidden length' due to forced unfolding occurs by unfolding the tertiary structure prior to the change in the secondary structure for the healthy and mutated structures. SMD simulations help deliver a hierarchical level of stiffness values for the tetramerization site which is shown to be similar for both the healthy and the mutated structures. It is important to monitor the stability of the healthy versus mutated cases locally.

5 Discussion

The main focus of this work was to explore and assess, from a mechanical perspective, the effects of point mutations on the SPTA1 gene which cause HE (Hereditary Elliptocytosis). The crystal structure of the spectrin tetramerization site provides novel insights and enables us to do molecular testing to discuss the potential effects of mutations [22]. It was shown here that the mechanical stiffness of the tetramerization site is not directly affected by the point mutations. This suggests that the local structural disturbances the mutations cause, will affect the spectrin scaffold on the network-level rather than on the on the single chain level implying more complicated molecular interactional disorders. The local disturbances the mutations cause; due to different side-chain conformations/interactions; examined at different high-energy regions over long time periods could reveal insight to the "stability of the structure-lethality of the mutations" correlation.

Application of the SMD procedure to the tetramerization site here highlighted the unfolding pattern for a structure with folded domains where the sequence of unfolding was presented to comply: tertiary structure unraveling followed by the secondary structure change giving rise to a "softening" behaviour. From the SMD analyses, the stiffness of the backbone and the stiffness of the structure in general are discussed and compared. This provides insight into the prospective mechanical analyses that can be conducted to model different networks of poly-peptide chains [36].

Acknowledgements This work was supported by TUBITAK (The Scientific and Technological Research Council of Turkey), grant no: 114Z733 and TED University.

References

1. M. Rief, M. Gautel, F. Oesterhelt, J.M. Fernandez, H.E. Gaub, Science **276**, 1109–1112 (1997)
2. M. Rief, J.M. Fernandez, H.E. Gaub, Phys. Rev. Lett. **81**, 4764–4767 (1998)
3. M. Rief, J. Pascual, M. Saraste, H.E. Gaub, J. Mol. Biol. **286**, 553–561 (1999)
4. T.E. Fisher, A.F. Oberhauser, M. Carrion-Vazquez, P.E. Marszalek, J.M. Fernandez, TIBS **24**, 379–384 (1999)
5. J. Fernandez, P. Marszalek, H. Lu, H. Li, M. Carrion-Vazquez, A. Oberhauser, K. Schulten, Nature **402**, 100103 (1999)
6. P.-F. Lenne, A.J. Raae, S.M. Altmann, M. Saraste, J.K.H. Hörber, FEBS Lett. **476**, 124–128 (2000)
7. E. Paci, M. Karplus, J. Mol. Biol. **288**, 441–459 (1999)
8. S.M. Altmann, R.G. Grünberg, P.F. Lenne, J. Ylänne, A. Raae, K. Herbert, M. Saraste, M. Nilges, J.K. Hörber, Structure **10**, 1085–1096 (2002)
9. R. Law, P. Carl, S. Harper, P. Dalhaimer, D. Speicher, D.E. Discher, Biophys. J. **84**, 533–544 (2003)
10. H.J. Qi, M.C. Boyce, J. Mech. Phys. Solids **52**, 2187–2205 (2004)
11. V. Ortiz, S.O. Nielsen, M.L. Klein, D.E. Discher, J. Mol. Biol. **349**, 638–647 (2005)

12. H.J. Qi, C. Ortiz, M.C. Boyce, Trans. ASME, J. Eng. Mater. Technol. **128**, 509–518 (2006)
13. C.P. Johnson, H. Tang, C. Carag, D.W. Speicher, D.E. Discher, Science **317**, 663–666 (2007)
14. M. Arslan, M.C. Boyce, H.J. Qi, C. Ortiz, J. Appl. Mech. **75**, 536–543 (2008)
15. D.W. Speicher, J.S. Morrow, W.J. Knowles, V.T. Marchesi, J. Biol. Chem. **257**, 9093–9101 (1982)
16. D.M. Shotton, B.E. Burke, D. Branton, J. Mol. Biol. **131**, 303–329 (1979)
17. A.M. McGough, R. Josephs, Proc. Natl. Acad. Sci. U.S.A. **87**, 5208–5212 (1990)
18. T.L. Coetzer, K. Sahr, J. Prchal, H. Blacklock, L. Peterson, R. Koler, J. Doyle, J. Manaster, J. Palek, J. Clin. Invest. **88**, 743–749 (1991)
19. P.G. Gallagher, Semin. Hematol. **41**, 142–164 (2004)
20. M. Gaetani, S. Mootien, S. Harper, P.G. Gallagher, D.W. Speicher, Blood **111**(12), 5712–5720 (2008)
21. Z. Zhang, S.A. Weed, P.G. Gallagher, J.S. Morrow, Blood **98**, 1645–1653 (2001)
22. J.J. Ipsaro, S.L. Harper, T.E. Messick, R. Marmorstein, A. Mondragón, D.W. Speicher, Blood **115**, 4843–4852 (2010)
23. A.D. MacKerell, D. Bashford, M. Bellott, R.L. Dunbrack, J. D. Evanseck, M. J. Field, S. Fischer, J. Gao, H. Guo, S. Ha, D. Joseph-McCarthy, L. Kuchnir, K. Kuczera, F.T.K. Lau, C. Mattos, S. Michnick, T. Ngo, D.T. Nguyen, B. Prodhom, W.E. Reiher, B. Roux, M. Schlenkrich, J.C., Smith, R. Stote, J. Straub, M. Watanabe, J. Wiorkiewicz-Kuczera, D. Yin, M. Karplus, J. Phys. Chem. B, **102**, 3586–3616 (1998)
24. M.T. Nelson, W. Humphrey, A. Gursoy, A. Dalke, L.V. Kale´, R.D. Skeel, K. Schulten, Int. J. Supercomput. Appl. High Perform. Comput. **10**, 251–268 1996
25. W. Humphrey, A. Dalke, K. Schulten, J. Mol. Graph. **14**, 33 (1996)
26. H. Lu, B. Isralewitz, A. Krammer, V. Vogel, K. Schulten, Biophys. J. **75**, 662–671 (1998)
27. B. Isralewitz, J. Baudry, J. Gullingsrud, D. Kosztin, K. Schulten, J. Mol. Graph. Model. **19**, 13–25 (2001)
28. S. Park, F. Khalili-Araghi, E. Tajkhorshid, K. Schulten, J. Chem. Phys. **119**, 3559 (2003)
29. M. Schaefer, C. Froemmel, J. Mol. Biol. **216**, 1045–1066 (1990)
30. W.C. Still, A. Tempczyk, R.C. Hawley, T. Hendrickson, J. Am. Chem. Soc. **112**, 6127–6129 (1990)
31. G.D. Hawkins, C.J. Cramer, D.G. Truhlar, J. Phys. Chem. **100**, 19824–19839 (1996)
32. J. Srinivasan, M.W. Trevathan, P. Beroza, D.A. Case, Theor. Chem. Acc. **101**, 426–434 (1999)
33. A. Onufriev, D. Bashford, D.A. Case, J. Phys. Chem. **104**, 3712–3720 (2000)
34. A. Onufriev, D. Bashford, D.A. Case, Proteins: Struct., Func., Gen., **55**, 383–394 (2004)
35. W. Cornell, R. Abseher, M. Nilges, D.A. Case, J. Mol. Graph. Model. **19**, 136–145 (2001)
36. Z. Qin, M.J. Buehler, Phys. Rev. E **82**, 061906 (2010)

The Choice of a Performance Indicator of Release in Transdermal Drug Delivery Systems

Giuseppe Pontrelli and Laurent Simon

Abstract An effective time constant for first-order processes is defined to capture the dynamics of systems represented by partial differential equations. In this chapter, the methodology is applied to passive and electrically assisted drug controlled transdermal delivery devices in two case studies. The analysis, which is carried out using Laplace-transformed variables, results in a first-order approximation and does not require time-domain solutions. Numerical experiments are included to illustrate the effectiveness of the index under different conditions and to estimate the time it takes to establish a steady-state flux across the membrane.

1 Introduction

Traditional transdermal drug delivery (TDD) systems are based on the transport of therapeutic agents across the skin by passive diffusion. Despite being the subject of extensive research over the years because of its potential advantages, the exact release mechanism remains unclear in some cases and it is often difficult to predict the drug kinetics accurately [1, 2]. The solutes which can be administered by transdermal route are limited to molecules of low molecular weight, due to the excellent barrier properties of the stratum corneum, the outermost layer of the epidermis [3]. To increase skin's drug transport and overcome this limitation, innovative technologies have been developed, some of them based on the use of electrical current (*iontophoresis*). In these electrically assisted systems, an applied potential of low intensity ($\approx 1V$) generates an additional driving force for the drug motion in the skin [4, 5].

G. Pontrelli (✉)
IAC-CNR, Via Dei Taurini 19, Roma, Italy
e-mail: giuseppe.pontrelli@gmail.com

L. Simon
New Jersey Institute of Technology, Newark, NJ, USA
e-mail: laurent.simon@njit.edu

P. Wriggers and T. Lenarz (eds.), *Biomedical Technology*, Lecture Notes in Applied and Computational Mechanics 84, DOI 10.1007/978-3-319-59548-1_4

The application of transdermal patches for accurate delivery of medicaments to their target sites is another possible non-invasive technology: the drug is initially stored in the vehicle, a porous polymeric reservoir having an impermeable backing at one side and an adhesive in contact with the skin at the other side, and is subsequently released in a controlled manner [6, 7]. Compared to conventional TDD products, the rational design of these novel drug delivery devices poses further challenges, such as the complex mechanisms and the unknown significance of process parameters. Additional factors include the device polymeric microstructure characteristics and properties of the electric field.

In the absence of experimental data, mathematical modelling of TDD allows to predict drug release from the vehicle and its transport into the target tissue. The framework also offers insights into the factors governing drug delivery and provide quantitative relationships between drug concentration, or the delivery rate, and some key design drug/vehicle properties [8]. For traditional TDD, the coupling between the diffusion process in the reservoir and in the target tissue has been considered in [6, 9]. In the majority of TDD models, a constant flux enters the target tissue and the role of the reservoir finite capacity is neglected [10].

Moreover, the above models assume that the skin is homogeneous and ignore its composite structure. In fact, it is well accepted that the skin is an inhomogeneous medium, composed of several layers with different thickness and physico-chemical-electrical properties (Fig. 1). This aspect has a crucial importance since the drug transport critically relates to the local diffusive properties and, even more importantly in iontophoresis, the potential field relies on the layer-dependent electrical conductivities. The multi-layer structure of the biological media and other related issues have been addressed in other papers [11] and in a recent work, where a model of iontophoretic drug release from a vehicle into a multi-layered dermal tissue is presented [12]. However, even in situations where the transport phenomena are well represented mathematically, the need exists to develop analytical tools or simple indicators to extract meaning from the model and the data. These tools will make possible to answer certain questions, such as how long it takes to attain a therapeutic flux, or what processing conditions need to be adjusted and by how much, in order to reach a desired delivery rate without solving the full differential equations. Furthermore, when a full mathematical representation is not available, or is too complicated for being of practical use, simple performance indicators are required to elucidate the main transport mechanisms and identify the most critical components in TDD.

Among several mathematical techniques available for control systems analysis, Laplace transform and linearization are frequently applied to describe a process dynamics through an effective time constant (ETC)(denoted by t_{eff}) [13]: this represents a useful indicator of the time elapsed before reaching a steady state. The existence of a single ETC is of great importance in the design of drug delivery systems, because it would allow product manufacturers to tune specific properties to ensure that a constant release is reached at a specific time [7]. The problem is to find a formal definition of t_{eff} which makes the index precise for a general dynamical

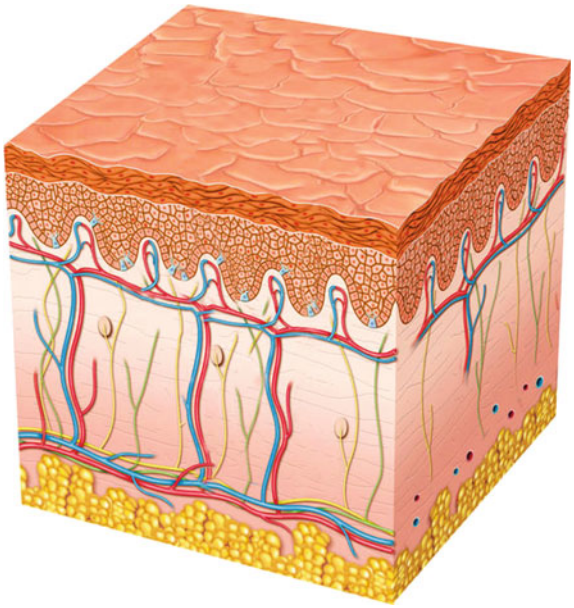

Fig. 1 An anatomic representation of the skin, composed by three main layers: epidermis (approximately 100 μm thick), dermis (between 1 and 3 mm thick, highly vascularized) and a subcutaneous tissue. The epidermis is divided into sub-layers where the stratum corneum (approximately 10 μm thick) is the outermost layer and is the major barrier to the drug migration, being composed of densely packed cells, with a typical *brick and mortar* structure. Each skin layer, due to its histological composition, has a different influence on the drug transport mechanism

system, no matter how complicated it is, even in cases when the time-dependence departs markedly from a simple exponential form. For a practical and useful definition, it must also be possible to compute t_{eff} in a simple and straightforward manner to enable different convective-diffusive systems to be compared on a common basis. Our goal is to relate ETC to the model parameters of a TDD device. This allows, with the aid of a single index, to understand the role of key factors influencing the release of active pharmaceutical ingredients and to assess the time drug reaches a target steady-state flux and to optimize the release performance.

The chapter is organized as follows. In Sect. 2, we introduce the concept of the ETC and its use in a general framework. In Sect. 3 the one-layer model in TDD is presented, and in Sect. 4 the computation of ETC is carried out. The mathematical problem in a multi-layered model is addressed in Sect. 5 followed by the correspondent ETC derivation (Sect. 6). Finally in Sect. 7 some numerical estimates of ETC and drug flux in the various cases, are presented and discussed for a realistic range of parameters and typical drugs.

2 The Concept of an Effective Time Constant: Definition and Applications

The introduction of a dynamic metric for controlled-release systems stems from the need to link the performance of formulations to measurable physico-chemical features of the drug and vehicle. For example, in transdermal heat-enhanced devices, manufacturers have the opportunity to design products that address the needs of patients suffering from breakthrough cancer pain. The idea is to dramatically tighten the pain-relief gap by triggering a prompt onset of drug effect. Although opioids are usually administered intravenously, there has been a growing interest in using physical enhancers to make transdermal patches designed to meet unique treatment protocols required by cancer patients. Preliminary studies, conducted by Ashburn et al., have shown some of the benefits of the application of local heat to transdermal fentanyl patches [14]. These researchers noticed that, when applying these patches with no controlled heat, attaining a steady-state blood level of the medicament may require a long time. One the contrary, an increase observed in the serum concentration immediately after the application of controlled heat, suggests that such technologies may prove effective in the delivery of analgesia [14]. A computational method to estimate the onset of action based on the properties of the active and inactive pharmaceutical ingredients, would be very useful in this case. It has also been shown that the period elapsed to reach 98% of the steady-state flux, defined by four times the first time constant, is related to the properties of the delivery system, although no analytical expression is available [15].

The ability of iontophoresis to deliver medicaments through the skin and quickly establish a therapeutic level has been studied. Song et al. [16] developed an alternating current technique to increase the permeation rate of urea and decrease the lag time in the human epidermal membrane. These researchers suggested that the design of iontophoretic drug-delivery devices would improve, considerably, if the transport lag time was well characterized and flux variability decreased [16]. Although the controlled-release community has expressed special interest in controlling the factors that delay the onset of the steady-state release rate [17], early efforts used compartmental models of transdermal iontophoretic transport [18]. This approach provides limited mechanistic insight and makes it difficult to extrapolate the findings to new iontophoretic products.

Laplace transform and linearization are commonly applied to examine the dynamic responses of many processes. These procedures help control engineers and process designers determine relevant characteristic parameters which affect the transient behavior of a plant [19]. For example, let us consider a storage tank with inlet and outlet flows: the time elapsed before reaching a steady-state liquid level, after changing the inlet flow rate, is related to the tank area and the flow resistance in the outlet pipe. The transfer function reveals that the product of these two factors represents the process time constant. Based on the success of these techniques, there have been significant efforts made, by researchers, toward implementing these tools to best describe the dynamics of diffusion [13]. A similar approach is considered

in this work to derive design equations that connect ETC to key properties. These features can be use by manufacturers of controlled-released systems to guarantee accurate release of active pharmaceutical ingredients to a selected site.

To assess the suitability of the method, let us start with a first-order system [19]:

$$\tau_p \frac{dy}{dt} + y = K_p u(t) \tag{1}$$

where τ_p (otherwise called t_{eff}) and K_p indicate the time constant and steady-state gain of the process, respectively; u and y are the input and output variables. While K_p is the ratio of the ultimate response (y_{ss}) to the size of a step change in u, τ_p is a measure of the time it takes to reach y_{ss}. The gain K_p determines the sensitivity of a system. For example, consider a process where saturated steam is supplied to heat the liquid in a vessel. A K_p value of 7 °F/(lb/min) suggests that an increase of 1.0 lb/min in the steam mass flow rate is necessary to raise the liquid temperature by 7 °F. It can be shown that y has achieved 63.2% of its steady-state value after one time constant. At $t_{res} = 4\tau_p$ (called the *response time*), y is at 98% of its ultimate value. In the previous example, the response time denotes the period elapsed before the temperature changes by 7 °F. By Eq. (1), using the Laplace variable s, often used to analyze the dynamics of linear systems, the response becomes:

$$Y(s) = \frac{K_p}{\tau_p s + 1} U(s) \tag{2}$$

The variables Y and U represent the Laplace transforms u and y assuming that $y(0) = u(0) = 0$.

This concept of a single time constant to describe a process dynamics is extended to systems in which the variable of interest can be approximated by a series of the form:

$$\chi(\mathbf{x}, t) = \sum_{n=1}^{\infty} f_n(\mathbf{x}) e^{-\lambda_n t} \tag{3}$$

where $\lambda_n = 1/t_n$ and f_n is a function of the space $\mathbf{x}$. The numbers t_n denote the characteristic time constants with $t_n > t_m$ or $\lambda_n < \lambda_m$ for $n < m$. In general, the system dynamics is represented by the first λ_n values. To use a single time constant that estimates how fast $\chi(\mathbf{x}, t)$ approaches the equilibrium $\chi_{eq}(\mathbf{x})$, a first-order moment with a normalized probability density function $\Omega(\mathbf{x}, t)$ is applied:

$$t_{eff}(\mathbf{x}) = \int_0^{\infty} t\Omega(\mathbf{x}, t)\, dt \tag{4}$$

where

$$\Omega(\mathbf{x},t)=\frac{\chi_{eq}(\mathbf{x})-\chi(\mathbf{x},t)}{\int_0^{\infty}\left(\chi_{eq}(\mathbf{x})-\chi(\mathbf{x},t)\right)dt}$$

The properties of Laplace transforms can be used to write ETC defined in Eq. (4) in terms of s [7]:

$$t_{eff}(\mathbf{x})=\frac{\lim_{s\to 0}\left(\frac{\chi_{eq}(\mathbf{x})}{s^2}+\frac{d\bar{\chi}}{ds}(\mathbf{x},s)\right)}{\lim_{s\to 0}\left(\frac{\chi_{eq}(\mathbf{x})}{s}-\bar{\chi}(\mathbf{x},s)\right)} \tag{5}$$

with $\bar{\chi}(\mathbf{x},s)$ the Laplace transform of $\chi(\mathbf{x},t)$. An inspection of Eq. (4) shows that $t_{eff}(\mathbf{x})$ is guaranteed to have a positive value as long as the difference $\frac{\chi_{eq}(\mathbf{x})}{s}-\bar{\chi}(\mathbf{x},t)$ does not change sign. Although there are other performance indicators (e.g., lag time) that have been defined to describe process dynamics [7], ETC remains the most effective indicator for our purposes. In the following, we apply the previous concepts to a one and multi-layered cases. The ETC is defined and computed for both systems.

3 A One-Layer Model for TDD

Let us consider a TDD system, where the skin is modeled as a planar membrane in contact with an infinite reservoir (i.e., constant drug concentration) and a receiver chamber. Because most of the mass transfer occurs along the direction normal to the skin surface, we restrict our study to a simplified 1D model. In particular, we consider a Cartesian coordinate and draw a line pointing inwards which crosses the vehicle and the skin. The skin surface is located at $x=0$; $x=x_1$ is the thickness of the SC (Fig. 2). Here, diffusion is assumed to take place only in the stratum corneum (SC) instead of the full-thickness skin, due to the formidable barrier posed by this layer. Permeation through the SC is the rate-limiting step [8]. We use $c\approx 0$ at the SC limit $x=x_1$ to show rapid removal of the drug from the interface between the SC and the viable epidermis by rapid diffusion followed by absorption by the blood vessels [20].

Iontophoretic transport

To promote TDD, an electric field is locally applied in the area where the therapeutic agent has to be released (*iontophoresis*): for example, the anode is at $x=0$ and the cathode is at $x=x_1$. Let Ψ_0 and Ψ_1 ($\Psi_0>\Psi_1$) be the correspondent applied potential at the endpoints (Fig. 2). By mass conservation, the drug concentration[1] satisfies the following equation:

[1] A mass volume-averaged concentration $c_1(x,t)$ (mg/cm^3) is considered in this chapter.

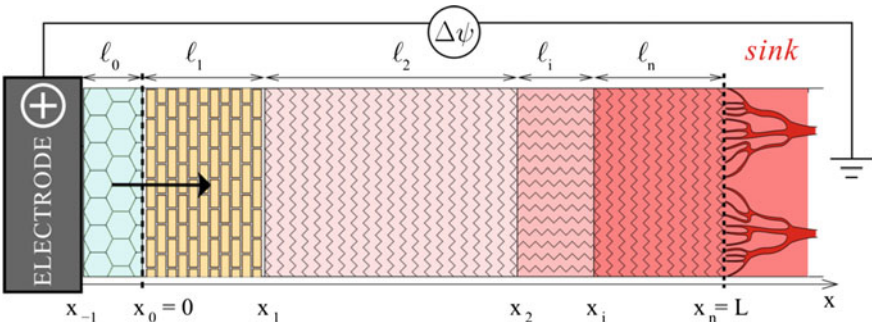

Fig. 2 A diagram of a n-layered tissue ($\ell_1, \ell_2, ..., \ell_n$) with a vehicle ℓ_0. In some cases, the model is confined to SC layer only (Sect. 3), while in a more realistic situation, it includes several layers (Sect. 5) The 1D model is defined along the line normal to the skin surface and extends with a sequence of n contiguous layers from the vehicle interface $x_0 = 0$ up to the skin bound $x_n = L$, where capillaries sweep the drug away to the systemic circulation (sink). In iontophoresis, a difference of potential is applied to facilitate drug penetration across the skin's layers (figure not to scale)

$$\frac{\partial c_1}{\partial t} + \nabla \cdot J_1 = 0 \tag{6}$$

and the mass flux is defined by the Nernst-Planck flux equation [10]:

$$J_1 = -D_1 \nabla c_1 - u_1 c_1 \nabla \phi_1, \tag{7}$$

where ϕ_1 is the electric potential and the convective (electroosmotic) term is omitted. Equation (7) is the generalized Fick's first law with an additional driving force which is proportional to the electric field. The electric mobility is related to the diffusivity coefficient through the Einstein relation:

$$u_1 = \frac{D_1 z F}{RT}, \tag{8}$$

($\mathrm{cm}^2\ V^{-1}\ s^{-1}$), where z ion valence, F the Faraday constant, R the gas constant, T the absolute temperature. The boundary conditions are:

$$c_1 = c_{10} \qquad \text{at} \quad x = 0 \tag{9}$$

$$c_1 = 0 \qquad \text{at} \quad x = x_1 \tag{10}$$

where c_{10} is related to the vehicle concentration c_0 by $c_0 = K_0^1 c_{10}$ with K_0^1 the reservoir/skin partition coefficient. The Eq. (10) arises because, in deep skin, drug is uptaken by capillary network and is lost in the systemic circulation: we refer to this as systemically absorbed drug.

The initial conditions is set as:

$$c_1(x,0) = 0 \tag{11}$$

The electric potential field

To solve Eqs. (6)–(8) in $[0, x_1]$, we first seek a solution of the Poisson equation [10]:

$$\begin{aligned} &\nabla \cdot (\sigma_1 \nabla \phi_1) = \rho(x) \simeq 0 \\ &\phi_1 = \Psi_0 \qquad \text{at} \quad x = 0 \\ &\phi_1 = \Psi_1 \qquad \text{at} \quad x = x_1 \end{aligned} \tag{12}$$

with $\sigma_1(\mathrm{cm}^{-1}\,\Omega^{-1})$ the skin electrical conductivity and $\rho(x)$ is the charge density over the permittivity [4]. It is straightforward to verify that the exact solution of the problem (12) is

$$\phi_1(x) = a_1 x + b_1 \tag{13}$$

with the expressions of a_1 (V/cm) and $b_1(V)$ given in Sect. 7.

4 Computation of the ETC for a One-Layer Skin Model

For the system described by Eqs. (6)–(11), the goal is to determine the period elapsed before reaching a steady-state flux by first estimating the ETC. Therefore, the cumulative amount of drug released at $x = x_1$ and into the systemic circulation is also an increasing function:

$$M(t) = \int_0^t -D\frac{\partial c_1}{\partial x}(x_1, \tau)d\tau \tag{14}$$

and, by definition of a monotonic function, the time derivative of $M(t)$ (e.g., the flux at $x = x_1$) does not change sign. It starts at 0 and reaches a steady-state value.

After applying the definition of the Laplace transform to c_1, we get

$$\bar{c}_1(x,s) = \int_0^\infty c_1(x,t)\exp(-st)dt \tag{15}$$

where $\bar{c}_1(x,s)$ is the Laplace transform of $c_1(x,t)$. Substituting $\bar{c}_1(x,s)$ into Eqs. (6)–(7) leads to the following solution:

$$\bar{c}_1(x,s) = k_1 \exp\left[\frac{1}{2}x\left(-\frac{\gamma_1}{D_1} - \frac{\sqrt{\gamma_1^2 + 4D_1 s}}{D_1}\right)\right] + k_2 \exp\left[\frac{1}{2}x\left(\frac{\sqrt{\gamma_1^2 + 4D_1 s}}{D_1} - \frac{\gamma_1}{D_1}\right)\right] \tag{16}$$

with $\gamma_1 = u_1 a_1$. Equation (16) is solved for k_1 and k_2 after imposing the boundary conditions (9) and (10). These integration constants are replaced in (16) to give $\bar{c}_1(x, s)$. An expression for the flux at $x = x_1$ in terms of s gives

$$J_1(s) = \frac{c_{10}\sqrt{\gamma_1^2 + 4D_1 s}\ \exp\left[\dfrac{x_1\left(\sqrt{\gamma_1^2 + 4D_1 s} - \gamma_1\right)}{2D_1}\right]}{s\left[\exp\left(\dfrac{x_1\sqrt{\gamma_1^2 + 4D_1 s}}{D_1}\right) - 1\right]} \tag{17}$$

The ETC, obtained from Eq. (4), and the steady-state flux are

$$t_{eff} = \frac{\gamma_1^2 {x_1}^2\left[2\mathrm{csch}^2\left(\dfrac{\gamma_1 x_1}{2D_1}\right) + 1\right] - 2\gamma_1 D_1 x_1 \coth\left(\dfrac{\gamma_1 x_1}{2D_1}\right) - 4D_1^2}{2\gamma_1^2\left[\gamma_1 x_1 \coth\left(\dfrac{\gamma_1 x_1}{2D_1}\right) - 2D_1\right]} \tag{18}$$

and

$$J_{1eq} = \frac{c_{10}\gamma_1}{\exp\left(\dfrac{\gamma_1 x_1}{D_1}\right) - 1} \tag{19}$$

respectively. Note that

$$\lim_{\gamma_1 \to 0} t_{eff} = \frac{7{x_1}^2}{60D_1} \qquad \lim_{\gamma_1 \to 0} J_{1eq} = \frac{c_{10}D_1}{x_1}$$

recover the expressions for the passive (simple) diffusion [7].

5 A Multi-layer Model for TDD

The skin has a typical composite structure, constituted by a sequence of contiguous layers of different physical properties and extensions. To be more realistic, let us generalize the previous model and consider the skin made of several layers of thicknesses $l_1, l_1, ..., l_n$, each treated as a macroscopically homogeneous porous medium. Therefore, a set of intervals $[x_{i-1}, x_i]$, $i = 1, \ldots, n$ ($x_n = L$) are defined (Fig. 2).

Iontophoretic transport

As in the case of the one-layer model, the concentration satisfies the following equation:

$$\frac{\partial c_i}{\partial t} + \nabla \cdot J_i = 0 \tag{20}$$

and in each layer i the mass flux is defined by the Nernst-Planck flux equation [10]:

$$J_i = -D_i \nabla c_i - u_i c_i \nabla \phi_i, \qquad u_i = \frac{D_i z F}{RT}, \qquad i = 1, \dots, n \tag{21}$$

where ϕ_i is the electric potential in layer i. The boundary conditions are:

$$c_1 = c_{10} \quad \text{at} \quad x = 0 \tag{22}$$

$$c_n = 0 \quad \text{at} \quad x = x_n \quad \text{(sink condition due to the capillary washout)} \tag{23}$$

At the layer interfaces, we impose continuity of mass fluxes and ratio of equilibrium concentrations equal to partition coefficients:

$$J_i = J_{i+1} \qquad c_i = K_{i,i+1}\, c_{i+1} \qquad \text{at} \quad x = x_i, \qquad i = 1, 2, \dots, n-1 \tag{24}$$

The initial conditions are:

$$c_i(x, 0) = 0 \qquad i = 1, 2, \dots, n \tag{25}$$

The electric potential field

In this multi-layer model, the potential is the solution of the multiple Poisson equations [10]:

$$\begin{aligned} &\nabla \cdot (\sigma_i \nabla \phi_i) = \rho(x) \simeq 0 \qquad i = 1, \dots, n \\ &\phi_1 = \Psi_0 \qquad \text{at} \quad x = 0 \\ &\phi_n = \Psi_1 \qquad \text{at} \quad x = x_n \end{aligned} \tag{26}$$

with $\sigma_i(\,\mathrm{cm}^{-1}\,\Omega^{-1})$ the electrical conductivities in the layer i. At the interfaces we assume an electrically perfect contact and we impose continuity of potential and fluxes:

$$-\sigma_i \nabla \phi_i = -\sigma_{i+1} \nabla \phi_{i+1} \qquad \phi_i = \phi_{i+1} \qquad \text{at} \quad x = x_i \qquad i = 1, \dots, n-1 \tag{27}$$

It is straightforward to verify that the exact solution of the problem (26)–(27) is

$$\phi_i(x) = a_i x + b_i \qquad i = 1, \dots, n \tag{28}$$

with the expressions of $a_i\,(\mathrm{V/cm})$ and $b_i(V)$ are computed as in [12] (see Sect. 7).

6 Computation of the ETC for a Multi-layer Skin Model

For simplicity, a three-layer skin model ($n = 3$) is studied. The governing Eqs. (20)–(21) read:

$$\frac{\partial c_1}{\partial t} = D_1 \frac{\partial^2 c_1}{\partial x^2} + \frac{\partial}{\partial x}\left(u_1 c_1 \frac{\partial \phi_1}{\partial x}\right) \qquad \text{in } [0, x_1] \tag{29}$$

$$\frac{\partial c_2}{\partial t} = D_2 \frac{\partial^2 c_2}{\partial x^2} + \frac{\partial}{\partial x}\left(u_2 c_2 \frac{\partial \phi_2}{\partial x}\right) \qquad \text{in } [x_1, x_2] \tag{30}$$

$$\frac{\partial c_3}{\partial t} = D_3 \frac{\partial^2 c_3}{\partial x^2} + \frac{\partial}{\partial x}\left(u_3 c_3 \frac{\partial \phi_3}{\partial x}\right) \qquad \text{in } [x_2, L] \tag{31}$$

The equilibrium partition relations at the boundaries are

$$c_0 = K_{0,1} c_1 \qquad \text{at} \quad x = 0 \tag{32}$$

$$c_1 = K_{1,2} c_2 \qquad \text{at} \quad x = x_1 \tag{33}$$

$$c_2 = K_{2,3} c_3 \qquad \text{at} \quad x = x_2 \tag{34}$$

The flux continuity equations at the boundaries are

$$D_1 \frac{\partial c_1}{\partial x} + u_1 c_1 \frac{\partial \phi_1}{\partial x} = D_2 \frac{\partial c_2}{\partial x} + u_2 c_2 \frac{\partial \phi_2}{\partial x} \qquad \text{at} \quad x = x_1 \tag{35}$$

$$D_2 \frac{\partial c_2}{\partial x} + u_2 c_2 \frac{\partial \phi_2}{\partial x} = D_3 \frac{\partial c_3}{\partial x} + u_3 c_3 \frac{\partial \phi_3}{\partial x} \qquad \text{at} \quad x = x_2 \tag{36}$$

At the dermis/capillary interface, we have

$$c_3 = 0 \qquad \text{at} \quad x = L \tag{37}$$

Following a method similar to the one described in Sect. 4, the Laplace transformed concentrations are:

$$\bar{c}_1(x, s) = k_1 \exp\left[\frac{1}{2}x\left(-\frac{\gamma_1}{D_1} - \frac{\sqrt{\gamma_1^2 + 4D_1 s}}{D_1}\right)\right] + k_2 \exp\left[\frac{1}{2}x\left(\frac{\sqrt{\gamma_1^2 + 4D_1 s}}{D_1} - \frac{\gamma_1}{D_1}\right)\right]$$

$$\bar{c}_2(x, s) = k_3 \exp\left[\frac{1}{2}x\left(-\frac{\gamma_2}{D_2} - \frac{\sqrt{\gamma_2^2 + 4D_2 s}}{D_2}\right)\right] + k_4 \exp\left[\frac{1}{2}x\left(\frac{\sqrt{\gamma_2^2 + 4D_2 s}}{D_2} - \frac{\gamma_2}{D_2}\right)\right]$$

and

$$\bar{c}_3(x, s) = k_5 \exp\left[\frac{1}{2}x\left(-\frac{\gamma_3}{D_3} - \frac{\sqrt{\gamma_3^2 + 4D_3 s}}{D_3}\right)\right] + k_6 \exp\left[\frac{1}{2}x\left(\frac{\sqrt{\gamma_3^2 + 4D_3 s}}{D_2} - \frac{\gamma_3}{D_3}\right)\right]$$

with $\gamma_1 = u_1 a_1, \gamma_2 = u_2 a_2$ and $\gamma_3 = u_3 a_3$. The integration constants k_i with $i = 1, ..., 6$ are obtained after solving Eqs. (32)–(37) in the Laplace domain. Using these results, expressions for ETC and the steady flux are derived at $x = L$. The functions are not shown here because of page limitation, but the numerical results are given in the next section.

7 Computational Results

To evaluate the dynamic behavior of a transdermal drug delivery, with a possible iontophoretic enhancement, an estimate of ETC is made in the one-layer and multi-layer model.

One-layer model

In the case where the skin is modelled by a single layer, we use the following nominal parameters corresponding to the permeation of arginine vasopressin through hairless rat skin [21]:

$$x_1 = 10^{-3}\,\text{cm} \qquad D_1 = 1.1 \times 10^{-11}\,\text{cm}^2/\text{s} \qquad z_1 = +2 \tag{38}$$

With these data at hand, it results: $\text{csch}^2\left(\frac{\gamma_1 x_1}{2D_1}\right) \approx 0$ and $\coth\left(\frac{\gamma_1 x_1}{2D_1}\right) \approx -1$, and Eq. (18) reduces to:

$$t_{eff} \approx \frac{\gamma_1^2 x_1^2 + 2\gamma_1 D_1 x_1}{-2\gamma_1^2(\gamma_1 x_1 + 2D_1)} \approx -\frac{1}{2}\frac{x_1}{\gamma_1}$$

Similarly, in Eq. (19), given that $\exp\left(\frac{\gamma_1 x_1}{D_1}\right) \approx 0$, the steady flux velocity at x_1 reduces to:

$$\frac{J_{1eq}}{c_{10}} \approx -\gamma_1$$

Therefore, the dependence of ETC on $\Delta\Psi$ is roughly inversely linear. The steady-state flux is quasi-linear to the DelPhi. Although the procedure yields fairly complex expressions (Eqs. 18 and 19), in the physiological range, a simple dependence on $\gamma_1 = u_1 a_1$ (see Eqs. (8) and (13)) results (Fig. 3).

Multi-layer model

Here, the skin is assumed to be composed of three main layers, the SC, the viable epidermis, and the dermis (Fig. 4). The model parameters are given in Table 1. In the absence of direct measurements, indirect data are inferred from previous studies in literature [22, 23]. Diffusivities depend on the type and size of the transported molecules and are affected of a high degree of uncertainty. Representative values of partition coefficients are listed [21, 24]. The $K_{2,3}$ value of 1.0 was selected because

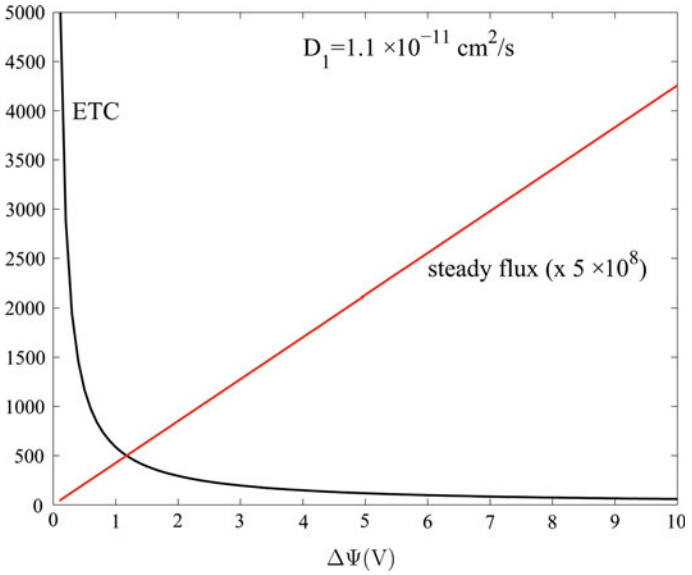

Fig. 3 The near-linear inverse dependence of ETC and the quasi-linear dependence for steady flux J_{1eq}/c_{10} on $\Delta\Psi$ (case one-layer). A similar trend is reported for varying D_1, at a fixed $\Delta\Psi$

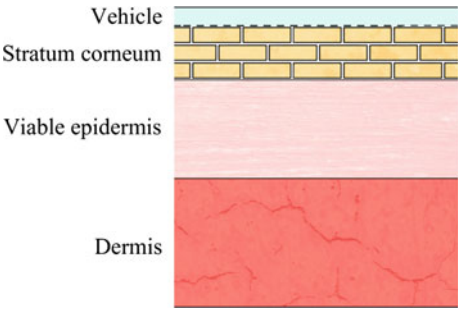

Fig. 4 A schematic section representing the three-layer model (figure not to scale)

Table 1 The parameters used in the simulations for the three-layer model

—	Stratum corneum (SC) (1)	Viable epidermis (2)	Dermis (3)
$l_i = x_i - x_{i-1}$ (cm)	1.75×10^{-3}	3.5×10^{-3}	0.11
D_i (cm^2/s)	10^{-10}	10^{-7}	10^{-7}
σ_i (S/cm)	10^{-7}	10^{-4}	10^{-4}
$K_{i-1,i}$	0.01	2.2	1.0

Table 2 The ETC and steady flux as a function of different currents with $D_1 = 10^{-11}\,\mathrm{cm}^2/\mathrm{s}, D_2 = 10^{-7}\,\mathrm{cm}^2/\mathrm{s}, D_3 = 10^{-7}\,\mathrm{cm}^2/\mathrm{s}$

$\Delta\Psi(V)$	$a_1/a_2/a_3$ (V/cm)	ETC(s)	J_{1eq}/c_{10} (cm/s)
0	0/0/0	5.41×10^4	5.71×10^{-7}
1.0	$-538.1/-0.54/-0.54$	3.89×10^4	2.08×10^{-5}
1.5	$-807.2/-0.81/-0.81$	1.22×10^4	3.12×10^{-5}
1.7	$-914.8/-0.91/-0.91$	8.00×10^3	3.54×10^{-5}
2.0	$-1076.3/-1.08/-1.08$	4.10×10^3	4.16×10^{-5}

Table 3 The ETC and steady flux as a function of different diffusivities with $\Delta\Psi = 1.0\,V$

D_1 ($\mathrm{cm}^2\mathrm{s}^{-1}$)	D_2 ($\mathrm{cm}^2\mathrm{s}^{-1}$)	D_3 ($\mathrm{cm}^2\mathrm{s}^{-1}$)	ETC(s)	J_{1eq}/c_{10} (cm/s)
10^{-11}	10^{-7}	10^{-7}	3.89×10^4	2.08×10^{-5}
2.0×10^{-11}	2.0×10^{-7}	2.0×10^{-7}	1.94×10^4	4.16×10^{-5}
3.0×10^{-11}	3.0×10^{-7}	3.0×10^{-7}	1.30×10^4	6.25×10^{-5}
4.0×10^{-11}	4.0×10^{-7}	4.0×10^{-7}	9.73×10^3	8.33×10^{-5}

the viable epidermis is usually treated as an aqueous tissue nearly equivalent to the dermis [25]. The coefficients a_i of the potential ϕ_i in Eq. (28) have the following expressions:

$$a_1 = -\frac{\Delta\Psi\sigma_2\sigma_3}{G} \qquad a_2 = -\frac{\Delta\Psi\sigma_1\sigma_3}{G} \qquad a_3 = -\frac{\Delta\Psi\sigma_1\sigma_2}{G}$$

where $G = l_3\sigma_1\sigma_2 + l_1\sigma_3(\sigma_2 - \sigma_1) + l_2\sigma_1(\sigma_3 - \sigma_2)$ and $\Delta\Psi = \Psi_0 - \Psi_1$.

The results are shown in Tables 2 and 3. As in the one-layer case, an electrical current—as well as increasing layer diffusivities—promotes a more effective release and enhances the drug flux in a nearly linear way, leading a reduced ETC. Nevertheless, since the thicknesses and compositions of the tissues are different in the one- and three-layer cases, the numerical values of ETC and flux are not directly comparable.

Although the model parameters are subject to some degree of uncertainty, estimation of the ETC is an important tool that can be applied for the successful release of new molecules and the improved delivery of conventional drugs.

8 Conclusions

The dynamic behavior of a finite physical system can often be described by a single relaxation time constant. In this chapter we have defined such an effective time constant as a design tool for transdermal drug release, possibly enhanced by iontophoresis. As a single index of release performance, the ETC has the advan-

tage that it can be evaluated from Laplace transforms without the need of explicit inversions, and can be used to describe the different effective speeds of relaxation of an extended system. Although closed-form expressions of ETC are not always easy to obtain and analyze, ETC has been derived and computed for two case studies: the transdermal drug delivery in one-layer and multi-layer models, with convection terms present in the case of electrically-assisted release.

References

1. M. Prausnitz, R. Langer, Transdermal drug delivery. Nat. Biotech. **26**, 1261–1268 (2008)
2. O. Perumal, S. Murthy, Y. Kalia, Tuning theory in practice: the development of modern transdermal drug delivery systems and future trends. Skin Pharm. Physiol. **26**, 331–342 (2013)
3. H. Trommer, R. Neubert, Overcoming the stratum corneum: the modulation of skin penetration. Skin Pharmacol. Physiol. **19**, 106–121 (2006)
4. S. Becker, B. Zorec, D. Miklavčič, N. Pavšelj: Transdermal transport pathway creation: electroporation pulse order. Math. Biosci. **257**, 60–68 (2014)
5. Y.N. Kalia, A. Naik, J. Garrison, R.H. Guy, Iontophoretic drug delivery. Adv. Drug Deliv. Rev. **56**, 619–658 (2004)
6. G. Pontrelli, F. de Monte, A two-phase two-layer model for transdermal drug delivery and percutaneous absorption. Math. Biosci. **257**, 96–103 (2014)
7. L. Simon, Timely drug delivery from controlled-release devices: Dynamic analysis and novel design concepts. Math. Biosci. **217**, 151–158 (2009)
8. Y.N. Kalia, R.H. Guy, Modeling transdermal drug release. Adv. Drug Del. Rev. **48**, 159–172 (2001)
9. L. Simon, A.N. Weltner, Y. Wang, B. Michniak, A parametric study of iontophoretic transdermal drug-delivery systems. J. Membr. Sci. **278**, 124–132 (2006)
10. T. Gratieri, Y. Kalia, Mathematical models to describe iontophoretic transport in vitro and in vivo and the effect of current application on the skin barrier. Adv. Drug Deliv. Rev. **65**, 315–329 (2013)
11. G. Pontrelli, F. de Monte, A multi-layer porous wall model for coronary drug-eluting stents. Int. J. Heat Mass Trans. **53**, 3629–3637 (2010)
12. G. Pontrelli, M. Lauricella, J.A. Ferreira, G. Pena, Iontophoretic transdermal drug delivery: a multi-layered approach. Math. Med. Biol. online (2016)
13. R. Collins, The choice of an effective time constant for diffusive processes in finite systems. J. Phys. D Appl. Phys. **13**, 1937–1947 (1980)
14. M.A. Ashburn, L.L. Ogden, J. Zhang, G. Love, S.V. Basta, The pharmacokinetics of transdermal fentanyl delivered with and without controlled heat. J. Pain **4**, 291–297 (2003)
15. L. Simon, Analysis of heat-aided membrane-controlled drug release from a process control perspective. Int. J. Heat Mass Trans. **50**, 2425–2433 (2007)
16. Y. Song, S.K. Li, K.D. Peck, H. Zhu, A. Ghanem, W.I. Higuchi, Human epidermal membrane constant conductance iontophoresis: alternating current to obtain reproducible enhanced permeation and reduced lag times of a nonionic polar permeant. Int. J. Pharm. **232**, 45–57 (2002)
17. A. Luzardo-Alvarez, M.B. Delgado-Charro, J. Blanco-Mendez, Iontophoretic delivery of ropinirole hydrochloride: effect of current density and vehicle formulation. Pharm. Res. **18**, 1714–1720 (2001)
18. A.K. Nugroho, O. Della Pasqua, M. Danhof, J.A. Bouwstra, Compartmental modeling of transdermal iontophoretic transport II: in vivo model derivation and application. Pharm. Res. **22**, 335–346 (2005)
19. L. Simon, *Control of Biological and Drug-Delivery Systems for Chemical, Biomedical, and Pharmaceutical Engineering* (Wiley, Hoboken, NJ, 2013)

20. Y.G. Anissimova, Mathematical models for skin toxicology. Expert Opin. Drug Metab. Toxicol. **10**, 551–560 (2014)
21. K. Tojo, *Mathematical models of transdermal and topical drug delivery* (Biocom Systems Inc., Fukuoka, Japan, 2005)
22. P.F. Millington, R. Wilkinson, Skin Cambridge University Press, 2009
23. S. Becker, Transport modeling of skin electroporation and the thermal behavior of the stratum corneum. Int. J. Thermal Sci. **54**, 48–61 (2012)
24. M. Fernandes, L. Simon, N.W. Loney, Mathematical modeling of transdermal drug deliverysystems: analysis and applications. J. Membr. Sci. **256**, 184–192 (2005)
25. J.M. Nitsche, G.B. Kasting, A microscopic multiphase diffusion model of viable epidermis permeability. Biophys. J. **104**, 2307–2320 (2013)

Part II
Cardiovascular Medicine

Multiscale Multiphysic Approaches in Vascular Hemodynamics

Michael Neidlin, Tim A.S. Kaufmann, Ulrich Steinseifer and Thomas Schmitz-Rode

Abstract Vascular hemodynamics are an important part of many medical and engineering applications. The advances in imaging technologies, modeling methods and the increasing computational power allow for sophisticated in-depth studies of the fluid dynamical behavior of blood. The integration of patient-specific geometries, the consideration of dynamical boundary conditions and the interaction between fluid and solid structures play the major role in all numerical modeling frameworks. The following chapter gives a brief summary on each of these topics providing a concise guideline for the interested modeler. In the end three applications are provided. Studies on Fluid-Structure-Interaction in the aortic arch, multiscale CFD simulations of heart support and the vascular hemodynamics in the cerebral arteries (Circle of Willis) are shown. The cases are chosen to emphasize the emerging complexity of fluid dynamics in biological systems and the methods to tackle these obstacles.

1 Introduction

The fluid mechanics of blood play a major role in many problems of biomedical engineering. Medical devices such as stents, heart valves and pumps are in constant contact with blood and therefore need to be carefully designed with respect to their influence on the flow field. Another important question is the blood flow through parts of the human vascular system. Hereby the interaction with these devices may be of interest. Further on, investigations of various physiological and pathological scenarios increases the understanding of the underlying mechanisms and ultimately help improving the clinical outcome.

From the numerical modeling viewpoint there are several aspects which need to be considered. First of all, the investigated geometries are rather complex and

M. Neidlin (✉) · T.A.S. Kaufmann · U. Steinseifer · T. Schmitz-Rode
Department of Cardiovascular Engineering, Institute of Applied Medical Engineering, Helmholtz Institute, RWTH Aachen University, Aachen, Germany
e-mail: michael.neidlin@rwth-aachen.de

P. Wriggers and T. Lenarz (eds.), *Biomedical Technology*, Lecture Notes in Applied and Computational Mechanics 84, DOI 10.1007/978-3-319-59548-1_5

exhibit high variability. As patient specific considerations gain more and more importance, (non-invasive) imaging techniques need to be incorporated in the model creation process. Secondly, boundary conditions need to be defined carefully with respect to the cardiovascular system as a whole. Finally, vessel elasticity and wall movement address the need of fluid-structure interaction (FSI) simulations.

This book chapter gives a concise overview of the current methods and challenges in the field of vascular hemodynamics with a focus on clinical application. It should be seen as a starting point for a numerical modeler interested in these scientific questions. The explanations do not claim to be exhaustive. In the second part, some examples of these methods are presented.

2 Geometry Creation and General Simulation Settings

As stated in the introduction, patient specificity is of course defined by the input data of the geometric anatomy. Non-invasive imaging techniques such as magnetic resonance imaging (MRI) and computer tomography (CT) are the common data sources. The geometry is created by surface reconstruction from these grayscale images. Semi-automated processes as region growing algorithms increase the model creation speed. Some exemplary applications can be found in [1, 7–9]. However the error probability can be quiet high in low-resolution imaging or the visualization of moving objects like heart valves. Feedback from clinicians at this stage can omit unrealistic geometrical representations and improve the meaningfulness of the acquired results.

After model creation the meshing is usually done by unstructured tetrahedral elements. As wall shear stress plays a major role in almost all clinical questions, the boundary layer needs to be carefully represented by prismatic elements. The shear-thinning behavior of blood can be expressed by the appropriate material models (Power-law, Carreau-model etc.). However, these phenomenological models are based on experimental data. Especially in the low shear regime $<5\ s^{-1}$ the model predictions show limitations. An a priori estimation of the shear rates can help to judge whether a non-Newtonian blood model is necessary. At last, turbulent effects need to be considered in the simulations. Comparison of a peak Reynolds number with a critical Reynolds number (Eq. 1) is a possible approach Peacock et al. [14]

$$Re_{peak,\,c} = 169\alpha^{0.83} St^{-0.27} \tag{1}$$

With α as the Womersley number and St as the Strouhal number. In case of turbulence the Shear Stress Transport model is a common RANS description.

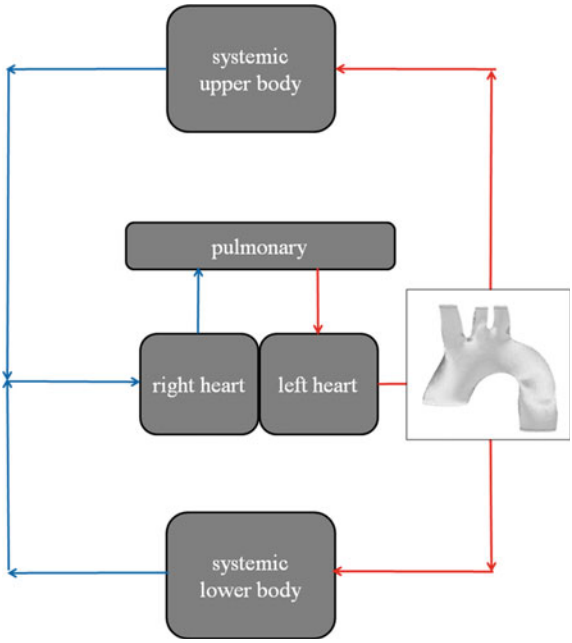

Fig. 1 Aortic arch in a simplified model of the cardiovascular system

3 Boundary Conditions

As we are only able to consider a selected region of interest of the cardiovascular system, regarding its pathological-anatomical specific features, (mostly a piece of the bigger sized arteries or veins), the question arises how to include the remaining part of the circulation.

Figure 1 shows the 3-D model of the aortic arch embedded in the entire cardiovascular system. It is evident, that one should try and model the system as a closed-loop to get a realistic simulation. With a multiscale description it is possible to solve this problem. At first, we model the entire cardiovascular circulation as a 0-D lumped parameter (LP) network leading to a system of ordinary differential equations (ODE). Then the ODEs are coupled to the fluid solver to combine the high resolution of computational fluid dynamics (CFD) with the overall dynamical behavior. The final model is adaptable to patient specific measurements of pressures and flows in the various parts of the cardiovascular system. Further on pathologies like valve insufficiencies, hypertension or diminished autoregulation capabilities can be represented by adjustments of the lumped parameters.

3.1 Lumped Parameter Modeling

Basically LP modeling uses elements of hydraulic circuits such as resistances, capacitors and inductances to express the flow resistance, the vessel compliance and the inertance of the blood. The so-called Windkessel models describe the combination of these elements to express the pressure/flow relationship of an elastic vessel segment. There has been extensive research on Windkessel modeling and on LP modeling of the cardiovascular system [4, 10, 13, 17]. The reader is referred to these works for more information.

A very simple case, a resistance with a capacitor (two-element Windkessel), is presented in Eqs. 2a and 2b:

$$Q_{out} = \frac{p_i - p_{i+1}}{R_i} \tag{2a}$$

$$\frac{dp_i}{dt} = \frac{Q_{in} - Q_{out}}{C_i} \tag{2b}$$

Q_{in} and Q_{out} are the incoming and outgoing flows into the compartment i (R_i and C_i). p_i and p_{i+1} are the pressures of the corresponding and the downstream compartment, respectively. This procedure is repeated for every block of the cardiovascular circulation, until there is a coupled system of ODEs. Elements as valves, cardiac chambers and coronary arteries have more sophisticated descriptions than Eqs. 2a and 2b. Again [10] give a thorough explanation.

3.2 0-D/3-D Coupling

The coupling between LP and CFD is achieved with the consolidated approach from [12] by an interchange of flows (CFD) and pressures (LP) at the boundary faces. At each timestep the flows Q_i across the boundaries are calculated by the CFD solver and serve as the input for the LP model. The ODE system is solved and the interface pressures are imposed as uniformly distributed pressure boundary conditions in the CFD solver.

4 Fluid-Structure-Interaction

There are mainly two approaches to perform a two-way coupled FSI simulation, the monolithic and the partitioned approach. The monolithic approach solves the fluid and solid domain simultaneously within the same solver and thus by using one set of equations, resulting in relatively stable simulations. The downside is the rather complicated formulation of the equations.

The second approach for FSI simulations is the partitioned approach, in which the fluid and solid domain are solved separately with two different solvers and the information between both systems is transferred through a domain interface. The CFD solver calculates the solution of the fluid domain and thereby also the load on the fluid-solid interface. The structural solver receives the load and calculates the displacement of the vessel wall, which is transferred back to the fluid domain. This procedure is one iteration loop and is repeated until the loading and the displacement are converged. The main challenge is the instability of the simulations due to the explicit nature of the fluid and structural iterations.

This means that displacements of the interface are not included in the fluid domain and the fluid pressures are not considered in the structural domain during each stagger iteration [3, 16]. After each iteration loop the differences of the calculated interface displacements lead to large pressure gradients in the incompressible fluid domain and destabilize the computations. This is known as the "artificial added-mass instability" [2, 6, 11] and can occur in fluid-structure interactions of an incompressible fluid with a slender flexible structure.

To overcome this obstacle the interface artificial compressibility method, which has been introduced by Degroote et al. [3] can be applied. Hereby, an additional source term in the continuity equations for elements adjacent to the interface imitates the structural displacement and dampens out the arising disturbances. With progressing iteration loops the displacement differences vanish and both solvers converge. The choice of an appropriate time step is critical to achieve a stable coupling scheme and two contrasting factors need to be considered. First of all, the time step has to be small enough to limit the fluid pressure changes. Secondly, and counterintuitively, the "artificial added-mass instability" increases with a decreasing time step.

As the displacements of the interface deform the elements in the fluid domain, changes in mesh quality need to be considered. A possibility to maintain high mesh quality and prevent folding of mesh elements is to adapt the mesh stiffness (or mesh diffusivity) such that the deformation is compensated by less skewed elements. Another approach is adaptive remeshing of highly deformed mesh regions. This numerically expensive option should only be considered if the deformations are too high to be compensated by an increase of mesh stiffness.

4.1 0-D/3-D Coupling of FSI Simulations

The coupling of an LP network to the FSI domain works with the same procedure as for the CFD domain. One additional aspect is the reflection of pressure waves and the unrealistic structural deformations [5, 15]. As a solution an additional resistance representing the characteristic impedance of the truncated artery can be included in the LP network. With this modification the incoming pressure wave is absorbed at the 3-D/0-D interface. The characteristic impedance can be calculated from geometrical dimensions (inertance L) and material properties (compliance C) according to Eq. 3:

$$Z_c = \sqrt{\frac{L}{C}} \tag{3}$$

5 Examples

5.1 An FSI Model of Cardiopulmonary Bypass with Cerebral Autoregulation

Neurological complications often occur during cardiopulmonary bypass (CPB). Hypoperfusion of brain tissue due to diminished cerebral autoregulation (CA), atherosclerotic disease and consecutive thromboembolism reduce the cerebral oxygen supply and increase the risk of perioperative stroke. To improve the outcome of cardiac surgery, patient-specific FSI models can be used to investigate the blood flow during CPB. In this study, a computational model of CPB which includes cerebral autoregulation and movement of aortic walls on the basis of in vivo measurements is established.

First, the Baroreflex mechanism, which plays a leading role in CA, is represented with a 0-D control circuit. The model parameters are assessed with respect to their physiological meaning and their influence on the cerebral blood flow (CBF). Pathologies like hypertension or impaired autoregulation can be expressed by the adjustment of the parameters. Further on, the effect of drugs on the static and dynamic behavior of the Baroreflex can be reproduced.

Additionally a two-way coupled fluid-structure interaction (FSI) model with CA is set up. The wall shear stress (WSS) distribution is computed for the whole FSI domain and a comparison to rigid wall CFD is made. Constant flow and pulsatile flow CPB is considered.

Rigid wall CFD delivers higher wall shear stress values than FSI simulations, especially during pulsatile perfusion. The flow rates through the supraaortic vessels are almost not affected, if considered as percentages of total cannula output. The developed multiphysic multiscale framework (Fig. 2) allows deeper insights into the underlying mechanisms during CPB on a patient-specific basis.

5.2 A CFD Model of VAD Support Using Closed-Loop Multiscale Simulations to Evaluate Various Cannulation Strategies

Left ventricular assist devices (LVADs) are a common therapy for end-stage heart failure patients. As the heart cannot supply enough blood into the systemic circulation, a blood pump is put in parallel to the left ventricle to unload the heart and

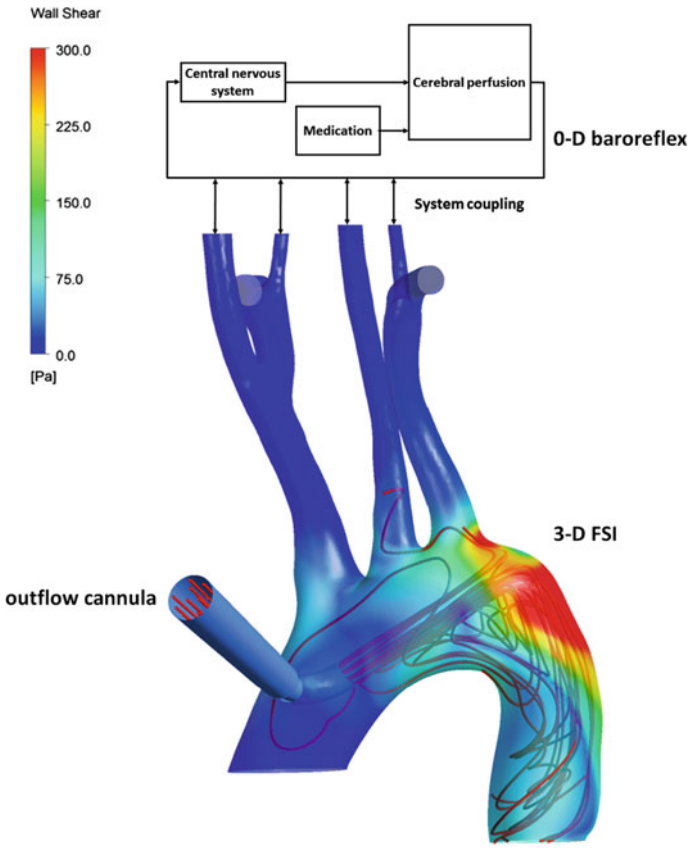

Fig. 2 0-D model of cerebral autoregulation coupled to a 3-D FSI model of the aortic arch. Streamlines and wall shear stress distribution during cardiopulmonary bypass

increase the blood flow. One open question investigates the positioning of the outflow cannula in the aortic arch. Several techniques as ascending or descending aortic grafting exist, which have an influence on the hemodynamics in the aortic arch and on the therapy outcome. A CFD model which takes the patient specific variability and the interaction between cardiac function and pump speed needs an addition of a lumped parameter model to the 3-D domain.

The cardiovascular system is divided into twelve compartments describing the systemic and pulmonary circulation, the four heart chambers and the coronary arteries. Further on, the VAD is modeled as a pressure and rotational speed dependent flow source. The entire model with exemplary results is shown in Fig. 3.

Physiological non-heart failure (NHF) and pathological heart failure (HF) conditions can be set by decreasing the elastance of the left ventricle. The effect is seen in the left ventricular pressure-volume loop. Reduced elastance decreases the stroke volume and the aortic pressure from 120/80 mmHg to 80/60 mmHg. VAD support

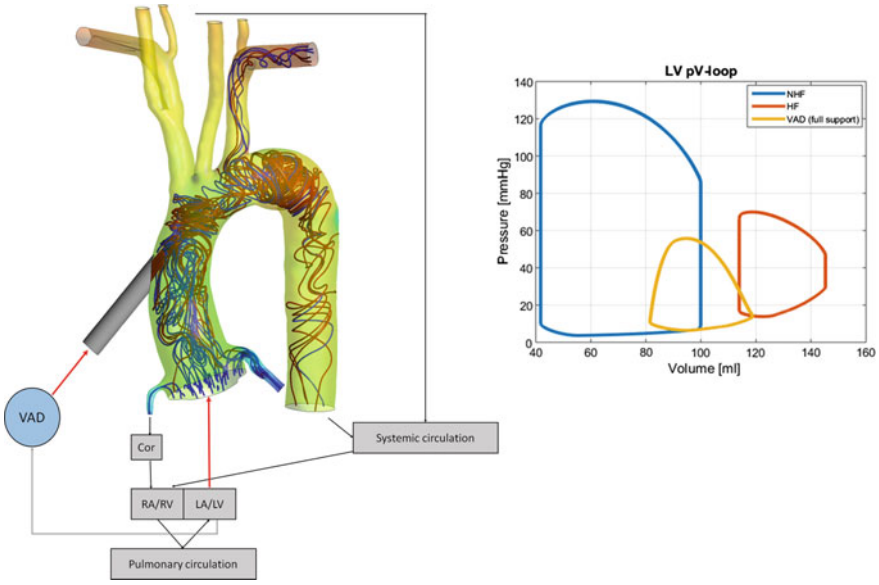

Fig. 3 *Left* multiscale model of aortic flow during VAD support. *Right Left* ventricular pV-loop during physiologic (*blue*), pathologic (*red*) and LVAD full support (*yellow*)

(in constant flow full support conditions) reduces the ventricular afterload and pulsatility and increases the blood flow from 3 l/min to 5 l/min (results not shown). This behavior has also been observed in several in vitro and in vivo studies. With this numerical framework the position of the outflow cannula can be varied to see its effect on the hemodynamics in the aortic arch.

5.3 A Numerical Framework to Investigate Hemodynamics During Endovascular Mechanical Recanalization in Acute Stroke

Ischemic stroke, caused by embolism of cerebral vessels is accompanied by high morbidity and mortality. Endovascular aspiration of the blood clot is an interventional technique for the recanalization of the occluded arteries. However, the hemodynamics in the Circle of Willis (CoW) is not completely understood, which results in medical misjudgment and complications during surgical intervention. In this study a multiscale description of cerebral hemodynamics during aspiration thrombectomy is established.

First, the CoW is modeled as a 1-D pipe network on the basis of CT angiography (CTA) scans and different vascular configurations are investigated regarding the overall flow distribution in the arterial network (Fig. 4, center)

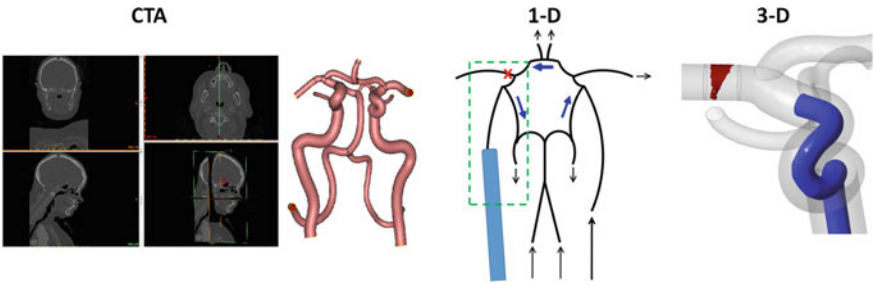

Fig. 4 1-D/3-D representation of aspirational thrombectomy. Geometry extraction (*left*), 1-D model (*center*), 3-D multiphase thrombus aspiration (*right*)

Afterwards, a vascular occlusion is placed in the middle cerebral artery and the relevant section of the CoW is transferred to a 3-D computational fluid dynamic (CFD) domain. A suction catheter in different positions is included in the CFD simulations. The boundary conditions of the 3-D domain are taken from the 1-D domain to ensure system coupling. An Eulerian-Eulerian multiphase simulation describes the process of thrombus aspiration (Fig. 4, right).

The physiological blood flow in the 1-D and 3-D domain is validated with literature data. Further on, it is proven that domain reduction and pressure coupling at the boundaries is an appropriate method to reduce computational costs.

6 Conclusion

Vascular hemodynamics play an important role in many research areas of biomedical engineering. The presented methodology can of course be extended to other problems. As patient-specific models play an important role in current investigations, the behavior of the entire system should be taken into account. With a combination of lumped parameter and 3-D models it is now not only possible to look beyond one patient condition (geometry A with boundary conditions B), but to cover several scenarios which include different pathologies, the effect of medication and the remodeling of the system. Multiple projects which deal with patient cohort measurements can serve as a valuable source to combine the different scales of numerical modeling to draw to new and insightful conclusions. As computational power increases multiphysic approaches, which are right now still numerically expensive, will become increasingly important.

References

1. A. Assmann, A.C. Benim, F. Guel, P. Lux, P. Akhyari, U. Boeken, F. Joos, P. Feindt, A. Lichtenberg, Pulsatile extracorporeal circulation during on-pump cardiac surgery enhances aortic wall shear stress. J. Biomech. **45**(1), 156–163 (2012)
2. P. Causin, J. Gerbeau, F. Nobile, Added-mass effect in the design of partitioned algorithms for fluid structure problems. Comput. Methods Appl. Mech. Eng. **194**(42), 4506–4527 (2005)
3. J. Degroote, P. Bruggeman, R. Haelterman, J. Vierendeels, Stability of a coupling technique for partitioned solvers in FSI applications. Comput. Struct. **86**(23), 2224–2234 (2008)
4. G. Ferrari, M. Kozarski, K. Zielinski, L. Fresiello, A. Di Molfetta, K. Górczynska, K.J. Pako, M. Darowski, A modular computational circulatory model applicable to vad testing and training. J. Artif. Org. **15**(1), 32–43 (2012)
5. L. Formaggia, A. Moura, F. Nobile, On the stability of the coupling of 3D and 1D fluid-structure interaction models for blood flow simulations ESAIM. Math. Modell. Numer. Anal. **41**(04), 743–769 (2007)
6. C. Förster, W.A. Wall, E. Ramm, The artificial added mass effect in sequential staggered fluid-structure interaction algorithms, in *Prooceedings European Conference on Computational Fluid Dynamics ECCOMAS CFD*, 2006
7. I. Fukuda, S. Osanai, M. Shirota, T. Inamura, H. Yanaoka, M. Minakawa, K. Fukui, Computer-simulated fluid dynamics of arterial perfusion in extracorporeal circulation: from reality to virtual simulation. Int. J. Artif. Org. **32**(6), 362–370 (2009)
8. B. Ji, A. Undar, An evaluation of the benefits of pulsatile versus nonpulsatile perfusion during cardiopulmonary bypass procedures in pediatric and adult cardiac patients. ASAIO J. **52**(4), 357–361 (2006)
9. T.A.S. Kaufmann, M. Hormes, M. Laumen, D.L. Timms, T. Schmitz-Rode, A. Moritz, O. Dzemali, U. Steinseifer, Flow distribution during cardiopulmonary bypass in dependency on the outflow cannula positioning. Artif. Org. **33**(11), 988–992 (2009)
10. T. Korakianitis, Y. Shi, A concentrated parameter model for the human cardiovascular system including heart valve dynamics and atrioventricular interaction. Med. Eng. Phys. **28**(7), 613–628 (2006)
11. P. Le Tallec, J. Mouro, Fluid structure interaction with large structural displacements. Comput. Methods Appl. Mech. Eng. **190**(24), 3039–3067 (2001)
12. F. Migliavacca, R. Balossino, G. Pennati, G. Dubini, T.-Y. Hsia, M.R. de Leval, E.L. Bove, Multiscale modelling in biofluidynamics: application to reconstructive paediatric cardiac surgery. J. Biomech. **39**(6), 1010–1020 (2006)
13. J.T Ottesen, M.S. Olufsen, J.K. Larsen, *Applied Mathematical Models in Human Physiology*, *Society for Industrial and Applied Mathematics* (2004)
14. J. Peacock, T. Jones, C. Tock, R. Lutz, The onset of turbulence in physiological pulsatile flow in a straight tube. Exp. Fluids **24**(1), 1–9 (1998)
15. P. Reymond, P. Crosetto, S. Deparis, A. Quarteroni, N. Stergiopulos, Physiological simulation of blood flow in the aorta: comparison of hemodynamic indices as predicted by 3-D FSI, 3-D rigid wall and 1-D models. Med. Eng. Phys. **35**(6), 784–791 (2013)
16. S.J. Sonntag, T.A. Kaufmann, M.R. Büsen, M. Laumen, T. Linde, T. Schmitz-Rode, U. Steinseifer, Simulation of a pulsatile total artificial heart: development of a partitioned fluid structure interaction model. J. Fluids Struct. **38**, 187–204 (2013)
17. N. Westerhof, J.-W. Lankhaar, B.E. Westerhof, The arterial windkessel. Med. Biol. Eng. Comput. **47**(2), 131–141 (2009)

Heart Valve Flow Computation with the Space–Time Slip Interface Topology Change (ST-SI-TC) Method and Isogeometric Analysis (IGA)

Kenji Takizawa, Tayfun E. Tezduyar, Takuya Terahara and Takafumi Sasaki

Abstract We present a heart valve flow computation with the Space–Time Slip Interface Topology Change (ST-SI-TC) method and Isogeometric Analysis (IGA). The computation is for a realistic heart valve model with actual contact between the valve leaflets. The ST-SI-TC method integrates the ST-SI and ST-TC methods in the framework of the ST Variational Multiscale (ST-VMS) method. The ST-VMS method functions as a moving-mesh method, which maintains high-resolution boundary layer representation near the solid surfaces. The ST-TC method was introduced for moving-mesh computation of flow problems with TC, such as contact between the leaflets of a heart valve. It deals with the contact while maintaining high-resolution representation near the leaflet surfaces. The ST-SI method was originally introduced to addresses the challenge involved in high-resolution representation of the boundary layers near spinning solid surfaces. The mesh covering a spinning solid surface spins with it, and the SI between that mesh and the rest of the mesh accurately connects the two sides. This maintains the high-resolution representation near solid surfaces. In the context of heart valves, the SI connects the sectors of meshes containing the leaflets, enabling a more effective mesh moving. In that context, the ST-SI-TC method enables high-resolution representation even when the contact is between leaflets that are covered by meshes with SI. It also enables dealing with contact location change or contact and sliding on the SI. With IGA, in addition to having a more accurate representation of the surfaces and increased accuracy in the flow solution, the element density in the narrow spaces near the contact areas is kept at a reasonable level. Furthermore, because the flow representation in the contact area has a wider support in IGA, the flow computation method becomes more robust. The computation we present for an aortic-valve model shows the effectiveness of the ST-SI-TC-IGA method.

K. Takizawa (✉) · T. Terahara · T. Sasaki
Department of Modern Mechanical Engineering, Waseda University,
1-6-1 Nishi-Waseda, Shinjuku-ku, Tokyo 169-8050, Japan
e-mail: Kenji.Takizawa@tafsm.org

T.E. Tezduyar
Mechanical Engineering, Rice University, 6100 Main Street, Houston,
TX 77005, USA

P. Wriggers and T. Lenarz (eds.), *Biomedical Technology*, Lecture Notes in Applied and Computational Mechanics 84, DOI 10.1007/978-3-319-59548-1_6

1 Introduction

Heart valve flow computation is challenging because it requires accurate representation of boundary layers near moving solid surfaces, including the valve leaflet surfaces, even when the leaflets come into contact. In computation of flows with moving boundaries and interfaces (MBI), accurate representation of boundary layers near moving solid surfaces requires moving-mesh (interface-tracking) methods, where the fluid mesh moves to follow (track) the fluid–solid interfaces, enabling us to control the mesh resolution near the interface and have high-resolution representation of the boundary layers.

The Space–Time Variational Multiscale (ST-VMS) method [1, 2], which is the core computational method we are using here in addressing the challenges of heart valve flow computation, is a moving-mesh method. It was introduced mainly for fluid–structure interactions (FSI) and, in a more general context, for MBI. It is the VMS version of the Deforming-Spatial-Domain/Stabilized ST (DSD/SST) method [3–5], with the VMS components coming from the residual-based VMS (RBVMS) method [6–9]. The stabilization components of the original DSD/SST method are the Streamline-Upwind/Petrov-Galerkin (SUPG) [10] and Pressure-Stabilizing/Petrov-Galerkin (PSPG) [3] stabilizations, and for that the method is also called "ST-SUPS." Functionally, the ST-VMS method can be seen as an augmented version of the ST-SUPS method, with two additional stabilization terms beyond the three of the ST-SUPS method, or the ST-SUPS method can be seen as a reduced version of the ST-VMS method.

The ALE-VMS method [11, 12], first presented in [13], is the VMS version of the Arbitrary Lagrangian–Eulerian (ALE) finite element method [14], which is a more commonly used moving-mesh method. The RBVMS and ALE-VMS methods have been successfully used for different types of FSI, MBI and fluid mechanics problems (see, for example, [12, 13, 15–39]).

The ST-SUPS and ST-VMS methods have also been successfully used for different classes of FSI, MBI and fluid mechanics problems. The classes of problems include spacecraft parachute FSI [24, 40–44], wind-turbine aerodynamics [20, 24, 28, 40, 45–49], flapping-wing aerodynamics [24, 40, 48, 50–56], cardiovascular fluid mechanics [40, 48, 54, 57–61], spacecraft aerodynamics [62, 63], thermo-fluid analysis of ground vehicles and their tires [64], thermo-fluid analysis of disk brakes [65], flow-driven string dynamics in turbomachinery [66], flow analysis of the turbine part of a turbocharger [67], flow around a tire with road contact and deformation [68], and ram-air parachutes [69].

The challenges associated with using a moving-mesh method in a heart valve flow computation even when the valve leaflets come into contact and create a topology change (TC) in the fluid mechanics domain is addressed with the ST-TC method. The method was introduced in [54]. Even before the ST-TC method, the ST-SUPS and ST-VMS methods, when used with robust mesh update methods, have been proven effective in flow computations where the solid surfaces are in near contact or create other near TC, if the "nearness" is sufficiently "near" for the purpose of solving

the problem. For examples of such computations, see the references mentioned in [54]. Flow computation of heart valves, however, is an example of the class of computations where the "nearness" that can be modeled with a moving-mesh method without actually bringing the surfaces into contact might not be "near" enough. That is because an actual contact is required for blocking the flow when the valve closes. The Fluid–Solid Interface-Tracking/Interface-Capturing Technique (FSITICT) [70] was motivated by that class of problems. In the FSITICT, we track the interfaces wherever and whenever we can with a moving mesh, and capture over that moving mesh the interfaces we cannot track, specifically the interfaces where and when we need to have an actual contact between the solid surfaces. As commented in [61], essentially, the FSITICT is based on giving up on the interface-tracking accuracy in the parts of the domain where and when we expect an actual contact. The FSITICT has been successfully extended in [33] to 3D FSI computation of a bioprosthetic heart valve. In that case the interface-tracking technique was the ALE-VMS method, and the interface-capturing technique was a variational immersed-boundary method, later referred to as the Immersogeometric method in [71].

The ST-TC method does not give up on interface-tracking (moving-mesh) accuracy even when there is an actual contact between solid surfaces or other TC. It can handle an actual TC while maintaining high-resolution boundary layer representation near solid surfaces. The ST-TC method is based on special mesh generation and update, and a master–slave system that maintains the connectivity of the "parent" mesh when there is a TC. The ST-TC method has been successfully applied to 3D computational analysis of heart valve models [61] and wing clapping [56].

Considering that heart valve flow computations involve a high level of geometric complexity, it is desirable to have a good level of freedom in mesh generation and mesh moving. This is accomplished with the ST Slip Interface (ST-SI) method [49]. The method was originally introduced to retain the desirable moving-mesh features of the ST-VMS method when we have spinning solid surfaces, such as a wind-turbine rotor. With the ST-SI method, the mesh covering the spinning solid surface spins with it and we maintain the high-resolution representation of the boundary layers. Earlier methods to accomplish that objective in the ST framework were the Shear–Slip Mesh Update Method (SSMUM) [72–74], which was introduced in [72, 73] and named "SSMUM" in [74], and the ST/NURBS Mesh Update Method (STNMUM), which was introduced in [50–52] and named "STNMUM" in [47]. In the ST-SI method NURBS basis functions can be used for the temporal representation of the spinning motion. With the spinning motion represented by quadratic temporal NURBS basis functions, and with sufficient number of temporal patches for a full rotation, the circular paths associated with the spinning motion can be represented exactly. An added "secondary mapping" [1, 2, 24, 50] enables also specifying a constant angular velocity corresponding to the invariant speeds along those paths. For more on how the ST-SI method compares to the two earlier methods, see [68].

The starting point in the development of the ST-SI method was the version of the ALE-VMS method designed for computations with "sliding interfaces" [23, 75]. This ALE-VMS version has been used successfully in a number of computations with spinning solid surfaces [23, 26, 29, 30, 75]. In the ST-SI method, interface terms similar to those in the ALE-VMS version are added to the ST-VMS formulation to account for the compatibility conditions for the velocity and stress. That way, the SI between the spinning mesh and the rest of the mesh accurately connects the two sides. While having high-resolution representation of the boundary layers near a spinning solid surface, by using NURBS functions in temporal representation of the spinning motion, the ST-SI method has exact representation of the circular paths associated with the spinning. The ST-SI method has been successfully applied to aerodynamic analysis of vertical-axis wind turbines [49], thermo-fluid analysis of disk brakes [65], flow-driven string dynamics in turbomachinery [66], and flow analysis for the turbine part of a turbocharger [67]. In the context of heart valves, the SI connects the sectors of meshes containing the leaflets, enabling a more effective mesh moving.

The "ST-SI-TC" method, introduced in [68], integrates the ST-SI and ST-TC methods in the ST-VMS framework. The initial target was to enable accurate flow analysis when we have a spinning solid surface that is in contact with a solid surface. In that context, the ST-SI-TC method was successfully applied to flow around a tire with road contact and deformation [68]. In the context of heart valves, the ST-SI-TC method enables high-resolution representation of boundary layers even when the contact is between leaflets that are in mesh sectors connected by SIs. It also enables dealing with contact location change or contact and sliding on the SI, which of course can also be encountered in the context of spinning solid surfaces.

The RBVMS test computations in [8] with the Isogeometric Analysis (IGA) [15] showed that using quadratic or cubic NURBS basis functions in space significantly improves the solution accuracy compared to the finite element analysis with trilinear basis functions. Computations with the ST-VMS method and ST-IGA (with NURBS basis functions in space) were first reported in [1] in a 2D context. The ST-IGA method has been successfully applied to flow analysis of the turbine part of a turbocharger [67] and ram-air parachutes [69]. In this paper, we integrate the ST-SI-TC and ST-IGA methods. The "ST-SI-TC-IGA" method, beyond enabling a more accurate representation of the surfaces and increased accuracy in the flow solution, keeps the element density in the narrow spaces near the contact areas at a reasonable level. When solid surfaces come into contact, the elements between the surface and the SI collapse. Before the elements collapse, the boundaries could be curved and rather complex, and the narrow space might have high-aspect-ratio elements. With NURBS elements, we can deal with such adverse conditions rather effectively. Furthermore, because the flow representation in the contact area has a wider support in IGA, the flow computation method becomes more robust.

In Sect. 2 we describe the ST-VMS and ST-SI formulations. The ST-SI-TC-IGA method is described in Sect. 3. A heart-valve flow computation with an aortic-valve model is presented in Sect. 4, and the concluding remarks are given in Sect. 5.

2 ST-VMS and ST-SI Formulations

In this section, we include from [49] the ST-VMS and ST-SI formulations.

2.1 ST-VMS Formulation

The ST-VMS formulation is given as

$$
\begin{aligned}
&\int_{Q_n} \mathbf{w}^h \cdot \rho \left(\frac{\partial \mathbf{u}^h}{\partial t} + \mathbf{u}^h \cdot \boldsymbol{\nabla} \mathbf{u}^h - \mathbf{f}^h \right) \mathrm{d}Q + \int_{Q_n} \boldsymbol{\varepsilon}(\mathbf{w}^h) : \boldsymbol{\sigma}(\mathbf{u}^h, p^h) \mathrm{d}Q \\
&- \int_{(P_n)_{\mathrm{h}}} \mathbf{w}^h \cdot \mathbf{h}^h \mathrm{d}P + \int_{Q_n} q^h \boldsymbol{\nabla} \cdot \mathbf{u}^h \mathrm{d}Q + \int_{\Omega_n} (\mathbf{w}^h)_n^+ \cdot \rho \left((\mathbf{u}^h)_n^+ - (\mathbf{u}^h)_n^- \right) \mathrm{d}\Omega \\
&+ \sum_{e=1}^{(n_{\mathrm{el}})_n} \int_{Q_n^e} \frac{\tau_{\mathrm{SUPS}}}{\rho} \left[\rho \left(\frac{\partial \mathbf{w}^h}{\partial t} + \mathbf{u}^h \cdot \boldsymbol{\nabla} \mathbf{w}^h \right) + \boldsymbol{\nabla} q^h \right] \cdot \mathbf{r}_{\mathrm{M}}(\mathbf{u}^h, p^h) \mathrm{d}Q \\
&+ \sum_{e=1}^{(n_{\mathrm{el}})_n} \int_{Q_n^e} \nu_{\mathrm{LSIC}} \boldsymbol{\nabla} \cdot \mathbf{w}^h \rho r_{\mathrm{C}}(\mathbf{u}^h) \mathrm{d}Q \\
&- \sum_{e=1}^{(n_{\mathrm{el}})_n} \int_{Q_n^e} \tau_{\mathrm{SUPS}} \mathbf{w}^h \cdot \left(\mathbf{r}_{\mathrm{M}}(\mathbf{u}^h, p^h) \cdot \boldsymbol{\nabla} \mathbf{u}^h \right) \mathrm{d}Q \\
&- \sum_{e=1}^{(n_{\mathrm{el}})_n} \int_{Q_n^e} \frac{\tau_{\mathrm{SUPS}}^2}{\rho} \mathbf{r}_{\mathrm{M}}(\mathbf{u}^h, p^h) \cdot \left(\boldsymbol{\nabla} \mathbf{w}^h \right) \cdot \mathbf{r}_{\mathrm{M}}(\mathbf{u}^h, p^h) \mathrm{d}Q \\
&= 0, \qquad (1)
\end{aligned}
$$

where

$$
\mathbf{r}_{\mathrm{M}}(\mathbf{u}^h, p^h) = \rho \left(\frac{\partial \mathbf{u}^h}{\partial t} + \mathbf{u}^h \cdot \boldsymbol{\nabla} \mathbf{u}^h - \mathbf{f}^h \right) - \boldsymbol{\nabla} \cdot \boldsymbol{\sigma}(\mathbf{u}^h, p^h), \qquad (2)
$$

$$
r_{\mathrm{C}}(\mathbf{u}^h) = \boldsymbol{\nabla} \cdot \mathbf{u}^h \qquad (3)
$$

are the residuals of the momentum equation and incompressibility constraint. Here, ρ, $\mathbf{u}$, p, $\mathbf{f}$, $\boldsymbol{\sigma}$, $\boldsymbol{\varepsilon}$, and $\mathbf{h}$ are the density, velocity, pressure, external force, stress tensor, strain rate tensor, and the traction specified at the boundary. The test functions associated with the velocity and pressure are $\mathbf{w}$ and q. A superscript "h" indicates that the function is coming from a finite-dimensional space. The symbol Q_n represents the ST slice between time levels n and $n+1$, $\left(P_n\right)_{\mathrm{h}}$ is the part of the lateral boundary of that slice associated with the traction boundary condition $\mathbf{h}$, and Ω_n is the spatial domain at time level n. The superscript "e" is the ST element counter, and n_{el} is the number of ST elements. The functions are discontinuous in time at each time level,

and the superscripts "−" and "+" indicate the values of the functions just below and just above the time level. There are various ways of defining the stabilization parameters τ_{SUPS} and ν_{LSIC}. See [4, 5, 47, 49, 64] for the stabilization parameter definitions used here. For more ways of calculating the stabilization parameters in finite element computation of flow problems, see [76–97].

The expression for $\mathbf{r}_{\mathrm{M}}(\mathbf{u}^h, p^h)$ includes second derivatives of the velocity. For linear basis functions these terms vanish, and for bilinear and trilinear basis functions they are very much underrepresented. This means that $\mathbf{r}_{\mathrm{M}}(\mathbf{u}^h, p^h)$ does not explicitly depend on the Reynolds number. When we use quadratic or higher-order basis functions, on the other hand, the term is nonzero and therefore explicit dependence of the residual on the Reynolds number is taken into account.

2.2 ST-SI Formulation

2.2.1 Two-Side Formulation

We use the labels "Side A" and "Side B" to represent the two sides of the SI. In the ST-SI formulation, we add boundary terms to Eq. (1). The boundary terms for the two sides are first added separately, using test functions $\mathbf{w}_{\mathrm{A}}^h$ and q_{A}^h and $\mathbf{w}_{\mathrm{B}}^h$ and q_{B}^h. Then, putting together the terms added to each side, the complete set of terms added becomes

$$
\begin{aligned}
&- \int_{(P_n)_{\mathrm{SI}}} \left(q_{\mathrm{B}}^h \mathbf{n}_{\mathrm{B}} - q_{\mathrm{A}}^h \mathbf{n}_{\mathrm{A}}\right) \cdot \frac{1}{2} \left(\mathbf{u}_{\mathrm{B}}^h - \mathbf{u}_{\mathrm{A}}^h\right) \mathrm{d}P \\
&- \int_{(P_n)_{\mathrm{SI}}} \rho \mathbf{w}_{\mathrm{B}}^h \cdot \frac{1}{2} \left(\left(\mathcal{F}_{\mathrm{B}}^h - \left|\mathcal{F}_{\mathrm{B}}^h\right|\right) \mathbf{u}_{\mathrm{B}}^h - \left(\mathcal{F}_{\mathrm{B}}^h - \left|\mathcal{F}_{\mathrm{B}}^h\right|\right) \mathbf{u}_{\mathrm{A}}^h\right) \mathrm{d}P \\
&- \int_{(P_n)_{\mathrm{SI}}} \rho \mathbf{w}_{\mathrm{A}}^h \cdot \frac{1}{2} \left(\left(\mathcal{F}_{\mathrm{A}}^h - \left|\mathcal{F}_{\mathrm{A}}^h\right|\right) \mathbf{u}_{\mathrm{A}}^h - \left(\mathcal{F}_{\mathrm{A}}^h - \left|\mathcal{F}_{\mathrm{A}}^h\right|\right) \mathbf{u}_{\mathrm{B}}^h\right) \mathrm{d}P \\
&+ \int_{(P_n)_{\mathrm{SI}}} \left(\mathbf{n}_{\mathrm{B}} \cdot \mathbf{w}_{\mathrm{B}}^h + \mathbf{n}_{\mathrm{A}} \cdot \mathbf{w}_{\mathrm{A}}^h\right) \frac{1}{2} \left(p_{\mathrm{B}}^h + p_{\mathrm{A}}^h\right) \mathrm{d}P \\
&- \int_{(P_n)_{\mathrm{SI}}} \left(\mathbf{w}_{\mathrm{B}}^h - \mathbf{w}_{\mathrm{A}}^h\right) \cdot \left(\hat{\mathbf{n}}_{\mathrm{B}} \cdot \mu \left(\boldsymbol{\varepsilon}(\mathbf{u}_{\mathrm{B}}^h) + \boldsymbol{\varepsilon}(\mathbf{u}_{\mathrm{A}}^h)\right)\right) \mathrm{d}P \\
&- \gamma \int_{(P_n)_{\mathrm{SI}}} \hat{\mathbf{n}}_{\mathrm{B}} \cdot \mu \left(\boldsymbol{\varepsilon}\left(\mathbf{w}_{\mathrm{B}}^h\right) + \boldsymbol{\varepsilon}\left(\mathbf{w}_{\mathrm{A}}^h\right)\right) \cdot \left(\mathbf{u}_{\mathrm{B}}^h - \mathbf{u}_{\mathrm{A}}^h\right) \mathrm{d}P \\
&+ \int_{(P_n)_{\mathrm{SI}}} \frac{\mu C}{h} \left(\mathbf{w}_{\mathrm{B}}^h - \mathbf{w}_{\mathrm{A}}^h\right) \cdot \left(\mathbf{u}_{\mathrm{B}}^h - \mathbf{u}_{\mathrm{A}}^h\right) \mathrm{d}P, \qquad (4)
\end{aligned}
$$

where

$$\mathcal{F}_{\mathrm{B}}^{h} = \mathbf{n}_{\mathrm{B}} \cdot \left(\mathbf{u}_{\mathrm{B}}^{h} - \mathbf{v}_{\mathrm{B}}^{h}\right), \tag{5}$$

$$\mathcal{F}_{\mathrm{A}}^{h} = \mathbf{n}_{\mathrm{A}} \cdot \left(\mathbf{u}_{\mathrm{A}}^{h} - \mathbf{v}_{\mathrm{A}}^{h}\right), \tag{6}$$

$$h = \frac{h_{\mathrm{B}} + h_{\mathrm{A}}}{2}, \tag{7}$$

$$h_{\mathrm{B}} = 2\left(\sum_{\alpha=1}^{n_{\mathrm{ent}}} \sum_{a=1}^{n_{\mathrm{ens}}} \left|\mathbf{n}_{\mathrm{B}} \cdot \boldsymbol{\nabla} N_a^{\alpha}\right|\right)^{-1} \text{(for Side B)}, \tag{8}$$

$$h_{\mathrm{A}} = 2\left(\sum_{\alpha=1}^{n_{\mathrm{ent}}} \sum_{a=1}^{n_{\mathrm{ens}}} \left|\mathbf{n}_{\mathrm{A}} \cdot \boldsymbol{\nabla} N_a^{\alpha}\right|\right)^{-1} \text{(for Side A)}, \tag{9}$$

$$\hat{\mathbf{n}}_{\mathrm{B}} = \frac{\mathbf{n}_{\mathrm{B}} - \mathbf{n}_{\mathrm{A}}}{\left\|\mathbf{n}_{\mathrm{B}} - \mathbf{n}_{\mathrm{A}}\right\|}. \tag{10}$$

Here, $\left(P_n\right)_{\mathrm{SI}}$ is the SI in the ST domain, $\mathbf{n}$ is the unit normal vector, $\mathbf{v}$ is the mesh velocity, n_{ens} and n_{ent} are the number of spatial and temporal element nodes, N_a^{α} is the basis function associated with spatial and temporal nodes a and α, $\gamma = 1$, and C is a nondimensional constant. From our experience, for our element length definition, usually $C = 1$ is large enough for stability.

A number of remarks were provided in [49] to explain the added terms and to comment on related interpretations. We refer the reader interested in those details to [49].

Remark 1 In [49], the expression given by Eq. (7) was in the form

$$h = \min(h_{\mathrm{B}}, h_{\mathrm{A}}). \tag{11}$$

With the new form in Eq. (7), which was introduced in [68], the expression gives zero value only if the element length is zero on both sides.

Remark 2 The ST-SI method was generalized in [68] by adding a coefficient γ to the sixth integration so that we have the option of using $\gamma = -1$. Using $\gamma = 1$ in a discontinuous Galerkin method was introduced in the symmetric interior penalty Galerkin method [98], and using $\gamma = -1$ was introduced in the nonsymmetric interior penalty Galerkin method [99]. Stabilized methods based on both $\gamma = 1$ and -1 were reported in [100] in the context of the advection–diffusion equation.

Remark 3 It was proposed in [68] to use, in general, the ST-SI method also as a way of imposing the periodicity in ST-VMS computations with spatial periodicity, including rotational periodicity (i.e., discrete rotational symmetry). In such cases, we place an SI where we want to impose the periodicity and carry out the computations while including the corresponding ST-SI terms.

2.2.2 One-Side Formulation

On solid surfaces where we prefer to have weakly-imposed Dirichlet conditions for the fluid [22, 100], we use the ST-SI version where the SI is between the fluid and solid domains. This version is obtained (see [49]) by starting with the terms added to Side B and replacing the Side A velocity with the velocity $\mathbf{g}^h$ coming from the solid domain. Then the terms added to Eq. (1) to represent the weakly-imposed Dirichlet conditions become

$$
\begin{aligned}
&- \int_{(P_n)_{\mathrm{SI}}} q_{\mathrm{B}}^h \mathbf{n}_{\mathrm{B}} \cdot \mathbf{u}_{\mathrm{B}}^h \mathrm{d}P - \int_{(P_n)_{\mathrm{SI}}} \rho \mathbf{w}_{\mathrm{B}}^h \cdot \mathcal{F}_{\mathrm{B}}^h \mathbf{u}_{\mathrm{B}}^h \mathrm{d}P + \int_{(P_n)_{\mathrm{SI}}} q_{\mathrm{B}}^h \mathbf{n}_{\mathrm{B}} \cdot \mathbf{g}^h \mathrm{d}P \\
&+ \int_{(P_n)_{\mathrm{SI}}} \rho \mathbf{w}_{\mathrm{B}}^h \cdot \frac{1}{2} \left(\left(\mathcal{F}_{\mathrm{B}}^h + \left| \mathcal{F}_{\mathrm{B}}^h \right| \right) \mathbf{u}_{\mathrm{B}}^h + \left(\mathcal{F}_{\mathrm{B}}^h - \left| \mathcal{F}_{\mathrm{B}}^h \right| \right) \mathbf{g}^h \right) \mathrm{d}P \\
&- \int_{(P_n)_{\mathrm{SI}}} \mathbf{w}_{\mathrm{B}}^h \cdot \left(\mathbf{n}_{\mathrm{B}} \cdot \boldsymbol{\sigma}_{\mathrm{B}}^h \right) \mathrm{d}P - \gamma \int_{(P_n)_{\mathrm{SI}}} \mathbf{n}_{\mathrm{B}} \cdot 2\mu \boldsymbol{\varepsilon} \left(\mathbf{w}_{\mathrm{B}}^h \right) \cdot \left(\mathbf{u}_{\mathrm{B}}^h - \mathbf{g}^h \right) \mathrm{d}P \\
&+ \int_{(P_n)_{\mathrm{SI}}} \frac{\mu C}{h_{\mathrm{B}}} \mathbf{w}_{\mathrm{B}}^h \cdot \left(\mathbf{u}_{\mathrm{B}}^h - \mathbf{g}^h \right) \mathrm{d}P. \qquad (12)
\end{aligned}
$$

3 ST-SI-TC-IGA Method

We first overview the aspects of the ST-SI [49] and ST-TC [54] methods relevant to their integration as the ST-SI-TC method [68], and then describe the advantages of the IGA in this context and integration of all three components as the ST-SI-TC-IGA method.

3.1 ST-SI Method

We note that the ST-SI method allows mesh slipping also in the one-side formulation, that is, when the SI is between the fluid and solid domains where we have weakly-imposed Dirichlet conditions. The boundary terms added to Eq. (1) to connect the two sides and to connect the fluid to the solid in the one-side formulation were given in Sects. 2.2.1 and 2.2.2. The added terms (see Eqs. (4) and (12)) include derivatives in the direction normal to the SI. Therefore the elements bordering the SI need to have finite thickness in the normal direction. This places a limitation on the meshes that can be used with the ST-SI method because if an element bordering the interface degenerates it might lead to a zero element thickness in the normal direction.

3.2 ST-TC Method

The ST-TC method can deal with TC in ST moving-mesh computations. The discretization is unstructured in time, but based on a "parent" mesh that is structured in time. The ST parent mesh is extruded from a single spatial mesh. The key technology is massive element degeneration by using a special master–slave system. This special system allows changing, within an ST slab, master nodes to slave nodes and slave nodes to master nodes. With that, elements can collapse or be reborn. This way, within an ST slab, we can represent closing and opening motions. Since an ST method naturally allows discretizations that are unstructured in time, the rest of the method needs no modification. The method is very flexible, and computationally as effective as a typical moving-mesh method. However, the master–slave relationship has to be node to node; a point on a solid surface that is not a node cannot be a master or slave node.

3.3 ST-IGA Method

With NURBS meshes, we can represent curved boundaries with less elements compared to finite element meshes. With this desirable feature, a volume can also be meshed with high aspect ratio elements. This is particularly helpful when we need to generate meshes in very narrow spaces.

3.4 Integration of the ST-SI, ST-TC and ST-IGA Methods

Integration of these three methods brings a number of advantages. (i) It enables high-resolution boundary layer representation near the solid surfaces in contact even when the surfaces are covered by meshes with SI. (ii) It enables dealing with contact location change or contact and sliding on the SI. This overcomes the ST-TC restriction that a point on a solid surface that is not a node cannot be a master or slave node. (iii) When surfaces contact each other, the elements between the surface and the SI collapse. Before the elements collapse, the boundaries could be curved and complex, and the narrow space might have high-aspect-ratio elements. With NURBS elements, we can deal with such adverse conditions rather effectively. (iv) Because the flow representation in the contact area has a wider support in IGA, the flow computation method becomes more robust.

To illustrate how the ST-SI-TC-IGA method works, we show with a 2D example how we deal with two valve leaflets flapping and coming into contact in an asymmetric fashion. Figure 1 shows the mesh motion, and Fig. 2 shows the corresponding control mesh.

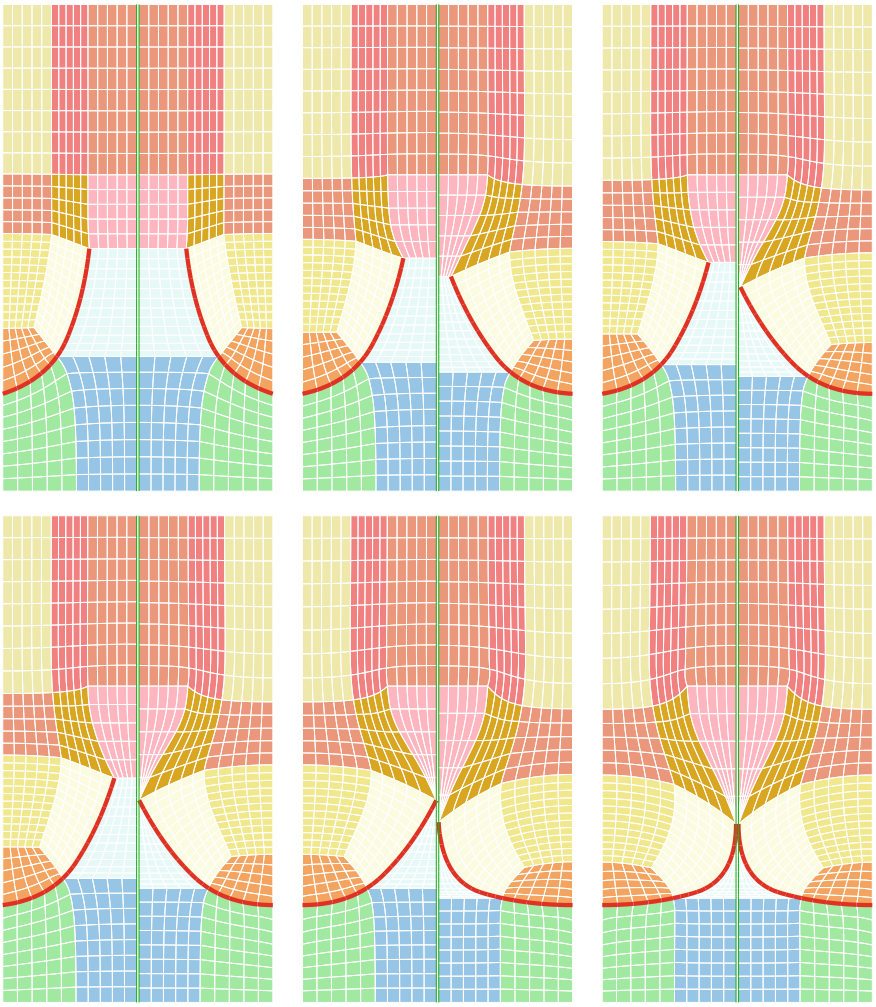

Fig. 1 An example of contact and sliding (element representation). Element colors indicate the NURBS patches the elements belong to. The *thick red curves* are the leaflets. The two *green vertical lines*, with the narrow space between them added only for illustration purposes, represent the two sides of an SI

Remark 4 As can be seen in Fig. 1, we have high-aspect-ratio elements near the contact region, and the NURBS elements can deal with that without mesh entanglement.

Remark 5 We allow situations where a surface from only one of the two sides coincides with the SI. This gives us the freedom of the two sides of the SI having their own master–slave relationships. For the surface that coincides with the SI, the SI serves the purpose of enforcing the weak Dirichlet condition.

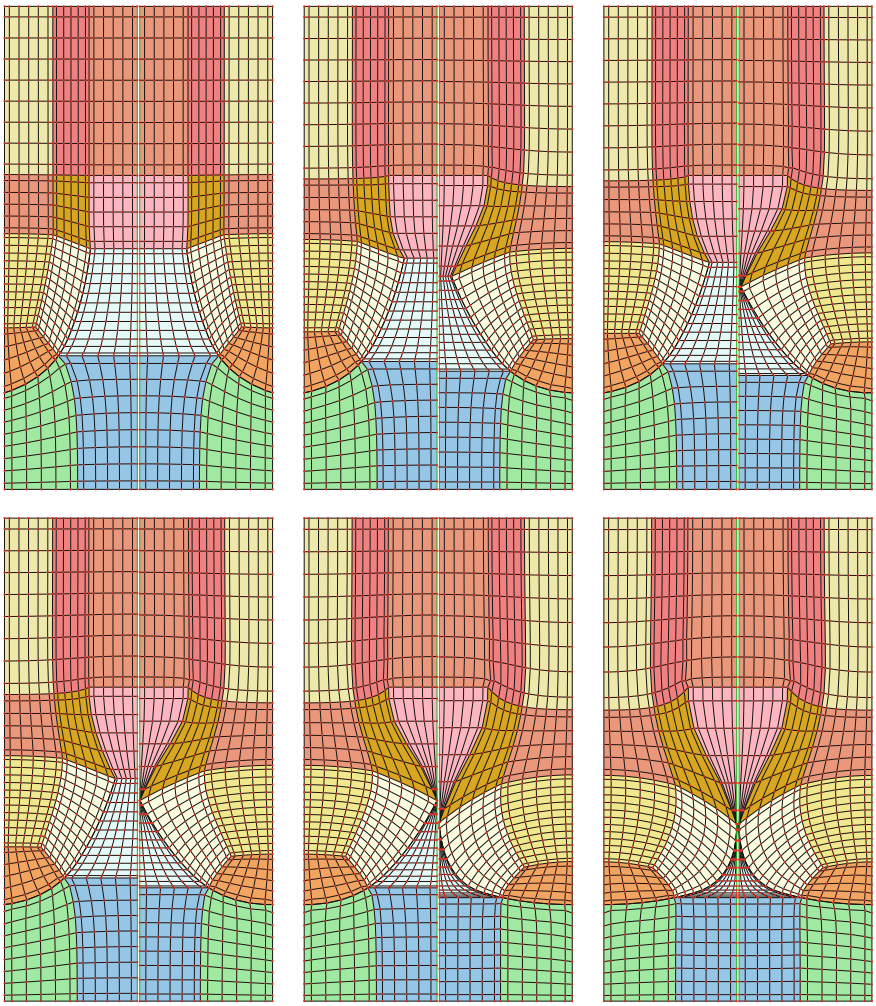

Fig. 2 An example of contact and sliding (control mesh). Shading colors indicate the NURBS patches. The black curves represent the control-mesh surfaces corresponding to the leaflets. The control points on the two sides of the narrow vertical gap correspond to the two sides of the SI. When control points coincide, they are in a master–slave relationship

Remark 6 In the case of quadratic NURBS elements, three control points along each of the two parametric directions aligned with the SI must coalesce with the corresponding control points in the third direction to result in a zero-volume element (see Fig. 2 for the 2D version of that). Unless that happens, the element is treated as an element with nonzero volume, and the element integrations are performed using all the integration points of the element. We also note that even if a spatial element belonging to an ST element has zero volume, as long as the ST element has nonzero volume, we integrate over that ST element (see [54] for details).

4 Aortic-Valve Model

4.1 Geometry

We have a typical aortic-valve model, such as the one in [56]. The model, shown in Fig. 3, has three leaflets and one main outlet, corresponding to the beginning of the aorta. The leaflet motion is prescribed.

4.2 Mesh and Flow Conditions

We create the mesh with five SIs, with three of them connecting the mesh sectors containing the leaflets in the valve region of the aorta (see Fig. 4). The other two SIs, which are the top and bottom circular planes in Fig. 4, connect the meshes in the inlet and outlet regions to the valve region. They are for independent meshing in the inlet and outlet regions.

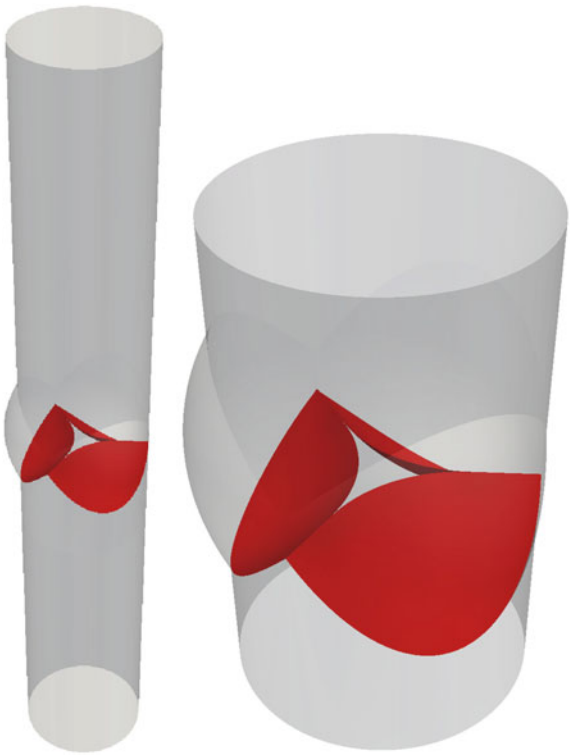

Fig. 3 Aortic-valve model geometry. Aorta, leaflets, and sinuses. The *left* picture shows the entire computational domain, and the *right* picture is the zoomed view of the valve

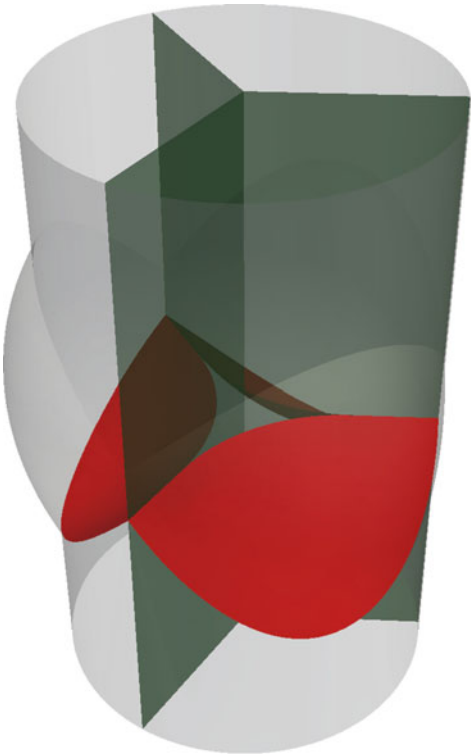

Fig. 4 Aortic valve and the three SIs

The volume mesh is made of quadratic NURBS elements. The number of control points is 84,534, and the number of elements is 54,000. We prescribe the motion of the interior control points, and specify in each domain the master–slave mapping for all leaflet positions. Figure 5 shows a set of selected NURBS elements to illustrate how elements collapse.

The boundary conditions are no-slip on the arterial walls and the leaflets, traction-free at the outflow boundary, and uniform velocity at the inflow boundary, with a temporal profile as shown in Fig. 6. The cycle period is 0.71 s. The no-slip condition on the arterial walls is based on the weakly-imposed Dirichlet condition given by Eq. (12).

4.3 Computational Conditions

We use the ST-SUPS method, which can obtained by dropping the last two series of integrations in Eq. (1). The time-step size is 4.00×10^{-3} s. There are three nonlinear iterations at each time step. The number of GMRES iterations per nonlinear iteration is 300.

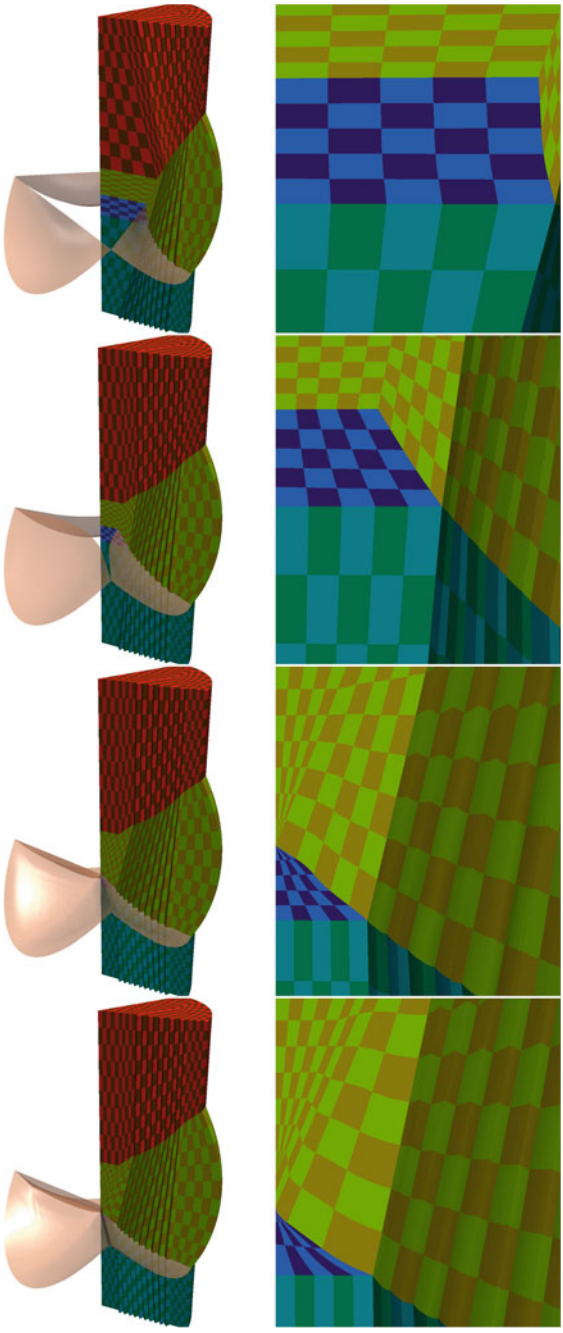

Fig. 5 A set of selected NURBS elements, from when the valve is fully open (*top*) to when it is fully closed (*bottom*). The *right* pictures are the zoomed views around the leaflet

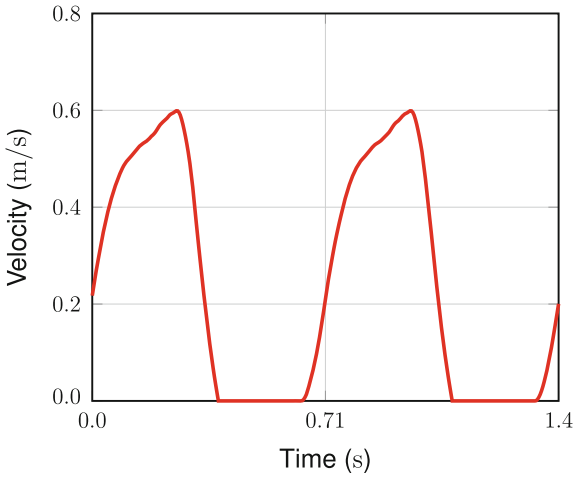

Fig. 6 Inflow velocity (two cycles)

4.4 Results

Figures 7 and 8 show the isosurfaces corresponding to a positive value of the second invariant of the velocity gradient tensor, colored by the velocity magnitude.

The result shows how effectively the flow separation is captured near the leaflet edges and the solution is obtained as the surfaces come into contact.

Remark 7 We note that there is a thin vortex sheet near the aorta wall in the second and third pair of pictures in Fig. 8, which correspond to the fully closed positions of the valve. That is because full blocking of the flow requires a collapsed (i.e. zero-volume) element, which in turn requires that the control points of the element coalesce as described in Remark 6, and that is not happening for the elements with two edges on the leaflet edges and two edges on the aorta wall. In the current setting, the control points associated with the two edges on the aorta wall cannot coalesce.

5 Concluding Remarks

We presented a heart valve flow computation with the ST-SI-TC-IGA method, which integrates the ST-SI, ST-TC and ST-IGA methods in the framework of the ST-VMS method. The computation was for a realistic aortic-valve model with prescribed valve leaflet motion and actual contact between the leaflets. The ST-VMS method functions as a moving-mesh method, which maintains high-resolution boundary layer representation near the solid surfaces, including the leaflet surfaces. The ST-TC method was introduced for moving-mesh computation of flow problems with TC, such as contact between the leaflets of a heart valve. It deals with the contact while maintaining high-resolution representation near the leaflet surfaces. The ST-SI method

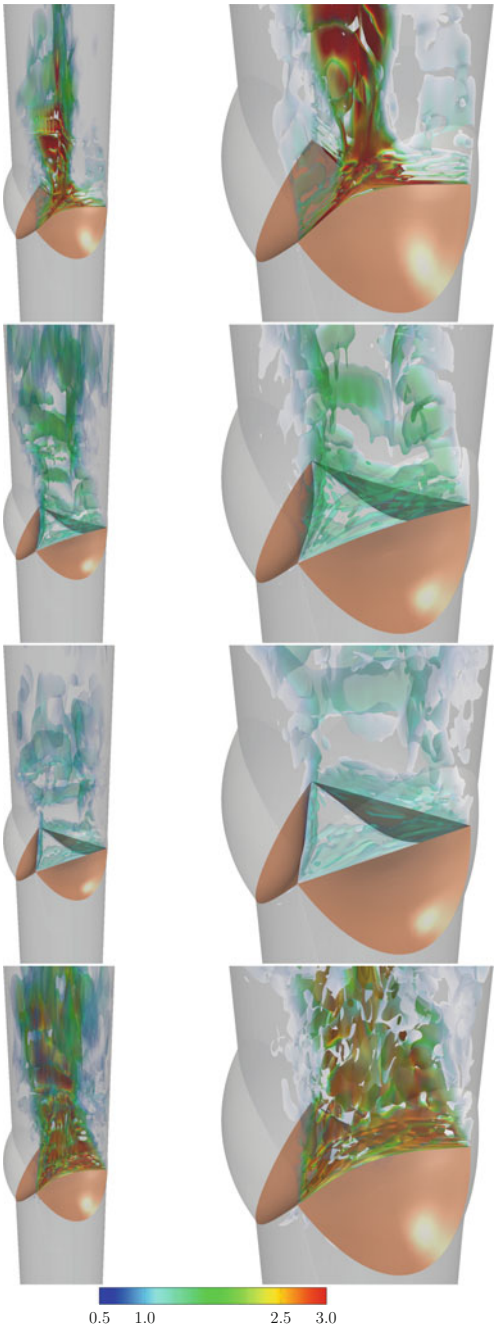

Fig. 7 Isosurfaces corresponding to a positive value of the second invariant of the velocity gradient tensor, colored by the velocity magnitude (m/s). The frames are for $t = 0.716$, 0.804, 0.892, and 0.984 s

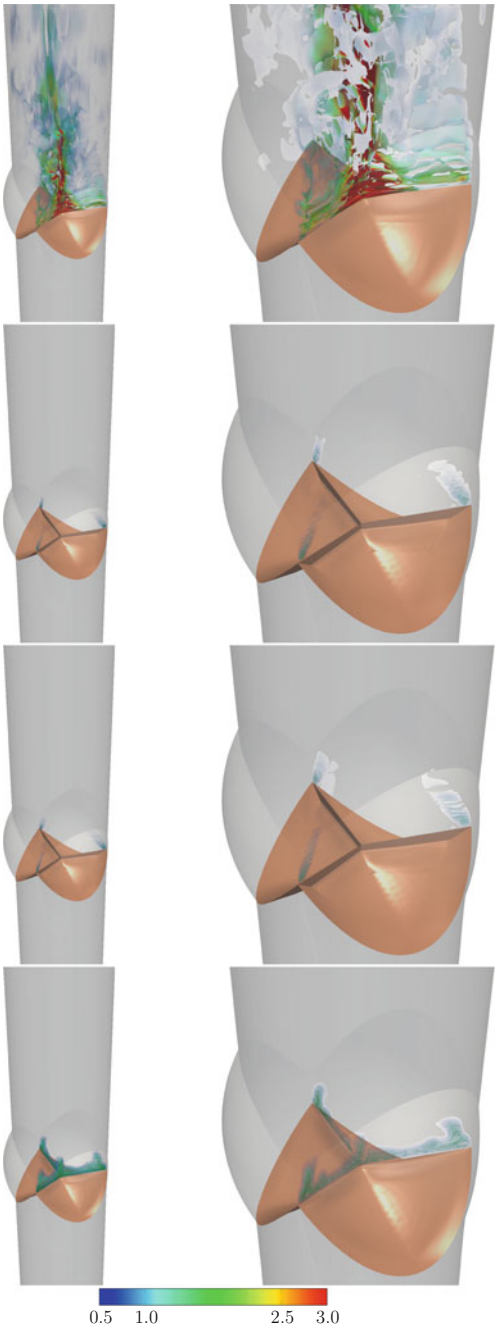

Fig. 8 Isosurfaces corresponding to a positive value of the second invariant of the velocity gradient tensor, colored by the velocity magnitude (m/s). The frames are for $t = 1.072$, 1.160, 1.252, and 1.340 s

was originally introduced to addresses the challenge involved in high-resolution representation of the boundary layers near spinning solid surfaces. The mesh covering a spinning solid surface spins with it, and the SI between that mesh and the rest of the mesh accurately connects the two sides. This maintains the high-resolution representation near solid surfaces. In the context of heart valves, the ST-SI method gives us more freedom in mesh generation and mesh moving, and that helps us deal with the high level of geometric complexity involved. The SIs connect the sectors of meshes containing the leaflets, enabling a more effective mesh moving. The ST-SI-TC method enables high-resolution representation of boundary layers even when the contact is between leaflets that are in mesh sectors connected by SIs. It also enables dealing with contact location change or contact and sliding on the SI. With the ST-SI-TC-IGA method, beyond having a more accurate representation of the surfaces and increased accuracy in the flow solution, we keep the element density in the narrow spaces near the contact areas at a reasonable level. When solid surfaces come into contact, before the elements between the surface and the SI collapse, the boundaries could be curved and rather complex, and the narrow space might have high-aspect-ratio elements. The ST-SI-TC-IGA method can deal with such adverse conditions rather effectively. In addition, because the ST-SI-TC-IGA method provides a wider support for the flow representation in the contact area, we have a flow computation method with increased robustness. The computation we present for the aortic-valve model shows the effectiveness of the ST-SI-TC-IGA method.

Acknowledgements This work was supported (first, third, and fourth authors) in part by JST-CREST; Grant-in-Aid for Young Scientists (B) 24760144 from Japan Society for the Promotion of Science (JSPS); Grant-in-Aid for Scientific Research (S) 26220002 from the Ministry of Education, Culture, Sports, Science and Technology of Japan (MEXT); and Rice–Waseda research agreement.

References

1. K. Takizawa, T.E. Tezduyar, Multiscale space-time fluid-structure interaction techniques. Comput. Mech. **48**, 247–267 (2011). doi:10.1007/s00466-011-0571-z
2. K. Takizawa, T.E. Tezduyar, Space-time fluid-structure interaction methods. Math. Models Methods Appl. Sci. **22**(supp02), 1230001 (2012). doi:10.1142/S0218202512300013
3. T.E. Tezduyar, Stabilized finite element formulations for incompressible flow computations. Adv. Appl. Mech. **28**, 1–44 (1992). doi:10.1016/S0065-2156(08)70153-4
4. T.E. Tezduyar, Computation of moving boundaries and interfaces and stabilization parameters. Int. J. Numer. Methods Fluids **43**, 555–575 (2003). doi:10.1002/fld.505
5. T.E. Tezduyar, S. Sathe, Modeling of fluid-structure interactions with the space-time finite elements: solution techniques. Int. J. Numer. Methods Fluids **54**, 855–900 (2007). doi:10.1002/fld.1430
6. T.J.R. Hughes, Multiscale phenomena: Green's functions, the Dirichlet-to-Neumann formulation, subgrid scale models, bubbles, and the origins of stabilized methods. Comput. Methods Appl. Mech. Eng. **127**, 387–401 (1995)
7. T.J.R. Hughes, A.A. Oberai, L. Mazzei, Large eddy simulation of turbulent channel flows by the variational multiscale method. Phys. Fluids **13**, 1784–1799 (2001)

8. Y. Bazilevs, V.M. Calo, J.A. Cottrell, T.J.R. Hughes, A. Reali, G. Scovazzi, Variational multiscale residual-based turbulence modeling for large eddy simulation of incompressible flows. Comput. Methods Appl. Mech. Eng. **197**, 173–201 (2007)
9. Y. Bazilevs, I. Akkerman, Large eddy simulation of turbulent Taylor-Couette flow using isogeometric analysis and the residual-based variational multiscale method. J. Comput. Phys. **229**, 3402–3414 (2010)
10. A.N. Brooks, T.J.R. Hughes, Streamline upwind/Petrov-Galerkin formulations for convection dominated flows with particular emphasis on the incompressible Navier-Stokes equations. Comput. Methods Appl. Mech. Eng. **32**, 199–259 (1982)
11. K. Takizawa, Y. Bazilevs, T.E. Tezduyar, Space-time and ALE-VMS techniques for patient-specific cardiovascular fluid-structure interaction modeling. Arch. Comput. Methods Eng. **19**, 171–225 (2012). doi:10.1007/s11831-012-9071-3
12. Y. Bazilevs, M.-C. Hsu, K. Takizawa, T.E. Tezduyar, ALE-VMS and ST-VMS methods for computer modeling of wind-turbine rotor aerodynamics and fluid-structure interaction. Math. Models Methods Appl. Sci. **22**(supp02), 1230002 (2012). doi:10.1142/S0218202512300025
13. Y. Bazilevs, V.M. Calo, T.J.R. Hughes, Y. Zhang, Isogeometric fluid-structure interaction: theory, algorithms, and computations. Comput. Mech. **43**, 3–37 (2008)
14. T.J.R. Hughes, W.K. Liu, T.K. Zimmermann, Lagrangian-Eulerian finite element formulation for incompressible viscous flows. Comput. Methods Appl. Mech. Eng. **29**, 329–349 (1981)
15. T.J.R. Hughes, J.A. Cottrell, Y. Bazilevs, Isogeometric analysis: CAD, finite elements, NURBS, exact geometry, and mesh refinement. Comput. Methods Appl. Mech. Eng. **194**, 4135–4195 (2005)
16. Y. Bazilevs, V.M. Calo, Y. Zhang, T.J.R. Hughes, Isogeometric fluid-structure interaction analysis with applications to arterial blood flow. Comput. Mech. **38**, 310–322 (2006)
17. Y. Bazilevs, T.J.R. Hughes, NURBS-based isogeometric analysis for the computation of flows about rotating components. Comput. Mech. **43**, 143–150 (2008)
18. Y. Bazilevs, J.R. Gohean, T.J.R. Hughes, R.D. Moser, Y. Zhang, Patient-specific isogeometric fluid-structure interaction analysis of thoracic aortic blood flow due to implantation of the Jarvik, left ventricular assist device. Comput. Methods Appl. Mech. Eng. **198**(2009), 3534–3550 (2000)
19. Y. Bazilevs, M.-C. Hsu, D. Benson, S. Sankaran, A. Marsden, Computational fluid-structure interaction: methods and application to a total cavopulmonary connection. Comput. Mech. **45**, 77–89 (2009)
20. Y. Bazilevs, M.-C. Hsu, I. Akkerman, S. Wright, K. Takizawa, B. Henicke, T. Spielman, T.E. Tezduyar, 3D simulation of wind turbine rotors at full scale. Part I: geometry modeling and aerodynamics. Int. J. Numer. Methods Fluids **65**, 207–235 (2011). doi:10.1002/fld.2400
21. Y. Bazilevs, M.-C. Hsu, J. Kiendl, R. Wüchner, K.-U. Bletzinger, 3D simulation of wind turbine rotors at full scale. Part II: fluid–structure interaction modeling with composite blades. Int. J. Numer. Methods Fluids **65**, 236–253 (2011)
22. M.-C. Hsu, I. Akkerman, Y. Bazilevs, Wind turbine aerodynamics using ALE-VMS: validation and role of weakly enforced boundary conditions. Comput. Mech. **50**, 499–511 (2012)
23. M.-C. Hsu, Y. Bazilevs, Fluid-structure interaction modeling of wind turbines: simulating the full machine. Comput. Mech. **50**, 821–833 (2012)
24. Y. Bazilevs, K. Takizawa, T.E. Tezduyar, *Computational Fluid–Structure Interaction: Methods and Applications*. (Wiley, 2013). ISBN 978-0470978771
25. Y. Bazilevs, K. Takizawa, T.E. Tezduyar, Challenges and directions in computational fluid-structure interaction. Math. Models Methods Appl. Sci. **23**, 215–221 (2013). doi:10.1142/S0218202513400010
26. A. Korobenko, M.-C. Hsu, I. Akkerman, J. Tippmann, Y. Bazilevs, Structural mechanics modeling and FSI simulation of wind turbines. Math. Models Methods Appl. Sci. **23**, 249–272 (2013)
27. A. Korobenko, M.-C. Hsu, I. Akkerman, Y. Bazilevs, Aerodynamic simulation of vertical-axis wind turbines. J. Appl. Mech. **81**, 021011 (2013). doi:10.1115/1.4024415

28. Y. Bazilevs, K. Takizawa, T.E. Tezduyar, M.-C. Hsu, N. Kostov, S. McIntyre, Aerodynamic and FSI analysis of wind turbines with the ALE-VMS and ST-VMS methods. Arch. Comput. Methods Eng. **21**, 359–398 (2014). doi:10.1007/s11831-014-9119-7
29. Y. Bazilevs, A. Korobenko, X. Deng, J. Yan, M. Kinzel, J.O. Dabiri, FSI modeling of vertical-axis wind turbines. J. Appl. Mech. **81**, 081006 (2014). doi:10.1115/1.4027466
30. M.-C. Hsu, I. Akkerman, Y. Bazilevs, Finite element simulation of wind turbine aerodynamics: Validation study using NREL Phase VI experiment. Wind Energy **17**, 461–481 (2014)
31. C.C. Long, M. Esmaily-Moghadam, A.L. Marsden, Y. Bazilevs, Computation of residence time in the simulation of pulsatile ventricular assist devices. Comput. Mech. **54**, 911–919 (2014). doi:10.1007/s00466-013-0931-y
32. C.C. Long, A.L. Marsden, Y. Bazilevs, Shape optimization of pulsatile ventricular assist devices using FSI to minimize thrombotic risk. Comput. Mech. **54**, 921–932 (2014). doi:10.1007/s00466-013-0967-z
33. M.-C. Hsu, D. Kamensky, Y. Bazilevs, M.S. Sacks, T.J.R. Hughes, Fluid-structure interaction analysis of bioprosthetic heart valves: significance of arterial wall deformation. Comput. Mech. **54**, 1055–1071 (2014). doi:10.1007/s00466-014-1059-4
34. B. Augier, J. Yan, A. Korobenko, J. Czarnowski, G. Ketterman, Y. Bazilevs, Experimental and numerical FSI study of compliant hydrofoils. Comput. Mech. **55**, 1079–1090 (2015). doi:10.1007/s00466-014-1090-5
35. Y. Bazilevs, A. Korobenko, J. Yan, A. Pal, S.M.I. Gohari, S. Sarkar, ALE-VMS formulation for stratified turbulent incompressible flows with applications. Math. Models Methods Appl. Sci. **25**, 2349–2375 (2015). doi:10.1142/S0218202515400114
36. Y. Bazilevs, K. Takizawa, T.E. Tezduyar, New directions and challenging computations in fluid dynamics modeling with stabilized and multiscale methods. Math. Models Methods Appl. Sci. **25**, 2217–2226 (2015). doi:10.1142/S0218202515020029
37. Y. Bazilevs, A. Korobenko, X. Deng, J. Yan, FSI modeling for fatigue-damage prediction in full-scale wind-turbine blades. J. Appl. Mech. **83**(6), 061010 (2016)
38. J. Yan, B. Augier, A. Korobenko, J. Czarnowski, G. Ketterman, Y. Bazilevs, FSI modeling of a propulsion system based on compliant hydrofoils in a tandem configuration. Comput. Fluids (2015). doi:10.1016/j.compfluid.2015.07.013
39. J. Yan, A. Korobenko, X. Deng, Y. Bazilevs, Computational free-surface fluid-structure interaction with application to floating offshore wind turbines. Comput. Fluids (2016). doi:10.1016/j.compfluid.2016.03.008
40. K. Takizawa, Y. Bazilevs, T.E. Tezduyar, M.-C. Hsu, O. Øiseth, K.M. Mathisen, N. Kostov, S. McIntyre, Engineering analysis and design with ALE-VMS and space-time methods. Arch. Comput. Methods Eng. **21**, 481–508 (2014). doi:10.1007/s11831-014-9113-0
41. K. Takizawa, T.E. Tezduyar, R. Kolesar, C. Boswell, T. Kanai, K. Montel, Multiscale methods for gore curvature calculations from FSI modeling of spacecraft parachutes. Comput. Mech. **54**, 1461–1476 (2014). doi:10.1007/s00466-014-1069-2
42. K. Takizawa, T.E. Tezduyar, C. Boswell, R. Kolesar, K. Montel, FSI modeling of the reefed stages and disreefing of the Orion spacecraft parachutes. Comput. Mech. **54**, 1203–1220 (2014). doi:10.1007/s00466-014-1052-y
43. K. Takizawa, T.E. Tezduyar, C. Boswell, Y. Tsutsui, K. Montel, Special methods for aerodynamic-moment calculations from parachute FSI modeling. Comput. Mech. **55**, 1059–1069 (2015). doi:10.1007/s00466-014-1074-5
44. K. Takizawa, T.E. Tezduyar, R. Kolesar, FSI modeling of the Orion spacecraft drogue parachutes. Comput. Mech. **55**, 1167–1179 (2015). doi:10.1007/s00466-014-1108-z
45. K. Takizawa, B. Henicke, T.E. Tezduyar, M.-C. Hsu, Y. Bazilevs, Stabilized space-time computation of wind-turbine rotor aerodynamics. Comput. Mech. **48**, 333–344 (2011). doi:10.1007/s00466-011-0589-2
46. K. Takizawa, B. Henicke, D. Montes, T.E. Tezduyar, M.-C. Hsu, Y. Bazilevs, Numerical-performance studies for the stabilized space-time computation of wind-turbine rotor aerodynamics. Comput. Mech. **48**, 647–657 (2011). doi:10.1007/s00466-011-0614-5

47. K. Takizawa, T.E. Tezduyar, S. McIntyre, N. Kostov, R. Kolesar, C. Habluetzel, Space-time VMS computation of wind-turbine rotor and tower aerodynamics. Comput. Mech. **53**, 1–15 (2014). doi:10.1007/s00466-013-0888-x
48. K. Takizawa, Computational engineering analysis with the new-generation space-time methods. Comput. Mech. **54**, 193–211 (2014). doi:10.1007/s00466-014-0999-z
49. K. Takizawa, T.E. Tezduyar, H. Mochizuki, H. Hattori, S. Mei, L. Pan, K. Montel, Space-time VMS method for flow computations with slip interfaces (ST-SI). Math. Models Methods Appl. Sci. **25**, 2377–2406 (2015). doi:10.1142/S0218202515400126
50. K. Takizawa, B. Henicke, A. Puntel, T. Spielman, T.E. Tezduyar, Space-time computational techniques for the aerodynamics of flapping wings. J. Appl. Mech. **79**, 010903 (2012). doi:10.1115/1.4005073
51. K. Takizawa, B. Henicke, A. Puntel, N. Kostov, T.E. Tezduyar, Space-time techniques for computational aerodynamics modeling of flapping wings of an actual locust. Comput. Mech. **50**, 743–760 (2012). doi:10.1007/s00466-012-0759-x
52. K. Takizawa, N. Kostov, A. Puntel, B. Henicke, T.E. Tezduyar, Space-time computational analysis of bio-inspired flapping-wing aerodynamics of a micro aerial vehicle. Comput. Mech. **50**, 761–778 (2012). doi:10.1007/s00466-012-0758-y
53. K. Takizawa, B. Henicke, A. Puntel, N. Kostov, T.E. Tezduyar, Computer modeling techniques for flapping-wing aerodynamics of a locust. Comput. Fluids **85**, 125–134 (2013). doi:10.1016/j.compfluid.2012.11.008
54. K. Takizawa, T.E. Tezduyar, A. Buscher, S. Asada, Space-time interface-tracking with topology change (ST-TC). Comput. Mech. **54**, 955–971 (2014). doi:10.1007/s00466-013-0935-7
55. K. Takizawa, T.E. Tezduyar, N. Kostov, Sequentially-coupled space-time FSI analysis of bio-inspired flapping-wing aerodynamics of an MAV. Comput. Mech. **54**, 213–233 (2014). doi:10.1007/s00466-014-0980-x
56. K. Takizawa, T.E. Tezduyar, A. Buscher, Space-time computational analysis of MAV flapping-wing aerodynamics with wing clapping. Comput. Mech. **55**, 1131–1141 (2015). doi:10.1007/s00466-014-1095-0
57. K. Takizawa, K. Schjodt, A. Puntel, N. Kostov, T.E. Tezduyar, Patient-specific computer modeling of blood flow in cerebral arteries with aneurysm and stent. Comput. Mech. **50**, 675–686 (2012). doi:10.1007/s00466-012-0760-4
58. K. Takizawa, K. Schjodt, A. Puntel, N. Kostov, T.E. Tezduyar, Patient-specific computational analysis of the influence of a stent on the unsteady flow in cerebral aneurysms. Comput. Mech. **51**, 1061–1073 (2013). doi:10.1007/s00466-012-0790-y
59. K. Takizawa, Y. Bazilevs, T.E. Tezduyar, C.C. Long, A.L. Marsden, K. Schjodt, ST and ALE-VMS methods for patient-specific cardiovascular fluid mechanics modeling. Math. Models Methods Appl. Sci. **24**, 2437–2486 (2014). doi:10.1142/S0218202514500250
60. H. Suito, K. Takizawa, V.Q.H. Huynh, D. Sze, T. Ueda, FSI analysis of the blood flow and geometrical characteristics in the thoracic aorta. Comput. Mech. **54**, 1035–1045 (2014). doi:10.1007/s00466-014-1017-1
61. K. Takizawa, T.E. Tezduyar, A. Buscher, S. Asada, Space-time fluid mechanics computation of heart valve models. Comput. Mech. **54**, 973–986 (2014). doi:10.1007/s00466-014-1046-9
62. K. Takizawa, D. Montes, M. Fritze, S. McIntyre, J. Boben, T.E. Tezduyar, Methods for FSI modeling of spacecraft parachute dynamics and cover separation. Math. Models Methods Appl. Sci. **23**, 307–338 (2013). doi:10.1142/S0218202513400058
63. K. Takizawa, D. Montes, S. McIntyre, T.E. Tezduyar, Space-time VMS methods for modeling of incompressible flows at high Reynolds numbers. Math. Models Methods Appl. Sci. **23**, 223–248 (2013). doi:10.1142/s0218202513400022
64. K. Takizawa, T.E. Tezduyar, T. Kuraishi, Multiscale ST methods for thermo-fluid analysis of a ground vehicle and its tires. Math. Models Methods Appl. Sci. **25**, 2227–2255 (2015). doi:10.1142/S0218202515400072

65. K. Takizawa, T.E. Tezduyar, T. Kuraishi, S. Tabata, H. Takagi, Computational thermo-fluid analysis of a disk brake. Comput. Mech. **57**, 965–977 (2016). doi:10.1007/s00466-016-1272-4
66. K. Takizawa, T.E. Tezduyar, H. Hattori, Computational analysis of flow-driven string dynamics in turbomachinery. Comput. Fluids (2016). doi:10.1016/j.compfluid.2016.02.019
67. K. Takizawa, T.E. Tezduyar, Y. Otoguro, T. Terahara, T. Kuraishi, H. Hattori, Turbocharger flow computations with the space-time isogeometric analysis (ST-IGA). Comput. Fluids (2016). doi:10.1016/j.compfluid.2016.02.021
68. K. Takizawa, T.E. Tezduyar, S. Asada, T. Kuraishi, Space-time method for flow computations with slip interfaces and topology changes (ST-SI-TC). Comput. Fluids (2016). doi:10.1016/j.compfluid.2016.05.006
69. K. Takizawa, T.E. Tezduyar, T. Terahara, Ram-air parachute structural and fluid mechanics computations with the space-time isogeometric analysis (ST-IGA). Comput. Fluids (2016). doi:10.1016/j.compfluid.2016.05.027
70. T.E. Tezduyar, K. Takizawa, C. Moorman, S. Wright, J. Christopher, Space-time finite element computation of complex fluid-structure interactions. Int. J. Numer. Methods Fluids **64**, 1201–1218 (2010). doi:10.1002/fld.2221
71. D. Kamensky, M.-C. Hsu, D. Schillinger, J.A. Evans, A. Aggarwal, Y. Bazilevs, M.S. Sacks, T.J.R. Hughes, An immersogeometric variational framework for fluid-structure interaction: application to bioprosthetic heart valves. Comput. Methods Appl. Mech. Eng. **284**, 1005–1053 (2015)
72. V. Kalro, T.E. Tezduyar, Parallel finite element computation of 3D incompressible flows on MPPs, in *Solution Techniques for Large-Scale CFD Problems*, ed. by W.G. Habashi (Wiley, 1995)
73. T. Tezduyar, S. Aliabadi, M. Behr, A. Johnson, V. Kalro, M. Litke, Flow simulation and high performance computing. Comput. Mech. **18**, 397–412 (1996). doi:10.1007/BF00350249
74. M. Behr, T. Tezduyar, The shear-slip mesh update method. Comput. Methods Appl. Mech. Eng. **174**, 261–274 (1999). doi:10.1016/S0045-7825(98)00299-0
75. Y. Bazilevs, A. Korobenko, X. Deng, J. Yan, Novel structural modeling and mesh moving techniques for advanced FSI simulation of wind turbines. Int. J. Numer. Methods Eng. **102**, 766–783 (2015). doi:10.1002/nme.4738
76. T.E. Tezduyar, D.K. Ganjoo, Petrov-Galerkin formulations with weighting functions dependent upon spatial and temporal discretization: applications to transient convection-diffusion problems. Comput. Methods Appl. Mech. Eng. **59**, 49–71 (1986). doi:10.1016/0045-7825(86)90023-X
77. G.J. Le Beau, S.E. Ray, S.K. Aliabadi, T.E. Tezduyar, SUPG finite element computation of compressible flows with the entropy and conservation variables formulations. Comput. Methods Appl. Mech. Eng. **104**, 397–422 (1993). doi:10.1016/0045-7825(93)90033-T
78. T.E. Tezduyar, Finite elements in fluids: stabilized formulations and moving boundaries and interfaces. Comput. Fluids **36**, 191–206 (2007). doi:10.1016/j.compfluid.2005.02.011
79. T.E. Tezduyar, M. Senga, Stabilization and shock-capturing parameters in SUPG formulation of compressible flows. Comput. Methods Appl. Mech. Eng. **195**, 1621–1632 (2006). doi:10.1016/j.cma.2005.05.032
80. T.E. Tezduyar, M. Senga, SUPG finite element computation of inviscid supersonic flows with YZβ shock-capturing. Comput. Fluids **36**, 147–159 (2007). doi:10.1016/j.compfluid.2005.07.009
81. T.E. Tezduyar, M. Senga, D. Vicker, Computation of inviscid supersonic flows around cylinders and spheres with the SUPG formulation and YZβ shock-capturing. Comput. Mech. **38**, 469–481 (2006). doi:10.1007/s00466-005-0025-6
82. T.E. Tezduyar, S. Sathe, Enhanced-discretization selective stabilization procedure (EDSSP). Comput. Mech. **38**, 456–468 (2006). doi:10.1007/s00466-006-0056-7
83. A. Corsini, F. Rispoli, A. Santoriello, T.E. Tezduyar, Improved discontinuity-capturing finite element techniques for reaction effects in turbulence computation. Comput. Mech. **38**, 356–364 (2006). doi:10.1007/s00466-006-0045-x

84. F. Rispoli, A. Corsini, T.E. Tezduyar, Finite element computation of turbulent flows with the discontinuity-capturing directional dissipation (DCDD). Comput. Fluids **36**, 121–126 (2007). doi:10.1016/j.compfluid.2005.07.004
85. T.E. Tezduyar, S. Ramakrishnan, S. Sathe, Stabilized formulations for incompressible flows with thermal coupling. Int. J. Numer. Methods Fluids **57**, 1189–1209 (2008). doi:10.1002/fld.1743
86. F. Rispoli, R. Saavedra, A. Corsini, T.E. Tezduyar, Computation of inviscid compressible flows with the V-SGS stabilization and YZβ shock-capturing. Int. J. Numer. Methods Fluids **54**, 695–706 (2007). doi:10.1002/fld.1447
87. Y. Bazilevs, V.M. Calo, T.E. Tezduyar, T.J.R. Hughes, YZβ discontinuity-capturing for advection-dominated processes with application to arterial drug delivery. Int. J. Numer. Methods Fluids **54**, 593–608 (2007). doi:10.1002/fld.1484
88. A. Corsini, C. Menichini, F. Rispoli, A. Santoriello, T.E. Tezduyar, A multiscale finite element formulation with discontinuity capturing for turbulence models with dominant reactionlike terms. J. Appl. Mech. **76**, 021211 (2009). doi:10.1115/1.3062967
89. F. Rispoli, R. Saavedra, F. Menichini, T.E. Tezduyar, Computation of inviscid supersonic flows around cylinders and spheres with the V-SGS stabilization and YZβ shock-capturing. J. Appl. Mech. **76**, 021209 (2009). doi:10.1115/1.3057496
90. A. Corsini, C. Iossa, F. Rispoli, T.E. Tezduyar, A DRD finite element formulation for computing turbulent reacting flows in gas turbine combustors. Comput. Mech. **46**, 159–167 (2010). doi:10.1007/s00466-009-0441-0
91. M.-C. Hsu, Y. Bazilevs, V.M. Calo, T.E. Tezduyar, T.J.R. Hughes, Improving stability of stabilized and multiscale formulations in flow simulations at small time steps. Comput. Methods Appl. Mech. Eng. **199**, 828–840 (2010). doi:10.1016/j.cma.2009.06.019
92. A. Corsini, F. Rispoli, T.E. Tezduyar, Stabilized finite element computation of NOx emission in aero-engine combustors. Int. J. Numer. Methods Fluids **65**, 254–270 (2011). doi:10.1002/fld.2451
93. A. Corsini, F. Rispoli, T.E. Tezduyar, Computer modeling of wave-energy air turbines with the SUPG/PSPG formulation and discontinuity-capturing technique. J. Appl. Mech. **79**, 010910 (2012). doi:10.1115/1.4005060
94. A. Corsini, F. Rispoli, A.G. Sheard, T.E. Tezduyar, Computational analysis of noise reduction devices in axial fans with stabilized finite element formulations. Comput. Mech. **50**, 695–705 (2012). doi:10.1007/s00466-012-0789-4
95. P.A. Kler, L.D. Dalcin, R.R. Paz, T.E. Tezduyar, SUPG and discontinuity-capturing methods for coupled fluid mechanics and electrochemical transport problems. Comput. Mech. **51**, 171–185 (2013). doi:10.1007/s00466-012-0712-z
96. A. Corsini, F. Rispoli, A.G. Sheard, K. Takizawa, T.E. Tezduyar, P. Venturini, A variational multiscale method for particle-cloud tracking in turbomachinery flows. Comput. Mech. **54**, 1191–1202 (2014). doi:10.1007/s00466-014-1050-0
97. F. Rispoli, G. Delibra, P. Venturini, A. Corsini, R. Saavedra, T.E. Tezduyar, Particle tracking and particle-shock interaction in compressible-flow computations with the V-SGS stabilization and YZβ shock-capturing. Comput. Mech. **55**, 1201–1209 (2015). doi:10.1007/s00466-015-1160-3
98. M.F. Wheeler, An elliptic collocation-finite element method with interior penalties. SIAM J. Numer. Anal. **15**, 152–161 (1978)
99. P. Houston, C. Schwab, E. Suli, Discontinuous hp-finite element methods for advection-diffusion reaction problems. SIAM J. Numer. Anal. **39**, 2133–2163 (2002)
100. Y. Bazilevs, T.J.R. Hughes, Weak imposition of Dirichlet boundary conditions in fluid mechanics. Comput. Fluids **36**, 12–26 (2007)

Estimation of Element-Based Zero-Stress State in Arterial FSI Computations with Isogeometric Wall Discretization

Kenji Takizawa, Tayfun E. Tezduyar and Takafumi Sasaki

Abstract In patient-specific arterial fluid–structure interaction computations the image-based arterial geometry does not come from a zero-stress state (ZSS), requiring an estimation of the ZSS. A method for estimation of element-based ZSS (EBZSS) was introduced earlier in the context of finite element wall discretization. The method has three main components. 1. An iterative method, which starts with a calculated initial guess, is used for computing the EBZSS such that when a given pressure load is applied, the image-based target shape is matched. 2. A method for straight-tube segments is used for computing the EBZSS so that we match the given diameter and longitudinal stretch in the target configuration and the "opening angle." 3. An element-based mapping between the artery and straight-tube is extracted from the mapping between the artery and straight-tube segments. This provides the mapping from the arterial configuration to the straight-tube configuration, and from the estimated EBZSS of the straight-tube configuration back to the arterial configuration, to be used as the initial guess for the iterative method that matches the image-based target shape. Here we introduce the version of the EBZSS estimation method with isogeometric wall discretization. With NURBS basis functions, we may be able to use larger elements, consequently less number of elements, compared to linear basis functions. Higher-order NURBS basis functions allow representation of more complex shapes within an element. To show how the new EBZSS estimation method performs, we present 2D test computations with straight-tube configurations.

K. Takizawa (✉) · T. Sasaki
Department of Modern Mechanical Engineering, Waseda University,
1-6-1 Nishi-Waseda, Shinjuku-ku, Tokyo 169-8050, Japan
e-mail: Kenji.Takizawa@tafsm.org

T.E. Tezduyar
Department of Mechanical Engineering, Rice University, 6100 Main Street,
Houston, TX 77005, USA

P. Wriggers and T. Lenarz (eds.), *Biomedical Technology*, Lecture Notes in Applied and Computational Mechanics 84, DOI 10.1007/978-3-319-59548-1_7

1 Introduction

In the last decade, we have seen a major expansion in computational cardiovascular fluid mechanics research (see, for example, [1–56]). Much of the emphasis has been on computations involving moving boundaries and interfaces (MBI), including fluid–structure interaction (FSI) between the blood flow and cardiovascular wall. While these are challenging classes of computations, advances in core MBI and FSI methods (see, for example, [36, 37, 47, 56–59] and references therein) and development of special methods targeting cardiovascular MBI and FSI (see, for example, [29, 33, 36, 46, 51] and references therein) helped address a large number of computational challenges.

In patient-specific arterial FSI computations the image-based arterial geometry does not come from a zero-stress state (ZSS). Special methods targeting cardiovascular MBI and FSI include those designed to take that into account. The attempt to find a ZSS for the artery was first made in a conference paper [60], where the concept of estimated zero-pressure (EZP) arterial geometry was introduced. The method introduced in [60] for calculating an EZP geometry was also included in one of the earlier journal papers on space–time arterial FSI methods [9] as "a rudimentary technique" for addressing the issue. It was pointed out in [9, 60] that quite often, the image-based geometries were used as arterial geometries corresponding to zero blood pressure, and that it would be more realistic to use the image-based geometry as the arterial geometry corresponding to the time-averaged value of the blood pressure. Given that arterial geometry at the time-averaged pressure value, an estimated arterial geometry corresponding to zero blood pressure needed to be constructed. Special methods developed to address the issue include the newer EZP versions [17, 26, 29, 33, 36] and the prestress technique introduced in [24], which was further refined in [30] and presented also in [33, 36].

A method for estimation of element-based ZSS (EBZSS) was introduced in [42] in the context of finite element wall discretization. The method has three main components. 1. An iterative method, which starts with a calculated initial guess, is used for computing the EBZSS such that when a given pressure load is applied, the image-based target shape is matched. 2. A method for straight-tube segments is used for computing the EBZSS so that we match the given diameter and longitudinal stretch in the target configuration and the "opening angle." 3. An element-based mapping between the artery and straight-tube is extracted from the mapping between the artery and straight-tube segments. This provides the mapping from the arterial configuration to the straight-tube configuration, and from the estimated EBZSS of the straight-tube configuration back to the arterial configuration, to be used as the initial guess for the iterative method that matches the image-based target shape. The method was used successfully in [42] in test computations based on straight-tube configurations with single and three layers, and a curved-tube configuration with single layer. The method was used successfully also in [52] in coronary arterial dynamics computations with medical-image-based time-dependent anatomical models.

In this article, we introduce the version of the EBZSS estimation method with isogeometric wall discretization. With NURBS basis functions, we may be able to use larger elements, consequently less number of elements, compared to linear basis functions. Higher-order NURBS basis functions allow representation of more complex shapes within an element. To explain how the new EBZSS estimation method works and to demonstrate how it performs, we carry out 2D test computations with straight-tube configurations.

In Sect. 2, we describe, in the context of isogeometric discretization, the Element-Based Total Lagrangian (EBTL) method, including the EBZSS concept. Section 3, extracted from [42], is an overview of the analytical relationship between the ZS and reference states of straight-tube segments, and here we call that relationship "straight-tube ZSS template." The test computations are presented in Sect. 4, and the concluding remarks are given in Sect. 5.

2 Element-Based Total Lagrangian (EBTL) Method

In this section we provide an overview of the EBTL method [42], including the EBZSS concept, and describe the version of the method with NURBS wall discretization.

Let $\Omega_0 \in \mathbb{R}^3$ be the material domain of a structure in the ZSS, and let Γ_0 be its boundary. Let $\Omega_t \in \mathbb{R}^3$, $t \in (0, T)$, be the material domain of the structure in the deformed state, and let Γ_t be its boundary. The structural mechanics equations based on the total Lagrangian formulation can be written as

$$\int_{\Omega_0} \mathbf{w} \cdot \rho_0 \frac{\mathrm{d}^2 \mathbf{y}}{\mathrm{d}t^2} \, \mathrm{d}\Omega + \int_{\Omega_0} \delta \mathbf{E} : \mathbf{S} \, \mathrm{d}\Omega - \int_{\Omega_0} \mathbf{w} \cdot \rho_0 \mathbf{f} \, \mathrm{d}\Omega = \int_{(\Gamma_t)_\mathrm{h}} \mathbf{w} \cdot \mathbf{h} \, \mathrm{d}\Gamma. \tag{1}$$

Here, $\mathbf{y}$ is the displacement, $\mathbf{w}$ is the virtual displacement, $\delta\mathbf{E}$ is the variation of the Green–Lagrange strain tensor, $\mathbf{S}$ is the second Piola–Kirchhoff stress tensor, ρ_0 is the mass density in the ZSS, $\mathbf{f}$ is the body force per unit mass, and $\mathbf{h}$ is the external traction vector applied on the subset $\left(\Gamma_t\right)_\mathrm{h}$ of the total boundary Γ_t.

2.1 EBZSS

In the EBTL method the ZSS is defined with a set of positions $\mathbf{X}_0^e$ for each element e. Positions of nodes from different elements mapping to the same node in the mesh do not have to be the same. In the reference state, $\mathbf{X}_\mathrm{REF}$, all elements are connected by nodes, and we measure the displacement $\mathbf{y}$ from that connected state. The implementation of the method is simple. The deformation gradient tensor $\mathbf{F}$ is evaluated for each element:

$$\mathbf{F}^e \equiv \frac{\partial \mathbf{x}}{\partial \mathbf{X}_0^e}, \tag{2}$$

$$= \frac{\partial \left(\mathbf{X}_{\mathrm{REF}} + \mathbf{y} \right)}{\partial \mathbf{X}_0^e}. \tag{3}$$

The deformation gradient tensors for different elements are on different states, but the terms in Eq. (1), including the second term, do not depend on the orientation. Therefore the rest of the process is the same as it is in the total Lagrangian formulation.

2.2 NURBS Basis Functions

In representation of the EBZSS with NURBS basis functions, we may be able to use larger and less number of elements compared to linear basis functions. Higher-order NURBS basis functions allow representation of more complex shapes within an element. Curvature representation requires at least quadratic NURBS, and to have a continuous curvature, cubic or higher-order NURBS is required.

In the case of 1D parametric space, a curve segment can be represented by NURBS as

$$\mathbf{z}(\xi) = \sum_{a=1}^{n_{\mathrm{en}}} R_a(\xi) \mathbf{z}_a, \tag{4}$$

where n_{en} is the number of control points in the element, $\mathbf{z}_a$ is the position of the control point (node) a,

$$R_a(\xi) = \frac{N_a(\xi) w_a}{\sum_{b=1}^{n_{\mathrm{en}}} N_b(\xi) w_b}, \tag{5}$$

$N_a(\xi)$ is the B-spline basis function for point a, and w_a is the NURBS weight for point a. An equivalent form can be obtained by using the homogeneous coordinates [61], where $\mathbf{z}_a$ is augmented as

$$\mathbf{z}_a^{\mathrm{w}} = \begin{bmatrix} w_a \mathbf{z}_a \\ w_a \end{bmatrix}. \tag{6}$$

With that, we represent the curve segment as

$$\mathbf{z}^{\mathrm{w}}(\xi) = \sum_{a=1}^{n_{\mathrm{en}}} N_a(\xi) \mathbf{z}_a^{\mathrm{w}}, \tag{7}$$

and

$$\mathbf{z}(\xi) = \begin{bmatrix} 1\,0\,0\,0 \\ 0\,1\,0\,0 \\ 0\,0\,1\,0 \end{bmatrix} \frac{\mathbf{z}^{\mathrm{w}}(\xi)}{\sum_{a=1}^{n_{\mathrm{en}}} N_a(\xi) w_a}. \tag{8}$$

The forms given by Eqs. (4) and (8) are equivalent.

As proposed in [61], we represent the B-spline basis functions with the Bernstein basis functions $B_b(\xi)$:

$$N_a(\xi) = \sum_{b=1}^{n_{\mathrm{en}}} C_{ab} B_b(\xi), \tag{9}$$

where C_{ab} denotes the components of the Bézier extraction operator. See [61] for how to obtain the operator from the B-spline knots. With that,

$$\mathbf{z}^{\mathrm{w}}(\xi) = \sum_{a=1}^{n_{\mathrm{en}}} \sum_{b=1}^{n_{\mathrm{en}}} C_{ab} B_b(\xi) \mathbf{z}_a^{\mathrm{w}}. \tag{10}$$

From that, we can first operate with C_{ab}, and obtain the Bézier control positions as

$$\hat{\mathbf{z}}_b = \sum_{a=1}^{n_{\mathrm{en}}} \mathbf{z}_a^{\mathrm{w}} C_{ab}. \tag{11}$$

The extension to multi-dimensional parametric spaces is straightforward.

Given the control position $\mathbf{z}_a$ for a point a, the corresponding homogeneous coordinates $\mathbf{z}_a^{\mathrm{w}}$, its Bézier representation $\hat{\mathbf{z}}_a$, and the Bézier extraction operator components C_{ab}, we move to an array notation where

$$\mathbf{Z} = \left[\mathbf{z}_a\right], \tag{12}$$

$$\mathbf{Z}^{\mathrm{w}} = \left[\mathbf{z}_a^{\mathrm{w}}\right], \tag{13}$$

$$\hat{\mathbf{Z}} = \left[\hat{\mathbf{z}}_a\right], \tag{14}$$

$$\mathbf{C} = \left[C_{ab}\right]. \tag{15}$$

Then, Eq. (11) can be written as

$$\hat{\mathbf{Z}} = \mathbf{Z}^{\mathrm{w}} \mathbf{C}. \tag{16}$$

With that, the transformation from the Bézier representation to NURBS representation becomes

$$\mathbf{Z}^{\mathrm{w}} = \hat{\mathbf{Z}} \mathbf{C}^{-1}. \tag{17}$$

2.3 EBZSS Representation with NURBS Basis Functions

When we are designing a ZSS, we have the corresponding reference state $\mathbf{X}_{\mathrm{REF}}$. Therefore we have $\left(\mathbf{X}_{\mathrm{REF}}\right)_a$, w_a, and the Bézier extraction operator corresponding to the element. We obtain the homogeneous coordinates $\left(\mathbf{X}_{\mathrm{REF}}\right)_a^{\mathrm{w}}$ and then convert that to $\left(\hat{\mathbf{X}}_{\mathrm{REF}}\right)_a$. From that and the Bernstein basis functions, we can design the EBZSS as $\left(\hat{\mathbf{X}}_0^e\right)_a$. For implementation convenience, we convert the control points to $\left(\mathbf{X}_0^e\right)_a^{\mathrm{w}}$ by using Eq. (17).

Remark 1 Although in the ZSS we could have element-based w_a values, that would in general require using different basis functions between the ZS and reference states. Here we do not consider that option.

With the EBZSS, under a given load we would like to reach a configuration that matches the target shape, and we take $\mathbf{X}_{\mathrm{REF}}$ as the target state. Here we assume that we have a reasonably good initial guess for the EBZSS, and explain the iterative method used in calculating the EBZSS that results in the target state associated with the given load. In doing that, we use many pieces of the method described in [42] for linear elements.

In our iterative method, we estimate $\mathbf{F}$ from the ith solution. We use the notation

$$\mathbf{F}\left(\mathbf{x},\mathbf{X}\right)=\mathbf{R}\left(\mathbf{x},\mathbf{X}\right)\mathbf{U}\left(\mathbf{x},\mathbf{X}\right), \tag{18}$$

which is the polar decomposition of $\mathbf{F}$ into rotation $\mathbf{R}$ and right stretch tensor $\mathbf{U}$. The arguments in the tensors represent the numerator and denominator in the partial derivatives. With that, $\mathbf{F}$ at $(i+1)$th iteration is expressed as

$$\mathbf{F}^{i+1}=\mathbf{R}\left(\mathbf{X}_{\mathrm{REF}},\mathbf{x}^i\right)\mathbf{F}^i\mathbf{R}\left((\mathbf{X}_0^e)^i,(\mathbf{X}_0^e)^{i+1}\right). \tag{19}$$

With the approximation

$$\mathbf{R}\left((\mathbf{X}_0^e)^i,(\mathbf{X}_0^e)^{i+1}\right)=\mathbf{I}, \tag{20}$$

we obtain

$$\mathbf{F}^{i+1}=\mathbf{R}\left(\mathbf{X}_{\mathrm{REF}},\mathbf{x}^i\right)\mathbf{F}^i, \tag{21}$$

and from that we obtain

$$\left(\mathbf{F}^{i+1}\right)^{-1}=\left(\mathbf{F}^i\right)^{-1}\mathbf{R}(\mathbf{x}^i,\mathbf{X}_{\mathrm{REF}}), \tag{22}$$

$$=\left(\mathbf{U}^i\right)^{-1}\mathbf{R}((\mathbf{X}_0^e)^i,\mathbf{X}_{\mathrm{REF}}). \tag{23}$$

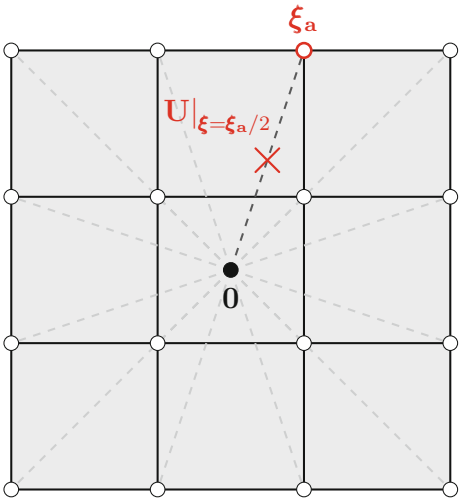

Fig. 1 The representative parametric position $\boldsymbol{\xi}_a$ assigned to the Bézier control point a, and the straight path from $\mathbf{0}$ to $\boldsymbol{\xi}_a$. When performing the integration with the midpoint rule, the evaluation point is $\boldsymbol{\xi}_a/2$

In this article, in calculating $(\mathbf{X}_0^e)^{i+1}$, instead of doing the tensor evaluations at $\boldsymbol{\xi} = \mathbf{0}$, we do integrations from $\boldsymbol{\xi} = \mathbf{0}$ to the corresponding positions:

$$(\mathbf{X}_0^e)^{i+1}\Big|_{\boldsymbol{\xi}=\boldsymbol{\xi}_a} - (\mathbf{X}_0^e)^{i+1}\Big|_{\boldsymbol{\xi}=\mathbf{0}} = \int_{\mathbf{X}^e_{\mathrm{REF}}|_{\boldsymbol{\xi}=\mathbf{0}}}^{\mathbf{X}^e_{\mathrm{REF}}|_{\boldsymbol{\xi}=\boldsymbol{\xi}_a}} \left(\mathbf{F}^{i+1}\right)^{-1} \mathrm{d}\mathbf{X}_{\mathrm{REF}}. \tag{24}$$

Here $\boldsymbol{\xi}_a$ is the representative parametric position assigned to the Bézier control point for a (see Fig. 1), and we use a straight path from $\mathbf{0}$ to $\boldsymbol{\xi}_a$. The representative parametric positions are equally spaced. The first approximation here is performing the integration with the midpoint rule:

$$(\mathbf{X}_0^e)^{i+1}\Big|_{\boldsymbol{\xi}=\boldsymbol{\xi}_a} - (\mathbf{X}_0^e)^{i+1}\Big|_{\boldsymbol{\xi}=\mathbf{0}} \approx \left(\mathbf{F}^{i+1}\right)^{-1}\Big|_{\boldsymbol{\xi}=\boldsymbol{\xi}_a/2} \left(\mathbf{X}^e_{\mathrm{REF}}|_{\boldsymbol{\xi}=\boldsymbol{\xi}_a} - \mathbf{X}^e_{\mathrm{REF}}|_{\boldsymbol{\xi}=\mathbf{0}}\right). \tag{25}$$

The second approximation is to assume that the relationship given by Eq. (25) between $(\mathbf{X}_0^e)^{i+1}\Big|_{\boldsymbol{\xi}=\boldsymbol{\xi}_a}$ and $\mathbf{X}^e_{\mathrm{REF}}\Big|_{\boldsymbol{\xi}=\boldsymbol{\xi}_a}$ can also be used between the control points $(\hat{\mathbf{X}}_0^e)_a^{i+1}$ and $(\mathbf{X}^{\hat{e}}_{\mathrm{REF}})_a$:

$$(\hat{\mathbf{X}}_0^e)_a^{i+1} - (\mathbf{X}_0^e)^{i+1}\Big|_{\boldsymbol{\xi}=\mathbf{0}} \approx \left(\mathbf{F}^{i+1}\right)^{-1}\Big|_{\boldsymbol{\xi}=\boldsymbol{\xi}_a/2} \left((\mathbf{X}^{\hat{e}}_{\mathrm{REF}})_a - \mathbf{X}^e_{\mathrm{REF}}|_{\boldsymbol{\xi}=\mathbf{0}}\right). \tag{26}$$

This is the new version of the "direct-update (DU)" process (see [42] for the original DU process). The "recursive-update (RU)" process is given as

$$(\hat{\mathbf{X}}_0^e)_a^{i+1} - (\mathbf{X}_0^e)^{i+1}\Big|_{\boldsymbol{\xi}=\mathbf{0}} \approx \left(\mathbf{F}^{i+1}\right)^{-1}\Big|_{\boldsymbol{\xi}=\boldsymbol{\xi}_a/2} \mathbf{F}\left(\mathbf{X}_{\mathrm{REF}}, (\mathbf{X}_0^e)^i\right)\Big|_{\boldsymbol{\xi}=\boldsymbol{\xi}_a/2} \left((\hat{\mathbf{X}}_0^e)^i{}_a - (\mathbf{X}_0^e)^i\Big|_{\boldsymbol{\xi}=\mathbf{0}}\right) \tag{27}$$

$$= \left(\mathbf{U}^i\right)^{-1}\Big|_{\boldsymbol{\xi}=\boldsymbol{\xi}_a/2} \mathbf{U}\left(\mathbf{X}_{\mathrm{REF}}, (\mathbf{X}_0^e)^i\right)\Big|_{\boldsymbol{\xi}=\boldsymbol{\xi}_a/2} \left((\hat{\mathbf{X}}_0^e)^i{}_a - (\mathbf{X}_0^e)^i\Big|_{\boldsymbol{\xi}=\mathbf{0}}\right). \tag{28}$$

We note that the tensor–vector operations in Eqs. (26)–(28) actually involve the augmented versions of the tensors, where the augmented version of a tensor $\mathbf{F}$ is defined as

$$\begin{bmatrix} \mathbf{F} & \mathbf{0} \\ \mathbf{0}^T & 1 \end{bmatrix}, \tag{29}$$

and the augmented versions of the vectors $(\mathbf{X}_0^e)^{i+1}\Big|_{\boldsymbol{\xi}=\mathbf{0}}$, $\mathbf{X}_{\text{REF}}^e\Big|_{\boldsymbol{\xi}=\mathbf{0}}$ and $(\mathbf{X}_0^e)^i\Big|_{\boldsymbol{\xi}=\mathbf{0}}$, as defined by Eq. (7).

In the actual computations, we start from the "ZSS template": $(\mathbf{X}_0^e)^0 = (\mathbf{X}_0^e)_{\text{TEMP}}$ (see Sect. 3). In the steady-state structural mechanics computations, it is reasonable to start from displacement $\mathbf{y} = \mathbf{0}$. However, it is unlikely for that to be a good match for the ZSS. To improve the convergence of the structural mechanics solution for $i = 0$, we use an incremental loading and modify the initial guess for the EBZSS based on that ramping:

$$\left((\mathbf{X}_0^e)^0\right)^j = (1 - t^j)\mathbf{X}_{\text{REF}} + t^j(\mathbf{X}_0^e)_{\text{TEMP}}. \tag{30}$$

Here $0 < t^1 \leq t^2 \leq \cdots \leq t^N = 1$, N is the number of nonlinear-iteration steps used in computing $\mathbf{y}^0$, and the iterations start with $(\mathbf{y}^0)^0 = \mathbf{0}$. We also ramp the load:

$$(\mathbf{h}^h)^j = t^j \mathbf{h}^h, \tag{31}$$

where $\mathbf{h}^h$ is the target load. The ramping options include having a ramping profile where the t^j values change at every certain number of nonlinear-iteration steps. With that, we obtain the steady-state solution $\mathbf{y}^0$ for $(\mathbf{X}_0^e)^0 = (\mathbf{X}_0^e)_{\text{TEMP}}$ based on the full load. For $i = 1$ and beyond, $(\mathbf{X}_0^e)^i$ is calculated from Eq. (28), and the nonlinear iterations used in computing $\mathbf{y}^i$ start with $(\mathbf{y}^i)^0 = \mathbf{0}$.

3 Modeling the Artery ZSS: Straight-Tube ZSS Template

An analytical relationship between the ZS and reference states of straight-tube segments was given in [42]. Here we will call that relationship "straight-tube ZSS template." We describe the straight tube in the target state, which is here the reference state, with three lengths: $\overline{\ell}$, h and L. They are the circumferential length of the arterial-wall midsurface, wall thickness, and the longitudinal length. The tube volume is

$$V = \overline{\ell} hL. \tag{32}$$

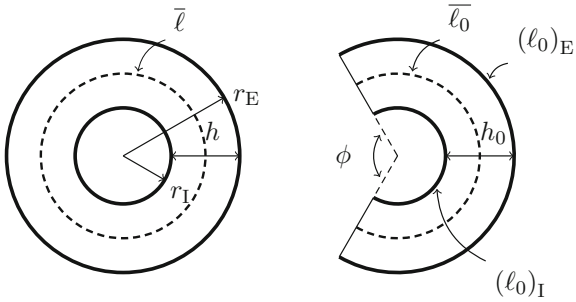

Fig. 2 Straight tube in the target (*left*) and ZS (*right*) states. The *dashed lines* denote the arterial-wall midsurface in each state

For an artery, beyond having a target shape under a given load, there are some significant properties. One of them is the opening angle, ϕ, seen after a longitudinal cut, which we call the "LC state." Fig. 2 summarizes the template.

Remark 2 We note that in general it is not necessary for the LC state to be a ZSS.

4 2D Test Computations

We define a parameter α:

$$\overline{\ell_0} = \alpha \ell_{\mathrm{I}}, \tag{33}$$

where ℓ_{I} is the circumferential length of the inner tube surface in the target state. The task of calculating $\overline{\ell_0}$ becomes the task of calculating α.

4.1 Meshes

In the test computations here, we use quadratic and cubic NURBS basis functions. Although NURBS can represent a circular arc exactly, it cannot do that throughout a full circle while retaining the C^1 continuity of the basis functions. Therefore, here we simplify the basis functions to uniform B-splines. Figures 3 and 4 show the meshes used.

We evaluate how well the meshes represent the circular arcs. For that, we inspect the radius of curvature, ρ. Figures 5 and 6 show $\rho/\overline{\rho}$ as a function of the circumferential parametric coordinate, ξ, where $\overline{\rho}$ is the average radius.

Remark 3 The highest shape function value is at $\xi = 0$ for the quadratic B-splines, and at $\xi = -1$ and $\xi = 1$ for the cubic B-splines. From that, and from Figs. 5 and 6, we conclude that the radius of curvature will be lowest at points closest to the control points, and highest between those points.

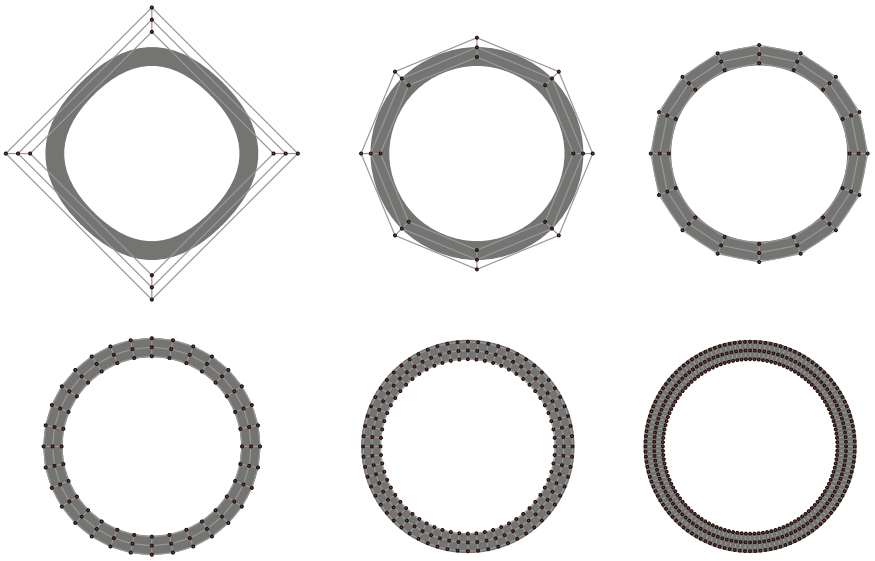

Fig. 3 Quadratic B-spline meshes with 4, 8, 16, 32, 64, and 128 elements. The *red* circles are the control points and the *gray* part is the actual tube

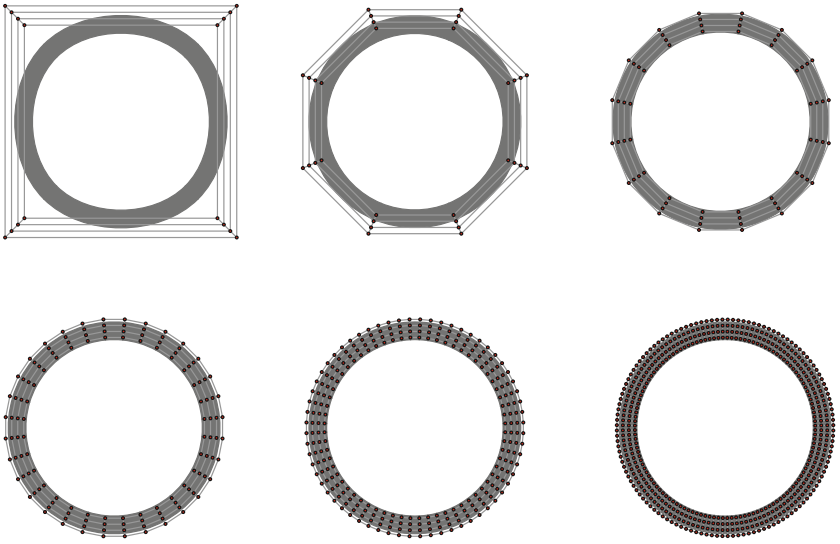

Fig. 4 Cubic B-spline meshes with 4, 8, 16, 32, 64, and 128 elements. The *red* circles are the control points and the *gray* part is the actual tube

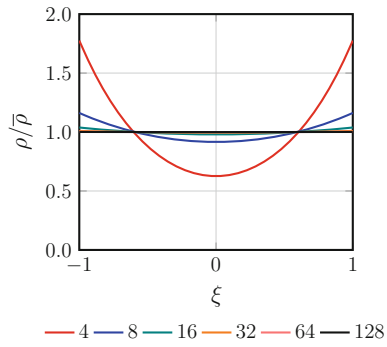

Fig. 5 Representation of the radius of curvature within an element with quadratic B-splines. The curves are for the six meshes, ξ is the circumferential parametric coordinate, and $\overline{\rho}$ is the average radius

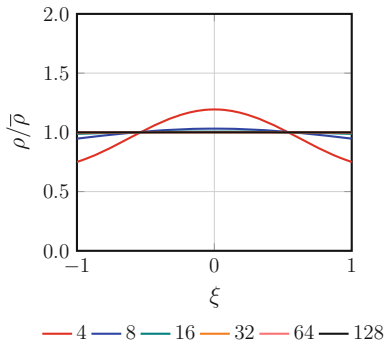

Fig. 6 Representation of the radius of curvature within an element with cubic B-splines. The curves are for the six meshes, ξ is the circumferential parametric coordinate, and $\overline{\rho}$ is the average radius

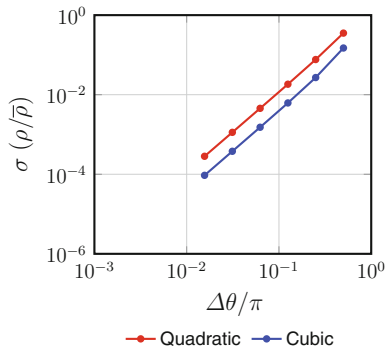

Fig. 7 Standard deviation of $\rho/\overline{\rho}$ as a function of the arc angle $\Delta\theta$ represented by a B-spline element, where $\overline{\rho}$ is the average radius

Figure 7 shows the standard deviation of $\rho/\overline{\rho}$, as a function of the arc angle $\Delta\theta$ represented by an element, where $\Delta\theta = 2\pi/n_{el}$, and n_{el} is the number of elements. We note that both quadratic and cubic B-splines have second-order accuracy.

4.2 Curvature Matching in the ZSS

Curvature matching in the ZSS is done by first converting the B-spline element in the target state to Bézier representation. After that, for the specified ϕ, we generate element configurations with the objective of having a constant radius of curvature in the ZSS. Then we convert that back to B-spline representation. Figures 8 and 9 show examples of the process for $\phi = 5\pi/2$, which results in Bézier elements with $\Delta\theta = (2\pi - \phi)/n_{el} = -\pi/(2n_{el})$, and for a given value of α. The negative value implies that the outer surface is smaller than the inner surface.

In the case of quadratic Bézier functions, we choose the middle control point to be on the tangents to the inner surface at the two other control points. This determines the curvature in the ZSS. For cubic Bézier functions, we have an additional degree of freedom, and we use that by choosing the control points to be also at equally-spaced angular positions. Figure 10 shows the convergence rate for the standard deviation of $\rho_0/\overline{\rho_0}$ for the Bézier elements, where $\overline{\rho_0}$ is the average radius. We note from Figs. 7 and 10 that Bézier elements yield the same representation quality as the B-spline elements for quadratic functions, and slightly better quality for cubic functions.

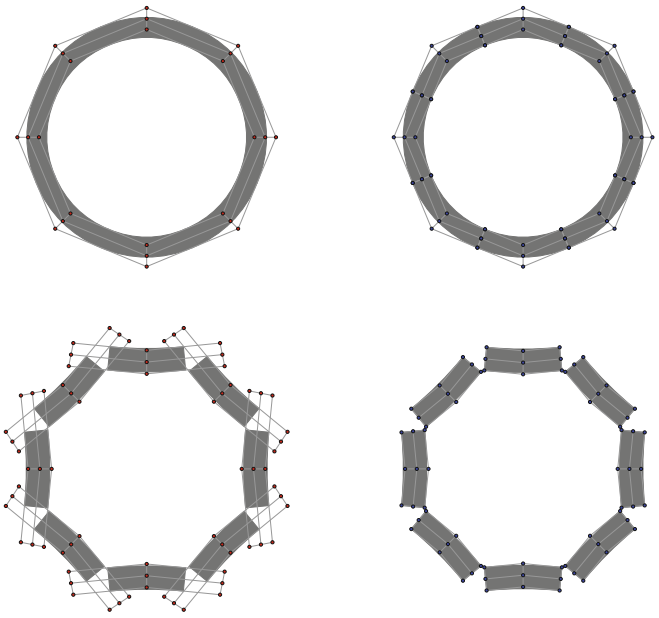

Fig. 8 Curvature matching in the ZSS. Quadratic basis functions with 8 elements. The B-spline mesh in the target state (*top left*) is converted to Bézier representation (*top right*). From that, for the specified ϕ and for a given value of α, we generate element configurations with the objective of having constant radius of curvature in the ZSS (*bottom right*). Then we convert that back to B-spline representation (*bottom left*)

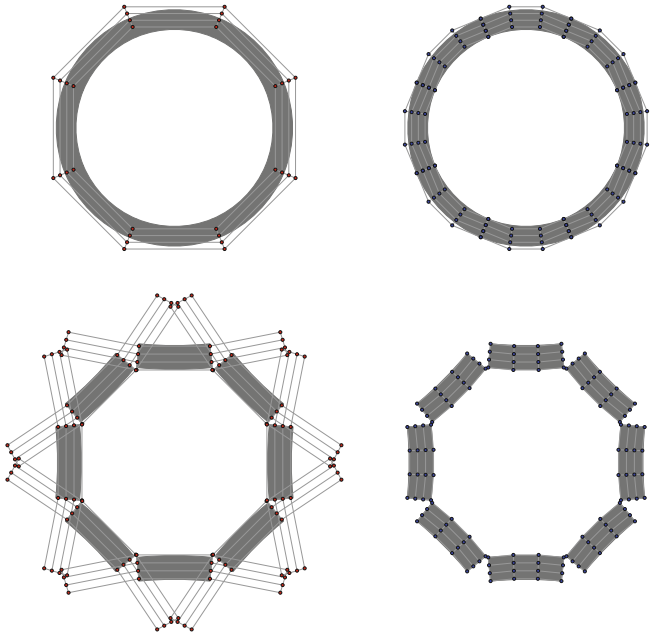

Fig. 9 Curvature matching in the ZSS. Cubic basis functions with 8 elements. The B-spline mesh in the target state (*top left*) is converted to Bézier representation (*top right*). From that, for the specified ϕ and for a given value of α, we generate element configurations with the objective of having constant radius of curvature in the ZSS (*bottom right*). Then we convert that back to B-spline representation (*bottom left*)

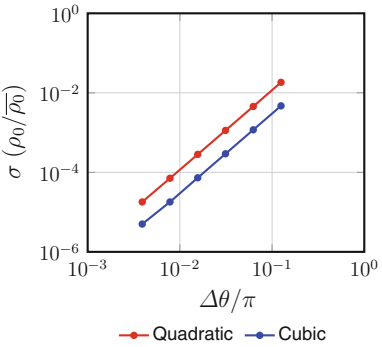

Fig. 10 Curvature matching in the ZSS. Standard deviation of $\rho_0/\overline{\rho_0}$ as a function of the arc angle $\Delta\theta$ represented by a Bézier element, where $\overline{\rho_0}$ is the average radius

4.3 Computational Results

For a range of α values, we go through the process described in Sect. 4.2 and, using the B-spline elements with curvature matching in the ZSS, we do structural mechanics computations. We obtain the steady-state solutions corresponding to a constant pressure value of $p_0 = 92$ mm Hg. In these computations, the arterial wall is made of hyperelastic (Fung) material. The material constants D_1 and D_2 are 2.6447×10^3 N/m^2 and 8.365, and the penalty Poisson's ratio is 0.45. We note that, because of the process in Sect. 4.2, the inner-surface shapes obtained from the computations will be at the best as good as those in the upper-left picture in Figs. 8 and 9, for whatever the number of elements are.

The structural mechanics computations generate a relationship between the curvature in the deformed state and α, and from that we select the α value that matches the curvature in the target state. Figures 11 and 12 show the average curvature of the inner surface in the deformed state as a function of α for the six meshes with quadratic and cubic B-splines. For quadratic functions, with the mesh made of 4 elements, the α value that matches the target curvature is very different than the value obtained with the other meshes. For cubic functions, except for the mesh made of

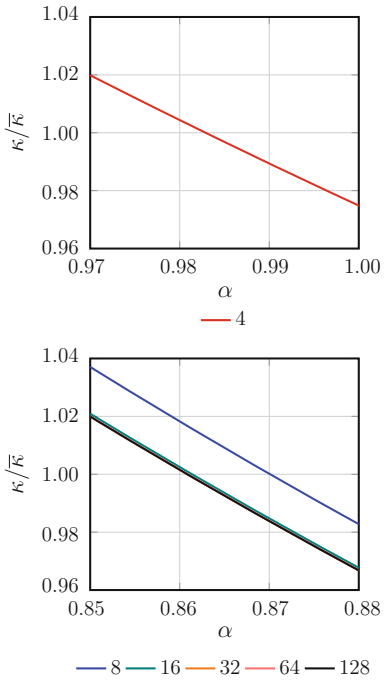

Fig. 11 Average curvature in the deformed state as a function of α for the six meshes with quadratic B-splines, where $\overline{\kappa}$ is the curvature in the target state

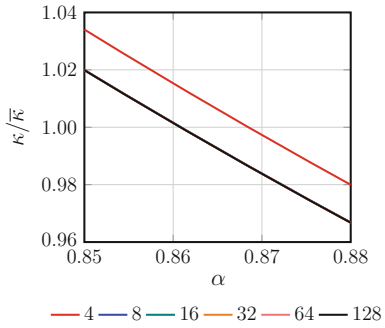

Fig. 12 Average curvature in the deformed state as a function of α for the six meshes with cubic B-splines, where $\overline{\kappa}$ is the curvature in the target state

4 elements, curves for all the meshes coincide. Figure 13 shows, for all the meshes, the α value that matches the target curvature.

With all the meshes and the α values displayed in Fig. 13, we compute the steady-state structural mechanics solutions to examine the stretches. We evaluate the stretches at the 4×4 Gaussian quadrature points (see Fig. 14).

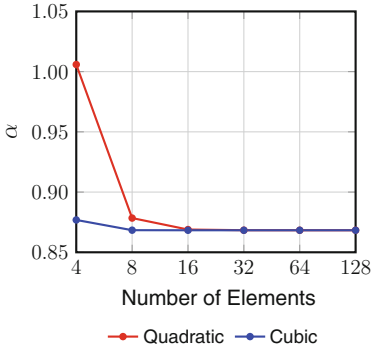

Fig. 13 For all the meshes, the α value that matches the target curvature

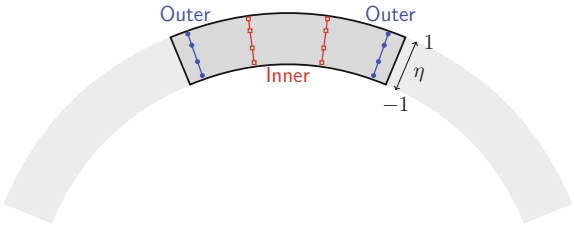

Fig. 14 Schematic display of the integration points

Remark 4 In the structural mechanics computations with quadratic functions, we use only 3×3 quadrature points.

Remark 5 The integration points are defined over the ZSS.

Because of the circular symmetry, the stretches should depend only on the radial position. Here we check that by examining their values along different radial lines in the element, which are called "Inner" and "Outer" in Fig. 14. Figure 15 shows, for the meshes with 8 elements, the radial stretches. For the meshes with 16 or more elements, the radial stretches along the inner and outer lines are basically indistinguishable.

Remark 6 The precise definitions of the radial and circumferential directions for the stretch components are based on the parametric coordinates.

Figure 16 shows, for the meshes with 16 elements, the circumferential stretches. For the meshes with 32 or more elements, the circumferential stretches along the inner and outer lines are basically indistinguishable.

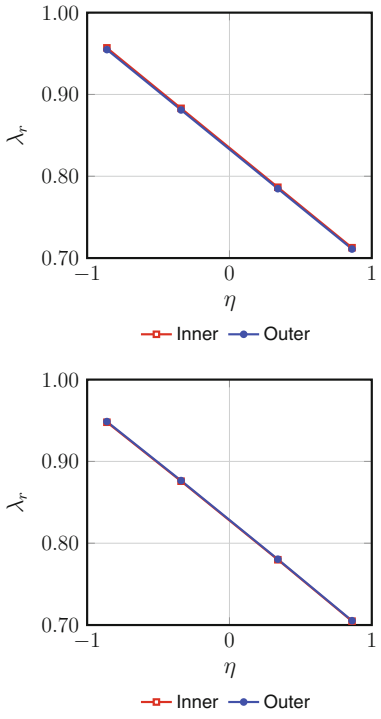

Fig. 15 Radial stretches for the meshes with 8 elements and quadratic (*top*) and cubic (*bottom*) B-splines

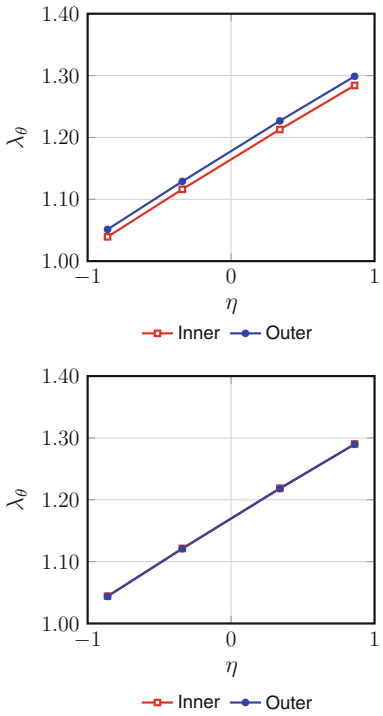

Fig. 16 Circumferential stretches for the meshes with 16 elements and quadratic (*top*) and cubic (*bottom*) B-splines

Table 1 Stretch values at the integration points for the mesh with 128 elements and cubic B-splines. The values along the inner and outer lines are identical for the number of digits displayed

η	λ_r	λ_θ
−0.86114	0.9481	1.044
−0.33998	0.8760	1.121
0.33998	0.7800	1.218
0.86114	0.7049	1.289

Table 1 shows, for the mesh with 128 elements and cubic B-splines, the stretch values at the integration points. We assume the values in Table 1 to be the actual values and calculate based on that the relative error for the other meshes. Figure 17 shows the relative error in the radial and circumferential stretches at all 8 integration points for all those other meshes.

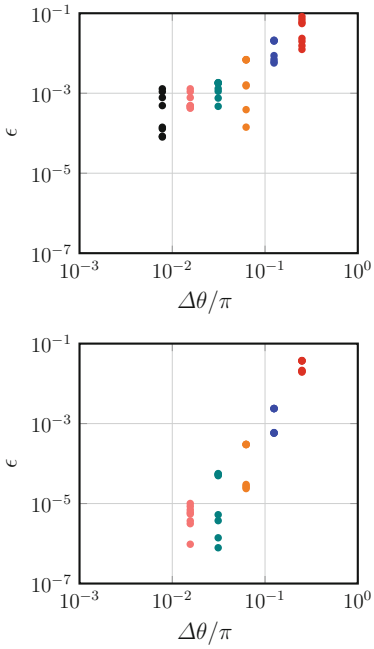

Fig. 17 Relative error in the radial and circumferential stretches at all 8 integration points for the meshes with quadratic (*top*) and cubic (*bottom*) B-splines. The colors represent different meshes, with the same color convention used in Fig. 11. The relative error is calculated based on the value obtained from the mesh with 128 elements and cubic B-splines

5 Concluding Remarks

We have introduced the version of the EBZSS estimation method with isogeometric wall discretization. The EBZSS estimation method, which was originally introduced in the context of finite element wall discretization, will help us estimate the ZSS in patient-specific arterial FSI computations, where the image-based arterial geometry does not come from a ZSS. The method consists of three main components. 1. An iterative method, which starts with a calculated initial guess, is used for computing the EBZSS such that under a given load, the image-based target shape is matched. 2. A method for straight-tube segments is used for computing the EBZSS so that the given diameter and longitudinal stretch in the target configuration are matched together with the opening angle. 3. An element-based mapping between the artery and straight-tube configurations. This provides the mapping from the arterial configuration to the straight-tube configuration, and from the estimated EBZSS of the straight-tube configuration back to the arterial configuration, to be used as the initial guess for the iterative method that matches the target shape. With NURBS basis functions, we may be able to use larger and less number of elements compared to linear basis functions. Higher-order NURBS basis functions allow representation of more complex shapes within an element. To demonstrate how the new EBZSS estimation method performs, we presented 2D test computations with straight-tube configurations, carried out with quadratic and cubics basis functions and meshes made of different number of elements.

Acknowledgements This work was supported in part by JST-CREST; Grant-in-Aid for Scientific Research (S) 26220002 from the Ministry of Education, Culture, Sports, Science and Technology of Japan (MEXT); Rice–Waseda research agreement.

References

1. R. Torii, M. Oshima, T. Kobayashi, K. Takagi, T.E. Tezduyar, Influence of wall elasticity on image-based blood flow simulations. Trans. Jpn. Soc. Mech. Eng. Ser. A, **70**, 1224–1231 (2004). doi:10.1299/kikaia.70.1224. in Japanese
2. R. Torii, M. Oshima, T. Kobayashi, K. Takagi, T.E. Tezduyar, Computer modeling of cardiovascular fluid-structure interactions with the Deforming-Spatial-Domain/Stabilized Space-Time formulation. Comput. Methods Appl. Mech. Eng. **195**, 1885–1895 (2006). doi:10.1016/j.cma.2005.05.050
3. R. Torii, M. Oshima, T. Kobayashi, K. Takagi, T.E. Tezduyar, Fluid-structure interaction modeling of aneurysmal conditions with high and normal blood pressures. Comput. Mech. **38**, 482–490 (2006). doi:10.1007/s00466-006-0065-6
4. Y. Bazilevs, V.M. Calo, Y. Zhang, T.J.R. Hughes, Isogeometric fluid-structure interaction analysis with applications to arterial blood flow. Comput. Mech. **38**, 310–322 (2006)
5. T.E. Tezduyar, S. Sathe, T. Cragin, B. Nanna, B.S. Conklin, J. Pausewang, M. Schwaab, Modeling of fluid-structure interactions with the space-time finite elements: arterial fluid mechanics. Int. J. Numer. Methods Fluids **54**, 901–922 (2007). doi:10.1002/fld.1443
6. R. Torii, M. Oshima, T. Kobayashi, K. Takagi, T.E. Tezduyar, Influence of wall elasticity in patient-specific hemodynamic simulations. Compu. Fluids **36**, 160–168 (2007). doi:10.1016/j.compfluid.2005.07.014
7. R. Torii, M. Oshima, T. Kobayashi, K. Takagi, T.E. Tezduyar, Numerical investigation of the effect of hypertensive blood pressure on cerebral aneurysm–dependence of the effect on the aneurysm shape. Int. J. Numer. Methods Fluids **54**, 995–1009 (2007). doi:10.1002/fld.1497
8. Y. Bazilevs, V.M. Calo, T.E. Tezduyar, T.J.R. Hughes, YZβ discontinuity-capturing for advection-dominated processes with application to arterial drug delivery. Int. J. Numer. Methods Fluids **54**, 593–608 (2007). doi:10.1002/fld.1484
9. T.E. Tezduyar, S. Sathe, M. Schwaab, B.S. Conklin, Arterial fluid mechanics modeling with the stabilized space-time fluid-structure interaction technique. Int. J. Numer. Methods Fluids **57**, 601–629 (2008). doi:10.1002/fld.1633
10. R. Torii, M. Oshima, T. Kobayashi, K. Takagi, T.E. Tezduyar, Fluid-structure interaction modeling of a patient-specific cerebral aneurysm: influence of structural modeling. Comput. Mech. **43**, 151–159 (2008). doi:10.1007/s00466-008-0325-8
11. Y. Bazilevs, V.M. Calo, T.J.R. Hughes, Y. Zhang, Isogeometric fluid-structure interaction: theory, algorithms, and computations. Comput. Mech. **43**, 3–37 (2008)
12. J.G. Isaksen, Y. Bazilevs, T. Kvamsdal, Y. Zhang, J.H. Kaspersen, K. Waterloo, B. Romner, T. Ingebrigtsen, Determination of wall tension in cerebral artery aneurysms by numerical simulation. Stroke **39**, 3172–3178 (2008)
13. T.E. Tezduyar, M. Schwaab, S. Sathe, Sequentially-Coupled Arterial Fluid-Structure Interaction (SCAFSI) technique. Comput. Methods Appl. Mech. Eng. **198**, 3524–3533 (2009). doi:10.1016/j.cma.2008.05.024
14. R. Torii, M. Oshima, T. Kobayashi, K. Takagi, T.E. Tezduyar, Fluid-structure interaction modeling of blood flow and cerebral aneurysm: significance of artery and aneurysm shapes. Comput. Methods Appl. Mech. Eng. **198**, 3613–3621 (2009). doi:10.1016/j.cma.2008.08.020
15. Y. Bazilevs, J.R. Gohean, T.J.R. Hughes, R.D. Moser, Y. Zhang, Patient-specific isogeometric fluid-structure interaction analysis of thoracic aortic blood flow due to implantation of the Jarvik, left ventricular assist device. Comput. Methods Appl. Mech. Eng. **198**(2009), 3534–3550 (2000)

16. Y. Bazilevs, M.-C. Hsu, D. Benson, S. Sankaran, A. Marsden, Computational fluid-structure interaction: methods and application to a total cavopulmonary connection. Comput. Mech. **45**, 77–89 (2009)
17. K. Takizawa, J. Christopher, T.E. Tezduyar, S. Sathe, Space-time finite element computation of arterial fluid-structure interactions with patient-specific data. Int. J. Numer. Methods Biomed. Eng. **26**, 101–116 (2010). doi:10.1002/cnm.1241
18. T.E. Tezduyar, K. Takizawa, C. Moorman, S. Wright, J. Christopher, Multiscale sequentially-coupled arterial FSI technique. Comput. Mech. **46**, 17–29 (2010). doi:10.1007/s00466-009-0423-2
19. K. Takizawa, C. Moorman, S. Wright, J. Christopher, T.E. Tezduyar, Wall shear stress calculations in space-time finite element computation of arterial fluid-structure interactions. Comput. Mech. **46**, 31–41 (2010). doi:10.1007/s00466-009-0425-0
20. R. Torii, M. Oshima, T. Kobayashi, K. Takagi, T.E. Tezduyar, Influence of wall thickness on fluid-structure interaction computations of cerebral aneurysms. Int. J. Numer. Methods Biomed. Eng. **26**, 336–347 (2010). doi:10.1002/cnm.1289
21. R. Torii, M. Oshima, T. Kobayashi, K. Takagi, T.E. Tezduyar, Role of 0D peripheral vasculature model in fluid-structure interaction modeling of aneurysms. Comput. Mech. **46**, 43–52 (2010). doi:10.1007/s00466-009-0439-7
22. Y. Bazilevs, M.-C. Hsu, Y. Zhang, W. Wang, X. Liang, T. Kvamsdal, R. Brekken, J. Isaksen, A fully-coupled fluid-structure interaction simulation of cerebral aneurysms. Comput. Mech. **46**, 3–16 (2010)
23. K. Sugiyama, S. Ii, S. Takeuchi, S. Takagi, Y. Matsumoto, Full Eulerian simulations of biconcave neo-Hookean particles in a Poiseuille flow. Comput. Mech. **46**, 147–157 (2010)
24. Y. Bazilevs, M.-C. Hsu, Y. Zhang, W. Wang, T. Kvamsdal, S. Hentschel, J. Isaksen, Computational fluid-structure interaction: methods and application to cerebral aneurysms. Biomech. Model. Mechanobiol. **9**, 481–498 (2010)
25. Y. Bazilevs, J.C. del Alamo, J.D. Humphrey, From imaging to prediction: emerging non-invasive methods in pediatric cardiology. Prog. Pediatr. Cardiol. **30**, 81–89 (2010)
26. K. Takizawa, C. Moorman, S. Wright, J. Purdue, T. McPhail, P.R. Chen, J. Warren, T.E. Tezduyar, Patient-specific arterial fluid-structure interaction modeling of cerebral aneurysms. Int. J. Numer. Methods Fluids **65**, 308–323 (2011). doi:10.1002/fld.2360
27. M. Manguoglu, K. Takizawa, A.H. Sameh, T.E. Tezduyar, Nested and parallel sparse algorithms for arterial fluid mechanics computations with boundary layer mesh refinement. Int. J. Numer. Methods Fluids **65**, 135–149 (2011). doi:10.1002/fld.2415
28. R. Torii, M. Oshima, T. Kobayashi, K. Takagi, T.E. Tezduyar, Influencing factors in image-based fluid-structure interaction computation of cerebral aneurysms. Int. J. Numer. Methods Fluids **65**, 324–340 (2011). doi:10.1002/fld.2448
29. T.E. Tezduyar, K. Takizawa, T. Brummer, P.R. Chen, Space-time fluid-structure interaction modeling of patient-specific cerebral aneurysms. Int. J. Numer. Methods Biomed. Eng. **27**, 1665–1710 (2011). doi:10.1002/cnm.1433
30. M.-C. Hsu, Y. Bazilevs, Blood vessel tissue prestress modeling for vascular fluid-structure interaction simulations. Finite Elem. Anal. Des. **47**, 593–599 (2011)
31. M. Manguoglu, K. Takizawa, A.H. Sameh, T.E. Tezduyar, A parallel sparse algorithm targeting arterial fluid mechanics computations. Comput. Mech. **48**, 377–384 (2011). doi:10.1007/s00466-011-0619-0
32. K. Takizawa, T. Brummer, T.E. Tezduyar, P.R. Chen, A comparative study based on patient-specific fluid-structure interaction modeling of cerebral aneurysms. J. Appl. Mech. **79**, 010908 (2012). doi:10.1115/1.4005071
33. K. Takizawa, Y. Bazilevs, T.E. Tezduyar, Space-time and ALE-VMS techniques for patient-specific cardiovascular fluid-structure interaction modeling. Arch. Comput. Methods Eng. **19**, 171–225 (2012). doi:10.1007/s11831-012-9071-3
34. K. Takizawa, K. Schjodt, A. Puntel, N. Kostov, T.E. Tezduyar, Patient-specific computer modeling of blood flow in cerebral arteries with aneurysm and stent. Comput. Mech. **50**, 675–686 (2012). doi:10.1007/s00466-012-0760-4

35. J.Y. Yao, G.R. Liu, D.A. Narmoneva, R.B. Hinton, Z.-Q. Zhang, Immersed smoothed finite element method for fluid-structure interaction simulation of aortic valves. Comput. Mech. **50**, 789–804 (2012)
36. Y. Bazilevs, K. Takizawa, T.E. Tezduyar, *Computational Fluid–Structure Interaction: Methods and Applications*. (Wiley, 2013). ISBN 978-0470978771
37. Y. Bazilevs, K. Takizawa, T.E. Tezduyar, Challenges and directions in computational fluid-structure interaction. Math. Models Methods Appl. Sci. **23**, 215–221 (2013). doi:10.1142/S0218202513400010
38. K. Takizawa, K. Schjodt, A. Puntel, N. Kostov, T.E. Tezduyar, Patient-specific computational analysis of the influence of a stent on the unsteady flow in cerebral aneurysms. Comput. Mech. **51**, 1061–1073 (2013). doi:10.1007/s00466-012-0790-y
39. C.C. Long, A.L. Marsden, Y. Bazilevs, Fluid-structure interaction simulation of pulsatile ventricular assist devices. Comput. Mech. **52**, 971–981 (2013). doi:10.1007/s00466-013-0858-3
40. M. Esmaily-Moghadam, Y. Bazilevs, A.L. Marsden, A new preconditioning technique for implicitly coupled multidomain simulations with applications to hemodynamics. Comput. Mech. **52**, 1141–1152 (2013). doi:10.1007/s00466-013-0868-1
41. C.C. Long, M. Esmaily-Moghadam, A.L. Marsden, Y. Bazilevs, Computation of residence time in the simulation of pulsatile ventricular assist devices. Comput. Mech. **54**, 911–919 (2014). doi:10.1007/s00466-013-0931-y
42. K. Takizawa, H. Takagi, T.E. Tezduyar, R. Torii, Estimation of element-based zero-stress state for arterial FSI computations. Comput. Mech. **54**, 895–910 (2014). doi:10.1007/s00466-013-0919-7
43. K. Takizawa, T.E. Tezduyar, A. Buscher, S. Asada, Space-time interface-tracking with topology change (ST-TC). Comput. Mech. **54**, 955–971 (2014). doi:10.1007/s00466-013-0935-7
44. J. Yao, G.R. Liu, A matrix-form GSM-CFD solver for incompressible fluids and its application to hemodynamics. Comput. Mech. **54**, 999–1012 (2014). doi:10.1007/s00466-014-0990-8
45. C.C. Long, A.L. Marsden, Y. Bazilevs, Shape optimization of pulsatile ventricular assist devices using FSI to minimize thrombotic risk. Comput. Mech. **54**, 921–932 (2014). doi:10.1007/s00466-013-0967-z
46. K. Takizawa, Y. Bazilevs, T.E. Tezduyar, C.C. Long, A.L. Marsden, K. Schjodt, ST and ALE-VMS methods for patient-specific cardiovascular fluid mechanics modeling. Math. Models Methods Appl. Sci. **24**, 2437–2486 (2014). doi:10.1142/S0218202514500250
47. K. Takizawa, Y. Bazilevs, T.E. Tezduyar, M.-C. Hsu, O. Øiseth, K.M. Mathisen, N. Kostov, S. McIntyre, Engineering analysis and design with ALE-VMS and space-time methods. Arch. Comput. Methods Eng. **21**, 481–508 (2014). doi:10.1007/s11831-014-9113-0
48. K. Takizawa, Computational engineering analysis with the new-generation space-time methods. Comput. Mech. **54**, 193–211 (2014). doi:10.1007/s00466-014-0999-z
49. H. Suito, K. Takizawa, V.Q.H. Huynh, D. Sze, T. Ueda, FSI analysis of the blood flow and geometrical characteristics in the thoracic aorta. Comput. Mech. **54**, 1035–1045 (2014). doi:10.1007/s00466-014-1017-1
50. K. Takizawa, T.E. Tezduyar, A. Buscher, S. Asada, Space-time fluid mechanics computation of heart valve models. Comput. Mech. **54**, 973–986 (2014). doi:10.1007/s00466-014-1046-9
51. K. Takizawa, Y. Bazilevs, T.E. Tezduyar, C.C. Long, A.L. Marsden, K. Schjodt, Patient-specific cardiovascular fluid mechanics analysis with the ST and ALE-VMS methods, in *Numerical Simulations of Coupled Problems in Engineering*, ed. by S.R. Idelsohn. Computational Methods in Applied Sciences, vol. 33, Chapter 4 (Springer, 2014), pp. 71–102. ISBN 978-3-319-06135-1
52. K. Takizawa, R. Torii, H. Takagi, T.E. Tezduyar, X.Y. Xu, Coronary arterial dynamics computation with medical-image-based time-dependent anatomical models and element-based zero-stress state estimates. Comput. Mech. **54**, 1047–1053 (2014). doi:10.1007/s00466-014-1049-6
53. M.-C. Hsu, D. Kamensky, Y. Bazilevs, M.S. Sacks, T.J.R. Hughes, Fluid-structure interaction analysis of bioprosthetic heart valves: significance of arterial wall deformation. Comput. Mech. **54**, 1055–1071 (2014). doi:10.1007/s00466-014-1059-4

54. M.-C. Hsu, D. Kamensky, F. Xu, J. Kiendl, C. Wang, M.C.H. Wu, J. Mineroff, A. Reali, Y. Bazilevs, M.S. Sacks, Dynamic and fluid-structure interaction simulations of bioprosthetic heart valves using parametric design with T-splines and Fung-type material models. Comput. Mech. **55**, 1211–1225 (2015). doi:10.1007/s00466-015-1166-x
55. D. Kamensky, M.-C. Hsu, D. Schillinger, J.A. Evans, A. Aggarwal, Y. Bazilevs, M.S. Sacks, T.J.R. Hughes, An immersogeometric variational framework for fluid-structure interaction: application to bioprosthetic heart valves. Comput. Methods Appl. Mech. Eng. **284**, 1005–1053 (2015)
56. K. Takizawa, T.E. Tezduyar, New directions in space-time computational methods, in *Advances in Computational Fluid-Structure Interaction*, ed. by Y. Bazilevs, K. Takizawa (Engineering and Technology (Springer, Modeling and Simulation in Science, 2016)
57. K. Takizawa, T.E. Tezduyar, Space-time fluid-structure interaction methods. Math. Models Methods Appl. Sci. **22**(supp02), 1230001 (2012). doi:10.1142/S0218202512300013
58. K. Takizawa, Y. Bazilevs, T.E. Tezduyar, M.-C. Hsu, O. Øiseth, K.M. Mathisen, N. Kostov, S. McIntyre, Computational engineering analysis and design with ALE-VMS and ST methods, in *Numerical Simulations of Coupled Problems in Engineering*, ed. by S.R. Idelsohn. Computational Methods in Applied Sciences, vol. 33, Chapter 13 (Springer, 2014), pp. 321–353. ISBN 978-3-319-06135-1
59. Y. Bazilevs, K. Takizawa, T.E. Tezduyar, New directions and challenging computations in fluid dynamics modeling with stabilized and multiscale methods. Math. Models Methods Appl. Sci. **25**, 2217–2226 (2015). doi:10.1142/S0218202515020029
60. T.E. Tezduyar, T. Cragin, S. Sathe, B. Nanna, FSI computations in arterial fluid mechanics with estimated zero-pressure arterial geometry, in *Marine 2007*, ed. by E. Onate, J. Garcia, P. Bergan, T. Kvamsdal, CIMNE, Barcelona, Spain (2007)
61. M.J. Borden, M.A. Scott, J.A. Evans, T. Hughes, Isogeometric finite element data structures based on Bézier extraction of NURBS. Int. J. Numer. Methods Eng. **87**, 15–47 (2011)

Fluid-Structure Interaction Modeling in 3D Cerebral Arteries and Aneurysms

Yue Yu

Abstract In recent years, there have been great interests in fluid-structure interaction (FSI) problems due to their relevance in biomedical applications. However, several difficulties have hindered the development of partitioned FSI algorithms in modeling cerebral arteries and aneurysms. For example, the relatively small values of the mass ratio between the arterial wall and the blood will cause instabilities in coupled solvers, the arterial wall responses are very complicated therefore difficult to be described by classical structural models, accurate simulations in patient-specific geometries require large CPU time, and so on. To resolve these difficulties, the investigation of proper models for the aneurysms and the design of efficient and stable numerical schemes of these models are considered in this chapter. To be specific, we first contribute on stabilizing the partitioned fluid-structure interaction procedure and resolving the added-mass effect, then develop and employ fractional PDEs to model the complex biomechanical viscoelastic properties of patient-specific aneurysms. To validate the optimal coefficient analysis, the FSI framework is applied to patient-specific aneurysms, hence demonstrating the general applicability of the proposed model and the developed methodology.

1 Introduction

A cerebral aneurysm is a pathological dilatation of the intracranial artery, and its rupture is the leading cause of subarachnoid hemorrhage [53]. However, the current clinical technology could not provide a lot of detailed information *in vivo*. Computational simulations then appear as an effective alternative approach for understanding the mechanisms behind aneurysm growth and rupture [8, 15, 16, 25, 28, 39, 50, 51], which rely heavily on the fluid-structure interaction (FSI) methods [3, 4, 6, 17, 22, 24, 29, 37–39, 47]. Regarding the numerical approaches, the high-order spectral/*hp* element method has demonstrated particular advantages, because of its high resolution in space. With the high-order method, it is possible to capture

Y. Yu (✉)
Department of Mathematics, Lehigh University, Bethlehem, PA 18015, USA
e-mail: yuy214@lehigh.edu

P. Wriggers and T. Lenarz (eds.), *Biomedical Technology*, Lecture Notes in Applied and Computational Mechanics 84, DOI 10.1007/978-3-319-59548-1_8

the complicated patient-specific aneurysm geometry, as well as to predict possible flow instabilities. Therefore, this note focuses on developing and bringing to real-life applications high-fidelity and high-performance numerical tools for fluid-structure interaction, with spectral/*hp* element methods.

This chapter is organized as follows. In Sect. 2 we describe the FSI governing equations and discretization methods and the interface transmission conditions. The FSI coupling procedure at each time step for the full partitioned algorithm without special stabilization is summarized in Sect. 2.1.

To stabilize the fluid-structure interaction solver, in Sect. 3 we present the general fictitious methods for fluid-structure interaction (FSI) problems for the partitioned coupling approach [6, 55]. The fictitious pressure method involves modification of the fluid solver whereas the fictitious mass and damping methods modify the structure solver. Therefore, the generalized fictitious methods can provide not only software modularity but also great flexibility for implementation. For example, one can combine a fluid open source code with a black box structure code by employing the fictitious pressure method, or a fluid black box code with a structure open source code by employing the fictitious mass (or damping) method. We analyze *all* fictitious methods for simplified problems and obtain explicit expressions for the optimal reduction factor (convergence rate index) at the FSI interface [23]. This analysis also demonstrates an apparent similarity of fictitious methods to the FSI approach based on Robin boundary conditions, while the Robin boundary conditions have been found to be very effective in FSI problems. All methods were implemented in the context of spectral element discretization, which is more sensitive to temporal instabilities than low-order methods. In numerical tests, we verify the selection of optimal values for the fictitious parameters for simplified problems, and also also develop an empirical a posteriori analysis for complex geometries. The empirical a posteriori analysis is applied to 3D patient-specific flexible brain arteries with aneurysms for very large deformations. We demonstrate that the fictitious pressure method enhances stability and convergence, and is comparable or better in most cases to the Robin approach or to the other fictitious methods.

Based on the stabilized FSI method, in Sect. 4 we then demonstrate a new fractional-order PDE model for arterial walls introduced in [56]. Typically, integer-order differential equations are used to model the stress-strain relations for arterial walls [1, 21, 43]. However, although the integer-order model can capture the time-dependent response of the arterial wall, in [18] it was reported that this model's viscoelastic response is very sensitive to the relaxation parameters. In arterial simulations, these relaxation parameters vary significantly among patients and anatomic locations, which makes the estimation of these parameters a challenging task and hinders the use of the integer order model. Therefore, in [12–14, 18, 40] fractional time derivatives [34, 35, 41] are introduced to describe the layered structure of arterial walls and to capture the continuous relaxation spectrum of soft tissue. In Sect. 4, we develop fundamental new numerical methods for 3D fractional order PDEs, and investigate the fractional order models for 3D arterial walls in FSI simulations. To deal with the high memory requirements and in order to accelerate the numerical evaluation of hereditary integrals, we employ a fast convolution method [32]

that reduces the memory cost to $O(\log(N))$ and the computational complexity to $O(N\log(N))$. Furthermore, we combine the fast convolution with high-order backward differentiation to achieve third-order time integration accuracy. We confirm that in 3D viscoelastic simulations, the integer order models strongly depends on the relaxation parameters, while the fractional order models are less sensitive. As an application to *long-time* simulations in complex geometries, we also apply the method to modeling fluid-structure interaction of a 3D patient-specific *compliant* cerebral artery with an aneurysm.

Lastly, we summarize in Sect. 6, and suggest several problems as a natural next step.

2 Fluid-Structure Interaction: Mathematical Formulation

In the arterial flow simulations, the domain $\Omega \subset \mathbb{R}^3$ can be composed of two parts: the fluid subdomain $\Omega_f(t)$ occupied by the fluid (blood), and the structure subdomain Ω_s occupied by a deformable structure (arterial walls), as shown in Fig. 1. There is a common boundary between the two subdomains, which is the fluid-structure interface $\Sigma(t) = \Omega_f(t) \cap \Omega_s$. The fluid problem is stated in an arbitrary Lagrangian-Eulerian framework [26] since the fluid domain is changing with the movement of the interface, while for the structure kinematics a purely Lagrangian approach is adopted. Therefore, we aim to solve for three sets of variables in this FSI system: the fluid velocity $\mathbf{u}(\mathbf{x}, t)$, the fluid mesh velocity $\mathbf{w}(\mathbf{x}, t)$, and the structure displacement $\eta(\mathbf{X}, t)$. Here $\mathbf{x} = \mathbf{x}(t)$ and $\mathbf{X}$ are the position vectors in the deformed configuration and initial configuration, respectively.

In this section, we present the general settings for fluid and structure subdomains, respectively, and describe a *strong* coupling partitioned method, which solves the FSI system with the standard Dirichlet-Neumann boundary condition at the interface. In the following, we assume that suitable Dirichlet or Neumann boundary conditions are imposed on the boundaries $\partial\Omega_f(t)\backslash\Sigma(t)$ and $\partial\Omega_s\backslash\Sigma(t)$, and therefore omit them in the descriptions. To ensure the continuity on the interface, subiterations are

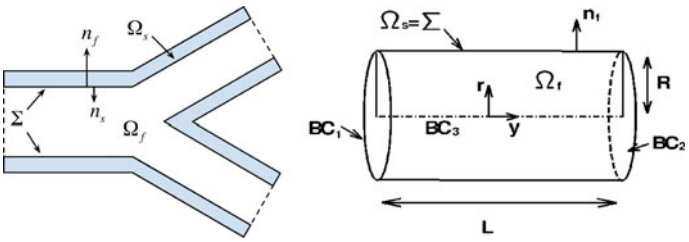

Fig. 1 Sketches for problems of interest: *Left* flow inside an arterial bifurcation; *Right* domain for the flow in a tube arterial model

employed on each time step. In the following sections, we denote the subiteration number by the subscript k, and the time step number by the superscript n.

Fluid Model: The fluid is assumed to be incompressible and Newtonian, hence, we describe it by the incompressible Navier-Stokes equation in the arbitrary Lagrangian-Eulerian (ALE) framework,

$$\frac{\partial \mathbf{u}}{\partial t} + (\mathbf{u} - \mathbf{w}) \cdot \nabla \mathbf{u} = -\frac{\nabla p}{\rho_f} + \nu \nabla^2 \mathbf{u}, \quad \text{in } \Omega_f(t), \tag{1a}$$

$$\nabla \cdot \mathbf{u} = 0, \quad \text{in } \Omega_f(t), \tag{1b}$$

combined with the initial condition $\mathbf{u}(\mathbf{x}, t = 0) = \mathbf{u}_0(\mathbf{x})$, in $\Omega_f(0)$, and the Dirichlet boundary conditions on the interface, i.e., $\mathbf{u} = \frac{\partial \eta}{\partial t}$, on $\Sigma(t)$, which enforces the continuity of velocities. Here, $\mathbf{w}$, p, ρ_f, and ν stand for the mesh velocity, pressure, fluid density, and the kinematic viscosity, respectively.

To solve numerical equations (1), we employ the parallel Navier-Stokes solver NEKTAR [31] where the Navier-Stokes equation is discretized in time using a high-order splitting scheme, with three parts: first the nonlinear terms are treated explicitly, then the pressure is obtained by a Poisson equation solver, and finally the viscous terms are treated implicitly [30]. At time step n and subiteration step k, we solve for $\mathbf{u}_k^n$ and p_k^n from previous time step results $\mathbf{u}^{n-i}$ and previous subiteration solution $\mathbf{u}_{k-1}^n$ [5]:

$$\frac{\tilde{\mathbf{u}}^n - \sum_{i=1}^{J} \alpha_i \mathbf{u}^{n-i}}{\Delta t} = -\mathbf{N}_{k-1}^n, \tag{2a}$$

$$\frac{\tilde{\tilde{\mathbf{u}}}^n - \tilde{\mathbf{u}}^n}{\Delta t} = -\frac{\nabla p_k^n}{\rho_f}, \tag{2b}$$

$$\frac{\beta \mathbf{u}_k^n - \tilde{\tilde{\mathbf{u}}}^n}{\Delta t} = \nu \nabla^2 \mathbf{u}_k^n, \tag{2c}$$

where

$$\frac{\partial p_k^n}{\partial \mathbf{n}_f} = -\rho_f \left(\frac{\partial \mathbf{u}_k^n}{\partial t} + \nu \nabla \times \nabla \times \mathbf{u}_{k-1}^n + \mathbf{N}_{k-1}^n \right) \cdot \mathbf{n}_f, \quad \text{on } \Sigma(t), \tag{3}$$

and $\mathbf{N}_{k-1}^n := (\mathbf{u}_{k-1}^n - \mathbf{w}^{n-1}) \cdot \nabla \mathbf{u}_{k-1}^n$. Here J denotes the time integration order, and α_i, β are the corresponding coefficients of the $J-$th order backward differentiation formulas [31]. In (3), $\mathbf{n}_f$ is the normal vector of fluid subdomain pointing outward on the interface $\Sigma(t)$.

The current configuration $\mathbf{x}$ of the fluid subdomain is defined as a lifting from the structure displacement on the interface: given the displacement on the interface $\eta|_\Sigma$, we construct a mapping from the initial fluid configuration $\Omega_f(0)$ to the current configuration $\Omega_f(t)$, based on a harmonic extension operator. At each time step, the mesh position $\mathbf{x}$ is obtained from the integration of the mesh velocity. Similar to the Navier-Stokes equation, at each time step the mesh velocity is obtained by solving

the Laplace equation with the spectral element method. For more details about the fluid solver, we refer the interested readers to [6].

Structure Model: For the structure subdomain we follow the Lagrangian approach, so all physical variables are described in the initial configuration $\mathbf{X}$. We are going to start with a linear elastic model and infinitesimal deformations in this section and Sect. 3, then modify the model to an viscoelastic Kelvin-Zener (Standard Linear Solid or SLS) model in Sect. 4. Note that a hyperelastic model with finite deformations [54] can also readily be substituted in. The equation describing the deformation can be expressed as follows:

$$\rho_s \frac{\partial^2 \eta}{\partial t^2} - \text{div}(\mathbf{S}) = \rho_s \mathbf{f}, \quad \text{in } \Omega_s, \tag{4}$$

with the *Neumann* boundary condition at the interface

$$\mathbf{S}\mathbf{n}_s = -[-p\mathbf{I} + \rho_f \nu(\nabla \mathbf{u} + (\nabla \mathbf{u})^T)]\mathbf{n}_f, \quad \text{on } \Sigma(t), \tag{5}$$

and the proper initial deformation $\eta(\mathbf{x}, t = 0) = \eta_0(\mathbf{x}), \quad \text{in } \Omega_s$. In the above equations, $\mathbf{S}$, $\mathbf{f}$ and ρ_s are the second Piola-Kirchhoff stress tensor for the specific material, the body load on the structure, and the structure density, respectively. On the interface $\Sigma(t)$, $\mathbf{n}_s$ stands for the normal vector pointing outward from the structure subdomain. When considering the geometrically linear elastodynamics, the second Piola-Kirchhoff stress tensor is given by

$$\mathbf{S} = \frac{\lambda E}{2(1+\lambda)(1-2\lambda)} \left[\text{tr} \left(\frac{\partial \eta}{\partial \mathbf{X}} + \frac{\partial \eta}{\partial \mathbf{X}}^T \right) \right] + \frac{E}{2(1+\lambda)} \left(\frac{\partial \eta}{\partial \mathbf{X}} + \frac{\partial \eta}{\partial \mathbf{X}}^T \right), \tag{6}$$

where E and λ are the Young's modulus and the Poisson ratio of the material, respectively. On the right hand side of (5), we note that $-p\mathbf{I} + \rho_f \nu[\nabla \mathbf{u} + (\nabla \mathbf{u})^T]$ represents the hydrodynamic stresses at the interface from the flow. Therefore, while the transmission condition $\mathbf{u} = \frac{\partial \eta}{\partial t}$ enforces the continuity of velocities, the Neumann boundary condition in (5) enforces the continuity of the normal stresses at the interface.

The structure problem is solved with a parallel spectral element method code, StressNEKTAR [20]. Spatially, the variables in StressNEKTAR are discretized in a similar way as in NEKTAR. To discretize in time, we implement a three-step backward differentiation formula (BDF) [19] which can be defined by different expressions for the displacement and velocity at the next time step. From (4) and (5) we have

$$\rho_s \ddot{\eta}_k^n - \text{div}(\mathbf{S}(\eta_k^n)) = \rho_s \mathbf{f}_k^n, \tag{7}$$

and

$$\mathbf{S}(\eta_k^n)\mathbf{n}_s = -[-p_{k-1}^n \mathbf{I} + \rho_f \nu(\nabla \mathbf{u}_{k-1}^n + (\nabla \mathbf{u}_{k-1}^n)^T)](\mathbf{n}_f)^n, \quad \text{on } \Sigma(t), \tag{8}$$

where we have used "$\cdot$" to denote the temporal derivatives. In the *three-step BDF scheme*, the acceleration and velocity approximations are also expressed based on

the current information $(\eta_k^n, \dot{\eta}_k^n)$ and previous time steps results $(\eta^{n-i}, \dot{\eta}^{n-i})$ as:

$$\dot{\eta}_k^n = A_1\eta_k^n + B_1\eta^{n-1} + C_1\eta^{n-2} + D_1\eta^{n-3}, \tag{9a}$$
$$\ddot{\eta}_k^n = A_2\dot{\eta}_k^n + B_2\dot{\eta}^{n-1} + C_2\dot{\eta}^{n-2} + D_2\dot{\eta}^{n-3}. \tag{9b}$$

Here A_i, B_i, C_i and D_i $(i = 1, 2)$ are related following the rule

$$A_1 = \frac{\theta_1}{\Delta t},\ B_1 = \frac{2.5 - 3\theta_1}{\Delta t},\ C_1 = \frac{3\theta_1 - 4}{\Delta t},\ D_1 = \frac{1.5 - \theta_1}{\Delta t}, \tag{10a}$$
$$A_2 = \frac{\theta_2}{\Delta t},\ B_2 = \frac{2.5 - 3\theta_2}{\Delta t},\ C_2 = \frac{3\theta_2 - 4}{\Delta t},\ D_2 = \frac{1.5 - \theta_2}{\Delta t}, \tag{10b}$$

and (θ_1, θ_2) are also decided based on considerations of stability and dissipation. When taking $(\theta_1, \theta_2) = (0, 0)$, the three-step BDF scheme reaches its highest accuracy, i.e., the third-order convergence in time.

2.1 Partitioned Algorithm

To strongly impose the continuity of the interface, at each time step we perform subiterations for the FSI system until a convergence is obtained. In each subiteration step, the fluid and structure solvers work separately, then interact by exchanging suitable transmission conditions at the interface $\Sigma(t)$. Here the Aitken relaxation, see the appendix of [55], is employed in both the structure and fluid solvers, to accelerate the convergence. At the n-th time step, we solve the FSI system following the fixed point algorithm:

1. Set

$$\text{(Solid) } \eta_0^n = \eta^{n-1},\ \dot{\eta}_0^n = \dot{\eta}^{n-1},\ \ddot{\eta}_0^n = \ddot{\eta}^{n-1}, \tag{11a}$$
$$\text{(Fluid) } \mathbf{u}_0^n = \mathbf{u}^{n-1},\ p_0^n = p^{n-1}. \tag{11b}$$

2. **for** $k = 1 : k_{max}$, **do**
   a. (Solid) Solve the elastodynamics equation (7) with external traction force $-[-p_{k-1}^n\mathbf{I} + \rho_f\nu(\nabla\tilde{\mathbf{u}}_{k-1}^n + (\nabla\tilde{\mathbf{u}}_{k-1}^n)^T)](\mathbf{n}_f)^n$ applied on the interface, and update the displacement results η_k^n.
   b. (Solid) Perform the Aitken relaxation on η_k^n, and obtain the relaxed displacement $\tilde{\eta}_k^n$.
   c. (Solid) From $\tilde{\eta}_k^n$, calculate the velocity and acceleration $\dot{\eta}_k^n$ and $\ddot{\eta}_k^n$ based on the BDF scheme (9).
   d. (Solid) Pass the velocity and acceleration at the interface to the fluid solver.

e. (Fluid) Update the velocity boundary condition $\mathbf{u}_k^n = \dot{\eta}_k^n$ and the pressure boundary condition $\partial p_k^n / \partial \mathbf{n}_f = -\rho_f \left(\ddot{\eta}_k^n + \nu \nabla \times \nabla \times \mathbf{u}_{k-1}^n + \mathbf{N}_{k-1}^n \right) \cdot (\mathbf{n}_f)^n$ at the interface.
f. (Fluid) Solve the Navier-Stokes equation (2), and obtain updated velocity and pressure $(\mathbf{u}_k^n, p_k^n)$.
g. (Fluid) Apply the Aitken relaxation on $\mathbf{u}_k^n$ to obtain the relaxed velocity $\tilde{\mathbf{u}}_k^n$.
h. (Fluid) Calculate the normal stress $-[-p_k^n \mathbf{I} + \rho_f \nu (\nabla \tilde{\mathbf{u}}_k^n + (\nabla \tilde{\mathbf{u}}_k^n)^T)](\mathbf{n}_f)^n$ at the interface
i. (Fluid) Pass the normal stress at the interface to the structure solver.
j. (Solid and Fluid) Check convergence on both solvers. If

$$||\tilde{\eta}_k^n - \tilde{\eta}_{k-1}^n||, \ ||\tilde{\mathbf{u}}_k^n - \tilde{\mathbf{u}}_{k-1}^n||, \ ||p_k^n - p_{k-1}^n|| < \varepsilon, \tag{12}$$

set $k = k_{max}$ and update the results as

$$\text{(Solid) } \eta^n = \tilde{\eta}_k^n, \ \dot{\eta}^n = \dot{\eta}_k^n, \ \ddot{\eta}^n = \ddot{\eta}_k^n, \tag{13a}$$

$$\text{(Fluid) } \mathbf{u}^n = \tilde{\mathbf{u}}_k^n, \ p^n = p_k^n. \tag{13b}$$

Else, continue to the $(k+1)$-th subiteration.

3. (Mesh) Update the mesh velocity boundary condition at the interface with $\mathbf{w}^n = \dot{\eta}^n$ and get the mesh velocity $\mathbf{w}^n$.
4. (Mesh) Update the mesh positions for the fluid subdomain.
5. Go to time step $n+1$.

3 Fictitious Methods

In the presence of large added-mass, the coupling procedure introduced in Sect. 2.1 exhibits very slow convergence, or sometimes even no convergence at all [9]. To overcome this problem, fictitious methods were introduced in [6, 55], as an effective way of stabilization and convergence acceleration. A brief review of these methods are given in this section, and a convergence analysis is derived for all cases for simplified problems, which provide us with some guidance in choosing the optimal parameters in the applications.

Fictitious Mass and Damping Methods: In the fictitious mass and damping methods [6], the structure momentum equation is solved with additional acceleration and damping terms. These terms aim to balance the added-mass operator. Considering the fictitious mass coefficient f_m and damping coefficient f_d, equation (7) is modified as

$$\rho_s (1 + f_m) \ddot{\eta}_k^n + \rho_s f_d \dot{\eta}_k^n - \text{div}(\mathbf{S}(\eta_k^n)) = \rho_s \mathbf{f}_k^n + \rho_s f_m \ddot{\eta}_{k-1}^n + \rho_s f_d \dot{\eta}_{k-1}^n. \tag{14}$$

Here we note that when the subiteration is converged, we have $\eta_k^n \approx \eta_{k-1}^n$ and $\dot{\eta}_k^n \approx \dot{\eta}_{k-1}^n$. Therefore, the scheme with fictitious mass and damping of Eq. (14) should converge to the same results as the original scheme of Eq. (7) at the end of each time step. The fictitious mass method can be thought of as mimicking an exact coupled solver, with the optimal value of f_m being a good approximation to $\frac{\rho_f \mathscr{M}}{\rho_s H_s}$ where $\mathscr{M}$ is the added-mass operator as defined in [55].

Fictitious Pressure Method: Now we also apply the idea of fictitious methods to the fluid solver, on the pressure term in (1a). By introducing the fictitious pressure coefficient f_p, the splitting scheme for the Navier-Stokes equation (2) can be written as

$$\frac{\beta \mathbf{u}_k^n - \sum_{i=1}^{J} \alpha_i \mathbf{u}^{n-i}}{\Delta t} + \mathbf{N}_{k-1}^n - f_p \frac{\nabla p_{k-1}^n}{\rho_f} = -(1+f_p)\frac{\nabla p_k^n}{\rho_f} + \nu \nabla^2 \mathbf{u}_k^n. \tag{15}$$

As in the fictitious mass and damping methods, the new scheme (15) converges to the same values as the original one (2) at the end of each time step, and therefore it does not change the physical solution of the FSI problem.

3.1 Analysis of an Idealized Artery Model

We now consider a simple model for an artery modeled as a straight tube. The problem is solved in a cylinder with radius R and length L, as shown in the right plot of Fig. 1, in which a Neumann boundary condition $\frac{\partial \mathbf{u}}{\partial \mathbf{n}} = 0$ is set on BC_1 and BC_2, and Dirichlet boundary condition $p = \bar{p}(t)$ for pressure. In the cylindrical coordinate system (r, θ, y), this problem is independent of the angle θ, therefore a tube domain $\Omega = \{(r, y) \in [0, R) \times [0, L]\} \subset \mathbb{R}^2$ is considered, with the fluid subdomain $\Omega_f = \Omega$ as and the structure subdomain coincides with the interface $\Sigma = \{(r, y) | r = R \text{ and } y \in [0, L]\}$. In this simplified model, the deformation of the structure is assumed to be very small, therefore the fluid domain can be considered fixed. Here we use a linear incompressible inviscid model for the fluid, and a generalized string model as described in [42] for the structure:

$$\rho_f \frac{\partial \mathbf{u}}{\partial t} + \nabla p = 0, \text{ in } \Omega_f, \tag{16a}$$

$$\frac{1}{r}\frac{\partial (r u_r)}{\partial r} + \frac{\partial u_y}{\partial y} = 0, \text{ in } \Omega_f, \tag{16b}$$

$$\mathbf{u} \cdot \mathbf{n} = \frac{\partial \eta}{\partial t}, \text{ on } \Sigma, \tag{16c}$$

$$\frac{\partial \mathbf{u}}{\partial \mathbf{n}} = 0, \ p = \bar{p}(t) \text{ on } BC_1 \cup BC_2, \tag{16d}$$

$$p = \rho_s H_s \frac{\partial^2 \eta}{\partial t^2} + G_1 H_s \eta - G_2 H_s \frac{\partial^2 \eta}{\partial y^2}, \text{ on } \Sigma, \tag{16e}$$

where the components of $\mathbf{u}$ in r and y directions are denoted as u_r and u_y, respectively. In the structure model, the displacement η lies in the r direction, with H_s, G_1, G_2 as the thickness and the material coefficients. Here H_s is the thickness of the structure, and $G_2 = \frac{KE}{1+\lambda}$ with K being the Timoshenko correction factor. The reaction term G_1 is introduced to take into account transverse membrane effects. For an arterial vessel with radius R_0, this term can be approximated as $G_1 \approx \frac{E}{(1-\lambda^2)R^2}$ under the assumption of linear elastic behavior, as illustrated in [42]. Here the pressure can be decomposed into two parts: one given by the interaction with the structure at the interface, and another one related to the other boundaries $\Omega_f \backslash \Sigma$ only. Our main focus is on the first part, which is influenced by the added-mass operator $\mathscr{M}$, and therefore the boundary conditions $p = \bar{p}(t)$ on $BC_1 \cup BC_2$ are assumed to be vanishing.

Now we investigate the effects of fictitious methods on this simplified tube problem. The following analysis is performed on the n-th step, therefore we omit the step numbers and analyze the convergence of pressure to the zero solution. Similar to the analysis in [23], our convergence analysis is based on the Fourier sine transform in the y direction. Since $p_k(r, y) = 0$ when $y = 0$ or $y = L$, for every fixed r, the Fourier sine series $\{\sin\left(\frac{\gamma\pi r}{L}\right)\}, \gamma = 1, 2, \cdots \infty$ forms a complete orthogonal basis for $p_k(r, y)$. In the following analysis, the reduction factor is defined by the Fourier sine coefficients: given a function $c(r, y) \in L^2(\mathbb{R}^2)$,

$$\hat{c}(r, \gamma) = \frac{2}{L} \int_0^L c(r, y) \sin\left(\frac{\gamma\pi y}{L}\right) dy. \tag{17}$$

which corresponds to the frequency γ. To quantify the error for pressure at the k-th subiteration, on the interface we define a reduction factor in the frequency space

$$\rho_k(\gamma) := \frac{|\hat{p}_k(0, \gamma) - \hat{p}(0, \gamma)|}{|\hat{p}_{k-1}(0, \gamma) - \hat{p}(0, \gamma)|}, \tag{18}$$

where $\hat{p}(r, \gamma)$ is the Fourier sine coefficient of the exact pressure $p(r, y)$ at the current time, and $\hat{p}_k(r, \gamma)$ is the Fourier coefficient of the numerical approximation for pressure at the k-th subiteration. If $\rho_k(\gamma)$ is less than 1 for all relevant frequencies at every subiteration step, the algorithm converges. Moreover, the smaller this reduction factor is, the faster the rate of convergence is.

In the fictitious mass and damping methods, the structure solver is modified as in (14), with the fluid solver unchanged. In [55] we have derived the following:

Theorem 1 *With fictitious mass and damping coefficients f_m and f_d, respectively, the reduction factor of frequency γ is independent of the subiteration step and it is given by:*

$$\rho^{FM}(\gamma) = \left| \frac{A_1(\beta\rho_f - \mu(\gamma)(f_m A_2 + f_d)\rho_s H_s \Delta t)}{\mu(\gamma)\Delta t((A_2 + f_m A_2 + f_d)A_1\rho_s H_s + G_1 H_s + \gamma^2 G_2 H_s)} \right|, \tag{19}$$

where $\mu(\gamma) := \frac{\gamma\pi I_0'(\frac{\gamma\pi R}{L})}{L I_0(\frac{\gamma\pi R}{L})}$ *depends on the modified Bessel function* $I_0(r) = \sum_{m=0}^{\infty} \frac{1}{m!}\left(\frac{r}{2}\right)^{2m}$, β *is the coefficient of the J-th splitting scheme for the fluid solver as defined in (2),* A_1, A_2 *are the coefficients of the BDF scheme for the structure solver as in (9), and* H_s, G_1, G_2 *are the thickness and material coefficients of the structure model.*

For the fictitious pressure method, we calculate the reduction factor from Fourier analysis for the coupling algorithm with the original structure solver and the fictitious pressure fluid solver as defined in (15). Given a fictitious pressure coefficient f_p, we have derived the following in [55]:

Theorem 2 *The reduction factor for the fictitious pressure coefficient* f_p *of frequency* γ *can be written as*

$$\rho^{FP}(\gamma) = \left| \frac{A_1\beta\rho_f - f_p\Delta t\mu(\gamma)(A_1A_2\rho_s H_s + G_1H_s + \gamma^2 G_2H_s)}{(1+f_p)\Delta t\mu(\gamma)(A_1A_2\rho_s H_s + G_1H_s + \gamma^2 G_2H_s)} \right| \tag{20}$$

which is independent of the subiteration number k.

Remark For the cases with small Young's modulus E or small time step size, we have $G_1\Delta t \ll 1$ and $G_2\Delta t \ll 1$. It was reported in [9] that such cases suffer from severe added-mass effect, and therefore very slow convergence. When taking $f_p = f_m + f_d/A_2$ for these cases, the two fictitious methods both have an equivalent reduction factor as the Dirichlet-Robin transmission condition given in [23]. The optimal coefficients from the fictitious methods should be comparable with each other.

Remark When the material has a large modulus or we use a large time step size, i.e., $G_1\Delta t \gg 1$ and $G_2\Delta t \gg 1$, the reduction factor for the fictitious pressure method reads $\rho^{FP}(\gamma) = \left|\frac{f_p}{1+f_p}\right|$. Therefore a small f_p would be preferred for a faster convergence in these cases.

4 Fractional-Order Viscoelastic Model for Aneurysm Walls

In this section, we extend the linear elastodynamics arterial wall model, to investigate the viscoelastic properties for arterial wall mechanics. To be specific, we study three-dimensional (3D) fractional PDEs that naturally model the continuous relaxation properties of soft tissue, and employ them to simulate flow structure interactions for patient-specific brain aneurysms [55].

Fractional-Order Model: Here we generalize the 1D fractional-order model described in [40] into the 3D case

$$\mathbf{S}(t) + \tau_\sigma^\alpha \frac{\partial^\alpha \mathbf{S}(t)}{\partial t^\alpha} = \mathbf{S}_0(t) + \tau_\varepsilon^\alpha \frac{\partial^\alpha \mathbf{S}_0(t)}{\partial t^\alpha}, \tag{21}$$

where $\mathbf{S}$ is the second Piola-Kirchhoff stress tensor, α is the fractional order, and τ_σ, τ_ε are the relaxation parameters. The Riemann-Liouville definition is employed for the fractional derivative $\frac{d^\alpha f(t)}{dt^\alpha}$ of order α $(0 \leq \alpha < 1)$

$$ {}_{a}^{RL}\mathbf{D}_{t}^{\alpha} f(t) = \frac{1}{\Gamma(1-\alpha)} \frac{d}{dt} \int_a^t (t-\upsilon)^{-\alpha} f(\upsilon) d\upsilon, \tag{22} $$

which is a non-local operator that depends on the history of function $f(t)$. The Γ function is defined as $\Gamma(r) = \int_0^\infty e^{-t} t^{r-1} dt$. We mainly focus on the linear elastic model with infinitesimal deformations for simplicity, i.e., taking the stress tensor $\mathbf{S}_0$ as the $\mathbf{S}$ in (6). However, the same methodology can also be applied on nonlinear materials if we take $\mathbf{S}_0$ as the stress tensor for hyperelastic materials and employ a Newton-Raphson procedure at each time step (more details can be found in [54]). We assume that both the stress tensor and the strain tensor are continuously differentiable, and the object is at a static equilibrium when $t \leq 0$. Then we can set the lower limit of the fractional derivative (22) to be $a = 0$. Consequently, as α approaches 1, the model (21) converges to the integer-order SLS model

$$ \mathbf{S}(t) + \tau_\sigma \frac{\partial \mathbf{S}(t)}{\partial t} = \mathbf{S}_0(t) + \tau_\varepsilon \frac{\partial \mathbf{S}_0(t)}{\partial t}. $$

In fact, we have also numerically verified that as the fractional order α approaches 1, the simulation results from the fractional-order model converges to the results from the integer order SLS model, and therefore increasingly more sensitive to the parameters (also shown in [40]).

Fast Convolution Method: Next we derive a time discretization formulation for (4), to compute the displacement field $\eta(\mathbf{X})$. When the integer-order derivative term $\frac{\partial^2 \eta}{\partial t^2}$ can be approximated by the three step BDF scheme (9), the fractional-order derivative is introduced when substituting (21) into (4), which requires special time integration approaches to be investigated in this section. One of the most popular ways of discretizing the fractional derivative is the Grüwald-Letnikov formula which is of first order accuracy in time and consumes $O(N^2)$ operations and $O(N)$ memory in evaluating the accumulated right-hand-side from deformation history. Here $N = T/\Delta t$ numbers of total time steps.

Since the Grüwald-Letnikov formula is limited by its first-order accuracy and the computational bottleneck, especially in long-term time integration as in the FSI problems of interest here. To improve both the accuracy as well as the efficiency, we now convert Eq. (21) to the convolution form. Applying the Laplace transform $\mathscr{L}$ to (21), we have

$$ \mathscr{L}(\mathbf{S})(s) = \left(\left(\frac{\tau_\varepsilon}{\tau_\sigma} \right)^\alpha + \frac{1}{\tau_\sigma^\alpha} \left(1 - \left(\frac{\tau_\varepsilon}{\tau_\sigma} \right)^\alpha \right) \frac{1}{\tau_\sigma^{-\alpha} + s^\alpha} \right) \mathscr{L}(\mathbf{S}_0)(s). \tag{23} $$

Then taking the inverse Laplace transform, we get the relation between $\mathbf{S}(t)$ and $\mathbf{S}_0(t)$

$$\mathbf{S}(t) = \left(\frac{\tau_\varepsilon}{\tau_\sigma}\right)^\alpha \mathbf{S}_0(t) + \frac{1}{\tau_\sigma^\alpha}\left(1 - \left(\frac{\tau_\varepsilon}{\tau_\sigma}\right)^\alpha\right)\int_0^t I(t-r)\mathbf{S}_0(r)dr, \tag{24}$$

where $I(t) := t^{\alpha-1}E_{\alpha,\alpha}\left(-\left(\frac{t}{\tau_\sigma}\right)^\alpha\right)$, $\mathscr{L}(I)(s) = \frac{1}{\tau_\sigma^{-\alpha}+s^\alpha}$, and $E_{\cdot,\cdot}(t)$ is the two parameter Mittag-Leffler function [41], which can be seen as the fractional generalization of the exponential. By substituting the relaxation form of constitutive law (24) into (7), at the n-th time step and the k-th subiteration, we obtain the discretized form

$$\rho_s\ddot{\eta}_k^n + \frac{\tau_\varepsilon^\alpha}{\tau_\varepsilon^\alpha}\mathbf{S}_0(\eta_k^n) = \frac{1}{\tau_\sigma^\alpha}\left(\left(\frac{\tau_\varepsilon}{\tau_\sigma}\right)^\alpha - 1\right)\int_0^{t^n} I(t^n - r)\mathbf{S}_0(\eta(r))dr + \rho_s\mathbf{f}_k^n. \tag{25}$$

When $t \to \infty$, the Mittag-Leffler function has a heavy tail and its decay is only algebraic. Therefore, although we may directly calculate the Mittag-Leffler function to compute the convolution integral $\int_0^t I(t-r)\mathbf{S}_0(\eta(r))dr$ in (25), such heavy tail behavior would prohibit us from alleviating the computational complexity. The methods introduced in [32, 33] then provide an effective alternative to evaluate such convolution integrals. The idea is to decompose the integral range $\int_0^{t^n}$ with base 2:

$$\int_0^{n\Delta t} = \int_0^{2^{m_1}\Delta t} + \int_{2^{m_1}\Delta t}^{(2^{m_1}+2^{m_2})\Delta t} + \cdots + \int_{(n-1)\Delta t}^{n\Delta t} \tag{26}$$

where $m_1 = [log_2(n)]$, $m_2 = [log_2(n - 2^{m_1})]$, etc. To approximate the l-th part of the convolution integral, we apply the trapezoidal rule to a parametrization of the contour integral for the inverse Laplace transform:

$$I(t) = \frac{1}{2\pi i}\int_{\Gamma_l} \mathscr{L}(I)(\gamma)e^{t\gamma}d\gamma \approx \sum_{j=-L}^{L} \omega_j^{(l)}\mathscr{L}(I)(\gamma_j^{(l)})e^{t\gamma_j^{(l)}}, \tag{27}$$

where the complex contour Γ_l is chosen to be the Talbot contour [44, 49], and $\omega_j^{(l)}$ and $\gamma_j^{(l)}$ are the weights and quadrature points on each Talbot contour:

$$\omega_j^{(l)} = -\frac{j}{4\pi(L+1)i}\frac{d\varpi_l}{d\kappa}(\kappa_j), \quad \gamma_j^{(l)} = \varpi_l(\kappa_j), \quad \kappa_j = \frac{j\pi}{L+1}.$$

The function $\varpi_l(\kappa)$ is chosen such that the singularities of $\mathscr{L}(I)(s)$ lie in the contour [33]. In the current method, we generate the quadrature points for all $O(\log N)$ numbers of Talbot contours before the first time step (pre-processing cost only). While computing the last part of the convolution integral in (26), we improve the linear approximation proposed in [33] by making a full use of the velocity $\dot{\eta}^{n-1}$ and acceleration $\ddot{\eta}^{n-1}$ information approximated following the three-step BDF scheme (9):

$$\int_{(n-1)\Delta t}^{n\Delta t} I(n\Delta t - r)\mathbf{S}_0(\eta(r))dr \approx H_1\mathbf{S}_0(\eta^{n-1}) + H_2\mathbf{S}_0(\dot{\eta}^{n-1}) + H_3\mathbf{S}_0(\ddot{\eta}^{n-1}) \tag{28}$$

which introduces an $O(\Delta t^4)$ error. Here the integrals can be calculated a priori as the inverse Laplace transforms

$$H_1 = \int_{(n-1)\Delta t}^{n\Delta t} I(n\Delta t - r)dr \approx \sum_{j=-L}^{L} \omega_j^{(0)} \frac{1}{\gamma_j^{(0)}\left(\tau_\sigma^{-\alpha} + \left(\gamma_j^{(0)}\right)^\alpha\right)} e^{t\gamma_j^{(0)}}$$

$$H_2 = \int_{(n-1)\Delta t}^{n\Delta t} (r - (n-1)\Delta t)I(n\Delta t - r)dr \approx \sum_{j=-L}^{L} \omega_j^{(0)} \frac{1}{(\gamma_j^{(0)})^2\left(\tau_\sigma^{-\alpha} + \left(\gamma_j^{(0)}\right)^\alpha\right)} e^{t\gamma_j^{(0)}}$$

$$H_3 = \int_{(n-1)\Delta t}^{n\Delta t} \frac{(r - (n-1)\Delta t)^2}{2} I(n\Delta t - r)dr \approx \frac{1}{2}\sum_{j=-L}^{L} \omega_j^{(0)} \frac{1}{(\gamma_j^{(0)})^3\left(\tau_\sigma^{-\alpha} + \left(\gamma_j^{(0)}\right)^\alpha\right)} e^{t\gamma_j^{(0)}}$$

and the weights as well as the quadrature points correspond to the Talbot contour chosen for $t = \Delta t$. For the rest of the convolution integrals $\int_a^b I(n\Delta t - r)\mathbf{S}_0(\eta(r))dr$ in (26), we can approximate them on the corresponding Talbot contour Γ_l

$$\begin{aligned}\int_a^b I(n\Delta t - r)\mathbf{S}_0(\eta(r))dr &= \int_a^b \frac{1}{2\pi i}\int_{\Gamma_l} \frac{1}{\tau_\sigma^{-\alpha} + \gamma^\alpha} e^{(n\Delta t - r)\gamma} d\gamma \mathbf{S}_0(\eta(r))dr \\ &\approx \sum_{j=-L}^{L} \omega_j^{(l)} \frac{1}{\tau_\sigma^{-\alpha} + \left(\gamma_j^{(l)}\right)^\alpha} e^{(n\Delta t - b)\gamma_j^{(l)}} \int_a^b e^{(b-r)\gamma_j^{(l)}} \mathbf{S}_0(\eta(r))dr,\end{aligned} \tag{29}$$

where the inner integral $\int_a^b e^{(b-r)\gamma_j^{(l)}} \mathbf{S}_0(\eta(r))dr$ can be updated recursively by solving

$$\frac{dy[b, a, \gamma_j^{(l)}](r)}{dr} = \gamma_j^{(l)} y[b, a, \gamma_j^{(l)}](r) + \mathbf{S}_0(\eta(r)), \quad y(a) = 0. \tag{30}$$

In the end of the n-th time step (when the subiteration has converged), we update $y^n \approx y[b, a, \gamma_j^{(l)}](n\Delta t)$ recursively after obtaining the approximated displacement η^n, velocity $\dot{\eta}^n$ and acceleration $\ddot{\eta}^n$:

$$\begin{aligned} y^n \approx e^{\gamma_j^{(l)}\Delta t} y^{n-1} &+ \frac{e^{\gamma_j^{(l)}\Delta t} - 1}{\gamma_j^{(l)}} \mathbf{S}_0(\eta^n) - \frac{e^{\gamma_j^{(l)}\Delta t}(\gamma_j^{(l)}\Delta t - 1) + 1}{(\gamma_j^{(l)})^2} \mathbf{S}_0(\dot{\eta}^n) \\ &+ \frac{e^{\gamma_j^{(l)}\Delta t}((\gamma_j^{(l)}\Delta t)^2 - 2\gamma_j^{(l)}\Delta t + 2) - 2}{2(\gamma_j^{(l)})^3} \mathbf{S}_0(\ddot{\eta}^n). \end{aligned} \tag{31}$$

Therefore, while the piecewise linear interpolant used in [33] introduces an $O(\Delta t^2)$ error, the time derivatives obtained from the three-step BDF scheme makes our algorithm more effective in long-term computation because it only gives $O(\Delta t^4)$ error at each time step which yields an $O(\Delta t^3)$ error accumulatively. This accuracy could be further improved by using higher-order BDF schemes. Since the Talbot contours are fixed, the computational cost in our algorithm for approximating the convolution integrals (26) are $O(N \log N)$ for multiplications, $O(\log N)$ for evaluations of the Laplace transform $\mathscr{L}(I)(s)$, and $O(\log N)$ active memory for storing y^n. Here N is the total number of time-history steps.

Combining (28) and (29), we can rewrite the right hand side of (25) as

$$\rho_s \mathbf{f}_k^n + \frac{1}{\tau_\sigma^\alpha}\left(\left(\frac{\tau_\varepsilon}{\tau_\sigma}\right)^\alpha - 1\right)\left(H_1 \mathbf{S}_0(\boldsymbol{\eta}^{n-1}) + H_2 \mathbf{S}_0(\dot{\boldsymbol{\eta}}^{n-1}) + H_3 \mathbf{S}_0(\ddot{\boldsymbol{\eta}}^{n-1}) + \sum_l \left(\sum_{j=-L}^{L} \omega_j^{(l)} \frac{1}{\tau_\sigma^{-\alpha} + \left(\gamma_j^{(l)}\right)^\alpha} e^{((n-1)\Delta t - b)\gamma_j^{(l)}} y[b, a, \gamma_j^{(l)}]((n-1)\Delta t) \right)\right) \tag{32}$$

and substitute it into the FSI partitioned algorithm in Sect. 2.1. Note that we only need to update the inner integral approximations y^n following (31) at the end of each time step, i.e., not for each subiteration. The estimated integrals in (28) and (29) introduce an $O(\Delta t^4)$ error each, which accumulatively give an $O(\Delta t^3)$ error from the fast convolution method. Regarding the efficiency, with $N = T/\Delta t$ numbers of total time steps, this resultant algorithm requires $O(N \log N)$ operations and $O(\log N)$ memory.

5 Numerical Simulations

We now present a series of numerical tests using the fictitious methods. With these tests, we aim to provide a validation for our theoretical analysis, and to demonstrate the capability of our fractional-order PDE solver in modeling realistic physiological problems in computational domains with a large number of elements. In particular, we consider two FSI problems which model compliant brain arteries and blood flow, where the mass ratio is relatively low and therefore the stabilization technique is required for the partitioned FSI approach.

5.1 Blood Flow in an Artery

In this section we consider a straight tube with pulsatile inflow as an idealization of an arterial flow. The fluid domain is as illustrated in the right plot of Fig. 1, with

$R = 1$ mm and $L = 4$ mm. The arterial wall is modeled by a layer of linear elastic material on the tube wall, with thickness $H_s = 0.105$ mm. In all tests we take the fluid density as $\rho_f = 1060$ kg/m^3, and the structure density $\rho_s = 1.2\rho_f$ since the material density of the arterial wall is known to be close to that of the blood. On the fluid solver, a Womersley velocity profile with 8 Fourier coefficients is imposed at the inlet boundary, with a mean velocity 0.106 m/s. For the fluid model, the kinematic viscosity for the fluid is set to 3.8×10^{-6} m^2/s. In the structural model, the Poisson ratio is set to $\lambda = 0.3$, and the Young's modulus of the vessel walls $E = 0.6$ MPa, which is in the physiological range of intracranial vessels of size 2–4 mm [2]. In the following simulations, we employ polynomial order 3 elements for the velocity, pressure and displacement. The first-order splitting scheme ($\beta = 1.0$) is applied on the fluid, and the BDF scheme on the structure, with time step size 1.9×10^{-5} (s).

Effect of Fictitious Methods on Number of Subiterations: Next we investigate the optimal values of the fictitious coefficients for the cylindrical artery, and test the effect of these coefficients for both fictitious mass and fictitious pressure methods. On the fluid outlet, a constant pressure boundary condition $p = 0$ MPa and a zero Neumann boundary condition for velocity are imposed. The similarity between the fictitious methods and Dirichlet-Robin transmission conditions suggests that their optimized coefficients should be close, if the same time integration schemes are applied for the fluid and structure solvers. For the simpliffied model described in Sect. 3.1, when apply the fluid and structure solvers in time with first-order accuracy, an optimized coefficient $\alpha_s = \frac{2\rho_f}{\Delta t \gamma_{max}}$ was provided in [23] for the Dirichlet-Robin conditions, where γ_{max} is the maximum frequency supported by the numerical grid (which is 8 in our simulations). Therefore, for the cylindrical case with first-order splitting scheme (which gives $\beta = 1$) for the fluid and the three-step BDF formula (which gives $A_1 = A_2 = \frac{5}{3\Delta t}$) for structure, we can derive the optimal fictitious mass coefficient for (19) as $f_m = \frac{2\beta\rho_f}{\mu(\gamma_{max})A_2\rho_s H_s \Delta t} \approx 1.7$ and the optimal fictitious pressure coefficient for (20) as $f_p = \frac{2\beta\rho_f A_1}{\mu(\gamma_{max})\Delta t(A_1A_2\rho_s H_s + G_1 H_s + \gamma_{max}^2 G_2 H_s)} \approx 1.3$, where $\Delta t = 1.89 \times 10^{-5}$ s. The estimated optimal coefficients are given based on the approximations that $G_1 \approx \frac{E}{(1-\lambda^2)R^2}$ and $G_2 \approx \frac{KE}{1+\lambda}$, with $K \approx \frac{(1+\lambda)}{2+\lambda}$ for the thin-walled cylinder [27].

To investigate the effect of different coefficients, we test the two fictitious methods with coefficients $f_p, f_m = \{0.44, 0.87, 1.3, 1.7, 2.16, 2.61\}$. The averaged subiteration numbers are listed in Table 1. We can see that among all fictitious mass coefficients, the smallest subiteration number is obtained by $f_m = 2.16$, while the theoretically optimal choice $f_m = 1.7$ gives a subiteration number slightly larger than this. On the other hand, for the fictitious pressure method, $f_p = 0.87$, $f_p = 1.3$ and $f_p = 1.7$ obtained similar subiteration numbers, while $f_p = 1.3$ is the best case over all. This finding is consistent with our estimations. In summary, in this case the fictitious pressure method gives a smaller subiteration number than the fictitious mass method.

Now we investigate the effects of different fictitious methods with various Young's modulus and time step sizes. In all cases, the averaged subiteration numbers are obtained with the theoretical optimal coefficients

Table 1 Averaged subiteration number for the cylindrical artery test: effect of different methods. $E = 0.6$ MPa, $\Delta t = 1.89 \times 10^{-5}$ s

Case	Fic mass	Fic pressure	Avg subiteration	Case	Fic mass	Fic pressure	Avg subiteration
T1	0.0	0.0	No convergence				
TM1	0.44	0.0	80.6	TP1	0.0	0.44	22.7
TM2	0.87	0.0	76.0	TP2	0.0	0.87	18.7
TM3	1.3	0.0	45.4	TP3	0.0	1.3(opt)	17.7
TM4	1.7(opt)	0.0	28.7	TP4	0.0	1.7	19.8
TM5	2.16	0.0	27.6	TP5	0.0	2.16	21.3
TM6	2.61	0.0	29.8	TP6	0.0	2.61	60.1

$$f_m = \frac{2\beta\rho_f}{\mu(\gamma_{max})A_2\rho_s H_s \Delta t}, \text{ or } f_p = \frac{2\beta\rho_f A_1}{\mu(\gamma_{max})\Delta t(A_1A_2\rho_s H_s + G_1 H_s + \gamma_{max}^2 G_2 H_s)}. \quad (33)$$

We first vary the Young's modulus from 0.15 to 19.2 MPa with fixed time step size $\Delta t = 1.89 \times 10^{-5}$ s, and obtain the averaged subiteration numbers as shown in the left plot of Fig. 2. When the Young's modulus is as small as 0.15 MPa, the fictitious mass method requires 251.2 averaged subiterations while the fictitious pressure method only requires 29.5. When the Young's modulus increases, both methods converge faster and the averaged subiteration number from the fictitious mass method is closer to that from the fictitious pressure method, but the latter still performs better. On the other hand, we fix the Young's modulus as $E = 0.6$ MPa and increase the time step sizes from 9.43×10^{-6}s to 1.51×10^{-4}s. The averaged subiteration numbers from the fictitious methods are plotted in the right plot of Fig. 2, from which we can see that when $\Delta t = 9.43 \times 10^{-6}$s, the fictitious mass method takes 270.1 averaged

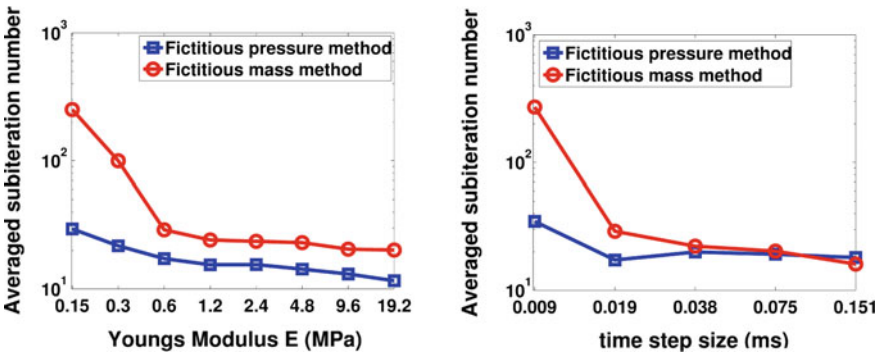

Fig. 2 Averaged subiteration number for the cylindrical artery test. *Left* varying Young's modulus; *right* varying time step sizes

subiterations while the fictitious pressure method only 34.7. However, if we increase the time step size to 1.51×10^{-4}s, the fictitious mass method preforms better (with 16.0 averaged subiteration number) than the fictitious pressure method (with 18.0 averaged subiteration number). Overall, from these results we can see that the fictitious pressure method is much more efficient when the Young's modulus and/or the time step size are small. When the Young's modulus and/or the time step size get increased, the performance from the fictitious mass method becomes comparable with that from the fictitious pressure method.

Sensitivity to Viscoelastic Coefficients: We now employ the fractional-order viscoelastic arterial wall model (21) in the FSI simulations, and evaluate the sensitivity of this model by varying the viscoelastic parameters α, τ_ε and τ_σ. In all tests we take a reduced Young's modulus $E = 0.3$ MPa. On the fluid solver, at the outlet the pressure $\bar{p}$ is flow-dependent and is determined from the flow rate $Q(t)$, given the resistant R, and the capacitance C as in [6], with coefficients $R = 2.8 \times 10^3 \text{dyn} \cdot \text{s/cm}^5$ and $C = 3.4 \times 10^{-7} \text{cm}^5/\text{dyn}$. The arterial outlet is assumed to be undeformed when the outlet pressure $\bar{p}(t)$ reaches its lowest point at $t = 0.0151$ s. To investigate how sensitive the solution is to the choice of relaxation parameters τ_ε and τ_σ, in the left plot of Fig. 3, we present the pressure-radial displacement hysteresis loops results at point $(1, 0, 2)$ for fixed $\alpha = 0.2$ with various relaxation time parameters. Correspondingly, the results for $\alpha = 1.0$ are displayed in the right plot. When $\alpha = 1.0$, a more noticeable viscous response can be observed, and the arterial wall deformation is more sensitive to the relaxation spectrum used. This means that when the fractional order α is relatively small, the effect of the fractional order SLS model (21) has low sensitivity on the relaxation parameters. Therefore, it overcomes the uncertainty for using the integer order SLS model in simulating arterial networks, where α is typically less than 0.3, since we can only hope to get accurate estimates of τ_ε and τ_σ at limited anatomic locations.

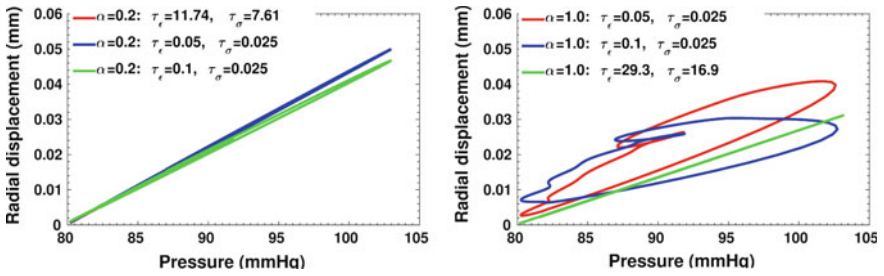

Fig. 3 Pressure-radial displacement hysteresis loops at point $(1, 0, 2)$ in the idealized artery simulations, from fixed and varying relaxation parameters. *Left* $\alpha = 0.2$; *Right* $\alpha = 1.0$

5.2 Blood Flow in a Patient-Specific Aneurysm

In this section patient-specific aneurysm models are tested, with the arterial geometry extracted from Magnetic Resonance Imaging data [6]. This aneurysm is located in the cavernous segment of the right internal carotid artery at the eye level. In all tests the structure subdomain covers the aneurysm sac only, as shown in the left plot of Fig. 4. Similar to the cylindrical artery model in the previous section, we imposed a Womersley velocity profile with 8 harmonics at the inlet boundary of the fluid solver, and a zero Neumann boundary condition for velocity at the outlet. The outlet pressure $\bar{p}$ is flow-dependent as in [6]. The arterial outlet is assumed to be undeformed when the outlet pressure $\bar{p}(t)$ reaches its lowest point at $t = 0.0571$ s. To integrate in time, we employed the second-order splitting scheme for the fluid solver, and the BDF formula for the structure side. All the simulations are done with the physical and numerical parameters summarized in Table 2. In the tests of this section we set $\rho_s/\rho_f = 1$. To investigate the displacement distribution on the whole aneurysm, we show the corresponding displacement amplitudes at the systolic peak in the right two plots of Fig. 4. We observe that the maximum displacement amplitude is about 0.8 mm, which is obtained near point 1. This is also consistent with the physiological range obtained from the measurements, as reported in [36].

Fictitious Method: Next, we investigate the effect of various fictitious methods, by comparing the subiteration numbers. Before demonstrating any results, an estima-

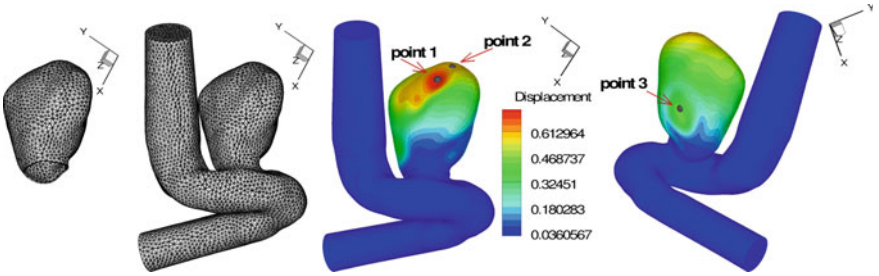

Fig. 4 *Left two plots* structure mesh and fluid mesh. *Right two plots* displacement magnitudes distribution and positions of the history points in patient-specific aneurysm test at $t = 3T/7$

Table 2 Parameters used in the patient-specific aneurysm simulations

Parameter	Value	Parameter	Value
Young's Modulus	3 Mpa	Poisson ratio	0.3
Blood density	1.06 g/cm^3	Wall thickness	0.01 cm
Kinematic viscosity	3.8×10^{-2} cm^2/s	Average flow rate	70 ml/min
Time step size	1.43×10^{-3} s	Polynomial order	2
Resistant parameter	7.844×10^2 dyn · s/cm^5	Capacitance parameter	7.285×10^{-5} cm^5/dyn

Table 3 Averaged subiteration number in patient-specific aneurysm test

	Fic mass	Fic pressure	Robin coef	Avg subiter		Fic mass	Fic pressure	Robin coef	Avg subiter
B1	0.0	0.0	0.0	18.4	BR1	0.0	0.0	350	12.4
BM1	0.5	0.0	0.0	16.2	BP1	0.0	0.2	0.0	14.7
BM2	2.08	0.0	0.0	12.4	BP2	0.0	0.119	0.0	12.3

tion of the optimal coefficients is needed. Since the artery with aneurysm is a complicated geometry, we cannot obtain any reasonable analytical value from Fourier analysis. Instead, this value is obtained from the post-processing of several sample tests. We first take three initial tests with three initial guesses of f_m and f_p, then estimate $f_m(opt)$ and $f_p(opt)$ from simulation of these three runs. More details can be found in [55].

In the following we confirm the previous estimate. The results are also compared with those from a Robin based semi-implicit coupling method proposed in [3]. Since the Young's modulus E is large in this example, based on our previous discussions in Sect. 3.1, we take a smaller value for f_p as the initial guess. Firstly, the averaged subiteration numbers for three sample cases $B1 : f_m = f_p = 0, BM1 : f_m = 0.5, f_p = 0$ and $BP1 : f_m = 0, f_p = 0.2$ are computed, as shown in Table 3. The estimates for $f_p(opt)$ and $f_m(opt)$ can be obtained: $f_p(opt) \approx 0.119, f_m(opt) \approx 2.08$. The averaged subiteration numbers obtained from $f_p(opt) = 0.119$ and $f_m(opt) = 2.08$ are also listed in Table 3. To demonstrate the effects of these coefficients, the subiteration numbers obtained from the Robin-based coupling method with its optimal coefficient 350 is also provided. It can be seen that the fictitious methods with estimated optimal coefficients require smaller subiteration numbers compared to the original sample simulations. Among all, the test with $f_p = 0.119$ has the best performance, which is slightly better than that from $f_m = 2.08$ and the Robin based coupling method. Comparing to the fictitious pressure method with its optimal coefficient, the optimized fictitious mass method has a similar efficiency here. Since the Young's modulus $E = 3$ MPa in these simulations is large, this finding actually confirms our previous discussion in Sect. 3.1.

Viscoelastic Model: The authors in [11–14, 18] have demonstrated that fractional orders would be able to properly predict the different mechanical behavior of the smooth muscle cell activities. Since the smooth muscle decrease plays a crucial role in the change of cerebral aneurysm walls [7, 46, 48, 52], in this section we investigate the fractional order models on the patient-specific aneurysm geometry demonstrated in Fig. 4. On the structure side, the fast convolution method introduced in Sect. 4 is used, with the fictitious mass method applied to stabilize the FSI partitioned procedure.

To compare the computed evolution of the aneurysm deformation from different models, we first display the displacement time traces of three points on the interface. The locations of these points are shown in the right two plots of Fig. 4. Two

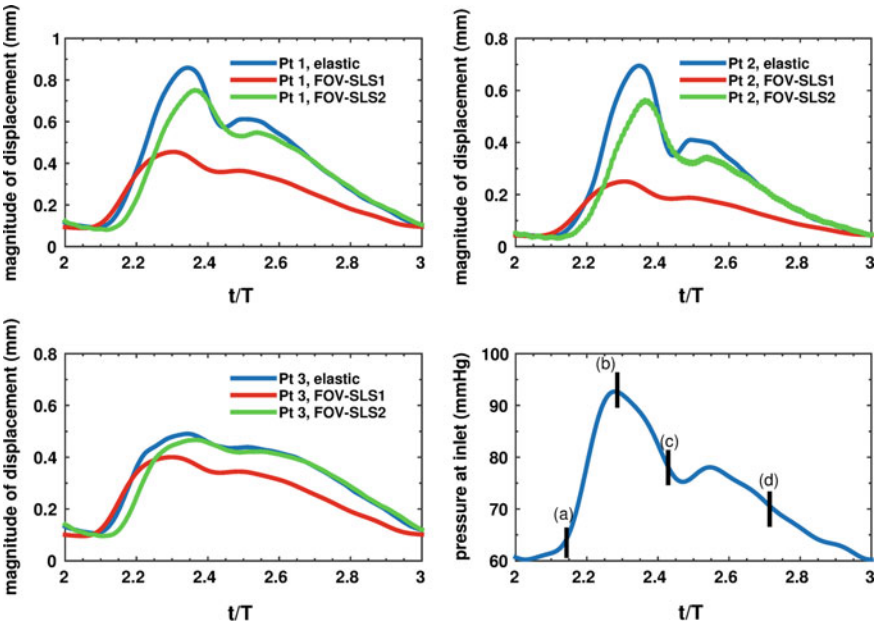

Fig. 5 Time traces in patient-specific aneurysm with viscoelastic arterial wall models. *Upper left*, *upper right*, *bottom left* displacement profiles for corresponding points; *bottom right* pressure imposed at the inlet

fractional-order viscoelastic models are studied for the aneurysm wall: FOV-SLS1 ($\alpha = 0.29$, $\tau_\varepsilon = 1.84\,(\mathrm{s})$, $\tau_\sigma = 0.076\,(\mathrm{s})$) and FOV-SLS2 ($\alpha = 0.2$, $\tau_\varepsilon = 11.74\,(\mathrm{s})$, $\tau_\sigma = 7.61\,(\mathrm{s})$) which were calibrated from arterial sample loading tests in the literatures [12–14, 18]. Then we compare the results against simulation results from the pure elastic model. The computed inlet pressure and the time traces for displacements at these three points are shown in Fig. 5, for the pure elastic model, the FOV-SLS1 and the FOV-SLS2 models. The FOV-SLS1 model predicts a much smaller deformation compared with that from the other two models, which results in a larger blood pressure drop in each cardiac cycle. A minor phase shift could be observed while comparing the location of the maximum displacement for each model: while the maximum displacements were achieved after the systolic peak in all cases, the case using the FOV-SLS1 model reaches its maximum deformation firstly, then the case using the elastic arterial wall model, and finally the case with the FOV-SLS2 model. It was also observed that although the displacement magnitudes vary for different arterial wall models, the displacement magnitude distribution pattern does not change much [56].

6 Conclusion and Future Work

This chapter centered around numerical analysis and large-scale scientific computing for cerebral artery and aneurysm applications with specific focus on fluid-structure interaction problems.

Specifically, we first introduced a family of fictitious methods and analyzed them for FSI problems, where additional terms are introduced in the fluid/structure equations to balance the added-mass effect and make the partitioned FSI solver perform more like an exact coupled solver [6, 55]. The fictitious methods can be implemented by changing the coefficients of the pressure or acceleration terms in the fluid or structure equations, respectively, and therefore can be easily extended and adopted in any existing FSI solver. We verified the a priori analysis of optimal fictitious coefficients with corresponding numerical tests, which suggest that for small Young's modulus and/or small time step size, the fictitious pressure method is a better choice for a faster convergence. However, when the Young's modulus or time step size increases, the performance of the fictitious pressure and fictitious mass methods is comparable. As validation for the methods on complex geometries, we also conducted simulations and provided theoretical analysis to obtain optimal values for the fictitious parameters in 3D patient-specific brain arterial geometries with aneurysms.

With the stabilized FSI framework, we have investigated a 3D viscoelastic arterial wall model, whose constitutive law is derived using fractional-order differential equations. To sustain the high-order accuracy of the backward differentiation formula (BDF), we designed a high-order fast convolution method with third-order convergence rate in time and $N \log(N)$ operation count. In numerical tests, we investigated the ability of fractional-order model to capture the viscoelastic behavior of arterial walls under fluid-structure interactions. On an idealized artery geometry, we compared several models with the same elasticity parameters and different viscoelastic parameters. This comparison study indicates that for the integer-order SLS models, the viscous behavior strongly depends on the relaxation parameters τ_ε and τ_σ, while the fractional order models are less sensitive. Especially when the fractional order $\alpha \to 0$, the viscous response is less pronounced, and the fractional model is tuned by a single parameter, the fractional order α. As an example of long-term large-scale simulations, we have also investigated the performance of this fractional-order arterial wall model on the 3D complex patient-specific brain aneurysm geometry.

In ongoing work, we are now investigating the proper fractional parameters specifically for the aneurysm sac using patient-specific data. Since the fractional order is related with the loss of smooth muscle cells, this aneurysm-specific model as well as the numerical tools developed here may help to understand the structural integrity of the aneurysm wall, and therefore contribute in studying the subclasses of unruptured aneurysm walls [10, 45]. In the future, we will further develop coupling schemes for FSI with better efficiency and accuracy, and apply the related domain decomposition approaches in other multiscale and multiphysics problems, for example, multi-phase flows, atomistic-to-continuum coupling problems, etc.

Acknowledgements The author would like to acknowledge support by the Simons collaboration grant, the NSF grant 1620434, and the computational resources of CCV at Brown University. She would also like to thank Professor George Karniadakis at Brown University for helpful discussions.

References

1. J. Alastruey, A.W. Khir, K.S. Matthys, P. Segers, S.J. Sherwin, P.R. Verdonck, K.H. Parker, J. Peiró, Pulse wave propagation in a model human arterial network: assessment of 1-d visco-elastic simulations against in vitro measurements. J. Biomech. **44**(12), 2250–2258 (2011)
2. J. Alastruey, K.H. Parker, J. Peiro, S.M. Byrd, S.J. Sherwin, Modelling the circle of Willis to assess the effects of anatomical variations and occlusions on cerebral flows. J. Biomech. **40**(8), 1794–1805 (2007)
3. M. Astorino, F. Chouly, M.A. Fernández, Robin based semi-implicit coupling in fluid-structure interaction: stability analysis and numerics. SIAM J. Sci. Comput. **31**(6), 4041–4065 (2009)
4. S. Badia, F. Nobile, C. Vergara, Fluid-structure partitioned procedures based on Robin transmission conditions. J. Comput. Phys. **227**(14), 7027–7051 (2008)
5. H. Baek, G.E. Karniadakis, Sub-iteration leads to accuracy and stability enhancements of semi-implicit schemes for the Navier-Stokes equations. J. Comput. Phys. **230**(12), 4384–4402 (2011)
6. H. Baek, G.E. Karniadakis, A convergence study of a new partitioned fluid-structure interaction algorithm based on fictitious mass and damping. J. Comput. Phys. **231**(2), 629–652 (2012)
7. A.J. Bank, D.R. Kaiser, S. Rajala, A. Cheng, In vivo human brachial artery elastic mechanics effects of smooth muscle relaxation. Circulation **100**(1), 41–47 (1999)
8. Y. Bazilevs, M.C. Hsu, Y. Zhang, W. Wang, X. Liang, T. Kvamsdal, R. Brekken, J.G. Isaksen, A fully-coupled fluid-structure interaction simulation of cerebral aneurysms. Comput. Mech. **46**(1), 3–16 (2010)
9. P. Causin, J.F. Gerbeau, F. Nobile, Added-mass effect in the design of partitioned algorithms for fluid-structure problems. Comput. Methods Appl. Mech. Eng. **194**(42–44), 4506–4527 (2005)
10. J.R. Cebral, X. Duan, B.J. Chung, C. Putman, K. Aziz, A.M. Robertson, Wall mechanical properties and hemodynamics of unruptured intracranial aneurysms. Am. J. Neuroradiol. **36**(9), 1695–1703 (2015)
11. D. Craiem, R.L. Magin, Fractional order models of viscoelasticity as an alternative in the analysis of red blood cell (RBC) membrane mechanics. Phys. Biol. **7**(1), 013,001 (2010)
12. D.O. Craiem, R.L. Armentano, A fractional derivative model to describe arterial viscoelasticity. Biorheology **44**(4), 251–263 (2007)
13. D.O. Craiem, F.J. Rojo, J.M. Atienza, R.L. Armentano, G.V. Guinea, Fractional-order viscoelasticity applied to describe uniaxial stress relaxation of human arteries. Phys. Med. Biol. **53**(17), 4543 (2008)
14. D.O. Craiem, F.J. Rojo, J.M. Atienza, G.V. Guinea, R.L. Armentano, Fractional calculus applied to model arterial viscoelasticity. Lat. Am. Appl. Res. **38**(2), 141–145 (2008)
15. P. Crosetto, S. Deparis, G. Fourestey, A. Quarteroni, Parallel algorithms for fluid-structure interaction problems in haemodynamics. SIAM J. Sci. Comput. **33**(4), 1598–1622 (2011)
16. P. Crosetto, P. Reymond, S. Deparis, D. Kontaxakis, N. Stergiopulos, A. Quarteroni, Fluid-structure interaction simulation of aortic blood flow. Comput. Fluids **43**(1), 46–57 (2011)
17. J. Degroote, J. Vierendeels, Multi-solver algorithms for the partitioned simulation of fluid-structure interaction. Comput. Methods Appl. Mech. Eng. **200**(25–28), 2195–2210 (2011)
18. T.C. Doehring, A.D. Freed, E.O. Carew, I. Vesely, Fractional order viscoelasticity of the aortic valve cusp: an alternative to quasilinear viscoelasticity. ASME J. Biomech. Eng. **127**(4), 700–708 (2005)
19. S. Dong, BDF-like methods for nonlinear dynamic analysis. J. Comput. Phys. **229**(8), 3019–3045 (2010)

20. S. Dong, Z. Yosibash, A parallel spectral element method for dynamic three-dimensional non-linear elasticity problems. Comput. Struct. **87**(1–2), 59–72 (2009)
21. Y.C. Fung, *Biomechanics: Mechanical Properties of Living Tissues*. Springer (1993)
22. M.W. Gee, U. Kuttler, W.A. Wall, Truly monolithic algebraic multigrid for fluid-structure interaction. Int. J. Numer. Methods Eng. **85**(8), 987–1016 (2011)
23. L. Gerardo-Giorda, F. Nobile, C. Vergara, Analysis and optimization of Robin-Robin partitioned procedures in fluid-structure interaction problems. SIAM J. Numer. Anal. **48**(6), 2091–2116 (2010)
24. G. Guidoboni, R. Glowinski, N. Cavallini, S. Canic, Stable loosely-coupled-type algorithm for fluid-structure interaction in blood flow. J. Comput. Phys. **228**(18), 6916–6937 (2009)
25. M.C. Hsu, Y. Bazilevs, Blood vessel tissue prestress modeling for vascular fluid-structure interaction simulation. Finite Elem. Anal. Des. **47**(6), 593–599 (2011)
26. T.J.R. Hughes, W.K. Liu, T.K. Zimmermann, Lagrangian-Eulerian finite element formulation for incompressible viscous flows. Comput. Methods Appl. Mech. Eng. **29**(3), 329–349 (1981)
27. J.R. Hutchinson, Shear coefficients for Timoshenko beam theory. J. Appl. Mech. **68**(1), 87–92 (2001)
28. E. Järvinen, P. Råback, M. Lyly, J.P. Salenius, A method for partitioned fluid-structure interaction computation of flow in arteries. Med. Eng. Phys. **30**(7), 917–923 (2008)
29. M.M. Joosten, W.G. Dettmer, D. Peric, Analysis of the block Gauss-Seidel solution procedure for a strongly coupled model problem with reference to fluid-structure interaction. Int. J. Numer. Methods Eng. **78**(7), 757–778 (2009)
30. G.E. Karniadakis, M. Israeli, S. Orszag, High-order splitting methods for the incompressible Navier-Stokes equations. J. Comput. Phys. **97**(2), 414–443 (1991)
31. G.E. Karniadakis, S.J. Sherwin, *Spectral/hp Element Methods for Computational Fluid Dynamics*, 2nd edn. (Numerical Mathematics and Scientific Computation (Oxford University Press, Oxford, 2005)
32. M. López-Fernández, C. Lubich, A. Schädle, Adaptive, fast, and oblivious convolution in evolution equations with memory. SIAM J. Sci. Comput. **30**(2), 1015–1037 (2008)
33. C. Lubich, A. Schädle, Fast convolution for nonreflecting boundary conditions. SIAM J. Sci. Comput. **24**(1), 161–182 (2002)
34. R.L. Magin, *Fractional Calculus in Bioengineering* (Begell House Publishers Inc., Redding, CT, 2006)
35. F. Mainardi, Fractional Calculus and Waves in Linear Viscoelasticity: An Introduction to Mathematical Models. (World Scientific, 2010)
36. F.B. Meyer, J. Huston, S.S. Riederer, Pulsatile increases in aneurysm size determined by cine phase-contrast MR angiography. J. Neurosurg. **78**(6), 879–883 (1993)
37. C. Michler, H. van Brummelen, R. de Borst, An investigation of interface-GMRES(R) for fluid-structure interaction problems with flutter and divergence. Comput. Mech. **47**(1), 17–29 (2011)
38. F. Nobile, Coupling strategies for the numerical simulation of blood flow in deformable arteries by 3D and 1D models. Math. Comput. Model. **49**(11–12), 2152–2160 (2009)
39. F. Nobile, C. Vergara, An effective fluid-structure interaction formulation for vascular dynamics by generalized Robin conditions. SIAM J. Sci. Comput. **30**(2), 731–763 (2008)
40. P. Perdikaris, G.E. Karniadakis, Fractional-order viscoelasticity in one-dimensional blood flow models. Ann. Biomed. Eng. **42**(5), 1012–1023 (2014)
41. I. Podlubny, *Fractional Differential Equations: An Introduction to Fractional Derivatives, Fractional Differential Equations, to Methods of Their Solution and Some of Their Applications*, vol. 198. (Academic Press, 1998)
42. A. Quarteroni, L. Formaggia, Mathematical modelling and numerical simulation of the cardiovascular system, in *Computational Models for the Human Body*, ed. by N. Ayache. Handbook of Numerical Analysis, vol. 12. (Elsevier, 2004), pp. 3–127
43. P. Reymond, Y. Bohraus, F. Perren, F. Lazeyras, N. Stergiopulos, Validation of a patient-specific one-dimensional model of the systemic arterial tree. Am. J. Physiol.-Heart Circ. Physiol. **301**(3), 1173–1182 (2011)

44. M. Rizzardi, A modification of talbot's method for the simultaneous approximation of several values of the inverse Laplace transform. ACM Trans. Math. Softw. (TOMS) **21**(4), 347–371 (1995)
45. A.M. Robertson, X. Duan, K.M. Aziz, M.R. Hill, S.C. Watkins, J.R. Cebral, Diversity in the strength and structure of unruptured cerebral aneurysms. Ann. Biomed. Eng. 1–14 (2015)
46. A.M. Robertson, M.R. Hill, D. Li, Structurally motivated damage models for arterial walls. theory and application, in *Modeling of Physiological Flows*. (Springer, 2012), pp. 143–185
47. F.X. Roux, J.D. Garaud, Domain decomposition methodology with Robin interface matching conditions for solving strongly coupled fluid-structure problems. Int. J. Multiscale Comput. Eng. **7**(1), 29–38 (2009)
48. C. Sadasivan, D.J. Fiorella, H.H. Woo, B.B. Lieber, Physical factors effecting cerebral aneurysm pathophysiology. Ann. Biomed. Eng. **41**(7), 1347–1365 (2013)
49. A. Talbot, The accurate numerical inversion of Laplace transforms. IMA J. Appl. Math. **23**(1), 97–120 (1979)
50. T.E. Tezduyar, K. Takizawa, T. Brummer, P.R. Chen, Space-time fluid-structure interaction modeling of patient-specific cerebral aneurysms. Int. J. Numer. Methods Biomed. Eng. **27**(11), 1665–1710 (2011)
51. R. Torii, M. Oshima, T. Kobayashi, K. Takagi, T.E. Tezduyar, Computer modeling of cardiovascular fluid-structure interactions with the deforming-spatial-domain/stabilized space-time formulation. Comput. Methods Appl. Mech. Eng. **195**(13–16), 1885–1895 (2006)
52. M. Toth, G.L. Nadasy, I. Nyary, T. Kerényi, M.s. Orosz, G. Molnarka, E. Monos, Sterically inhomogenous viscoelastic behavior of human saccular cerebral aneurysms. J. Vasc. Res. **35**(5), 345–355 (1998)
53. J. Van Gijn, G.J.E. Rinkel, Subarachnoid haemorrhage: diagnosis, causes and management. Brain **124**(2), 249–278 (2001)
54. Y. Yu, H. Baek, M.L. Bittencourt, G.E. Karniadakis, Mixed spectral/hp element formulation for nonlinear elasticity. Comput. Methods Appl. Mech. Eng. **213–216**, 42–57 (2012)
55. Y. Yu, H. Baek, G.E. Karniadakis, Generalized fictitious methods for fluidstructure interactions: Analysis and simulations. J. Comput. Phys. **245**, 317–346 (2013)
56. Y. Yu, P. Perdikaris, G.E. Karniadakis, Fractional modeling of viscoelasticity in 3d cerebral arteries and aneurysms. Submitted to J. Comput. Phys. (2016)

Large-Eddy Simulation of Turbulence in Cardiovascular Flows

F. Nicoud, C. Chnafa, J. Siguenza, V. Zmijanovic and S. Mendez

Abstract A 4th-order accurate, low dissipative flow solver is used to perform Large-Eddy Simulations of three typical hemodynamic situations: the flow through the idealized medical device proposed by the American Food and Drug Administration; the intracardiac flow within an actual human left heart whose morphology and deformations are deduced from medical imaging; the flow downstream of an artificial aortic valve which arises from the blood-leaflets interaction problem. In all the cases, the σ subgrid scale model designed to handle wall-bounded transitional flows is successfully used and the numerical simulations compare favourably with the experimental data available. These results illustrate the potential of the Large-Eddy Simulation methodology to properly handle blood flows. They also support the idea that turbulence, even if not fully developed, may be present in cardiovascular flows, including under non pathological conditions.

1 Introduction

Turbulence is a natural phenomenon in fluid mechanics, which gives rise to wide spectrum, chaotic fluctuations in the velocity/pressure fields, even in the absence of external forcing. This phenomenon arises when the inertia forces are significantly larger than the viscous effects, viz. when the Reynolds number R_e exceeds a few thousands in steady flow, most probably less for pulsatile flows [1]. This number usually reaches a few hundreds in medium-sized arteries and a few thousands in the largest vessels, in the heart itself or within biomedical systems such as total artificial hearts or ventricular assist devices. Thus, one may expect turbulence to be present in

F. Nicoud (✉) · J. Siguenza · V. Zmijanovic · S. Mendez
Institut Montpelliérain Alexander Grothendieck, CNRS, Univ. Montpellier, Montpellier, France
e-mail: franck.nicoud@umontpellier.fr

C. Chnafa
Biomedical Simulation Laboratory, Department of Mechanical & Industrial Engineering, University of Toronto, Toronto, Canada
e-mail: cchnafa@mie.utoronto.ca

P. Wriggers and T. Lenarz (eds.), *Biomedical Technology*, Lecture Notes in Applied and Computational Mechanics 84, DOI 10.1007/978-3-319-59548-1_9

the cardiovascular system, at least in some favourable regions in space (e.g. close to stenoses, valves, bifurcations) and during specific periods of the cardiac cycle (when the flow decelerates). Still, until recently turbulence was virtually not studied, at least non-invasively, in the cardiovascular biomechanics community, notably because in vivo 3D and unsteady measurements of the blood velocity are very challenging. Recent progresses in both computational fluid dynamics (CFD) and medical imaging techniques give rise to a renewed interest for the turbulent properties of blood flows. Unstable and/or turbulent flows have been observed in numerical simulations in abdominal aortic aneurysms [2], carotid siphons [3], cerebral aneurysms [4] as well as experimentally in an idealized left ventricle [5]. Thanks to an MRI method based on the intravoxel velocity standard deviation, it is now possible to estimate the turbulent kinetic energy in vivo. Significant levels of kinetic energy were found not only in pathological left atria [6] but also in normal left ventricles [7], supporting the idea that turbulence can also occur in healthy human subjects.

From a numerical point of view, representing turbulence is a challenge due to the wide variety of both temporal and spatial scales that are present at the same time. In the ideal case of a decaying isotropic turbulence, one may show that the largest-to-smallest length scales ratio behaves like $R_e^{3/4}$ [8]; as a consequence, the number of grid points necessary to properly represent a turbulent flow, including the whole range of fluctuations, increases as fast as $R_e^{9/4}$. This approach where turbulence is accounted for by just and only solving all the scales produced by the Navier-Stokes equations is called Direct Numerical Simulation and remains most of the times out of reach of the current computing power except in simple cases with moderate Reynolds number. The large variety of scales inherent to any turbulent flow motivated the development of turbulent models in order to complement the Reynolds-Averaged Navier-Stokes (RANS) equations which allow to compute the averaged flow quantities without explicitly representing the fluctuations. Despite decades of very active research and some successes in fully developped turbulent flows, there are still many controversies about the proper way to develop 'good' turbulent models [9] and the idea of a universal formulation able to properly deal with any turbulent flows is widely considered as hopeless. On top of not being predictive enough, RANS models are better suited for fully turbulent flows at very high Reynolds numbers than transitional flows. The ability of Large-Eddy Simulation (LES) to better predict a flow without prior knowledge, including regarding its laminar/turbulent nature, is one of the reasons why this technique is now being used in many applications. It is a method of choice for unsteady 3D flows at moderate Reynolds numbers, especially when transition from laminar to turbulence plays a key role. In this paper, we illustrate how LES can be used to represent three configurations typical of cardiovascular applications:

- an idealized medical device where a stationary flow goes from laminar to turbulent in a simple geometry [10],
- a realistic human left heart whose geometry and cyclic deformations are deduced from medical imaging and where CFD/LES in a time varying domain is used to generate the associated blood flow [11],

- the flow past an artificial aortic valve where the Fluid-Structure Interaction problem is solved to predict the leaflets dynamics and associated turbulent generation.

Some numerical and physical issues specific to each of these configurations will be discussed in Sects. 3, 4 and 5 respectively, together with comparison with experimental data when available. Some details about the numerics and the subgrid scale modelling strategy are first given in Sect. 2.

2 LES Requirements

In LES, the modelling effort focuses on the smallest length scales of fluctuations which are presumably less dependent on the geometry of the flow domain and thus more universal. The largest scales (which can be as small as twice the typical cell size, at least in theory) are explicitly resolved as solutions of the low-pass filtered Navier-Stokes equations [12]. Thus, the finer the mesh, the larger the range of resolved scales and the smallest the contribution of the subgrid scale model. In other words, the modelling effort in less intense in LES compared to RANS and this is all the more true that the grid is refined.

The price to pay is that the dynamics of the largest scales, as well as the related macroscopic mixing and turbulent stresses, must be properly represented by the numerics. As a consequence the numerical errors associated to both the spatial and temporal discretizations must be kept as small as possible. Notably, dissipation-free schemes must be preferred so that the (relative) intensity of the different resolved scales is not spoiled. An important feature of LES is that the scheme should be as accurate as possible for all the scales represented on the mesh, the largest as well as the smallest. This means that the order of accuracy of a numerical method is not a good measure of its capability to perform well in the LES; the effective wave number [13] and kinetic energy conservation [14] concepts are better suited to characterize a numerical scheme dedicated to LES. For example, better results may be obtained with a second order centered (dissipation-free at all scales) scheme than with a higher-order upwind biased (dissipative) scheme [15, 16]. As a consequence, a RANS solver, usually based on stabilized scheme coupled to implicit time marching methods designed to speed up the convergence towards a steady solution cannot be easily adapted to LES. In the present study, the in-house flow solver *YALES2BIO* (http://www.math.univ-montp2.fr/~yales2bio) was used to solve the filtered flow equations. Dedicated to the computations of blood flows, this general purpose solver relies on a 4th-order accurate centred (dissipation-free) finite-volume formulation where the projection method [17] is used to meet the divergence-free condition. The time-stepping is also 4th-order accurate, based on the dissipation-free explicit low-storage Runge-Kutta scheme [18]. At the end, the algorithm is non dissipative and one relies on the physical dissipation, either laminar or issued by the subgrid scale model, to ensure numerical stability. This is made possible because the Reynolds number is low to moderate in biomedical applications so that numer-

ical stabilization is not necessary; this also requires to use high quality 3D meshes. Finally, *YALES2BIO* inherits its parallel efficiency from the *YALES2* package developed by V. Moureau and co-workers [19, 20].

From the modelling point of view, the subgrid scale stress tensor τ_{SGS} which results from the filtering operation applied to the Navier-Stokes equations is most of the time modelled thanks to the eddy-viscosity assumption (introduced in the RANS concept in the 70s). In the case of an incompressible fluid, this reduces to

$$\tau_{SGS} = 2\rho\nu_{SGS}\mathbf{S}$$

where ρ is the fluid density, $\mathbf{S}$ is the strain rate tensor of the resolved scales and ν_{SGS} is the so-called subgrid scale viscosity. Several models were proposed over the years for this quantity and most of them share the following form:

$$\nu_{SGS} = (C\Delta)^2\,\mathscr{D}(\mathbf{u}) \tag{1}$$

where C is the model constant which is usually tuned (either theoretically or numerically) so that the model produces the proper amount of dissipation in the simple case of decaying isotropic turbulence. The length scale Δ denotes the typical size of the local cell of the mesh used to solve the filtered Navier-Stokes equations and $\mathscr{D}$ is a differential operator which defines the model and operates on the resolved velocity field $\mathbf{u}$. The $\boldsymbol{\sigma}$-model [21] is used in this study, meaning that:

$$\mathscr{D}(\mathbf{u}) = \frac{\sigma_3(\sigma_1-\sigma_2)(\sigma_2-\sigma_3)}{\sigma_1^2} \tag{2}$$

In this expression, $\sigma_1 \geq \sigma_2 \geq \sigma_3 \geq 0$ are the three singular values of the local velocity gradient tensor and can be efficiently computed [21]; the model constant is $C = 1.35$. This model was selected because it meets several useful properties relevant in terms of SGS modelling, although not shared by the other SGS models. On top of vanishing for a variety of canonical laminar flows for which no SGS viscosity is expected, it has the proper cubic behavior in near-wall regions. In [21], the model was implemented in different numerical solvers and validated in academic cases (homogeneous isotropic turbulence, turbulent channel); its effectiveness in a more demanding configuration was also demonstrated recently by considering the impingement of an unsteady jet with a rigid wall [22]. In this particular case which is relevant to intra-cardiac hemodynamics, the comparison with experimental data shows that the $\boldsymbol{\sigma}$-model outperforms the well-known Dynamic Smagorinsky model [23].

In the next three sections, results from the $\boldsymbol{\sigma}$-model as implemented in the *YALES2BIO* solver are discussed to illustrate how LES can be used to analyse flows relevant to cardiovascular applications.

3 The FDA Medical Device Test Case

The United States Food and Drug Administration (FDA) medical device benchmark was introduced at the beginning of the current decade as an answer to the ubiquitous presence of various numerical methods in biomedicine. The purpose of the proposed benchmark program was to validate the CFD codes on idealized medical device examples. The first FDA test model [10, 24] aims at challenging CFD codes on a case whith transition to turbulence, which is frequently encountered in biomedical devices. Accurately predicting turbulence is necessary to properly assess shear stresses, themselves relevant to blood damage prediction in ventricular assist devices (VAD) [25, 26], but also in blood flows through stents and pumps, to cite a few. Mispredicting the turbulent nature of blood flows heavily impacts the results and may cause critical faulty conclusions.

The FDA medical device model, as illustrated in Fig. 1, consists of a fixed axisymmetric geometry with a long inlet section, a convergent nozzle, a 10 diameters long throat section and a sudden expansion at the downstream end. This geometry submits the flowing fluid to several events as acceleration through the convergent, pipe type of flow in the throat where maximal Reynolds number (Re_{th}) is reached and jet formation into the sudden expansion section characterized by deceleration, mixing shear layer generation and possible turbulence transition. Five flow regimes were considered, which correspond to fully laminar case ($\mathrm{Re}_{th} = 500$), transient case ($\mathrm{Re}_{th} = 2000$), laminar inlet—transition to turbulence in sudden expansion ($\mathrm{Re}_{th} = 3500$), laminar inlet—turbulent case ($\mathrm{Re}_{th} = 5000$) and fully turbulent case ($\mathrm{Re}_{th} = 6500$).

The reported computational investigations on this FDA benchmark can be divided into two major groups: blinded studies that were conducted without foreknowledge of the experimental results and the studies conducted after the publication of first benchmark results. While none of the first 28 CFD research groups which used various RANS methods managed to fully reproduce the FDA experimental results [24], almost all succeeding CFD studies [27–30] reported good agreement with the FDA experiments. This raises a number of questions regarding both the numerical

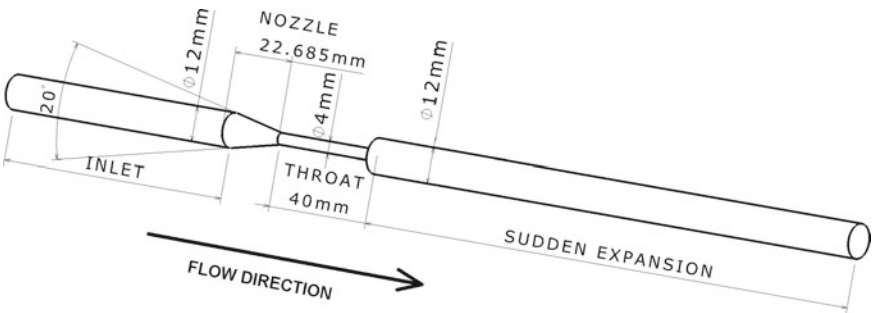

Fig. 1 Geometry specifications of the first FDA ideal medical device

methods for turbulence transitional blood flows and the overall methodology to represent the FDA blood flow case. While the RANS codes [24, 31] in this case clearly lag behind the LES due to their inability to accurately predict the laminar to turbulent transition, the absence of analysis of the sensitivity to numerical parameters in the reported DNS and LES results [27, 28, 30] questions the actual predictive character of these simulations. Indeed, the FDA case proves to be highly sensitive to any physical or numerical specificities as illustrated in the remaining of this section.

3.1 Simulations with Perturbation-Free Inlet

Investigation of the effects of numerics on the results was conducted by considering three grid levels as well as a variety of CFL numbers (dimensionless time step). In order not to presume the resulting flow field in any way, unstructured finite volume grids were designed with almost no-local refinement in the domain with only slight stretching towards the upstream and downstream ends. The three grids contain respectively 5 million tetrahedral elements with $h = 0.34$ mm average cell height (Coarse), 15 million with $h = 0.2$ mm (Medium) and 50 million with $h = 0.14$ mm (Fine). Further details on the numerics and grids are available in [32].

Snapshots of instantaneous velocity fields obtained with the medium grid are displayed in Fig. 2 for the transitional ($Re_{th} = 3500$) case. Except for the CFL number, the same physical and numerical conditions were used in both cases. This figure illustrates that the location of the transition to turbulence is very sensitive to the numerical details, as confirmed by the profiles displayed in Fig. 3. The latter also shows that the

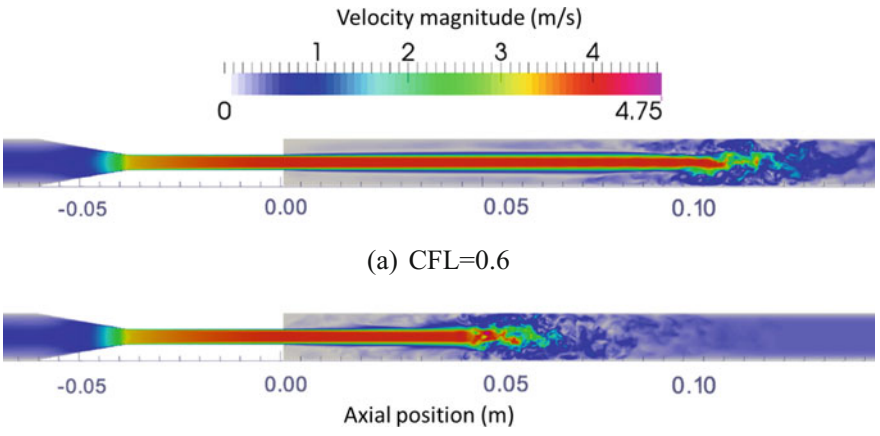

Fig. 2 Instantaneous velocity fields (medium grid) for two different values of the CFL numbers (*top* CFL = 0.6; *bottom* CFL = 0.1)—$Re_{th} = 3500$

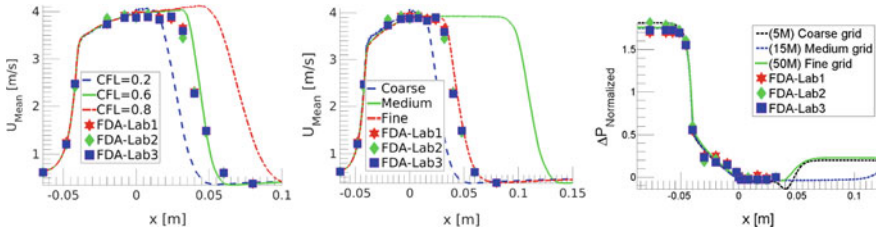

(a) Velocity – Coarse grid (b) Velocity – CFL=0.6 (c) Pressure – CFL=0.6

Fig. 3 Longitudinal evolutions of the streamwise velocity (*left* and *middle* plots) and wall-pressure (relative to the pressure at x = 0 and normalized by the dynamic pressure at the throat—*right* plot) for a variety of temporal and spatial resolutions—$Re_{th} = 3500$

upstream part of the flow (x < 0, the sudden expansion starts at x = 0) is robust to the details of the simulation. However, both the streamwise mean velocity and the static pressure strongly depend on the numerics in the downstream region. This means that the axisymmetric configuration considered, when fed with an ideal Poiseuille velocity profile without perturbation, is very sensitive to any physical (boundary conditions) or numerical (mesh stretching, schemes, time step) modification. This makes hopeless any effort towards a predictive simulation of this configuration. A cure to this issue is considered in the next section.

3.2 *Small Perturbations at the Inlet*

When dealing with transitional flows, the perturbations injected at the inlet of the computational domain are of prime importance as already discussed in the literature [33, 34]. In the particular case of the FDA nozzle, the absence of such inlet perturbations leads to an extreme sensitivity of the results which makes the simulations unreliable. Note that this may also lead to simulations which may compare well with the experimental data set but which are nonetheless inadequate since not robust (e.g. the case CFL = 0.6 and coarse grid in Fig. 3a agrees well with the measurements but should not be trusted since the results depend on the time step).

As shown in Fig. 4, even the smallest amount of perturbations injected at the inlet (thereafter denoted turbulence injection, TI) greatly improves the situation in the sense that the results are now robust to any tested numerical condition. More importantly, the numerical results are also systematically in good agreement with the experimental data, suggesting that the simulations outcomes are both robust and accurate. Profiles of the root-mean-square (RMS) velocity, Fig. 5a, show that the amount of flow perturbations at inlet is significantly increased by TI, as expected. The small amplitude perturbations are quickly dissipated downstream, being decreased by more than 2 orders of magnitude as shown in Fig. 5b. Figure 5c and d show that the flow in the throat is characterized by an increase of the near wall RMS. Just after the

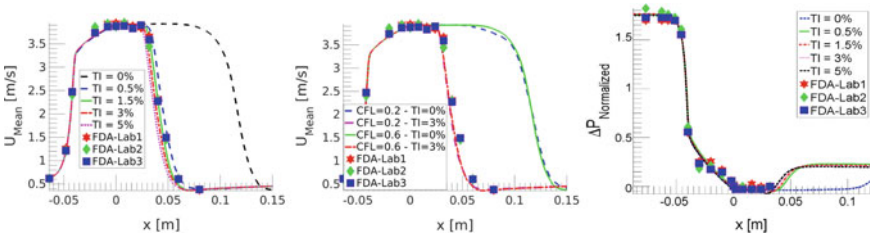

(a) CFL=0.6: TI range (b) CFL vs TI levels (c) Pressure,CFL=0.6: TI range

Fig. 4 Mean axial velocity and pressure profiles with small TI at inlet (Medium grid, $\mathrm{Re}_{th} = 3500$)

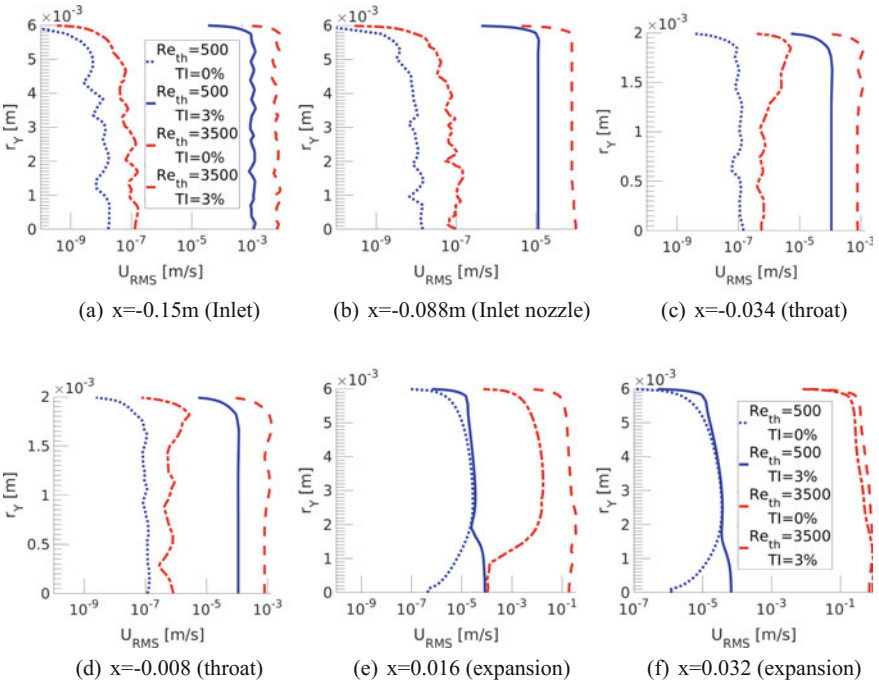

(a) x=-0.15m (Inlet) (b) x=-0.088m (Inlet nozzle) (c) x=-0.034 (throat)

(d) x=-0.008 (throat) (e) x=0.016 (expansion) (f) x=0.032 (expansion)

Fig. 5 Radial profiles of the root-mean-square (RMS) velocity for the laminar ($\mathrm{Re}_{th} = 500$) and transitional ($\mathrm{Re}_{th} = 3500$) regimes at a variety of axial positions with and without TI (Medium grid)

sudden-expansion, Fig. 5e and f, both RMS profiles obtained with TI are approaching the original no TI cases before merging into laminar flow profile ($\mathrm{Re}_{th} = 500$) or advancing into turbulence breakdown ($\mathrm{Re}_{th} = 3500$).

Figure 6 shows that TI greatly improves the LES prediction as well as its robustness for laminar, mildly turbulent cases and even in the most demanding, transitional case ($\mathrm{Re}_{th} = 2000$). The injected perturbations dissipate without inflicting transition in the laminar case, while in the transitional and turbulent cases they develop and contribute to more accurate and robust results.

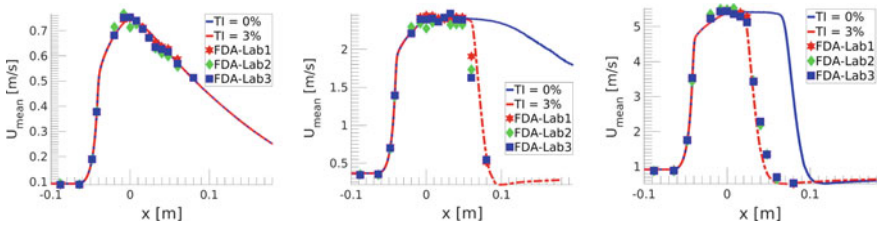

(a) Re_{th}=500 (b) Re_{th}=2000 (c) Re_{th}=5000

Fig. 6 Axial velocity profiles for the laminar, transitional and mildly turbulent cases with and without TI (Medium grid)

The study thus reveals that the upstream injection of small-scale perturbations into transition sensitive flows is an indispensable tool for any biomedical case where accurate prediction of turbulence is critical.

4 Intracardiac Turbulence

The hemodynamics of the left heart (LH) conveys information regarding the heart function [35, 36]. Observation of LH flow may thus reflect the presence of an existing pathology. In addition, there is substantial evidence that the LH hemodynamics can be responsible for the initiation of ventricular remodelling through mechanosensitive feedbacks modulating cardiomyocytes architecture [37, 38] and thus cardiac function [39]. Therefore, accurate assessment of the intracardiac flow is of paramount importance to get further comprehension of the role played by the hemodynamics in normal and abnormal LH. Used with caution, image-based computational fluid dynamics (CFD) can retrieve all the scales of the instantaneous flow, hence being able to capture disturbed flows. However, pioneering CFD studies focused only on the large-scale features of the ventricular flow i.e. the jets and the large recirculating cell. Apart from a few studies that mentioned the potential presence of flow instabilities [11, 40–42], little focus has been given to the disturbed nature of the LV flow, despite its potential importance.

4.1 Method

Large-eddy simulations were preformed to compute 35 cardiac cycles using the in-house YALES2BIO solver in a patient-specific left heart model obtained from CMR images. The set of images used to define the time evolution of the model over the cadiac cycle consists in 20 3D images of spatial resolution $5.0 \times 1.1 \times 1.1$ mm^3 ($21 \times 256 \times 256$ voxels). The subject was 26 years old and his cardiac cycles lasted

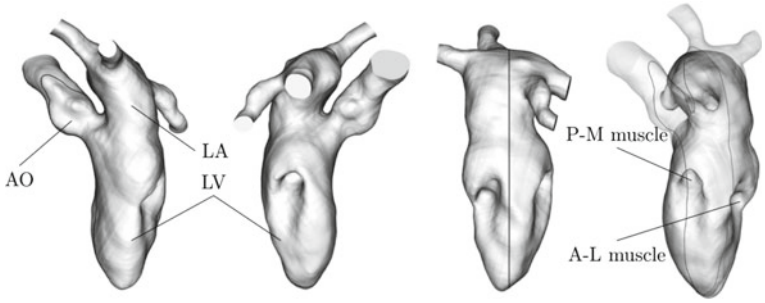

Fig. 7 Human left heart extracted from CMR images. The same domain is shown from four different points of view. The inlets and outlet flow extensions are visible in the *left figure*. The left ventricle (LV), left atrium (LA), Aorta (AO), Antero Lateral (A-L) and Postero Medial (P-M) papillary muscles are indicated. A *black line* passing through the LH indicates the position of the slice which will be used to display the results in Figs. 8 and 10

on average T = 750 ms. As shown in Fig. 7, the model includes the valves, atrium, ventricle, papillary muscles and ascending aorta. The deformations of the heart all along the heart cycle match the CMR exam thanks to an image registration technique. The technical procedure can be found in [11, 43]. The flow domain within the heart is discretized using ten million tetrahedral elements. The average edge length is close to 0.55 mm during diastole. The time step, based on a Courant-Friedrichs-Lewy stability number of 0.9, varies from 0.2 ms during the beginning of diastole to 0.5 ms during diastasis.

4.2 Results

The LV large-scale flow features i.e. the blood ejection, the two vortex rings for the E and A waves and the recirculating cell, are well retrieved (Fig. 8) in accordance with the numerous observations performed in vivo [42, 44], in silico [40, 45] and in vitro [46, 47]. However, our computation reveals also large velocity fluctuations, which are usually not reported in silico but which are in line with the results of previous experimental work that used both simplified ventricle geometries and inflow boundary condition [5, 47]. In order to quantify and study the regional distribution of these fluctuations, we computed them as the difference between the instantaneous velocity components u_i ($i = 1, 2, 3$) and the phase-averaged velocity components U_i. The fluctuating part of the fluid velocity is then:

$$u_i' = u_i - U_i = u_i - \langle u_i \rangle$$

while the corresponding fluctuating kinetic energy (FKE) per unit volume is:

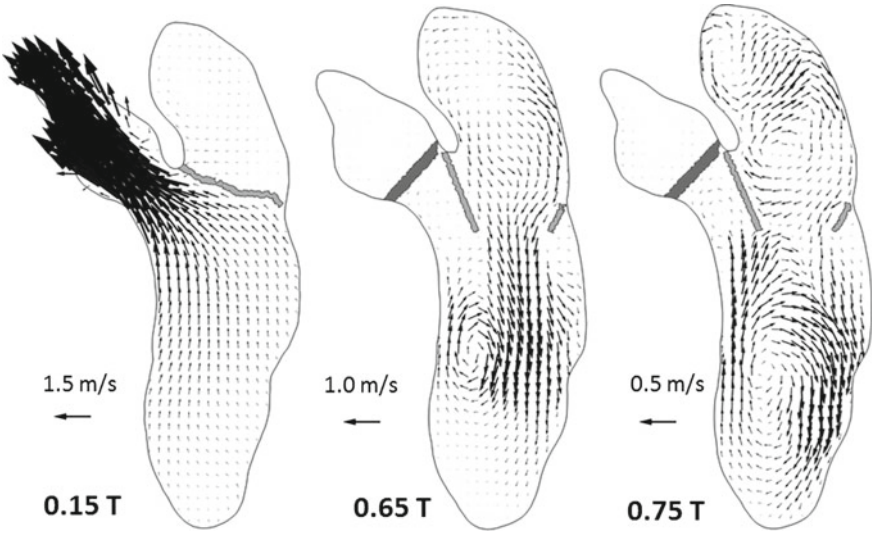

Fig. 8 Phase-averaged velocity field over a cutting plane through the LH (see Fig. 7 for the plane position). The mitral and the aortic valves are depicted in *grey*. The figure shows the classically reported structure of the heart cycle: the strong blood ejection at systole (0.15 T), the E wave-induced vortex ring at diastole (0.65 T) and the recirculating cell during diastasis (0.75 T)

$$FKE = \frac{\rho}{2} \left\langle u_i' u_i' \right\rangle ,$$

where $\langle\rangle$ denotes phase-averaged values, ρ is the fluid density (here 1040 kg/m^3) and the implicit summation rule over repeated indices is used. Figure 9 displays the FKE in the left heart during systole (left figure) and diastasis (right figure). Note that non negligible levels of FKE are visible at these instants. Detailed results of this simulation and its biomedical consequences can be found in [41].

4.3 Role of SGS Model

As a common practice when using properly resolved LES, all quantities are computed from the resolved velocity field in this study [48, 49]. We note that during our computations the subgrid scale viscosity remains low in the LV during the whole the heart cycle, showing that the subgrid scale model dissipates a moderate amount of energy. Figure 10 shows the ratio between the subgrid scale viscosity and the fluid viscosity. As expected, since the flow is laminar, the subgrid scale viscosity is virtually zero during the systole in the LV and has moderate values, but non-null, during the most turbulent part of the cycle. Thus, the σ-model [21] mainly introduces dissipation in regions where there are significant turbulent fluctuations and

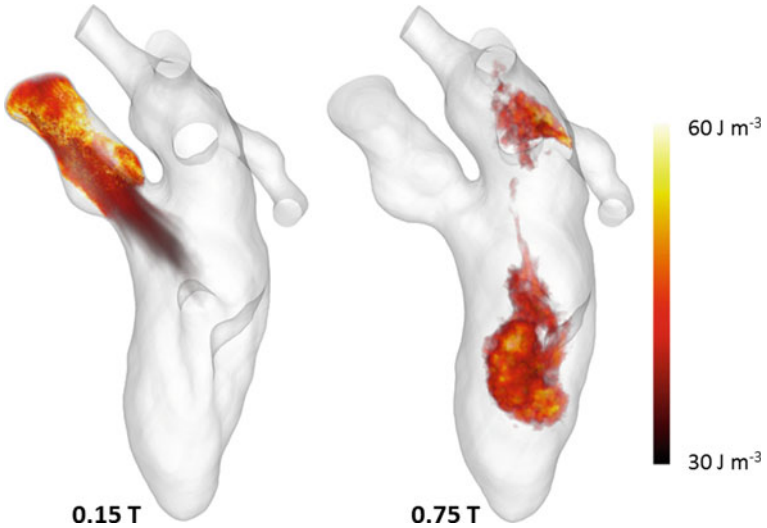

Fig. 9 3D volume rendering of the FKE in the left heart during systole (*left*, 0.15 T) and diastasis (*right*, 0.75 T). The opacity is set to 0% for FKE values below 30 J/m^3. The mitral and aortic valves are not displayed for more clarity but were accounted for in the simulation

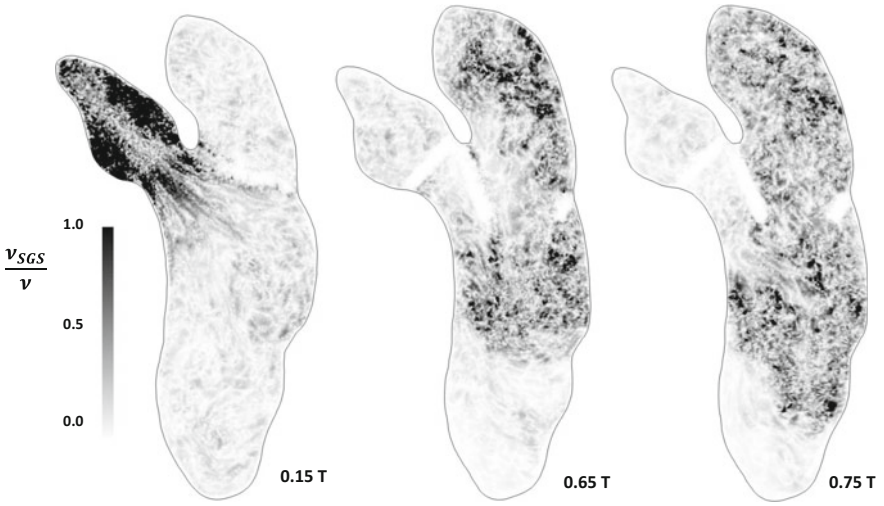

Fig. 10 Instantaneous fields of the SGS to fluid viscosity ratio. As expected the SGS viscosity tends to zero in the left ventricle during systole. The ν_{SGS}/ν ratio reaches approx. 0.2 in average in the LV during the most disturbed phase of the heart cycle. Maximum values are close to 5

almost no dissipation in regions where the flow is laminar. This is one of the features of the σ-model that makes it suitable for computing cardiovascular flows. For this particular simulation, an estimation of the Pope criterion [50] can be computed

as $k_{sgs}/k \approx 3C/2(\Delta/\pi L)^{2/3}$ [49] where $C = 1.5$, $\Delta = 0.55$ mm and $L = 0.04$ m is the characteristic length of the largest structures. For the present LES, this leads to $k_{sgs}/k \approx 0.06$ which remains three times below the 15–20% threshold usually used to evaluate if a LES is sufficiently resolved [50].

4.4 Discussion

The present results question the common idea of laminar flow in the normal left heart. Imposing the flow to be laminar (as often done in CFD for the LV using commercial software) may be sufficient to retrieve main large-scale hemodynamic features, namely jets, recirculating cell, and ejection. However, transitional or turbulent regimes feature small-scale phenomena that cannot be retrieved under the laminar hypothesis. The typical Reynolds number value (a few thousand) would make the DNS of one single cardiac cycle extremely CPU/memory demanding, if not impossible. For example, Chnafa et al. [11] estimated that more than 1 billion nodes would be necessary to represent the Kolmogorov scale in their realistic human heart model. On the contrary, well-resolved large-eddy simulation allows retrieving the main characteristics of the flow and its transient properties at a lower cost. This allows simulating several cycles (here 35) at a tractable numerical cost, thus studying more complex flow features compared to what is usually done based on RANS simulations, including cycle-to-cycle variations.

5 Cardiac Valves

The aortic heart valve separates the left ventricle from the aorta. It is composed of three thin deformable leaflets that open and close passively during the cardiac cycle, preventing blood from flowing back into the left ventricle, and thus ensuring an unidirectional flow through the cardiovascular system. Aortic valves often degenerate and lead to either insufficiency or stenosis, which can cause the death of the patient if not treated. Usually, medication is not a sufficient treatment, and the aortic valve needs to be replaced by a prosthesis. One of the basic engineering concern for artificial aortic valve design is the hemodynamics. Indeed, the ideal aortic valve design should minimize production of turbulence which is notably known to have effect on thrombus formation (blood coagulation) [51, 52]. In Sect. 4, the aortic valve was represented thanks to a simple model fed by morphological data gained from medical imaging [11, 41, 43]. A more realistic modelling based on a Fluid-Structure Interaction (FSI) formulation is described in this section where an experimental configuration relevant to an artificial aortic valve [53] is also considered for validation.

Numerical Method

The FSI model relies on the immersed thick boundary method (ITBM) [54] which was adapted from the original immersed boundary method (IBM) introduced by Peskin [55] to deal with 3D membranes. Two independent meshes are considered to discretize the solid valve and the fluid. The valve leaflets are represented by a moving Lagrangian mesh while the fluid is discretized by a fixed Eulerian unstructured mesh. The different steps of the ITBM are the following:

1. Knowing the displacement $\overrightarrow{U_m}$ of each Lagrangian node, the mechanical force $\overrightarrow{F_m}$ resulting from the membrane deformation is calculated,
2. The mechanical force $\overrightarrow{F_m}$ is regularized on the fluid mesh, giving rise to the volumetric force $\vec{f}_j$ on each fluid node,
3. The Navier-Stokes equations (forced by the regularized mechanical forces) are solved on the fluid mesh, yielding the velocity of the fluid $\vec{v}_j$ on each fluid node,
4. The velocity of the membrane $\overrightarrow{V_m}$ at each Lagrangian node is interpolated from the $\vec{v}_j$ field, enabling to deduce the new position $\overrightarrow{X_m}$ from the position at the previous timestep

$$\overrightarrow{X_m} = \overrightarrow{X_m}^{previous} + \Delta t \overrightarrow{V_m}$$

The displacement of each Lagrangian node is then updated thanks to $\overrightarrow{U_m} = \overrightarrow{X_m} - \overrightarrow{X_m^0}$, where $\overrightarrow{X_m^0}$ stands for the initial stress-free position (also referred to as the reference position).

The regularization and interpolation of steps 2 and 4 require dealing with Dirac functions that must be properly regularized on the Eulerian fluid mesh [56]. To this respect, the Reproducing Kernel Particle Method [57] is used to deal with unstructured meshes. The computation of the mechanical force $\overrightarrow{F_m}$ (step 1) is performed by the LMGC90 solid mechanics solver [58], using the classical finite-element method. In the present work, a quasi-incompressible Neo-Hookean material is used to model the valve, defined by its strain energy function:

$$W = \frac{G}{2}\left(\bar{I}_1 - 3\right) + \frac{K}{2}(\ln J)^2, \tag{3}$$

where G and K are the shear and bulk modulus, respectively. $\bar{I}_1$ is the first invariant of the isochoric right Cauchy-Green deformation tensor $\bar{\mathbf{C}}$, and J is the Jacobian of the transformation.

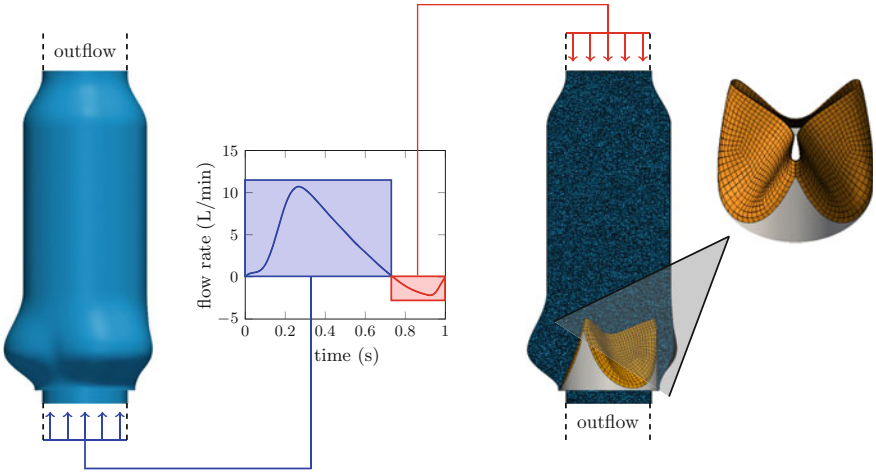

Fig. 11 Details of the computational setup. The flow is generated using switching inlet and outlet conditions, imposed far from the zone of interest. The assumption of a flat velocity profile is made to impose the inlet/outlet flow rate signal

Computational Setup

The computational setup was designed in such a way to represent the experimental test rig studied at the Helmholtz Institute of Aachen [53]. The aortic geometry includes the three sinuses of Valsalva after the calculations by Reul et al. [59] (see Fig. 11). The valve is built on a tri-commissure frame positioned within the aortic geometry, and is designed in an almost closed position (see Fig. 11). Both the arterial wall and the tri-commissure frame are defined as rigid bodies whose borders are non-slip wall boundary conditions of the fluid domain. As shown in Fig. 11, a flow rate signal is imposed as a periodic inlet condition either upstream or downstream of the valve, depending if the signal is positive or negative. The whole fluid geometry is represented by approx. 3.3 million tetrahedral elements, and the zone of interest (displayed in Fig. 11) is meshed with a uniform mesh resolution of 0.5 mm. The valve mesh is composed of approx. 1500 quadratic hexahedral elements, with an effective resolution of 0.5 mm.

The characteristics of the flow and the valve are relevant of physiological data and are summarized in Table 1. In view of the Reynolds (R_e) and Womersley (W_0) numbers, the viscosity of the Newtonian blood analogue fluid is set in the high-shear limit values [60].

Results and Discussion

Figure 12 shows the streamwise velocity field downstream of the valve. Four characteristic instants of the cardiac cycle are shown: $t = 0.20$ s, just before the flow rate reaches its maximal value, referred to as Early Systole (ES); $t = 0.26$ s, when the flow rate is maximal, referred to as Peak Systole (PS); $t = 0.35$ s, just after the flow

Table 1 Characteristics of the flow and the valve set to reproduce physiological flow conditions

Flow parameters	
Density	$\rho = 1100\,\text{kg/m}^3$
Dynamic viscosity	$\mu = 3.6 \times 10^{-3}$ Pa s
Heart rate	$n_{bpm} = 60$
Mean cardiac output	$Q_{mean} = 3.48$ L/min
Reynolds number	$R_e = 1388$
Womersley number	$W_0 = 17$
Valve parameters	
Density	$\rho_s = 1000\,\text{kg/m}^3$
Shear modulus	$G = 2.4$ MPa
Bulk modulus	$K = 1.6$ MPa
Thickness of the valve	$e = 0.15$ mm
Radius of the valve	$R = 12.5$ mm

rate reaches its maximal value and begins to decrease, referred to as Mid-Systole (MS); $t = 0.55$ s, when the flow rate is decreasing, referred to as Late Systole (LS). The main feature of the flow is the propagation of a jet emerging from the valve at ES (see label a), propagating between ES and MS (see labels b and c), and dissipating at LS. This jet is most probably hydro-dynamically unstable, promoting transition to turbulence downstream of the valve.

In order to analyse the structure of this jet and highlight the cycle-to-cycle variations of the flow, two velocity profiles are extracted over 10 distinct cycles (displayed in Fig. 12): profile 1 (P1), located immediately behind the valve; profile 2 (P2), located further downstream of the valve. Cycle-to-cycle variations are mainly observed on P2, suggesting that the jet emerging from the valve is mostly laminar and that it becomes turbulent when propagating further downstream. Regarding P2 at PS, MS and LS, it is seen that cycle-to-cycle variations increase as the inlet flow rate decreases, which is consistent with the observations made by Chnafa et al. [11, 41] in the case of whole heart geometries with simple (without FSI) valve model. This feature should be related to the general trend of all decelerated flows to destabilize. Few cycle-to-cycle variations are nonetheless observed on P1 at ES; these fluctuations are in fact induced by variations in the valve opening process and not related to any turbulent motion. This is illustrated in Fig. 13 which displays some typical shapes of the aortic valve. All these views correspond to the same three instants (the third one corresponding to ES) but were extracted at four different cycles. If the overall opening process is always the same (buckling of the leaflets, either successive or simultaneous), very large fluctuations are also present from one cycle to the other. These variations most probably result from two main ingredients: the sensitivity of the buckling phenomenon to the details of the load on the first hand, the existence of a chaotic pressure load induced by the downstream turbulent fluctuations on the other hand.

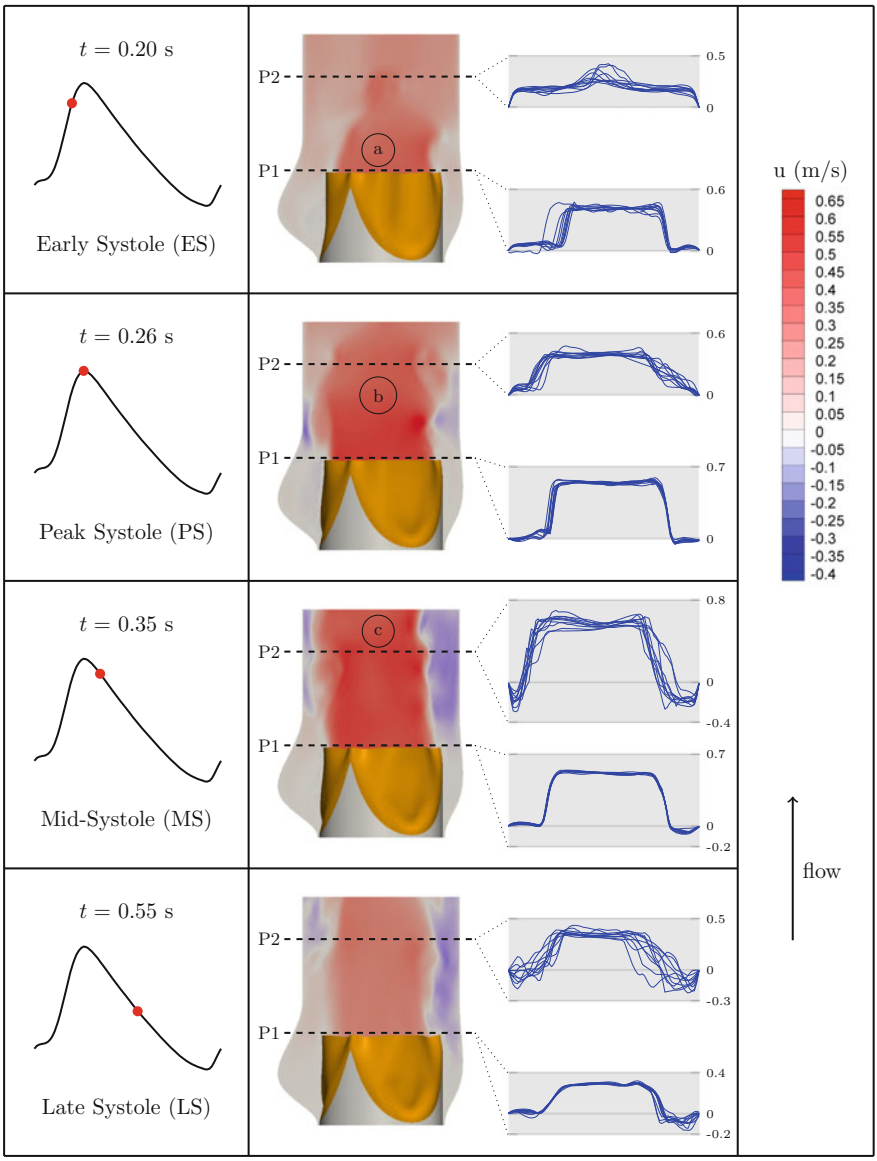

Fig. 12 Streamwise velocity field downstream of the valve. Two velocity profiles (P1 and P2) are extracted over 10 distinct cycles. Four different instants of the cardiac cycle are depicted (ES, PS, MS and LS)

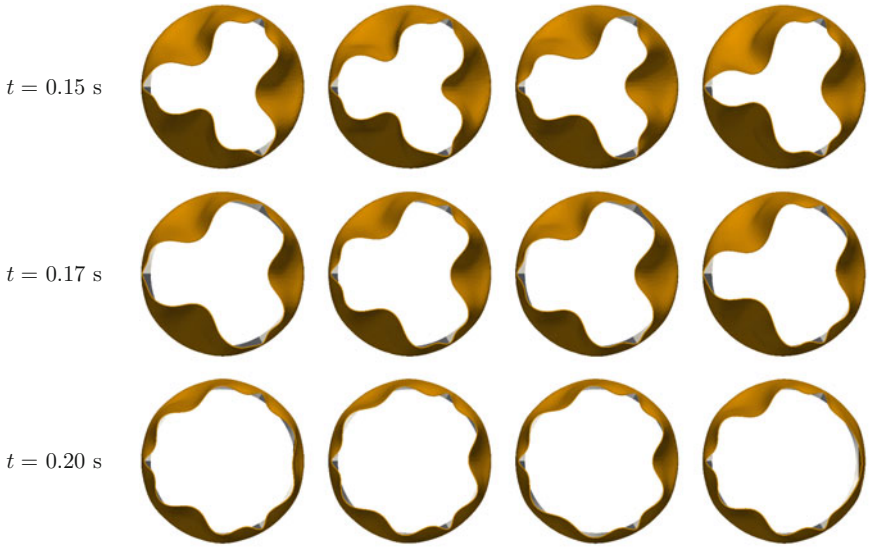

Fig. 13 Typical shapes of the aortic valve during the opening phase. The last instant (t = 0.20 s) corresponds to ES (see Fig. 12). Each column corresponds to a specific cycle

6 Conclusion

Given the flow regimes encountered in macro-circulation, turbulence is most probably present in many practical configurations, either physiological or within biomedical devices. Large-Eddy Simulation has the potential to properly represent the effects of turbulence provided that it is used with appropriate numerics, subgrid scale model and boundary conditions. The numerical solver YALES2BIO (http://www.math.univ-montp2.fr/~yales2bio/) gathers all the required properties and was successfully used in three different situations including the intracardiac flow and the interaction with a realistic aortic valve. Transitional flows are even more demanding and should be addressed very carefully since they may be extremely sensitive to the details of the simulation if no perturbation is introduced in the upstream condition. This is illustrated by considering the simplified medical device proposed by FDA as a validation test case.

Acknowledgements The authors thank ANR and BPI for their supports through the Laboratory of Excellence NUMEV (ANR-10-LABX-20), the FORCE (ANR-11-JS09-0011) and the DAT@DIAG (ISI-I1112018W) project. Dr S. Sonntag and PhD student D. Pott from the Helmholtz Institute of Aachen are gratefully acknowledged for providing the details of their experimental test rig about the aortic valve dynamics. CC also thanks CNRS for funding his thesis. Dr. V. Moureau is gratefully acknowledged for giving access to the YALES2 solver. This work was performed using HPC resources from GENCI-CINES (Grants 2014-, 2015- and 2016-c2015037194) and the HPC@LR Center.

References

1. S. Varghese, S. Frankel, P. Fischer, Direct numerical simulation of stenotic flows. Part 2. Pulsatile flow. J. Fluid Mech. **582**, 281 (2007)
2. A. Les, S. Shadden, C. Figueroa, J. Park, M. Tedesco, R. Herfkens, R. Dalman, C. Taylor, Quantification of hemodynamics in abdominal aortic aneurysms during rest and exercise using magnetic resonance imaging and computational fluid dynamics. Ann. Biomed. Eng. **38**(4), 1288–1313 (2010)
3. K. Valen-Sendstad, M. Piccinelli, D. Steinman, High-resolution computational fluid dynamics detects flow instabilities in the carotid siphon: implications for aneurysm initiation and rupture? J. Biomech. **47**(12), 3210–3216 (2014)
4. J. Mikhal, B. Geurts, Immersed boundary method for pulsatile transitional flow in realistic cerebral aneurysms. Comput. Fluids **91**, 144–163 (2014)
5. F. Domenichini, G. Querzoli, A. Cenedese, G. Pedrizzetti, Combined experimental and numerical analysis of the flow structure into the left ventricle. J. Biomech. **40**, 1988–1994 (2007)
6. P. Dyverfeldt, J. Kvitting, C. Carlhäll, G. Boano, A. Sigfridsson, U. Hermansson, A. Bolger, J. Enqwall, T. Ebbers, Hemodynamic aspects of mitral regurgitation assessed by generalized phase-contrast MRI. J. Magn. Reson. Imaging **33**, 582–588 (2011)
7. J. Zajac, J. Eriksson, P. Dyverfeldt, A. Bolger, T. Ebbers, C. Carlhäll, Turbulent kinetic energy in normal and myopathic left ventricles. J. Magn. Reson. Imaging **41**(4), 1021–1029 (2015)
8. U. Frisch, *Turbulence: The Legacy of A.N. Kolmogorov* (Cambridge University Press, 1996)
9. P. Spalart, Progress in aerospace sciences philosophies and fallacies in turbulence modeling. Prog. Aerosp. Sci. 1–15 (2015)
10. P. Hariharan, M. Giarra, V. Reddy, S. Day, K. Manning, S. Deutsch, S. Stewart, M. Myers, M. Berman, G. Burgreen, E. Paterson, R. Malinauskas, Multilaboratory particle image velocimetry analysis of the FDA benchmark nozzle model to support validation of computational fluid dynamics simulations. J. Biomech. Eng. **133**(4), 041002 (2011)
11. C. Chnafa, S. Mendez, F. Nicoud, Image-based large-eddy simulation in a realistic left heart. Comput. Fluids **94**, 173–187 (2014)
12. P. Sagaut, *Large Eddy Simulation for Incompressible Flows. An Introduction* (Springer, Berlin, 2001)
13. R. Vichnevetsky, J. Bowles, *Fourier Analysis of Numerical Approximations of Hyperbolic Equations*, Siam - stu edn. (1982)
14. Y. Morinishi, T. Lund, O. Vasilyev, P. Moin, Fully conservative higher order finite difference schemes for incompressible flow. J. Comput. Phys. **143**(1), 90–124 (1998)
15. R. Mittal, P. Moin, Suitability of upwind-biased finite differance schemes for large eddy simulation of turbulent flows. AIAA J. **35**(8), 1415–1417 (1997)
16. N. Park, J. Yoo, H. Choi, Discretization errors in large eddy simulation: on the suitability of centered and upwind-biased compact difference schemes. J. Comput. Phys. **198**(2), 580–616 (2004)
17. A. Chorin, Numerical solution of the Navier-Stokes equations. Math. Comput. **22**, 745–762 (1968)
18. J. Williamson, Low-storage Runge-Kutta schemes. J. Comput. Phys. **35**(1), 48–56 (1980)
19. V. Moureau, P. Domingo, L. Vervisch, Design of a massively parallel CFD code for complex geometries. Comptes Rendus Mécanique **339**(2–3), 141–148 (2011)
20. M. Malandain, N. Maheu, V. Moureau, Optimization of the deflated Conjugate Gradient algorithm for the solving of elliptic equations on massively parallel machines. J. Comput. Phys. **238**, 32–47 (2013)
21. F. Nicoud, H. Baya Toda, O. Cabrit, S. Bose, J. Lee, Using singular values to build a subgrid-scale model for large eddy simulations. Phys. Fluids **23**(8), 085106 (2011)
22. H. Baya Toda, O. Cabrit, K. Truffin, G. Bruneaux, F. Nicoud, Assessment of subgrid-scale models with a large-eddy simulation-dedicated experimental database: the pulsatile impinging jet in turbulent cross-flow. Phys. Fluids **26**(7), 075108 (2014)

23. M. Germano, U. Piomelli, P. Moin, W. Cabot, A dynamic subgrid-scale eddy viscosity model. Phys. Fluids A **3**, 1760–1766 (1991)
24. S. Stewart, E. Paterson, G. Burgreen, P. Hariharan, M. Giarra, V. Reddy, S. Day, K. Manning, S. Deutsch, M. Berman, M. Myers, R. Malinauskas, M. Berman, R. Malinauskas, Assessment of CFD performance in simulations of an idealized medical device: results of FDA's first computational interlaboratory study. Cardiovasc. Eng. Technol. **3**(2), 139–160 (2012)
25. A. Marsden, Y. Bazilevs, C. Long, M. Behr, Recent advances in computational methodology for simulation of mechanical circulatory assist devices. WIREs Syst. BiolMed. **6**, 169–188 (2014)
26. S. Mendez, V. Zmijanovic, E. Gibaud, J. Siguenza, F. Nicoud, Assessing macroscopic models for hemolysis from fully resolved simulations, in *4th International Conference on Computational and Mathematical Biomedical Engineering, CMBE2015 Proceedings*, ed. by P. Nithiarasu, E. Budyn (ENS Cachan, France, 2015), pp. 575–578
27. T. Passerini, A. Quaini, U. Villa, A. Veneziani, S. Canic, Validation of an open source framework for the simulation of blood flow in rigid and deformable vessels. Int. J. Numer. Methods Biomed. Eng. **29**(11), 1192–1213 (2013)
28. Y. Delorme, K. Anupindi, S. Frankel, Large eddy simulation of FDA's idealized medical device. Cardiovasc. Eng. Technol. **4**(4), 392–407 (2013)
29. S. Bhushan, D. Walters, G. Burgreen, Laminar, turbulent, and transitional simulations in benchmark cases with cardiovascular device features. Cardiovasc. Eng. Technol. **4**(4), 408–426 (2013)
30. G. Janiga, Large eddy simulation of the FDA benchmark nozzle for a Reynolds number of 6500. Comput. Biol. Med. **47**(April), 113–119 (2014)
31. F. Sotiropoulos, Computational fluid dynamics for medical device design and evaluation: are we there yet? Cardiovasc. Eng. Technol. **3**(2), 137–138 (2012)
32. V. Zmijanovic, S. Mendez, V. Moureau, F. Nicoud, About the numerical robustness of biomedical benchmark cases: Interlaboratory FDA's idealized medical device. Int. J. Numer. Methods Biomed. Eng. (2016). doi:10.1002/cnm.2789
33. X. Wu, P. Moin, R. Adrian, J. Baltzer, Osborne Reynolds pipe flow: direct simulation from laminar through gradual transition to fully developed turbulence. Proc. Natl. Acad. Sci. **112**(26), 7920–7924 (2015)
34. K. Avila, D. Moxey, A. de Lozar, M. Avila, D. Barkley, B. Hof, The onset of turbulence in pipe flow. Science **333**, 192–196 (2011)
35. A. Kheradvar, M. Gharib, On mitral valve dynamics and its connection to early diastolic flow. Ann. Biomed. Eng. **37**(1) (2009)
36. G. Pedrizzetti, F. Domenichini, G. Tonti, On the left ventricular vortex reversal after mitral valve replacement. Ann. Biomed. Eng. **38**(3), 769–773 (2010)
37. P. Davies, A. Remuzzi, E. Gordon, C. Dewey, M. Gimbrone, Turbulent fluid shear stress induces vascular endothelial cell turnover in vitro. Proc. Natl. Acad. Sci. **83**(7), 2114–2117 (1986)
38. S. Olesen, D. Clapham, P. Davies, Haemodynamic shear stress activates a K+ current in vascular endothelial cells. Nature **331**(6152), 168–170 (1988)
39. A. Pasipoularides, Mechanotransduction mechanisms for intraventricular diastolic vortex forces and myocardial deformations: Part 1. J. Cardiovasc. Transl. Res. **8**(1), 76–87 (2015)
40. F. Domenichini, G. Pedrizzetti, B. Baccani, Three-dimensional filling flow into a model left ventricle. J. Fluid Mech. **539**, 179–198 (2005)
41. C. Chnafa, S. Mendez, F. Nicoud, Image-based simulations show important flow fluctuations in a normal left ventricle: what could be the implications? Ann. Biomed. Eng. (2016). doi:10.1007/s10439-016-1614-6
42. T. Le, F. Sotiropoulos, On the three-dimensional vortical structure of early diastolic flow in a patient-specific left ventricle. Eur. J. Mech. B/Fluids **35**, 20–24 (2012)
43. C. Chnafa, S. Mendez, R. Moreno, F. Nicoud, Using image-based CFD to investigate the intracardiac turbulence, in *Modeling the Heart and the Circulatory System*, ed. by A. Quarteroni (Springer International Publishing, New York, 2015), pp. 97–117

44. P. Kilner, G. Yang, J. Wilkes, R. Mohiaddin, D. Firmin, M. Yacoub, Asymmetric redirection of flow through the heart. Nature **404**(6779), 759–761 (2000)
45. V. Mihalef, R. Ionasec, P. Sharma, B. Georgescu, I. Voigt, M. Suehling, D. Comaniciu, Patient-specific modelling of whole heart anatomy, dynamics and haemodynamics from four-dimensional cardiac CT images. Interface Focus **1**(3), 286–296 (2011)
46. A. Falahatpisheh, A. Kheradvar, High-speed particle image velocimetry to assess cardiac fluid dynamics in vitro: From performance to validation. Eur. J. Mech. B/Fluids **35**, 2–8 (2012)
47. G. Querzoli, S. Fortini, A. Cenedese, Effect of the prosthetic mitral valve on vortex dynamics and turbulence of the left ventricular flow. Phys. Fluids **22**, 1–10 (2010)
48. I. Celik, Z. Cehreli, I. Yavuz, Index of resolution quality for large eddy simulations. J. Fluid Eng. **127**(5), 949–958 (2005)
49. S. Pope, *Turbulent Flows* (Cambridge University Press, 2000)
50. S. Pope, Ten questions concerning the large-eddy simulation of turbulent flows. *New J. Phys.***6** (2004)
51. P. Stein, H. Sabbah, Measured turbulence and its effect on thrombus formation. Circ. Res. **35**, 608–614 (1974)
52. A. Yoganathan, Z. He, S. Jones, Fluid mechanics of heart valves. Annu. Rev. Biomed. Eng. **6**, 331–362 (2004)
53. D. Pott, J. Sigüenza, S. Sonntag, U. Steinseifer, S. Mendez, F. Nicoud, Dynamics of artificial aortic valves: a combined experimental and numerical study, in *42th ESAO meeting, Leuven* (2015)
54. J. Sigüenza, S. Mendez, D. Ambard, F. Dubois, F. Jourdan, R. Mozul, F. Nicoud, Validation of an immersed thick boundary method for simulating fluid-structure interactions of deformable membranes. J. Comput. Phys. **322**, 723–746 (2016). doi:10.1016/j.jcp.2016.06.041, http://dx.doi.org/10.1016/j.jcp.2016.06.041
55. C. Peskin, The immersed boundary method. Acta Numerica **11**, 479–517 (2002)
56. S. Mendez, E. Gibaud, F. Nicoud, An unstructured solver for simulations of deformable particles in flows at arbitrary Reynolds numbers. J. Computat. Phys. **256**, 465–483 (2014)
57. A. Pinelli, I. Naqavi, U. Piomelli, J. Favier, Immersed-boundary methods for general finite-difference and finite-volume Navier-Stokes solvers. J. Comput. Phys. **229**, 9073–9091 (2010)
58. F. Radjai, F. Dubois, *Discrete Numerical Modeling of Granular Materials* (Wiley-ISTE, 2011)
59. H. Reul, A. Vahlbruch, M. Giersiepen, T. Schmitz-Rode, V. Hirtz, S. Effert, The geometry of the aortic root in health, at valve disease and after valve replacement. J. Biomech. **23**(2), 181–191 (1990)
60. A. Robertson, A. Sequeira, R. Owens, Rheological models for blood, in *Cardiovascular Mathematics. Modeling and Simulation of the Circulatory System* (Springer, 2009), pp. 211–241

Computational Comparison Between Newtonian and Non-Newtonian Blood Rheologies in Stenotic Vessels

Bruno Guerciotti and Christian Vergara

Abstract This work aims at investigating the influence of non-Newtonian blood rheology on the hemodynamics of 3D patient-specific stenotic vessels, by means of a comparison of some numerical results with the Newtonian case. In particular, we consider two carotid arteries with severe stenosis and a stenotic coronary artery treated with a bypass graft, in which we virtually vary the degree of stenosis. We perform unsteady numerical simulations based on the Finite Element method using the Carreau-Yasuda model to describe the non-Newtonian blood rheology. Our results show that velocity, vorticity and wall shear stress distributions are moderately influenced by the non-Newtonian model in case of stenotic carotid arteries. On the other hand, we observed that a non-Newtonian model seems to be important in case of stenotic coronary arteries, in particular to compute the *relative residence time* which is greatly affected by the rheological model.

1 Introduction

Blood is a two-phase mixture comprising various types of formed elements (red blood cells, white blood cells, platelets) suspended in an aqueous solution of organic molecules, proteins, and salts called plasma. Because of this multi-component nature, blood exhibits complex rheological properties [1, 2]. In particular, several experimental investigations showed that blood features a so-called *shear-thinning* behavior, that is, its viscosity decreases with increasing shear rates, reaching a nearly constant value of approximately 0.035 poise only for shear rates grater than $200\,s^{-1}$ [3].

In computational fluid-dynamics, the assumption of Newtonian flow (i.e. constant viscosity) is generally accepted for blood flow in large-sized arteries, such as the aorta, where the shear rates are high, while the non-Newtonian behavior of blood

B. Guerciotti · C. Vergara (✉)
MOX, Dipartimento di Matematica, Politecnico di Milano, Piazza Leonardo da Vinci 32, 20133 Milan, Italy
e-mail: christian.vergara@polimi.it

P. Wriggers and T. Lenarz (eds.), *Biomedical Technology*, Lecture Notes in Applied and Computational Mechanics 84, DOI 10.1007/978-3-319-59548-1_10

has to be taken into account in small vessels like the capillaries [2]. For medium-sized vessels, such as the carotid arteries or the coronary arteries, the validity of the Newtonian hypothesis is still not completely clear, especially in the stenotic case. In addition to this, presently there is no universal agreement upon the correct model to represent the viscous properties of blood [4]. For these reasons, modelling of blood's non-Newtonian behavior is increasingly being performed and different non-Newtonian models have been used in order to study their effects on blood flow characteristics (e.g. flow field, secondary flow patterns, wall shear stresses).

We report in Table 1 the main computational studies regarding the use of non-Newtonian models in (possibly stenotic) carotid and coronary arteries, either in ideal or real (i.e. patient-specific) geometries. Most of the literature deals with healthy (i.e. non-stenotic) geometries, see [5–8, 12] for carotid arteries and [14, 15, 17, 18] for coronary arteries, whereas studies on stenotic geometries are still sparse. Among the studies in ideal stenotic districts, we cite e.g. Razavi et al. [9], who studied different non-Newtonian models in a 2D idealized stenotic carotid, and Chen et al. [13], who studied an ideal model of stenotic coronary artery treated with an end-to-side bypass graft. As for coronary bypasses, we mention Kabinejadian et al. [16], who studied a compliant model of an idealized sequential coronary artery bypass graft, but without including the stenosis in the 3D geometry. Even more rare are the studies on patient-specific stenotic vessels: Stroud et al. [11] compared Newtonian and non-Newtonian models in a severely stenotic patient-specific carotid, but only a two-dimensional model was examined; Shirmer et al. [10] studied a 3D

Table 1 Review of the literature regarding computational studies in carotid and coronary arteries using non-Newtonian models

	Arterial vessel	Geometry	Non-Newtonian model
Box et al. [5]	Non-stenotic carotids	Ideal, 3D	Carreau-Yasuda
Boyd et al. [6]	Non-stenotic carotids	Real, 2D	Carreau-Yasuda
Gijsen et al. [7]	Non-stenotic carotids	Ideal, 3D	Carreau-Yasuda
Perktold et al. [8]	Non-stenotic carotids	Ideal, 3D	Casson
Razavi et [9]	Stenotic carotids	Ideal, 2D	6 different models[a]
Shirmer et al. [10]	Stenotic carotids	Real, 3D	Carreau
Stroud et al. [11]	Stenotic carotids	Real, 2D	Power law
Valencia et al. [12]	Non-stenotic carotids	Real, 3D	Herschel-Bukley
Chen et al. [13]	Stenotic coronaries	Ideal, 3D	Carreau-Yasuda
Jeong et al. [14]	Non-stenotic coronaries	Ideal, 2D	Carreau
Johnston et al. [15]	Non-stenotic coronaries	Real, 3D	Generalised power law
Kabinejadian et al. [16]	Non-stenotic coronaries	Ideal, 3D	Carreau-Yasuda
Liu et al. [17]	Non-stenotic coronaries	Real, 3D	Power law
Soulis et al. [18]	Non-stenotic coronaries	Real, 3D	7 different models[b]
Vimmr et al. [19]	Stenotic coronaries	Real, 3D	Carreau-Yasuda

[a]Power law, Carreau, Carreau-Yasuda, Modified-Casson, Generalized power law, Walburn-Schneck

[b]Carreau, Carreau-Yasuda, Power law, Non-Newtonian power law, Generalized power law, Casson, Walburn-Schneck

patient-specific stenotic carotid artery, but no comparison was made with the Newtonian model; Vimmr et al. [19] performed a numerical comparison of Newtonian and non-Newtonian models in patient-specific aorto-coronary bypasses. At the best of our knowledge, no comparisons between Newtonian and non-Newtonian models have been made so far in patient-specific 3D stenotic carotid arteries. Furthermore, no attention has been given to the influence of the degree of stenosis on the non-Newtonian behavior of blood in 3D patient-specific aorto-coronary bypass configurations.

In this context, the aim of this work is to investigate the effects of non-Newtonian blood rheology on the hemodynamics of 3D patient-specific stenotic vessels. In particular, we studied two sets of geometries:

1. two carotid arteries with severe stenosis (i.e. greater than 70%);
2. a stenotic coronary artery treated with a bypass graft. In this case, we virtually vary the degree of stenosis in order to obtain three different degrees of coronary stenosis (50, 70, 90)%, with the aim of analysing the effects of the non-Newtonian rheology for different degrees of stenosis.

On these geometries, reconstructed from MRI or CT images, we performed unsteady numerical simulations based on the Finite Element method. In order to describe the non-Newtonian blood rheology, we choose the Carreau-Yasuda model, since this model is able to correctly describe the physiological shear-thinning behavior of blood [4].

2 Materials and Methods

2.1 Computational Domains and Mesh Generation

For this study, we consider two carotids with a degree of stenosis greater than 70% who underwent elective carotid endarterectomy, i.e. the surgical removal of atherosclerotic plaque (cases CA1, CA2), and one patient with isolated severe left anterior descending (LAD) coronary artery disease (i.e. stenosis greater than 70%) who underwent aorto-coronary bypass graft surgery by means of the left internal mammary artery (case CO1). Radiological images were acquired by means of Magnetic Resonance technology for CA1 and CA2 and Contrast Enhanced Computed Tomography for CO1.

Using the software VMTK (https://www.vmtk.org), we reconstructed from the radiological images a surface model of the interface between the blood and the arterial wall (see Fig. 1 for two examples of reconstructed surfaces). The corresponding computational domains were turned into volumetric meshes of tetrahedra, obtained after a refinement study (constant wall shear stresses up to a tolerance of 2%). A local mesh refinement was also performed in all the cases at the level of the stenosis. As examples, we report in Fig. 2a detail of the meshes for CA1 and CO1 cases.

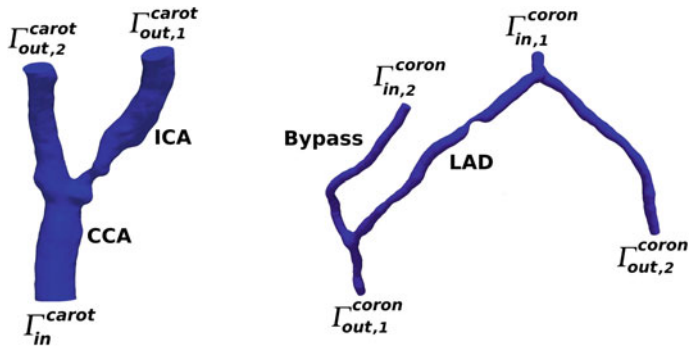

Fig. 1 Computational domains for the numerical simulations. *Left*: case CA2. *Right*: case CO1 with a 70% LAD stenosis

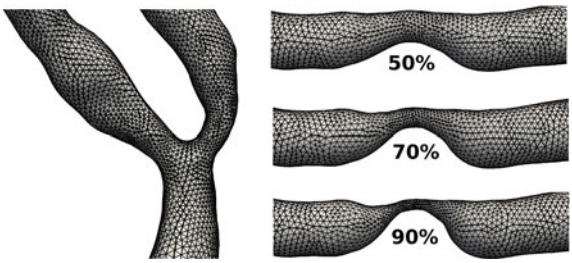

Fig. 2 Mesh details. *Left*: stenotic carotid bifurcation of case CA1. *Right*: different degrees of LAD stenosis of case CO1

2.2 Mathematical and Numerical Methods

We consider blood as a homogeneous and incompressible fluid described by the Navier-Stokes equations [20] and we assume either a Newtonian or a non-Newtonian rheology model. In particular, for the latter case we choose the *Carreau-Yasuda* model, with viscosity given by [3, 19]

$$\mu(\mathbf{x},t) = \mu_\infty + (\mu_0 - \mu_\infty)\left(1 + (\lambda\dot{\gamma}(\mathbf{x},t)^a\right)^{\frac{n-1}{a}}, \tag{1}$$

where $\dot{\gamma}$ is the shear rate defined by $\dot{\gamma} = 2\sqrt{D_{II}}$, $D_{II} = \frac{1}{2}\sum_{i,j=1}^{3} D_{ij}D_{ij}$ being the second invariant of the rate of deformation tensor $\mathbf{D}(\mathbf{u}) = \frac{1}{2}\left(\nabla\mathbf{u} + (\nabla\mathbf{u})^T\right)$, with $\mathbf{u} = \mathbf{u}(\mathbf{x},t)$ the fluid velocity. For the Newtonian case, we set $\mu = \mu_\infty$. Since the viscosity given by (1) is a function of the velocity, we will write in general $\mu = \mu(\mathbf{u})$. The values of the parameters that define the Carreau-Yasuda model are $\lambda = 1.902\,s$, $n = 0.22$, $a = 1.25$, $\mu_0 = 0.56\,P$, $\mu_\infty = 0.035\,P$.

As for time discretization, we consider the backward Euler method with a semi-implicit treatment of the convective term. The non-linearity arising from the non-Newtonian model (1) is treated semi-implicitly. This means that, indicating with z^n the approximation of a generic function $z(t)$ evaluated at $t^n = n\Delta t$, $n = 1, \ldots$, at each

time-step t^n we have the following discretized-in-time problem to be solved in the computational domain Ω:

$$\begin{cases} \rho \dfrac{\mathbf{u}^n - \mathbf{u}^{n-1}}{\Delta t} - \nabla \cdot \left[\mu(\mathbf{u}^{n-1}) \left(\nabla \mathbf{u}^n + (\nabla \mathbf{u}^n)^T \right) \right] + \rho \mathbf{u}^{n-1} \cdot \nabla \mathbf{u}^n + \nabla p^n = \mathbf{0} & \text{in } \Omega, \\ \nabla \cdot \mathbf{u}^n = 0 & \text{in } \Omega, \end{cases}$$

equipped with a suitable initial condition for the velocity, and where $\rho = 1.06\, g/cm^3$ is the fluid density and $p = p(\mathbf{x}, t)$ the fluid pressure.

As for the boundary conditions, we consider at each discrete time t^n a flow rate condition

$$\int_{\Gamma} \mathbf{u}^n \cdot \mathbf{n}\, d\gamma = Q(t^n),$$

for $\Gamma = \Gamma_{in}^{carot}$, $\Gamma_{out,1}^{carot}$, $\Gamma_{in,1}^{coron}$, $\Gamma_{in,2}^{coron}$, $\Gamma_{out,1}^{coron}$ (see Fig. 1) and where Q are the corresponding flow rates depicted in Fig. 3 for cases CA1 and CA2 and Fig. 4 for case CO1 (for each degree of stenosis). For the carotid cases, the patient-specific measures of flow rate were obtained by means of Doppler echocardiography technique (see [21] for more details). For the coronary cases, the prescribed flow rate at the coronary inlet $\Gamma_{in,1}^{coron}$ and at the graft inlet $\Gamma_{in,2}^{coron}$ were taken from literature [22, 23]. For the latter section, the amplitude of the signal was set in accordance to the degree of stenosis, in order to guarantee that the flow rate perfusing the myocardium at the outlet $\Gamma_{out,1}^{coron}$ (calibrated by means of an *healthy* simulation) remained constant, as observed in the clinical practice [24, 25] (see [26] for more details). In the remaining artificial sections $\Gamma_{out,2}^{carot}$ and $\Gamma_{out,2}^{coron}$, the following homogeneous Neumann condition is prescribed, in accordance with the fluid incompressibility:

$$-p^n \mathbf{n} + \mu \left(\mathbf{u}^{n-1} \right) \mathbf{D} \left(\mathbf{u}^n \right) = \mathbf{0}.$$

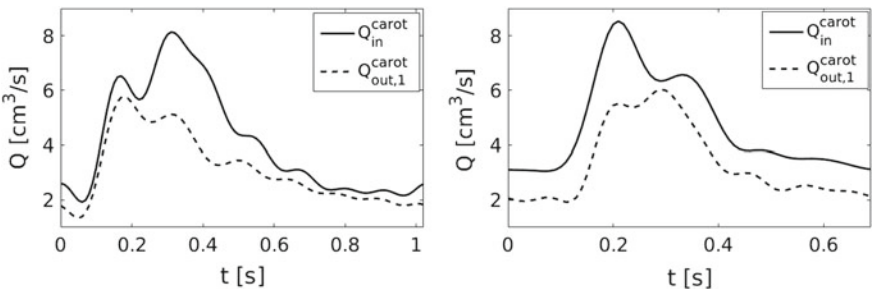

Fig. 3 Flow rates imposed as boundary conditions on the inlet and outlet of the computational domain for cases CA1 (*left*) and CA2 (*right*)

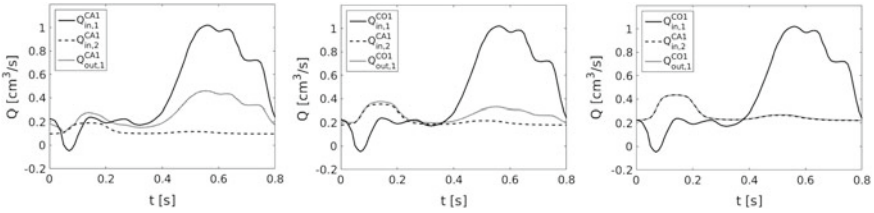

Fig. 4 Flow rates imposed as boundary conditions on the inlets and outlet of the computational domain for case CO1 for different degrees of stenosis: 50% (*left*), 70% (*middle*) and 90% (*right*)

We performed unsteady numerical simulations using the Finite Element library LifeV developed at MOX—Politecnico di Milano, INRIA—Paris, CMCS—EPF of Lausanne, and Emory University—Atlanta (https://www.lifev.org). The vessel walls were assumed to be rigid. In order to highlight the differences between Newtonian and non-Newtonian rheologies, we did not consider any turbulence model, although for stenotic carotids transition to turbulence may occur [27, 28]. We used $P1_{bubble} - P1$ finite elements for the space discretization and we set the time discretization parameter $\Delta t = 0.01\ s$. The flow rate conditions were prescribed by means of a Lagrange multipliers method, see [29, 30].

3 Results

3.1 Carotid Arteries

In order to investigate the differences between the Newtonian (N) and non-Newtonian (N-N) models, we report in Fig. 5 the velocity magnitude $v(\mathbf{x}, t) = \sqrt{u_x^2 + u_y^2 + u_z^2}$ at the systolic instant t_1 and at the post-systolic instant $t_2 = 0.41\ s$ on selected sections in cases CA1 and CA2, respectively. Furthermore, Fig. 6 shows the vorticity magnitude $w(\mathbf{x}, t) = \sqrt{\omega_x^2 + \omega_y^2 + \omega_z^2}$ [1] on the same sections for CA1 and CA2. These sections were selected so as to comprise the common carotid artery (CCA), the stenosis and the internal carotid artery (ICA). In the same images we also report, for t_1 and t_2 and on the same sections, the viscosity computed for the non-Newtonian model and the differences $d_V(\mathbf{x}, t) = |v_N - v_{NN}|$ and $d_w(\mathbf{x}, t) = |w_N - w_{NN}|$, where the subscripts N and NN refer to the Newtonian and non-Newtonian computations, respectively. From these results, small differences can be observed between the two models both for velocity and vorticity at systole (t_1). Instead, some differences are noticeable at t_2: for the velocity, at the distal ICA and, only for case CA2, at the CCA, whereas for the vorticity, mainly at the ICA for both the cases. As for the viscosity in the

[1] We recall that the vorticity, ω, is defined as $\omega = \nabla \times \mathbf{u}$.

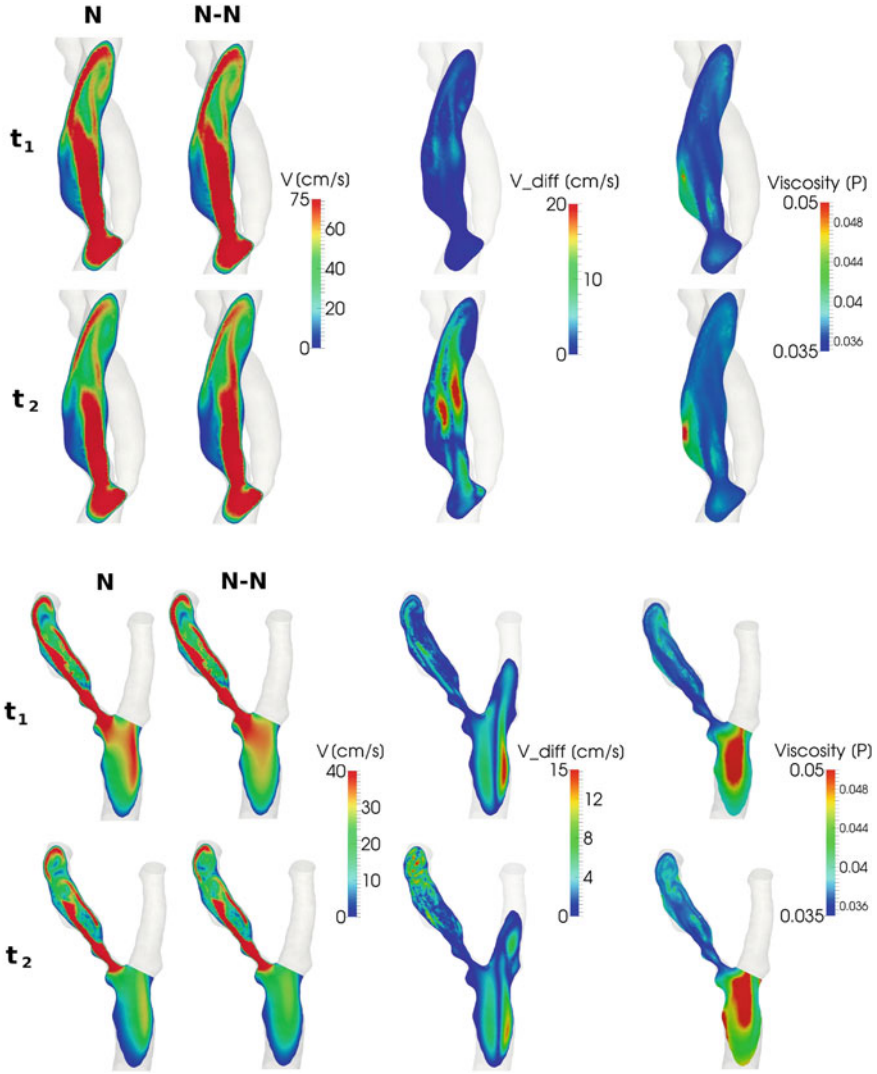

Fig. 5 *Left columns*: velocity magnitude v in the Newtonian (N) and non-Newtonian (N-N) models. *Middle column*: absolute value of the difference between the Newtonian and non-Newtonian velocity magnitudes. *Right column*: viscosity computed for the non-Newtonian model. *Top*: CA1 case; *bottom*: CA2 case. For each case, the quantities are reported on a selected section and at the systolic (t_1) and post-systolic (t_2) instants

non-Newtonian cases, we notice higher values in regions where the vessel diameter is large (e.g. in the CCA and in the region downstream the stenosis). This is due to lower velocities and shear rates at larger diameters, which result in higher viscosities due to the *shear-thinning* behavior of blood.

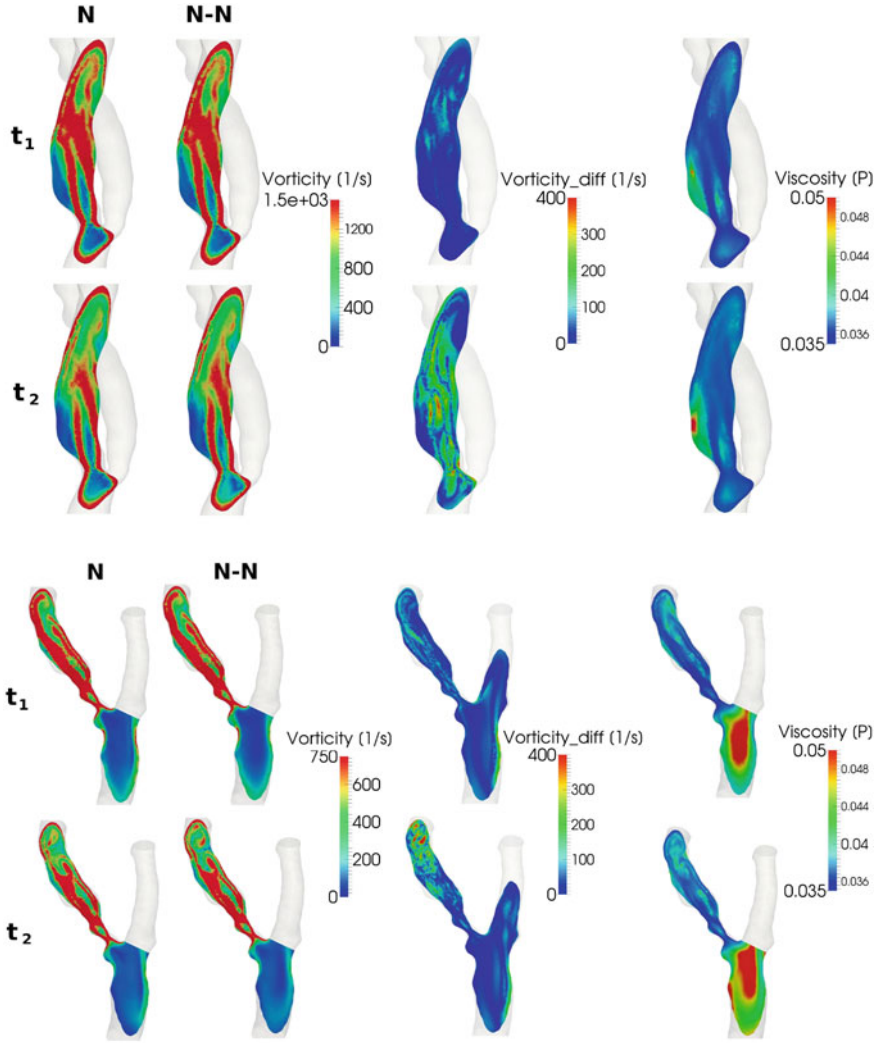

Fig. 6 *Left columns*: vorticity magnitude w in the Newtonian (N) and non-Newtonian (N-N) models. *Middle column*: absolute value of the difference between the Newtonian and non-Newtonian vorticity magnitudes. *Right column*: viscosity computed for the non-Newtonian model. *Top*: CA1 case; *bottom*: CA2 case. For each case, the quantities are reported on a selected section and at the systolic (t_1) and post-systolic (t_2) instants

Figure 7 shows the Wall Shear Stress (WSS) magnitude $t_w(\mathbf{x}, t)=\sqrt{\tau_{w,x}^2+\tau_{w,y}^2+\tau_{w,z}^2}$ at systole for CA1 and CA2, together with the viscosity computed for the non-Newtonian model. The Wall Shear Stress vector, τ_w, is defined as $\tau_w = \mathbf{t} - (\mathbf{t} \cdot \mathbf{n})\mathbf{n}$, where $\mathbf{t} = 2\mu\mathbf{D}\mathbf{n}$ is the traction vector acting on a surface with normal $\mathbf{n}$. Systolic

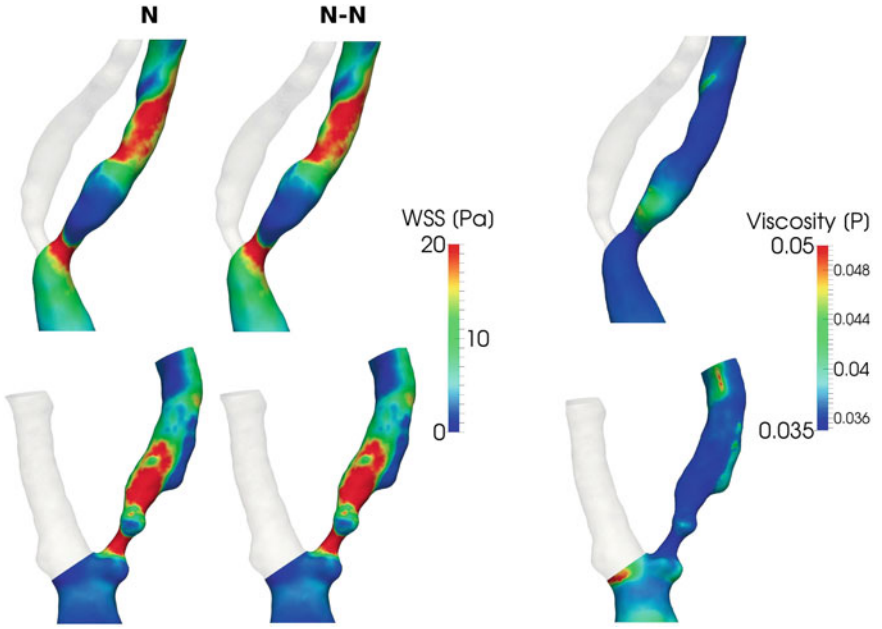

Fig. 7 WSS magnitude at the systolic instant t_1 in the Newtonian (N) and non-Newtonian (N-N) models. *Top*: case CA1; *bottom*: case CA2. The viscosity computed for the non-Newtonian model is also reported

WSS is an important index of risk of plaque rupture (see [31]), so that it is interesting to evaluate the possible effects of the non-Newtonian model on the quantification of this index. From the figures, no significant differences are observed between the Newtonian and non-Newtonian solutions. We notice that the regions where the viscosities are higher correspond to region of low WSS, which however are not regions of interest for stenotic carotids.

We finally report in Table 2 the mean relative differences between the Newtonian (N) and non-Newtonian (N-N) results at instants t_1 and t_2 for velocity, vorticity and WSS magnitudes, defined as

$$\frac{\int_\Omega |q_N - q_{NN}| d\mathbf{x}}{\int_\Omega |q_N| d\mathbf{x}} \quad q = v, w, t_w. \tag{2}$$

Table 2 Mean relative difference computed with (2) between the Newtonian (N) and non-Newtonian (N-N) cases for velocity, vorticity and WSS magnitudes for CA1 and CA2 at t_1 and t_2

	Velocity magnitude		Vorticity magnitude		WSS magnitude	
	t_1 (%)	t_2 (%)	t_1 (%)	t_2 (%)	t_1 (%)	t_2 (%)
CA1	4.8	9.1	5.8	11.8	3.6	6.5
CA2	9.5	24.0	10.9	30.4	7.2	18.4

Differences up to nearly 24 and 30% are visible for velocity and vorticity magnitudes, respectively, thus confirming what we observed in Figs. 5 and 6. For WSS magnitude, the differences are not so negligible as we inferred from Fig. 7. In any case, the differences are more pronounced at the deceleration phase (instant t_2).

3.2 Coronary Arteries

Figure 8 shows the diastolic (i.e. the maximum, see Fig. 4) velocity magnitude for the 3° of stenosis on a selected section at the region of the anastomosis. Furthermore, for the same section, we report the viscosity computed for the non-Newtonian model and the difference d_v between Newtonian and non-Newtonian results. We notice appreciable differences in the viscosity and, accordingly, in the velocity field. In particular, the latter are more localized in the native/stenotic artery (on the right in the figures) for smaller degrees of stenosis and at the anastomosis region for higher degrees of stenosis, and they are more pronounced for higher degree of stenosis. In Table 3,

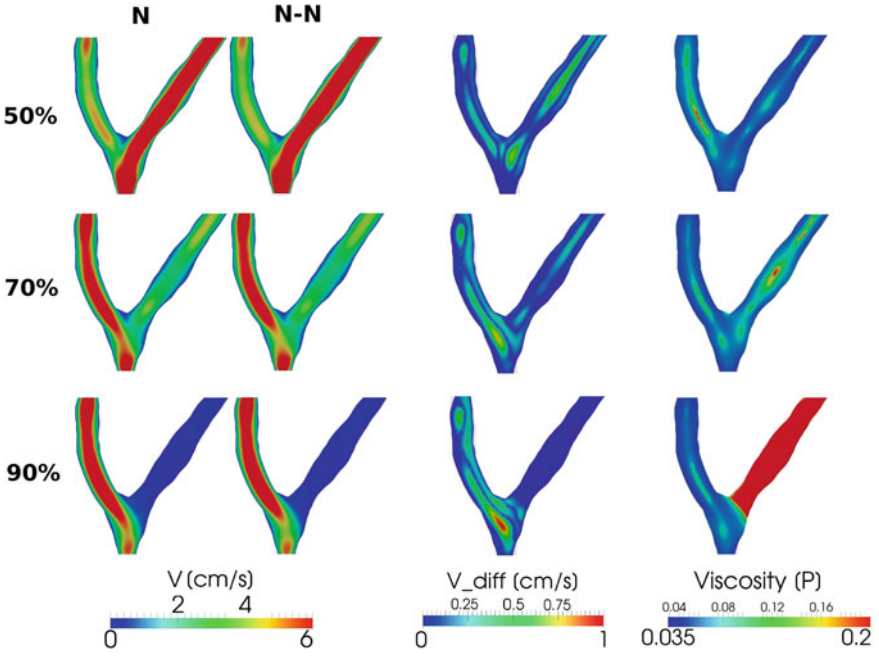

Fig. 8 *Left columns*: velocity magnitude v in the Newtonian (N) and non-Newtonian (N-N) models. *Middle column*: absolute value of the difference between the Newtonian and non-Newtonian velocity magnitudes. *Right column*: viscosity computed for the non-Newtonian model. *Top*: 50% degree of stenosis; *middle*: 70% degree of stenosis; *bottom*: 90% degree of stenosis. For each case, the quantities are reported on a selected section and at the diastolic instant

Table 3 Mean relative difference computed with (2) between the Newtonian (N) and non-Newtonian (N-N) cases for the diastolic velocity magnitude and RRT for different degree of stenosis

Stenosis (%)	v_{max} (%)	*RRT* (%)
50	2.7	34.3
70	2.8	51.5
90	6.9	91.5

we report the mean relative differences of diastolic velocity magnitude given by (2), $q = v$. These results confirm that the relative difference increases for increasing values of the stenosis degree.

In Fig. 9, we report the Relative Residence Time (RRT) distribution in a region comprising the coronary-bypass anastomosis and the stenosis for Newtonian and non-Newtonian models and for each degree of stenosis. RRT is a function of space defined on the lumen boundary given by

$$RRT(\mathbf{x}) = \frac{1}{(1 - 2OSI(\mathbf{x}))TAWSS(\mathbf{x})},$$

where *OSI* is the Oscillatory Shear Index

$$OSI(\mathbf{x}) = \frac{1}{2}\left(1 - \frac{\left\|\int_0^T \tau_w(t,\mathbf{x})dt\right\|}{\int_0^T \left\|\tau_w(t,\mathbf{x})\right\| dt}\right),$$

and *TAWSS* is the Time-Averaged Wall Shear Stress

$$TAWSS(\mathbf{x}) = \frac{1}{T}\int_0^T \left\|\tau_w(t,\mathbf{x})\right\| dt.$$

The choice of this index for the comparison between the models was driven by the fact that RRT is known to be related to the risk of plaque formation in coronary arteries [32] and, since restenosis is a known clinical problem in coronary artery bypasses (see [33]), it is interesting to investigate the effects of the non-Newtonian model on this index. We can see from the figure that RRT is greatly influenced by the choice of the rheological model for all stenosis degrees (notice that the scales are different for each stenosis degree, in order to better emphasize the differences). In particular, the Newtonian model overestimates RRT, especially at the anastomosis and in the native/stenotic branch. The reason for these differences may be attributed to the low flow rates in the stenotic vessel (in addition to the generally low flow rates in the coronary arteries), thus featuring very low shear rates. These results are also confirmed by the mean relative differences of RRT computed owing to (2), $q = RRT$, which are reported in Table 3 for each degree of stenosis and which feature very high values, especially for increasing values of the stenosis degree.

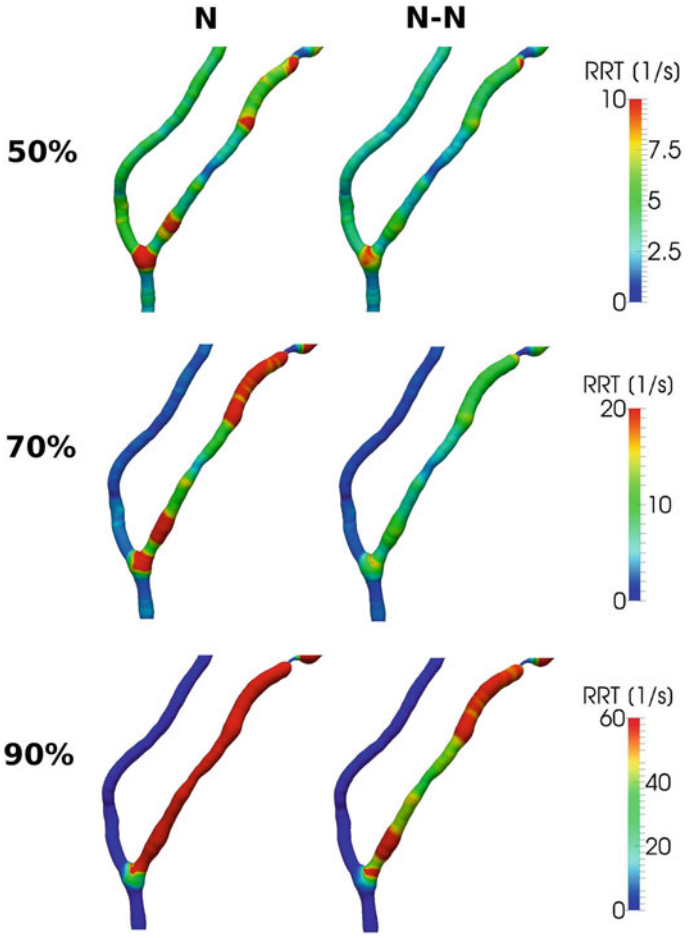

Fig. 9 RRT distribution in a region comprising the coronary-bypass anastomosis and the stenosis in the Newtonian (N) and non-Newtonian (N-N) cases for each degree of stenosis, case CO1

4 Conclusions

The purpose of this study was to investigate the influence of non-Newtonian blood rheology in stenotic vessels. In particular, we considered two carotid arteries with severe stenosis (i.e. greater than 70%) and one coronary vessel in which we virtually varied the stenosis degree (50, 70, 90)%. Our comparisons between Newtonian and non-Newtonian models showed that:

1. for stenotic carotid arteries, velocity and vorticity fields are influenced by blood rheology (mean differences of magnitudes up to 24 and 30%, respectively). Smaller differences were found in the quantification of WSS (mean difference of magnitude up to 18%);
2. also for stenotic coronary arteries, the velocity field is influenced by blood rheology. Moreover, great differences were found in the quantification of RRT (for all stenosis degrees). Thus, we believe that the non-Newtonian behavior of blood should not be neglected to accurately compute RRT, regardless of the degree of the stenosis.

Limitations of this work are the absence of turbulence models in the stenotic carotids and of a fluid-structure interaction model. We are working on both these topics to understand their importance in quantifying the differences between Newtonian and non-Newtonian models.

References

1. O.K. Baskurt, H.J. Meiselman, Blood rheology and hemodynamics. Semin. Thromb. Hemost. **29**(5), 435–450 (2003)
2. N. Bessonov, A. Sequeira, S. Simakov, Y. Vassilevskii, V. Volpert, Methods of blood flow modelling. Math. Model. Nat. Phenom. **11**(1), 1–25 (2006)
3. Y.I. Cho, K.R. Kensey, Effects of the non-Newtonian viscosity of blood on flows in a diseased arterial vessel. Biorheology **28**, 241–262 (1991)
4. S.S. Shibeshi, W.E. Collins, The rheology of blood flow in a branched arterial system. Appl. Rheo. **15**(6), 398–405 (2005)
5. F.M. Box, R.J. van der Geest, M.C. Rutten, J.H. Reiber, The influence of flow, vessel diameter, and non-Newtonian blood viscosity on the wall shear stress in a carotid bifurcation model for unsteady flow. Invest. Radiol. **40**(5), 277–294 (2005)
6. J. Boyd, J. Buick, Comparison of Newtonian and non-Newtonian flows in a two dimensional carotid artery model using the lattice Boltzmann method. Phys. Med. Biol. **52**(20), 6215–6228 (2007)
7. F.J.H. Gijsen, F.N. van de Vosse, J.D. Janssen, The influence of the non-Newtonian properties of blood on the flow in large arteries: steady flow in a carotid bifurcation model. J. Biomech. **32**(6), 601–608 (1999)
8. K. Perktold, R.O. Peter, M. Resch, G. Langs, Pulsatile non-Newtonian blood flow in a three-dimensional carotid bifurcation models: a numerical sudy of flow phenomena under different bifurcation angles. J. Biomed. Eng. **13**(6), 507–515 (1991)
9. A. Razavi, E. Shirani, M.R. Sadeghi, Numerical simulation of blood pulsatile flow in a stenosed carotid artery using different rheological models. J. Biomech. **44**(11), 2021–2030 (2011)
10. C.M. Shirmer, A.M. Malek, Computational fluid dynamic characterization of carotid bifurcation stenosis in patient-based geometries. Brain Behav. **2**(1), 45–52 (2012)
11. J.S. Stroud, S.A. Berger, D. Saloner, Numerical analysis of flow through a severely stenotic carotid artery bifurcation. J. Biomech. Eng. **124**(1), 9–20 (2002)
12. A. Valencia, A. Zarate, M. Galvez, L. Badilla, Non-Newtonian blood flow dynamics in a right internal carotid artery with a saccular aneurysm. Int. J. Numer. Method Fluid **50**, 751–764 (2006)
13. J. Chen, X.-Y. Lu, W. Wang, Non-Newtonian effects of blood flow on hemodynamics in distal vascular graft anastomoses. J. Biomech. **39**, 1983–1995 (2006)

14. W.W. Jeong, K. Rhee, Effects of surface geometry and non-Newtonian viscosity on the flow field in arterial stenoses. J. Mech. Sci. Technol. **23**, 2424–2433 (2009)
15. B.M. Johnston, P.R. Johnston, S. Corney, D. Kilpatrick, Non-Newtonian blood flow in human right coronary arteries: transient simulations. J. Biomech. **39**, 1116–1128 (2006)
16. F. Kabinejadian, D.N. Ghista, Compliant model of a coupled sequential coronary arterial bypass graft: effects of vessel wall elasticity and non-Newtonian rheology on blood flow regime and hemodynamic parameters distribution. Med. Eng. Phys. **34**, 860–872 (2012)
17. B. Liu, D. Tang, Influence of non-Newtonian properties of blood on the wall shear stress in human atherosclerotic right coronary arteries. Mol. Cell. Biomech. **8**(1), 73–90 (2011)
18. J.V. Soulis, G.D. Giannoglou, Y.S. Chatzizsis, K.V. Seralidou, G.E. Parcharidis, G.E. Louridas, Non-Newtonian models for molecular viscosity and wall shear stress in a 3D reconstructed human left coronary artery. Med. Eng. Phys. **30**, 9–19 (2008)
19. J. Vimmr, A. Jonašóvá, O. Bublík, Numerical analysis of non-Newtonian blood flow and wall shear stress in realistic single, double and triple aorto-coronary bypasses. Int. J. Numer. Method Biomed. Eng. **29**, 1057–1081 (2013)
20. L. Formaggia, A. Quarteroni, A. Veneziani, *Cardiovascular Mathematics: Modeling and Simulation of the Circulatory System, Modeling, Simulation and Application* (Springer, 2009)
21. B. Guerciotti, C. Vergara, L. Azzimonti, L. Forzenigo, A. Buora, P. Biondetti, M. Domanin, Computational study of the fluid-dynamics in carotis before and after endarterectomy. J. Biomech. **49**, 26–38 (2016)
22. J. Keegan, P.D. Gatehouse, G.Z. Yang, D.N. Firmin, Spiral phase velocity mapping of left and right coronary artery blood flow: correction for through-plane motion using selective fat-only excitation. J. Magn. Reson. Imaging **20**, 953–960 (2004)
23. H. Sakuma, S. Globits, M. O'Sullivan, A. Shimakawa, M.A. Berstein, T.K.F. Foo, T.M. Amidon, K. Takeda, T. Nakagawa, C.B. Higgins, Breath-hold MR measurements of blood flow velocity in internal mammary arteries and coronary artery bypass grafts. J. Magn. Reson. Im. **1**, 219–222 (1996)
24. X. Meng, Q. Fu, W. Sun, J. Yu, W. Yue, W. Bi, Competitive flow arising from varying degrees of coronary artery stenossi affects the blood flow and the production of nitric oxide and endothelin in the internal mammary artery. Eur. J. Cardio-Thorac. **4**3, 1022–1027 (2013)
25. S. Pagni, J. Storey, J. Ballen, W. Montgomery, B.Y. Chiang, S. Etoch, P.A. Spence, ITA versus SVG: a comparison of instantaneous pressure and flow dynamics during competitive flow. Eur. J. Cardio-Thorac. **11**, 1086–1092 (1997)
26. B. Guerciotti, C. Vergara, S. Ippolito, A. Quarteroni, C. Antona, R. Scrofani. Computational study of the risk of restenosis in coronary bypasses. Med. Eng. Phys. (2017 in press). doi:10.1016/j.medengphy.2017.05.008
27. R.M. Lancellotti, C. Vergara, L. Valdettaro, S. Bose, A. Quarteroni. Large eddy simulations for blood fluid-dynamics in real stenotic carotids. Int. J. Numer. Meth. Biomed. Eng. (2017 in press). doi:10.1002/cnm.2868
28. S. Lee, S. Lee, P. Fischer, H. Bassiouny, F. Loth, Direct numerical simulation of transitional flow in a stenosed carotid bifurcation. J Biomech **41**(11), 2551–2561 (2008)
29. L. Formaggia, J.F. Gerbeau, F. Nobile, A. Quarteroni, Numerical treatment of defective boundary conditions for the Navier-Stokes equation. SIAM J. Numer. Anal. **40**(1), 376–401 (2002)
30. A. Veneziani, C. Vergara, Flow rate defective boundary conditions in haemodynamics simulations. Int. J. Numer. Method Fluid **47**, 803–816 (2005)
31. C. Slager, J. Wentzel, F. Gijsen, J. Schuurbiers, A. van der Wal, A. van der Steen, P. Serruys, The role of shear stress in the generation of rupture-prone vulnerable plaques. Nat. Rev. Cardiol. **2**(9), 401–407 (2005)
32. J. Knight, U. Olgac, S.C. Saur, D. Poulikakos, W.J. Marshall, P.C. Cattin, H. Alkadhi, V. Kurtcuoglu, Choosing the optimal wall shear parameter for the prediction of plaque location—A patient-specific computational study in human right coronary arteries. Atherosclerosis **211**(2), 445–450 (2010)

33. A. Berger, P.A. MacCarthy, U. Siebert, S. Carlier, W. Wijns, G. Heyndrickx, J. Bartunek, H. Vanermen, B.D. Bruyne, Long-term patency of internal mammary artery bypass grafts—Relationship with preoperative severity of the native coronary artery stenosis. Circulation **110**, 36–40 (2004)

Artificial Textile Reinforced Tubular Aortic Heart Valves—Multi-scale Modelling and Experimental Validation

Deepanshu Sodhani, R. Varun Raj, Jaan Simon, Stefanie Reese, Ricardo Moreira, Valentine Gesché, Stefan Jockenhoevel, Petra Mela, Bertram Stier and Scott E. Stapleton

Abstract Tissue engineered valvular implants are in development as living and remodelling prostheses to replace damaged native valves. To improve the mechanical properties of the valve, textile is used as a reinforcing scaffold. To predict the behaviour and optimize the structure of such composites, it is necessary to understand the behaviour of the underlying components. The current study seeks to test a multi-scale approach often used in the field of composites to evaluate the behaviour of knitted textile reinforced elastomeric composites. The complex textile structure is divided into simplified models at different levels/structural units. Virtual experiments are conducted at each of these levels and their responses are fit to appropriate isotropic and anisotropic hyperelastic material models. The simulation responses obtained by conducting virtual experiments on the repeating unit cell (RUC) of the composite are then compared with experimental results, resulting in good agreement. After experimental validation, the multi-scale approach is used to predict the behaviour of artificial heart valves.

D. Sodhani (✉) · R. Varun Raj · J. Simon · S. Reese
Institute of Applied Mechanics, RWTH Aachen University,
Mies-van-der-Rohe-Str. 1, 52074 Aachen, Germany
e-mail: deepanshu.sodhani@rwth-aachen.de

R. Moreira · S. Jockenhoevel · P. Mela
Institute of Applied Medical Engineering, Helmholtz-Institute,
RWTH Aachen University, Pauwelsstr 20, 52074 Aachen, Germany

V. Gesché · S. Jockenhoevel
Institut Für Textiltechnik, RWTH Aachen University,
Otto-Blumenthal-Str. 1, 52074 Aachen, Germany

B. Stier
Hypersizer, 760 Pilot House Dr. Suite A Newport News,
Newport News, VA 23606, USA

S.E. Stapleton
Department of Mechanical Engineering, University of Massachusetts Lowell,
1 University Avenue, Lowell, MA 01854, USA

P. Wriggers and T. Lenarz (eds.), *Biomedical Technology*, Lecture Notes in Applied and Computational Mechanics 84, DOI 10.1007/978-3-319-59548-1_11

1 Introduction

1.1 Motivation

Engineered bio-materials are ubiquitous and have important functions in numerous bio-medical applications which are incentivized by advances in regenerative medicine. One such application of bio-material implants are artificial heart valves where replacement of load-bearing soft tissues has long been the impetus for the development of new materials. To achieve adequate mechanical properties required by such implants to sustain the pressures and flow of the systemic circulation, a three-dimensional textile scaffold is used as reinforcement on which cells can grow, proliferate and form into a functional tissue construct. The optimum scaffold architecture for artificial heart valves is a structure with high degree of interconnectivity (through continuous fibres or interconnected short fibres) allowing for continuous stress flow through the thin heart valve leaflets to the strong aortic wall, protecting the cusps from rupture and still porous enough to allow cellular migration and proliferation. A mismatch between highly deformable native tissue and engineered bio-material can lead to short and long term health impairments. The capability of implants to deform similar to the macroscopic mechanical response of the surrounding biological materials, is often associated with dissimilar micro structural deformation mechanisms. This mismatch on smaller length scales might lead to micro injuries, cell damage, inflammation, fibrosis or necrosis [33]. Hence, the mechanical bio-compatibility of soft implants depends not only on the properties and composition of the implant material, but also on its organization, distribution and motion at one or several length scales. To achieve such a design and mechanical bio-compatibility, modelling strategies need to be developed in order to rationalize experimental observations and predict implant performance.

1.2 Previous Work

A substantial amount of work has been done in the field of cardio-vascular engineering, from experiments to simulation. Cheung et al. [11] reviewed the current progress in tissue engineering of heart valves, looking at different fabricating strategies of tissue engineered heart valves (TEHVs), concluding that a clinically viable product has not yet been realized. Singh et al. [39] reviewed the design aspect of medical textiles (woven, knitted, braided, electro-spun) intended for vascular implant applications, concluding that mechanical properties of biological material such as anisotropy, non-linearity, compliance and visco-elasticity remain widely unconsidered while designing synthetic vascular implants. Mazza and Ehret [33] showed that the mechanical bio-compatibility of scaffolds is not only linked to adequate macroscopic properties (non-linear stress-strain response, ductility, strength) but also to the realization of micro structural deformation mechanisms, in particular, the deforma-

tion field at the cell length scale influences the mechano-transduction and mechano-biological response of the tissue surrounding the implant. Some years back, [43] reviewed the ability of material processing techniques to produce different mechanically sound tissue surrogates and highlighted the unique structural characteristics produced in these materials. Translations of these properties to distinct macroscopic bio-mechanical behaviours were also discussed.

Some of the works in the direction of stress and strain analysis of heart valves under its diastolic and systolic phase are detailed in this paragraph. Stapleton et al. [42] analysed the effect of fibre orientation and volume fraction on the macroscopic stress developed in a tubular three leaflet heart valve in its closed configuration, indicating that a non-uniform fibre distribution using tailored fibre placement could be used to optimize reinforcement design. Argento et al. [2] presented an approach of mechanical characterization of the electro-spun scaffolds for TEHVs, by accounting for the effect of underlying scaffold structure. The derived material properties were then used to simulate the stress and strain in a heart valve when it was closed. De Hart et al. [14] analysed the effects of collagen fibres (distributed short natural fibres) on the mechanics and hemodynamics of a trileaflet aortic valve using a numerical analysis of the systolic phase. It demonstrates that presence of distributed fibres substantially reduce stresses in the leaflets and provide smoother opening and closing while reducing the fluttering motion of the leaflets. Cacciola et al. [8, 9] produced stentless artificial aortic valve prosthesis and analysed different fibre-reinforced structures with respect to the stresses that are likely to contribute to the failure of fibre-reinforced prostheses and compared them with the results obtained for a stented prosthesis. The comparison showed that stress developed in the stentless models were significantly lower than the stented models with the same type of reinforcement. De Heart et al. [13] analysed three-dimensional finite element models for reinforced three-leaflet valve prosthesis for stress reduction. Different fibre reinforcements were investigated and the model responses were analysed for stresses showing that, in peak stress areas of reinforced models, up to 60% of the maximum principle stresses were taken over by fibres and that, in some cases of reinforcement, a more homogeneous stress distribution was obtained.

An experimental protocol along with a set of parameters addressing scaffold stiffness, anisotropy, influence of deformation history and change in properties when embedded in homogeneous matrix was proposed by [32]. They compared the performance of nine mesh types used for pelvic repair, covering a wide range of mechanical responses, comprehensively and extensively characterizing the mechanical biocompatibility of mesh prostheses. Jana et al. [26] compared the advantages and disadvantages of decellularized and fabricated scaffolds for use as TEHVs, concluding that synthetic scaffold-based TEHVs are more suited as an implant because they can be tailored to the requirement. Even though decellularized scaffolds retain the original valve structure and extra-cellular matrix, their low pore size, porosity and cell survivability limit their use for valve engineering. Van Lieshout et al. [48] tested various bio-compatible scaffold heart valves and fibrin under systemic circulation and compared the electro-spun valvular scaffold with knitted valvular scaffold in [49]. It was shown that the knitted textile scaffold lasted longer in the systemic circula-

tion as the electro-spun scaffold tore after a while. Yeoman et al. [54] developed a constitutive model to represent the non-linear warp-weft coupled mechanics by extending a strain energy function for soft tissue to include shear and by increasing the number and order of coefficients, which was validated for uniaxial tension tests. The model was successfully able to predict the macro behaviour of some textiles but fails to capture the micro mechanics and its effects. D'Amore et al. [12] simulated the mesoscopic in-plane mechanical behaviour of elastomeric electro-spun polyurethane membrane where the simulations were developed from experimentally-derived fibre network geometries. Effects on macro-mechanics based on fibre intersections, connectivity, orientation, and diameter were evaluated demonstrating good agreement with the experimental data.

Modelling approaches for different knitted/woven fabrics and their composites have been presented by [1, 27, 29, 31, 38, 51]. But to the knowledge of the authors, literature on multi-scale modelling of knitted textile reinforced elastomeric composites is scarce. Qi et al. [36] presented a repeating unit cell (RUC) based approach to determine the effective stiffness of a multi-layered biaxial weft-knitted fabric reinforced composite. Wan et al. [52] presented a multi-scale approach to analyse the damage behaviour of a multi-axial warp knitted composite. Ugbolue et al. [46] discusses a method to produce auxetic knit structures from non-auxetic yarns and their use as an engineering textile material that becomes wider when stretched and thinner when compressed. In [47], they examined the geometrical model of auxetic warp knitted structures and validated its characteristics with data obtained from experimental analysis.

Apart from geometric modelling, a significant amount of work has been invested in modelling the macroscopic behaviour of biological materials (which have differently oriented short fibres as reinforcement). Much of the works on continuum modelling of isotropic and anisotropic material behaviour has been reviewed in [10]. These materials are known to support large reversible deformations along with exhibiting hysteresis, stress softening or relaxation. A hyperelastic constitutive equation is typically the basis of the model that describes the behaviour of the material. The hyperelastic constitutive equation can be isotropic or anisotropic. Böl et al. [7] used a micro mechanically motivated tetrahedral element developed in [6] to create a predictive model of thin muscular films accounting for the muscle fibres. Auricchio et al. [4] tested the impact of using different material models in a patient-specific finite element analysis able to virtually reproduce stent-less valve implantation, on both the stress pattern and post-operative coaptation area, length and height. Also, physical and non-physical response from a few of these hyperelastic material models have been compared in [16].

In the field of traditional fibre reinforced composites, there has been tremendous development in multi-scale material modelling; investigating the effects of the micro structure on its macroscopic behaviour. Nguyen et al. [35] reviewed the recent developments in multi-scale modelling of continuous and discontinuous modelling of multi-phase heterogeneous materials. Vassiliadis et al. [50] discussed the challenges and solutions/modelling methodologies for woven fabrics at different scales accounting for micro to macro scale deformations. An extended literature review

of the computational models for the deformation of woven fabrics was presented. A review on homogenization and topology optimization of periodic structure was presented by [21]. Some of the recent works in the direction of multi-scale modelling of composites accounting for the micro structural effects are presented in [5, 15, 30, 44, 45].

1.3 Present Work

Even though there exists a considerable body of work in various disciplines like modelling of bio-materials, analysis of scaffolds, analysis of artificial and TEHVs and multi-scale modelling of fibre reinforced composites, there exists a scarcity in the synergistic approach towards the analysis and development of cardio-vascular bio-implants. In this work, a multi-scale method related to the modelling, simulation and analysis of bio-compatible mechanical deformations of knitted scaffold used in the development of tissue engineered tubular heart valve by [34, 53] is illustrated. Simulations are conducted on knitted PET fibre scaffold embedded in a silicone matrix (resulting in a two-phase composite) at various structural levels to predict their mechanical behaviour. Simulated predictions are then compared to the experimental results. Substituting the engineered tissue matrix (consisting of oriented elastin and collagen fibres) with silicone enables us to focus on understanding and predicting the behaviour of the knitted scaffold which is the underlying reinforcing structure. To predict the behaviour of the knitted scaffold embedded in silicone, henceforth referred to as composite, one needs to understand the structural response at different levels. Therefore, the composite used as an artificial heart valve was decomposed into multiple levels as shown in Fig. 1. A multi-scale modelling approach popular in the field of material mechanics is employed. The benefit of this approach is that individual components of the composite can be modelled by means of a simple material model which can be characterized using simple experiments.

This chapter is organized as follows. A brief introduction to the artificial heart valves used in this study is given in the next section. Then the experimental setup

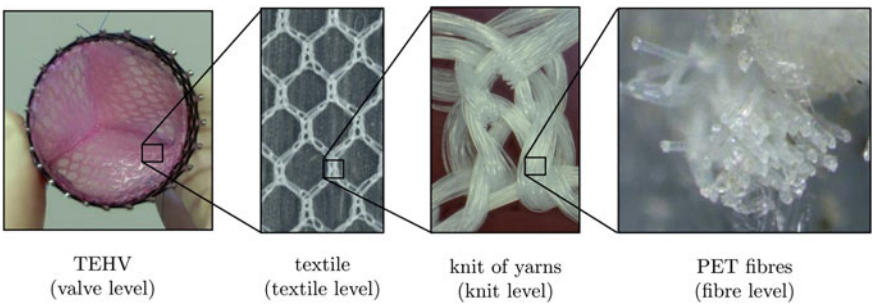

Fig. 1 Multi-scaling of a knitted scaffold embedded into silicone matrix [41]

for the composite is presented. The structural multi-scale levels, along with a small introduction to the modelling approach is provided in Sect. 4. This is followed by a brief overview of the constitutive material models used (Sect. 5). The results are discussed in Sect. 6. The chapter concludes with a summary and an outlook.

2 Bio-Engineered Aortic Heart Valves with a Tubular Leaflet Design

The tube-in-stent valve consists of a tubular tissue engineered fibrin based construct sewn into a stent at three single attachment points and along a circumferential line at the annulus according to the single point attachment commissure technique proposed by [20]. The valves are produced by using fibrin gel as a cell carrier embedding vascular cells isolated from human umbilical cord veins and a tubular warp knitted textile structure as a co-scaffold [34]. Initially, the knitted polyethylene terephthalate (PET) mesh is embedded into the fibrin gel containing the cells. The tubular mesh construct is fixed during the static cultivation for one week after which it is sutured into a self-expandable nitinol stent. First the construct is sewn at the three single points to form the commissure points and then circumferentially to define the annulus (Fig. 2).

After static conditioning, the TEHVs are conditioned for 14 days in a custom-made bioreactor positioned in an incubator. With the use of actuators and membranes, the bioreactor is able to create a flow to open and close the valve. At the end of the in vitro conditioning phase, the valve is tested under aortic flow and pressure conditions according to ISO 5840-3 i.e., cardiac output of 5 L/min, 100 mmHg mean aortic pressure and 70 bpm (beats per minute) frequency. The pressures are measured by pressure transducers positioned immediately upstream and downstream from the valves. The instantaneous flow is measured by a flow meter positioned upstream from the valves. Pressure and flow values are recorded by a LabVIEW™ application.

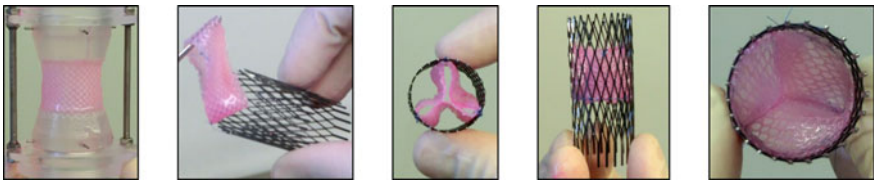

Fig. 2 Fabrication of the tube-in-stent valve. From *left* to *right*: tubular construct after one week of static cultivation still fixed at the silicone connectors, after release from the silicone connectors and placed into the stent, after suturing at the three commissure points and at the base of the tubular construct circumferentially (annulus), *top* view of tube-in-stent valve [34]

3 Experiments

Uniaxial tensile tests were conducted on the composite samples (knitted textile scaffold embedded in silicone matrix), results from which were used to validate the proposed modelling and simulation approach. Once the proposed approach was validated, it was used to predict the behaviour of an artificial heart valve which uses the same scaffold as reinforcement. As mentioned earlier, engineered tissue was substituted with silicone to focus on modelling and predicting the behaviour of the knitted scaffold, which is the underlying reinforcing structure.

The test setup, which includes a Zwick Z005 testing machine along with all the specimens are shown in Fig. 3. Force and global displacements were measured and recorded. The load cell signals were recorded using the control software TestXpert II. Time, force, cross head displacement and nominal strain were measured. The kinematic quantities were captured at the specimen in real time, providing global strain values. The results from the experiments are discussed in Sect. 6.

The textile mesh was produced using medical grade polyethylene terephthalate (PET) fibres. For the production, a tüll-fillet pattern, a needle gauge of E30 (i.e. 30 needles per inch) and a course density of 15 loops/cm were chosen. 52 PET yarns were processed into a tubular structure which was thermo-stabilized at 200 °C for 8 min before use. The textile mesh was then embedded into a medical grade silicone

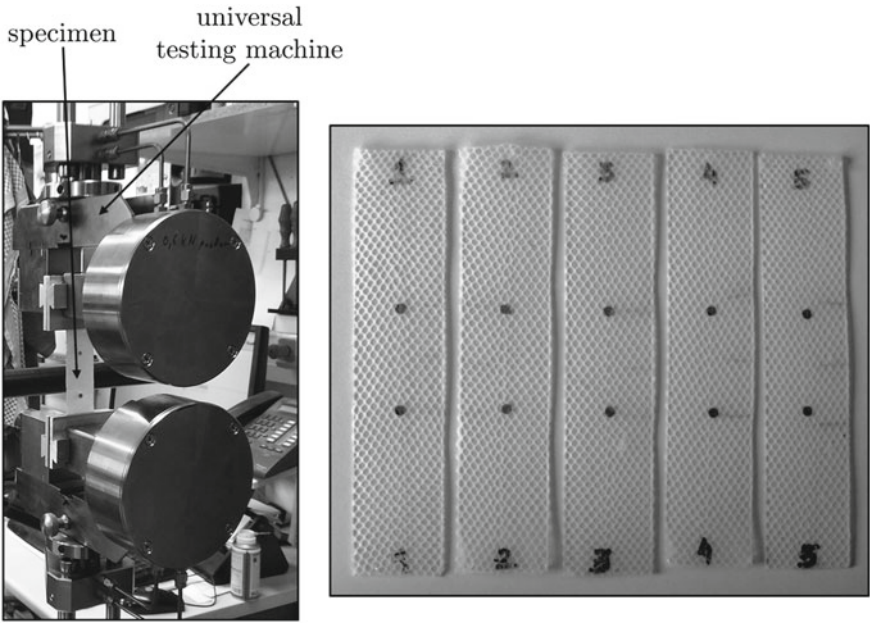

Fig. 3 Experimental setup; Zwick Z005 machine with clamped experimental sample (*left*), experimental samples with marked positions for measuring displacements (*right*)

Table 1 Dimensions of the specimen

Parameter	Value (mm)
Length (l)	120.00
Measuring length (l_m)	≈29
Width (w)	25.67 ± 0.28
Thickness (t)	1.245 ± 0.05

matrix and cured for around two hours. The final specimens are shown in Fig. 3 and the dimension of the produced specimens are provided in Table 1. Nominal strain was measured using an optical extensometer and two points.

Volume fraction of PET fibres in the samples were derived by considering the density of the PET fibres and its mass over a given area. Density of the PET fibres is 1.38 g/cm^3. The mass m of the textile mesh over an area of $A = 551.25$ mm^2 ($l = 17.5$ mm, $b = 31.5$ mm) was found to be 0.025 g. Hence, using $\phi = V_{textile}/V_{total} = (m/A)/(t\rho)$ the volume fraction of the composite for the same area A was determined to be approximately 2.564%.

4 Finite Element Simulations

All the finite element (FE) models were created using the commercial software Abaqus [22]. The elements used were C3D4 (linear tetrahedral) and C3D8R (eight-noded brick elements with reduced integration and enhanced hourglass stiffness) depending on the structural model in consideration. All the structural models were simulated using the implicit (standard) solver of Abaqus except the macroscopic heart valve model, which was simulated using the explicit solver.

4.1 Multi-scale Modelling

The multi-scale modelling approach has been divided into two cases, Case L and Case U. Case L is used to predict the tensile behaviour of the embedded textile scaffold for experimental validation of the approach, after which Case U is used to simulate and predict the behaviour of the heart valve composite subjected to the pressures of the cardiac cycle (i.e. fatigue loading). Apart from the geometric modelling, a principle difference between the two schemes is the material properties used for the elastomeric silicone matrix. It is well known that elastomeric matrix including biological tissues has a hysteresis when subjected to cyclic loading i.e. they show Mullins' effect (see Fig. 11). Therefore, the matrix properties were divided into loading and unloading sections. In Case L, the properties of the loading section are used because the experimental sample is only subjected to monotonic tensile loading. The properties of the unloading section are used for Case U because after the first few

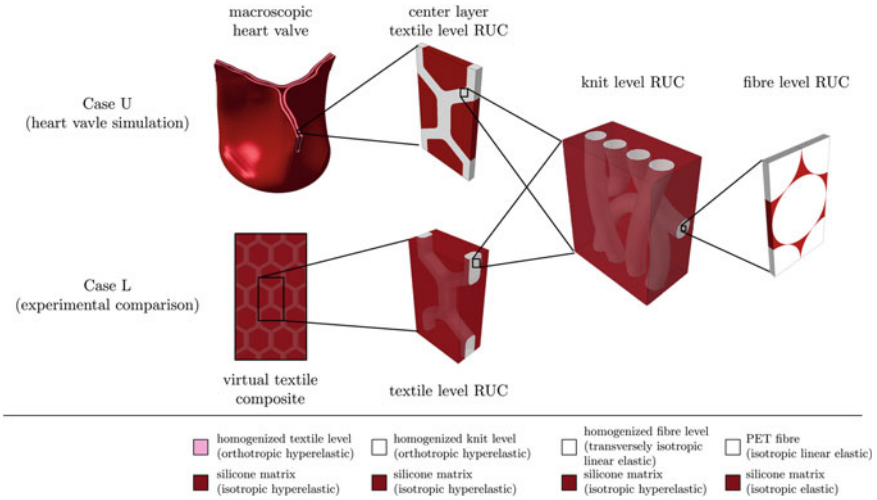

Fig. 4 Hierarchical multi-scaling of the textile reinforced silicone samples is divided into Case L (for experimental comparison) and Case U (for simulating the behaviour of the heart valve composite). The type of material models used to represent the components are also mentioned

cardiac cycles the virgin matrix softens and behaves elastically along the unloading path until the previous maximum deformation has been reached. Also, sine the heart valve will be simulated for the same maximum pressure difference, it is assumed that the maximum stretch reached by the matrix in the first cycle will not be exceeded in the consecutive cycles. The internal structure of the heart valve composite was simplified and divided into three levels for Case L and four levels for Case U. The schematic representation of the different levels used in multi-scale modelling of the heart valve composite is shown in Fig. 4.

The modelling approach of repeating unit cells (RUC) presented in [21] was implemented at the textile, knit and fibre levels. Virtual experiments were conducted at a lower level RUC by applying far-field strains. Volume averaging over the computed stress distribution within the RUC was carried out to determine the effective material response, which were then fitted by a material model to determine the material parameters for the upper level model. The same procedure was repeated until all the levels under investigation were accounted for. This approach is often referred to as hierarchical multi-scaling in the literature (for example see [5]). Displacement based 3D periodic boundary conditions (PBCs) as explained by [5] were used and modified to apply in-plane periodicity to predict the effective material response for different multi-scale levels. Material models used at different levels are shown in Fig. 4 and briefly discussed in Sect. 5.

An important aspect of hierarchical multi-scaling is to maintain the desired volume fraction of reinforcing fibres at the highest level, i.e. the volume fraction of the fibres at the textile level for Case L has to be $\approx$2.564% and at the macro-level heart valve model for Case U has to be $\approx$4.69%. To achieve this, the volume frac-

Table 2 Dimensions of the RUCs

Dimension	Fibre level RUC (μm)	Knit level RUC (mm)	Textile level RUC (mm)
Length	17.065	1.342	2.380
Width/diameter	29.557	1.647	4.122
Thickness	1.706	0.700	1.245

tion of different underlying models has to be chosen such that there is a trade off between reality and modelling convenience. Volume fraction of the textile structure for Case L and Case U, also referred to as homogenized knit level at the textile level was 15% and 36.61% respectively, which was modelled using the dimensions of the specimen measured under a microscope (see Sect. 4.5). In Case L, this implies that the volume fraction of the knit and the fibre levels have to be adjusted such that the overall volume fraction is achieved. For the ease of modelling the knit level RUC, the volume fraction of fibres at the fibre level was assumed to be 90%. This means that at the knit level, the yarns (also referred to as homogenized fibre level) needed to have a volume fraction of ≈19%. Hence, considering the volume fraction of the fibres at fibre level, yarns at the knit level and textile structure at the textile level, the overall volume fraction of the fibres in the composite was achieved to be 2.565% (= 90% × 19% × 15%). Similarly, in Case U the macro scale heart valve model was divided into three layers, where the centre layer was used to represent the textile scaffold. This layer forms 70% of the heart valve (see Sect. 4.6), resulting into the over all fibre volume fraction of 4.38% (= 90% × 19% × 36.61% × 70%).

It can be observed from the mentioned dimensions that there does not exist a scale separation between the knit level and the textile level RUC. The complexity of modelling the textile structure using intricately knitted textile patterns motivated the use of a volume averaged homogenization approach to capture the effective response of a knit. The material parameters obtained by fitting an appropriate material model to the effective response were then used for the textile structure in the textile level RUC (Table 2).

4.2 Fibre Level Structural Model

The fibre level model was used to evaluate the material parameters of the yarn. 24 PET fibres with a diameter of 17 μm were assumed to be tightly bundled together in a yarn. Although the number of fibres is probably not large enough to ignore the edge effects, the tow was idealized using a hexagonal dense packing (HDP) RUC considering the assumption of a periodic composite. As a result, yarns have a high fibre volume fraction which means that the fibre distribution does not play a role in it's effective response. The boundary effects on the peripheral fibres are assumed

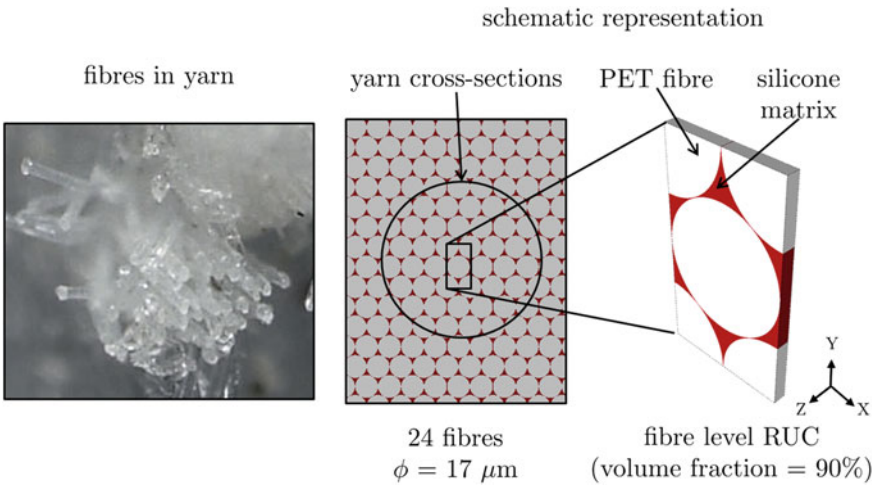

Fig. 5 Fibre level structural model [41]

to be restricted by modelling the yarn in the knit level model using a circular cross-section, with a volume fraction of 90%. Therefore, the HDP RUC was modelled with a volume fraction of 90% as shown in Fig. 5. The individual material response of the fibres and the matrix was captured using a linear elastic material model because a far field strain of only 1% is applied on the RUC. The homogenized material response from this level was used to represent the yarn in the knit level.

4.3 Knit Level Structural Model

Figure 6 shows a close-up of the textile where one of many interlocking yarn loops (knit) in the textile is visible. Modelling such a complex knit pattern is computationally challenging and expensive. Even though the knitted textile has a repetitive pattern, it is difficult to identify a consistent path along which the yarns are knit. Hence, it was found necessary to simplify the knit for computationally efficient modelling. The simplified knit pattern has to account for the continuous load transfer within the yarns from one knit to other along with the locking of yarn alignment in the loading direction due to the looping structure of the knit. Therefore, in this work, the complex knits was approximated by a simplified knit pattern with a volume fraction of 19% as shown in Fig. 6. The yarns were modelled using transversely isotropic elasticity. Material orientations are assigned to the yarns and the material properties are obtained from the homogenized response of the fibre level. The matrix was modelled as an incompressible hyperelastic material. The homogenized material response from this level was then used to represent the homogenized knit in the textile level RUCs.

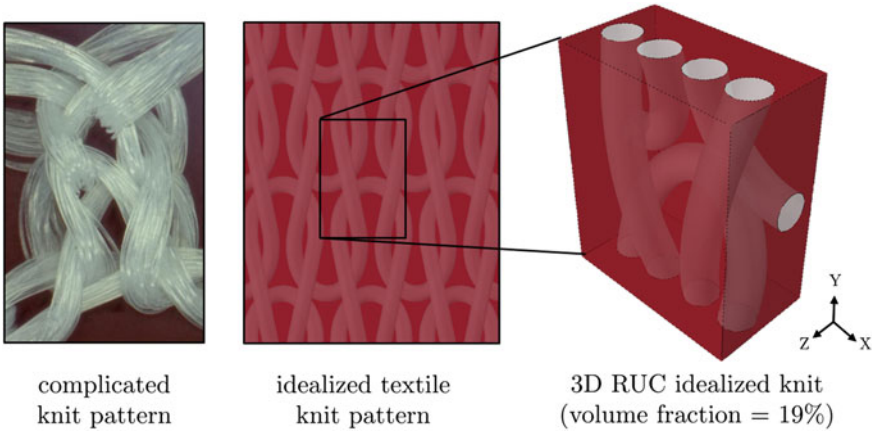

Fig. 6 Knit level structural model [41]

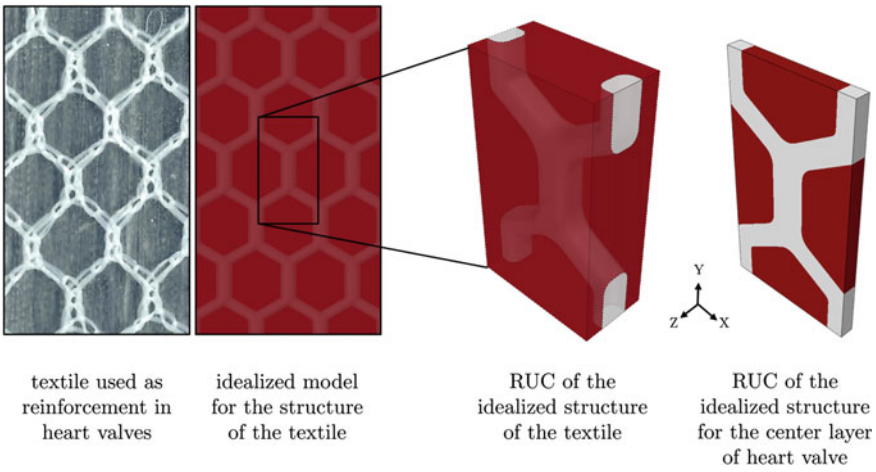

Fig. 7 Textile level structural model

4.4 Textile Level Structural Model

Figure 7 shows the textile pattern and the RUCs used to model it, with the homogenized knit volume fraction of 15% and 36.61% for Case L and Case U, respectively. These RUCs are periodic only in the XY plane. Orthotropic Fung's hyperelastic material model was used to represent the homogenized knit domain in these RUCs, and the matrix was modelled as an incompressible hyperelastic material. As mentioned earlier, there does not exist a scale transition between the knit level RUC and the textile level RUCs, but because the effective knit level response was averaged over the volume, it can be used to represent the homogenized knit domain. The

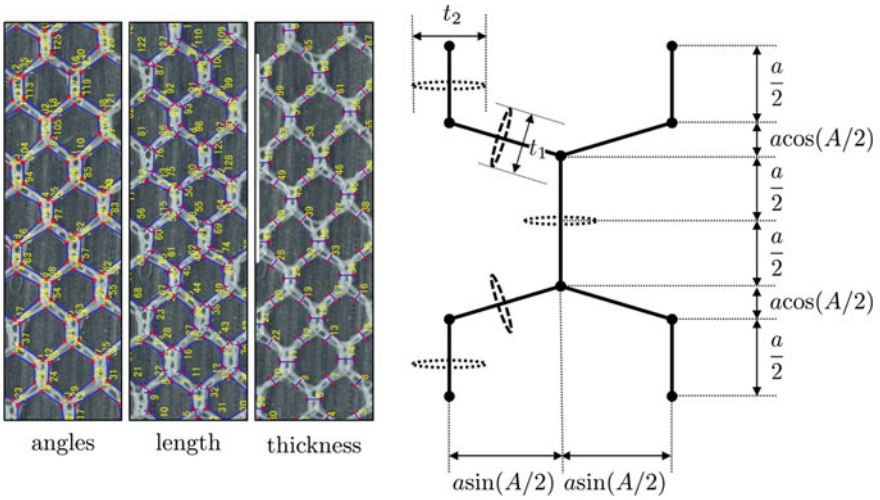

Fig. 8 Microscopic measurements of angle, length and thickness of the textile within the specimen and wire frame model of the textile structure at the textile level RUC

Table 3 Structural parameters for defining the textile structure

Dimension	Values
Edge length (a)	1.3560 mm
Thinner section (t_1)	0.4133 mm
Thicker section (t_2)	0.6008 mm
Angle (A)	120°

orthotropy was ensured using local orientations. These RUCs were then subjected to virtual experiments and the results were compared to the experimental results.

The homogenized knit domain in the textile level RUCs were modelled such that it forms a spatial envelope of the textile region within the composite. A rectangular cross-section with filleted edges was used to represent this domain in the textile level RUCs. Dimensions of this domain was measured from microscopic images of the silicone textile composite (Fig. 8). Mean value of the measured quantities; edge length (a), thickness of thinner section (t_1), thickness of thicker section (t_2) and angle distribution (A) are given in Table 3. Using these dimensions, a 2D wire-frame of the honeycomb fibre domain was constructed (Fig. 8), which was later extruded and filleted to obtain the desired geometries for both the RUCs. From the measurements, it was observed that the thickness of the textile region in the embedded textile scaffold composite (homogenized knit domain) was ≈1/3 of the composite thickness. Hence, as the RUC for Case L was modelled to have the same thickness as the composite and the homogenized knit domain was restricted to 1/3 of the RUC thickness. For Case U, the homogenized knit domain was modelled through the thickness because in the macro scale heart valve model, the textile scaffold region is sandwiched between two matrix layers.

4.5 Virtual Textile Composite

The textile level RUC was generated with an assumption that there are no boundary effects even though the specimen under consideration is of finite width considering the length scales at different levels. This assumption works reasonably well for composites undergoing small deformations with varying length scales, but the same cannot be stated for soft composites undergoing large deformations. Hence, a virtual textile composite that mimics the experimental sample as shown in Fig. 9 was generated with the intention to compare the effective response of the RUC with the full specimen simulation. Only a quarter of the entire sample was modelled and symmetric boundary conditions shown in Fig. 9 were applied (Table 4).

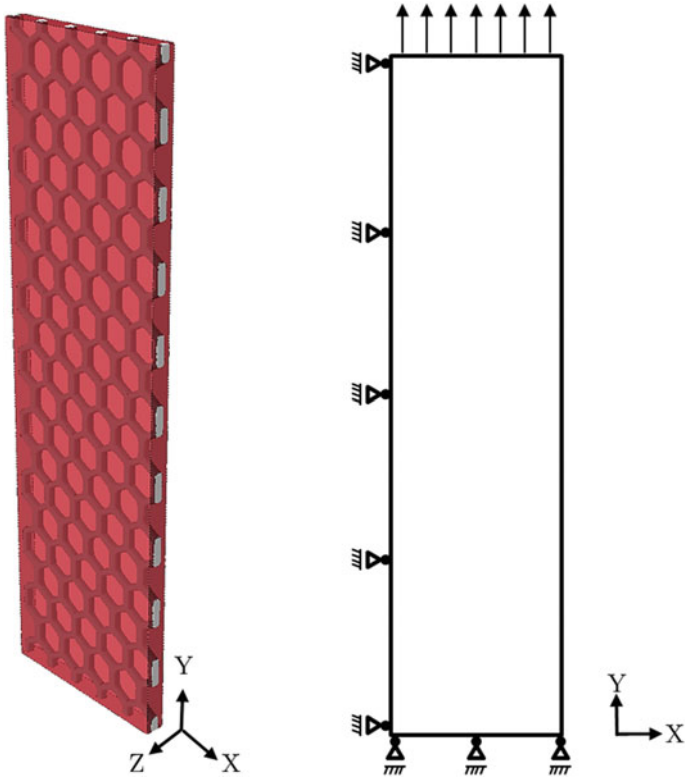

Fig. 9 Virtual textile composite and the boundary conditions applied on it

Table 4 Dimensions of the virtual textile sample

Dimension	Values (mm)
Length	41.22
Width	9.58
Thickness	1.254

4.6 Macro Level Heart Valve Model

Figure 10 shows the macro level heart valve model. The macro model of the heart valve is divided into three layers along the thickness. The centre layer is where the textile scaffold is present. This layer is modelled by the Fung's orthotropic hyperelastic material model, with material parameters obtained by fitting the Fung's model to the virtual experiments conducted at the textile level model in Case U. The outer and the inner layers are considered to be pure matrix (silicone or engineered tissue) layers and are modelled using the isotropic hyperelastic (Arruda Boyce) material model. The material properties for the matrix are obtained by fitting the Arruda Boyce model to the unloading part of the experimental results conducted on Elastosil samples. The macro heart valve level is now subjected to the loading of three cardiac cycles and compared to experimental results.

The simulations in the paper are based on the tubular valve construct as shown in Fig. 10 (see also [42]). The tubular construct is 18 mm long, has an outer diameter of 23 mm with a thickness of 0.7 mm. An initial simulation was carried out on the tubular construct to achieve the geometry of the sutured heart valve. The deformed geometry was then extracted from the output file to obtain a stress free initial sutured configuration. Aortic and ventricular surface pressures were applied to simulate the cardiac cycle while keeping the suture points and the base of the heart valve fixed. The boundary conditions are summarized in Fig. 10. Details about the aortic and the ventricular pressure applied as a periodic change in amplitude within Abaqus [22] are given in [41].

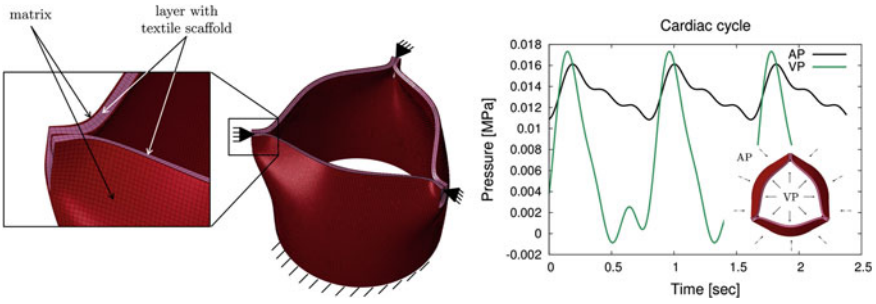

Fig. 10 Macro scale heart valve level; initial sutured configuration along with boundary conditions and pressure loads (AP: aortic pressure; VP: ventricular pressure)

5 Material Models

Four different material models were used across the different levels. The fibres were modelled as linear elastic and isotropic whereas an isotropic hyperelastic material model was applied for the matrix. The yarns were assumed to behave transversely isotropically as well as linear elastically. To fit the response at the knit and the textile levels, Fung's orthotropic hyperelastic material model [18] which is already implemented in Abaqus was used. Various other orthotropic/anisotropic hyperelastic material models such as the ones suggested by [17, 19, 23, 24, 37] could also be used to represent orthotropic/anisotropic material response. But, as the focus of this work was more on the methodology rather than material modelling, implementing any one of these models was outside the scope of this work.

5.1 Transversely Isotropic Material Model

The material properties of the yarn, used in the knit level RUC, are modelled using a transversely isotropic material law. Transverse isotropy is a special case of orthotropy, where the material has the same properties in one plane and different properties in the direction normal to this plane. These materials can be described by five independent elastic constants. By convention, the five elastic constants in transversely isotropic constitutive equations are the Young's modulus and Poisson's ratio in the symmetry plane, E_p and ν_p, the Young's modulus and Poisson's ratio in the normal direction, E_n and ν_{np}, and the shear modulus μ_{np}. Considering the out of plane direction to be the z-direction, the compliance matrix takes the form

$$\begin{bmatrix} \epsilon_{xx} \\ \epsilon_{yy} \\ \epsilon_{zz} \\ 2\epsilon_{yz} \\ 2\epsilon_{zx} \\ 2\epsilon_{xy} \end{bmatrix} = \begin{bmatrix} \frac{1}{E_p} & -\frac{\nu_p}{E_p} & -\frac{\nu_{np}}{E_n} & 0 & 0 & 0 \\ -\frac{\nu_p}{E_p} & \frac{1}{E_p} & -\frac{\nu_{np}}{E_n} & 0 & 0 & 0 \\ -\frac{\nu_{pn}}{E_p} & -\frac{\nu_{pn}}{E_p} & \frac{1}{E_n} & 0 & 0 & 0 \\ 0 & 0 & 0 & \frac{1}{\mu_{np}} & 0 & 0 \\ 0 & 0 & 0 & 0 & \frac{1}{\mu_{np}} & 0 \\ 0 & 0 & 0 & 0 & 0 & \frac{2(1+\nu_p)}{E_p} \end{bmatrix} \begin{bmatrix} \sigma_{xx} \\ \sigma_{yy} \\ \sigma_{zz} \\ \sigma_{yz} \\ \sigma_{zx} \\ \sigma_{xy} \end{bmatrix} \tag{1}$$

in Voigt notation.

5.2 Arruda Boyce Material Model

Elastosil silicone matrix material is modelled across all scales/levels (except the fibre level) using the Arruda Boyce model [3] which is an isotropic hyperelastic constitutive model used to describe the mechanical behaviour of rubber-like and other

polymeric substances. This model is based on the statistical mechanics of a material with a cubic repeating unit cell containing eight chains along the diagonal directions. The material is assumed to be incompressible. The strain energy density function for the incompressible [3] model is given by

$$W = Nk_B\theta\sqrt{n}\left[\beta\lambda_{\text{chain}} - \sqrt{n}\ln\left(\frac{\sinh\beta}{\beta}\right)\right] \tag{2}$$

where n is the number of chain segments, k_B is the Boltzmann's constant, θ is the temperature in Kelvin and N is the number of chains/density of chains in the network of cross-linked polymers.

$$\lambda_{\text{chain}} = \sqrt{\frac{I_1}{3}}\ ;\ \ \beta = \mathscr{L}^{-1}\left(\frac{\lambda_{\text{chain}}}{\sqrt{n}}\right)\ ;\ \ \mu_{ab} = Nk_B\theta \tag{3}$$

λ_{chain} represents the stretch of a chain. I_1 is the first invariant of the right Cauchy-Green deformation tensor, and $\mathscr{L}^{-1}$ is the inverse Langevin function. μ_{ab} is the shear modulus obtained by fitting the experimental results.

5.3 *Fung's Orthotropic Material Model*

The generalized Fung strain energy potential in Abaqus is based on the two-dimensional exponential form proposed by [18], which was suitably generalized to arbitrary three-dimensional states using [25]. It has the form

$$W = \frac{c}{2}(e^Q - 1) + \frac{K}{2}\left(\frac{(J^2) - 1}{2} - \ln J\right) \tag{4}$$

where c is the shear modulus, K is the bulk modulus, J is the change in volume and with Q being defined by

$$Q = \mathbf{E} : \mathbb{B} : \mathbf{E} \tag{5}$$

$\mathbb{B}$ is a dimensionless symmetric fourth-order tensor of anisotropic material constants and $\mathbf{E}$ represents the Green-Lagrange strain tensor. The orthotropic form of the generalized Fung model with eleven independent variables is used in this work. The Voigt notation of the $\mathbb{B}$ matrix is given by

$$\hat{\mathbf{B}} = \begin{bmatrix} b_1 & b_7 & b_8 & 0 & 0 & 0 \\ b_7 & b_2 & b_9 & 0 & 0 & 0 \\ b_8 & b_9 & b_3 & 0 & 0 & 0 \\ 0 & 0 & 0 & b_4 & 0 & 0 \\ 0 & 0 & 0 & 0 & b_5 & 0 \\ 0 & 0 & 0 & 0 & 0 & b_6 \end{bmatrix} \tag{6}$$

It is well known in literature that parameter fitting of the Fung model largely depends on the choice of the initial values. Hence, care has been taken to choose the initial values reasonably while fitting this model to the virtual experiments at different levels.

6 Results and Discussions

6.1 Characterization to Experimental Results

In this section we characterize the two phases of the soft composite. Silicone matrix was characterized with experiments conducted in house using linear elasticity for small deformations and with Arruda Boyce model for large deformations. PET fibres were characterized using the experimental data obtained from literature for a single fibre tensile test. The experimental results obtained from the uniaxial tension tests conducted in house on the soft composite were used for validating the modelling and simulation approach presented in this paper.

6.1.1 Silicone Matrix

The silicone matrix is characterized using tensile tests. The specimens had a gauge length of 31.28 mm, a width of 6.35 mm, and a nominal thickness of around 1.15 mm. The specimens were preloaded with 0.5 N, and stretched at 3 mm/min until failure. The engineering stress versus stretch is plotted in Fig. 11. As can be seen from Fig. 11a, silicone has a hyperelastic material response, which undergoes softening under cyclic loading representing the Mullins' effect. As the composite is subjected to monotonic uniaxial tensile loading, the silicone matrix is characterized only by the loading curve of both cycles. For the fibre level model, silicone matrix is characterized using linear elasticity (Fig. 11b) where the elastic constant E is found to be 1.1495 MPa, and for all the other scales, the matrix is characterized by the Arruda Boyce model where the constants μ_{ab} and n are found to be 0.2665 MPa and 1.2856 respectively. The heart valve is subjected to cyclic fatigue loading, therefore the silicone matrix is characterized only by the unloading curve of the last cycle. For the fibre level model, silicone matrix is characterized using linear elasticity (Fig. 11d) where the elastic constant E is found to be 0.7323 MPa, and for all the other scales, the matrix is characterized by the Arruda Boyce model where the constants μ_{ab} and n are found to be 0.0862 MPa and 1.0600 respectively. Silicone is modelled as nearly incompressible.

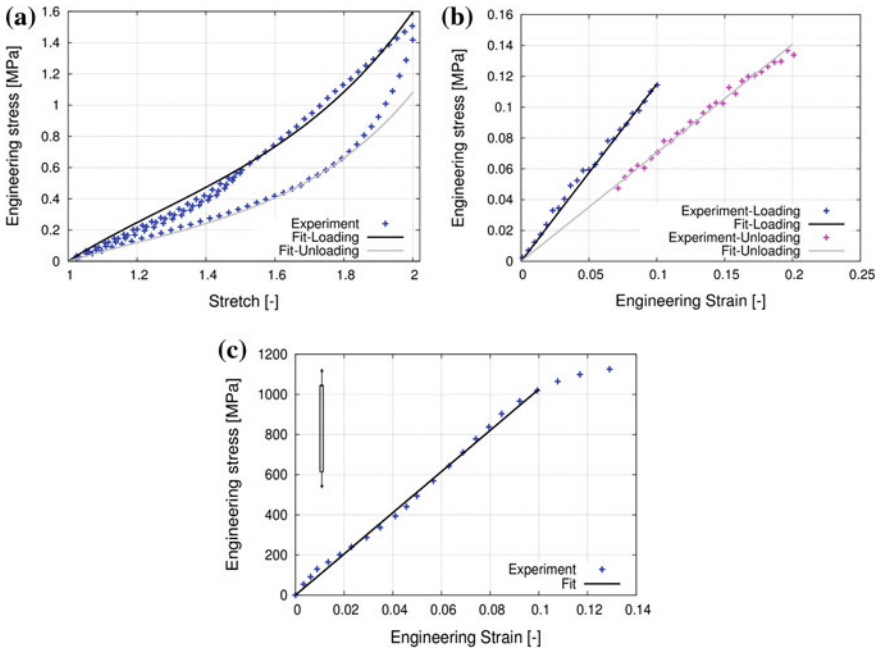

Fig. 11 Experimental data used for elastic fit of material models **a** silicone with Arruda Boyce model; **b** silicone for strain less than 10% with linear elasticity; **c** PET fibres [28] for strains less than 10% with linear elasticity

6.1.2 PET Fibres

The PET fibre material parameters were obtained by using experimental data from [28] as shown in Fig. 11c. This stress vs strain curve is from a tensile test on a single PET fibre. Since plasticity is not included in the present model, part of the curve before it becomes plastic can be approximated with linear elasticity where $E = 10.259\,\text{GPa}$ was found and $\nu = 0.35$ was assumed.

6.2 Numerical Results

In the sections below, results obtained from virtual experiments carried out to predict the effective behaviour at each structural level model are discussed. The effective response obtained were fitted with an appropriate material model to be used for carrying out virtual experiments at the higher level model. The results from the knit level structural model was used in both the textile level structural model and the virtual composite model, results from which are used for validation of the presented approach with experimental results. The results obtained were fitted using

Table 5 Parameters obtained by homogenizing the fibre level model

Parameters	Case L	Case U
E_p (MPa)	521.57	346.43
E_n (MPa)	9233.09	9233.01
μ_{np} (MPa)	21.47	13.72
μ_p (MPa)	183.49	122.33
ν_p	0.422	0.417
ν_{np}	0.020	0.013

a Monte Carlo multi-curve fitting algorithm. First the tensile tests were used to fit the corresponding parameters. Keeping the obtained parameters fixed, the remaining parameters were fitted to the shear response.

6.2.1 Fibre Level Structural Model

The material response of the yarn was derived from the homogenized response of the fibre level RUC. A far-field strain of 1% was applied to the RUC in three uniaxial strain and three shear deformation modes in order to fully populate the elasticity tensor (see [40]). The material parameters obtained are given in Table 5.

6.2.2 Knit Level Structural Model

To characterize the material response of the knit level model, virtual tensile and pure shear tests were carried out at the knit level RUC for a far field strain of 25% while applying periodic boundary conditions in all the three directions. The material response obtained was then fitted with the orthotropic hyperelastic Fung's model. The effective material response and the material fit are as shown in Figs. 12 and 13. c and K along with nine independent parameters constituting the $\hat{\mathbf{B}}$ matrix are given in Table 6.

6.2.3 Textile Level Structural Model

The material parameters obtained from the knit level model for Case L were then used to represent the textile structure in the textile level RUC of Case L. The RUC was subjected to a far field tensile strain of 75% and pure shear strain of 37.5% while applying the periodic boundary condition only in the XY and XZ plane. The material was free to deform in the YX plane because the RUC has been modelled with the same thickness as that of the specimen. The effective response obtained by subjecting this RUC to displacements in the Y direction were also used for comparison with the experimental results. This is discussed in Sect. 6.3.

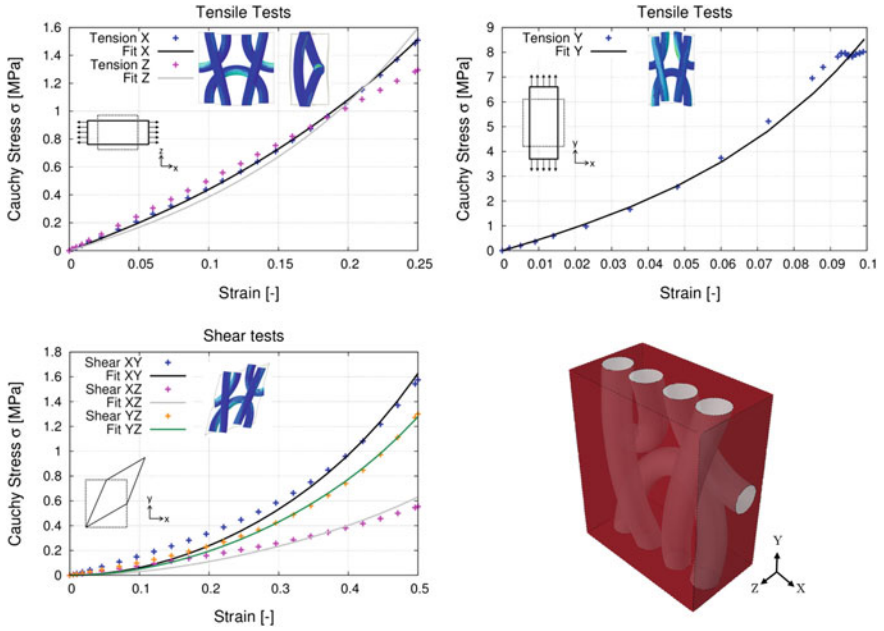

Fig. 12 Results and fit from virtual experiments at the knit level for Case L

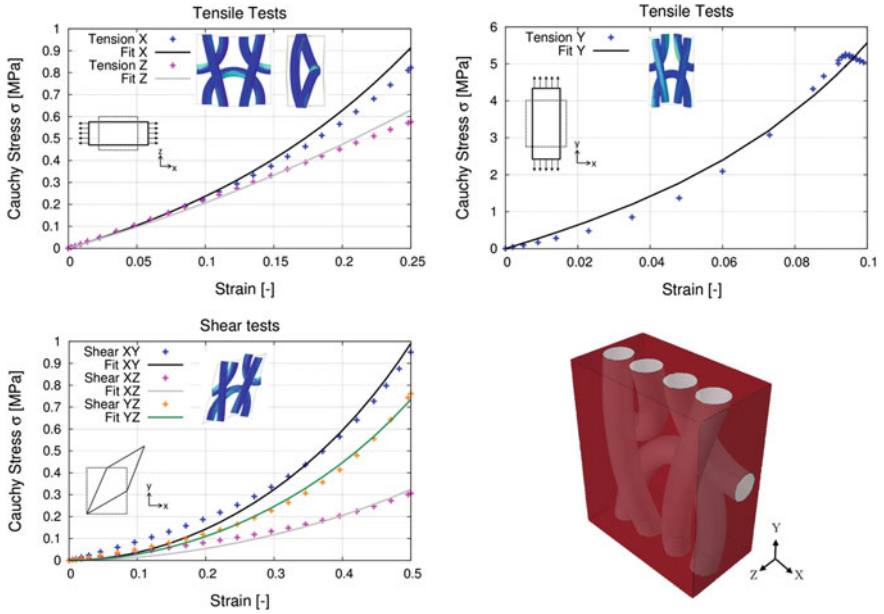

Fig. 13 Results and fit from virtual experiments at the knit level for Case U

Table 6 Parameters obtained by fitting the Fung's material model to virtual experiments conducted at the knit and the textile level models

Parameters	Case L		Case U	
	Knit level model	Textile level model	Knit level model	Textile level model
c (MPa)	1.241	3.580	1.008	1.1635
K (MPa)	11.6212	12.0	4.163	2.00
b_1	2.683	0.449	1.939	1.1957
b_2	38.792	0.480	33.412	1.2917
b_3	1.959	0.32	0.779	0.6059
b_4	20.524	4.50	14.649	12.5
b_5	10.463	4.50	6.039	12.5
b_6	17.088	4.50	11.409	12.5
b_7	2.498	0.0062	2.591	0.0828
b_8	0.570	0.2726	0.229	0.1396
b_9	1.501	0.0062	1.319	0.1493

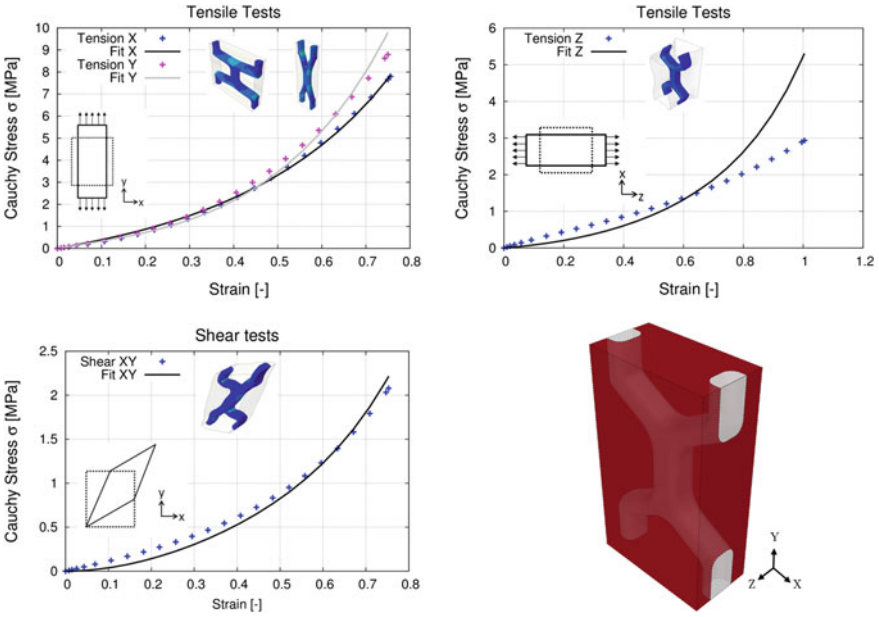

Fig. 14 Results and fit from virtual experiments at the textile level for Case L

The effective material response obtained were then fit with the Fung orthotropic hyperelastic model. Shear test was carried out only in the XY plane to obtain the b_4 parameter. Parameters b_5 and b_6 were assumed to be the same as b_4. The effective

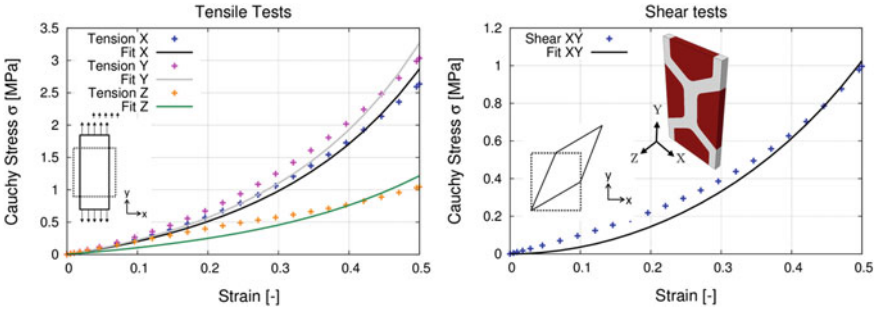

Fig. 15 Results and fit from virtual experiments at the textile level for Case U

material response and the material fit are as shown in Fig. 14. c and K along with nine independent parameters constituting the $\hat{\mathbf{B}}$ matrix are given in Table 6.

Similarly, material parameters obtained from the knit level model for Case U were then used to represent the textile structure in the textile level RUC of Case U. The RUC was subjected to a far field tensile strain of 50% and pure shear strain of 25% while applying the periodic boundary condition in all directions. The effective material response obtained were then fit with the Fung orthotropic hyperelastic model which was used to model the centre textile scaffold layer in the macro scale heart valve is shown in Fig. 15. c and K along with nine independent parameters constituting the $\hat{\mathbf{B}}$ matrix are given in Table 6.

6.2.4 Virtual Textile Composite

The material parameters obtained from the knit level model was also used to represent the textile structure in the virtual textile composite, which was then subjected to a global displacement of 75%. From the strain contour plots in Fig. 16, it can be observed that the strains localize in the pure silicone matrix pockets. For a global strain of 50% the matrix strains is around 60%. The localization is not very high because of the low fibre volume fraction in the composite. One can also observe a prominent Poisson's effect, i.e. there is a proportional decrease in the lateral measurement to the proportional increase in length of the virtual textile specimen.

The effective response obtained by subjecting the virtual textile composite to displacements in the Y direction are also used for comparison with the experimental results and with the results of the textile level RUC. This is discussed in Sect. 6.3.

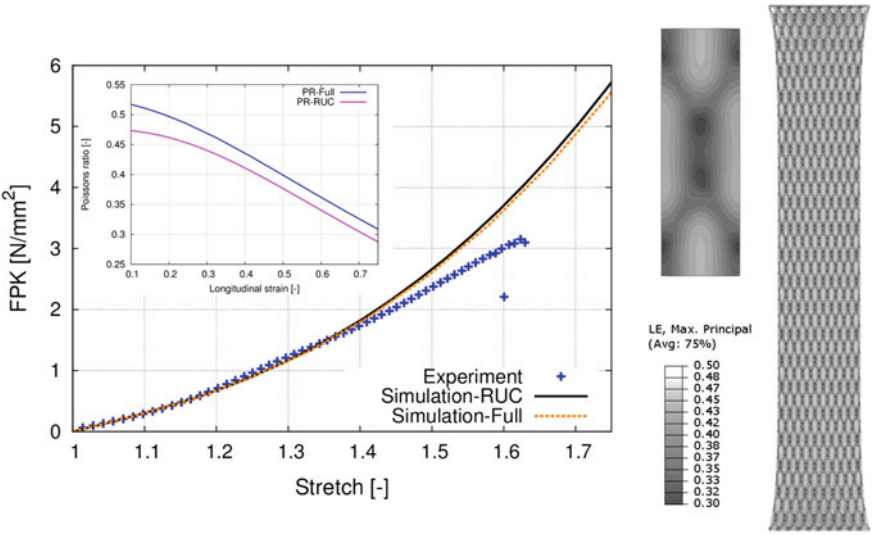

Fig. 16 Experimental and simulation comparison for the textile reinforced silicone: engineering (First Piola Kirchoff) stress versus stretch; contour plots of strain distribution in the textile level RUC and virtual textile composite; (inset) change in Poisson's ratio over longitudinal strain

6.3 Experimental Validation and Comparison

The material response of the textile level RUC and the virtual textile composite are in good agreement with the experimental results until a global strain of 40%. It then diverges as shown in Fig. 16. The good agreement of the stress-strain response at relatively low strains can be attributed to accurate capture of the scaffolding structure and the overall volume fraction of the scaffold in the composite. The divergence of the simulation which results into a stiffer response can be attributed to a couple of reasons; (i) matrix damage leading to localized damage, delamination (similar to [32]) and void formation resulting in matrix softening has not been considered and (ii) idealization of the underlying knit pattern does not accurately capture the mechanics of the knitted textile at large deformations.

The inset compares the change in lateral contraction with respect to axial stretch (i.e. Poisson's ratio) of the virtual samples. Even though the change in Poisson's ratio is qualitatively and quantitatively similar, there exists an offset, suggesting that the boundary effects under tension are not accurately captured by the RUC as expected. But as the heart valve undergoes large bending deformation and relatively small stretches, we consider the results obtained from the virtual experiments of the RUC for further computations. This is also a trade off between numerical accuracy and computation effort.

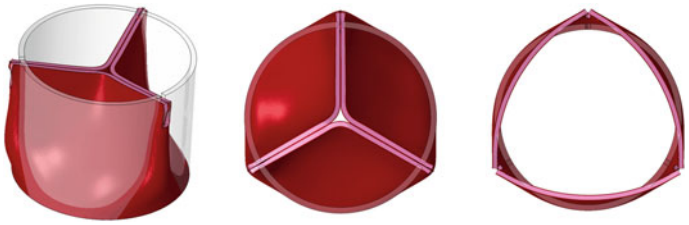

Fig. 17 Deformed and undeformed configuration in the iso-geometric view and *top* view

6.4 Heart Valve Model

After validation of the proposed multi-scale approach, it was used to predict the opening and closing behaviour of the macroscopic heart valve model (Fig. 10). As mentioned earlier, the heart valve model was divided into three layers. The center layer is the textile scaffold layer, whereas the inner and outer layers are pure matrix. The matrix layer was modelled using the Arruda Boyce material model, parameters for which are provided in Sect. 6.1.1. The center layer was modelled using the orthotropic Fung's material model, parameters for which were obtained through the proposed multi-scale modelling scheme. Results for the multi-scale modelling of various levels in Case U, to obtain the parameters of the homogenized center layer have been presented in Sect. 6.2. The parameters are provided in Table 6.

The deformed and undeformed configuration of the closed and open heart valve are shown in Fig. 17. Fifteen observation points on the loading cycle are pointed out and the logarithmic strain contour plots of the heart valve for these positions are shown in Fig. 18. From the contour plots, one can observe that the deformed geometry of the heart valve is symmetric. But in reality, different bifurcation modes might be present for the closing of the heart valve leaflets based on the position of the suture point in the corners, as explained by [42]. In our simulations, results are symmetric because of the choice of the fixed nodes at the suture points.

To further understand the deformation of the leaflets, the principle logarithmic strains along three pre-selected paths, at the top, middle and bottom of the heart valve, have been plotted in Fig. 19. All the paths start at the vertical line crossing suture point "S1", pass through the verticals along the suture points "S2" and "S3", before ending at its start point. Logarithmic strains are plotted over the circumferential length of the initial tubular construct. Five different graphs for all the aforementioned paths during the third loading cycle and comparing the logarithmic strain at the mentioned observation points, have been plotted. It can be observed that when the valve is completely closed (point 11), there are large strains in the centre, at the bottom of the leaflet (path "bottom"). Considerable strains also develop under the suture points (both at the top and in the middle). During the systole phase (points 12 and 13) of the cardiac cycle, strains in the entire heart valve are relaxed, because during this phase the pressure difference between the aortic and the ventricular side of the heart valve is very small and the deformed heart valve is close to its undeformed

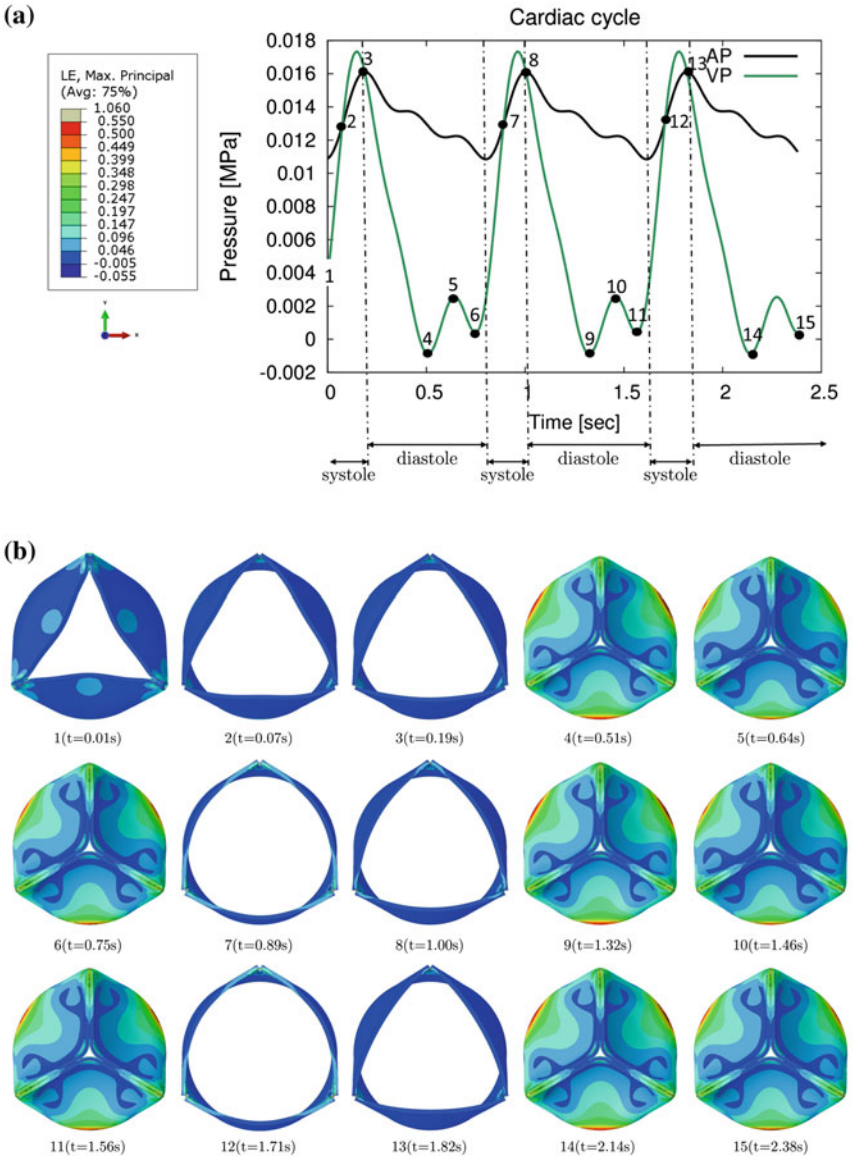

Fig. 18 Initial configuration **a** loading curve along with the legend of the logarithmic strain plot (AP: aortic pressure; VP: ventricular pressure); **b** logarithmic strain contour plot

configuration (see Fig. 17). In the initial diastolic phase (point 14), the strains developed in the centre, at the bottom are high compared to the other regions and other time points in the diastolic phase. This is because maximum difference between the

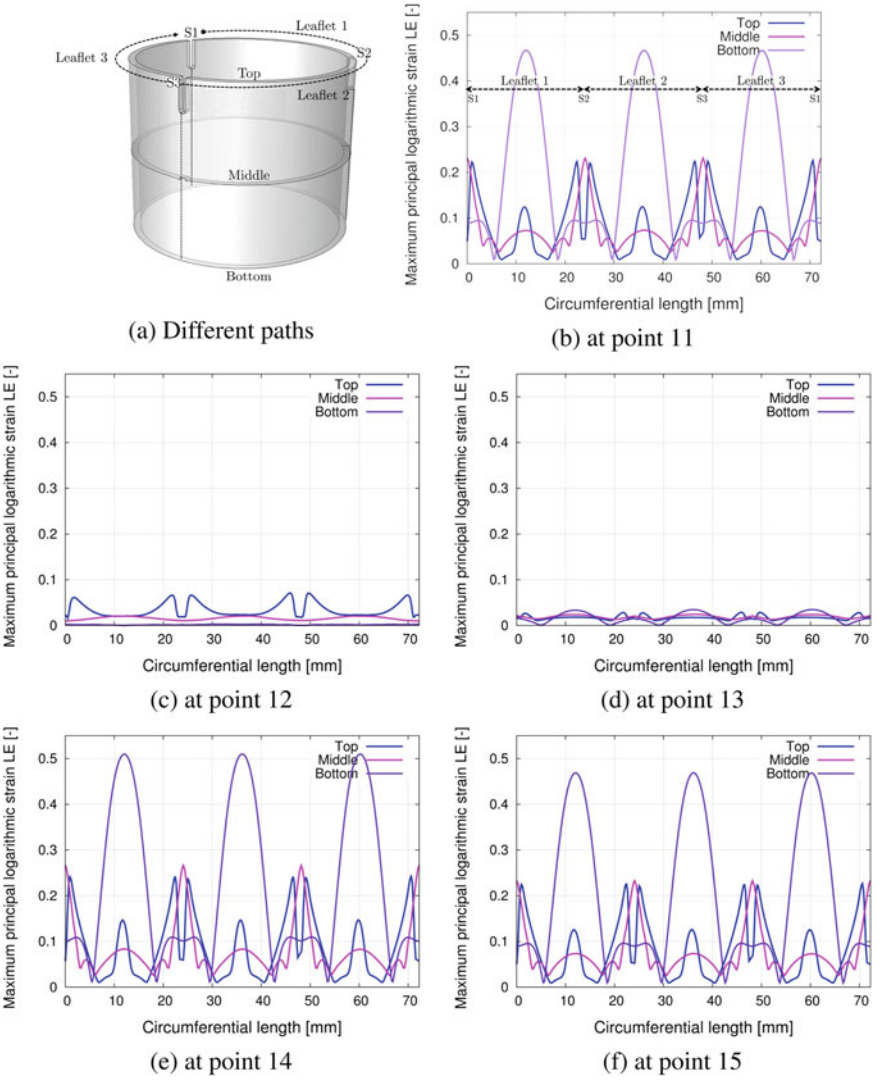

Fig. 19 Logarithmic strains versus for given time points along different paths (*top*, *middle* and *bottom*) on the heart valve, starting from suture point S1, passing through suture point S2 and S3 and finishing at S1

aortic and the ventricular pressure exist at this point. During this diastolic phase, point 15 is the same as point 11 in the previous diastolic phase.

The maximum principle logarithmic strain obtained in the heart valve is ≈0.5, which occurs at the constrained bottom of the heart valve. This is equivalent to nominal strains of ≈65%. In the remainder of the heart valve, the local maximum principle logarithmic strains are less than 0.25, which is equivalent to nominal strains of

≈28%. Therefore, the choice for taking the textile level model up to macro strains of 50% at the textile level model is adequate to capture the effective response of the reinforcing textile at the macro level. Furthermore, the lower two levels are idealizations, hence, it was assumed that the chosen macro stain limits are enough to predict the behaviour of the next upper level. To be more precise one will need to account for local damage in the matrix due to higher strains at the textile level.

7 Conclusion and Outlook

The goal of the current study was to show the competence of the multi-scale modelling approach to predict the behaviour of soft composites, with application to bio-materials. First, the complex structure of the textile reinforced composite was reduced to simplified structural models at different levels. Repeating unit cells (RUCs) of these simplified structural models were then meshed to obtain a finite element (FE) model. These were then subjected to periodic boundary conditions and loaded using far-field (macroscopic) strains to obtain an effective material response. The effective material responses were then fitted using the appropriate material models. Only the material models available in a commercial finite element tool were used.

The material behaviour of the considered orthotropic material derived from multi-scale simulation are in good agreement with the experimental results, implying that the technique can be used to study systems which are otherwise difficult to experiment on and optimize. The suggested method can now be used to optimize the textile structure along with its orientation, saving time and resources needed to create a prototype of each specimen for optimizing the end product.

The approach can further be made more reliable and robust by further investigations to quantify the deviation of the final result due to the change in volume fraction of individual structural levels, such that the modelling is faithful to the overall volume fraction of the composite. Also, further investigations are needed to determine the effect of different idealized knit patterns at the knit level model on the overall results. The changing cross-section of the yarn in the knit level model should also be considered during modelling.

To validate the simulation results of the heart valve, one can either use a digital image correlation to generate the strain patterns occurring in the tubular aortic heart valve or simulate fluid flow through the valve and compare the flow volumes.

Acknowledgements This research was funded by the Integrated Interdisciplinary Institute of Technology for Medicine (I^3TM) of RWTH Aachen University, through the Seed-Fund SF-14-04-08, "Hybrid scaffold for a transcatheter tissue engineered aortic valve". Additional funding was provided by the People Programme (Marie Curie Actions) of the European Union's Seventh Framework Programme FP7/2007-2013/ under REA grant agreement 317512.

References

1. S. Adanur, T. Liao, 3D modeling of textile composite preforms. Compos. Part B Eng. **29**, 787–793 (1998). doi:10.1016/S1359-8368(98)00036-5
2. G. Argento, M. Simonet, C. Oomens, F. Baaijens, Multi-scale mechanical characterization of scaffolds for heart valve tissue engineering. J. Biomech. **45**(16), 2893–2898 (2012)
3. E. Arruda, M. Boyce, A three-dimensional constitutive model for the large stretch behavior of rubber elastic materials. J. Mech. Phys. Solids (1993)
4. F. Auricchio, M. Conti, A. Ferrara, S. Morganti, A. Reali, Patient-specific simulation of a stentless aortic valve implant: the impact of fibres on leaflet performance. Comput. Methods Biomech. Biomed. Eng. (June 2014), 1–9 (2012). doi:10.1080/10255842.2012.681645
5. B.A. Bednarcyk, B. Stier, J.W. Simon, S. Reese, E.J. Pineda, Meso- and micro-scale modeling of damage in plain weave composites. Compos. Struct. **121**, 258–270 (2015). doi:10.1016/j.compstruct.2014.11.013
6. M. Böl, S. Reese, Finite element modelling of rubber-like polymers based on chain statistics. Int. J. Solids Struct. **43**(1), 2–26 (2006)
7. M. Böl, S. Reese, K.K. Parker, E. Kuhl, Computational modeling of muscular thin films for cardiac repair. Comput. Mech. **43**(4), 535–544 (2009). doi:10.1007/s00466-008-0328-5
8. G. Cacciola, G. Peters, P. Schreurs, A three-dimensional mechanical analysis of a stentless fibre-reinforced aortic valve prosthesis. J. Biomech. **33**(5), 521–530 (2000a)
9. G. Cacciola, G.W.M. Peters, F.P.T. Baaijens, A synthetic fiber-reinforced stentless heart valve. J. Biomech. **33**(6), 653–658 (2000b). doi:10.1016/S0021-9290(00)00003-8
10. G. Chagnon, M. Rebouah, D. Favier, Hyperelastic energy densities for soft biological tissues: a review. J. Elast. **120**(2), 129–160 (2015). doi:10.1007/s10659-014-9508-z
11. D.Y. Cheung, B. Duan, J.T. Butcher, Current progress in tissue engineering of heart valves: multiscale problems, multiscale solutions. Expert Opin. Biol. Ther. **2598**(October), 1–18 (2015). doi:10.1517/14712598.2015.1051527
12. A. D'Amore, N. Amoroso, R. Gottardi, C. Hobson, C. Carruthers, S. Watkins, W.R. Wagner, M.S. Sacks, From single fiber to macro-level mechanics: a structural finite-element model for elastomeric fibrous biomaterials. J. Mech. Behav. Biomed. Mater. **39**, 146–161 (2014). doi:10.1016/j.jmbbm.2014.07.016
13. J. De Hart, G. Cacciola, P. Schreurs, G. Peters, A three-dimensional analysis of a fibre-reinforced aortic valve prosthesis. J. Biomech. **31**(7), 629–638 (1998)
14. J. De Hart, G.W.M. Peters, P.J.G. Schreurs, F.P.T. Baaijens, Collagen fibers reduce stresses and stabilize motion of aortic valve leaflets during systole. J. Biomech. **37**(3), 303–311 (2004). doi:10.1016/S0021-9290(03)00293-8
15. O. Döbrich, T. Gereke, C. Cherif, Modeling the mechanical properties of textile-reinforced composites with a near micro-scale approach. Compos. Struct. **135**, 1–7 (2016). doi:10.1016/j.compstruct.2015.09.010
16. M.T. Duong, N.H. Nguyen, M. Staat, Physical response of hyperelastic models for composite materials and soft tissues. Asia Pac. J. Comput. Eng. **2**(3), 1–18 (2015). doi:10.1186/s40540-015-0015-x
17. A.E. Ehret, M. Itskov, A polyconvex hyperelastic model for fiber-reinforced materials in application to soft tissues. J. Mater. Sci. **42**(21), 8853–8863 (2007). doi:10.1007/s10853-007-1812-6
18. Y. Fung, K. Fronek, P. Patitucci, Pseudoelasticity of arteries and the choice of its mathematical expression. Am. J. Physiol.-Heart Circulatory Physiol. **237**(5), H620–H631 (1979)
19. T.C. Gasser, R.W. Ogden, H. Ga, Hyperelastic modelling of arterial layers with distributed collagen fibre orientations. J. R. Soc. Interface **3**(6), 15–35 (2006). doi:10.1098/rsif.2005.0073, 0312002v1
20. W. Goetz, H. Lim, E. Lansac, P. Weber, C. Duran, A temporarily stented, autologous pericardial aortic valve prosthesis. J. Heart Valve Dis. **11**(5), 696–702 (2002)

21. B. Hassani, E. Hinton, A review of homogenization and topology optimization i-homogenization theory for media with periodic structure. Comput. Struct. **69**(6), 707–717 (1998)
22. Hibbitt, Karlsson, Sorensen, ABAQUS/Standard User's Manual, vol 1. Hibbitt, Karlsson & Sorensen, 2001
23. G. Holzapfel, Computational biomechanics of soft biological tissue. Encycl. Comput. Mech. **2**, 605–635 (2004)
24. G.A. Holzapfel, T.C. Gasser, A viscoelastic model for fiber-reinforced composites at finite stains: continuum basis, computational aspects and applications. Comput. Methods Appl. Mech. Eng. **190**(34), 4379–4403 (2001). doi:10.1016/S0045-7825(00)00323-6
25. J.D. Humphrey, Mechanics of the arterial wall: review and directions. Crit. Rev. Biomed. Eng. **23**(1–2), 1–162 (1994)
26. S. Jana, B.J. Tefft, D.B. Spoon, R.D. Simari, Scaffolds for tissue engineering of cardiac valves. Acta Biomater. **10**(7), 2877–2893 (2014). doi:10.1016/j.actbio.2014.03.014
27. Y. Kyosev, Y. Angelova, R. Kovar, 3D Modelling of plain weft knitted structures from compressible yarn. Res. J. Text Appar. **9**(1), 88–97 (2005)
28. C. Lechat, A.R. Bunsell, P. Davies, Tensile and creep behaviour of polyethylene terephthalate and polyethylene naphthalate fibres. J. Mater. Sci. **46**(2), 528–533 (2011). doi:10.1007/s10853-010-4999-x
29. Y. Li, L. Yang, S. Chen, L. Xu, Three dimensional simulation of weft knitted fabric based on surface mode. Comput. Model. Technol. **18**, 52–57 (2014)
30. Y. Li, B. Stier, B. Bednarcyk, J.W. Simon, S. Reese, The effect of fiber misalignment on the homogenized properties of unidirectional fiber reinforced composites. Mech. Mater. **92**, 261–274 (2016). doi:10.1016/j.mechmat.2015.10.002
31. H. Lin, X. Zeng, M. Sherburn, A.C. Long, M.J. Clifford, Automated geometric modelling of textile structures. Text Res. J. **82**(16), 1689–1702 (2012). doi:10.1177/0040517511418562
32. M.M. Maurer, B. Röhrnbauer, A. Feola, J. Deprest, E. Mazza, Mechanical biocompatibility of prosthetic meshes: a comprehensive protocol for mechanical characterization. J. Mech. Behav. Biomed. Mater. **40**, 42–58 (2014). doi:10.1016/j.jmbbm.2014.08.005
33. E. Mazza, A.E. Ehret, Mechanical biocompatibility of highly deformable biomedical materials. J. Mech. Behav. Biomed. Mater. **48**, 100–124 (2015). doi:10.1016/j.jmbbm.2015.03.023
34. R. Moreira, T. Velz, N. Alves, V.N. Gesche, A. Malischewski, T. Schmitz-Rode, J. Frese, S. Jockenhoevel, P. Mela, Tissue-engineered heart valve with a tubular leaflet design for minimally invasive transcatheter implantation. Tissue Eng. Part C: Methods **21**(6), 530–540 (2014)
35. V.P. Nguyen, M. Stroeven, L.J. Sluys, Multiscale continuous and discontinuous modeling of heterogeneous materials: a review on recent developments. J. Multiscale Model. **03**(04), 229–270 (2011). doi:10.1142/S1756973711000509
36. Y. Qi, J. Li, L. Liu, Stiffness prediction of multilayer-connected biaxial weft-knitted fabric-reinforced composites. J. Reinf. Plast Compos. (399), 0731684415587, 346 (2015). doi:10.1177/0731684415587346
37. S. Reese, Meso-macro modelling of fibre-reinforced rubber-like composites exhibiting large elastoplastic deformation. Int. J. Solids Struct. **40**(4), 951–980 (2003)
38. M. Sherburn, Geometric and mechanical modelling of textiles. ph.d. thesis, university of nottingham, 2007
39. C. Singh, C. Wong, X. Wang, Medical textiles as vascular implants and their success to mimic natural arteries. J. Funct. Biomater. **6**(3), 500–525 (2015). doi:10.3390/jfb6030500
40. D. Sodhani, B. Stier, S. Reese, Evaluating the simulation of ideal filler reinforced elastomers using a full field modelling approach. Const. Models Rubber **IX**, 317 (2015)
41. D. Sodhani, S. Reese, R. Moreira, S. Jockenhoevel, P. Mela, S.E. Stapleton, Multi-scale modelling of textile reinforced artificial tubular aortic heart valves. Meccanica (2016). doi:10.1007/s11012-016-0479-y
42. S.E. Stapleton, R. Moreira, S. Jockenhoevel, P. Mela, S. Reese, Effect of reinforcement volume fraction and orientation on a hybrid tissue engineered aortic heart valve with a tubular leaflet design. Adv. Model. Simul. Eng. Sci. **2**(1), 1–17 (2015)

43. J.A. Stella, A. D'Amore, W.R. Wagner, M.S. Sacks, On the biomechanical function of scaffolds for engineering load-bearing soft tissues. Acta Biomater. **6**(7), 2365–2381 (2010). doi:10.1016/j.actbio.2010.01.001
44. B. Stier, J.W. Simon, S. Reese, Finite element analysis of layered fiber composite structures accounting for the materials microstructure and delamination. Appl. Compos. Mater. **22**(2), 171–187 (2015a). doi:10.1007/s10443-013-9378-8
45. B. Stier, J.W. Simon, S. Reese, Numerical and experimental investigation of the structural behavior of a carbon fiber reinforced ankle-foot orthosis. Med. Eng. Phys. **37**(5), 505–511 (2015). doi:10.1016/j.medengphy.2015.02.002
46. S.C. Ugbolue, Y.K. Kim, S.B. Warner, Engineered warp knit auxetic fabrics. J. Text Sci. Eng. **02**(01), 1–8 (2012). doi:10.4172/2165-8064.1000e103
47. C. Ugbolue, SYKKSBW, Geometrical analysis of warp knit auxetic fabrics. J. Text Sci. Eng. **5**(3), 1000, 201 (2015). doi:10.4172/2165-8064.1000201
48. M. Van Lieshout, G. Peters, M. Rutten, F. Baaijens, A knitted, fibrin-covered polycaprolactone scaffold for tissue engineering of the aortic valve. Tissue Eng. **12**(3), 7–481 (2006). doi:10.1089/ten.2006.12.481
49. M. Van Lieshout, C.M. Vaz, M.C.M. Rutten, G.W.M. Peters, F.P.T. Baaijens, Electrospinning versus knitting: two scaffolds for tissue engineering of the aortic valve. J. Biomater. Sci. Polym. Edition **17**(1–2), 77–89 (2006b). doi:10.1163/156856206774879153
50. S. Vassiliadis, A. Kallivretaki, C. Provatidis, D. Domvoglou, Mechanical analysis of woven fabrics: the state of the art. INTECH Open Access Publisher 2011
51. I. Verpoest, S.V. Lomov, Virtual textile composites software WiseTex: Integration with micro-mechanical, permeability and structural analysis. Compos. Sci. Technol. **65** (15-16 SPEC. ISS.), 2563–2574 (2005). doi:10.1016/j.compscitech.2005.05.031
52. Y. Wan, B. Sun, B. Gu, Multi-scale structure finite element analyses of damage behaviors of multi-axial warp-knitted composite materials subjected to quasi-static and high strain rate compressions. J. Text Inst. **5000**(February 2016), 1–26 (2015). doi:10.1080/00405000.2015.1070028
53. M. Weber, E. Heta, R. Moreira, V.N. Gesche, T. Schermer, J. Frese, S. Jockenhoevel, P. Mela, Tissue-engineered fibrin-based heart valve with a tubular leaflet design. Tissue Eng. Part C: Methods **20**(4), 265–275 (2013)
54. M. Yeoman, B. Reddy, H. Bowles, A constitutive model for the warp-weft coupled non-linear behavior of knitted textiles with potential use in tissue regenerative implants. J. Biomech. **31**(32), 1–21 (2010). doi:10.1016/j.biomaterials.2010.07.033

Preliminary Monolithic Fluid Structure Interaction Model for Ventricle Contraction

D. Cerroni, D. Giommi, S. Manservisi and F. Mengini

Abstract In this work we test the performance of different algorithms for the solution of a monolithic Fluid Structure Interaction (FSI) problem with a simplified ventricle model with the purpose to reduce the computational time. We study this challenging FSI problem by solving the fully coupled and the projection algorithm with a different number of penalty correction steps. The proposed FSI penalty projection algorithm is a modification of the Chorin method for fluids based on a predictor and a corrector step. The performance of the modified algorithm is tested by comparing the results obtained with the standard coupled algorithm with the ones obtained with the modified penalty projection scheme.

1 Introduction

In the last decades the number of Fluid-Structure studies has been increasing in various fields of engineering. Many early studies can be found with regard to wing or bridge response stability and biology applications but in recent years a great interest has been developed in FSI problems related to biological and medicine fields, e.g., see [1, 2] and citations therein. In particular very interesting works can be found on aneurysm growing, hearth valves mechanics and ventricle contraction dynamics. Such simulations represent an impressive step forward in the comprehension and the prediction of biological component behavior and dynamics. A fluid structure interaction problem solves the conservative set of equations over both fluid and solid domain. The most common solution strategy, implemented in software packages, is the so-called partitioned approach, which decouples the problem into two separate sub-problems and uses dedicated software for each different region. According to this solution strategy the coupling is achieved by enforcing continuity stress conditions along the fluid-solid interface. For details the interested reader can see [3]. It is worthwhile to remark that when large displacements occur, as in the case of biolog-

D. Cerroni (✉) · D. Giommi · S. Manservisi · F. Mengini
Montecuccolino Laboratory, DIN, Alma Mater, University of Bologna,
Via dei Colli 16, 40136 Bologna, Italy
e-mail: daniele.cerroni2@unibo.it

P. Wriggers and T. Lenarz (eds.), *Biomedical Technology*, Lecture Notes in Applied and Computational Mechanics 84, DOI 10.1007/978-3-319-59548-1_12

ical applications, explicit partitioned algorithms show instabilities due to the poor fluid-solid coupling matching with unbalanced solid-fluid stresses at the interface. In order to overcome this numerical problems one could implicitly enforce coupling conditions. These algorithms are called fully coupled or monolithic and solve simultaneously for the fluid and structure unknowns, so that the solid and fluid regions are treated as a single continuum and the interface conditions are automatically enforced [4, 5]. Moreover, in a typical biological FSI problem, the fluid and the solid material are characterized by a similar density leading to the so called "added mass effect". In this case it is well known that only fully coupled algorithms exhibit good stability properties [4]. For large displacements, as typical in biology, an accurate and detailed geometrical domain is important leading to computational expensive simulations [6]. The reduction of the computational cost of the monolithic approach motivated this work. The cpu time reduction can be achieved by using different resolutions in different regions or by using velocity-pressure uncoupling algorithms [2, 7, 8]. In order to reduce the computational cost of the ventricle model we explore the possibility to use a penalty-projection uncoupling and test the performance of the algorithm proposed in [9]. In this work we use a simplified model to simulate the ventricle contraction cycle and the results, obtained with the monolithic fully coupled algorithm, are compared with the ones obtained with the fully decoupled algorithm in order to explore the possibility to reduce the computational effort and introduce a more realistic ventricle model. The work is organized as follows. In Sects. 2 and 3 we give the mathematical description of the fluid structure interaction problem and the penalty projection algorithm. In Sect. 4 we present some numerical tests. We define the simplified model used to simulate the ventricle contraction and compare the results obtained with the pressure-velocity coupling and uncoupling algorithms.

2 Mathematical Model

In this Section we introduce mathematical notation used in the work together with the generic mathematical description of a fluid structure interaction problem. We denote by $H^s(\mathscr{O})$, $s \in \mathfrak{R}$, the standard Sobolev space of order s with respect to the set $\mathscr{O}$, which is either the flow domain Ω, or its boundary Γ, or part of its boundary. Whenever m is a non negative integer, the inner product over $H^m(\mathscr{O})$ is denoted by $(f,g)_m$ and (f,g) denotes the inner product over $H^0(\mathscr{O}) = L^2(\mathscr{O})$. Hence, we associate with $H^m(\mathscr{O})$ its natural norm $\|f\|_{m,\mathscr{O}} = \sqrt{(f,f)_m}$. For $1 \le p < \infty$ the Sobolev space $W^{m,p}(\mathscr{O})$ is defined as the closure of $C^\infty(\mathscr{O})$ in the norm

$$\|f\|^p_{W^{m,p}(\mathscr{O})} = \sum_{|\alpha|\le m} \int_{\mathscr{O}} |\Big(\frac{\partial}{\partial x}\Big)^\alpha f(x)|^p \, dx \,.$$

The closure of $C^\infty_0(\mathscr{O})$ under the norm $\|\cdot\|_{W^{m,p}(\mathscr{O})}$ will be denoted by $W^{m,p}_0(\mathscr{O})$. Whenever possible, we will neglect the domain label in the norm. For vector-valued

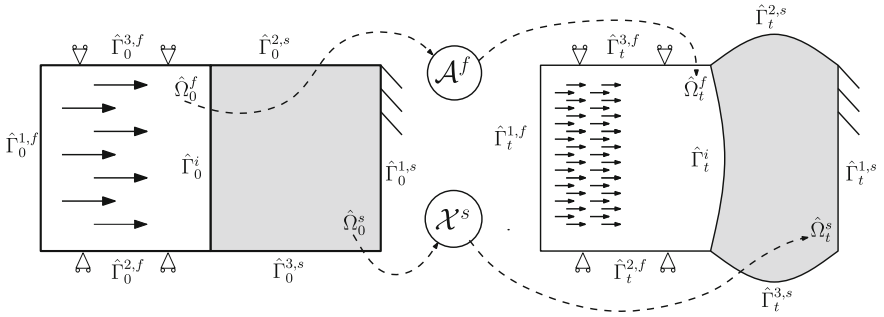

Fig. 1 Reference and current configurations for a generic FSI domain

functions and spaces, we use boldface notation. For example, $\mathbf{H}^s(\Omega) = [H^s(\Omega)]^n$ denotes the space of $\mathfrak{R}^n$-valued functions such that each component belongs to $H^s(\Omega)$. Of special interest is the space

$$\mathbf{H}^1(\Omega) = \left\{ v_j \in L^2(\Omega) \;\middle|\; \frac{\partial v_j}{\partial x_k} \in L^2(\Omega) \quad \text{for } j,k = 1,2 \right\}$$

equipped with the norm $\|\mathbf{v}\|_1 = (\sum_{k=1}^2 \|v_k\|_1^2)^{1/2}$. For details concerning the function spaces we have introduced, one may consult [10, 11].

In an ordinary FSI problem we consider a mechanical system composed by a laminar Newtonian fluid region and a solid one which defines a moving domain Ω_t. A schematic geometry of the problem is shown in Fig. 1. Let Ω_t^f and Ω_t^s be the fluid and the solid region at $t \in (0,T]$, respectively. At $t = 0$ the fluid and solid region are defined by $\hat{\Omega}_0^f$ and $\hat{\Omega}_0^s$. Let $\Gamma_t^i = \bar{\Omega}_t^f \cap \bar{\Omega}_t^s$ and $\hat{\Gamma}_0^i = \bar{\Omega}_0^f \cap \bar{\Omega}_0^s$ be the interface where solid and fluid interact. $\Gamma_t^k, k = 1,2,3$ and $\hat{\Gamma}_0^k, k = 1,2,3$ are defined to be the remaining external boundaries at $t \in (0,T]$ and $t = 0$, respectively. The evolution of the solid and fluid domain $\hat{\Omega}_0^f$ and $\hat{\Omega}_0^s$ are defined by

$$\mathscr{X}^s : \hat{\Omega}_0^s \times \mathbb{R}^+ \to \mathbb{R}^3,$$
$$\mathscr{A}^f : \hat{\Omega}_0^f \times \mathbb{R}^+ \to \mathbb{R}^3,$$

such that the range of $\mathscr{X}^s(\cdot,t)$ and $\mathscr{A}^f(\cdot,t)$ define Ω_t^s and Ω_t^f, respectively. $\mathscr{X}^s$ maps any material point $\hat{\mathbf{x}}_0^s$ from the given fixed reference configuration $\hat{\Omega}_0^s$ to the current solid material configuration Ω_t^s. The solid displacement is then defined as

$$\hat{\mathbf{u}}^s(\hat{\mathbf{x}}_0^s, t) = \mathscr{X}(\hat{\mathbf{x}}_0^s, t) - \hat{\mathbf{x}}_0^s. \tag{1}$$

The mapping $\mathscr{A}^f$ is such that $\mathscr{A}^f(\hat{\mathbf{x}}_0^f, t) = \hat{\mathbf{x}}_0^f + \hat{\mathbf{u}}^f(\hat{\mathbf{x}}_0^f, t)$, where $\hat{\mathbf{u}}^f(\hat{\mathbf{x}}_0^f, t)$ is defined as an arbitrary extension operator over the fluid domain $\hat{\Omega}_0^f$ and given by

$$\hat{\mathbf{u}}^f(\hat{\mathbf{x}}_0^f, t) = \mathrm{Ext}(\hat{\mathbf{u}}^s|_{\hat{\Gamma}_0^i}) \quad \text{in} \quad \hat{\Omega}_0^f . \tag{2}$$

The extension operator used to evaluate the fluid region displacement is the harmonic or Laplace operator. Other similar operators can be employed as described in [12–15]. The velocity $\hat{\mathbf{w}}^f$ is defined by

$$\hat{\mathbf{w}}^f = \frac{\partial \hat{\mathbf{u}}^f}{\partial t} \quad \text{in} \quad \hat{\Omega}_0^f . \tag{3}$$

This quantity represents the velocity in terms of the reference coordinate $\hat{\mathbf{x}}_0^f$.

2.1 The Coupled Fluid-Structure Problem

The behavior of the fluid is described by the Navier-Stokes equations for incompressible flows. For details the interested reader can also see [16–19].

$$\begin{aligned}
&\rho^f \frac{\partial \mathbf{v}^f}{\partial t}\bigg|_{\tilde{\mathscr{A}}} + \rho^f \left(\mathbf{v}^f - \mathbf{w}^f\right) \cdot \boldsymbol{\nabla}\mathbf{v}^f - \boldsymbol{\nabla} \cdot \boldsymbol{\sigma}^f = \mathbf{0} && \text{in} \quad (0,T) \times \Omega_t^f , \\
&\boldsymbol{\nabla} \cdot \mathbf{v}^f = \mathbf{0} && \text{in} \quad (0,T) \times \Omega_t^f , \\
&\mathbf{v}^f|_{t=0} = \mathbf{v}_0 && \text{in} \quad \hat{\Omega}_0^f , \\
&\mathbf{v}^f|_{\Gamma_{t,D}^{1,f} \cup \Gamma_{t,D}^{2,f}} = \mathbf{g}^f && \text{in} \quad (0,T) , \\
&\boldsymbol{\sigma}_f \cdot \mathbf{n}^f|_{\Gamma_{t,N}^{1,f} \cup \Gamma_{t,}^{2,f}} = \mathbf{h}^f && \text{in} \quad (0,T) ,
\end{aligned} \tag{4}$$

where ρ^f is the constant density, $\mathbf{v}^f$ is the fluid velocity, $\tilde{\mathscr{A}}$ denotes the ALE application that maps the reference fluid configuration $\hat{\Omega}_0^f$ onto the current fluid configuration Ω_t^f and $\mathbf{w}^f$ denotes the fluid domain velocity. $\mathbf{n}$ is the unit normal vector that points outward from the boundary $\partial\Omega_t^f$ and $\mathbf{g}^f$, $\mathbf{h}^f$, $\mathbf{v}_0$ are given data. The flow state variables in the incompressible case are the pressure p^f and the velocity $\mathbf{v}^f$. The contribution of external forces such as gravity is assumed to be negligible. The constitutive relation for the stress tensor in the Newtonian incompressible case reads

$$\boldsymbol{\sigma}^f = -p^f \mathbf{I} + \boldsymbol{\tau}^f = -p^f \mathbf{I} + 2\mu^f \boldsymbol{\varepsilon}\left(\mathbf{v}^f\right) , \tag{5}$$

where μ^f is the dynamic viscosity of the fluid, p^f the Lagrange multiplier associated to the incompressibility constraint and $\boldsymbol{\varepsilon}\left(\mathbf{v}^f\right)$ the strain rate tensor defined as

$$\boldsymbol{\varepsilon}\left(\mathbf{v}^f\right) = \frac{1}{2}\left(\boldsymbol{\nabla}\mathbf{v}^f + \left(\boldsymbol{\nabla}\mathbf{v}^f\right)^{\mathrm{t}}\right) . \tag{6}$$

The total time derivative is related to the adopted reference systems. The governing equations for structural mechanics are the following momentum equations

$$\rho^s \frac{\partial \mathbf{v}^s}{\partial t} - \boldsymbol{\nabla} \cdot \boldsymbol{\sigma}^s(\mathbf{u}^s) = \mathbf{0} \qquad \text{in} \quad \Omega_t^s \,, \tag{7}$$

where ρ^s is the density of the solid material, $\mathbf{v}^s$ is the velocity field and $\boldsymbol{\sigma}^s$ its Cauchy stress tensor, which is a function of the solid region displacement $\mathbf{u}^s$. Since the constitutive law for the solid stress tensor is expressed in terms of displacements one must solve both the balance equations (7) and the kinematic relation

$$\mathbf{v}^s = \frac{\partial \mathbf{u}^s}{\partial t} \,. \tag{8}$$

For the reference configuration we can introduce the right Cauchy-Green deformation tensor $\mathbf{C}$ as

$$C_{ij} = F_{ki} F_{kj} \qquad \forall\, i,j = 1, \ldots, 3 \,, \tag{9}$$

where $\mathbf{F}$ is the deformation gradient tensor defined by $\mathbf{F} = \mathbf{I} + \boldsymbol{\nabla}\mathbf{u}^s$. In a similar way in the current configuration we can introduce the left Cauchy-Green deformation tensor, $\mathbf{b}$, as

$$b_{ij} = F_{ik} F_{jk} \qquad \forall\, i,j = 1, \ldots, 3 \,. \tag{10}$$

According with this notation we can now express the Cauchy stress tensor, $\boldsymbol{\sigma}^s$, as [16]

$$\sigma_{ij}^s = \frac{2}{J} \left[b_{ij} \left(I\, b_{ij} - b_{im} b_{mj} \right) \frac{J \delta_{ij}}{2} \right] \begin{pmatrix} \frac{\partial W}{\partial I} \\ \\ \frac{\partial W}{\partial II} \\ \\ \frac{\partial W}{\partial J} \end{pmatrix} , \tag{11}$$

where $I = C_{ii}$, $II = 1/2 \left(I - C_{ij} C_{ji} \right)$ are the first and second invariant of the right Cauchy-Green strain tensor $\mathbf{C}$ and J its determinant. The quantity $W = W(I, II, J)$ is the strain energy of the system which depends on the constitutive law of the considered material. For example for a Neo-Hookian material, with respect to the current configuration, the energy function is defined by

$$\begin{aligned} W(I,J) = & \frac{1}{2} \mu_s \left(J^{-2/3} \mathrm{tr}\mathbf{C} - 3 \right) + \\ & \frac{1}{2} \left(\lambda + \frac{2}{3} \mu_s \right) \left(\frac{1}{2} (J^2 - 1) - \ln J \right) . \end{aligned} \tag{12}$$

In the case of incompressible solid, the third invariant is equal to one so the energy density function becomes

$$W(I) = \frac{1}{2} \mu_s \left(\mathrm{tr}\mathbf{C} - 3 \right) \tag{13}$$

and the Cauchy stress tensor is defined by

$$\boldsymbol{\sigma}^s = -p^s \mathbf{I} + \boldsymbol{\sigma}^{s*}, \tag{14}$$

where $\boldsymbol{\sigma}^{s*}$ is the tensor obtained by using the equations (11) and (13).

The problem defined by (4)–(7) is not well posed since we have not yet prescribed any boundary conditions at the interface Γ_t^i. The coupling between the fluid and the solid model determines the missing boundary conditions, which consist of imposing the continuity of velocity and stress at the interface Γ_t^i as

$$\mathbf{v}^f|_{\Gamma_t^i} = \mathbf{v}^s|_{\Gamma_t^i}, \tag{15}$$

$$\boldsymbol{\sigma}^f \cdot \mathbf{n}^f|_{\Gamma_t^i} + \boldsymbol{\sigma}^s \cdot \mathbf{n}^s|_{\Gamma_t^i} = \mathbf{0}. \tag{16}$$

In order to write the weak formulation of the coupled problem, let us consider the following functional spaces

$$\begin{aligned}
\mathbf{V}^t &= \{\boldsymbol{\phi} \in \mathbf{H}^1(\Omega_t^f) : \boldsymbol{\phi}|_{\Gamma_{t,D}^{1,f} \cup \Gamma_{t,D}^{2,f}} = \mathbf{0}\}, \\
\mathbf{V}_g^t &= \{\boldsymbol{\phi} \in \mathbf{H}^1(\Omega_t^f) : \boldsymbol{\phi}|_{\Gamma_{t,D}^{1,f} \cup \Gamma_{t,D}^{2,f}} = \mathbf{g}^f\}, \\
Q^t &= L^2(\Omega_t^f), \\
\mathbf{M}^0 &= \{\boldsymbol{\psi} \in \mathbf{H}^1(\hat{\Omega}_0^s) : \boldsymbol{\psi}|_{\hat{\Gamma}_{0,D}^{1,s} \cup \hat{\Gamma}_{0,D}^{2,s} \cup \hat{\Gamma}_{0,D}^{3}} = \mathbf{0}\}, \\
\mathbf{M}_g^0 &= \{\boldsymbol{\psi} \in \mathbf{H}^1(\hat{\Omega}_0^s) : \boldsymbol{\psi}|_{\hat{\Gamma}_{0,D}^{1,s} \cup \hat{\Gamma}_{0,D}^{2,s} \cup \hat{\Gamma}_{0,D}^{3}} = \mathbf{g}^s\}, \\
D^0 &= L^2(\hat{\Omega}_0^s).
\end{aligned}$$

In addition, let us introduce the following bilinear form

$$a^f(\mathbf{v}^f, \boldsymbol{\phi}) = \int_{\Omega^f} \boldsymbol{\tau}^f(\mathbf{v}^f) : \nabla\boldsymbol{\phi}\, d\mathbf{x} = \mu(\nabla\mathbf{v}^f + (\nabla\mathbf{v}^f)^T, \nabla\boldsymbol{\phi}), \tag{17}$$

where we denote with $\boldsymbol{\tau}^f$ the fluid viscosity tensor. The variational formulation of the fluid equations can be obtained through the usual method by multiplying the Eq. (4) with appropriate test functions, performing integrations on the whole domain and keeping into account the boundary and interface conditions. This procedure leads, for the velocity field $\mathbf{v} \in \mathbf{V}_g^t$ and pressure $p \in Q^t$, to the following fluid momentum equation

$$\begin{aligned}
\rho^f \left(\frac{\partial \mathbf{v}^f}{\partial t}\bigg|_{\mathscr{A}}, \boldsymbol{\phi} \right) + a(\mathbf{v}^f, \boldsymbol{\phi}) - \rho^f((\nabla \cdot \mathbf{w}^f)\mathbf{v}^f, \boldsymbol{\phi}) + \rho^f(\left(\mathbf{v}^f - \mathbf{w}^f\right) \cdot \nabla\mathbf{v}^f, \boldsymbol{\phi}) = \\
(p^f, \nabla \cdot \boldsymbol{\phi}) + \int_{\Gamma_t^i} (\boldsymbol{\sigma}^f \cdot \mathbf{n}^f) \cdot \boldsymbol{\phi}\, d\gamma + \int_{\Gamma_N^f} \mathbf{h}^f \cdot \boldsymbol{\phi}\, d\gamma,
\end{aligned} \tag{18}$$

$$(q, \nabla \cdot \mathbf{v}^f) = 0\,,$$
$$\mathbf{v}^f|_{t=0} = \mathbf{v}_0^f\,,$$

for all $\boldsymbol{\phi} \in \mathbf{V}^t$ and $q \in Q^t$. In a similar way, we define the following bilinear form

$$a^s(\mathbf{u}^s, \boldsymbol{\psi}) = (\boldsymbol{\sigma}^s(\mathbf{u}^s), \nabla \boldsymbol{\psi})\,. \tag{19}$$

By following the procedure briefly described above, we obtain at each time t, for the velocity $\mathbf{v}^s \circ \mathscr{X}^s \in \mathbf{M}_g^0$ and pressure $p^s \circ \mathscr{X}^s \in \mathbf{D}^0$, the following weak formulation for the solid problem

$$\rho^s\left(\frac{\partial^2}{\partial t^2}\mathbf{u}^s, \boldsymbol{\psi}\right) + a^s(\mathbf{u}^s, \boldsymbol{\psi}) - (p^s, \nabla \cdot \boldsymbol{\psi}) = \int_{\Gamma_t^i} (\boldsymbol{\sigma}^s \cdot \mathbf{n}^s) \cdot \boldsymbol{\psi}\, d\gamma + \int_{\Gamma_N^s} \mathbf{h}^s \cdot \boldsymbol{\psi}\, d\gamma\,,$$
$$(d, \nabla \cdot \mathbf{u}^s) = 0\,, \tag{20}$$
$$\mathbf{u}^s|_{t=0} = \mathbf{u}_0^s\,, \qquad \mathbf{v}^s|_{t=0} = \mathbf{v}_0^s\,,$$

for all $\boldsymbol{\psi} \circ \mathscr{X}^s \in \mathbf{M}^0$ and $d \circ \mathscr{X}^s \in \mathbf{D}^0$. Let us introduce a global weak formulation for the fluid-structure problem. If we define the functional space

$$\mathbf{S}^t = \{(\boldsymbol{\phi}, \boldsymbol{\psi} \circ \mathscr{X}^s) \in \mathbf{V}^t \times \mathbf{M}^0 \,:\, \boldsymbol{\psi}|_{\Gamma_t^i} = \boldsymbol{\phi}|_{\Gamma_t^i}\}\,, \tag{21}$$

from (15), (16), (18) and (20), we can write the FSI problem in the coupled formulation as

$$\rho^f\left(\left.\frac{\partial \mathbf{v}^f}{\partial t}\right|_{\mathscr{A}}, \boldsymbol{\varphi}\right) + a(\mathbf{v}^f, \boldsymbol{\varphi}) - \rho^f((\nabla \cdot \mathbf{w}^f)\mathbf{v}^f, \boldsymbol{\varphi}) + \rho^f\left(\left(\mathbf{v}^f - \mathbf{w}^f\right) \cdot \nabla \mathbf{v}^f, \boldsymbol{\varphi}\right) -$$
$$(p^f, \nabla \cdot \boldsymbol{\varphi}) + \rho^s\left(\frac{\partial^2}{\partial t^2}\mathbf{u}^s, \boldsymbol{\varphi}\right) + a^s(\mathbf{u}^s, \boldsymbol{\varphi}) - (p^s, \nabla \cdot \boldsymbol{\varphi}) \tag{22}$$
$$- \int_{\Gamma_N^s} \mathbf{h}^s \cdot \boldsymbol{\varphi}\, d\gamma - \int_{\Gamma_N^f} \mathbf{h}^f \cdot \boldsymbol{\varphi}\, d\gamma = 0\,, \quad \forall \boldsymbol{\varphi} \in \mathbf{S}^t$$
$$(q, \nabla \cdot \mathbf{v}^f) = 0 \qquad (d, \nabla \cdot \mathbf{u}^s) = 0, \tag{23}$$
$$\mathbf{v}^f|_{t=0} = \mathbf{v}_0^f \qquad \mathbf{u}^s|_{t=0} = \mathbf{u}_0^s \qquad \mathbf{v}^s|_{t=0} = \mathbf{v}_0^s\,. \tag{24}$$

It is worth noting that by using the coupling conditions (15) and (16) and this particular choice of the fluid-structure test functions, the boundary terms that appear in the fluid-solid interface Γ_t^i cancel out. This assures that forces at the interface are always computed in an exact way.

3 Numerical Penalty-Projection Algorithm

The solution of the system (22) and (23), due to its saddle-point nature, is CPU-time expensive and many authors have proposed different strategies to reduce the computational effort. Some of the most popular ones are decoupled fractional step strategies, domain decomposition methods and reduced models which try to decrease the degrees of freedom by splitting the discrete matrix or using boundary integral techniques [20]. Projection methods are widely used in fluid dynamics but they are not popular in incompressible structural mechanics due to the poor performance of the projection step itself over rigid media. In this work we propose to split the computation of the velocity and pressure degrees of freedom by introducing an iterative penalty-projection method. The standard projection method consists of two steps: a predictor step and a corrector one [21]. In the predictor step an auxiliary discrete velocity $\tilde{\mathbf{v}}_h$, which does not satisfy the divergence-free condition, is computed, while, in the corrector step, an iterative correction $\delta p^{s,n+1}_{h,proj}$ is introduced to enforce the incompressibility constraint. This projection allows us to solve the pressure and the velocity field separately but, at the same time, it does not recover the original boundary conditions on pressure which are defined implicitly in the original momentum equation [22]. This issue is particularly relevant on solid boundaries when incompressible materials are considered. In this case the boundary conditions involve the whole stress tensor and not only the pressure components. An error on the solid boundary, which deforms the solid surface in the wrong way, is introduced by setting the pressure or its normal derivative to zero. This is particular relevant when large displacements and moving meshes are considered. The iterative penalty procedure begins with the evaluation of an auxiliary velocity field $\tilde{\mathbf{v}}_h$ and a pressure correction term $\delta p^{s,n+1}_{h,pen}$. The quantity $\tilde{\mathbf{v}}_h = (\tilde{\mathbf{v}}^f_h, \tilde{\mathbf{v}}^s_h)$ is the solution of the following momentum balance equation

$$\begin{aligned} &\partial_t(\tilde{\mathbf{v}}^f_h, \boldsymbol{\varphi}_h) + \partial_t(\tilde{\mathbf{v}}^s_h, \boldsymbol{\varphi}_h) + c(\tilde{\mathbf{v}}^f_h, \boldsymbol{\varphi}_h) + d^s(\tilde{\mathbf{v}}^s_h, \boldsymbol{\varphi}_h) - (p^{f,k}_h, \boldsymbol{\nabla}\cdot\boldsymbol{\varphi}_h) \\ &- (\delta p^{f,k}_{h,proj}, \boldsymbol{\nabla}\cdot\boldsymbol{\varphi}_h) - (r_1 \delta p^{s,k+1}_{h,pen}, \boldsymbol{\nabla}\cdot\boldsymbol{\varphi}_h) = 0 \quad \forall \boldsymbol{\varphi}_h \in \mathbf{S}^t\,. \end{aligned} \tag{25}$$

where $\partial_t(\tilde{\mathbf{v}}^{\cdot}, \cdot)$ is the Eulerian time discretization of the velocity field defined by

$$\partial_t(\tilde{\mathbf{v}}^s_h, \boldsymbol{\psi}_h) = \frac{\rho^s}{\Delta t}(\tilde{\mathbf{v}}^{s,n+1}_h, \boldsymbol{\psi}_h) - \frac{\rho^s}{\Delta t}(\tilde{\mathbf{v}}^{s,n}_h, \boldsymbol{\psi}_h)\,. \tag{26}$$

The operator $c(\tilde{\mathbf{v}}^f_h, \boldsymbol{\phi}_h)$ is the fluid advection term modified by the ALE correction as

$$\begin{aligned} c(\tilde{\mathbf{v}}^f_h, \boldsymbol{\phi}_h) \;&= a(\tilde{\mathbf{v}}^{f,n+1}_h, \boldsymbol{\phi}_h) - \left(\rho^f \left(\boldsymbol{\nabla}\cdot\mathbf{w}^{f,n}_h\right)\tilde{\mathbf{v}}^{f,n+1}_h, \boldsymbol{\phi}_h\right) \\ &+ \rho^f \left(\left(\tilde{\mathbf{v}}^{f,n}_h - \mathbf{w}^{f,n}_h\right)\cdot\boldsymbol{\nabla}\tilde{\mathbf{v}}^{f,n+1}_h, \boldsymbol{\phi}_h\right) - \int_{\Gamma^f_N} \mathbf{h}^f \cdot \boldsymbol{\phi}_h \, d\gamma \end{aligned} \tag{27}$$

and $d^s(\tilde{\mathbf{v}}_h^s, \boldsymbol{\psi}_h)$ is

$$d^s(\tilde{\mathbf{v}}_h^s, \boldsymbol{\psi}_h) = \Delta t\, a^s(\tilde{\mathbf{v}}_h^{s,n+1}, \boldsymbol{\psi}_h) + a^s(\mathbf{u}_h^{s,n}, \boldsymbol{\psi}_h) - \int_{\Gamma_N^s} \mathbf{h}^s \cdot \boldsymbol{\psi}_h \, d\gamma \,. \tag{28}$$

The update of the penalty correction is obtained by using

$$\delta p_{h,pen}^{k+1,n+1} = \delta p_{h,pen}^{k,n+1} + r_2(\boldsymbol{\nabla} \cdot \tilde{\mathbf{v}}_h^k) \,, \tag{29}$$

where r_1, r_2 are real values that satisfy the following constraint [20]

$$0 < r_1 < 2r_2 \,. \tag{30}$$

It is important to remark that in case of large penalty values the numerical convergence may deteriorate quickly [20]. In order to accelerate the convergence a projection step can be introduced. The projector algorithm computes the L^2 orthogonal projection of $\tilde{\mathbf{v}}_h^{n+1}$ onto the space of divergence free vectors fields, which reads

$$\begin{aligned} \rho \frac{\mathbf{v}^{n+1} - \tilde{\mathbf{v}}^{n+1}}{\Delta t} + \boldsymbol{\nabla} \delta \tilde{p}_{proj}^{n+1} = 0 \qquad & \text{in} \quad \Omega_t \,, \\ \boldsymbol{\nabla} \cdot \mathbf{v}^{n+1} = 0 \qquad & \text{in} \quad \Omega_t \,. \end{aligned} \tag{31}$$

Now we reformulate this Darcy system by taking the divergence of the first expression in order to obtain a Poisson problem for $\delta \tilde{p}_{proj}^{n+1}$. The pressure variations $\delta \tilde{p}_{h,proj}^{f,n+1}$ and $\delta \tilde{p}_{h,proj}^{s,n+1}$ are the solutions of the following weak elliptic problem

$$(\boldsymbol{\nabla} \delta \tilde{p}_{h,proj}^{f,n+1}, \boldsymbol{\nabla} \zeta)_{\Omega_n^f} + (\boldsymbol{\nabla} \delta \tilde{p}_{h,proj}^{s,n+1}, \boldsymbol{\nabla} \zeta)_{\Omega_n^s} = -\frac{\rho^f}{\Delta t} (\boldsymbol{\nabla} \cdot \tilde{\mathbf{v}}^{f,n+1}, \zeta)_{\Omega_n^f} - \frac{\rho^s}{\Delta t} (\boldsymbol{\nabla} \cdot \tilde{\mathbf{v}}^{s,n+1}, \zeta)_{\Omega_n^s} \,, \tag{32}$$

for all ζ in $\mathbf{H}^1_{\Gamma_0}$, where Γ_0 is the region where the pressure is imposed. In the rest of the boundary $\Gamma - \Gamma_0$, where normal velocity are imposed, homogeneous Neumann boundary conditions must be applied. After solving these two sub-problems we project the predicted velocity onto the space of solenoidal vector fields as

$$\mathbf{v}_h^{f,n+1} = \tilde{\mathbf{v}}_h^{f,n+1} - \frac{\Delta t}{\rho^f} \boldsymbol{\nabla} \delta \tilde{p}_{h,proj}^{f,n+1} \qquad \text{in} \quad \Omega_t^f \,, \tag{33}$$

$$\mathbf{v}_h^{s,n+1} = \tilde{\mathbf{v}}_h^{s,n+1} - \frac{\Delta t}{\rho^s} \boldsymbol{\nabla} \delta \tilde{p}_{h,proj}^{s,n+1} \qquad \text{in} \quad \Omega_t^s \,, \tag{34}$$

and update both the pressure $p_h^{f,n+1}$ and $p_h^{s,n+1}$

$$p_h^{f,n+1} = p_h^{f,n} + \delta p_{h,proj}^{f,n+1} + \delta p_{h,pen}^{f,n+1} \quad \text{in} \quad \Omega_t^f \,, \tag{35}$$

$$p_h^{s,n+1} = p_h^{s,n} + \delta p_{h,proj}^{s,n+1} + \delta p_{h,pen}^{s,n+1} \quad \text{in} \quad \Omega_t^s \,. \tag{36}$$

We remark that the projection pressure field, on the boundary where the velocity field is imposed, has vanishing normal pressure derivative instead of the normal component of the Cauchy stress. This leads to a wrong representation of the pressure and stress components for an incompressible solid material which tends to reduce the bending displacement field. The iterative penalty correction is meant to reduce this boundary error and provide a stable behavior. The detailed description of the implementation of the penalty projection algorithm that has been used in this work can be found on [9].

4 Numerical Results

In this Section we describe the ventricle model used in this work and compare the results obtained with the fully coupled algorithm and those obtained with the penalty-projection algorithm for some penalty iteration cycles.

4.1 Ventricle Model

The domain Ω consists of a fluid and a solid region denoted by Ω_f and Ω_s, respectively. The overall dimensions of the geometrical model, shown in Fig. 2, are taken from a real standard heart ventricle. On the top of the fluid domain Ω_f there are two ventricle valves: the inlet and outlet valve. The heart valves are taken into account by using a simplified dynamical model. In order to reproduce the close-open valve movement we add a pressure loss term in (4) as $\Delta p = \beta \cdot \mathbf{v}|\mathbf{v}|$. Let Ω_i be the valve inlet region Ω_i defined as

$$\Omega_i = \{\mathbf{x} \in R^3 | \left[1 + \left(3 + \frac{z - 0.046}{0.04}\right)\left(\frac{y}{0.1} - 0.35 - 0.08\frac{z - 0.046}{0.04}\right)\right] 0.1|x|^{2.5}$$
$$+ \left|\frac{y}{0.1} - 0.32 - 0.08\left(\frac{z - 0.046}{0.04}\right)\right|^{2.5} - 0.005\left(1 + \frac{z - 0.046}{0.04}\right) < 0\} \tag{37}$$

where β is defined by the relation

$$\begin{cases} \beta = 0 & \mathbf{v} \leq 0 \\ \beta = 10^4 & \mathbf{v} > 0 \end{cases} . \tag{38}$$

The valve outlet region Ω_o is defined by

Fig. 2 Ventricle geometrical model

$$\Omega_o = \{\mathbf{x} \in R^3 | \left(\frac{y}{0.1} + 1.05\right)\left(\frac{|x|}{0.075}\right)^{2.5} + \left[\left(\frac{|y|}{0.1} + 0.05\right)0.9\right]^{2.5} - 0.01\left(1 + \frac{z-0.046}{0.025}\right) < 0\}, \tag{39}$$

where β is defined by

$$\begin{cases} \beta = 0 & \mathbf{v} > 0 \\ \beta = 10^4 & \mathbf{v} \leq 0 \end{cases}. \tag{40}$$

The inlet and outlet regions Ω_i and Ω_o are shown in the left part of Fig. 3. In the remaining part of the top region of the domain, shown in the right part of Fig. 3, we suppose that the value of β is 10^4. In this region we suppose that the fluid cannot

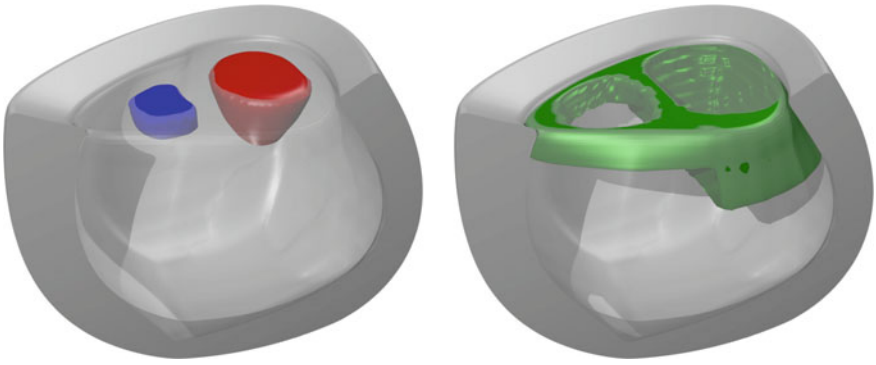

Fig. 3 Valve zones with reverse motion (on the left) and total occlusion (on the right)

flow because the valve is closed by its contraction and keep a constant pressure load with $p = 12{,}000$ Pa. The ventricle contraction is taking into account through a time dependent young modulus E_0 and a fixed ν value of 1/2. In particular we consider

$$E = \begin{cases} E_0 \frac{E_r - 1}{t^{*2}} t^2 + E_0 & t < t^* \\ E_0 (E_r - 1) e^{(t - t^*)} + E_0 & t \geq t^* \end{cases} \tag{41}$$

where E_0 is the young modulus of the tissues in the relaxed state, set to 2×10^5 *Pa*. E_r, which is set to 2, is the ratio between the Young modulus in the contracted state and E_0. The temporal parameter t, which is 0 at the beginning of the contraction, becomes 1 at the end of the pulse cycle. The ratio between the contraction and the relaxation period is defined as t^*. In this example we assume that the whole cardiac cycle has a duration of 1*s* and $t^* = 0.3$.

4.2 FSI Ventricle Simulations

In this Section we presents the numerical results obtained with the fully coupled algorithm. The solution overview at $t = 1, 1.4, 1.6$ and 1.86 s is shown in Fig. 4. We can notice that in the first two time steps, due to the ventricle contraction, the pressure inside the chamber is greater than the boundary pressure load and the fluid exits

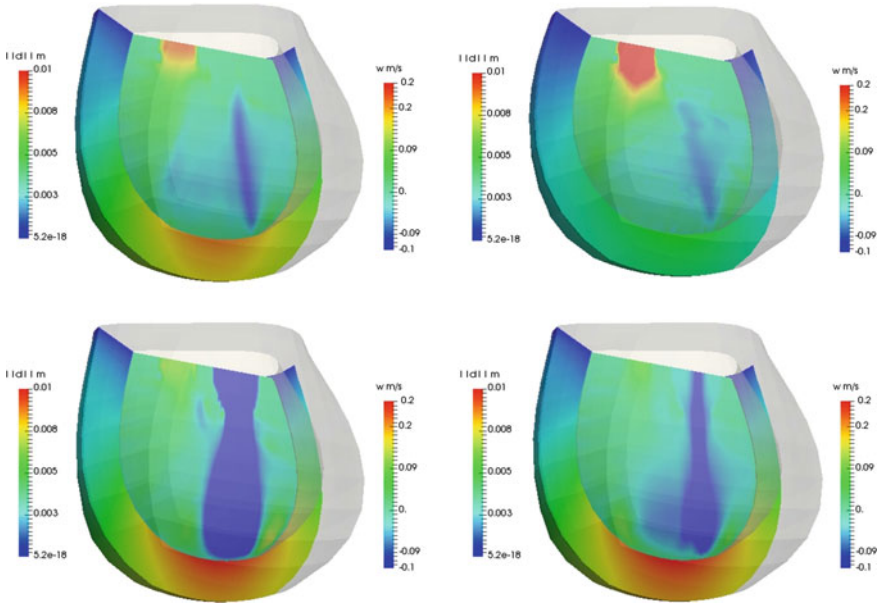

Fig. 4 Solution overview, obtained with the fully coupled algorithm, at $t = 1, 1.4, 1.6$ and 1.86 s

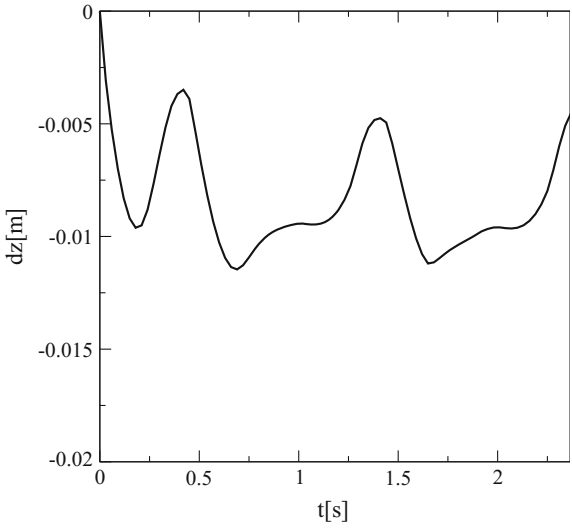

Fig. 5 Central point displacement over time

the fluid domain from the outflow region while it is blocked from flowing through the inlet by the values of β assumed in this valve region. When the young modulus reaches a low value, the last two steps of Fig. 4, we have the opposite: the pressure inside the chamber is lower than the boundary load and the fluid flows inside the domain only from the inlet region. We remark that these results are obtained The movement of the point at the bottom of the fluid region as a function of time is shown in Fig. 5. These computations, performed with the monolitic algorithm, are very expensive and the simulations can run for days even on multiprocessor clusters.

In order to reduce cpu time we perform the same simulation using the a penalty-projection algorithm based on FSI pressure-velocity uncoupling with different number of penalty iterations. The penalty-projection algorithm used is described in [9]. In Fig. 6 the axial displacement over time of the Fluid Structure interface point located at the bottom of the fluid domain is shown for different cases. The curve A is the displacement obtained with the fully coupled algorithm. The curve B, C and D are obtained with penalty value of 1/dt and with 0, 1 and 2 penalty iterations, respectively. With a further increase of the penalty iteration number the results obtained with the penalty projection algorithm are equal to the ones obtained with the fully coupled algorithm and the displacement of the reference point over time is again the curve A of Fig. 6. However the FSI pressure-velocity splitting can speed up the computation of a factor ten and more resources can be used to describe the ventricle geometry in details.

In Table 1 we report the time, needed by the coupled and decoupled algorithm, for solving a single time step of the problem described in the previous Sections in different cases. In particular we report the computational cost obtained with two computational grids, the first (Case 1) characterized by 66511 and the second (Case 2), obtained with a middle point refinement of the first one, characterized by 522469 nodes. From the first to the second case the number of unknowns of the problem

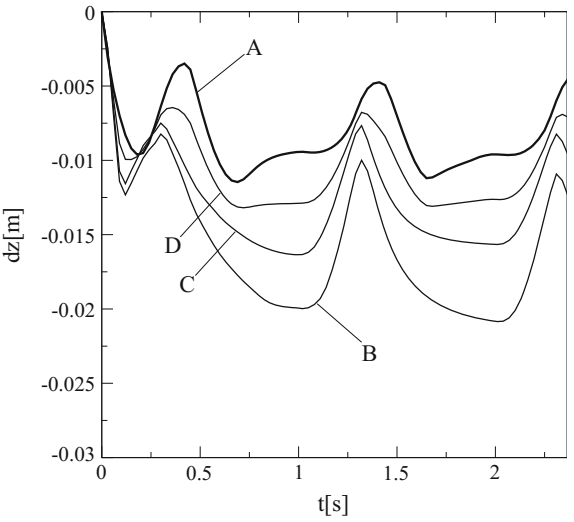

Fig. 6 Bottom fluid structure interface point displacement as a function of time for different cases. Curve *A* obtained with the fully couple algorithm and with the penalty projection scheme with 10 iterations. Curve *B*, *C* and *D* are obtained with the penalty projection algorithm with 0, 1 and 2 iterations

Table 1 Computational cost of a single time step iteration in the case of coupled and decoupled algorithm for different computational grids

	#Nodes	#Dofs	Coupled algorithm (s)	Decoupled algorithm (s)
Case 1	$\sim 7 \times 10^4$	$\sim 2 \times 10^5$	~80	~18
Case 2	$\sim 5 \times 10^5$	$\sim 2 \times 10^6$	~710	~67

(dofs) goes from 208797 to 1700429. From that Table we can notice that as we increase the number of dofs, the time reduction provided by the decoupled algorithm increases as well.

5 Conclusion

In this work a penalty projection algorithm, which provides an huge reduction of the computational cost for the solution of a monolithic fluid structure interaction problem, has been tested. A simplified geometrical and mathematical model for the ventricle contraction has been introduce and the results obtained with the fully coupled algorithm has been compared with the ones obtained with the penalty projection scheme. The results have shown that increasing the number of penalty iterations the solution, obtained with the splitting algorithm, leads to the same solution proving the consistency of the penalty projection method. We remark that in this work a simplified computational grid has been used in order to perform the fully coupled simulation. This coupled algorithm can not be used in realistic computational grids while the splitting scheme can easy deal with complex meshes without loosing the stability provided by the monolithic approach.

References

1. S. Turek, J. Hron, M. Madlik, M. Razzaq, H. Wobker, J. Acker, *Numerical Simulation and Benchmarking of a Monolithic Multigrid Solver for Fluid-structure Interaction Problems with Application to Hemodynamics* (Springer, 2010)
2. E. Aulisa, S. Manservisi, P. Seshaiyer, A multilevel domain decomposition approach to solving coupled applications in computational fluid dynamics. Int. J. Numer. Methods Fluids **56**(8), 1139–1145 (2008)
3. M. Bukač, S. Čanić, B. Muha, A partitioned scheme for fluid-composite structure interaction problems. J. Comput. Phys. **281**, 493–517 (2015)
4. P. Causin, J.-F. Gerbeau, F. Nobile, Added-mass effect in the design of partitioned algorithms for fluid-structure problems. Comput. Methods Appl. Mech. Eng. **194**(42), 4506–4527 (2005)
5. C. Michler, S. Hulshoff, E. Van Brummelen, R. De Borst, A monolithic approach to fluid-structure interaction. Comput. Fluids **33**(5), 839–848 (2004)
6. L. Formaggia, A. Quarteroni, A. Veneziani, *Cardiovascular Mathematics: Modeling and Simulation of the Circulatory System*, vol. 1 (Springer Science & Business Media, 2010)
7. F. Nobile, C. Vergara, An effective fluid-structure interaction formulation for vascular dynamics by generalized robin conditions. SIAM J. Sci. Comput. **30**(2), 731–763 (2008)
8. E. Aulisa, S. Manservisi, P. Seshaiyer, A computational multilevel approach for solving 2d navier-stokes equations over non-matching grids. Comput. Methods Appl. Mech. Eng. **195**(33), 4604–4616 (2006)
9. D. Cerroni, S. Manservisi, A penalty-projection algorithm for a monolithic fluid-structure interaction solver. J. Comput. Phys. **313**, 13–30 (2016)
10. R.A. Adams, J.J. Fournier, *Sobolev Spaces*, vol. 140 (Academic press, 2003)
11. P.G. Ciarlet, *The Finite Element Method for Elliptic Problems*, vol. 40 (Siam, 2002)
12. P. Sackinger, P. Schunk, R. Rao, A newton-raphson pseudo-solid domain mapping technique for free and moving boundary problems: a finite element implementation. J. Comput. Phys. **125**(1), 83–103 (1996)
13. J. Donea, S. Giuliani, J. Halleux, An arbitrary lagrangian-eulerian finite element method for transient dynamic fluid-structure interactions. Comput. Methods Appl. Mech. Eng. **33**(1), 689–723 (1982)
14. P. Le Tallec, J. Mouro, Fluid structure interaction with large structural displacements. Comput. Methods Appl. Mech. Eng. **190**(24), 3039–3067 (2001)
15. D. Cerroni, S. Manservisi, F. Menghini, A new moving mesh technique for monolithic multigrid fluid-structure interaction solver. Recent Adv. Civil Eng. Mech. **1**, 146–152 (2014)
16. O.C. Zienkiewicz, R.L. Taylor, O.C. Zienkiewicz, R.L. Taylor, *The Finite Element Method*, vol. 3 (McGraw-hill, London, 1977)
17. A. Guittet, M. Theillard, F. Gibou, A stable projection method for the incompressible navier-stokes equations on arbitrary geometries and adaptive quad/octrees. J. Comput. Phys. **292**, 215–238 (2015)
18. A.J. Chorin, Numerical solution of the navier-stokes equations. Math. Comput. **22**(104), 745–762 (1968)
19. C. Wang, J.D. Eldredge, Strongly coupled dynamics of fluids and rigid-body systems with the immersed boundary projection method. J. Comput. Phys. **295**, 87–113 (2015)
20. S.C. Brenner, R. Scott, *The Mathematical Theory of Finite Element Methods*, vol. 15 (Springer Science & Business Media, 2008)
21. M. Jobelin, C. Lapuerta, J.-C. Latché, P. Angot, B. Piar, A finite element penalty-projection method for incompressible flows. J. Comput. Phys. **217**(2), 502–518 (2006)
22. J. Guermond, P. Minev, J. Shen, An overview of projection methods for incompressible flows. Comput. Methods Appl. Mech. Eng. **195**(44), 6011–6045 (2006)

The Biomechanical Rupture Risk Assessment of Abdominal Aortic Aneurysms—Method and Clinical Relevance

T. Christian Gasser

Abstract An Abdominal Aortic Aneurysm (AAA) is an enlargement of the infrarenal aorta, a serious condition whose clinical treatment requires assessing its risk of rupture. This chapter reviews the current state of the Biomechanical Rupture Risk Assessment (BRRA), a non-invasive diagnostic method to calculate such AAA rupture risk, and emphasizes on constitutive modeling of AAA tissues. Histology and mechanical properties of the normal and aneurysmatic walls are summarized and related to proposed constitutive descriptions. Models for the passive vessel wall as well as their adaptation in time are discussed. Reported clinical BRRA validation studies are summarized and their clinical relevance is discussed. Despite open problems in AAA biomechanics, like robust modeling vascular tissue adaptation to mechanical and biochemical environments, a significant body of current validation evidence suggests integrating the BRRA method into the clinical decision-making process.

1 Introduction

Abdominal Aortic Aneurysm (AAA) disease is a serious condition and causes many deaths, especially in men above the age of 65. Progressive treatment i.e. either surgical or endovascular AAA repair, cannot (and should not) be offered to all patients. AAA repair is recommended if AAA rupture risk exceeds the interventional risks. While the hospital-specific treatment risks are reasonably predictable, assessing AAA rupture risk for individual patients remains the bottle neck in clinical decision making.

According to the current clinical practice AAA rupture risk is assessed by the aneurysm's largest transverse diameter and its change over time. Specifically, AAA repair is generally recommended if the largest diameter exceeds 55 mm or if it grows faster than 10 mm per year [1, 2]. The majority of clinicians follow this advice (see

T.C. Gasser (✉)
KTH Royal Institute of Technology, Stockholm, Sweden
e-mail: gasser@kth.se

P. Wriggers and T. Lenarz (eds.), *Biomedical Technology*, Lecture Notes in Applied and Computational Mechanics 84, DOI 10.1007/978-3-319-59548-1_13

the performed survey amongst vascular clinicians at http://www.vascops.com/files/survey2006.pdf) and use both indication criteria for clinical decision making. However, this kind of somewhat crude rupture risk assessment is the subject of much debate and AAAs with a diameters of less than 55 mm can and do rupture (even under surveillance), whereas many aneurysms larger than 55 mm never rupture [3, 4]. Most importantly, due to the poor specificity and sensitivity of the diameter criterion, the cost-effectiveness of patient treatment is not optimal. A more individualized AAA repair indication would be of great help. The drawbacks of the currently used AAA repair indicators triggered considerable research in the field and, besides the diameter and its change over time, many other clinical risk factors have been proposed. The Biomechanical Rupture Risk Assessment (BRRA) being one of such methods [5–12].

2 The Basic Concept of the Biomechanical Rupture Risk Assessment (BRRA)

Raising the blood pressure leads to local stress concentrations in the wall, and, if high enough, starts damaging the wall at specific spots which weakens/softens the vessel wall. Because of the compromised biological integrity of aneurysm tissue [13] and/or the supra-physiological wall stress level, healing cannot fully repair these micro defects. Consequently, the vessel wall continues to accumulate weak links. If the damage level, i.e. the numbers of defects per tissue volume exceeds a certain threshold, micro defects join each other and form macro-defects. Finally, a single macro-defect may propagate and rupture the vessel through the whole thickness, i.e. the AAA ruptures. Different engineering concepts are known to study initiation and propagation of failure (macro-defects) in materials. One of the simplest approaches is introducing a risk factor by relating local wall stress and local wall strength, i.e. introducing a Wall Rupture Index WRI= σ/σ_Y, where σ and σ_Y denote von Mises stress and tissue strength, respectively. The WRI is calculated all over the aneurysmatic sack, i.e. between the level of the infrarenal arteries and the aortic bifurcation. Finally, the peak of WRI, Peak Wall Rupture Index (PWRI) say, is extracted and serves as BRRA risk index.

2.1 Work Flow and Diagnostic Information

In order to implement the BRRA in the clinical work flow, a robust, fast, and operator-insensitive simulation pipeline is required. As an example Fig. 1a illustrates the BRRA work flow using the A4clinics software (VASCOPS GmbH, Graz, Austria). During an *Image Segmentation* step an accurate three-dimensional model of the aneurysm is derived by segmenting luminal and exterior surfaces from

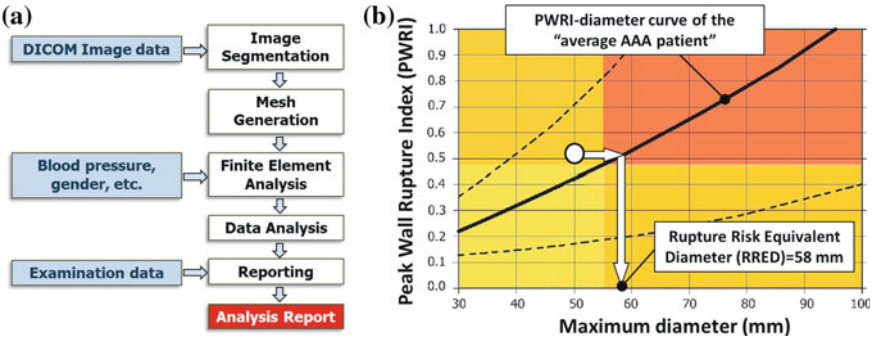

Fig. 1 **a** Work flow of the Biomechanical Rupture Risk Assessment (BRRA) of Abdominal Aortic Aneurysms (AAAs) using the A4clinics software (VASCOPS GmbH, Graz, Austria). **b** Definition of the Rupture Risk Equivalent Diameter (RRED) for an individual AAA patient. The RRED denotes the diameter of an average AAA that experiences the same Peak Wall Rupture Index (PWRI) as the individual case. Image taken from [76]

Computed Tomography-Angiography (CT-A) images in DICOM (Digital Imaging and Communications in Medicine) format [14]. In CT-A images, the interface between the vessel wall and the Intra-luminal thrombus (ILT) tissue (a pseudo-tissue seen in the majority of AAAs [15]) cannot be detected, such that the mean-population AAA wall thickness is pre-defined. Then, a *Mesh Generation* step uses the segmented surfaces and meshes vessel wall and ILT by pure hexahedral and hexahedral-dominated elements, respectively [14]. During the *Finite Element Analysis* step the user sets the patient-individual mean arterial pressure and other characteristics, and the wall stress σ that is required to carry the blood pressure for the individual aneurysm shape and ILT topology, is computed. This calculation uses mean-population elastic tissue properties and applies mixed Q1P0 finite elements [16] to prevent volume locking. Simultaneously the wall stress is locally related to an estimated wall strength σ_Y, which in turn defines the WRI= σ/σ_Y all over the aneurysmatic sack. Finally, a *Data Analysis* step extracts key geometrical and biomechanical information, which together with other examination input is compiled by a *Reporting* step into an Analysis Report. All steps can be executed by clinical users and the whole process, i.e. from reading the CT-A images to receiving the *Analysis Report*, takes about 10–20 min using standard laptops or PCs.

In order to assess the relative risk of rupture with respect to the mean population AAA patient, the Rupture Risk Equivalent Diameter (RRED) is introduced, see Fig. 1b. The RRED reflects the size of the average aneurysm that experiences the same PWRI as the individual case [7]. This is done by translating the individual biomechanical analysis into a diameter risk, i.e. the currently applied risk stratification parameter in the clinics. The RRED connects the individual biomechanical assessment with the outcome of large diameter-based clinical trials, like the small UK aneurysm trial [2, 7].

2.2 Complexity Versus Uncertainty of Model Predictions

Naturally, every model involves making modeling assumptions (see Fig. 2 for the BRRA) and reflects the real object always only up to a certain degree of completeness (see A. Einstein: "Everything should be made as simple as possible, but no simpler". http://quoteinvestigator.com/2011/05/13/einstein-simple/#more-2363), and a model should be verified and validated to the degree needed for the model's intended purpose or application [17]. *For a BRRA simulation the required level of modeling details can only be defined in the context of the clinical outcome.* Consequently, a good model will only include modeling details that improve the clinical outcome and disregard all the other information that reflects our current knowledge about the biomechanical problem. For example, the required degree of complexity of the aneurysm wall model (isotropic vs. anisotropic modeling; single phase vs. multiphase modeling; constant wall thickness vs. variable wall thickness; etc.) used by the BRRA can only be evaluated in relation to the wall model's implication on the clinical outcome—*a complex model does not necessarily give better diagnostic information*.

Wall stress computations are not particularly sensitive to constitutive descriptions [10, 18] as long as the wall's low initial stiffness, followed by its strong stiffening at higher strains, is captured [19]. Similarly, despite the fact that ITL tissue is highly porous [20, 21], previous biomechanical studies have demonstrated that a single phase model predicts AAA wall stress with sufficient accuracy [22, 23]. In contrast, wall stress predictions are sensitive to AAA geometry, such that an accurate three-dimension AAA representation is critically important for accurate predictions. Finally, the Finite Element Method (FEM) solves a discretized biomechanical model, and also the discretization error needs to be assessed in relation to the uncertainty of the input information.

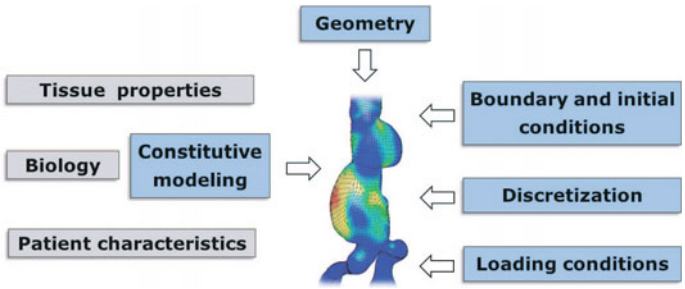

Fig. 2 Modeling assumptions and input uncertainties entering the Biomechanical Rupture Risk Assessment (BRRA) of Abdominal Aortic Aneurysms (AAAs). The validity of each assumption needs to be validated with respect to the clinical outcome of the BRRA prediction, i.e. a measurable benefit of the computed diagnostic information. Image taken from [76]

3 AAA Tissue Characterization

The characterization of vascular tissue is an active field of research and numerous studies with application to AAA tissue have been reported. AAA wall pathology is driven by the complex interaction of biochemical and biomechanical events [24], such that AAA tissue characterization requires multi-disciplinary investigations. Specifically, the development of robust and reliable constitutive modeling asks for profound histological and mechanical understandings of AAA tissues.

3.1 Properties of the Normal Aorta

Histology and morphology. In the arterial wall, ExtraCellular Matrix (ECM) components (elastin, collagen, ProteoGlycans (PGs), fibronectin, fibrilin, etc.) ensure the vessel's structural integrity, whereas cells (endothelial cells, Smooth Muscle Cells (SMC), fibroblasts, myofibroblasts, etc.) maintain its metabolism. Specifically, the proteins elastin and collagen, and their interactions, almost entirely define the vessel's passive mechanical properties [25].

Collagen fibrils organize into suprafibrilar structures (see Fig. 3), where PG bridges seem to provide interfibrillar load transition [26–29]. Physiological maintenance of the collagen structure relies on a delicate turnover at a normal half-life time of 60–70 days [30] between degradation (mainly through Matrix MetalloProteinases (MMPs)) and synthesis by cells like SMCs, fibroblasts and myofibroblasts, [31].

Elastin functions in partnership with collagen and mainly determines the mechanical properties of arterial tissue at low strain levels [25]. In the vessel wall, elastin is predominantly seen in the media, within which it is organized in sheets (71%), fibers (27%) and radial struts (2%) [32], see Fig. 3. Elastin is synthesized and secreted by vascular SMCs and fibroblasts, a process that normally stops soon after puberty once the body has reached maturity. Elastin degradation (by selective MMPs known as elastase) is related to several diseases (atherosclerosis, Marfan syndrome, Cutis laxa, etc.), but also important for many physiological processes such as growth, wound healing, pregnancy and tissue remodeling [33]. Finally, SMCs at the differentiated/contractile phenotype equip the vessel wall with active properties for quickly adjusting vessel caliber and stiffness.

At the organ level the vessel wall is composed of intimal, medial and adventitial layers, see Fig. 3. The intima is the innermost layer and comprises primarily of a single layer of endothelial cells lining the arterial wall. The media is the middle layer of the artery and consists of a complex three-dimensional network of SMCs, elastin and collagen fibers and fibrils. These structural components are preferentially aligned along the circumferential vessel direction [32, 34] and organized in repeating MLUs of 13–15 μm thickness [32, 35, 36]. The media's discrete laminated architecture is gradually lost towards the periphery and hardly present in muscular arteries. Finally, the adventitia is the outermost layer of the artery and consists mainly of fibroblasts

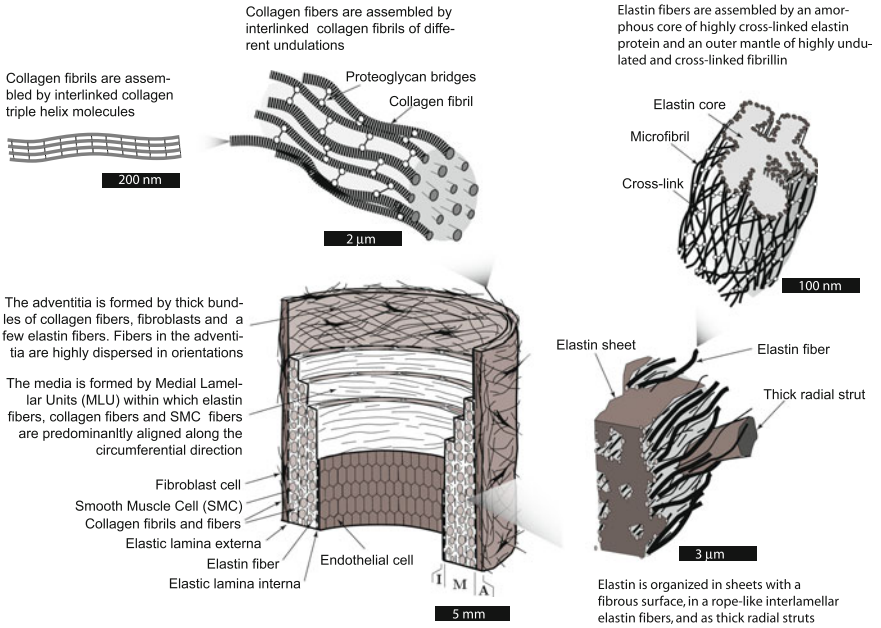

Fig. 3 Histological idealization of an artery. It is composed of three layers: intima (*I*), media (*M*), adventitia (*A*). The intima is the innermost layer consisting of a single layer of endothelial cells, a thin basal membrane and a subendothelial layer. Smooth Muscle Cells (SMCs), elastin and collagen are key mechanical constituents in the media and are arranged in a number (up to 60 in the aorta) of 13–15 µm thick Medial Lamellar Units (MLUs). In the adventitia the primary constituents are collagen fibers and fibroblasts. Collagen fibers with a thickness in the range of micrometers are assembled by collagen fibrils (50–300 nm thick) of different undulations. Load transition between collagen fibrils is maintained by Proteoglycan (PG) bridges. Elastin fibers with a thickness of hundreds of nanometers are formed by an amorphous core of highly cross-linked elastin protein that is encapsulated by 5 nm thick microfibrils. Elastin fibers are organized in thin concentric elastic sheets (about 1–2 µm thick), in a rope-like interlamellar elastin fibers (about 100–500 nm thick), and as thick radial struts (about 1.5 µm thick). Image taken from [135]

and fibrocytes and ECM of thick bundles of collagen fibrils. The strong adventitial layer protects the biologically vital medial layer from overstretching and anchors the artery to its surrounding.

Mechanical properties and experimental observations. The vessel wall is a mixture of solid components (elastin, collagen, SMCs, PGs, etc.) and water, much of which is not particularly mobile but bound to PGs, elastin, and the like. In-vivo the volumetric strain is three orders of magnitude smaller than the circumferential strain [37], such that, for many mechanical problems, it seems reasonable that the artery wall can be regarded as an incompressible homogenized solid.

The normal (non-calcified) artery is highly deformable and exhibits anisotropic [38, 39] and nonlinear [40] stress versus strain response. It stiffens typically at around the physiological strain level in response to the recruitment of the embedded wavy

collagen fibrils [25, 41, 42]. The vessel's load-free state is determined by a residual stress state [43], which biomechanical consequences are well discussed in the literature [44–47]. Clearly, residual stresses are multidimensional and circumferential [44, 47] as well as longitudinal [48] stresses have been reported in the load-free vessel. Arteries are axially pre-stretched, which seem to prevent their axial pulsation in the body [49].

Even when preconditioned, the aortic wall shows typical strain rate dependency like creep, relaxation and (almost frequency-independent [50]) dissipation under cyclic loading. Exposing vascular tissue to supra-physiological mechanical stresses rearranges the tissue's microstructure through irreversible deformations; damage-related effects [51, 52] and plasticity-related effects [52, 53] have been documented.

The level of vascular SMC activation or basal tone changes in response to biomechanical stimuli such as flow [54], pressure [55], circumferential and longitudinal stretching [56], hormonal stimuli, neural stimuli, and drugs. Finally, the normal vessel seems to follow the concept of homeostasis, i.e. it adapts to changes in the mechanical environment such that target mechanical properties are kept relatively constant. Specifically, target values for Wall Shear Stress (WSS) [57, 58], circumferential wall stress [59, 60] and axial stretch [61] have been shown to be regained after alterations.

3.2 Aneurysm-Related Alteration of the Aorta

AAAs are the end-result of irreversible pathological remodeling of the ECM [13, 62]. Specifically, the walls of larger AAAs show (i) degradation of the elastin, (ii) compensatory increased collagen synthesis and content, (iii) excessive inflammatory infiltration, and (iv) apoptosis of vascular SMC [13, 24, 63–65]. It is widely accepted that loss of elastin (and possibly SMC) triggers initial dilatation, while collagen turnover promotes enlargement and local wall weakening that eventually leads to AAA rupture [13].

With progressing aneurysm disease, the well-defined organization of normal vessel wall (Fig. 3), is lost; in larger AAA sometimes not even a distinct differentiation of individual vessel wall layers is possible. The entire wall seems to resemble a fibrous collagenous tissue similar to the adventitial layer in the normal aorta [34]. Blood flow within AAAs is complex [66] and triggers the formation of strong Vortical Structures (VSs) [67], which seem to play a critical role in blood coagulation [68] and could explain the formation of ILT. The ILT has solid-like properties [21, 69] and is composed of a fibrin mesh, traversed by a continuous network of interconnected canaliculi incorporated with blood cells, e.g., erythrocytes and neutrophils, aggregated platelets, blood proteins, and cellular debris [20, 70]. It creates an environment for increased proteolytic activity [71, 72] that may cause the observed weakening [73] and thinning [63] of the vessel wall.

Due to the above mentioned aneurysm-related proteolytic degeneration of structural proteins, an AAA wall mechanically differs significantly from a normal aorta.

Specifically, the AAA wall is less anisotropic, and, at the same time, the non-linearity of the stress-strain relation is more pronounced [38]. As already indicated by the AAA wall's inhomogeneous patho-histology [74], wall strength also shows significant inter- and intra-patient variability [75]. Strength values of the AAA wall reported in the literature are summarized elsewhere [76], and several factors that influence wall strength are already identified [77–81]. Such wall strength information is, with very few exceptions [82], usually derived from uniaxial tensile testing, which unfortunately does not reflect the biaxial in-vivo loading of the AAA wall.

Local variations of wall thickness and wall strength partly compensate for each other (wall strength and thickness are strongly negatively correlated [76]), and wall tension, i.e. stress multiplied by wall thickness, seems to be a more robust rupture risk predictor [83]. The inverse correlation between wall thickness and wall strength also justifies, to some extent, the typically-used uniform wall thickness for the BRRA computations. Consequently, FEM models that assume both, wall strength and wall thickness homogenous may give better results than models using an inhomogeneous wall thickness together with a homogenous wall strength.

3.3 Modeling Frameworks

While purely phenomenological approaches can successfully fit experimental data, such models show limited robustness for predictions beyond the strain range within which model parameters have been identified. Structural (or histo-mechanical) constitutive descriptions overcome such limitation and integrate histological and mechanical information of the arterial wall. Such formulations are not only more robust but also help to understand load carrying mechanisms in the vessel wall. Clearly, modeling assumptions need to fit the objective of the particular simulation [17], and for most applications the artery can be regarded as a single phase incompressible solid.

3.3.1 Descriptions for Passive Vessel Wall Properties

In arterial biomechanics, hyperelasticity of incompressible solids is a popular modeling approach in order to derive the Cauchy stress

$$\boldsymbol{\sigma} = 2\mathbf{F}\frac{\partial \psi(\mathbf{C})}{\partial \mathbf{C}}\mathbf{F}^T - p\mathbf{I} \tag{1}$$

from the strain energy density $\psi(\mathbf{C})$ in reference volume. Here, tissue deformation is determined by the right Cauchy-Green strain $\mathbf{C} = \mathbf{F}^T\mathbf{F}$, which is a function of the deformation gradient $\mathbf{F}$. The hydrostatic pressure p acts on the identity $\mathbf{I}$ and serves as a Lagrange parameter to enforce incompressibility. All constitutive information (mechanical and histological) is captured by a particular form of the strain energy

function ψ. The spatial elasticity tensor for a FEM implementation can be derived according to the classical framework of hyperelasticity [84].

Besides models originally proposed for rubber [85, 86], constitutive descriptions tailored for vascular tissue include exponential terms in the strain energy ψ [87, 88] and account for material anisotropy [89–101]. The stress in the wall of inflated structures like the AAA is mainly determined by its geometry and the inflation pressure, such that validation results [10, 18, 102] indicated that a reduced Yeoh potential $\psi = c_1(I_1 - 3) + c_2(I_1 - 3)^2$ provided reasonable results. Here, $I_1 = \mathrm{tr}\mathbf{C}$ denotes the first invariant of the right Cauchy Green strain. Despite the Yeoh potential being inherently phenomenological, the parameter c_1 relates to elastin-dominated low strain properties, while c_2 determines the collagen-dominated large strain properties of the vessel wall. In the present study these parameters are set to capture mean-population AAA wall properties, i.e. $c_1 = 177.0$ kPa and $c_2 = 1881.0$ kPa [10].

Despite ILT tissue being much softer than the vessel wall, it can occupy large volumes and can have a significant structural impact. ILT was modeled by an Ogden-like strain energy function $\psi = c_0 \sum_{i=1}^{3}(\lambda_i^4 - 1)$, whose properties change from its luminal ($c_0 = 2.62$ kPa) to the abluminal ($c_0 = 1.73$ kPa) site [21]. Here, λ_i denote the principal stretches, and such structural response also matches experiential ILT data reported elsewhere [69].

3.3.2 Descriptions for Adaptive Vessel Wall Properties

From a mechanical perspective, aneurysm pathology tends towards a wall, within which collagen remains the only protein able to provide structural integrity [65]. Consequently, collagen (and its turnover) determines the properties of the AAA wall and motivates the application of the general theory of fibrous connective tissue [103] by integrating fibers of dispersed orientation. The superposition of such fibers determines the tissue's Cauchy stress

$$\boldsymbol{\sigma} = \frac{2}{\pi} \int_{\phi=0}^{\pi/2} \int_{\theta=0}^{\pi/2} \rho(\phi, \theta)\sigma(\lambda)\mathrm{dev}(\mathbf{m} \otimes \mathbf{m}) \cos\phi \mathrm{d}\phi \mathrm{d}\theta - p\mathbf{I} \,, \tag{2}$$

where the hydrostatic pressure p enforces incompressibility, and $\mathbf{m} = \mathbf{FM}/|\mathbf{FM}|$ denotes the spatial collagen fiber orientation; $\mathbf{M}$ is their orientation in the reference configuration. The spatial deviator operator is denoted by $\mathrm{dev}(\bullet) = (\bullet) - \mathrm{tr}(\bullet)\mathbf{I}/3$, and θ and ϕ are the azimuth and elevation angles, respectively. The orientation density function $\rho(\phi, \theta)$ reflects the orientation of collagen fibers in the reference configuration and integrates histological information into Eq. (2). In addition, the mechanics of the collagen fibers are captured by the Cauchy stress $\sigma(\lambda)$ of the individual fiber as a function of its stretch λ.

A collagen fiber is thought of to be assembled of numerous PG-interlinked and undulated collagen fibrils (see Fig. 3), which gradually engage according to a trian-

gular Probability Density Function (PDF) [104]. In addition, the first Piola-Kirchhoff stress versus stretch relation $T = c\lambda\log\lambda$ captures the mechanics of the approximately linear [105, 106] collagen fibrils [104]. In contrast to other formulations [107, 108], the triangular PDF combined with the selected stress versus stretch law, allowed an analytic integration of fibril engagement, fast enough to support organ-level AAA computations. The model exhibited the typically non-linear property of soft biological tissues [104], and accurately described in-vitro experimental data over a wide range of biaxial deformations of the normal aorta [109] and the AAA wall [34].

Finally, a neoHookean model $\psi = \mu(I_1 - 3)/2$ captured the constitution of the matrix, within which collagen fibers are embedded. Dependent on the progress of aneurysmal disease, such matrix contribution is almost negligible, but helped to stabilize the numerical computations.

Collagen turnover model. The present model assumes that cells (fibroblasts, myofibroblasts, SMCs) sense the state of strain and pre-stretch collagen fibrils prior to their deposition. This requires three distinct sub-models, denoted as *Sensing Model*, *Mass Turnover Model* and *Structure Update Model*, respectively.

The Sensing Model defined the physical quantity ξ that stimulates collagen synthesis, i.e. the production of new collagen. Specifically, the model assumed that collagen stretch tends towards its homeostatic value of λ_{ph} (a stretch at which 10% of the collagen fibrils are engaged [110]) by satisfying the optimality condition

$$\xi(\mathbf{M}) = \frac{\lambda(\mathbf{M})}{\lambda_{\text{ph}}}\frac{\overline{\rho}}{\rho} \to 1\,. \tag{3}$$

Here, ρ denotes the specific collagen density that aims at approaching the target density of $\overline{\rho}$. The use of $\overline{\rho}$ substituted the maximum collagen turnover rate, which was introduced previously [110]. It is emphasized that ξ depends on $\mathbf{M}$, i.e. the orientation of the particular collagen fiber in the reference configuration.

The Mass Turnover Model quantified the relation between the sensed stimulus $\xi(\mathbf{M})$ and the change of the specific collagen density, i.e. the relation between degraded $\dot{\rho}^-$ and synthesized $\dot{\rho}^+$ collagen density rates, respectively. Despite experimental data hinting towards a stretch-based degradation of collagen (see [111] and references therein), in the present model collagen degraded independently from the orientation $\mathbf{M}$ and according to $\dot{\rho}^- = -\eta\rho$, where η defines the time-scale of the degradation process. In contrast, collagen syntheses was related to the stimulus $\xi(\mathbf{M})$ and followed $\dot{\rho}(\mathbf{M})^+ = \eta\rho\xi(\mathbf{M})$.

Finally, the Structure Update Model specified how collagen was integrated/disintegrated into/from the existing collagen structure. The model assumed that collagen fibrils are disintegrated without changing their undulation characteristics, i.e. without changing their triangular PDF. In contrast synthesized collagen fibrils are integrated at a certain distribution of pre-stretches, i.e. according to a triangular PDF with pre-defined $\overline{\lambda}_{\text{min}}$ and $\overline{\lambda}_{\text{max}}$; details are reported elsewhere [110]. Note that the triangular PDF, which describes the deposited collagen also defines the above intro-

duced homeostatic stretch λ_{ph}. Specifically, for 10% of the collagen fibrils being engaged, this stretch reads $\lambda_{ph} = \overline{\lambda}_{min} + 0.224(\overline{\lambda}_{max} - \overline{\lambda}_{min})$ [110].

In order to ensure a time step Δt small enough to accurately integrate the outlined rate equations a 'look-ahead' technique was used. Specifically, the largest collagen density increment $\max[\dot{\rho}^-, \dot{\rho}^+]\Delta t$ over all Gauss points of all finite elements was used to control the time step through FEAP's *AUTO MATErial* command [112].

4 Clinical Validation

Prior to the implementation of the BRRA into the regular clinical workflow, its validity needs to be tested with respect to its specific simulation objective [17], i.e. the clinical value of the BRRA diagnosis. Specifically, it is not important that all underlying modeling assumptions (sub-models) reflect current knowledge (see Sect. 2.2), but the whole system needs to demonstrate an improvement over state-of-the-art clinical practice.

4.1 Quasi-static BRRA Computations

Quasi-static computations are based on CT-A image data at a single time point and used the purely passive AAA tissue descriptions detailed in Sect. 3.3.1.

Operator variability. Intra- and inter-operator variability of the A4clinics (VASCOPS GmbH, Graz, Austria) rupture risk assessment system has been tested in clinical environments [113, 114], and own (unpublished) data showing an intra-operator variability of 3.5% for PWRI predictions and of 1.5% for maximum diameter measurements. This high precision could only be achieved with active (deformable) image segmentation models, which are known to have sub-pixel accuracy [14, 115]. In contrast, other segmentation tools (like MIMICS, Materialise, Leuven, Belgium) apply low-level segmentation methods based on threshold approaches, which not only require intensive manual interactions but also leads to high operator variability of the results.

Retrospective comparison between ruptured and non-ruptured AAAs. The diagnostic value of the BRRA method has been studied for almost 20 years [5–12]. During such studies Peak Wall Stress (PWS) has been regularly shown to be higher in ruptured/symptomatic AAAs than in intact/non-symptomatic AAAs [116]. Integrating wall strength (based on a statistical model that correlates mechanical in-vitro tests with patient characteristics [117]) in the BRRA further improved its diagnostic value, i.e. led to an improved retrospective discrimination between ruptured and non-ruptured cases [6, 8]. For example, a size-adjusted comparison showed that the RRED was, on average, 14.0 mm larger in ruptured than in non-ruptured cases, see Fig. 4 taken from [7].

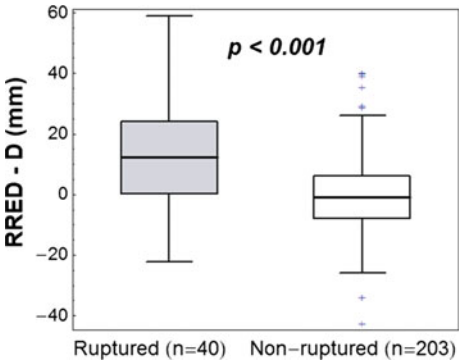

Fig. 4 Size-adjusted comparison between ruptured and non-ruptured Abdominal Aortic Aneurysms (AAAs). The comparison is based on the difference between Rupture Risk Equivalent Diameter (RRED) and the maximum transversal Diameter (*D*). The number of patients and the one-sided p-valuea are denoted by *n* and *p*, respectively. Image has been adjusted from [7]

Quasi-prospective comparison between ruptured and non-ruptured AAAs. CT-A scans of AAA patients that eventually experienced rupture (e.g., because the patient refused treatment) provide ideal data for a validation of the BRRA, and, to the best knowledge of the author, one such study has already been published [118]. The results showed that the BRRA method was able to significantly discriminate between AAAs that would rupture, when compared to a baseline-matched control group that did not rupture or was treated. The study [118] also found that in more than half of the cases, the rupture sites correlated with calculated pre-rupture PWRR locations. Consequently, the authors concluded that asymptomatic AAA patients with high PWRR and RRED values have an increased rupture risk.

Female versus male AAA rupture risk. Despite the fact that AAA prevalence is several times lower in females, female aneurysms rupture at smaller diameters [119–121]. Independently from this clinical observation, in-vitro failure testing of female AAA wall samples showed a lower strength compared to male samples [117, 122]. This gender-specific wall weakening effect is integrated into the PWRI, and the biomechanical risk of an average 53 mm large female AAA relates to an average 13.2 mm larger male case [7]. This BRRA simulation result nicely matches data from above mentioned clinical observations.

Correlation of PWRI and FDG-uptake. The vascular wall's biological activity can be evaluated indirectly through energy consumption, using 18-fluoro-deoxy-glucose (18F-FDG), as a tracer for positron emission tomography (PET) imaging [123]. Vascular cells respond to mechanical loads [24], such that an 18F-FDG-uptake can, in principle, be used to qualitatively explore wall stress. Despite the fact that the aneurysmatic wall loses its biological vitality [13, 64] PET-scan images still showed a considerable correlation between wall stress and an 18F-FDG-uptake [80, 124].

Correlation of PWRI and wall histopathology. Biomechanical stress is a common denominator of several aortic pathologies [24]. The complex geometry and morphology of AAAs cause highly inhomogeneous wall stress, and WRI correlated with wall's histopathology. Specifically, wall segments that in-vivo experienced high WRI showed fewer smooth muscle cells and elastic fibres, more soft and hard plaques, as well as a trend towards more fibrosis, when compared to wall samples at low WRI [74].

4.2 AAA Growth Prediction

Experimental AAA growth data was collected from analyzing CT-A images at at least two time points [125–127]. In a cohort of almost one hundred AAAs, diameter growth was continuously distributed all over the aneurysmal sac, reaching median absolute and relative peaks of 3.06 mm/year and 7.3 %/year, respectively [126]. Most interestingly, the local growth rate depended on the *local baseline diameter*, the *local ILT thickness* and (for wall segments not covered by ILT) also on the *local wall stress level*. Despite these complex influences, AAA growth was simulated based on the adaptive AAA wall description detailed in Sect. 3.3.2. For simplicity, and to avoid coupling with blood flow computations (in order to predict the formation of ILT [67, 68]), only cases with negligible or no ILT were considered; the expansion over time for an individual AAA is shown in Fig. 5. The performed growth simulation showed promising correlations with experimental data (for example in terms of coupled circumferential and longitudinal growth of the AAA wall), and structural instability (similar to the snap-through phenomena of an inflated rubber balloon) was observed at stress levels in the range of reported AAA wall strengths.

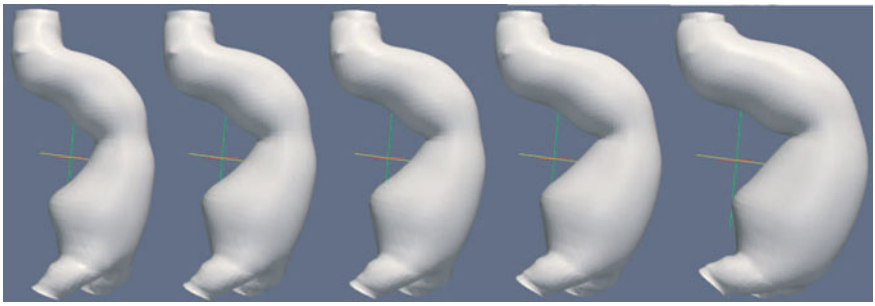

Fig. 5 Evolution of Abdominal Aortic Aneurysm (AAA) shape predicted by the adaptive AAA wall descriptions detailed in Sect. 3.3.2. The simulation covered four years of AAA growth and used parameters listed in Table 1

Table 1 Parameters used to simulate Abdominal Aortic Aneurysm (AAA) growth according to constitutive model described in Sect. 3.3.2

Parameter	Value	Description
μ	21.0 kPa	neoHookean parameter of the matrix
c	60.0 MPa	Collagen fibril stiffness
λ_{min}	1.045	Initial collagen minimum straightening stretch
λ_{max}	1.117	Initial collagen maximum straightening stretch
$\overline{\rho}$	0.4	Specific collagen target mass density
$\overline{\lambda}_{\text{min}}$	0.94	Minimum straightening stretch of deposited collagen
$\overline{\lambda}_{\text{max}}$	1.117	Maximum straightening stretch of deposited collagen
η	0.167 years	Collagen turn over rate

5 Conclusions

AAA wall pathology is driven by the complex interaction of biochemical and biomechanical events [24], such that a multi-disciplinary approach, involving also biomechanics, is needed to better understand and more effectively treat AAA disease. AAA rupture is a *local* event in the aneurysm wall and *global* parameters like the maximum diameter and its expansion over time frequently fail to predict individual risk for AAA rupture. In contrast the BRRA method assesses the wall's local mechanical loading and quantitatively integrates many known risk factors for AAA rupture like large size, asymmetric shape, female gender, and hypoxia due to a thick ILT layer. From a single CT-A scan, the biomechanical risk for rupture is best expressed by the RRED, which relates the individual case to the size of an average aneurysm at the same biomechanical risk for rupture. A significant and still growing body of validation evidence suggests using the RRED as an additional parameter for clinal decision making. Apart from other challenges, biomechanical predictions critically depend on an accurate constitutive description of the AAA tissue. Most important for the BRRA is to estimate AAA wall strength, which by itself is influenced by many factors. It is crucial in development of a constitutive model not only to understand the (passive) interaction of structural components within the vascular wall, but also how cells dynamically maintain such a structure.

Computational mechanics may advance our understanding of physiological and pathological mechanisms of organs, interaction between medical devices and biological material, drug delivery pathways, the interplay between structure and function of tissues, mechanotransduction and many others. Although to some extent traditional applied mechanics concepts are directly applicable to solve cardiovascular problems,

the inherent property of vascular tissue to adapt to mechanical and biochemical environments, remains a challenging modeling task. The normal vessel wall responds to mechanical stimuli [96], and seems to alter its mechanical properties towards approaching conditions for optimal mechanical operation [128]. However, cardiovascular diseases compromise such a mechanism and can lead to the formation of life-threatening aneurysms.

Despite modeling aneurysm development and progression being an active field of research [110, 129–133], most of these models are characterized by a high degree of phenomenology, and all of them are poorly validated. Consequently, significant further development is required to improve the reliability of growth and remodeling descriptions of the AAA wall. Modern image modalities allow the extraction of biomechanical functional information (gated CT-A, 3D ultrasound, Magnetic Resonance (MR) imaging) as well as biological activity (PET-scan) of the wall. Such information might provide valuable insights into growth-related effects and directly inform biomechanical AAA models, which in turn might further improve the sensitivity and specificity of the BRRA.

Many biomechanical models are overloaded with mechanical complexities and fail to address clinical problems adequately, and hence, do not enjoy clinician acceptance. Even after decades of biomechanics research the huge chasm between engineering and clinical approaches, that address the same cardiovascular problem, remains. A simulation model represents the real objective or process towards the desired degree of complexity, and should be guided by clinical needs rather than by integrating all available (biomechanical) information of the problem [17, 134]. Computational biomechanical models do not only require careful selection and combination of modelling assumptions but also rigorous clinical validation. Specifically, biomechanics researcher should be advised that *more complexity does not necessarily give better predictions.*

References

1. R.M. Greenhalgh, J.T. Powell, Endovascular repair of abdominal aortic aneurysm. N. Engl. J. Med. **358**, 494–501 (2008)
2. The U.K. Small, Aneurysm Trial Participants, Mortality results for randomised controlled trial of early elective surgery or ultrasonographic surveillance for small abdominal aortic aneurysms. Lancet **352**, 1649–1655 (1998)
3. R.C. Darling, C.R. Messina, D.C. Brewster, L.W. Ottinger, Autopsy study of unoperated Abdominal Aortic Aneurysms. Circulation **56**, 161–164 (1977) (II suppl)
4. S.C. Nicholls, J.B. Gardner, M.H. Meissner, H.K. Johansen, Rupture in small abdominal aortic aneurysms. J. Vasc. Surg. **28**, 884–888 (1998)
5. M.F. Fillinger, S.P. Marra, M.L. Raghavan, F.E. Kennedy, Prediction of rupture risk in abdominal aortic aneurysm during observation: wall stress versus diameter. J. Vasc. Surg. **37**, 724–732 (2003)
6. T.C. Gasser, M. Auer, F. Labruto, J. Swedenborg, J. Roy, Biomechanical rupture risk assessment of abdominal aortic aneurysms. Model complexity versus predictability of finite element simulations. Eur. J. Vasc. Endovasc. Surg. **40**, 176–185 (2010)

7. T.C. Gasser, A. Nchimi, J. Swedenborg, J. Roy, N. Sakalihasan, D. Böckler, A. Hyhlik-Dürr, A novel strategy to translate the biomechanical rupture risk of abdominal aortic aneurysms to their equivalent diameter risk: method and retrospective validation. Eur. J. Vasc. Endovasc. Surg. **47**, 288–295 (2014)
8. A. Maier, M.W. Gee, C. Reeps, J. Pongratz, H.H. Eckstein, W.A. Wall, A comparison of diameter, wall stress, and rupture potential index for abdominal aortic aneurysm rupture risk prediction. Ann. Biomed. Eng. **38**, 3124–3134 (2010)
9. J.P. Vande Geest, E.S. DiMartino, A. Bohra, M.S. Makaroun, D.A. Vorp, A biomechanics-based rupture potential index for abdominal aortic aneurysm risk assessment: demonstrative application. Ann. N.Y. Acad. Sci. **1085**, 11–21 (2006)
10. M.L. Raghavan, D.A. Vorp, Toward a biomechanical tool to evaluate rupture potential of abdominal aortic aneurysm: identification of a finite strain constitutive model and evaluation of its applicability. J. Biomech. **33**, 475–482 (2000)
11. M. Truijers, J.A. Pol, L.J. Schultzekool, S.M. van Sterkenburg, M.F. Fillinger, J.D. Blankensteijn, Wall stress analysis in small asymptomatic, symptomatic and ruptured abdominal aortic aneurysms. Eur. J. Vasc. Endovasc. Surg. **33**, 401–407 (2007)
12. A.K. Venkatasubramaniam, M.J. Fagan, T. Mehta, K.J. Mylankal, B. Ray, G. Kuhan, I.C. Chetter, P.T. McCollum, A comparative study of aortic wall stress using finite element analysis for ruptured and non-ruptured abdominal aortic aneurysms. Eur. J. Vasc. Surg. **28**, 168–176 (2004)
13. E. Choke, G. Cockerill, W.R. Wilson, S. Sayed, J. Dawson, I. Loftus, M.M. Thompson, A review of biological factors implicated in abdominal aortic aneurysm rupture. Eur. J. Vasc. Endovasc. Surg. **30**, 227–244 (2005)
14. M. Auer, T.C. Gasser, Reconstruction and finite element mesh generation of Abdominal Aortic Aneurysms from computerized tomography angiography data with minimal user interaction. IEEE T. Med. Imaging **29**, 1022–1028 (2010)
15. S.S. Hans, O. Jareunpoon, M. Balasubramaniam, G.B. Zelenock, Size and location of thrombus in intact and ruptured Abdominal Aortic Aneurysms. J. Vasc. Surg. **41**, 584–588 (2005)
16. J.C. Simo, R.L. Taylor, Quasi-incompressible finite elasticity in principal stretches. Continuum basis and numerical algorithms. Comput. Meth. Appl. Mech. Eng. **85**, 273–310 (1991)
17. R.G. Sargent, *Verification and Validation Of Simulation Models* (2011) pp. 183–198
18. E.S. DiMartino, D.A. Vorp, Effect of variation in intraluminal thrombus constitutive properties on abdominal aortic wall stress. Ann. Biomed. Eng. **31**, 804–809 (2003)
19. S. Polzer, J. Bursa, T.C. Gasser, R. Staffa, R. Vlachovsky, Numerical implementation to predict residual strains from the homogeneous stress hypothesis with application to abdominal aortic aneurysms. Ann. Biomed. Eng. **41**, 1516–1527 (2013)
20. R. Adolph, D.A. Vorp, D.L. Steed, M.W. Webster, M.V. Kameneva, S.C. Watkins, Cellular content and permeability of intraluminal thrombus in Abdominal Aortic Aneurysm. J. Vasc. Surg. **25**, 916–926 (1997)
21. T.C. Gasser, G. Görgülü, M. Folkesson, J. Swedenborg, Failure properties of intra-luminal thrombus in abdominal aortic aneurysm under static and pulsating mechanical loads. J. Vasc. Surg. **48**, 179–188 (2008)
22. A. Ayyalasomayajula, J.P. Vande, Geest, B.R. Simon, Porohyperelastic finite element modeling of abdominal aortic aneurysms. J. Biomech. **132**, 371–379 (2010)
23. S. Polzer, T.C. Gasser, B. Markert, J. Bursa, P. Skacel, Impact of poroelasticity of the intraluminal thrombus on the wall stress of abdominal aortic aneurysms. Biomed. Eng. **11** (2012). doi:10.1186/1475-925X-11-62
24. M. Bäck, T.C. Gasser, J.-B. Michel, G. Caligiuri, Review. biomechanical factors in the biology of aortic wall and aortic valve diseases. Cardiovasc. Res. **99**, 232–241 (2013)
25. M.R. Roach, A.C. Burton, The reason for the shape of the distensibility curve of arteries. Can. J. Biochem. Physiol. **35**, 681–690 (1957)
26. J. Liao, I. Vesely, Skewness angle of interfibrillar proteoglycans increases with applied load on mitral valve chordae tendineae. J. Biomech. **40**, 390–398 (2007)

27. P.S. Robinson, T.F. Huang, E. Kazam, R.V. Iozzo, D.E. Birk, L.J. Soslowsky, Influence of decorin and biglycan on mechanical properties of multiple tendons in knockout mice. J. Biomech. Eng. **127**, 181–185 (2005)
28. J.E. Scott, Elasticity in extracellular matrix 'shape modules' of tendon, cartilage, etc. a sliding proteoglycan-filament model. J. Physiol. **553**(2), 335–343 (2003)
29. J.E. Scott, Cartilage is held together by elastic glycan strings. Physiological and pathological implications. Biorheology **45**, 209–217 (2008)
30. R. Nissen, G.J. Cardinale, S. Udenfriend, Increased turnover of arterial collagen in hypertensive rats. Proc. Natl. Acad. Sci. USA **75**, 451–453 (1978)
31. W.W. Nichols, M.F. O'Rourke, C. Vlachopoulos, McDonald's blood flow in arteries, in *Theoretical, Experimental and Clinical Principles*, 6th edn. (Arnold, London, 2011)
32. M.K. O'Connell, S. Murthy, S. Phan, C. Xu, J. Buchanan, R. Spilker, R.L. Dalman, C.K. Zarins, W. Denk, C.A. Taylor, The three-dimensional micro- and nanostructure of the aortic medial lamellar unit measured using 3d confocal and electron microscopy imaging. Matrix Biol. **27**, 171–181 (2008)
33. Z. Werb, M.J. Banda, J.H. McKerrow, R.A. Sandhaus, Elastases and elastin degradation. J. Invest. Dermatol. **79**, 154–159 (1982)
34. T.C. Gasser, S. Gallinetti, X. Xing, C. Forsell, J. Swedenborg, J. Roy, Spatial orientation of collagen fibers in the abdominal aortic aneurysm wall and its relation to wall mechanics. Acta Biomater. **8**, 3091–3103 (2012)
35. J.M. Clark, S. Glagov, Transmural organization of the arterial media: the lamellar unit revisited. Arteriosclerosis **5**, 19–34 (1985)
36. K.P. Dingemans, P. Teeling, J.H. Lagendijk, A.E. Becker, Extracellular matrix of the human aortic media: an ultrastructural histochemical and immunohistochemical study of the adult aortic media. Anat. Rec. **258**, 1–14 (2000)
37. T.E. Carew, R.N. Vaishnav, D.J. Patel, Compressibility of the arterial wall. Circ. Res. **23**, 61–68 (1968)
38. J.P. Vande Geest, M.S. Sacks, D.A. Vorp, The effects of aneurysm on the biaxial mechanical behavior of human abdominal aorta. J. Biomech. **39**, 1324–1334 (2006)
39. D.J. Patel, J.S. Janicki, T.E. Carew, Static anisotropic elastic properties of the aorta in living dogs. Circ. Res. **25**, 765–779 (1969)
40. C. S. Roy. The elastic properties of the arterial wall. J. Physiol. **3**, 125–159 (1880–82)
41. Z.J. Samila, S.A. Carter, The effect of age on the unfolding of elastin lamellae and collagen fibers with stretch in human carotid arteries. Can. J. Physiol. Pharm. **59**, 1050–1057 (1981)
42. H. Wolinsky, S. Glagov, Structural basis for the static mechanical properties of the aortic media. Circ. Res. **14**, 400–413 (1964)
43. D.H. Bergel, The static elastic properties of the arterial wall. J. Physiol. **156**, 445–457 (1961)
44. C.J. Choung, Y.C. Fung, Residual stress in arteries, in G.W. Schmid-Schoenbein, S.L. Woo, B.W. Zweifach, ed. by *Frontiers in Biomechanics* 1(986) pp. 117–129
45. Y.C. Fung, What are the residual stresses doing in our blood vessels? Ann. Biomed. Eng. **19**, 237–249 (1991)
46. A. Rachev, S.E. Greenwald, Residual strains in conduit arteries. J. Biomech. **36**, 661–670 (2003)
47. R.N. Vaishnav, J. Vossoughi, Residual stress and strain in aortic segments. J. Biomech. **20**, 235–239 (1987)
48. J. Vossoughi, Longitudinal residual strains in arteries, in *Proceedings of the 11th Southern Biomedical Engineering Conference*, Memphis, TN, 1992. 2–4 Oct 1992, pp. 17–19
49. H.W. Weizsäcker, H. Lambert, K. Pascale, Analysis of the passive mechanical properties of rat carotid arteries. J. Biomech. **16**, 703–715 (1983)
50. T.T. Tanaka, Y.C. Fung, Elastic and inelastic properties of the canine aorta and their variation along the aortic tree. J. Biomech. **7**, 357–370 (1974)
51. J.L. Emery, J.H. Omens, A.D. McCulloch, Strain softening in rat left ventricular myocardium. J. Biomech. Eng. **119**, 6–12 (1997)

52. H.S. Oktay, T. Kang, J.D. Humphrey, G.G. Bishop, Changes in the mechanical behavior of arteries following balloon angioplasty, in *ASME 1991 Biomechanics Symposium, AMD-Vol. 120* (American Society of Mechanical Engineers, 1991)
53. N.V. Salunke, L.D.T. Topoleski, Biomechanics of atherosclerotic plaque. Crit. Rev. Biomed. Eng. **25**, 243–285 (1997)
54. P.F. Davies, Flow-mediated endothelial mechanotransduction. Physiol. Rev. **75**, 519–560 (1995)
55. P. Fridez, A. Makino, H. Miyazaki, J.J. Meister, K. Hayashi, N. Stergiopulos, Short-term biomechanical adaptation of the rat carotid to acute hypertention: contribution of smooth muscle. Ann. Biomed. Eng. **29**, 26–34 (2001)
56. M.A. Zulliger, A. Rachev, N. Stergiopulos, A constitutive formulation of arterial mechanics including vascular smooth muscle tone. Am. J. Physiol. Heart Circ. Physiol. **287**, H1335–H1343 (2004)
57. Y. Castier, R.P. Brandes, G. Leseche, A. Tedgui, S. Lehoux, p47phox-dependent NADPH oxidase regulates flow-induced vascular remodeling. Circ. Res. **97**, 533–540 (2005)
58. R.J. Guzman, K. Abe, C.K. Zarins, Flow-induced arterial enlargement is inhibited by suppression of nitric oxide synthase activity in vivo. Surgery **122**, 273–279 (1997)
59. T. Matsumoto, K. Hayashi, Stress and strain distribution in hypertensive and normotensive rat aorta considering residual strain. J. Biomech. **118**, 62–73 (1996)
60. H. Wolinsky, Effects of hypertension and its reversal on the thoracic aorta of male and female rats. Circ. Res. **28**, 622–637 (1971)
61. R.L. Gleason, E. Wilson, J.D. Humphrey, Biaxial biomechanical adaptations of mouse carotid arteries cultured at altered axial extension. J. Biomech. **40**, 766–776 (2007)
62. M.J. Davis, Aortic aneurysm formation: lessons from human studies and experimental models. Circulation **98**, 193–195 (1998)
63. M. Kazi, J. Thyberg, P. Religa, J. Roy, P. Eriksson, U. Hedin, J. Swedenborg, Influence of intraluminal thrombus on structural and cellular composition of Abdominal Aortic Aneurysm wall. J. Vasc. Surg. **38**, 1283–1292 (2003)
64. J.B. Michel, J.L. Martin-Ventura, J. Egido, N. Sakalihasan, V. Treska, J. Lindholt, E. Allaire, U. Thorsteinsdottir, G. Cockerill, J. Swedenborg, Novel aspects of the pathogenesis of aneurysms of the abdominal aorta in humans. Cardiovasc. Res. (2011)
65. R.J. Rizzo, W.J. McCarthy, S.N. Dixit, M.P. Lilly, V.P. Shively, W.R. Flinn, J.S.T. Yao, Collagen types and matrix protein content in human abdominal aortic aneurysms. J. Vasc. Surg. **10**, 365–373 (1989)
66. J. Biasetti, T.C. Gasser, M. Auer, U. Hedin, F. Labruto, Hemodynamics conditions of the normal aorta compared to fusiform and saccular abdominal aortic aneurysms with emphasize on thrombus formation. Ann. Biomed. Eng. **38**, 380–390 (2009)
67. J. Biasetti, F. Hussain, T.C. Gasser, Blood flow and coherent vortices in the normal and aneurysmatic aortas. A fluid dynamical approach to Intra-Luminal Thrombus formation. J. R. Soc. Interface **8**, 1449–1461 (2011)
68. J. Biasetti, P.G. Spazzini, T.C. Gasser, An integrated fluido-chemical model towards modeling the formation of intra-luminal thrombus in abdominal aortic aneurysms. Front. Physiol. **3**, article 266 (2011)
69. J.P. Vande Geest, M.S. Sacks, D.A. Vorp, A planar biaxial constitutive relation for the luminal layer of intra-luminal thrombus in abdominal aortic aneurysms J. Biomech. **39**, 2347–2354 (2006)
70. T.C. Gasser, G. Martufi, M. Auer, M. Folkesson, J. Swedenborg, Micro-mechanical characterization of intra-luminal thrombus tissue from abdominal aortic aneurysms. Ann. Biomed. Eng. **38**, 371–379 (2010)
71. M. Folkesson, A. Silveira, P. Eriksson, J. Swedenborg, Protease activity in the multi-layered intra-luminal thrombus of abdominal aortic aneurysms. Atherosclerosis **218**, 294–299 (2011)
72. J. Swedenborg, P. Eriksson, The intraluminal thrombus as a source of proteolytic activity. Ann. N.Y. Acad. Sci. **133–138**, 2006 (1085)

73. D.A. Vorp, P.C. Lee, D.H. Wang, M.S. Makaroun, E.M. Nemoto, S. Ogawa, M.W. Webster, Association of intraluminal thrombus in abdominal aortic aneurysm with local hypoxia and wall weakening. J. Vasc. Surg. **34**, 291–299 (2001)
74. P. Erhart, C. Grond-Ginsbach, M. Hakimi, F. Lasitschka, S. Dihlmann, D. Böckler, A. Hyhlik-Dürr, Finite element analysis of abdominal aortic aneurysms: predicted rupture risk correlates with aortic wall histology in individual patients. J. Endovas. Ther. **21**, 556–564 (2014)
75. C. Reeps, A. Maier, J. Pelisek, F. Hartl, V. Grabher-Maier, W.A. Wall, M. Essler, H.-H. Eckstein, M.W. Gee, Measuring and modeling patient-specific distributions of material properties in abdominal aortic wall. Biomech. Model. Mechanobio. **12**, 717–733 (2013)
76. T.C. Gasser, Biomechanical rupture risk assessment: a consistent and objective decision-making tool for abdominal aortic aneurysm patients. AORTA (2016). doi:10.12945/j.aorta.2015.15.030 (in press)
77. W.-I. Yang M.-K. Kang S. Park J.-W. Ha Y. Jang N. Chung C.Y. Shim, I.J. Cho, Central aortic stiffness and its association with ascending aorta dilation in subjects with a bicuspid aortic valve. J. Am. Soc. Echoradiogr. **24**, 847–852 (2011)
78. C. Forsell, H.M. Björck, P. Eriksson, A. Franco-Cereceda, T.C. Gasser, Biomechanical properties of the thoracic aneurysmal wall; differences between bicuspid aortic valve (BAV) and tricuspid aortic valve (TAV) patients. Ann. Thorac Surg. **98**, 65–71 (2014)
79. C. Forsell, T. C. Gasser, J. Swedenborg, J. Roy, The quasi-static failure properties of the abdominal aortic aneurysm wall estimated by a mixed experimental-numerical approach. Ann. Biomed. Eng. **11** (2012). doi:10.1007/s10439-012-0712-3
80. A. Maier, M. Essler, M.W. Gee, H.H. Eckstein, W.A. Wall, C. Reeps, Correlation of biomechanics to tissue reaction in aortic aneurysms assessed by finite elements and [18f]-fluorodeoxyglucose-pet/ct. Int. J. Numer. Meth. Biomed. Eng. **28**, 456–471 (2012)
81. V. Marque, P. Kieffer, B. Gayraud, I. Lartaud-Idjouadiene, F. Ramirez, J. Atkinson, Aortic wall mechanics and composition in a transgenic mouse model of Marfan syndrome. Arterioscl. Thromb. Vasc. Biol. **21**, 1184–1189 (2001)
82. A. Romo, P. Badel, A. Duprey, J.P. Favre, S. Avril, In vitro analysis of localized aneurysm rupture. J. Biomech. **189**, 607–616 (2014)
83. M.L. Raghavan, M.M. Hanaoka, J.A. Kratzberg, M. de Lourdes, Higuchi, E.S. da Silva, Biomechanical failure properties and microstructural content of ruptured and unruptured abdominal aortic aneurysms. J. Biomech. **44**, 2501–2507 (2011)
84. J.C. Simo, T.J.R. Hughes, *Computational Inelasticity* (Springer, New York, 1998)
85. R.W. Ogden, Large deformation isotropic elasticity—on the correlation of theory and experiment for incompressible rubberlike solids. Proc. R. Soc. Lond. A **A326**, 565–584 (1972)
86. O.H. Yeoh, Some forms of strain energy functions for rubber. Rubber Chem. Technol. **66**, 754–771 (1993)
87. H. Demiray, A note on the elasticity of soft biological tissues. J. Biomech. **5**, 309–311 (1972)
88. Y.C. Fung, K. Fronek, P. Patitucci, Pseudoelasticity of arteries and the choice of its mathematical expression. Am. J. Physiol. **237**, H620–H631 (1979)
89. C.A. Basciano, C. Kleinstreuer, Invariant-based anisotropic constitutive models of the healthy and aneurysmal abdominal aortic wall. J. Biomech. Eng. **131**(021009), 11 (2009)
90. S. Celi , S. Berti, Biomechanics and fe modelling of aneurysm: Review and advances in computational models, in: Y. Murai, ed. by Aneurysm, chapter 1. InTech (2012)
91. H.S. Choi, R.P. Vito, Two-dimensional stress-strain relationship for canine pericardium. J. Biomech. Eng. **112**, 153–159 (1990)
92. C.J. Chuong, Y.C. Fung, Three-dimensional stress distribution in arteries. J. Biomech. Eng. **105**, 268–274 (1983)
93. T.C. Gasser, R.W. Ogden, G.A. Holzapfel, Hyperelastic modelling of arterial layers with distributed collagen fibre orientations. J. R. Soc. Interface **3**, 15–35 (2006)
94. G.A. Holzapfel, T.C. Gasser, R.W. Ogden, A new constitutive framework for arterial wall mechanics and a comparative study of material models. J. Elasticity **61**, 1–48 (2000)
95. C.O. Horgan, G. Saccomandi, A description of arterial wall mechanics using limiting chain extensibility constitutive models. Biomech. Model. Mechanobio. **1**, 251–266 (2003)

96. J.D. Humphrey, K.R. Rajagopal, A constrained mixture model for growth and remodeling of soft tissues. Math. Model. Meth. Appl. Sci. **12**, 407–430 (2002)
97. F. Riveros, S. Chandra, E.A. Finol, T.C. Gasser, J.F. Rodriguez, A pull-back algorithm to determine the unloaded vascular geometry in anisotropic hyperelastic aaa passive mechanics. Ann. Biomed. Eng. **41**, 694–708 (2013)
98. J.F. Rodríguez, C. Ruiz, M. Doblaré, G.A. Holzapfel, Mechanical stresses in abdominal aortic aneurysms: influence of diameter, asymmetry, and material anisotropy. J. Biomech. Eng. **130**, 021023 (2008)
99. D.P. Sokolis, E.M. Kefaloyannis, M. Kouloukoussa, E. Marinos, H. Boudoulas, P.E. Karayannacos, A structural basis for the aortic stressstrain relation in uniaxial tension. J. Biomech. **39**, 1651–1662 (2006)
100. K. Takamizawa, K. Hayashi, Strain energy density function and uniform strain hypothesis for arterial mechanics. J. Biomech. **20**, 7–17 (1987)
101. R.N. Vaishnav, J.T. Young, J.S. Janicki, D.J. Patel, Nonlinear anisotropic elastic properties of the canine aorta. Biophys. J. **12**, 1008–1027 (1972)
102. S. Polzer, T.C. Gasser, C. Forsell, H. Druckmullerova, M. Tichy, R. Vlachovsky, J. Bursa, Automatic identification and validation of planar collagen organization in the aorta wall with application to abdominal aortic aneurysm. Micros. Microanal. **19**, 1395–1404 (2013)
103. Y. Lanir, Constitutive equations for fibrous connective tissues. J. Biomech. **16**, 1–12 (1983)
104. G. Martufi, T.C. Gasser, A constitutive model for vascular tissue that integrates fibril, fiber and continuum levels. J. Biomech. **44**, 2544–2550 (2011)
105. H. Miyazaki, K. Hayashi, Tensile tests of collagen fibers obtained from the rabbit patellar tendon. Biomed. Microdevices **2**, 151–157 (1999)
106. Z.L. Shen, M.R. Dodge, Kahn, R. Ballarini, S.J. Eppell, Stress-strain experiments on individual collagen fibrils. Biophys. J. **95**, 3956–3963 (2008)
107. F.L. Wuyts, V.J. Vanhuyse, G.J. Langewouters, W.F. Decraemer, E.R. Raman, S. Buyle, Elastic properties of human aortas in relation to age and atherosclerosis: a structural model. Phys. Med. Biol. **40**, 1577–1597 (1995)
108. M.A. Zulliger, P. Fridez, K. Hayashi, N. Stergiopulos, A strain energy function for arteries accounting for wall composition and structure. J. Biomech. **37**, 989–1000 (2004)
109. S. Polzer, T.C. Gasser, K. Novak, V. Man, M. Tichy, P. Skacel, J. Bursa, Structure-based constitutive model can accurately predict planar biaxial properties of aortic wall tissue. Acta Biomater. **14**, 133–145 (2015)
110. G. Martufi, T.C. Gasser, Turnover of fibrillar collagen in soft biological tissue with application to the expansion of abdominal aortic aneurysms. J. R. Soc. Interface **9**, 3366–3377 (2012)
111. S. Loerakker, C. Obbink-Huizer, F.P.T. Baaijens, A physically motivated constitutive model for cell-mediated compaction and collagen remodeling in soft tissues. Biomech. Model. Mechanobio. **13**, 985–1001 (2014)
112. R.L. Taylor, *FEAP—A Finite Element Analysis Program, Version 8.2 User Manual*. University of California at Berkeley, Berkeley, California, 2007
113. A. Hyhlik-Dürr, T. Krieger, P. Geisbüsch, D. Kotelis, T. Able, D. Böckler, Reproducibility of deriving parameters of AAA rupture risk from patient-specific 3d finite element models. J. Endovas. Ther. **18**, 289–298 (2011)
114. A. Teutelink, E. Cancrinus, D. van de Heuvel, F. Moll, J.P. de Vries, Preliminary intraobserver and interobserver variability in wall stress and rupture risk assessment of abdominal aortic aneurysms using a semiautomatic finite element model. J. Vasc. Surg. **55**, 326–330 (2012)
115. C. Xu, D.L. Pham, J.L. Prince, Image segmentation using deformable models, in *Handbook of Medical Imaging*, vol. 2, Medical Image Processing and Analysis, ed. by M. Sonka, J.M. Fitzpatrick (Spie press, Bellingham, 2000), pp. 129–174
116. S. Khosla, D.R. Morris, J.V. Moxon, P.J. Walker, T.C. Gasser, J. Golledge, Meta-analysis of peak wall stress in ruptured, symptomatic and intact abdominal aortic aneurysms. Br. J. Surg. **101**, 1350–1357 (2014)
117. J.P. Vande Geest, D.H.J. Wang, S.R. Wisniewski, M.S. Makaroun, D.A. Vorp, Towards a noninvasive method for determination of patient-specific wall strength distribution in abdominal aortic aneurysms. Ann. Biomed. Eng. **34**, 1098–1106 (2006)

118. P. Erhart, J. Roy, J-P. de Vries, M. Lindquist Liljeqvist, C. Grond-Ginsbach, A. Hyhlik-Dürr, D. Böckler, Prediction of rupture sites in abdominal aortic aneurysms after finite element analysis J. Endovas. Ther. **23**, 121–124 (2016)
119. B.G. Derubertis, S.M. Trocciola, E.J. Ryer, F.M. Pieracci, J.F. McKinsey, P.L. Faries, K.C. Kent, Vascular endothelium responds to fluid shear stress gradients. J. Vasc. Surg. **46**, 630–635 (2007)
120. M. Heikkinen, J. Salenius, R. Zeitlin, J. Saarinen, V. Suominen, R. Metsanoja, O. Auvinen, The fate of aaa patients referred electively to vascular surgical unit. Scand. J. Surg. **91**, 354–352 (2002)
121. E. Larsson, Abdominal Aortic Aneurysm—Gender Aspects on Risk Factors and Treatment. PhD Thesis, Karolinska Institute, Stockholm, Sweden, 2011
122. J.P. Vande Geest, E.D. Dillavou, E.S. DiMartino, M. Oberdier, A. Bohra, M.S. Makaroun, D.A. Vorp, Gender-related differences in the tensile strength of abdominal aortic aneurysm. Ann. N.Y. Acad. Sci. **1085**, 400–402 (2006)
123. N. Sakalihasan, H. Van Damme, P. Gomez, P. Rigo, C.M. Lapiere, B. Nusgens, R. Limet, Positron emission tomography (pet) evaluation of abdominal aortic aneurysm (aaa). Eur. J. Vasc. Endovasc. Surg. **23**, 431–436 (2002)
124. A. Nchimi, J.-P. Cheramy-Bien, T.C. Gasser, G. Namur, P. Gomez, A. Albert, L. Seidel, J.O. Defraigne, N. Labropoulos, N. Sakalihasan, Multifactorial relationship between 18f-fluoro-deoxy-glucose positron emission tomography signaling and biomechanical properties in unruptured aortic aneurysms. Circ. Cardiovasc. Imaging **7**, 82–91 (2014)
125. M. Lindquist Liljeqvist, R.Hultgren, T.C. Gasser, J. Roy, Volume growth of abdominal aortic aneurysms correlates with baseline volume and increasing finite element analysis-derived rupture risk. J. Vasc. Surg. **63**, 1434–1442 (2016)
126. G. Martufi, M. Lindquist Liljeqvist, N. Sakalihasan, G. Panuccio, R. Hultgren, J. Roy, T.C. Gasser, Local diameter, wall stress and thrombus thickness influence the local growth of abdominal aortic aneurysms. J. Endovas. Ther. (2016) (in press)
127. G. Martufi, J. Roy, J. Swedenborg, N. Sakalihasan, G. Panuccio, T.C. Gasser, Multidimensional growth measurements of abdominal aortic aneurysms. J. Vasc. Surg. (2013) (in press)
128. A. Rachev, S.E. Greenwald, T. Shazly, Are geometrical and structural variations along the length of the aorta governed by a principle of "Optimal Mechanical Operation"? J. Biomech. Eng. **135** (2013). doi:10.1115/SBC2013-14427
129. M. Kroon, G.A. Holzapfel, A theoretical model for fibroblast-controlled growth of saccular cerebral aneurysms. J. Theor. Biol. **257**, 73–83 (2009)
130. K.Y. Volokh, D.A. Vorp, A model of growth and rupture of abdominal aortic aneurysm. J. Biomech. **41**, 1015–1021 (2008)
131. P.N. Watton, N.A. Hill, Evolving mechanical properties of a model of abdominal aortic aneurysm. Biomech. Model. Mechanobio. **8**, 25–42 (2009)
132. J.S. Wilson, S. Baek, J.D. Humphrey, Importance of initial aortic properties on the evolving regional anisotropy, stiffness and wall thickness of human abdominal aortic aneurysms. J. R. Soc. Interface (2012) (ahead of print)
133. S. Zeinali-Davarani, S. Baek, Medical image-based simulation of abdominal aortic aneurysm growth. Mech. Res. Commun. **42**, 107–117 (2012)
134. T.C. Gasser, Patient-specific computational modeling, in *Lecture Notes in Computational Vision and Biomechanics, chapter Bringing Vascular Biomechanics into Clinical Practice*. Simulation-Based Decisions for Elective Abdominal Aortic Aneurysms Repair (Springer, 2012) pp. 1–37
135. T.C. Gasser, Aorta—Mechanical properties, histology, and biomechanical modeling. ed. by Yohan Payan, Jacques Ohayon in Biomechanics of Living Organs. Hyperelastic Constitutive Laws for Finite Element Modeling. Academic Press (2017) (Chapter 7)

Part III
Dentistry

A Deeper Insight of a Multi-dimensional Continuum Biofilm Growth Model: Experimental Observation and Parameter Studies

Dianlei Feng, Henryke Rath, Insa Neuweiler, Nico Stumpp, Udo Nackenhorst and Meike Stiesch

Abstract *Streptococcus gordonii* is one of the first colonizing bacteria on tooth or dental implant materials forming so-called biofilm. These biofilms cause severe inflammation that, as a consequence, lead to tooth or implant failure. A promising way to study the *S. gordonii* biofilm formation is by combining experimental investigations and numerical simulation. Our previous research has shown the potential to model the growth process of the *S. gordonii* biofilm in a mimic human oral environment by using a mathematical model developed by Alpkvist and Klapper (the A-K model). The parameters used for the simulation were calibrated by the experimental results. However, what are the crucial parameters that have a strong influence on the biofilm growth behavior and thus need to be determined accurately is an open question. In this paper, parameter studies on four independent parameters are carried out.

D. Feng (✉) · I. Neuweiler
Institute of Fluid Mechanics and Environmental Physics in Civil Engineering, Leibniz Universität Hannover, Appelstrae 9a, 30167 Hannover, Germany
e-mail: feng@hydromech.uni-hannover.de

I. Neuweiler
e-mail: neuweiler@hydromech.uni-hannover.de

H. Rath · N. Stumpp · M. Stiesch
Department of Prosthetic Dentistry and Biomedical Material Sciences, Hanover Medical School, Carl-Neuberg-Strasse 1, 30625 Hannover, Germany
e-mail: henryke.rath@ibnm.uni-hannover.de

N. Stumpp
e-mail: stumpp.nico@mh-hannover.de

M. Stiesch
e-mail: stiesch.meike@mh-hannover.de

U. Nackenhorst
Institute of Mechanics and Computational Mechanics, Leibniz Universität Hannover, Appelstrae 9a, 30167 Hannover, Germany
e-mail: nackenhorst@ibnm.uni-hannover.de

P. Wriggers and T. Lenarz (eds.), *Biomedical Technology*, Lecture Notes in Applied and Computational Mechanics 84, DOI 10.1007/978-3-319-59548-1_14

1 Introduction

Due to the demographical change in the world, the human population grows older nowadays. This gives clinicians the major challenge to guarantee patients best healthcare and secure best quality of life in every stage of age. Special attention was drawn on dental implants within the last decades. In Germany about 1 million dental implants are inserted each year. They are among the most widely used medical implant systems. Despite the striking advantages of dental implant treatment, about 20% of patients develop bacteria-induced implant infections [1]. In many cases treatment of peri-implantatis is complicated and requires a surgical intervention since antibiotic therapy can be ineffective.

The human oral cavity is inhabited by over more than 700 bacterial species [2]. The oral microbiota contains harmless as well as (opportunistic) pathogens. The latter is directly involved in the development of oral infectious diseases like periodontitis, peri-implantitis and tooth decay [2, 3]. Surfaces within the oral cavity are covered with bacterial agglomerates, referred to as biofilms. These are complex structured microbial communities in which bacteria are embedded in a self secreted extracellular polymeric substance (EPS) [4]. This matrix shields the bacteria from external threats. It acts as a potent diffusion barrier so that the antibiotic resistance is up to 5000 fold higher in biofilms compared to planktonic bacteria [5, 6]. As a consequence, the conventional treatments fail.

If the adhesion of so called first colonizers is controlled, also further stages of biofilm development are influenced. The periodontopathogenic late colonizing species will decrease as they cannot attach to the biofilm in a stable way. One of these first colonizers is the *Streptococcus gordonii* [7–9]. This is an opportunistic-pathogen, gram positive bacterium that adheres to tooth or implant substratum [10–12]. For the better analysis of the bacterial biofilm, new studies must be taken into account. Since 1994, so called flow chamber systems are the gold standard [13]. The biofilm formation is influenced by environmental conditions: (a) the transport of nutrients, oxygen or signaling molecules (b) contribution to gene expression, (c) biotransformation reaction [14–18]. Therefore, the establishment of a flow chamber concerning the saliva flow is an option to study the biofilm formation. As it was described by literature, a saliva flow velocity of 100 μL/min is used [19]. For this specific study, we have designed an open flow chamber system and a strategy to study the *S. gordonii* biofilm formation by combining the experimental studies together with numerical simulation [18]. Numerical simulations help to identify situations that lead to fast biofilm growth.

A mathematical model developed by Alpkvist and Klapper (A-K model)[20] has been used to simulate the *S. gordonii* biofilm formation. Our previous study shows that the A-K model has a good potential to describe the *S. gordonii* biofilm formation under the experimental condition for physiologic fluid oral environment [18]. A comparison of the simulation results and experimental observations, which has been reported in [18] (as shown in Sect. 4) is presented again in this paper. However, quite a few parameters are required for the numerical modeling and only few of them are

quantitatively measured from experiments. Therefore, parameter studies are useful in order to identify the crucial parameters that need to be well determined to make prediction with the model. In this study, we introduce the A-K model briefly in Sect. 2 and the numerical strategy developed by Feng et al. [21] to solve the model is shortly presented in Sect. 3. Both the experimental and numerical setups are described in Sect. 4. In Sect. 5 an analysis of the independence of the parameters is carried out and four independent parameters are found. Then parameter studied are presented on those four crucial parameters.

2 Mathematical Model

2.1 Governing Equations

Based on our previous study [18], the mathematical model (A-K model) developed by Alpkvist and Klapper has been founded to be suitable to model the *S. gordonii* biofilm growth in human oral environment. We briefly describe the mathematical model in this section which was originally presented in [20]. The numerical study in this paper limits to a two-dimensional (2D) model. The 2D A-K model is considered within a computational domain of $\Omega :\rightarrow \{\mathbf{x} = (x, z) : 0 \leq x \leq W, \quad 0 \leq z \leq H\}$ as illustrated in Fig. 1. The computational domain Ω is composed of a time changing biofilm domain B_t and a fluid domain F_t. The biofilm-fluid interface is denoted as $\Gamma_{int} = F_t \cap B_t$. Even though the input medium is fully mixed with a concentration of $\bar{s}$, there still exists a very thin boundary layer above the biofilm-fluid interface within which the transport of substrates is dominated by molecular diffusion. Therefore, a diffusive boundary layer of a constant thickness H_b is assumed above the biofilm-fluid interface. The domain below the top of the boundary layer Γ_h is a substrate transport domain S_t in which the governing transport equation of the substrate is solved.

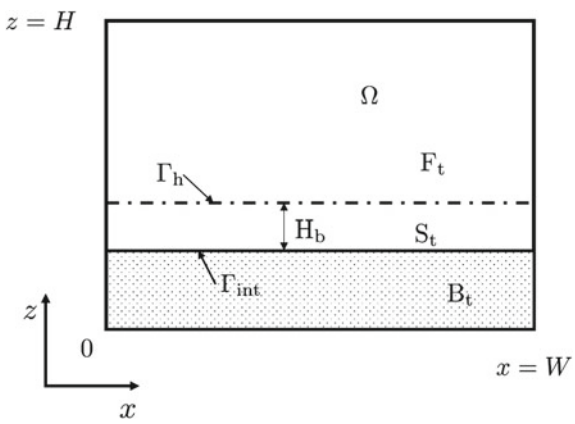

Fig. 1 Two-dimensional illustration of the computational domain

The nutrient, namely, the Tryptic Soy Broth with yeast and glucose (TSBYG) medium is considered as the only biofilm growth limiting substrate in this paper. Therefore, the biofilm growth rate is limited by the concentration of TSBYG medium s ($\mathrm{kg/m^3}$). Due to the time scale of the medium transport process is much smaller than the time scale of biofilm growth, the transport of the medium is usually considered as quasi-steady and the mass balance for the medium reads

$$\begin{aligned} -D\nabla^2 s &= r(\boldsymbol{\upsilon}, s), & \mathbf{x} &\in \mathrm{S_t}, \\ s &= \bar{s}, & \mathbf{x} &\in \Gamma_\mathrm{h}, \\ \frac{\partial s}{\partial \mathbf{n}_s} &= 0, & \mathbf{x} &\in \Gamma_\mathrm{s}, \end{aligned} \tag{1}$$

where D is of the diffusion coefficient of the medium and $r(\boldsymbol{\upsilon}, s)$ describes the consumption rate of the medium by the active biomass. $\boldsymbol{\upsilon} = (\upsilon_1, \upsilon_2, \upsilon_3 ...)^T$ refers to the volume fractions of different biomass components. No-flux boundary is applied at $\Gamma_\mathrm{s} :\rightarrow \partial \mathrm{S_t} \cap \partial\Omega$ and $\mathbf{n}_s$ here refers to the normal vector of Γ_s.

We consider two components of biomass, namely the active biomass and inactive biomass that are distinguished by indexes 1 and 2 respectively. The mass balance for biomass reads

$$\begin{aligned} \frac{\partial \boldsymbol{\upsilon}}{\partial t} + \nabla \cdot (\mathbf{u}\boldsymbol{\upsilon}) &= \mathbf{g}(\boldsymbol{\upsilon}, s), & \mathbf{x} &\in \Omega, \\ \frac{\partial \boldsymbol{\upsilon}}{\partial \mathbf{n}_b} &= 0, & \mathbf{x} &\in \partial\Omega, \end{aligned} \tag{2}$$

where the right hand side term $\mathbf{g}(\boldsymbol{\upsilon}, s) = \big(g_1(\boldsymbol{\upsilon}, s), g_2(\boldsymbol{\upsilon}, s)\big)^T$ describes the transformation process of each component of biomass. $\boldsymbol{\upsilon} = (\upsilon_1, \upsilon_2)^T$ refers to the volume fractions of the active biomass and inactive biomass respectively and they grow with a common velocity $\mathbf{u}$. The biofilm growth velocity $\mathbf{u}$ is assumed to be irrotational. Therefore, there exists a potential $\boldsymbol{\Phi}$ that satisfies

$$\nabla \cdot \mathbf{u} = \nabla^2 \boldsymbol{\Phi} = g_1 + g_2, \qquad \mathbf{x} \in \mathrm{B_t}. \tag{3}$$

Equations. (1)–(3) compose the full A-K model used in this paper.

2.2 Transformation Processes

It is assumed that the medium is consumed as a consequences of self-reproduction of the active biomass. The reaction term $r(\boldsymbol{\upsilon}, s)$ reads

$$r(\boldsymbol{\upsilon}, s) = -\upsilon_1 \rho \frac{1}{Y} \frac{\mu s}{k_s + s}, \tag{4}$$

where ρ is the density of biofilm and Y is the biofilm yield, μ and k_s are constant parameters required in the Monod kinetic. The inactive biomass is generated by the transformation of the active biomass and the transformation process here is noted as inactivation which is described by introducing an inactivation rate κ_i in the mathematical model. With all these arguments above, the terms g_1 and g_2 can be eventually written as

$$g_1(\boldsymbol{v}, s) = v_1 \left(\frac{\mu s}{k_s + s} - \kappa_i \right), \qquad g_2(\boldsymbol{v}, s) = v_1 \kappa_i. \tag{5}$$

3 Numerical Strategy

To solve the governing equations (1)–(3) numerically is challenging. Equations (1) and (3) are second order elliptic partial differential equations (PDEs) which can be solved easily by using the standard finite element method. However, the boundaries Γ_{int} and Γ_{h} change over time due to the growth of biofilm. Therefore, one needs special treatment for the moving boundaries. We use the iso-line of the total biomass concentration of a threshold value as the biofilm-fluid interface and Γ_{h} is determined by using a rolling ball algorithm.

More challenges arise when solving Eq. (2) which is a set of hyperbolic PDEs with nonlinear reaction terms. To solve such PDEs accurately, higher order stable numerical schemes in both time and space are required. However, it is well known that higher order schemes suffer from instability problems. For this reason, the combined TDG-FIC (time discontinuous Galerkin [22]—finite increamental calculus [23]) method is applied for solving Eq. (2). We refer to [21, 24] for more detailed information of the numerical aspects.

4 Biofilm Height After 24 h: Experimental Observation and Numerical Simulation

4.1 Experiment Setup

S. gordonii DSM 20568 was acquired from the German Collection of Microorganisms and Cell Cultures (DSMZ). The bacterium was pre-cultivated in Tryptic Soy Broth (TSB) supplemented with 10% yeast extract (TSBY). The bacterial solution was incubated at 37 °C for 18 h under agitation. For biofilm cultivation in the flow chamber, the overnight culture was adjusted to an optical density (OD_{600}) of 0.016 with modified (50 mM glucose) TSBY (TSBYG). The OD equaled 1.94×10^6 colony forming units (CFU)/mL. The flow chamber system is a devise for the

in vitro analysis of biofilm formation under flow conditions. The flow chamber itself was 7.0 cm × 5.5 cm × 3.5 cm in size. For macroscopic and microscopic analysis, the system was provided with a 28 mm glass cover slip. The 12 mm titanium (grade 4) was used as test specimen. The system was applied and analyzed as described in [18]. Within this study we focused on the influence of different flow velocities. Therefore, the bacteria solution was pumped through the system at flow discharge rates between 100–400 μL/min over 24 h at 37 °C. The influence of nutrient supply on biofilm formation was tested with TSBYG media concentrations between 0.1x and 1.0x (0.01; 0.03; 0.05; 0.06; 0.07; 0.1; 0.3; 0.5; 0.7; 1.0). The biofilm formation was performed at 37 °C for 24 h with a flow velocity of constant 100 μL/min. Both experiments were performed in triplicates of independent experiments.

4.2 Numerical Simulation and Results

The study in [18] shows that there is no significant change of biofilm height after 24 h's growth under the flow discharges of 100 and 200 μL/min. This indicates that the detachment effect can be omitted in the case with a flow discharge rate of 100 μL/min.

The initial thickness of biofilm is set to be 1 μm which is of the length scale of single bacterium. Therefore, the initial biofilm-fluid interface reads

$$\Gamma_{\text{int}}^{0} :\rightarrow z = 1(\mu\text{m}). \tag{6}$$

Parameters used for the simulation are listed in Table 1. Experimental observations as well as numerical simulation results are presented in Fig. 2. Error bars of the experimental results are the standard deviation calculated from different repeating measurements. The active biofilm height h_1 and inactive biofilm height h_2 used in the figure are defined as

$$h_i = \vartheta_i h_{\text{biofilm}} \qquad (i = 1, 2), \tag{7}$$

where ϑ_i refers to the mass fraction of the corresponding biomass in the system and h_{biofilm} is the total biofilm height. Specially, we define the inactivation fraction f of the biofilm as

$$f = \frac{\vartheta_2}{\vartheta_1 + \vartheta_2}. \tag{8}$$

The mathematical model used in this paper was calibrated using the experimental data shown in Fig. 2 and it was validated with a time series of the biofilm heights measurements. However, it would have been beneficial to have some of the parameters pre-determined. Also, the parameters need to be determined, if the model should be used to predict biofilm growth under different conditions. On the other hand, it is very difficult to measure all parameters of a biology system experimentally.

Table 1 Parameters used for the simulation

Quantity name	Symbol	Value	Unit
Length of the computational domain	W	100	μm
Height of the computational domain	H	100	μm
Thickness of the boundary layer	H_b	15	μm
Maximum input medium concentration (1x TSBYG medium)	s_{max}	43.9	kg/m^3
Diffusion coefficient of TSBYG medium	D	5×10^{-10}	m$^{2/s}$
Biofilm density	ρ	1100	kg/m^3
Biofilm yield	Y	10^{-1}	$(-)$
Maximum growth rate of biofilm	μ	3.0×10^{-5}	s^{-1}
Monod half-rate constant	k_s	$0.020 \times s_{max}$	kg/m^3
Inactivation rate	κ_i	4.0×10^{-6}	s^{-1}

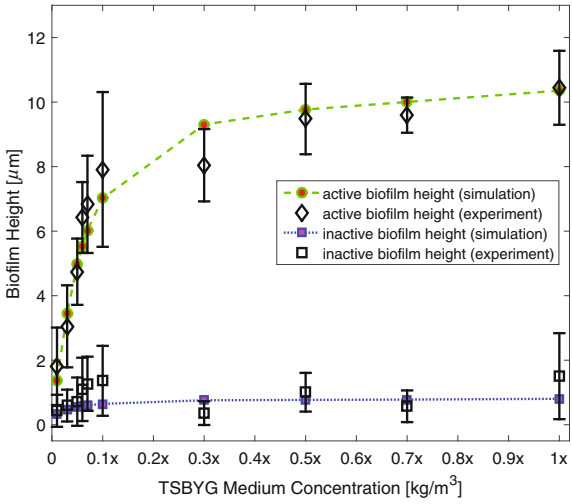

Fig. 2 Comparison of experimental results and numerical simulation results of the biofilm height at different concentrations of medium after 24 h's growth

For this reason, it is useful to study how the change of parameters' values influence the simulation results by carrying out parameter studies. This allows to identify those parameters that are crucial and are really needed to be measured accurately. Meanwhile, the studies can also uncover (not in a comprehensive way) the abilities of the mathematical model for predicting the biofilm growth process.

5 Parameter Study of the Mathematical Model

As shown in Sect. 4, the simulation results have good agreement with the experimental measurements when the parameters listed in Table 1 are used. To investigate the sensitivity of the biofilm growth on the different parameters, parameter studies

are carried out in the following sections. We focus here explicitly on the *S. gordonii* biofilm and consider the parameters that were calibrated with experiments as reference values. Different sets of parameters are applied for numerical simulation and the influences of the parameters on active biofilm height h_1, inactive biofilm height h_2 as well as inactivation fraction f are studied by changing these values. The results also provide an illustration of what kind of bio-dynamics behaviors of biofilm can be simulated by using the A-K model. Of course, one may argue that these cases (different sets of parameters) studied in this paper cannot represent all possible results gained from the A-K model and the bio-dynamic behaviors of biofilm obtained from the parameter studies are not comprehensive. The system here is restricted to the *S. gordonii* systems that close to the reference system presented in Sect. 4. Therefore, only one parameter (the being studied one) is changed while the others are the same as the ones listed in Table 1 for each study in the following sections. Moreover, the results also show the sensitivities of the biofilm heights (active and inactive) and inactivation fraction to each parameter.

There are 10 parameters listed in Table 1. Several of those parameters are fixed due to the set up of the experiments and simulations. Those include the size of the computational domain W and H and the maximum input TSBYG medium concentration $s_{\max}$. The remaining 7 parameters are not all independent as can be seen in the dimensionless governing equations. For instance, one can expect with a thicker boundary layer, less TSBYG medium will access to the biofilm-fluid surface and same effect can be achieved by using a smaller diffusion coefficient of the TSBYG medium D. Actually, the penetration properties of the TSBYG medium in the biofilm is mainly controlled by a dimensionless variable $\Theta^2 = \frac{H^2\mu\rho^2}{YD\bar{s}}$ which is known as the Thiele modulus. Changing of the Thiele modulus Θ^2 can be achieved by changing either biofilm density ρ, maximum growth rate μ, biofilm yield Y or TSBYG medium diffusion coefficient D. For this reason, we carry out parameter studies of the biofilm yield Y and the results can be also viewed as results of Θ^2, ρ, D or $\mathrm{H_b}$. What should be noted is that the maximum biofilm growth rate μ appears in more than one dimensionless variables (not only in the Thiele modulus Θ^2) in the governing equations which demonstrates that we need to carry out parameter study on μ separately. By the end, only four parameters, namely the biofilm yield Y (can be viewed as the inverse of the Thiele modulus Θ^2), maximum biofilm growth rate μ, Monod half-rate constant k_s and the inactivation rate κ_i, are left for parameter studies.

5.1 Influence of Maximum Growth Rate μ

Studies on the influence of the maximum biofilm growth rate μ are carried out with three different values of μ as $1.0 \times 10^{-5}\mathrm{s}^{-1}$, $3.0 \times 10^{-5}\mathrm{s}^{-1}$ and $5.0 \times 10^{-5}\mathrm{s}^{-1}$. The simulation results of the active biofilm height, inactive biofilm height and inactivation fraction over the input TSBYG medium concentrations are shown in Fig. 3.

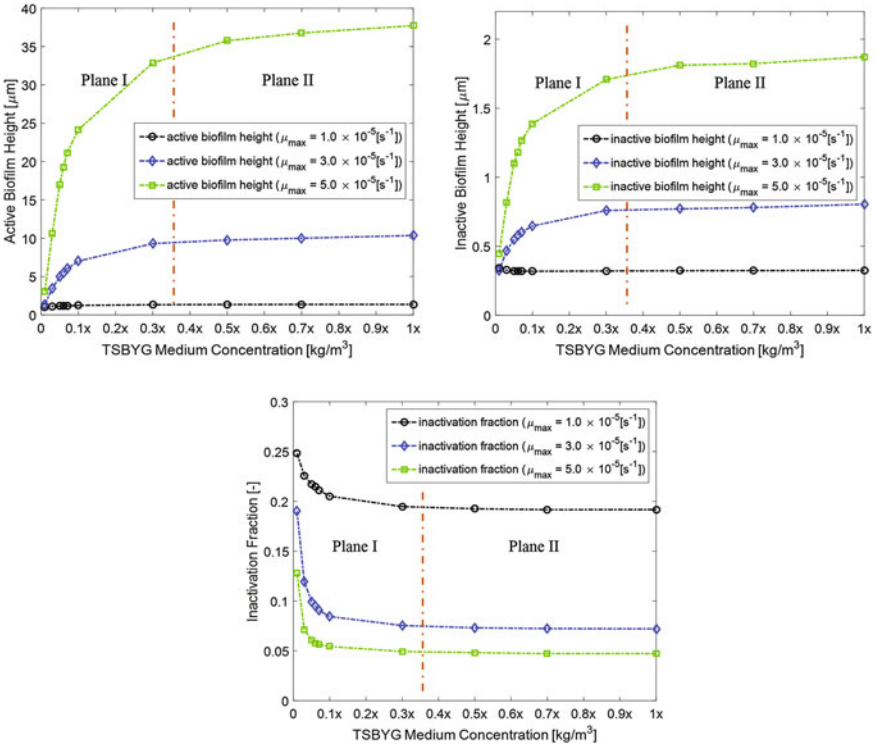

Fig. 3 Influence of the maximum biofilm growth rate μ on the active biofilm height, inactive biofilm height and inactivation fraction over different input TSBYG medium concentrations

The dependency of the biofilm heights on the maximum growth rate μ is, however, not linear. Also, for a very small value of $\mu = 1.0 \times 10^{-5} s^{-1}$, the inactive biofilm height decreases with increasing nutrient concentrations. As we expected, the results demonstrate that the biofilm heights (active and inactive) as well as the inactivation fraction are very sensitive to the maximum biofilm growth rate μ due to the proportional behavior, which means a properly determined (by experimental study or numerical calibration) μ is important for modeling the biofilm growth numerically. As a remark, the real role of the maximum growth rate μ in the mathematical model is not limited to the results presented in this study. For instance, one may imagine that if the TSBYG medium cannot fully penetrate the biofilm, the biofilm heights could be less sensitive to μ. However, as mentioned previously, we only look into biofilm systems that are close to the reference one.

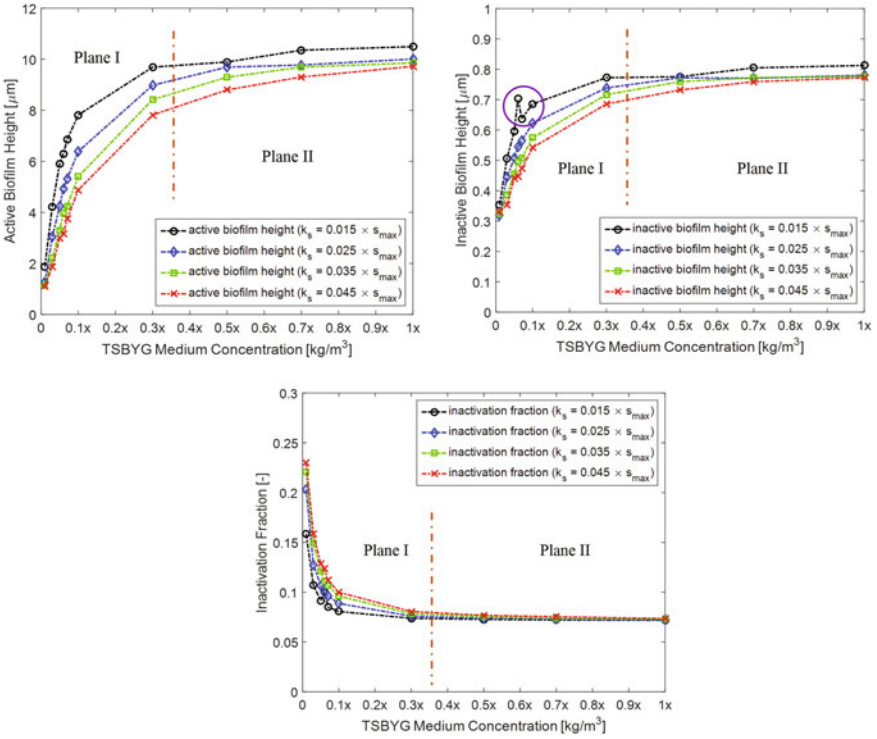

Fig. 4 Influence of the Monod half-rate constant k_s on the active biofilm height, inactive biofilm height and inactivation fraction over different input TSBYG medium concentrations

5.2 *Influence of Monod Half-Rate Constant k_s*

The influence of the Monod half-rate constant k_s are studied using four different values of k_s as shown in Fig. 4 where again the results after 24 h are plotted depending on the TSBYG medium concentrations. It is shown that the TSBYG medium concentration does not influence the biofim heights much in Plane II and the results even show a trend of converging in the cases of $k_s = 0.015 \times s_{max}$, $k_s = 0.025 \times s_{max}$, $k_s = 0.035 \times s_{max}$ and $k_s = 0.045 \times s_{max}$ in Plane II.

An interesting observation from the results is that non-monotonic behaviors (as the results plotted in the circle) of the inactive biofilm height as well as the inactivation fraction are observed in the case of $k_s = 0.015 \times s_{max}$. After checking the simulation results corresponding to the plots presented in the circle, we found both the active biomass and the inactive biomass increase over an increment of the TSBYG medium concentrations. However, the inactivation fraction could increase or decrease (see Eq. 8) over the TSBYG medium concentration as a result of competition of the active biomass production and inactivation processes. This leads to the

non-monotonic behavior of the inactivation fraction and naturally leads to a similar behavior of the inactive biofilm height as shown in the circle.

5.3 Influence of Inactivation Rate κ_i

Another important parameter used in the model is the inactivation rate κ_i, which is introduced to describe the inactivation process. However, the mechanism of the inactivation is still not clear from a biologist's point of view [18]. Our experimental results (as shown in Fig. 2) demonstrate that the inactivation process happens anyway no matter how large the input concentration of the TSBYG medium is in the system. For this reason, the inactivation process is modeled as a reaction transforming the active biomass into inactive biomass with a constant rate. Obviously, one expects that with a larger value of the inactivation rate κ_i, more inactive biomass is produced and the simulation results are as expected sensitive to the inactivation rate κ_i as a result of that. The results of three cases with inactivation rates of $\kappa_i = 4.0 \times 10^{-7}\text{s}^{-1}$, $\kappa_i = 4.0 \times 10^{-6}\text{s}^{-1}$ and $\kappa_i = 4.0 \times 10^{-5}\text{s}^{-1}$ are illustrated in Fig. 5. It is shown that the simulation results agree with our expectation.

Specially, in the case of $\kappa_i = 4.0 \times 10^{-7}\text{s}^{-1}$, the inactivation fraction is larger than 0.6 even in the Plane II. This indicates that the amount of inactive biomass is always more than the active biomass in this case regardless of how much medium is in the system.

5.4 Influence of Biofilm Yield Y

The influence of biofilm yield Y on the biofilm heights and the inactivation fraction is discussed in the following. The biofilm yield is widely used and can be interpreted as with one unit growth limiting substrate consumed, Y unit mass of active biomass is produced. The value of the biofilm yield depends on the species of bacteria as well as the growth limiting substrate.

Simulation results of the influence of the biofilm yield Y (or Thiele modulus Θ^2) on active biofilm height, inactive biofilm height and inactivation fraction are presented in Fig. 6. It is shown that the curves corresponding to $Y = 1 \times 10^{-1}$ and $Y = 1 \times 10^{-2}$ are almost coincident. This is because in both of these two cases, the biofilm yield Y is large enough to guarantee that the TSBYG medium fully penetrates the biofilm and all bacteria have enough medium to reproduce themselves. The result also demonstrates that changing of the diffusion coefficient of the medium a little bit in the biofilm or in the water will not change the final result significantly when the parameters listed in Table 1 are used. What should be noted is that in the case of $Y = 1 \times 10^{-3}$, the TSBYG medium also fully penetrates the biofilm. However, the concentration is not large enough to ensure the bacteria at the bottom of the biofilm have enough TSBYG medium supply and the growth of the biofilm is partly lim-

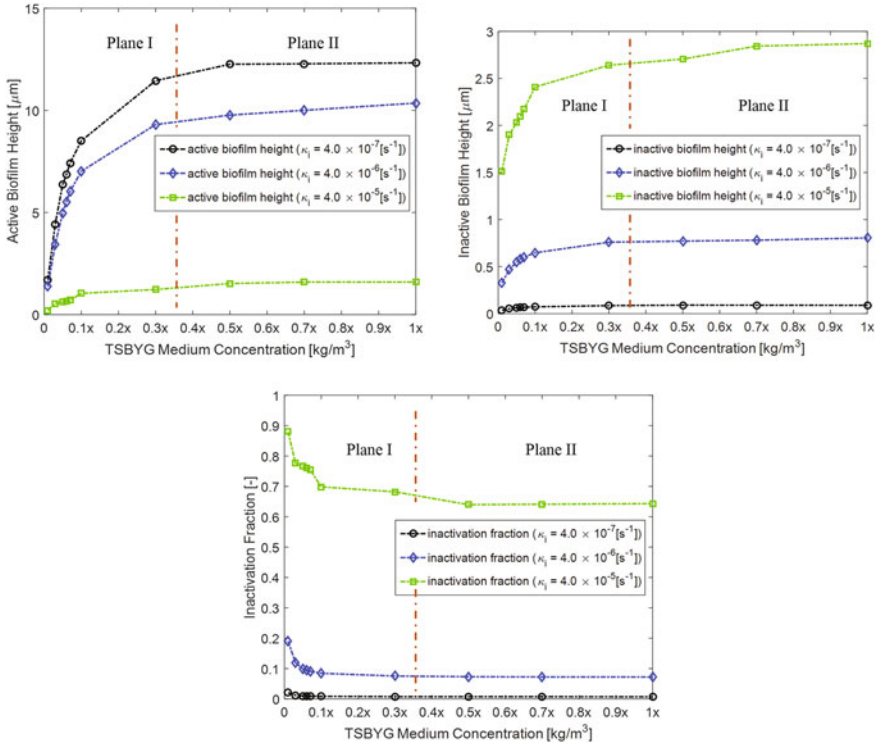

Fig. 5 Influence of the inactivation rate κ_i on the active biofilm height, inactive biofilm height and inactivation fraction over different input TSBYG medium concentrations

ited by the medium concentration (especially in Plane I). Therefore, smaller active biofilm heights and inactive biofilm heights compared to the cases of $Y = 1 \times 10^{-1}$ and $Y = 1 \times 10^{-2}$ are observed in Plane I. With increase of the medium concentration, this partly limiting phenomenon is less pronounced and the results converge to the same value again. This can be verified by the time behavior of the active biofilm height shown in Fig. 7. The results of the development of the active biofilm height over time with an input TSBYG medium concentration of 0.05x kg/m^3 are shown in the left figure in Fig. 7 and the right figure illustrates the results with an input TSBYG medium concentration of 1x kg/m^3. The time dependent results demonstrate that the biofilm growth velocity is not influenced much by different biofilm yield values if the values are large (e.g. $Y = 1 \times 10^{-1}$ and $Y = 1 \times 10^{-2}$). However, the biofilm grows slower in the case of $Y = 1 \times 10^{-3}$ when a small input TSBYG medium concentration (0.05x kg/m^3) is applied. But almost no difference is observed on the biofilm growth speed if large enough TSBYG medium concentration (1x kg/m^3) is supplied. This explains why the curves corresponding to $Y = 1 \times 10^{-1}$, $Y = 1 \times 10^{-2}$ and $Y = 1 \times 10^{-3}$ in Fig. 6 converge to the same value when the TSBYG medium concentration is 1x kg/m^3.

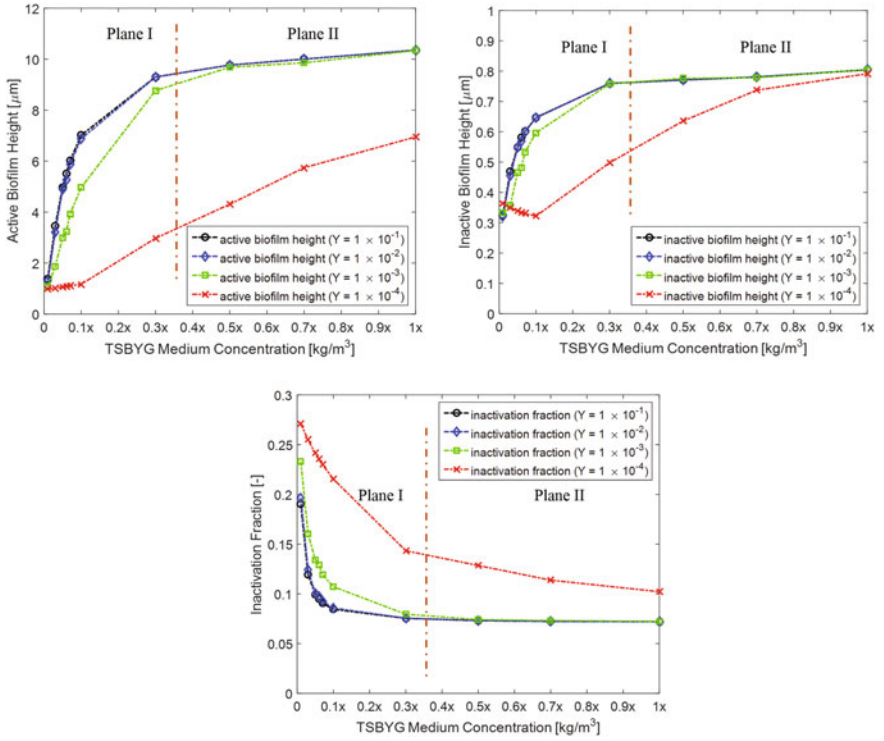

Fig. 6 Influence of the biofilm yield Y on the active biofilm height, inactive biofilm height and inactivation fraction (from top to bottom) over different input TSBYG medium concentrations

The results of an extreme case of $Y = 1 \times 10^{-4}$ are presented as the red curves in Fig. 6. The TSBYG medium concentration is almost zero at the bottom of the biofilm which limits the biofilm growth significantly. The results shown in Fig. 7 also indicate that the biofilm growth is limited all the time in the case of $Y = 1 \times 10^{-4}$ even with an input TSBYG medium concentration of 1x. Overall, one can draw the conclusion that the biofilm heights as well as inactivation fraction are sensitive to the biofilm yield (or Thiele modulus Θ^2) only when the biofilm yield is small enough (Θ^2 is large enough). Another interesting observation is that the inactivation fraction of the case $Y = 1 \times 10^{-4}$ also shows non-monotonic behavior. This is also due to the competition between the active biomass production and the inactive biomass transformation as explained in Sect. 5.2.

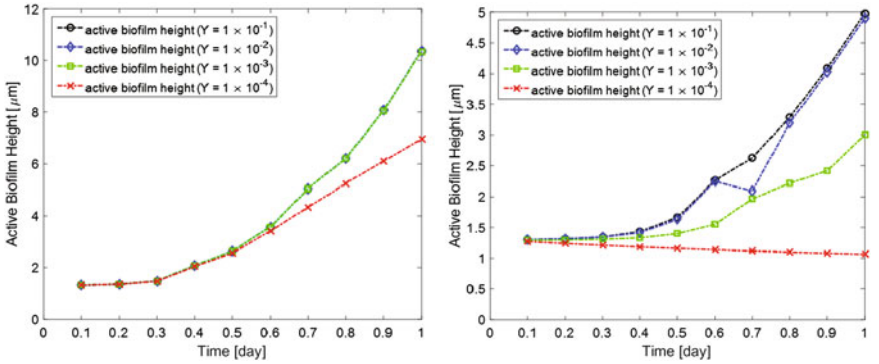

Fig. 7 Influence of the biofilm yield Y on the active biofilm height over time with input TSBYG medium concentrations of 0.05x (*left*) and 1x (*right*)

6 Summary and Conclusion

The *S. gordonii* biofilm formation within 24 h is studied by combining experimental investigations and numerical simulations. Here, the biofilm behavior was studied in a flow chamber system mimicking the physiological flow within the oral cavity. A multi-species continuum biofilm growth model (the A-K model) is applied for numerical simulation. Our previous research demonstrated that the mathematical model as well as the numerical strategy used for solving the model are capable to present the biology behavior of the *S. gordonii* biofilm formation in such an environment. In this study, parameter studies are carried out for better understanding of the model as well as the biological processes and to identify the requirments for accurately measured parameters.

Influence of the maximum biofilm growth rate μ, the Monod half-rate constant k_s, the inactivation rate κ_i and the biofilm yield Y (or the Thiele modulus Θ^2) on the biofilm heights (active and inactive) as well as the inactivation fraction are studied. The parameters that corresponding to the realistic *S. gordonii* biofilm system are taken as the references parameter and all the parameter studies are carried out based on the reference set. As expected that the solutions are rather sensitive to the TSBYG medium concentrations in most of the cases when the concentration is under a certain value (in Plane I) while the results are not depending on the TSBYG medium concentration much with larger concentrations (in Plane II).

The simulation results demonstrate that both the biofilm heights and the inactivation fraction are sensitive to the maximum growth rate μ and inactivation rate κ_i. This is also not surprising, because the biological definitions of these two parameters relate to the biofilm heights directly. One can expect that by using a larger maximum growth rate shall lead to a thicker biofilm. However, even though our simulation results agree with our expectation, this is not always the golden rule. For instance, the biofilm growth process could also be limited as a result of too thick of a biofilm

Table 2 Sensitivity of the biofilm heights h_1, h_2 and inactivation fraction f to the parameters μ, k_s, κ_i and Y

	Small TSBYG medium concentrations			Large TSBYG medium concentrations		
	h_1	h_2	f	h_1	h_2	f
μ	High	High	High	High	High	High
k_s	Fair	Fair	Small to fair	Small	Small	None
κ_i	High	High	High	High	High	High
$Y \geq Y_{crt}$	Small	Small	Small	None	None	None
$Y < Y_{crt}$	High	High	High	High	Small to none	High

and the TSBYG medium can hardly fully penetrate the biofilm. This did not happen in our simulations that are close to the reference *S. gordonii* biofilm system described in Sect. 4. We also found that the influences of the Monod half-rate constant k_s on the simulation results differ for small and large TSBYG medium concentrations. The simulation results demonstrate that the biofilm heights as well as the inactivation fraction are sensitive to k_s if the nutrient concentration is low while are not very sensitive to the k_s if the nutrient is sufficient. Parameter studies on the biofilm yield Y (or could also be viewed as studies on ρ, H_b or D in the Thiele modulus Θ^2) showed that the solution are significantly influenced by the parameter only when Y is below a threshold value Y_{crt} ($Y < Y_{crt} = 1 \times 10^{-3}$). This is due to the TSBYG medium, which cannot fully penetrate the biofilm and the biofilm growth is limited by the lack of the nutrient supply. As a summary, the sensitivities of the results to these parameters are presented in Table 2.

Acknowledgements Financial support of Dianlei Feng and Henryke Rath were provided by the Ministry of Science and Culture of Lower Saxony within the framework of the Doctoral Program MARIO (Multifunctional Active and Reactive Interfaces and Surfaces).

References

1. A. Mombelli, N. Müller, N. Cionca, Clin. Oral Implant. Res. **23**(s6), 67 (2012)
2. J.A. Aas, B.J. Paster, L.N. Stokes, I. Olsen, F.E. Dewhirst, J. Clin. Microbiol. **43**(11), 5721 (2005). doi:10.1128/JCM.43.11.5721-5732.2005
3. L. Makesh Raj, J. Jude, I. Kannan, P. Sai Krishna, K. Shankar, J. Clin. Diagn. Res. JCDR **8**(11), ZC48 (2014)
4. H.C. Flemming, T.R. Neu, D.J. Wozniak, J. Bacteriol. **189**(22), 7945 (2007)
5. H. Anwar, J. Costerton, Antimicrob. Agents Chemother. **34**(9), 1666 (1990)
6. J.W. Costerton, B. Ellis, K. Lam, F. Johnson, A.E. Khoury, Antimicrob. Agents Chemother. **38**(12), 2803 (1994). doi:10.1128/AAC.38.12.2803
7. L. Hall-Stoodley, J.W. Costerton, P. Stoodley, Nat. Rev. Microbiol. **2**(2), 95 (2004). doi:10.1038/nrmicro821
8. C.J. Jung, C.Y. Yeh, C.T. Shun, R.B. Hsu, H.W. Cheng, C.S. Lin, J.S. Chia, J. Infect. Dis. **205**(7), 1066 (2012). doi:10.1093/infdis/jis021

9. P. Moreillon, Y.A. Que, Lancet (London, England) **363**(9403), 139 (2004). doi:10.1016/S0140-6736(03)15266-X
10. P.I. Diaz, N.I. Chalmers, A.H. Rickard, C. Kong, C.L. Milburn, R.J. Palmer, P.E. Kolenbrander, Appl. Environ. Microbiol. **72**(4), 2837 (2006). doi:10.1128/AEM.72.4.2837-2848.2006
11. M. Kilian, L. Mikkelsen, J. Henrichsen, Int. J. Sys. Evol. Microbiol. **39**(4), 471 (1989)
12. B. Nyvad, M. Kilian, Eur. J. Oral Sci. **95**(5), 369 (1987). doi:10.1111/j.1600-0722.1987.tb01627.x
13. G.M. Wolfaardt, Lawrence, R.D. Robarts, S.J. Caldwell, D.E. Caldwell, Appl. Environ. Microbiol. **60**(2), 434 (1994)
14. D. de Beer, P. Stoodley, Z. Lewandowski, Biotechnol. Bioeng. **44**(5), 636 (1994)
15. T.R. De Kievit, B.H. Iglewski, Infect. Immun. **68**(9), 4839 (2000)
16. M.B. Miller, B.L. Bassler, Annu. Rev. Microbiol. **55**(1), 165 (2001)
17. A. Park, H.H. Jeong, J. Lee, K.P. Kim, C.S. Lee, BioChip J. **5**(3), 236 (2011). doi:10.1007/s13206-011-5307-9
18. H. Rath, D. Feng, N. Stumpp, I. Neuweiler, U. Nackenhorst, M. Stiesch, FEMS Microbiol. Ecol. **93**(3), (2017). doi:https://doi.org/10.1093/femsec/fix010
19. C. Dawes, S. Watanabe, P. Biglow-Lecomte, G.H. Dibdin, J. Dent. Res. **68**(11), 1479 (1989). doi:10.1177/00220345890680110201
20. E. Alpkvista, I. Klapper, Bull. Math. Biol. **69**(2), 765 (2007)
21. D. Feng, I. Neuweiler, U. Nackenhorst, Comput. Mech. **59**(6), 1049 (2017). doi:10.1007/s00466-0171388-1
22. T.J. Hughes, G.M. Hulbert, Comput. Methods Appl. Mech. Eng. **66**(3), 339 (1988)
23. E. Oñate, J. Miquel, F. Zárate, Comput. Fluids **36**(1), 92 (2007)
24. A. Sapotnick, U. Nackenhorst, Int. J. Numer. Methods Eng. **92**(3), 301 (2012)

Multiscale Experimental and Computational Investigation of Nature's Design Principle of Hierarchies in Dental Enamel

Songyun Ma, Ingo Scheider, Ezgi D. Yilmaz, Gerold A. Schneider and Swantje Bargmann

Abstract Dental enamel possesses extraordinary mechanical properties due to a complex hierarchical and graded microstructure. In this study, multiscale experimental and computational approaches are employed and combined to study nature's design principle of the hierarchical structure of bovine enamel for developing bio-inspired advanced ceramics with hierarchical microstructure. Micro-cantilever beam tests are carried out to characterize the mechanical properties from nano- to meso-scale experimentally. In order to understand the relationship between the hierarchical structure and the flaw-tolerance behavior of enamel, a 3D representative volume element (RVE) is used in a numerical analysis to study the deformation and damage process at two hierarchical levels. A continuum damage mechanics model coupled to hyperelasticity is developed for modeling the initiation and evolution of damage in the mineral fibers as well as protein matrix. Moreover, debonding of the interface between mineral fiber and protein is captured by a cohesive zone model. The effect of an initial flaw on the overall mechanical properties is analyzed at different hierarchical levels to understand the superior damage tolerance of dental enamel. Based

S. Ma (✉)
Institute of General Mechanics, RWTH Aachen University, Aachen, Germany
e-mail: ma@iam.rwth-aachen.de

I. Scheider
Institute of Materials Research, Materials Mechanics/ACE-Centre, Helmholtz-Zentrum, Geesthacht, Germany
e-mail: ingo.scheider@hzg.de

E.D. Yilmaz · G.A. Schneider
Institute of Advanced Ceramics, Hamburg University of Technology, Hamburg, Germany
e-mail: e.yilmaz@tuhh.de

S. Bargmann
Chair of Solid Mechanics, School of Mechanical Engineering and Safety Engineering, University of Wuppertal, Wuppertal, Germany
e-mail: bargmann@uni-wuppertal.de

P. Wriggers and T. Lenarz (eds.), *Biomedical Technology*, Lecture Notes in Applied and Computational Mechanics 84, DOI 10.1007/978-3-319-59548-1_15

on the experimental and computational investigation, the role of hierarchical levels on the multiscale design of structure in dental enamel is revealed for optimizing bio-inspired composites.

1 Introduction

The unique microstructure of highly-mineralized biological composites results in optimized mechanical properties in terms of being stiff, hard and damage-tolerant at the same time, whereas many load-bearing engineering materials with high stiffness and hardness suffer from limited deformability and brittle failure [9]. Therefore, extensive experimental and computational studies at different length-scales have been contributed to identify relationships between hierarchical biological structures and properties that have been unknown until recently in order to develop novel design strategies and large-scale and low-cost production methods for next-generation man-made materials [28].

Hierarchical materials are designed from the nano- to the macroscale with characteristic structural features on several length scales, which is often correlated with their improved fracture toughness and damage-tolerance of biological materials in comparison to their constituents [14]. However, there has been a key gap in knowledge of how this exactly occurs. Previous experimental studies on the mechanical characterization of biological materials are mostly based on the macroscopic testing of bulk samples or indentation at nano- and micro-scale [1, 16, 17]. Large-scale measurements alone embrace the synergistic contribution of all hierarchical levels, and do not elucidate the contribution of individual hierarchical levels. Indentation approaches, on the other hand, characterize the materials' properties at small spots but under highly complex and constrained conditions so that the critical strength of the material cannot be determined. For modeling the damage behavior and obtaining a deeper insight into the relationship between structure and damage resistance of biocomposites, different computational approaches have been employed in recent years, e.g. [13, 15, 20, 25]. The majority of these models are based on the small deformation theory and restricted to 2D numerical analysis, ignoring the geometrical details of the microstructure as well as complex deformation and failure mechanisms of biocomposites.

To fill this gap and provide accurate information of the hierarchical structure-property relationship, we study dental enamel as a model material, since the evolution of enamel microstructure is known to have an adaptive relationship to the stresses generated during mastication [21, 31]. On the one hand, dental enamel allows the preparation of samples in different sizes. Micro-cantilever beam tests are performed for a systematic experimental characterization of bovine enamel at different length scales. On the other hand, 3D micromechanical simulations in the framework of finite strain theory are carried out to provide accurate information on the damage tolerance behavior of enamel. The computational results are verified by

micro-cantilever experiments at two hierarchical levels. The influence of initial flaws on the mechanical properties at different hierarchical levels is analyzed to understand the superior damage tolerance of dental enamel based on computational analysis.

2 Microstructural Characteristics of Bovine Enamel

The structural motifs of bovine enamel varying between nano- to macroscale and between different locations is summarized in this section before introducing the findings of mechanical characterization. The smallest structural units in bovine enamel are hydroxyapatite (HAP) nanofibers (15–50 nm in thickness and 40–150 nm in width) that assemble into quasi-cylindrically shaped μ-sized enamel rods extending from the dentin-enamel junction to the outer enamel surface with certain angulations α with respect to the outer surface of the tooth as shown in Fig. 1. This angle may vary between different species and also from cusp to cervical region of an individual tooth. The diameter of rods ranges between 1 and 7 µm in different regions of bovine enamel with respect to the distance from the dentin-enamel junction. Another remarking structure observed at the second level is the so-called interrod, which is a continuous layer of nanofibers, lying outside the rods and crossing them at almost right angles (Fig. 1). The appearance of rod boundaries and the arrangement of rods and interrods define rod patterns [8, 26], which diverge among different species and enamel regions. In bovine enamel, three types of rod pattern can be distinguished as shown in Fig. 1. In pattern A, detected in inner regions, rod boundaries seem "closed"

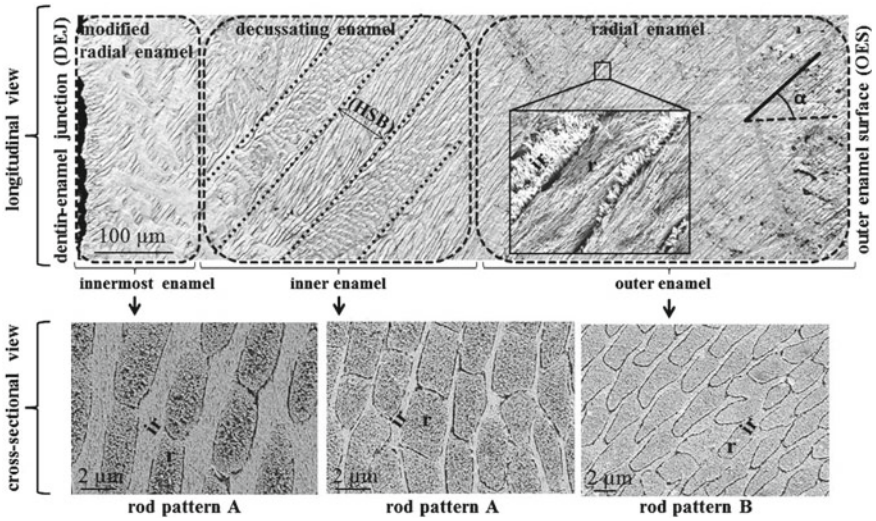

Fig. 1 Microstructural characteristics of bovine enamel (*ir* interrod. *r* rod. *HSB* Hunter-Schreger bands)

(complete) and interrods form inter-row sheets, which assemble into a plywood-like structure with rows of rods (Fig. 1). In the outer enamel region pattern B dominates, where rod boundary appearances are mostly "open" (incomplete) and interrods serve as a matrix anastomosing to the rod in their open ends. Another class of characters specified in describing enamel microstructures is the "enamel type" defining the alignment of rod bundles [21]. In the outer enamel region, rods are aligned roughly parallel to one another forming the so-called "radial enamel", which underwent a specific modification in hypsodont (high-crowned teeth) taxa by increasing the thickness of inter-row sheets. This is known as "modified radial enamel" and locates in the innermost layer near to the dentin-enamel junction. The layer between the innermost and outer enamel is occupied by a more derived enamel type "decussating enamel". By definition, decussating enamel describes groups of rod bundles crossing each other, which can occur in a regular (as in bovine enamel) or irregular fashion. In bovine enamel, uniformly aligned rod bundles form well-defined bands (Hunter-Schreger bands) that decussate with adjacent bands at high angles.

Although it is widely stated that enamel constitutes little amount of remnant organic material and water besides its major component HAP, the exact nature, location and amount of it is still an unresolved issue. The reported volume fraction of mineral, organic, firmly and loosely bound water components vary among different sources between 71–99 vol%, 0.02–8 vol%, 3–9 vol% and 0.02–3.3 vol%, respectively [3, 11, 12, 18, 19, 23, 33]. Soft matter in enamel is reported to be enriched substantially in the vicinity of the dentin-enamel junction [10, 27] and is believed to accumulate at the free space between nanofibers and rods [29].

3 Multiscale Experimental Study of Mechanical Behavior of Dental Enamel

The main objective of the series of experiments is to quantify how the mechanical properties of bovine enamel change over different hierarchical levels. In counting the hierarchical order of bovine enamel, here we consider nanostructural elements (hydroxyapatite nanofibers) as level-1, microstructural elements (rods and interrods) as level-2, and the complex assembly organized by microstructural elements (bulk enamel) as level-3. Enamel mainly operates under compressive stresses but due to the conical shape of teeth, tensile stresses are generated as well. The latter are more critical for crack propagation [31]. Thus, we conducted three point bending[1] tests. Bulk enamel specimens were fabricated with successive cutting and grinding steps, whereas micron-sized specimens of different sizes to characterize level-1 and level-2 were machined using focused-ion beam milling as shown in Fig. 2.[2] The resultant mechanical properties are listed in Table 1.

[1]Fracture is induced in bending experiments in the tensile stress region of the specimen.

[2]For more detailed information about specimen fabrication and testing methods, the reader is referred to [6, 7, 34–37].

Table 1 Hierarchical mechanical properties of dental enamel

Specimen level	Fracture strength σ_B (MPa)	Elastic modulus E_B (GPa)
Level-1	978 ± 52	54 ± 2
Level-2	478 ± 93	36 ± 8

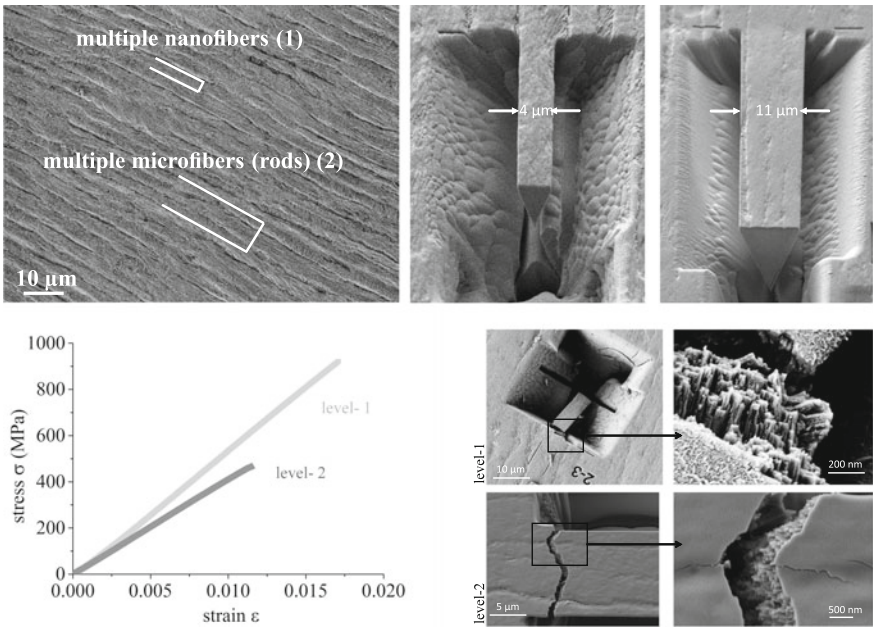

Fig. 2 Multiscale experimental study of mechanical response of bovine enamel at different hierarchical levels

The comparison of bending tests of bovine enamel performed at different hierarchical levels reveals a consistent reduction in fracture strength σ_B with increasing number of hierarchy level. The specific nanometer-sized scale of the enamel HAP nanofibers has evolved by nature as postulated by Gao et al. [13] in order to ensure optimum fracture strength of the mineral particles. If the dimension of the biomineral crystallites drops below a critical size, they become defect insensitive and the atomic bonds control the strength [14]. Thus, the HAP nanofibers were fractured at stress levels reaching up to 1 GPa under bending (macroscopic bending strength of HAP mineral is 100 MPa [1]). However, in the hierarchical level-2, the rods come along with rod boundaries, which are protein-rich regions and, thus, weaker than the nanofiber boundaries since they are predominantly the preferred sites for crack initiation [5]. This could be the reason for the reduction of the fracture strength from level-1 to level-2 and from level-2 to bulk enamel with a greater extend. However, in the latter, the orientation of nanofibers and rods has an impact as well. In the micro-cantilevers, the long axes of nanofibers and rods were parallel to the tensile

stress direction. However, in the bulk samples, the majority of rods were loaded perpendicularly to the tensile stress direction leading to delamination at the weaker rod boundaries. As an alternative explanation for the decreasing trend in σ_B as a function of hierarchy, the overall mineral content of the composite structure might decrease with each additional level of hierarchy [6, 36].

4 Multiscale Computational Simulation of Damage Behavior of Dental Enamel

In addition to the experimental investigations for studying nature's design principle of the hierarchical structure in dental enamel, computational modeling provides detailed insight into initiation and development of damage processes of enamel for understanding the failure mechanisms, which are not fully understood in the experiments due to limitations of experimental techniques. In the present work, micromechanical analyses based on a 3D representative volume element (RVE) are carried out for investigating the different deformation and damage behavior on the first and second hierarchy levels. For this purpose, physically based damage models are required to capture the failure mechanisms of mineral fibers and protein layers, as well as the interface between fibers and protein.

A continuum damage model is formulated in the framework of finite strain theory to map the non-linear deformation behavior and degradation process of protein and mineral fibers in enamel, since the protein layer transfers load between hydroxyapatite (HAP) fibers through large shear deformation in enamel. The debonding of the interface between mineral fiber and protein is captured by a cohesive zone model, since this debonding path is predefined by the geometry.

4.1 Continuum Damage Model for Mineral Fiber and Protein

4.1.1 Free Energy Density Function

The modeling of damage for mineral fibers has to take brittle failure into account. The main mechanism here is nucleation and growth of microcracks and their coalescence leading to fracture of the material. The difference between tensile and compressive loading due to crack closure must also be appropriately considered [22]. For mineral fibers, an isotropic damage theory coupled to Neo-Hookean hyperelasticity is introduced in order to initiate and evolve damage in the fibers. The corresponding Helmholtz free energy function is postulated as

$$\begin{aligned}\Psi_{\mathrm{m}}(J,\bar{I}_1,D_{\mathrm{m}}) &= [1-\alpha H(\sigma_{\mathrm{h}})D_{\mathrm{m}}]\Psi^0_{\mathrm{m,\,vol}}(J)+[1-D_{\mathrm{m}}]\Psi^0_{\mathrm{m,\,iso}}(\bar{I}_1)\\ &= [1-\alpha H(\sigma_{\mathrm{h}})D_{\mathrm{m}}]\frac{\mu_{\mathrm{m}}}{2}\left[\bar{I}_1-3\right]+\left[1-D_{\mathrm{m}}\right]\frac{K_{\mathrm{m}}}{2}\left[(J-1)\right]^2, \quad (1)\end{aligned}$$

where σ_{h} represents the hydrostatic stress and D_{m} is damage variable of fiber. $\Psi^0_{\mathrm{m,\,vol}}$, $\Psi^0_{\mathrm{m,\,iso}}$ are the volumetric and isochoric damage-free parts of the Helmholtz energy, respectively. The first strain invariant of the modified symmetric Cauchy-Green tensors $\bar{C}$ is defined as $\bar{I}_1 = \mathrm{tr}\bar{C}$ with $\bar{C} = \bar{F}^t \cdot \bar{F}$. The modified deformation gradient $\bar{F}$ is isochoric part of deformation gradient F: $\bar{F} = J^{-1/3}F$, with $J = \det F$. μ_{m} and K_{m} are the shear and bulk modulus of fibers, respectively.

Damage acts on the volumetric and the isochoric part in different ways: While the damage term $[1 - D_{\mathrm{m}}]$ is fully multiplied to the isochoric part, damage is only partially coupled with the volumetric energy (via model parameter α) under tensile loading, controlled by the Heaviside function $H(\sigma_{\mathrm{h}})$. This formulation is in accordance with the fact that microcracks are only active if the crack opens under tension, while they close and transfer stresses under compression. The isochoric part is more relevant to shear deformation where the microcracks are active independent of the shear direction.

The protein transmits the load between mineral fibers and is subjected to large shear deformation. Due to the large deformation of protein, the fracture energy is absorbed and dissipated, which leads to a high fracture toughness of the composite. In order to model the characteristics of the deformation and damage behavior of the protein, an Arruda-Boyce hyperelastic model is coupled to damage. Compared to the Helmholtz free energy for the mineral, the damage associated with the protein matrix is only related to distortional energy and independent of the hydrostatic pressure following [30]:

$$\begin{aligned}\Psi_{\mathrm{p}}(J,\bar{I}_1,D_{\mathrm{p}}) &= \Psi^0_{\mathrm{p,\,vol}}(J)+[1-D_{\mathrm{p}}]\Psi^0_{\mathrm{p,\,iso}}(\bar{I}_1)\\ &= \frac{K_{\mathrm{p}}}{2}\left[\frac{J^2-1}{2}-\ln J\right]+\left[1-D_{\mathrm{p}}\right]\mu_{\mathrm{p}}\sum_{i=1}^{5}\left[\frac{C_i}{\lambda_m^{2i-2}}\left[\bar{I}_1^i-3^i\right]\right], \quad (2)\end{aligned}$$

where D_{p} is damage variable of protein. Thus, the isochoric deformation induces the damage of protein. The values of the coefficients C_i arise from a series expansion of the inverse Langevin function

$$C_1=\frac{1}{2},\quad C_2=\frac{1}{20},\quad C_3=\frac{11}{1050},\quad C_4=\frac{19}{7000},\quad C_5=\frac{519}{673750}. \quad (3)$$

Further, $\mu^0_{\mathrm{p}} = \mu_{\mathrm{p}}\left[1+\frac{3}{5\lambda^2}+\frac{99}{175\lambda^4}+\frac{513}{875\lambda^6}+\frac{42039}{67375\lambda^8}\right]$ relates the initial shear modulus to μ_{p}, and λ is referred to as the locking stretch and assumed to be 1.0 for protein.

The second Piola-Kirchhoff stress of mineral fiber and protein is then derived from the Helmholtz free energy density

$$S_{\mathrm{i}} = J\frac{\partial \Psi_{\mathrm{i,\,vol}}}{\partial J}C^{-1} + 2\mathbb{P} : \frac{\partial \Psi_{\mathrm{i,\,iso}}}{\partial \bar{C}}, \tag{4}$$

where the fourth-order projection tensor $\mathbb{P}$ is defined as $\mathbb{P} = \frac{\partial \bar{C}}{\partial C} = J^{-2/3}[\mathbb{I} - \frac{1}{3}C \otimes C^{-1}]$. Here, $\mathbb{I}$ denotes the fourth-order identity tensor. With the postulated Helmholtz free energy density for the fiber and protein in Eqs. (2) and (1), the second Piola-Kirchhoff stress of mineral fiber and protein are written

$$\begin{aligned} S_{\mathrm{m}} &= [1 - \alpha H(\sigma_h)D_{\mathrm{m}}]\frac{K_{\mathrm{m}}}{2}\left[J^2 - J\right]C^{-1} + [1 - D_{\mathrm{m}}]\mu_{\mathrm{m}}\mathbb{P} : I, \\ S_{\mathrm{p}} &= \frac{K_{\mathrm{p}}}{2}\left[J^2 - 1\right]C^{-1} + 2[1 - D_{\mathrm{p}}]J^{-2/3}\mu_{\mathrm{p}}\sum_{i=1}^{5}\left[i\frac{C_i}{\lambda_p^{2i-2}}\bar{I}_1^{i-1}\right]\mathbb{P} : I, \end{aligned} \tag{5}$$

respectively.

4.1.2 Damage Initiation Criteria and Evolution Laws

The thermodynamic force Y_{m} associated with damage variable D_{m} in fibers is derived as

$$Y_{\mathrm{m}} = -\left[\frac{\partial \Psi_{\mathrm{m,\,vol}}}{\partial D_{\mathrm{m}}} + \frac{\partial \Psi_{\mathrm{m,\,iso}}}{\partial D_{\mathrm{m}}}\right]. \tag{6}$$

Using Eq. (1), the damage driving force of the fiber can be formulated as

$$Y_{\mathrm{m}} = \begin{cases} \alpha\Psi^0_{\mathrm{m,\,vol}} + \Psi^0_{\mathrm{m,\,iso}} & \sigma_{\mathrm{h}} \geq 0 \\ \Psi^0_{\mathrm{m,\,iso}} & \sigma_{\mathrm{h}} < 0 \end{cases}. \tag{7}$$

With the postulated Helmholtz free energy density function of protein (Eq. (2)), the damage driving force Y_{p} of protein is given

$$Y_{\mathrm{p}} = -\frac{\partial \Psi_{\mathrm{p,\,iso}}}{\partial D_{\mathrm{p}}} = \Psi^0_{\mathrm{p,\,iso}}, \tag{8}$$

which is the isochoric part of the strain energy density in the undamaged configuration.

The damage potential functions of fiber and matrix are proposed as

$$F_{\mathrm{dam}} = Y_{\mathrm{i}} - Z(D_{\mathrm{i}}) = Y_{\mathrm{i}} - \left[Y^0_{\mathrm{i}} + \frac{1}{b_{\mathrm{i}}}\ln\left(\frac{D_{\mathrm{c}}}{D_{\mathrm{c}} - D_{\mathrm{i}}}\right)\right], \tag{9}$$

with $i = \{\mathrm{m}, \mathrm{p}\}$, which lead to an exponential damage evolution law for fiber and protein. Here, Z is the material resistance against material damage. Y_{i}^{0} are the initial resistances to damage and b_{i} control the evolution rate of damage resistance with increasing values of D_{i}. D_{c} represents the critical value of the damage, that is, D_{i} can take values from 0 (undamaged state) to D_{c} (critical state of damage leading to fracture).

The damage evolution law is derived based on the maximum dissipation principle

$$\dot{D}_{\mathrm{i}} = \dot{\lambda}_{\mathrm{i}} \frac{\partial F_{\mathrm{dam}}}{\partial Y_{\mathrm{i}}} = \dot{\lambda}_{\mathrm{i}}. \tag{10}$$

In case of damage, the damage rate $\dot{D}_{\mathrm{i}}$ is determined by the damage consistency condition

$$\mathrm{d}F_{\mathrm{dam}} = \frac{\partial F_{\mathrm{dam}}}{\partial Y_{\mathrm{i}}} \dot{Y}_{\mathrm{i}} + \frac{\partial F_{\mathrm{dam}}}{\partial Z} \frac{\partial Z}{\partial D_{\mathrm{i}}} \dot{D}_{\mathrm{i}} = 0. \tag{11}$$

The damage evolution equation is then derived using Eq. (9) as

$$\dot{D}_{\mathrm{i}} = D_{\mathrm{c}}\, b_{\mathrm{i}}\, \exp\left[-b_{\mathrm{i}}\, \langle Y_{\mathrm{i}} - Y_{\mathrm{i}}^{0} \rangle\right]\, \dot{Y}_{\mathrm{i}}, \tag{12}$$

where $\langle \cdot \rangle$ are the Macaulay brackets, i.e., $\langle x \rangle = [|x| + x]/2$.

The viscous regularization method is incorporated into the model to reduce damage localization and improve convergence, which is a generalization of the Duvaut-Lions viscoplasticity regularization method.

4.2 Protein–Mineral Interface

The interface between protein and mineral is modeled by a cohesive zone model that has previously been used in [32]. The constitutive model for the material separation is based on a bi-linear traction separation law, which is defined by three parameters for each direction (normal and shear): the initial elastic stiffness of the interface, K_{int}, the cohesive strength T_0 and the fracture energy Γ_0. The critical separation, at which the interface has completely failed is then given by $\delta_c = 2\Gamma_0/T_0$.

The maximum stress criterion is chosen to determine the initiation of damage in the interface. The effect of the mode mixity on the damage evolution law is not taken into account in the present work, the parameters in normal and shear direction are denoted as T_0^N and T_0^S with $T_0^N = \sqrt{3} T_0^S$, respectively. For more information on the applied cohesive zone model in general, the interested reader is referred to [4].

4.3 3D Computational Model of the Microstructure

4.3.1 Setup of the 3D RVE Model

The first and second hierarchical levels of enamel can be assumed to be organized in a self-similar way. The geometrical modeling of the microstructure at the first and second hierarchical levels are illustrated in Fig. 3. The HAP fibers and enamel rods are assumed to be unidirectionally aligned and surrounded by protein in the enamel. In order to simplify the RVE and reduce the computational cost without loss of essential information, we assume that the nanofibers and enamel rods are periodically arranged in a staggered manner and represented by prisms with a hexagonal cross-section.

At the first hierarchical level, the volume fraction of the mineral fibers is taken as 90%. According to the average size of the fiber cross section (approx. 50 nm [4]), the side length of RVE shown in Fig. 3(left) is $S = 52$ nm at the first hierarchical level of enamel, the thickness of the protein layer is 2 nm. The resulting hexagon side length of the fiber is approximately $e_{\text{fib}} = 29$ nm. Experimental observations show that the length of the HAP fibers is several μm [6]. Therefore, the fiber length is assumed to be 3 μm according to the computational analysis in [24], which leads the failure of the level-1 composite caused by the breaking of mineral fiber.

At the second hierarchical level, the fiber is the level-1 composite consisting of HAP and protein. Nanofibers in the interlayer at the second hierarchical level are neglected in the RVE model. For the second hierarchy level, it is reported that the

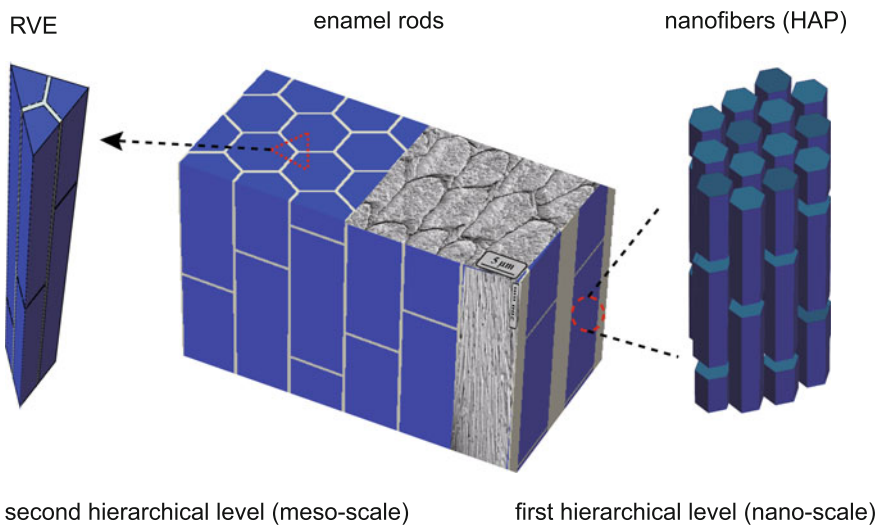

Fig. 3 Three-dimensional representative volume element with periodically staggered structure for modeling the microstructure of the first and second hierarchical levels of dental enamel

diameter of the fiber at this hierarchical level ranges from 1 to 7 μm [36]. Therefore, the hexagon side length of fiber at this level is set as $e_{\text{fib}} = 4\,\mu\text{m}$. The length of fiber is taken as 45 μm [6]. The thickness of protein layer is chosen to be 0.2 μm, so that the overall volume fraction of fiber at the second hierarchical level is 84%. The length of enamel rods is 45 μm [6].

The smallest unit of the periodic structure is the triangular prism, which is regarded as RVE for the 3D simulations. All simulations are conducted using ABAQUS®/standard. The finite element model consists of 8-node linear brick elements with full integration (designation: C3D8) for the fibers and the protein. Cohesive surfaces are inserted at the physical interface between protein and mineral fibers to model the interaction and damage behavior between the protein and mineral fibers. The 3D RVE model is subjected to a uniaxial displacement in fiber direction. Symmetric boundary conditions are applied to the bottom and side faces to keep the faces remaining plane and reproduce the constraint to deformation of the RVE from neighboring elements.

4.3.2 Material Properties

The mechanical properties of enamel on the different hierarchical levels have experimentally been determined based on micro-pillar and micro cantilever tests. However, the elastic properties and strengths of its constituents, protein and HAP, cannot directly be tested due to the limits of experimental methods. The mechanical properties of protein and HAP can only be inversely derived by combining mechanical model and experimental data. Elastic properties have already been identified in [4], strengths of the protein and the fibers were estimated in [32]. The HAP fiber in enamel is strong and has a brittle failure behavior, while the protein possesses a high capacity in dissipating energy during deformation. The model parameters b_{i} and Y_{i}^0 with respect to the damage process in the fiber and the protein have obtained by adjusting the values to reproduce the strength and damage behavior of the fiber and the protein in [24]. The respective values at level-1 are listed in Table 2.

The critical value of damage D_{c} is set to 1 according to the definition of damage, since the material loses the whole loading capacity for $D = D_{\text{c}} = 1$. In the damage model of the fiber, the additional parameter α in Eq. (1) maps the different damage behavior under tension and compression according to the crack closure effect. Due to the lack of experimental data for determining this parameter, we assume $\alpha = 1$ in all computations.

The properties of the interface between protein and mineral (cohesive strength T_0 and fracture energy Γ_0) have also been rationalized by comparison to experiments in [32] and are given in Table 2 as well.

The material properties of interface and protein at level 2 are not yet clearly determined. In this investigation, the microstructure at level 2 is assumed to be similar to the first hierarchy level. Therefore, the same model parameters are taken for the protein matrix acting between the rods and for the interface between fiber and matrix. Further, Ang et al. [2] investigated the behavior of crack propagation along

Table 2 Mechanical properties of protein, fiber and interface in enamel

1st hierarchical level:			
Mineral fiber:			
$\mu_m = 32.5\,\text{GPa}$,	$K_m = 49.4\,\text{GPa}$,	$b_m = 0.2\,\text{mm}^3/\text{J}$,	$Y_m^0 = 0.025\,\text{J/mm}^3$
Protein:			
$\mu_p = 89.1\,\text{MPa}$,	$K_p = 30.0\,\text{GPa}$,	$b_p = 0.015\,\text{mm}^3/\text{J}$,	$Y_p^0 = 0.004\,\text{J/mm}^3$
Interface:			
$T_0 = 60\,\text{MPa}$,	$\Gamma_0 = 1.5\,\text{J/m}^2$		
2nd hierarchical level:			
Enamel rod:			
$\mu_m = 27.4\,\text{GPa}$,	$K_m = 45.6\,\text{GPa}$,	$b_m = 0.2\,\text{mm}^3/\text{J}$,	$Y_m^0 = 0.01\,\text{J/mm}^3$
Protein:			
$\mu_p = 89.1\,\text{MPa}$,	$K_p = 30.0\,\text{GPa}$,	$b_p = 0.015\,\text{mm}^3/\text{J}$,	$Y_p^0 = 0.004\,\text{J/mm}^3$
Interface:			
$T_0 = 60\,\text{MPa}$,	$\Gamma_0 = 64.3\,\text{J/m}^2$		

the interface between protein and fiber using Vickers indentation at second hierarchical level of enamel. The critical stress intensity factor K_{Ic} is reported to be around $1.5\,\text{MPa m}^{0.5}$. With the elastic modulus $E_{L2} = 36\,\text{GPa}$ at this level the fracture toughness of the interface is estimated by $G_{\text{deb}} = K_{Ic}^2/E_{L2} = 64.3\ \text{J/m}^2$, which leads to the critical separation value of $1.286\,\mu\text{m}$.

The material parameters at the second hierarchical level are estimated based on the stress-strain curve of the level-1 composite as shown in Fig. 4a, since the average behavior of the first level of hierarchy consisting of fibers and protein is different to the HAP fibers. The Young's modulus at the first level of hierarchy, $E_{L1} = 64\,\text{GPa}$, is identified directly from the stress strain curve of the level-1-composite from the simulation. The Poisson's ratio is estimated to be 0.25 by the rule of mixture, $\nu_1 = \nu_m f_m + \nu_p f_p$, where the ν_m, f_m and ν_p, f_p are Poisson's ratio and volume fraction of mineral fiber and protein, respectively. The damage parameters, $Y = 0.01\,\text{J/mm}^3$ and $b = 0.18$ at the first level of hierarchy are obtained by iterative analysis to reproduce the strength and softening behavior as shown in Fig. 4a.

4.4 Simulation Results of First and Second Hierarchy Levels

In this section, the 3D finite element simulations are validated by comparing the simulation results with the stress-strain curve obtained from micro cantilever beam experiments at the first and second hierarchical levels of enamel. In Fig. 4, it is seen that the predicted results are in good agreement with experimental data for both hierarchical levels. The strength and nonlinear deformation behavior of the level-1 and level-2 composites are captured by the multiscale simulations.

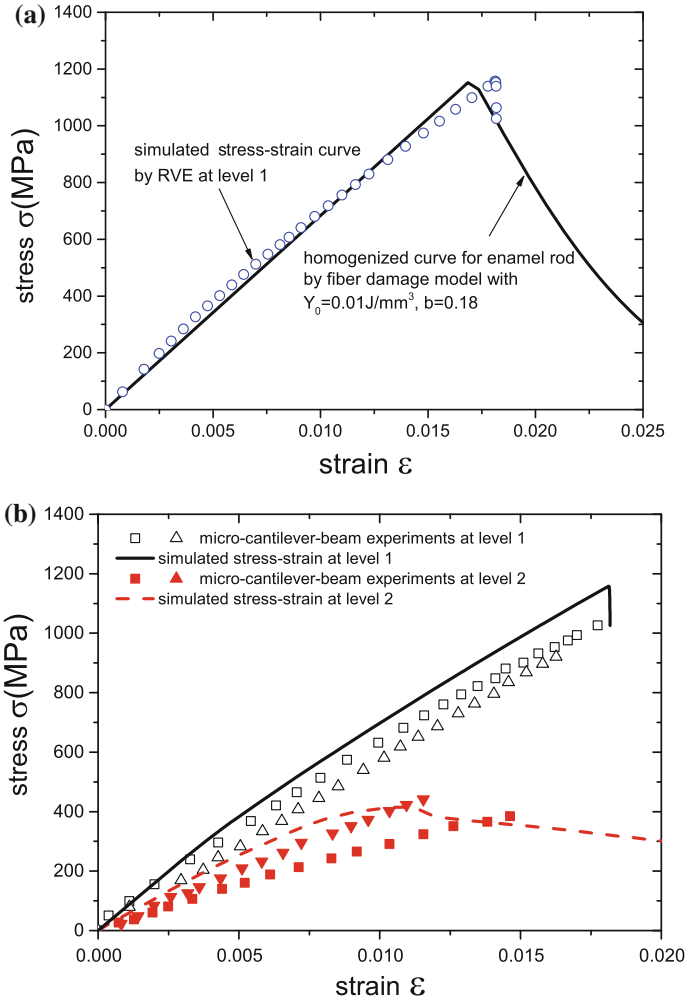

Fig. 4 **a** Stress-strain curve of damage model at level 1. **b** Comparison of experimental and simulation results at first and second level of hierarchy

The damage mechanisms for the level-1 and level-2 composites in the simulations are illustrated in Fig. 5. For the level-1 composite, the crack is deflected after forming a microcrack at the fiber end due to progressive debonding of the vertical interfaces. The interface debonding is confined close to the end of the fibers. The damage of fibers leads to the final failure of the level-1 composite. At this point a sharp drop in the stress-strain curve can be seen (Fig. 4a) and the level-1 composite fails. In contrast, the interface debonding initiates near the fiber end and then propagates along the interface, leading to a progressive degradation of the level-2 composite. Due to the debonding in a large portion of interface, the loading on the enamel rods

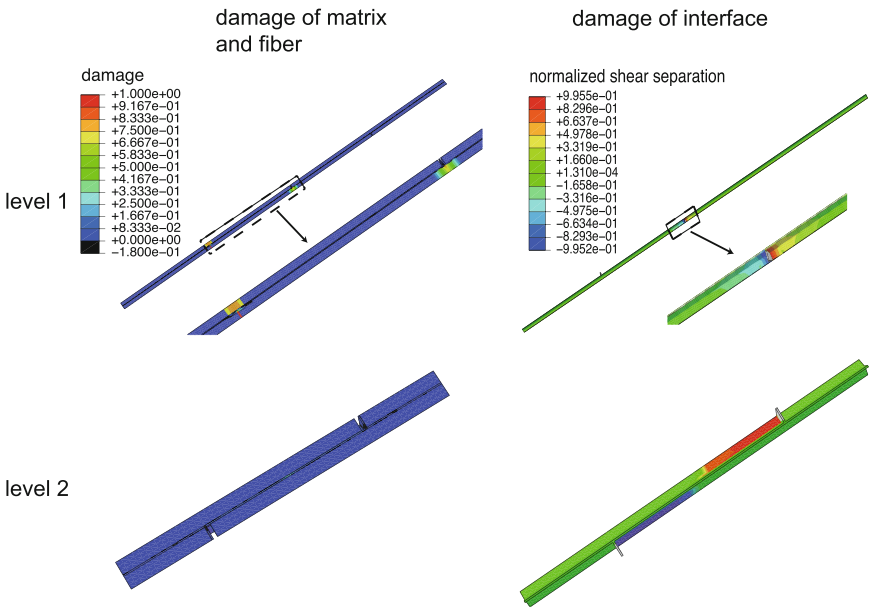

Fig. 5 Damage distribution in protein, mineral fibers and interface in the simulation of level-1 and level-2 composites

is reduced during the deformation process of the level-2 composite. Therefore, the enamel rods remain intact even when the level-2 composite fails.

The debonding of the interface leading to failure at the second level of hierarchy is consistent with experimental observations. The change of fracture mode from a catastrophic fracture due to failure of fiber at level 1 to progressive damage along prism boundaries of the fiber at level 2 is reproduced in the simulation. Further, it is clearly shown that the nonlinear deformation at the second level is more apparent due to debonding of interface and damage of protein, leading to a higher fracture dissipation energy that increases the damage-resistance at the second hierarchical level of enamel.

4.5 Influence of Initial Flaw at Different Hierarchical Levels

In order to investigate the flaw-tolerance behavior at different hierarchical levels, an initial flaw is introduced on the interface of the level-1 and level-2 composites. These imperfections can be a result of biomineralization and are visible under high-resolution electron microscopy [36].

Five sizes of initial flaws in the range 4–16% (defined as the area of unbonded interface A_{flaw} divided by total area of the interface in the RVE A_{total}, $A_{\text{flaw}}/A_{\text{total}}$)

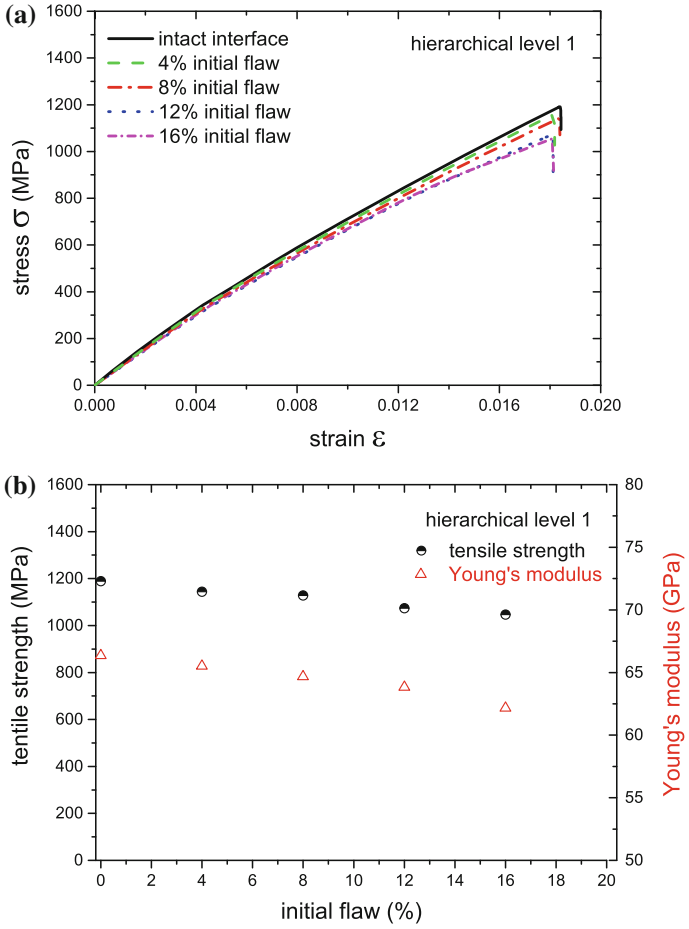

Fig. 6 Influence of initial flaw on mechanical properties at first hierarchical level

are considered to analyze the effect of structural imperfections on the degradation of the mechanical properties of the level-1 composite. The stress-strain curves in Fig. 6a show that the general damage mechanism is not affected by the presence of the structural imperfections. The fracture strain of the level-1 composites is not obviously affected by the size of the initial flaw. The variations of the tensile strength and Young's modulus with the size of initial flaw are displayed in Fig. 6b. It is seen that the tensile strength and Young's modulus are not sensitive to the size of initial flaw at the first hierarchical level of dental enamel. With an initial flaw size of 16%, the tensile strength is only reduced from 1175 to 1110 MPa and Young's modulus drops from 65 to 62 GPa.

At the second hierarchical level, the composite becomes more sensitive to the size of initial flaw compared to the level-1 composite as shown in Fig. 7. The tensile

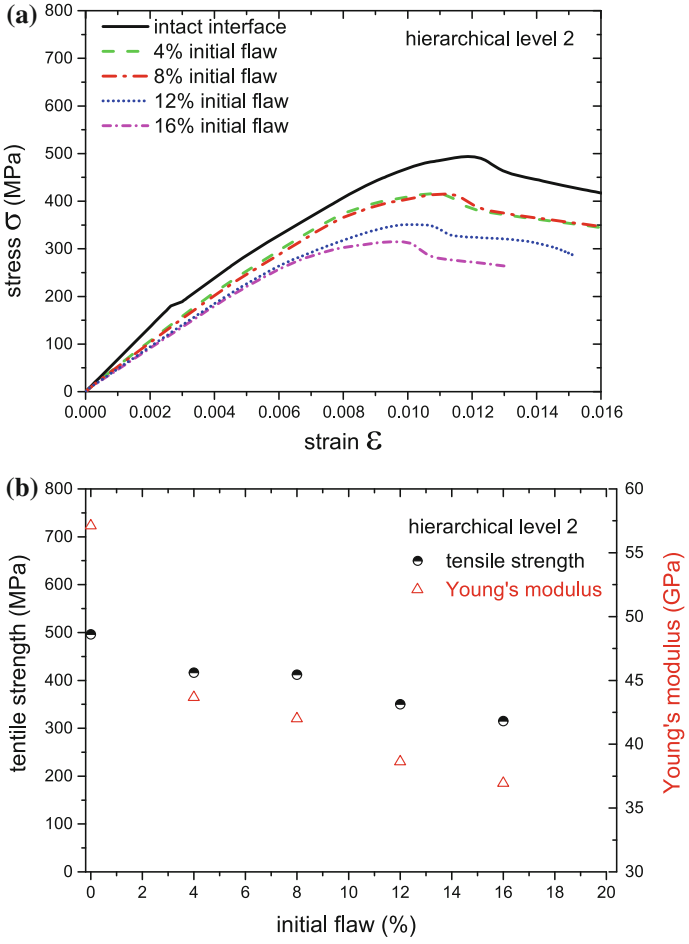

Fig. 7 Influence of initial flaw on mechanical properties at second hierarchical level

strength of the level-2 composite is reduced from 500 to 360 MPa due to the presence of an initial flaw with the size 16%. The Young's modulus dramatically drops from 56 to 43 GPa even if the level-2 composite only has a 4% initial flaw.

The computational analysis shows the different flaw-tolerance behavior of the composite at the first and second hierarchical levels in dental enamel. Compared to the second hierarchical level, the amount of interface between HAP and protein at the first hierarchical level is much larger due to the nano-sized fibers. As a results, the possibility for the formulation of a initial flaw on the interface at the first hierarchical level during the biomineralization process becomes higher. However, dental enamel becomes flaw-insensitive, if the initial flaw or the crack along the interface formulated during loading cycles is present at the first hierarchical level on the nano-scale.

5 Conclusions

In this work, multiscale experimental and computational approaches have been employed and combined to study nature's design principle of the hierarchical structure of bovine enamel. Small-scale experimental investigations have been performed to determine the mechanical properties at different hierarchical levels using micro-cantilever specimens. Three-dimensional finite element simulations incorporating damage have been performed to understand the hierarchical structure and damage-tolerance behavior of dental enamel. The simulation results were validated by comparison to experimental results from micro-cantilever beam experiments at two hierarchical levels. The dependence of the deformation and damage behavior on the hierarchical level are very well captured by the numerical simulations. The predicted different failure mechanisms at the first and second hierarchical level of enamel are consistent with experimental observations.

Summarizing the studies on the effects of feature of structure on the flaw-tolerance behavior of enamel, the following conclusions are drawn:

- The experimental results of micro-cantilever tests on bovine enamel at different hierarchical levels reveal a consistent reduction in fracture strength and Young's modulus with an increasing number of hierarchy levels. This results from the overall HAP content of the composite decreasing with each additional level of hierarchy. In addition, the computational analysis shows that the significant debonding of interface with a large portion reduces the stress-transfer between fibers at the second hierarchical level, which leads to the lower strength and Young's modulus of the level-2 composite.
- In the 3D multiscale simulations it is seen that the predicted results are in good agreement with experimental data for both hierarchical levels. The predicted different failure mechanisms at the first and second hierarchical level of enamel are consistent with experimental observations. The presence of initial imperfections significantly reduces the mechanical properties of the level-2 composite. The Young's modulus and tensile strength dramatically drop even if the level-2 composite only has a initial flaw with the size 4%. In contrast, tensile strength and Young's modulus are not sensitive to the size of an initial flaw at the first hierarchical level of dental enamel.
- Based on the computational analysis of the influence of thr hierarchical structure on the mechanical behavior of enamel, it is found that the first hierarchical level of enamel with very long fibers on the nano-scale is evoluted to be insensitive to initial flaws and achieve a high strength and stiffness. At the second hierarchical level, the microstructure is designed for the damage resistance of enamel.

The experimental and computational results from the study provide the knowledge for designing the hierarchical microstructure of bio-inspired advanced ceramics with a high flaw-tolerance.

Acknowledgements Partial financial support by the ACE-Centre (Institute of Materials Research, Helmholtz-Zentrum Geesthacht, Germany) is gratefully acknowledged. Partial financial support by the German Research Foundation (DFG) via SFB 986 "M^3" (projects A5, A6) is also gratefully acknowledged.

References

1. M. Akao, H. Aoki, K. Kato, Mechanical properties of sintered hydroxyapatite for prosthetic applications. J. Mater. Sci. **16**, 809–12 (1981)
2. S.F. Ang, A. Schulz, R. Pacher Fernandes, G.A. Schneider, Sub-10-micrometer toughening and crack-tip toughness of dental enamel. J. Mech. Behav. Biomed. Mater. **4**, 423–432 (2011)
3. B. Angmar, D. Carlström, J. Glas, Studies on the ultrastructure of dental enamel. J. Ultrastruct. Res. **8**, 12–23 (1963)
4. S. Bargmann, I. Scheider, T. Xiao, E. Yilmaz, G.A. Schneider, N. Huber, Towards bio-inspired engineering materials: modeling and simulation of the mechanical behavior of hierarchical bovine dental structure. Comput. Mater. Sci. **79**, 390–401 (2013)
5. S. Bechtle, S. Habelitz, A. Klocke, T. Fett, G.A. Schneider, The fracture behaviour of dental enamel. Biomaterials **31**, 375–84 (2010)
6. S. Bechtle, H. Özcoban, E.T. Lilleodden, N. Huber, A. Schreyer, M.V. Swain, G.A. Schneider, Hierarchical flexural strength of enamel: transition from brittle to damage-tolerant behaviour. J. R. Soc. Interface **9**, 74–1265 (2012)
7. S. Bechtle, H. Özcoban, E.D. Yilmaz, T. Fett, G. Rizzi, E.T. Lilleodden, N. Huber et al., A method to determine site-specific, anisotropic fracture toughness in biological materials. Scr. Mater. **66**, 8–515 (2012)
8. A. Boyde, L. Martin, The microstructure of primate dental enamel, in *Food Acquisition and Processing in Primates: The Microstructure of Primate Dental Enamel*, ed. by D.J. Chivers, B.A. Wood, A. Bilsborough (Springer, Boston, MA, US, 1984), pp. 341–367
9. P. Chen, A. Lin, Y. Lin, Y. Seki, A. Stokes, J. Peyras, E. Olevsky et al., Structure and mechanical properties of selected biological materials. J. Mech. Behav. Biomed. Mater. **1**, 26–208 (2008)
10. V. Dusevich, C. Xu, Y. Wang, M.P. Walker, J.P. Gorski, Identification of a protein-containing enamel matrix layer which bridges with the dentine-enamel junction of adult human teeth. Arch. Oral Biol. **57**, 1585–1594 (2012)
11. J.E. Eastoe, Organic matrix of tooth enamel. Nature **187**, 411–412 (1960)
12. J.C. Elliott, Structure, crystal chemistry and density of enamel apatites. Ciba Found. Symp. **205**, 54–67; discussion 67–72 (1997)
13. H. Gao, B. Ji, I.L. Jager, E. Arzt, P. Fratzl, Materials become insensitive to flaws at nanoscale: lessons from nature. Proc. Nat. Acad. Sci. **100**, 600–5597 (2003)
14. H. Gao, Application of fracture mechanics concepts to hierarchical biomechanics of bone and bone-like materials. Int. J. Fract. **138**, 101–137 (2006)
15. E. Hamed, I. Jasiuk, Multiscale damage and strength of lamellar bone modeled by cohesive finite elements. J. Mech. Behav. Biomed. Mater. **28**, 94–110 (2013)
16. L.H. He, N. Fujisawa, M.V. Swain, Elastic modulus and stressstrain response of human enamel by nano-indentation. Biomaterials **27**, 4388–98 (2006)
17. L.H. He, M.V. Swain, Understanding the mechanical behaviour of human enamel from its structural and compositional characteristics. J. Mech. Behav. Biomed. Mater. **1**, 18–29 (2008)
18. J. Holager, Thermogravimetric examination of enamel and dentin. J. Dent. Res. **49**, 546–548 (1970)
19. D.W. Holcomb, R.A. Young, Thermal decomposition of human tooth enamel. Calcif. Tissue Int. **31**, 189–201 (1980)
20. I. Jäger, P. Fratzl, Mineralized collagen fibrils: a mechanical model with a staggered arrangement of mineral particles. Biophys. J. **79**, 1737–1746 (2000)

21. W.V. Koenigswald, W.A. Clemens, Levels of complexity in the microstructure of mammalian enamel and their application in studies of systematics. Scanning Microsc. **6**, 195–217; discussion 217–218 (1992)
22. J. Lemaitre, R. Desmorat, *Engineering Damage Mechanics—Ductile, Creep, Fatigue and Brittle Failures*. Springer, 2005
23. M.F. Little, F. Casciani, The nature of water in sound human enamel. Arch. Oral Biol. **11**, 565–571 (1966)
24. S. Ma, I. Scheider, S. Bargmann, Continuum damage modeling and simulation of hierarchical dental enamel. Model. Simul. Mater. Sci. Eng. **24**, 045014 (2016)
25. S. Ma, I. Scheider, S. Bargmann, Anisotropic constitutive model incorporating multiple damage mechanisms for multiscale simulation of dental enamel. J. Mech. Behav. Biomed. Mater. **62**, 515–533 (2016)
26. M.C. Maas, E.R. Dumont, Built to last: the structure, function, and evolution of primate dental enamel. Evol. Anthropol. **8**, 52–133
27. J.D. McGuire, M.P. Walker, A. Mousa, Y. Wang, J.P. Gorski, Type VII collagen is enriched in the enamel organic matrix associated with the dentin-enamel junction of mature human teeth. Bone **63**, 29–35 (2014)
28. M. Mirkhalaf, A.K. Dastjerdi, F. Barthelat, Overcoming the brittleness of glass through bio-inspiration and micro-architecture. Nat. Commun. **5** (2014)
29. A. Nanci, *Ten Cates's oral histology: development, structure, and function*, 7th edn. (Mosby, St. Louis, Mo, London, 2007)
30. E. Peña, Prediction of the softening and damage effects with permanent set in fibrous biological materials. J. Mech. Phys. Solids **59**, 1808–1822 (2011)
31. J.M. Rensberger, Pathways to functional differentiation in mammalian enamel, in *Development, Function and Evolution of Teeth*, ed. by M.F. Teaford, M.M. Smith, M.W.J. Ferguson (Cambridge University Press, Cambridge, New York, 2000), pp. 252–268
32. I. Scheider, T. Xiao, E. Yilmaz, G.A. Schneider, N. Huber, S. Bargmann, Damage modeling of small scale experiments on dental enamel with hierarchical microstructure. Acta Biomater. **15**, 244–253 (2015)
33. M. Setally Azevedo Macena, de M.L. Alencar e Silva Leite, de C. Lima Gouveia, de T.A.S. Lima, P.A.A. Athayde, de F.B. Sousa, A comparative study on component volumes from outer to inner dental enamel in relation to enamel tufts. Arch. Oral Biol. **59**, 568–577 (2014)
34. E.D. Yilmaz, S. Bechtle, H. Özcoban, A. Schreyer, G.A. Schneider, Fracture behavior of hydroxyapatite nanofibers in dental enamel under micropillar compression. Scripta Mater. **68**, 7–404 (2013)
35. E.D. Yilmaz, S. Bechtle, H. Özcoban, J.A. Kieser, M.V. Swain, G.A. Schneider, Micromechanical characterization of prismless enamel in the tuatara, Sphenodon punctatus. J. Mech. Behav. Biomed. Mater. **39**, 7–210 (2014)
36. E.D. Yilmaz, H. Jelitto, G.A. Schneider, Uniaxial compressive behavior of micro-pillars of dental enamel characterized in multiple directions. Acta Biomater. **16**, 95–187 (2015)
37. E.D. Yilmaz, G.A. Schneider, M.V. Swain, Influence of structural hierarchy on the fracture behaviour of tooth enamel. Philos. Trans. Ser. A Math. Phys. Eng. Sci. **373** (2015)

Part IV
Orthopaedics

Challenges in Total Hip Arthroplasty

Gabriela von Lewinski and Thilo Floerkemeier

Abstract Challenges in total hip arthroplasty have several aspects. The current chapter discusses the changes of indication, the influence of demographic changes and the challenges of THA during different lifetimes periods. For younger patients the use of short stems becomes more and more popular. It is important to gain more information about the long-term survival rate, the extent of stress shielding and the osseointegration of the implants. With increasing numbers of THA the problem of revision THA becomes more and more important. For elderly patients custom-made implants are helpful to solve situations with a huge bone loss and to achieve a stable situation to allow a full weight bearing postoperatively.

1 Challenges of Total Hip Arthroplasty (THA)

1.1 Changes in Indication for Implantation of a Total Hip Arthroplasty

In the 1960s the indication for implantation of a total hip arthroplasty (THA) was given especially for elderly patients with the underlying diagnosis of osteoarthritis of the hip [1, 2]. Over the last decades the survival rate after THA increased and showed satisfying data [3]. Furthermore, pain and restrictions in function can be addressed very well by implantation of a THA [1, 4]. This concept of success resulted in the fact that THA designated as the operation of the century [2]. These facts lead to the enlargement of the indication for THA. Today the indication is given also for younger patients with osteoarthritis of the hip in order to regain activities, allow reintegration in working life and not to lose quality of life [5–8].

G. von Lewinski (✉) · T. Floerkemeier
Orthopaedic Department, Hannover Medical School,
Anna-von-Borries Strasse 1-7, 30625 Hannover, Germany
e-mail: Gabriela.lewinski@diakovere.de

T. Floerkemeier
e-mail: Thilo.Floerkemeier@diakovere.de

P. Wriggers and T. Lenarz (eds.), *Biomedical Technology*, Lecture Notes in Applied and Computational Mechanics 84, DOI 10.1007/978-3-319-59548-1_16

However, this implies changes in requirements of hip arthroplasty. Patients, who receive a THA in progressed age, are unlikely to have a revision of the THA or at least one, whereas patients, who were implanted a THA in younger age, are likely to receive one or more revision of the THA. With increasing number of revisions of the THA also the complexity of the surgical intervention due to less bone substance and thus problems for a sufficient fixation of the revision implant [9, 10]. Advanced in biomedical engineering new designs of implants were developed. In the meanwhile a variety of short stem arthroplasties exist [11, 12]. Standard stems reveal a primary diaphyseal anchorage, which means that load were transferred via arthroplasty to the diaphyses of the femur [13]. According to Wolf's law bone relieves in region with less loading, while bone strengthened in stressed regions [14]. This can result in a so called stress-shielding effect, which may be associated with an increased risk of THA loosening. In contrast to standard stems short stem THA are supposed to reveal a primary metaphyseal anchorage, which may reduce the stress-shielding effect and thus the risk of aseptic loosening [15]. However, short stem are not only shorter than standard stems, but they are also more bone preserving due to a more proximal osteotomy [16]. Along with that the implantation of a short stem arthroplasty irritates the gluteus muscles less than the implantation of a standard stem.

2 Influence of Demographic Changes on Osteoarthritis of the Hip

Demographic changes describe the size, composition and structure of populations. Thus, it is used to show shifts in population structure. Thus, demographic changes also influence the incidence of osteoarthritis of the hip and the number of implanted THAs per year.

Demographic changes in Germany reveal declining birth rates, longer life expectancy and increasing immigration [17]. This results in a shift to an increasing ageing of the population over the next decades. This demographic ageing is associated with the necessity of cost-effective THA in elderly trauma-patients with low demands as well as with the necessity of innovative THA with good survival rates and low wear for elective patients with high demands. While the majority of the German population is between 40 and 60 years at the moment, for the year 2040 the majority of the German population is supposed to be older than 60 years of age [17]. The risk of osteoarthritis of the hip and other joint increased with the age above 65 [18].

Furthermore, the life expectancy will increase continuously. While the life expectancy of a person at the age of 65 was about 10 years at the end of the 19th century and about 15 years in the 1980s, the life expectancy in Germany in 2050 is predicted to be greater than 20 years [17].

In addition, the demands of the activity level in progressed age within the population will increase. Seniors do not want to be limited in their daily life- and sportive activity. A study by Moschny et al. gathered the barriers to physiological activities in elderly population in Germany (mean age 77 years) [19]. The main reason for limitation of physical activity was a poor health (57.7%). In addition, more the half of the participants stated pain and more of one-third stated osteoarthritis as a concurrent cause for physical limitations.

As a consequence of these facts an increase in THAs as well as revision of THA each year will increase. Kurtz et al. for example predicted for the USA in increase in demand for THA between 2005 and 2030 of 174% [20]. In addition, a doubling of the revision of THA in the USA between 2005 and 2026 is expected. Nemes et al. stated that growing incidence, population growth, and increasing life expectancy will probably result in increased demand for hip replacement surgery in Sweden [21].

Therefore, it is important to assess the outcome, revision rates and risk factors of arthroplasties.

3 Joint Replacement Registers

Joint Arthroplasty Registers give helpful information for arthroplasties. They focus on the outcome of primary arthroplasties. Almost every western European, the United States and Australia country has a joint arthroplasty register by now. The longer a joint arthroplasty register exits, the more information is enclosed. Therefore a lot of information comes for e.g. from the older registers in Scandinavia [22, 23].

In 2010 a quality safety system started as a campaign of the German Orthopaedic Society to improve the quality of knee and hip arthroplasties in Germany. It is called the Endocert® system [24, 25]. The system is based on a DIN ISO 9001:2008 certification. Beside the quality of the results, the quality of the processes and the structures of each center is considered and required. One of the key points of the system is that joint replacement surgeries of hip and knee are only performed by high volume surgeons who do at least 50 arthroplasty procedures in hip and knee per year. Furthermore each X-ray is evaluated and quality indicators such as the inclination angle of the acetabular cup are measured. This leads to a very detailed data collection in each center. In contrast to the national joint arthroplasty register, which focus on the primary arthroplasty, also data from revision arthroplasties of the hip and knee are collected.

4 Challenges of THA During Different Lifetime Periods

Despite more than 2,00,000 implanted THA in Germany every year [17] remaining challenges exist. There seems to be a correlation between prolonged surgical time and difficult cases. Therefore, we determined the number of cases in our center with

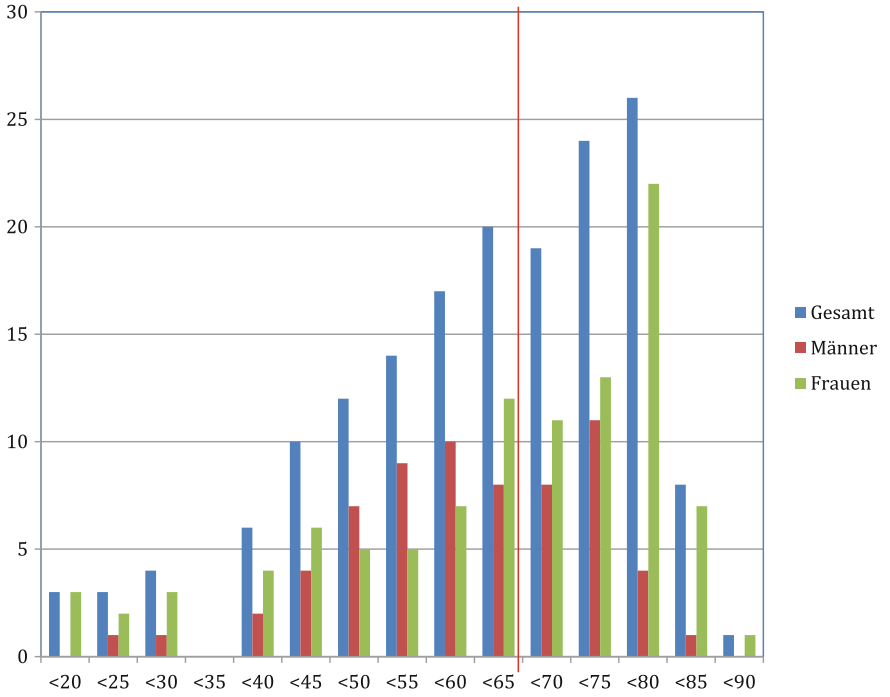

Fig. 1 Age distribution in quintels of patients with THA requiring an operating time > 90 min

a prolonged (>90 min) surgical duration. In 2014 17% of all primary THAs took more than 90 min. Distributing the patients of prolonged surgical duration gender-specific in quintile according to their age at the time of surgery (Fig. 1), three groups of patients are to the fore:

- Young (female) patients with secondary osteoarthritis of the hip
- (Male) mid-life patients
- "Elderly" (female) patients

The group of young patients with osteoarthritis of the hip represent a challenge for different reasons. Most of the patients with osteoarthritis of the hip in young age have the underlying diagnosis of a secondary osteoarthritis [7, 26]. Typical secondary osteoarthritis of the hip represent hip dysplasia, osteonecrosis of the femoral head and femoroacetabular impingement. The osteoarthritis due to hip dysplasia can represent a major challenge for the surgeon depending of the extend of dysplasia (Fig. 2). Hip dysplasia is defined as insufficient coverage of the femoral head. This can result in problems for anchorage of the cup of a THA. Hip dysplasia is often associated with a coxa valga on the femoral side. Along with that the implantation of the stem with reconstruction of the center of the hip can be aggravated by the increased CCD-angle of the femoral neck. Due to the young age of patients with hip dysplasia more than one revision of the THA is expected for the

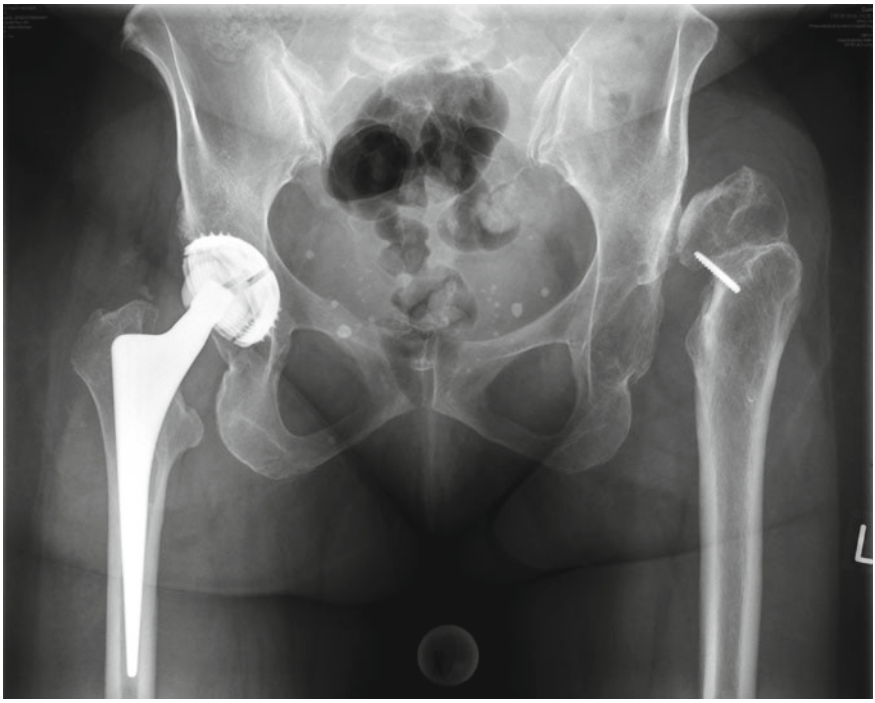

Fig. 2 Pelvic X-ray of an 50-year old patient with a hip dysplasia und congential high hip dislocation. Femoral osteotomy was performed in childhood

future. Thus, bone preserving strategies with low risk of aseptic loosening is desirable. Short stem THA are part of such approaches [11, 12].

Short stem THAs only exist since the end of the 1990s. Thus, by now longterm results do not exist [11, 12]. In order to gain midterm results our workgroup conducted a study to determine the outcome and survival rate after implantation of a short stem THA with primary metaphyseal anchorage in patients with osteoarthritis of the hip due to hip dysplasia [27]. Therefore, clinical and radiological outcome after implantation of a METHA® short stem THA in patients with progressive osteoarthritis of the hip (58 patients) were compared to the group of patients with primary osteoarthritis (59 patients). After a mean follow-up of 2.9 ± 1.1 years both groups showed a significant increase in clinical outcome according to the Harris Hip Score without significant difference between both groups. The mean Harris Hip Score in the group of primary osteoarthritis increased from 43.1 ± 17.8 points preoperatively (range 7.0–92.0) to 91.2 ± 11.1 postoperatively (range 47.0–100.0) ($p < 0.0001$), while in the group of osteoarthritis due to hip dysplasia the mean Harris Hip Score increased from a preoperative mean of 38.1 ± 11.4 points (range 19–72) to 88.8 ± 12.9 postoperatively (range 54–100, $p < 0.0001$). The outcome was categorized as excellent in 78 of 117 hips (66.6%), good in 19 (16.2%), fair in 11 (9.4%), and poor in 9 (7.7%). Summarizing the data revealed the METHA® short

stem as a good option for osteoarthritis of the hip even in patients with osteoarthritis due to hip dysplasia. The implant also allows a good reconstruction of the center of the hip and thus of the biomechanics resulting in good clinical outcome.

The second group with certain challenge is the so called “Mid-life group”. It is the group of dominantly manly patients with progressive osteoarthritis at the age between 50 and 70 years. These patients are limited due to pain and restriction in function so that a THA is a reasonable treatment option. However, it is uncertain which type of implant is best suited for these group of patients: short stem THA or standard stem THA. Long-term results exist only for standard stems, while only short- to midterm results are present for short stem THA. As mentioned previously short stem THA are supposed to be more bone preserving than standard stems due to a more proximal osteotomy and less stress-shielding effects as well as the implantation is more muscle protective than the one of standard stems. However, these supposed benefits of short stems are clinically not proven as short stem THA exist only since the end of the 1990s. Short stem THAs exhibit a smaller surface than standard stems. Thus, direct postoperatively the micromotion is increased compared to standard stems. Do these micromotion exceed certain amounts, the risk of failed osseointegration exist. In these cases factors like minor bone quality, e.g. osteoporosis or osteonecrosis of the femoral head, or increased loads due to high body weight or high body mass index influence the osseointegration of implants. In the certified center of arthroplasty of the orthopaedic department of the Hannover Medical School the revisions of short stem THA were analyzed in order to identify risk factors [28]. Of the 1953 short stem THAs, which were implanted between 2005 and 2012, 38 patients required a revision of the THA. In 12 cases, the modular titanium neck adapter failed. In 19 cases, reason for revision was aseptic loosening of the implant; of these, 11 cases were due to major stem subsidence, 2 due to via falsa (cortical penetration) implantation and 5 due to periprosthetic fractures. This corresponds to an aseptic total revision rate of 1.3% for 26 short stems and 1.9% including the cases of all 38 documented revision cases. Thirty-four cases could be revised with cementless standard hip stems, while 2 cases were revised with short stems, and 2 cases were revised with long revision stems. The main reason for revision was undersizing (58% of aseptic revisions). Fifty-four percent of revisions were conducted in male patients—23% with osteonecrosis of the femoral head, and 7% with short hip stems positioned in varus in coxa vara deformities. Seventy-two percent of revisions after marked early stem subsidence and position change into valgus were conducted in female patients.

The third group of patients with special focus is the group of elderly female patients with an age above 75 years with supposed minor bone quality due osteoporosis. These patients are unlikely to expect a revision of the THA due to aseptic loosening. Thus, and due to the fact of supposed minor bone quality a standard stem is normally chosen. However, it is uncertain whether the THA should be cemented or not. A cemented THA may be superior to non-cemented THA in elderly patients.

5 Challenges of Revision THA

Revision surgery of THA has to be differentiated between the revision surgery of the acetatabular cup and the femur. Today implants allow the replacement of the complete femur. Problem is the bone loss of the greater trochanter, which is an important muscular insertion of the gluteus medius and minimus. These muscles stabilize the pelvis. With deinsertion of the muscles the patient will limp and there is the risk for luxation of the hip replacement. However, special tripolar inlay will help to avoid this complication.

In contrast to this revision surgery of the acetabular cup is more complex insofar that with increasing loss of bone the anchorage of the acetabular cup the limited.

The acetabular bone defect was categorized according to the Method by Paprosky as reporting [29] (Table 1) and the method of the American Academy of Orthopedic Surgeons (AAOS) as reported by D' Antonio et al. [30] (Table 2).

An implant migration of more than 2 cm (Paprosky type 3A and 3B) and the pelvic discontinuity can be a resulting problem. These problems can also be a result of infection, osteolysis and casually fracture. In these situations, the pillars are no longer in sufficient condition to allow a conventional anchoring of the implants. After all the revision THA generate major acetabular defects and pelvic discontinuity. This is still a great challenge in the orthopedic surgery.

There are several adequate options mentioned in the literature, which is depending on the severity of defect situation. Small pelvic bone defects can be successfully rebuilt with or without supplementary allograft. A lager uncontained defect surgical options include elongated acetabular component extra—large hemispheric cups, structural allograft with planting, and reconstruction cages with ischial or iliac screw fixation. The available several surgical options reflect the difficulty to solve this problem [31].

Although the methods differ, general principle in the revision surgery of the acetabular cup with severe bone loss is to achieve a stable restoration of the continuity between the ischium and the ileum with reconstruction of the anatomical hip

Table 1 Paprosky classification [29]

Type		
I		Acetabular rim, anterior and posterior column intact. Local, contained defects
II		Destroyed hemisphere with intact supportive columns and <2 cm superomedial or superolateral migration
	A	Moderate superomedial migration
	B	Moderate superolateral migration with more destruction of superior dome
	C	Isolated medial migration
III		Superior migration >2 cm and destruction of the acetabular rim and supporting structures
	A	Köhlers line intact (the rim defect from 10 o'clock to 2 o'clock)
	B	Köhlers line not intact (the rim defect from 9 o'clock to 5 o'clock position)

Table 2 AAOS classification

Type 1		Segmental defects
	A	Peripheral: superior–anterior–posterior
	B	central (lack of medial wall)
Type 2		Cavitary defects
	A	Peripherals: superior–anterior–posterior
	B	Central (intact medial wall)
Type 3		Combined defects (Segmental and cavitary)
Type 4		Pelvic discontinuity
Type 5		Arthrodesis

center. However, currently, in the setting of massive periacetabular bone loss none of these options has been shown to clear advantageous results. Complications of acetabular revisions include component loosening, cup migration, alteration in the biomechanics, changes in the center of rotation of the hip joint, nerve palsies, chronic weakness, and dislocation.

They have on the one hand often the problem of reduced bone quality and on the other hand there is a reduced compliance in performing a partial weight bearing on crutches due to a limited mental and physical fitness. Thus, there is not only the problem of periacetabular bone loss, but also the anchorage of the revision of the acetubular cup surgery should be stable enough to allow a postoperative full weight bearing.

6 Patients and Methods

We evaluated in a retrospective designed study was between January 2010 and May 2016, a total of 44 patients with bone loss and pelvic discontinuity were treated with a custom acetabular component. (31 female and 13 male, both sides = 0; right n = 24; left n = 20).

The indication for the custom made acetabular components was that conventional cup replacement and revision cup system were expected not to achieve a successful result because of massive bone loss and pelvic discontinuity in the setting of failed THA. In contrast to other custom made acetabular revision cups, most custom made cups in the present study had not only flanges but also ilical stem —similar to the pedestral cups published by Schoellner in 2000 [32].

The patients were invited as part of a routine follow-up. From the 44 patients 31 could be included. Four patients died already and one was in coma. Because of dementia one patient could be followed up but was not included in the study. Neither death nor coma was related to their arthroplasty. Seven patients could not be contacted by phone or mail. Mean age of the patient at the time of the surgery was 71 years (range 38–86 years) (Table 3). The mean follow up was 27 months (range 7–51). The average duration of the surgery was 245 min (range 127–424). Length of the stay in hospital was 20 days (range 9–60 days).

Table 3 Preoperative patient characteristics

	n	%
Number of total triflange acetabular component	31	100%
Sex Female Male	23 8	74 26
Age (Years)	71 (range 38–86)	
Previous revision surgery		%
0	0	0
1	4	13
2	12	39
3	7	22
4	3	10
5	2	6
>5	3	10
Reason for surgery	Total	%
Aseptic bone loosening with cup migration	16	51
Aseptic & implant fracture	4	13
Recurrent dislocation	4	13
Girdlestone pseudarthrosis after Septic bone loosening	7	23
Preoperative walking aid	Total	%
No walking aids	2	6
Not mentioned	1	3
Crutch	14	45
Rollator	3	10
Wheelchair	7	23
Reclining	4	13
Operation Time min (range)	245 (range: 127–424)	
Duration of hospital stay	20 (range: 9–60)	

All patients received a previous revision surgery before the custom-made acetabular component was used. Four (13%) patients received a minimum of one revision, 12 (39%) a minimum of 2 revisions, 7 (23%) a minimum of 3 revisions, 3 (10%) a minimum of 4 revisions and 2 (6%) a minimum of 5 revisions. In 3 (10%) patients no precise information about the number of foregoing revisions was available.

Reason for revision surgery included aseptic bone loosening with cup migration in 16 hips (51%), aseptic and implant fracture in 4 (13%) and recurrent dislocation also in (13%) and so-called girdlestone situation with complete removal of the acetabular and femoral components after septic bone loosening with (22%).

Preoperative anteroposterior (a.p.) x-rays and 3-D CT-reconstruction based on preoperative radiographic evaluation analysis showed that most of patients had massive periacetabular bone loss (Paprosky Type 3A and 3B by (97%) (Figs. 3, 4, 5 and 6).

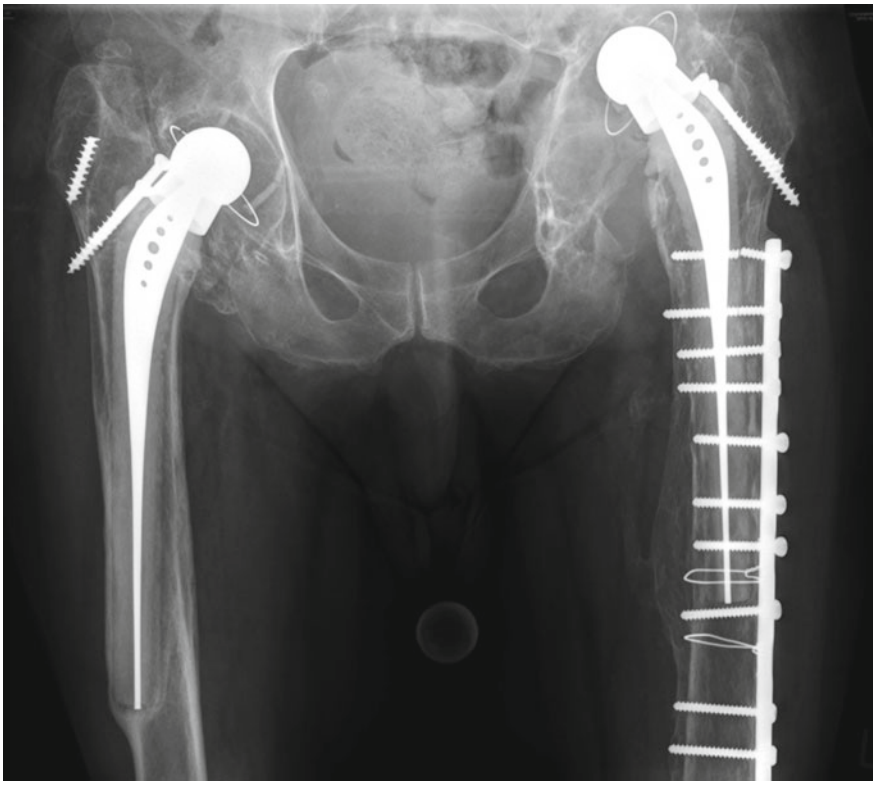

Fig. 3 Preoperative anteroposterior radiograph of a 71-year-old patient with an aseptic loosening, and migration of the acetabular cup. A massive bone loss in the os ilium is seen

Bone loss grading was performed using preoperative radiographs, and written reports about the surgery and CT reconstructed pelvic models. With this information the classification became accurate.

Outcome assessment included intraoperative and postoperative complications, reason for revision like dislocation, infection or revision of any reason, surgery and implant failure, surgery time, duration of the hospital stay.

Failure was defined according to Friedrich et al. [33] if custom-made implant had to be expanded or replaced with other methods.

One important criterion for evaluating the clinical outcome is the mobility of the patients. Therefore we compared the degree of mobility pre- and postoperatively and asked if any supports such a wheelchair or crutches were needed.

Clinical evaluation of the postal-surgical function was performed by using the validated disease-specific assessment tool, the Harris Hip score [34]. The patient activity level was assessed using the University of California Los Angeles (UCLA)

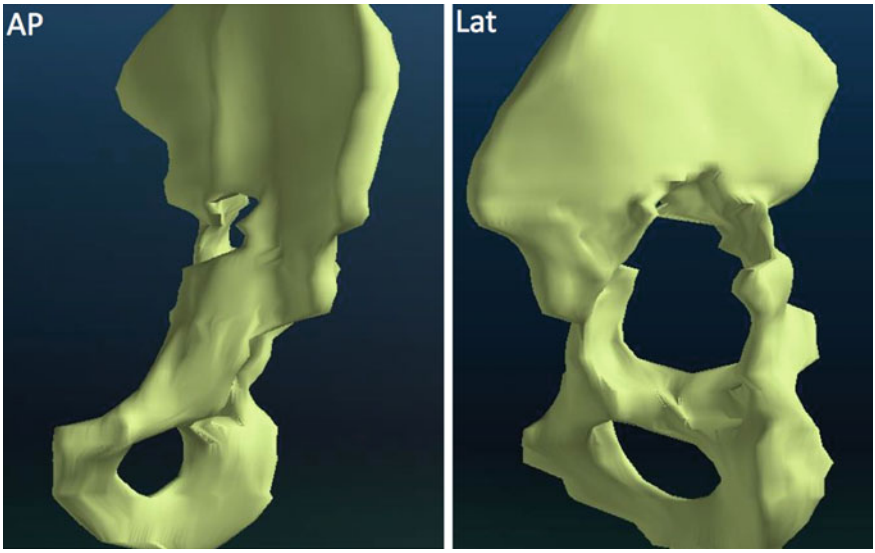

Fig. 4 Preoperative 3D reconstruction based on patient CT data. Medial breakthrough and cranial defect, unstable dorsal and ventral pillars. Classified as Paprosky Type IIIb

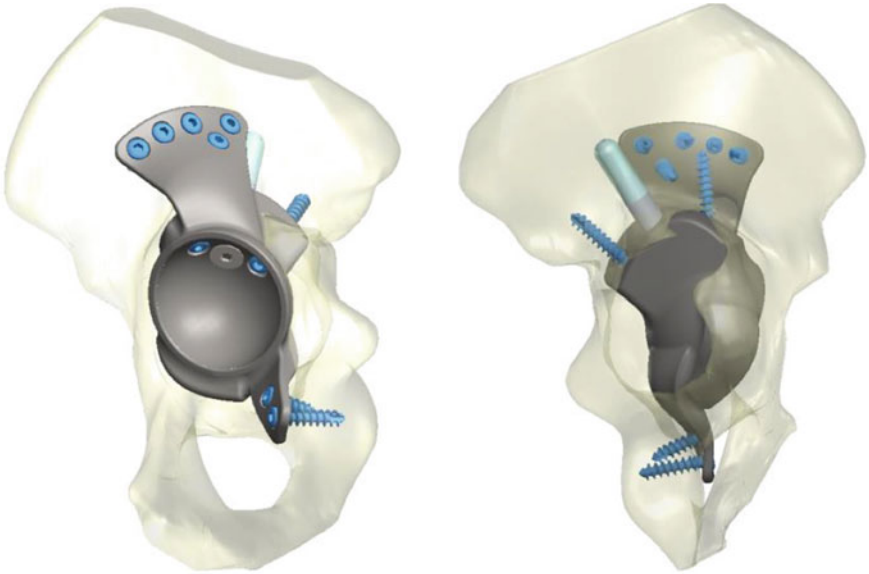

Fig. 5 3D reconstruction of the custom-made acetabular implant bridging the defect, position of the flanges and the ilical stem

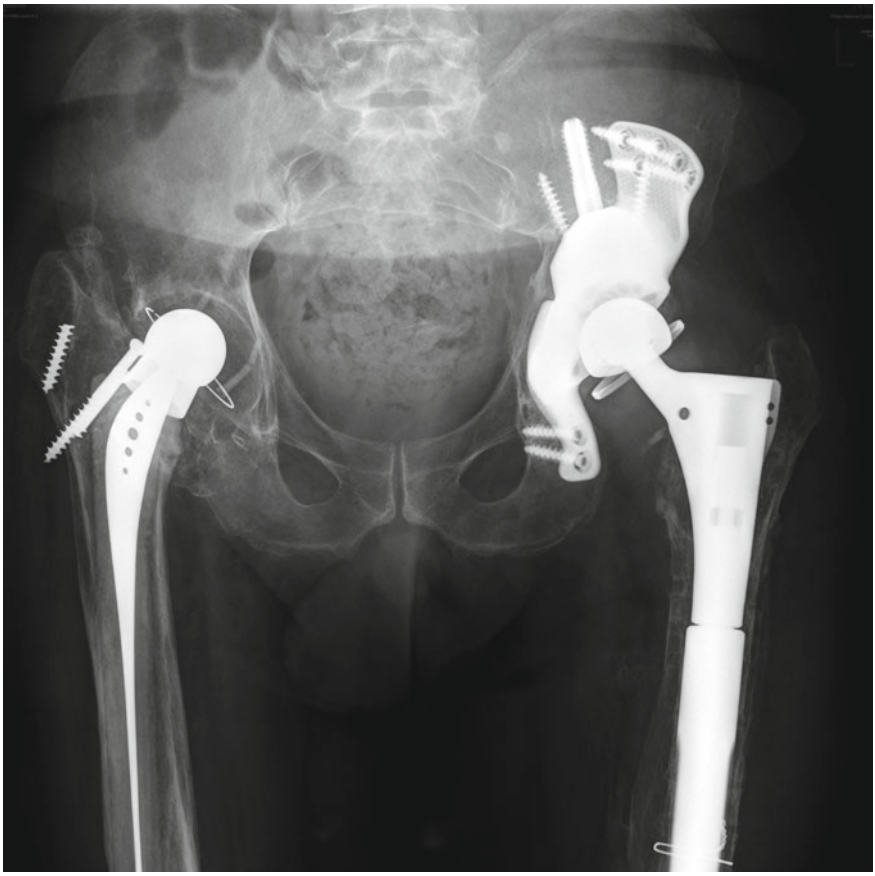

Fig. 6 Postoperative anterior-posterior pelvic X-ray. A well-fixed custom-made acetabular component with flanges and ilical stem is seen

[35] and the survey about the 38 modified HOOS items. Five subscales "Pain", "Symptoms", "Activities of Daily Living", "Sport and Recreation Function" and "Hip Related Quality of Life" which have in described from Nilsdotter et al. [36] were considered.

7 Results

Thirty (96%) procedures were considered clinically successful. Failure occured by one patient (4%). In this case the patient had a deep infection. The patient underwent an antibiotic treatment and girdlestone-situation. After healing of the infection reimplantation of THA with a new custom-made acetabular component was performed.

Three patients (10%) had an infection and all of them underwent surgical debridement and treatment with antibiotics. Two of these three patients had a girdlestone situation before implantation due to a deep joint infection before. Hip dislocation was seen in five (16%) cases, one could be solved with closed reduction. Four patients required further surgical intervention. Two of them were treated by exchanging the inlay into a tripolar anti-luxation inlay and the remaining two had an exchange of the inlay and the femoral head.

All in all seven 7 of 31 (23%) patients had a reoperation for any reason; four because of dislocation and three because of infection. All were successfully treated.

All patients were followed postoperatively with an anterior-posterior pelvis radiography. For the latest follow-up only 25 patients were able to come to an outpatient visit.

Radiological evaluation at the time of follow-up showed no signs of loosening or cup migration in none of the patients. In two patients the custom-made acetabular component demonstrated a loosening of the screws in the flange of the os ischium, without any signs of loosening of the cup itself.

In the clinical assessment the average Harris hip scores for 31 patients in this study reached a mean value of 70.4 points (range: 19–95 points). The mean of the UCLA Score was 4 points (range: 1–8 points) which stands for regularly participation in mild activities such as walking, limited housework, and limited shopping.

The survey about the 38 HOOS items resulted a mean of 56.4 points (range: 20–91 points).

The assessment of the use of walking aids pre- and postoperative was impressive. 91% of the patients needed at least crutches as a walking aid preoperatively. 13% of the patients were even not able to sit in a wheelchair. The postoperative evaluation showed that only 45% of the patients were depended on walking aids and only one patient (3.2%) was sitting in a wheelchair.

8 Discussion

The revision THA and the resulting major acetabular defects and pelvic discontinuity is still a great challenge in the orthopedic surgery [37–40]. There are several options mentioned in the literature, which is depending on the severity of defect situation. The diversity surgical options shows the difficulty to solve this problem [33, 37, 41]. The custom-made acetabular is a possibility which is according to the literature seems to be a favorable option for massive periacetabular bone loss.

The results of the present study are compared with other studies using custom made implants in the literature (Table 4). A direct comparison is difficult because patient groups and the design of the custom made implants differ. Beside the study of Taunton [42] (n = 57 hips) it is the largest patient group evaluating a custom made implant. Most of the published studies used a triflange custom-made acectabular implant. The use of the short iliacal stem in combination with the custom made implant—similar to the pedesdal cup is new. Furthermore with an

Table 4 Literature review with custom-made acetabular components in revision THA with severe bone loss

Author (Year)	Num-ber of patients (hips)	Period of surgery	Score	Result	Radiological classification of defect	Follow-up time (FUT) (average/month)	Average age at Surgery	Dislocation Rate	Revision rate (any reason)	Failure or removal	Infection
Joshi AB et al. [43]	27 (27)	1993-1996	/	/	AAOS Type 3	58	68	4%	2/27(7%)	1/27(4%)	2/27 (7%)
Holt GE et al. [44]	26 (26)		HHS	78	Paprosky Type 3B; AAOS Type III or IV 5	54	69	8%	1/26 (4%)	3/26 12%	0
DeBoer DK et al. [41]	18 (20)	1992–1998	HHS	80	AAOS Type 4	123	56	30%	6/20 (30%)	0/20 (0%)	0
Colen S et al. [45]	6 (6)	2007–2011	HHS, HOOS	61 HHS 74 HOOS	AAOS Type 3/4	28	69	0	0/6 (0%)	0/6 (0%)	0
Taunton MJ et al. [42]	57 (57)	1992–2008	HHS	75	Paprosky types 3A/3B, AAOS. Type3/4	65	61	NR	20/57 (30%)	3(5%)	2/57 (4%)
Wind MA et al. [46]	19 (19)	2001–2005	HHS	63	Paprosky types 3A/3B AAOS types 3/4	31	58	26%	6/19 (32%)	2(11)%)	2 (11)%
Li H et al. [47]	26 (26)	2003–2013	HHS	82	Paprosky 3B	67		1/26 (3,8%)	2/26 (7,6%)	0/26	2 (7,6%)
Berasi CC et al. [37]	23 (24)	2003–2012	HHS	65	Paprosky 3B	57	67	4%	4/24 (17%)	2/24(8%)	2/24 (8%)
Current Study	31 (31)	2010–2015	HHS; HOOS; UCLA	72 HHS 57 HOOS 4 UCLA	Paprosky 2A,3A,3B/ AOOS 2/3/4	26	73	16.2%	7/31(22.5%)	1/31 (3.2%)	3/31 (9.6%)

average age of 73 years at the time of the operation it is the oldest patient group receiving an custom made implant for an acetabular revision surgery. However, as mentioned at the beginning these elderly patients are a special challenge because of the reduced bone quality. But the concept seems to make sense. The walking ability could be clearly improved comparing the pre- and postoperative status. The UCLA activity score demonstrated that the patients can participate in mild activities of the daily life. Considering the age group this can be assessed as a success, too.

Most of the published studies used the Harris-Hip-Score for evaluation of the clinical results. It ranges between 61 and 80 points in the literature. With 72 points in the present study the result fits into the range. Furthermore, we used the HOOS with mean 54 (range 21–96) points and the UCLA with mean 4 (range 1–8) points. These score are more detailed and gave us additional options to measure the patient skills.

Unfortunately a comparison with results presented in the literature was not possible because of none used this score in the past studies.

Although the patient condition could be detected with all three methods, with the HOOS and UCLA score we could better assess the skills of the Patient. With the huge survey, considering the five subscales “Pain”, “Symptoms”, “Activities of Daily Living”, “Sport”, “Recreation”, “Function” and “Hip Related Quality of Life”, we get a holistic picture of the patients. The disadvantage in HOOS and UCLA is that because of co-morbidities some elderly patients could not accurately distinguish the reason for their restrictions. With investigating an older patient group with more co-morbidities in comparison to the literature this could be a reason for the limited mobility and inducing a reduced HOOS and UCLA score although the custom made implant has an accurate fitting.

Apart from these clinical scores it was important to know how satisfied the patients were with the result of the operative treatment. We could note that a very large proportion about 80% would repeat this treatment again and in 76% quality of life could be increased.

9 Conclusion

A challenging mission is the managing of massive acetabular bone loss in revision THA. Despite the high rate of complications, which has much to do with the prior surgircal conditions, the patients show a large satisfaction. Overall a custom-made acetabular component can be a valuable solution for pelvic discontinuity and acetabular bone loss.

Questions to the Engineers

- Long-term results for short-stem arthroplasty are missing by now. In order to gain information about long-term survival rate the extent of stress-shielding and osseointegration, which can be determined by finite-element analysis, can help. Furthermore, similar approaches can be done for simulation of short stem arthroplasty in deformities.
- The reconstruction of the acetabular cup in cases of severe periacetbular bone should be stable enough to allow a postoperative full weight bearing for the patients. Custom made implants seems to be a promising solution for this complex problem. It would be helpful to construct implants that have a stable anchorage in the bony defect.

References

1. C. Eingartner, Current trends in total hip arthroplasty. Ortop. Traumatol. Rehabil. **9**, 8–14 (2007)
2. I.D. Learmonth, C. Young, C. Rorabeck, The operation of the century: total hip replacement. Lancet **370**, 1508–1519 (2007)
3. C. Merle, M. Clarius, P.R. Aldinger, Long-term results of uncemented stems in total hip arthroplasty: analysis of survival rates with a minimum 15-year follow-up. Orthopade **39**, 80–86 (2010)
4. J.J. Branson, W.M. Goldstein, Primary total hip arthroplasty. AORN J. **78**, 947–953, 956–969; quiz 971–944 (2003)
5. R. D'Ambrosi, L. Marciandi, P.V. Frediani, R.M. Facchini, Uncemented total hip arthroplasty in patients younger than 20 years. J. Orthop. Sci. (2016)
6. T. Siddique, R.K. Sah, F. Masood, S.M. Awais, Improvement in Harris hip score after cementless total hip arthroplasty in young active adults with secondary hip arthritis: a short-term follow-up result. J. Pak. Med. Assoc. **65**, S63–66 (2015)
7. I. Swarup, A.C. Marshall, Y.Y. Lee, M.P. Figgie, Implant survival and patient-reported outcomes after total hip arthroplasty in young patients with developmental dysplasia of the hip. Hip. Int. **0** (2016)
8. E.T. Skytta, L. Jarkko, E. Antti, H. Huhtala, R. Ville, Increasing incidence of hip arthroplasty for primary osteoarthritis in 30- to 59-year-old patients. Acta Orthop. **82**, 1–5 (2011)
9. P.T. Lee et al., Mid-to long-term results of revision total hip replacement in patients aged 50 years or younger. Bone Joint J. **96-B**, 1047–1051 (2014)
10. B.W. Schreurs et al., Acetabular reconstruction with impaction bone-grafting and a cemented cup in patients younger than fifty years old. J. Bone Joint Surg. Am. **86-A**, 2385–2392 (2004)
11. F. Falez, F. Casella, M. Papalia, Current concepts, classification, and results in short stem hip arthroplasty. Orthopedics **38**, S6–13 (2015)
12. R.M. Patel, S.D. Stulberg, The rationale for short uncemented stems in total hip arthroplasty. Orthop. Clin. North Am. **45**, 19–31 (2014)
13. J. Gronewold et al., Changes in strain patterns after implantation of a short stem with metaphyseal anchorage compared to a standard stem: an experimental study in synthetic bone. Orthop. Rev. (Pavia) **6**, 5211 (2014)
14. J. Wolff, D. Wessinghage, *Das Gesetz der Transformation der Knochen*. Schattauer, (1991)

15. L. Cavalli, M.L. Brandi, Periprosthetic bone loss: diagnostic and therapeutic approaches. F1000Res. **2**, 266 (2013)
16. H. Feyen, A.J. Shimmin, Is the length of the femoral component important in primary total hip replacement? Bone Joint J. **96-B**, 442–448 (2014)
17. S. Bundesamt, https://www.destatis.de, (2016)
18. N. Rani et al., Infiltrative therapy as conservative treatment in hip osteoarthritis: a literature review. Hip Int. **0** (2016)
19. A. Moschny, P. Platen, R. Klaassen-Mielke, U. Trampisch, T. Hinrichs, Barriers to physical activity in older adults in Germany: a cross-sectional study. Int. J. Behav. Nutr. Phys. Act **8**, 121 (2011)
20. S. Kurtz, K. Ong, E. Lau, F. Mowat, M. Halpern, Projections of primary and revision hip and knee arthroplasty in the United States from 2005 to 2030. J. Bone Joint Surg. Am. **89**, 780–785 (2007)
21. S. Nemes, M. Gordon, C. Rogmark, O. Rolfson, Projections of total hip replacement in Sweden from 2013 to 2030. Acta Orthop. **85**, 238–243 (2014)
22. P. Herberts, H. Malchau, Long-term registration has improved the quality of hip replacement: a review of the Swedish THR Register comparing 160,000 cases. Acta Orthop. Scand. **71**, 111–121 (2000)
23. O. Robertsson, M.J. Dunbar, K. Knutson, S. Lewold, L. Lidgren, The Swedish Knee Arthroplasty Register. 25 years experience. Bull. Hosp. Jt. Dis. **58**, 133–138 (1999)
24. H. Haas, W. Mittelmeier, Implementation of the EndoCert system for certification of arthroplasty centers. Experiences from the pilot phase. Orthopade **43**, 534–540 (2014)
25. G. von Lewinski et al., Experience in establishing a certified endoprosthesis center. Orthopade **44**, 193–202 (2015)
26. J. Klit, Results of total joint arthroplasty and joint preserving surgery in younger patients evaluated by alternative outcome measures. Dan. Med. J. **61**, B4836 (2014)
27. S. Budde *et al.*, A short-stem hip implant with metaphyseal anchorage in patients with developmental dysplasia of the hip. Technol. Health Care, (2016)
28. G. von Lewinski, T. Floerkemeier, 10-year experience with short stem total hip arthroplasty. Orthopedics **38**, S51–S56 (2015)
29. W.G. Paprosky, P.G. Perona, J.M. Lawrence, Acetabular defect classification and surgical reconstruction in revision arthroplasty. A 6-year follow-up evaluation. J. Arthroplast. **9**, 33–44 (1994)
30. J.A. D'Antonio et al., Classification and management of acetabular abnormalities in total hip arthroplasty. Clin. Orthop. Relat. Res. 126–137 (1989)
31. A.Q. Ahmad, R. Schwarzkopf, Clinical evaluation and surgical options in acetabular reconstruction: a literature review. J. Orthop. **12**, S238–S243 (2015)
32. C. Schoellner, D. Schoellner, Pedestal cup operation in acetabular defects after hip cup loosening. A progress report. Z. Orthop. Ihre Grenzgeb. **138**, 215–221 (2000)
33. M.J. Friedrich et al., Management of severe periacetabular bone loss combined with pelvic discontinuity in revision hip arthroplasty. Int. Orthop. **38**, 2455–2461 (2014)
34. W.H. Harris, Traumatic arthritis of the hip after dislocation and acetabular fractures: treatment by mold arthroplasty. An end-result study using a new method of result evaluation. J. Bone Joint Surg. Am. **51**, 737–755 (1969)
35. C.A. Zahiri, T.P. Schmalzried, E.S. Szuszczewicz, H.C. Amstutz, Assessing activity in joint replacement patients. J. Arthroplasty **13**, 890–895 (1998)
36. A.K. Nilsdotter, L.S. Lohmander, M. Klassbo, E.M. Roos, Hip disability and osteoarthritis outcome score (HOOS)–validity and responsiveness in total hip replacement. BMC Musculoskelet. Disord. **4**, 10 (2003)
37. C.C.t. Berasi, K.R. Berend, J.B. Adams, E.L. Ruh, A.V. Lombardi, Jr., Are custom triflange acetabular components effective for reconstruction of catastrophic bone loss? Clin. Orthop. Relat. Res. **473**, 528–535 (2015)

38. K.P. Gunther, T. Wegner, S. Kirschner, A. Hartmann, Modular reconstruction in acetabular revision with antiprotrusio cages and metal augments: the cage-and-augment system. Oper. Orthop. Traumatol. **26**, 141–155 (2014)
39. P.E. Beaule, F.J. Dorey, R. Hoke, M. Le Duff, H.C. Amstutz, The value of patient activity level in the outcome of total hip arthroplasty. J. Arthroplast. **21**, 547–552 (2006)
40. S. Gravius, T. Randau, D.C. Wirtz, What can be done when hip prostheses fail? New trends in revision endoprosthetics. Orthopade **40**, 1084–1094 (2011)
41. D.K. DeBoer, M.J. Christie, M.F. Brinson, J.C. Morrison, Revision total hip arthroplasty for pelvic discontinuity. J. Bone Joint Surg. Am. **89**, 835–840 (2007)
42. M.J. Taunton et al., Pelvic discontinuity treated with custom triflange component: a reliable option. Clin. Orthop. Relat. Res. **470**, 428–434 (2012)
43. A.B. Joshi, J. Lee, C. Christensen, Results for a custom acetabular component for acetabular deficiency. J. Arthroplasty **17**, 643–648 (2002)
44. G.E. Holt, D.A. Dennis, Use of custom triflanged acetabular components in revision total hip arthroplasty. Clin. Orthop. Relat. Res. 209–214 (2004)
45. S. Colen, R. Harake, J. De Haan, M. Mulier, A modified custom-made triflanged acetabular reconstruction ring (MCTARR) for revision hip arthroplasty with severe acetabular defects. Acta Orthop. Belg. **79**, 71–75 (2013)
46. M.A. Wind, Jr., M.L. Swank, J.I. Sorger, Short-term results of a custom triflange acetabular component for massive acetabular bone loss in revision THA. Orthopedics **36**, e260–e265 (2013)
47. H. Li, X. Qu, Y. Mao, K. Dai, Z. Zhu, Custom acetabular cages offer stable fixation and improved hip scores for revision THA with severe bone defects. Clin. Orthop. Relat. Res. **474**, 731–740 (2016)

Personalized Orthopedic Trauma Surgery by Applied Clinical Mechanics

M. Roland, T. Tjardes, T. Dahmen , P. Slusallek, B. Bouillon and S. Diebels

Abstract In this study, the concept of applied clinical mechanics is used to present first steps in the direction of personalized orthopedic trauma surgery. As example process, a complex distal tibia fracture treated with an implant is chosen. Based on an automated workflow, routinely acquired tomographic data is segmented, assigned with material parameters and extended to an adaptive volume-mesh with hanging nodes. For the finite element simulations, this bone-implant system is equipped with realistic axial loading conditions. An optimization algorithm is then used to analyze the amount of fracture healing that will provide a full weight bearing capacity of the injured extremity in combination with the implant.

1 Introduction

Fractures are a neglected mass disease. With an incidence of about 140,000 tibial and 165,000 femoral fractures per year in Germany the cost of fracture care is a relevant burden for health care systems. Today the gold standard of fracture care is surgical treatment, i.e. open or, in an increasing number of cases, minimally invasive reconstruction of the fractured bone and mechanical neutralization of forces and loads acting on the fractured bone by implants such that immediate functional and physiotherapeutic training of the injured extremity is possible.

M. Roland (✉) · S. Diebels
Saarland University, Chair of Applied Mechanics, Campus A4 2, 66123 Saarbrücken, Germany
e-mail: m.roland@mx.uni-saarland.de

T. Tjardes · B. Bouillon
Department of Trauma and Orthopedic Surgery, Cologne Merheim Medical Center, Ostmerheimerstr. 200, 51109 Cologne, Germany
e-mail: ttjardes@me.com

T. Dahmen · P. Slusallek
DFKI GmbH, German Research Center for Artificial Intelligence, Agents and Simulated Reality, Campus D3 2, 66123 Saarbrücken, Germany
e-mail: Tim.Dahmen@dfki.de

P. Wriggers and T. Lenarz (eds.), *Biomedical Technology*, Lecture Notes in Applied and Computational Mechanics 84, DOI 10.1007/978-3-319-59548-1_17

From the biological point of view, fracture care by means of surgical fracture reduction and stabilization aims to provide the best environment possible for the complex process of fracture healing, which is a cellular process mediated by a complex network of mediators, to occur. Thus, the surgeon has a double role in the treatment process. First, to decide whether a given patient will benefit from surgical therapy of a fracture. This decision is guided by different factors, including the knowledge on comorbidities, the patient's ability to compliantly follow the rehabilitation plan, and the patient's functional expectations and needs, to name but a few. This part of the surgeon's role in fracture care is guided by sound understanding of clinical medicine and clinical experience but also requires a set of soft skills in order to guide the each patient individually through the therapeutic process.

The surgeon's second role is to manually implement the mechanical solution onto the fracture of the patient, i.e. to operate on the patient. The surgeon has to make a choice concerning the appropriate implant and position the implant such that the result of surgery provides better conditions for the micro-scale processes of fracture healing than non-operative therapy. This again requires a great amount of manual experience but also a deep understanding of mechanical laws and principles and their effects in the given case. While clinical experience cannot be substituted or augmented by any sort of technical device or algorithm, the understanding of the mechanical performance of an implant, i.e. the application of the general laws of (bio-) mechanics in a given case, is amenable to modeling, simulation and optimization.

Thus the question arises whether the opportunities offered by image processing, simulation of mechanical processes using the finite element method and the point-of-care availability of sufficient computational power might combine to a tool that can assist the surgeon to anticipate the optimal osteosynthetic strategy preoperatively on an individualized basis. Technically speaking, the aforementioned aim requires a simulation solution that allows to run simulations of an osteosynthesis on the individual patient's imaging data to provide understanding of the interplay between fixation strength of an implant and the amount of new bone formation, i.e. fracture healing, that is necessary to provide full weight bearing capacity of an extremity. The interaction between an implant and the dynamical process of fracture healing is extremely difficult to anticipate prior to surgery as the mechano-induction of fracture healing is a micro-scale process, which is directly influenced by fracture stabilization, i.e. by a macro-scale process. Due to the trans-scale nature of surgical fracture care, technical support in the sense of a software based, personalized analysis and simulation approach were a meaningful progress. Before this concept will be available as a point-of-care solution, algorithms have to be developed providing this information within a time frame that is compatible with clinical routine processes.

The work presented in this chapter examines whether an integrated workflow, which uses routine CT imaging data of a complex distal tibia fracture, can be implemented such that information on the amount of fracture healing that will provide a full weight bearing capacity (in combination with a given implant) of the injured

extremity is achieved. Once this proof of concept is accomplished, further options regarding an integration of biomechanics into the actual treatment process in surgical fracture care have to be explored.

2 Methods

The methods presented in the beginning of this work are based on the integrated workflow presented in [1]. Thereafter, the concept of patient-specific and personalized simulations directly on computed tomography data from medical imaging is combined with the optimization strategy introduced in [2, 3]. For the simulation setup, several algorithmic parameter variations and their influence on the interpretation from the viewpoint of orthopedic trauma surgery are analyzed and discussed.

2.1 Preparation and Tomography of the Fracture Model

Starting with a routinely acquired tomogram of a real patient or, alternatively, an artificial bone-implant-system based on real patient data, such artificial bone models of clinical relevant conditions are widely used to design mechanical experiments as well as to set up biomechanical FEM simulations.

Here, an AO type 42–B1.1 was implemented in a tibia model (Sawbones Europe, Malmø, Sweden). This fracture classification represents multifragmentary diaphyseal fractures of the tibia with a spiral wedge third fragment that, once reduced, maintains contact between the proximal and distal fragments [4].

To improve the radiographic visibility of the bone model, the surface of the sawbone was treated with zinc spray. The fracture was fixed using a 14 hole-titanium distal tibia-locking compression plate (anatomical LCP, Synthes, Oberdorf, Switzerland). A computed tomography scan of the fracture model and of a real patient was performed (Somatom Definition Flash, Siemens, Germany).

The tomogram consist of the gray-scale values in the `uint12` format, which can be mapped linearly to the Hounsfield scale (HU). The density values are arranged on a regular grid, with a series of 582 single CT images. The slice thickness of the dataset is constant, with a distance of 0.6 mm between two pictures. All images are square with 512 pixels as height and width with a constant pixel spacing of 0.318 mm. The tomogram is passed to the segmentation and the meshing procedure as individual gray-scale images.

2.2 Image Processing

In order to identify the pixels addressing the bone-implant-system in each image, a segmentation process is necessary. For this study, the adaptive thresholding method

was implemented and the interval was selected using histogram analysis. Due to the fact that adaptive thresholding as segmentation method only produces satisfactory results in conjunction with a selective low-pass filtering, here the edge-enhancing non-linear anisotropic diffusion (EED) filter was applied [5]. Hereby, the tomogram is preprocessed to cut off high frequencies or noise, but edges are detected, and blurring orthogonal to the edge direction is avoided so that features are preserved. Suitable choices of the diffusion tensor in the implemented EED method allow the design of filters that are going around the structures of the image and preserve the edges. The method is explained in all details in [6]. The computed tomography images were segmented automatically, using the diffusion process in two dimensions, i.e. the tomogram was processed slice-by-slice, and the individual slices were segmented separately. The fracture area was marked in an additional step in a semi-automatic way by an orthopedic trauma surgeon, cf. red parts in Fig. 1c.

2.3 Mesh Generation

The result of the segmentation process is a segmented tomogram, stored in an image stack, in which each image represents one slice of the tomogram. In every slice, the CT gray-scale values and in addition, the corresponding material class information are stored to allow an adaptive coarsening of individual material classes. This image information is placed at a uniform resolution on a homogeneous grid given by the pixel spacing and the slice thickness. In order to analyze the mechanical properties, a FEM simulation needs to be executed on the tomogram. FEM simulations typically operate on so-called volume-mesh data [7, 8]. Therefore, a program based on the OpenFlipper framework [9] was created to transfer tomograms to volume meshes. Tomographic data provided in the format of a uniform grid can be trivially transferred to a volume mesh by limiting the polyhedral topology to hexagons. For each voxel in the grid, a cuboid hexagon is created that represents the extent of this voxel, leading to a 1:1 relation between voxels and cells. The material information of the voxel can thus trivially be stored in the cell corresponding to the voxel.

However, this obvious approach leads to a simulation mesh with a large number of cells, which often exceeded the capabilities of the available hardware. As a consequence, the volume mesh resolution needs to be reduced. As shown in [1], uniform downsampling via 2D or 3D box filtering yields in less accurate simulation results compared with feature adaptive downsampling based on a hanging node strategy. To realize a hanging node based meshing concept, some properties of the tomography data must be exploited in the following way: The bone-implant-system consists of several materials. When building the FEM model in the segmentation step, the material properties of the voxels were simplified by mapping each density value to one material of a finite set (air, soft tissue, cortical bone, trabecular bone, broken bone, marrow and implant metal). Those material classes have different mechanical properties and thus require different spatial resolutions in the FEM simulation. Parts that can take high mechanical stresses need to be expressed at full tomographic reso-

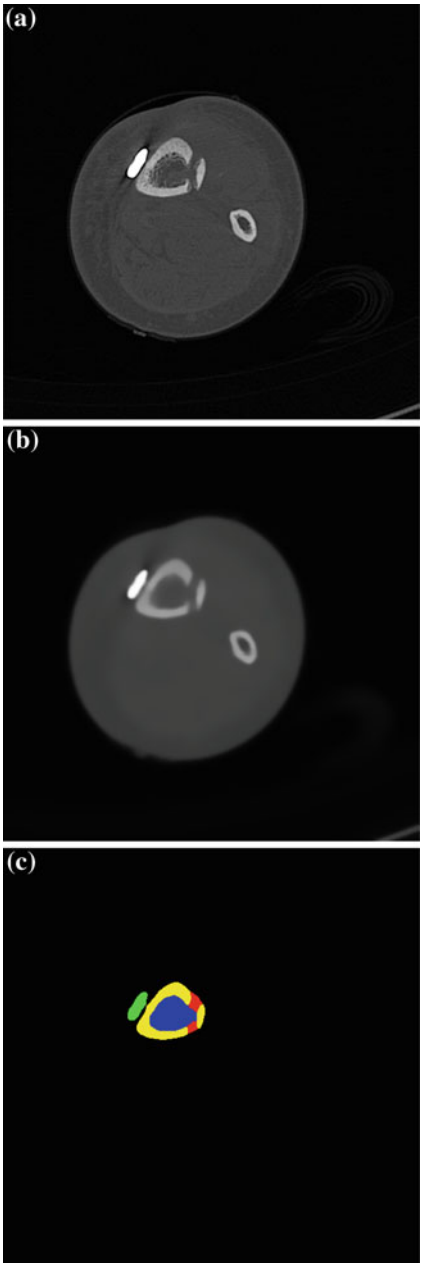

Fig. 1 **a** Original computed tomography image routinely acquired during the clinical workup; **b** EED filtered image; **c** applied adaptive thresholding and mapping to material classes

Table 1 Impact of the adaptive coarsening on the number of mesh cells for each material class

Mesh type	Cortical bone	Trabecular bone	Implant	Fracture area	Mesh cells
Full tomographic resolution	2,990,879	1,663,007	312,109	103,748	5,069,743
Applied adaptive coarsening	693,885	245,654	312,109	103,748	1,355,396

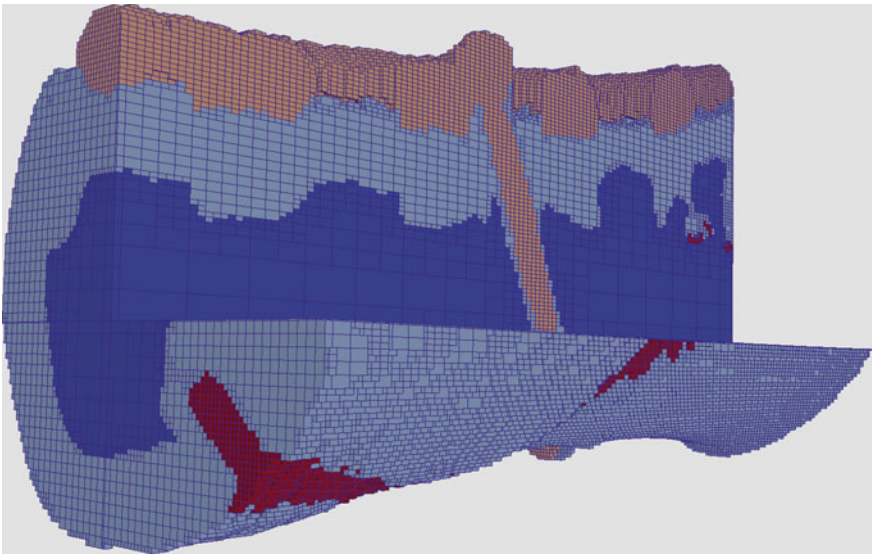

Fig. 2 Cut through the mesh to visualize the concept of hanging nodes. Different colors represent sets of different material classes: implant (), cortical bone (*light blue*), trabecular bone (*blue*) and fracture area (*red*); coarsening of the mesh via collapsing cells

lution, while soft parts that can take less mechanical stresses can be expressed safely using a coarser resolution. A detailed description of this meshing concept and some numerical examples for a bone-implant-system can be found in [1].

Here, for the implant and the fracture area, the full tomographic resolution is chosen without any coarsening. For the cortical bone, one level of coarsening is applied and for the trabecular bone, three levels of coarsening are allowed. In [1], it is shown that this strategy leads to a good relation of mesh coarsening on the one hand and the increase of computational errors on the other hand. Table 1 shows the impact of the algorithmic coarsening on the mesh size and Fig. 2 illustrates the hanging node concept.

2.4 Material Assignment

Besides the geometric properties of the volume-mesh structure, material properties had to be assigned to every mesh cell [10]. In order to derive an empirical elasticity-bone density relationship for the real and the artificial bone, the gray-scale values given in terms of Hounsfield Units can be mapped to local bone properties [11–13]. Therefore, the following linear conversion between HUs and equivalent mineral density ρ_{eqm} in g/cm^3 is used:

$$\rho_{\text{eqm}} = 10^{-3}(0.793) \times \text{HU}.$$

An isotropic heterogeneous material is assumed, having a different value for the Young's modulus and a fixed value for the Poisson ratio inside each mesh cell based on the segmented material classes. This type of material model has shown a good agreement with experimental observations [14, 15]. Depending on the local ash density, the mapping for the cortical and the trabecular bone is defined as follows [10, 16]:

$$\begin{aligned}
\rho_{\text{ash}} &= 1.22\rho_{\text{eqm}} + 0.0523\,\text{g/cm}^3 \\
\text{E}_{\text{cort}} &= 10,200 \times \rho_{\text{ash}}^{2.01}\,\text{MPa} \\
\text{E}_{\text{trab}} &= 5,307 \times \rho_{\text{ash}} + 469\,\text{MPa},
\end{aligned}$$

with a fixed Poisson ratio of $\nu = 0.30$. The ash density relation corresponding to the equivalent mineral density is in accordance with [17]. For the fracture area, the material parameters of the corresponding mesh cells are set to experimentally established soft tissue parameters [18]. The implant is assumed to be an Ti-6Al-7Nb alloy with literature values between 114 GPa [19] and 108 GPa [20] for the Young's modulus.

2.5 Set-up of the Numerical Simulations

For the numerical simulations, the standard linear elasticity model [21] was implemented in the `deal.II` environment. Assume that the boundary of the elastic body is divided into two disjoint sets Γ_D (Dirichlet boundary) and Γ_N (Neumann boundary) and assume that a system of body forces $\mathbf{f} : \Omega \to \mathbb{R}^3$ and surface tractions $\mathbf{g}_N : \Gamma_N \to \mathbb{R}^3$ act on the body. On the other part Γ_D of the boundary, the body is rigidly fixed in space. Under the assumption of small displacements, the displacement $\mathbf{u} = (u_i)_{1 \le i \le 3}$ satisfies the following problem:

$$
\begin{aligned}
-\sum_{j=1}^{3} \frac{\partial \sigma_{ij}}{\partial x_j}(\mathbf{u}) &= f_i \ \text{ in } \Omega, \\
u_i &= 0 \ \text{ on } \Gamma_D, \\
\sum_{j=1}^{3} \sigma_{ij}(\mathbf{u})\, n_j &= g_i \ \text{on } \Gamma_N,
\end{aligned}
$$

where $\mathbf{n} = (n_i)_{1 \le i \le 3}$ is the unit outward normal to the boundary Γ_D, f_i and g_i are the components of the forces $\mathbf{f}$ and $\mathbf{g}_N$, and $\sigma_{ij}(\mathbf{u})$ is the stress tensor [22].

Appropriate boundary conditions were specified consistently in all simulations. The elastic body was fixed at the side pointing to the foot. At the side of the knee, forces were applied representing the body weight of the patient (80 kg) with the original fracture.

The FEM simulations were realized using the `deal.II` software library [23, 24]. The system matrices and the right-hand side vectors were built using linear Lagrange finite elements. The systems were solved using the standard conjugate gradient (cg) method [25] and a symmetric successive over-relaxation (SSOR) preconditioner with a relaxation parameter $\omega = 1.3$ [26].

All simulations were executed on a DELL PowerEdge with 2 Intel Xeon 5680 CPUs and 72 GB main memory. As described above, the adaptive meshing strategy leads to a computing grid with 1,355,396 mesh cells. For the chosen linear Lagrange finite elements this concept results in 5,608,551 degrees of freedom (d.o.f.) for every simulation run.

2.6 Optimization Strategy

The presented algorithmic optimization strategy is introduced and analyzed in [2, 3]. The algorithm seeks the minimal amount of fracture union necessary to allow physiological loading of the limb without subjecting the implant to stresses and strains that might result in an implant failure or in pain occuring during the mobilization of the patient.

The boundary conditions for the optimization algorithm are given by a complete union of the pseudarthrosis, below called best-case scenario, and by a complete nonunion of the pseudarthrosis, below called worst-case scenario. First, the worst-case scenario is computed. For this purpose, the material parameters of the region marked as the nonunion or fracture area during the segmentation process are set to the parameters of soft tissue [18]. Here, the maximum possible von Mises stress arising in the bone-implant system during the optimization process can be quantified for the given set of loading parameters. Second, the best-case scenario is computed by setting the material parameters of the nonunion area to the parameters of cortical bone.

The goal of the optimization procedure is to gradually approach the minimum amount and location of bone bridging over the nonunion area that will protect the implant from overloading. As described in [2], the criterion when the algorithm moves to the next iteration needs to be defined a priori by a so-called `stop criterion`. Therefore, the stop criterion is set to X% of the maximum von Mises stress arising in the current step of the algorithm in the region marked as the nonunion area, i.e. if a mesh cell carries less than X% of the load it is considered omittable. Several stop criterions are tested and analyzed in this study. For that purpose, the X is set to 5, 10, 15, 20, 25 and 30%. In all cases it is assumed that nonunion area mesh cells sharing less than X% of the load can be eliminated such that the load can be dissipated over the neighboring mesh cells. This procedure is repeated until no more nonunion area mesh cell can be eliminated. With the number of unfilled areas increasing with every run of the optimization algorithm, the maximum of the von Mises stress in the remaining area and the implant increases constantly.

Starting with the best-case scenario as state of complete union, fracture area mesh cells with von Mises stress < `threshold`$\times$`max` are identified. The material parameters for these mesh cells are set from cortical bone to soft tissue in an update step. After one cycle over all fracture area mesh cells, the new material parameters are used as starting point for the next optimization run.

3 Results and Discussion

The methods presented in Sect. 2 demonstrates that, given today's technical possibilities in terms of point-of-care availability and affordability of computational power as well as the advancements in image processing and finite element modeling, a state of the art has been reached such that, from a technological point of view, biomechanics is ready to evolve from a theoretical and laboratory discipline into a discipline that actively participates in the treatment process in orthopedic trauma surgery (Table 2).

A crucial step in every workflow using imaging data is the segmentation process which is necessary to transfer the image data into a format such that different tissue types with different mechanical characteristics, i.e. material classes, can be simulated simultaneously, cf. Fig. 1.

Once the segmentation process is completed, the different materials have to be transferred into a finite element model. The finite element model is the key structure of the simulation process. Understanding biomechanics as applied clinical biomechanics means to accept that the simulation has to include the complete anatomical target structure, i.e. the extend of the model is determined not by the mechanical but by the anatomical needs. Thus in applied clinical mechanics the subject of simulation is usually much larger than in conventional biomechanical investigations. This notion results in a conflict of interest with the necessity to provide point-of-care solutions that can be operated on commercially available personal computers.

The application of modified finite element modeling approaches has overcome this problem. By using the hanging node concept, the size of the finite element model

Table 2 Optimization algorithm in pseudo-code from [2]

Algorithm Reduction of the filling capacity

initialization:
    compute the worst–case scenario
        set the material parameters of each fracture area mesh cell to soft tissue
        compute the von Mises stress for the tibia
        search for the maximum stress value
        define `max` := maximum stress value
    compute the initial scenario
        set the material parameters of each fracture area mesh cell to cortical bone
        compute the von Mises stress for the tibia
    define the stress `threshold`
    define the `stop_criterion`
repeat
    if von Mises stress of fracture area mesh cell < `threshold`×`max`
        set the material parameters of each fracture area mesh cell from cortical bone to soft tissue
    compute the von Mises stresses for the tibia
    search for the maximum stress value
until stop criterion is reached

can be reduced such that the consumption of computational resources during the iterative simulation processes is drastically reduced, cf. Fig. 2. As the number of mesh cells is reduced only in areas that contribute little to the overall mechanical behavior, the reduction of nodes, and thus the increased speed of computation, can be expected not to worsen the overall mechanical validity. On the contrary, when modeling bone anatomy, a reduction of mesh cells e.g. in the medullary cavity results in a model that is closer to the anatomy of bone than a model with homogeneously distributed mesh cells.

However, the fact that image processing algorithms are available and computational power is at hand does not guarantee the clinical validity of solutions generated with an applied clinical mechanics approach. To ensure that algorithms which develop mechanical solutions for clinical problems, be it individualized implants or a weight-bearing protocol for fracture aftercare, are safe and robust for implementation in clinical routine processes, some questions related to the interaction between the algorithm and individual imaging data, i.e. individual fractures and their plethora of mechanical constellations, need to be understood.

Given the high variability of mechanical fracture constellations mentioned above, the analysis of the simulation models derived from the individual imaging data, which has been implemented in a bone model (Sawbones, Sweden), is best carried out from the extremes, i.e. from a state of complete fracture consolidation, referred to as best-case scenario, and from a state of fracture nonunion, referred to a worst-case scenario.

3.1 Numerical Simulation with Perfect Bone Formation in the Pseudarthrosis Area—Best-Case Scenario

For this numerical simulation, the complete fracture area was assigned to the mechanical characteristics of cortical bone. Physiologically this means that the fracture can be considered completely healed. This situation is, especially with respect to complex fracture patterns and the fact that the distal tibia is a high-risk region in terms of the probability of fracture healing disorders, a rare situation in clinical medicine.

However, given the loading pattern chosen for this numerical simulation, it becomes obvious that the maximum stress occurs in the diaphyseal area, i.e. the area that is physiologically subjected to bending and torsional forces during axial loading, cf. Figs. 3 and 5. Thus if a metaphyseal distal tibia fracture is completely consolidated, the metaphyseal portion of the implant does not show any substantial loading. This observation is easily explained by the fact that the cancellous nature of metaphyseal bone architecture dissipates loads more efficiently away from the implant than diaphyseal bone (Figs. 4 and 6).

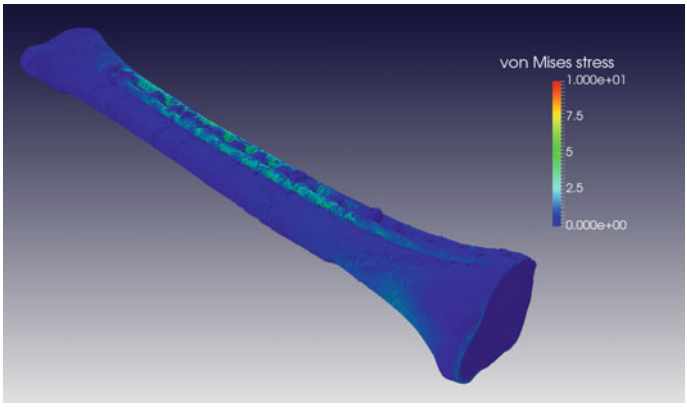

Fig. 3 Best-case scenario for the full bone-implant-system

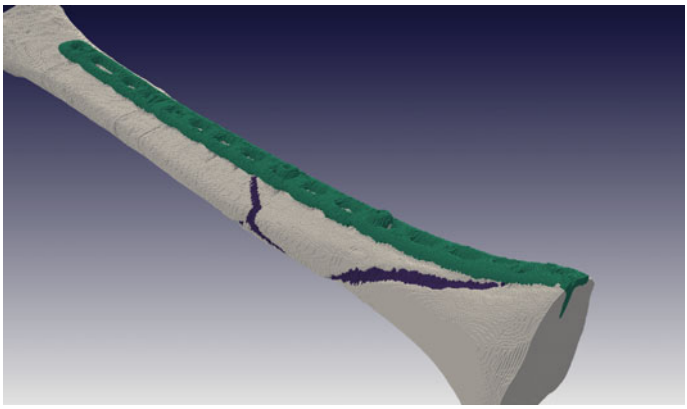

Fig. 4 Bone-implant system with different material classes

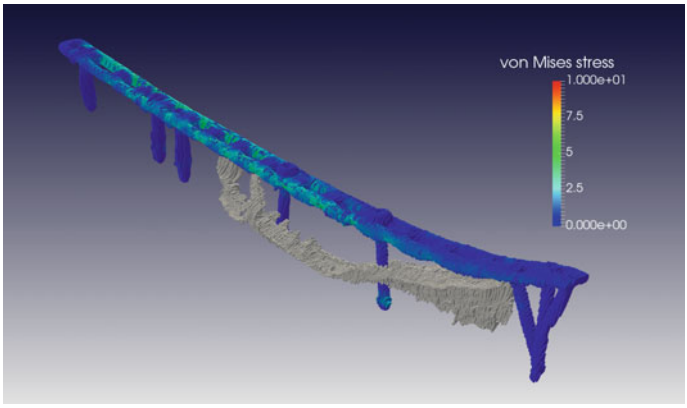

Fig. 5 von Mises stress focused on the implant in the best-case scenario

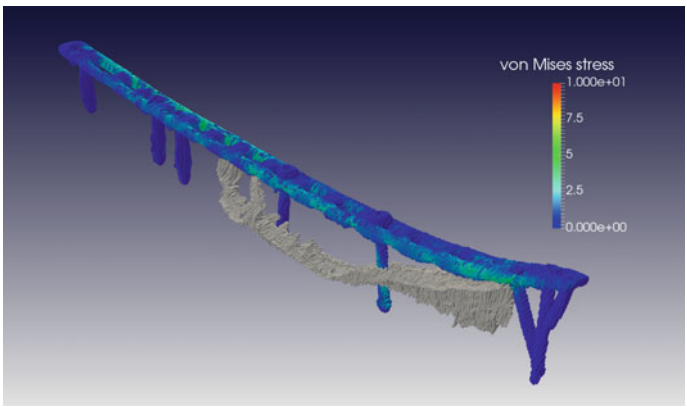

Fig. 6 von Mises stress focused on the implant in the worst-case scenario

3.2 Numerical Simulation with Totally Absent Bone Formation in the Pseudarthrosis Area—Worst-Case Scenario

A state with no fracture healing at all is found either directly after the fracture has been subjected to surgical treatment, i.e. reduction of the fracture and neutralization of displacing forces with an implant, or if fracture healing is disturbed and a nonunion has developed. In this case the pattern of tension in the diaphyseal portion of the implant is very similar to the best-case scenario while the tension in the metaphyseal portion of the implant increases drastically. In clinical reality there are two noteworthy consequences. First, if functional treatment with early weight bearing is allowed, the portion of the implant that is mechanically the weakest (due to soft tissue restraints in the distal tibia, the thickness of the implant decreases towards its distal end) is subjected to increased cyclic loading, i.e. the risk of implant failure increases. Second, the loading of the bone, which is mediated by the implant, is essentially uncontrollable. With respect to the mechanobiological importance of controlled, cyclic loading for bone healing, this is a clinically highly important consequence, as uncontrolled loading significantly increases the risk of incomplete or absent fracture healing. This results in the well-known phenomenon of only partially, i.e. incomplete, healed fractures.

The pattern of partial fracture consolidation cannot be predicted based on morphological fracture classifications like the AO classification of fractures. For clinical decision making the pattern of incomplete fracture consolidation is difficult to evaluate for the physician in terms of which pattern of fracture consolidation will progress to complete union, which pattern of consolidation is sufficient for full weight bearing, and which pattern will end up in nonunion and/or implant failure. Today, this decision is thus still based on the clinical experience of the physician.

From a mechanical point of view, the process of fracture healing in the distal tibia is caught in a dilemma: the portion of the tibia where the fracture pattern becomes most complex and most variable is addressed by the mechanically weakest portion of the implant which at the same time is subjected to the highest loads in the case of partial or complete weight bearing.

Before clinical decision making can really be improved, a deeper understanding of how much fusion, i.e. fracture healing, is necessary to allow full weight bearing without subjecting the implant to loads that result in unphysiological loading of the healing bone or, in the long run, in implant failure.

In the present study, an optimization algorithm is used that iteratively reduces the fusion area of a complex distal tibia fracture until a predefined stop parameter is reached. In the first instance, the optimization parameters have been set arbitrarily. Setting the stop criterion to 20%, the remaining fusion area reaches an impressive minimum (Figs. 7 and 8) after four simulation/optimization iterations, cf. Figs. 9, 10, 11, 12 and 13.

Thus the analysis of the extreme cases of complete and completely absent fracture healing has shown straight-forward results in terms of the loading of the implant.

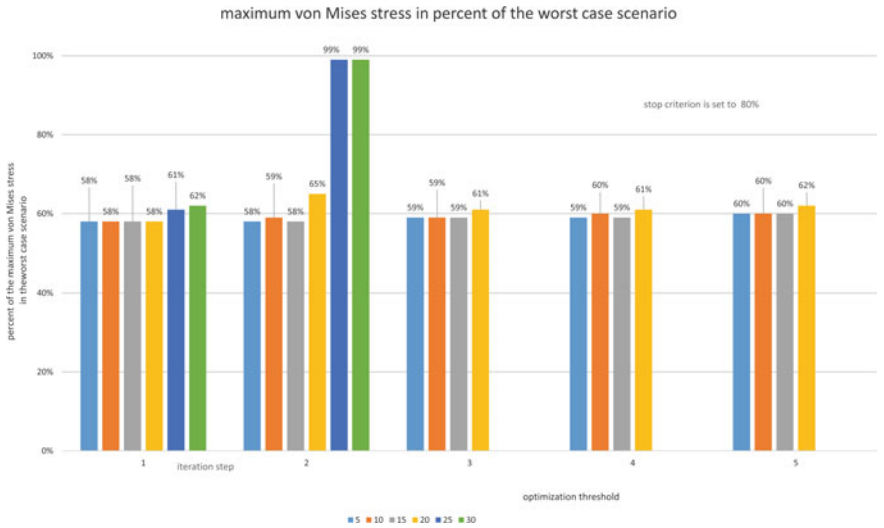

Fig. 7 This table illustrates the maximum value of the von Mises stress in every iteration step for all different optimization thresholds. The stop criterion is set to 80% of the maximum value of the von Mises stress of the worst-case scenario

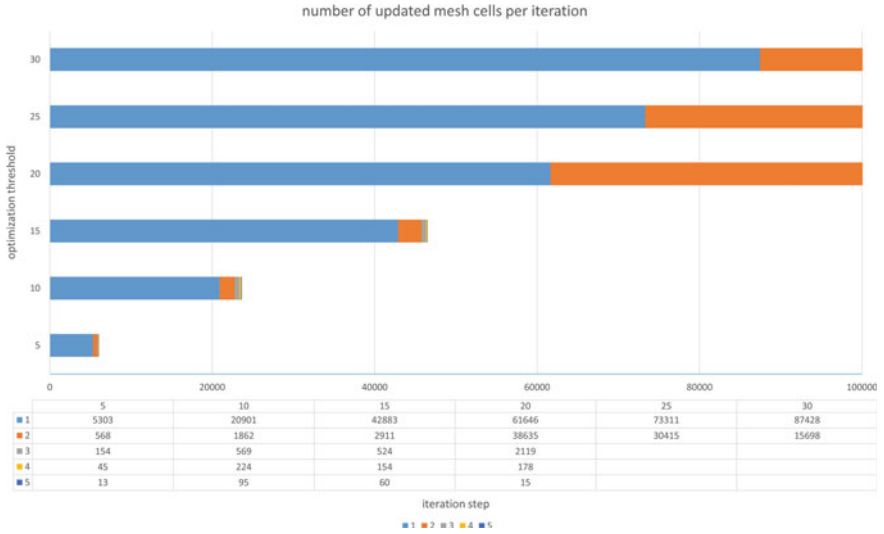

	5	10	15	20	25	30
1	5303	20901	42883	61646	73311	87428
2	568	1862	2911	38635	30415	15698
3	154	569	524	2119		
4	45	224	154	178		
5	13	95	60	15		

Fig. 8 This table shows the number of updated mesh cells per iteration step for all different optimization thresholds. For the optimization threshold values of 25 and 30%, the stop criterion is reached after the second iteration step

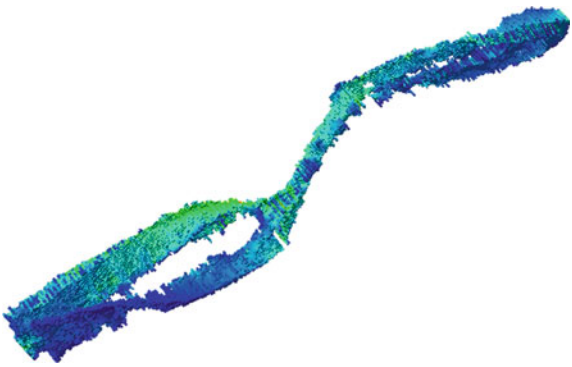

Fig. 9 Complete fracture area

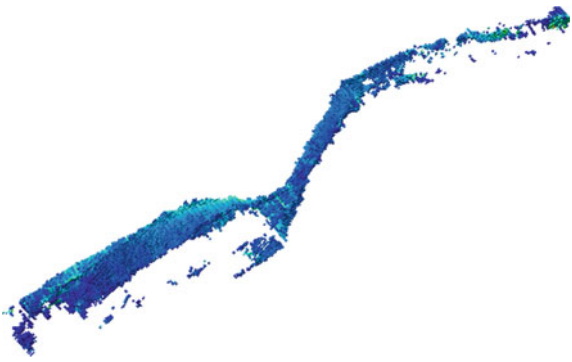

Fig. 10 Remaining fusion area after the fourth iteration

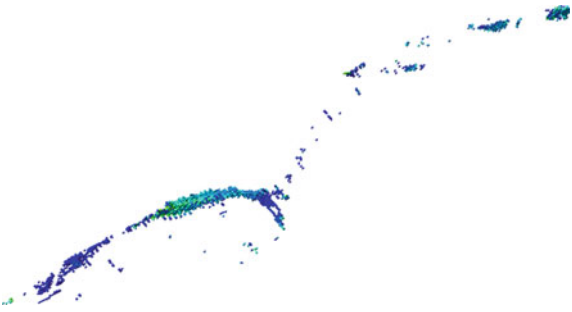

Fig. 11 Remaining fusion area after the first iteration

As fracture healing is a dynamic biological and not a technical process, it is impossible to predict the course of fracture healing from occasional CT imaging. The only mechanically valid information that can be extracted so far is the estimation of implant failure due to fatigue in the case of a nonunion. (Fig. 14)

Fig. 12 Remaining fusion area after the second iteration

Fig. 13 Remaining fusion area after the third iteration

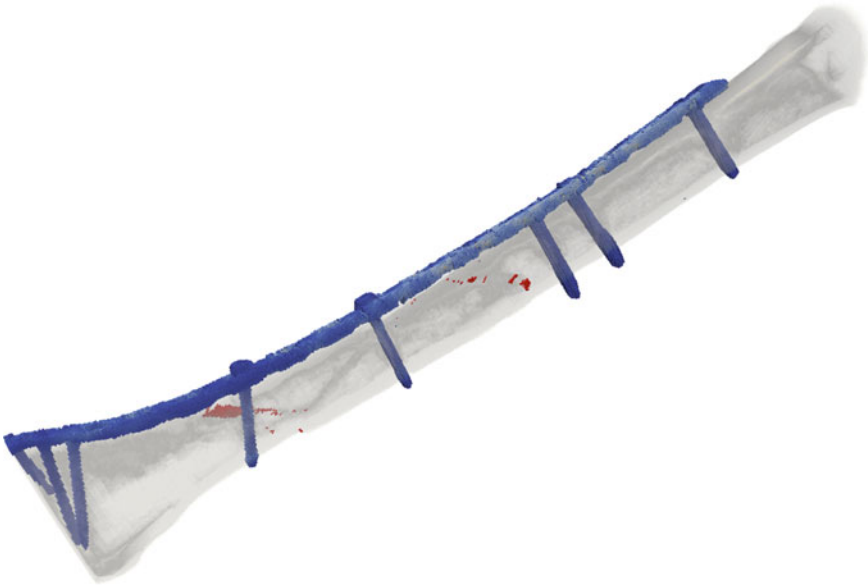

Fig. 14 Localization of the optimized union area in the full bone-implant-system

3.3 Impact of the Optimization Parameter on the Results

To understand the processes between the extremes described above, an optimization algorithm was developed gradually reducing the number of mesh cells in the fracture area according to a priori specifications of the load in a mesh cell. The iterative approach of algorithmic optimization combined with simulation of the optimized situation is a key principle to connect biomechanical analysis to clinical judgement and decision making. However, the choice of the stop criterion is basically a teleological choice that necessitates further investigation concerning the robustness of the algorithm against different values of the stop criterion. If the stop criteria are varied from 5 to 30% in 5% increments, the number of updated mesh cells per iteration varies considerably (Figs. 7 and 8).

Regardless of the actual optimization threshold the number of cells updated per iteration decreases exponentially. For optimization thresholds between 5 and 15%, the optimization process reaches a minimum of updated cells after five iterations of the algorithm, with more than 50% of the cells remaining. If the optimization threshold is set to 25–30%, only two iterations are sufficient to reduce the number of cells in the fracture area by more than 95%. Thus there is a considerable dependence of the performance of the optimization algorithm on the choice of the optimization threshold. The experience from clinical medicine that a full circumferential consolidation of a fracture is not a prerequisite for full weight bearing and function is confirmed by these results.

4 Conclusion and Outlook

The studies presented confirm the hypothesis that routinely acquired imaging data from complex distal fractures of tibia can be processed such that the fracture can be analyzed using an optimization algorithm that detects the fracture fusion area which is necessary to achieve full weight bearing, thereby also confirming the hypothesis that full circumferential fusion of a fracture is not a prerequisite to achieve full weight bearing from a mechanical point of view. At the current stage of development, these observations are a promising proof of concept. The major limitations from a clinical point of view result from the fact that the experiment was performed on an artificial bone model. Thus, the mechanical loads and strains measured cannot be directly translated directly to clinical cases. Furthermore, the percentages of mesh cells updated depending on the setting of the optimization criterion cannot be transferred directly into clinical decisions. To get the workflow closer to reality, the next stages of dement need to be a further investigation of the algorithm's performance for different fracture types and an evaluation of the simulation results with cadaver experiments and mechanical parameters fitted to natural bone. However, the results indicate that the integration of biomechanics into the actual therapeutic process in fracture care is a promising concept that needs further evaluation.

5 Conflict of Interest

This article has been prepared in accordance with all ethical and scientific guidelines. The authors declare that no conflict of interest nor competing interests are associated with this manuscript.

Acknowledgements Michael Roland and Thorsten Tjardes contributed equally to this work. The financial support for a dated back project from the Deutsche Forschungsgemeinschaft (DFG) under the grant DI 430/17–1 is gratefully acknowledged.

References

1. T. Dahmen, M. Roland, T. Tjardes, B. Bouillon, P. Slusallek, S. Diebels, An automated workflow for the biomechanical simulation of a tibia with implant using computed tomography and the finite element method. Comput. Math. Appl. **70**(5), 903–916 (2015)
2. M. Roland, T. Tjardes, R. Otchwemah, B. Bouillon, S. Diebels, An optimization algorithm for individualized biomechanical analysis and simulation of tibia fractures. J. Biomech. **48**, 1119–1124 (2015)
3. T. Tjardes, M. Roland, R. Otchwemah, T. Dahmen, S. Diebels, B. Bouillon, Less than full circumferential fusion of a tibial nonunion is sufficient to achieve mechanically valid fusion - Proof of concept using a finite element modeling approach. BMC Musculoskel. Dis. **15**, 434 (2014)
4. T.P. Ruedi, R.E. Buckley, C.G. Moran, AO principles of fracture management. Thieme (2007)
5. J. Weickert, Theoretical foundations of anisotropic diffusion in image processing. Comput. Suppl. **11**, 221–236 (1996)
6. J. Weickert, *Anisotropic Diffusion in Image Processing*, (Teubner, 2005)
7. M. Mäntylä, *An Introduction to Solid Modeling*, (Computer Science Press Inc, New York, 1987)
8. M. Kremer, D. Bommes, L. Kobbelt, OpenVolumeMesh—a versatile index-based data structure for 3D polytopal complexes, in *Proceedings of the 21st International Meshing Roundtable*, (Springer, Berlin, 2012), pp. 531–548
9. J. Möbius, L. Kobbelt, OpenFlipper: an open source geometry processing and rendering framework, in *Lecture Notes in Computer Science, Curves and Surfaces* ed. by J.-D. Boissonnat, P. Chenin, A. Cohen, C. Gout, T. Lyche, M.-L. Mazure, L. Schumaker, (Springer, Berlin 2012), pp. 488–500
10. J. Keyak, Y. Falkinstein, Comparison of in situ and in vitro CT-scan-based finite element model predictions of proximal femoral fracture load. J. Med. Eng. Phys. **25**, 781–787 (2003)
11. I. Hvid, S.M. Bentzen, F. Linde, L. Mosekilde, B. Pongsoipetch, X-ray quantitative computed tomography: the relations to physical properties of proximal tibial trabecular bone specimens. J. Biomech. **22**, 837–844 (1989)
12. J.Y. Rho, M.C. Hobatho, R.B. Ashman, Relations of mechanical properties to density and CT numbers in human bone Med. Eng. Phys. **17**, 347–355 (1995)
13. C. Zannoni, R. Mantovani, M. Viceconti, Material properties assignment to finite element models of bone structures: a new method. Med. Eng. Phys. **20**, 735–740 (1998)
14. Z. Yosibash, R. Padan, L. Joscowicz, C. Milgrom, A CT-based high-order finite element analysis of the human proximal femur compared to in-vitro experiments. ASME J. Biomech. Eng. **129**(3), 297–309 (2007)
15. N. Trabelsi, Z. Yosibash, C. Milgrom, Validation of subject-specific automated p-FE analysis of the proximal femur. J. Biomech. **42**, 234–241 (2009)

16. M. Ruess, D. Tal, N. Trabelsi, Z. Yosibash, E. Rank, The finite cell method for bone simulations: verification and validation. Biomech. Model. Mechanobiol. **11**, 425–437 (2012)
17. C. Les, J. Keyak, S. Sover, K. Taylor, A. Kaneps, Estimation of material properties in the equine metacarpus with use of quantitative computed tomography. J. Orthop. Res. **12**, 822–833 (1994)
18. E.J. Chen, J. Novakofski, W.K. Jenkins, W.D. O'Brien, Young's modulus measurements of soft tissues with application to elasticity imaging. IEEE Trans. Ultrason. Ferroelect. Freq. Control **43**(1), 191–194 (1996)
19. K.-H. Kramer, Metallische Implantatwerkstoffe—ein Überblick BIOmaterialien **2**, 4 (2001)
20. M. Ashraf Imam, A.C. Fraker, Titanium alloys as implant materials. Medical application of titanium and it's alloy: the material and biological Issues. ASTM STP **1272**, 1–16 (1996)
21. S. Timoshenko, *Strength of Materials*, (RE Krieger Pub. Co., Huntington, 1976)
22. B. Riviere, *Discontinuous Galerkin Methods for Solving Elliptic and Parabolic Equations: Theory and Implementation*, (Society for Industrial and Applied Mathematics (SIAM), 2008)
23. W. Bangerth, T. Heister, L. Heltai, G. Kanschat, M. Kronbichler, M. Maier, B. Turcksin, T.D. Young, The `deal.II Library, version 8.1` (2013), arXiv:1312.2266v4
24. W. Bangerth, R. Hartmann, G. Kanschat, `deal.II—a General Purpose Object Oriented Finite Element Library`. ACM T. Math. Softw. **33**(4), 24/1–24/27 (2007)
25. A. Meister, *Numerik linearer Gleichungssysteme*, (Vieweg-Verlag, Wiesbaden, 2007)
26. D. Braess, *Finite Elemente*, (Springer, Berlin, 2003)

Part V
Otology

Measurement of Intracochlear Pressure Differences in Human Temporal Bones Using an Off-the-Shelf Pressure Sensor

Martin Grossöhmichen, Rolf Salcher, Thomas Lenarz and Hannes Maier

Abstract Before clinical data are available, the achievable output levels of Implantable Middle Ear Hearing Devices (IMEHDs) are usually characterized in human cadaveric temporal bones (TBs) by measuring the vibration response of the stapes footplate with a laser Doppler vibrometer. However, this method is accurate only if the ossicular chain is stimulated and the cochlea is intact. For other stimulations, such as perilymph stimulation with a Direct Acoustic Cochlear Implant (DACI) and round window stimulation an alternative measurement method is needed. The sound pressure difference between scala vestibuli (SV) and scala tympani (ST) is a good candidate for such a method as it correlates with evoked potentials in animals. Using a custom-made pressure sensor it has been successfully measured and used to characterize acoustical and mechanical stimulation in human cadaveric TBs. In order to make this method accessible to a wider community, an off-the-shelf pressure sensor (Samba Preclin 420 LP, Samba Sensors) was tested here for intracochlear sound pressure measurements in cadaver ears. During acoustic stimulation, intracochlear sound pressures were simultaneously measurable in SV and ST between 0.1 – 8 kHz with sufficient signal-to-noise ratios with this sensor. The intracochlear sound pressure differences were comparable to results obtained with custom-made sensors. Our results demonstrated that the pressure sensor Samba Preclin 420 LP is usable for measurements of intracochlear sound pressures in SV and ST and for the determination of differential intracochlear sound pressures.

Parts of this chapter have been published in: M. Grossöhmichen, R. Salcher, K. Püschel, T. Lenarz, and H. Maier: "Differential Intracochlear Sound Pressure Measurements in Human Temporal Bones with an off-the-shelf Sensor." *BioMed Research International*, vol. 2016, Article ID 6059479, 2016 [1].

M. Grossöhmichen (✉) · R. Salcher · T. Lenarz · H. Maier
Cluster of Excellence Hearing4all, Oldenburg, Germany
e-mail: Grossoehmichen.Martin@mh-hannover.de

M. Grossöhmichen · R. Salcher · T. Lenarz · H. Maier
Department of Otolaryngology, Hannover Medical School,
Institute of Audioneurotechnoloy (VIANNA), Hanover, Germany

P. Wriggers and T. Lenarz (eds.), *Biomedical Technology*, Lecture Notes in Applied and Computational Mechanics 84, DOI 10.1007/978-3-319-59548-1_18

1 Introduction

The majority of Implantable Middle Ear Hearing Devices (IMEHDs) as the Carina® and MET® (Cochlear Ltd.) or the Vibrant Soundbridge (MED-EL) were developed for the treatment of sensorineural hearing loss [2, 3]. Here, the implant commonly stimulates the ossicular chain (e.g. incus body) with an actuator. To quantify the equivalent sound pressure output level in such applications, the ASTM standard 2504-05 [4] provides an experimental method in human cadaveric temporal bones (TBs). This method is commonly used and compares the vibration amplitude of the stapes footplate (SFP) in response to sound and to actuator stimulation measured with a Laser Doppler vibrometer (LDV). This method has been demonstrated to be reliable for applications that stimulate the ear in the physiological forward direction [3, 5–7].

More recently, the indication of IMEHDs was extended to conductive and mixed hearing loss applications where the implant vibrates the SFP or the round window (RW) [8–10]. Additionally, the direct acoustic stimulation of the cochlea by a Direct Acoustic Cochlear Implant (DACI, e.g. Codacs™, Cochlear Ltd.) was introduced for the treatment of severe to profound mixed hearing loss [11, 12]. Quantifying the output level of these new stimulation modes by LDV measurements in TBs according to ASTM standard 2504-05 [4] is not appropriate. Alternatively vibration responses of the RW determined by LDV can be used in a DACI stimulation [13, 14], but alterations of the complex vibration pattern at frequencies >1.5 kHz limit the reliability [13, 15, 16]. In the other case, where the RW is excited by an IMEHD, the ear is stimulated in reverse direction compared to the physiological sound transmission. Although SFP vibration responses are commonly measured to estimate the stimulation efficiency in reverse stimulation [17–19], it has been demonstrated that this method markedly underestimates the real output level [7].

In conclusion, measuring stapes vibration responses according to ASTM standard 2504-05 [4] is a reliable method to determine the output level of IMEHDs only during forward stimulation when the ossicular chain and cochlea are left intact. In all other stimulation modes an alternative measurement method is needed to quantify the output level of IMEHDs and DACIs in human cadaveric TBs. The sound pressure difference between the scala vestibuli (SV) and scala tympani (ST) correlates with cochlear excitation [20] and pressure differences have successfully been used to characterize the output level in forward and reverse stimulation in TB experiments [7, 21–23]. In these studies the sound pressure in SV and ST was measured with a custom-made pressure sensor developed by E. Olson [24]. This sensor is commercially not available and difficult to build. Therefore the much-needed technique of intracochlear sound pressure measurement is currently available only for a limited group of researchers.

In order to make this method accessible to a wider community, the goal of our study was to demonstrate that an off-the-shelf pressure measurement system can be successfully used for intracochlear sound pressure measurement. This may contribute to establish intracochlear sound pressure measurements as a generally accessible and commonly used technique.

2 Materials and Methods

In this study intracochlear sound pressures in response to acoustic stimulation of the tympanic membrane were measured in SV (P_{SV}) and ST (P_{ST}) in cadaveric human TBs with the off-the-shelf pressure transducer Samba Preclin 420 LP.

2.1 TB Preparation

Human cadaveric TBs obtained from the Institute for Pathology of the Hannover Medical School and the Department of Legal Medicine of the University Medical Center Hamburg-Eppendorf [25] were used for this study. Harvesting and anonymous use of the TBs was approved by the ethics committee of the Hannover Medical School (2168-2014). All TBs were harvested within 48 h *post mortem*, immediately frozen at approx. −19 °C and thawed shortly before preparation at room temperature. A mastoidectomy, removal of the facial nerve and thinning of the RW niche overhang down to approx. 0.5–1 mm were performed. After preparation the TBs were stored in saline containing ~0.005‰ thimerosal at approx. −19 °C until the experiments. During experiment the TBs were kept moist with saline to avoid changes in mechanical behavior [4].

2.2 Experimental Setup

TBs were fixed in a laboratory clamp on a vibration isolated table (LW3048B, Newport, Germany). A custom-made sound application setup containing a probe microphone (ER-7C, Etymotic Research Inc., USA) and a loudspeaker (DT48, beyerdynamic, Germany) was cemented (Paladur, Heraeus Kulzer GmbH, Germany) to the outer ear canal (OEC). The tip of the probe microphone tube was positioned 1–2 mm from the tympanic membrane (TM). To prevent unwanted vibrations from the loudspeaker to the TB, the TB was embedded in modelling clay (Play-Doh, Hasbro, Germany).

2.3 Intracochlear Pressure Measurement

Intracochlear pressures in SV and ST were measured simultaneously with two off-the-shelf pressure fiber-optic transducers (Samba Preclin 420 LP, Samba Sensors AB, Sweden) connected to a two-channel control unit (Samba control unit 202, Samba Sensors AB, Sweden). The pressure transducer has an outer diameter of 0.42 mm, is calibrated by the manufacturer, valid for lifetime with a long term

stability of <0.5% of range [26, 27], and can be reused for several measurements. The pressure measurement system has a maximum measurement frequency of 40 kHz, a pressure range of −50 to +350 hPa and a sensitivity of approx. −80 dB re 1 V/Pa. The control unit provides a proportional voltage signal at each analog output channel. Each transducer was mounted to a custom made holder attached to a 3-axis micromanipulator (M3301R, World Precision Instruments Germany GmbH, Germany), allowing the adjustment in all three spatial directions.

2.4 Vibration Measurement

SFP vibration responses were measured with a single-point LDV system (OFV 534, OFV 5000, A HLV MM 30, Polytec, Germany) attached to a surgical microscope (OPMI-1, Zeiss, Germany). The laser beam was directed at a small piece (<0.3 mm × 0.3 mm) of reflective tape on the SFP at a visually estimated incident angle of ≤45° to the SFP normal. During analysis the incident angle was considered by a cosine correction.

2.5 Experimental Procedure

(1) The TB preparation was checked visually using a surgical microscope.
(2) The loudspeaker was driven by a custom multi-sine signal, with equal amplitudes of approx. −25 dB re 1 V_{rms} at 0.125, 0.25, 0.5, 1, 2, 3, 4, 6, 8 and 10 kHz. The vibration of the SFP was measured with the LDV and the sound pressure level (SPL) in the OEC was recorded by the probe microphone. Only if the SFP vibration response was within the modified acceptance range [5] of the ASTM standard F2504-05 [4], the experiment was continued.
(3) Two Samba Preclin 420 LP transducers were placed in SV and ST (Fig. 1).
(4) For this purpose the promontory was thinned and a fenestration of approx. 0.5 mm diameter was made in SV and ST. After insertion of the transducer (100–300 µm, visually estimated) into the scalae it was sealed with dental impression material alginate (Alginoplast®, Heraeus Kulzer GmbH) in TB05–07 or a silicone rubber plug (Silikonkautschuk RTV, Wacker-Chemie GmbH, Germany) permanently mounted to the optical fiber in TB16, 18, 19. During cochleostomy, sensor insertion and sealing, the middle ear cavity was immersed in saline to prevent air from entering the cochlear.
(5) SFP vibrations in response to the acoustic multi-sine stimulation were measured again.
(6) The TM was stimulated acoustically between 0.1 and 10 kHz by a sequence of sine wave signals with a frequency resolution of 3/octave (23 frequencies

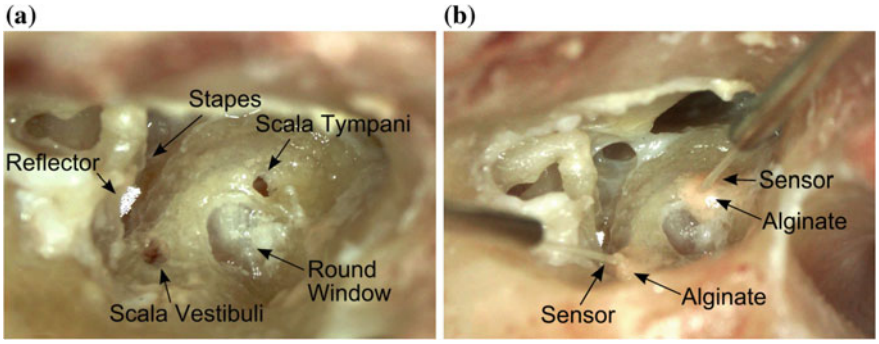

Fig. 1 Temporal bone preparation. **a** Cochleostomies of ~0.5 mm diameter in scala vestibuli (SV) and scala tympani (ST). A reflector was placed on the stapes footplate for LDV measurement. **b** Samba Preclin 420 LP transducers placed in SV (*left*) and ST (*right*) sealed with Alginate. Taken from [1]

between 0.1 and 10 kHz) at levels of 105–130 dB SPL. The sound pressures in SV and ST were measured by the pressure transducers, the vibration of the SFP was measured with the LDV and the SPL in the OEC was recorded by the probe microphone.

(7) After completing all measurements the pressure transducers were removed and the correct positioning of the cochleostomies in SV and ST was confirmed visually by dissection of the TB.

In total, three out of 19 TBs were excluded due to damages of anatomical structures. Of the remaining 16 TBs, six had SFP vibration responses compliant to the modified acceptance range of ASTM F2504-05 [5] and were used for intracochlear sound pressure measurements.

2.6 Signal Generation, Acquisition and Analysis

For signal generation and acquisition a commercial 16-bit, 4 channel data acquisition system (PC-D and VIB-E-400, Polytec, Germany) with commercial software (VibSoft 4.8.1, Polytec, Germany) was used. Electric input signals to the loudspeaker were buffered by an amplifier (SA1, Tucker-Davis Technologies, USA). Input signals were acquired simultaneously as averaged complex spectra (800 FFT lines, 0–10 kHz, 12.5 Hz resolution). The complex signal-spectra were averaged 500–1000 times. At each stimulation frequency the SNR was determined using the average of the three adjacent FFT lines below and above as noise level estimate. Vibration responses with SNR < 12 dB and intracochlear sound pressure responses with SNR < 7 dB were excluded from analysis.

3 Results

3.1 SFP Vibration Responses Before and After Cochleostomy

Six TBs showed vibration responses of the SFP to sound [dB re μm/Pa] at 0.25–4 kHz (Fig. 2a) compliant to the modified acceptance range [5] of ASTM F2504-05 [4] and were used for intracochlear sound pressure measurements. Even after the insertion of the pressure transducer, the SFP responses (Fig. 2b) were inside the range, except TB06 at 4 kHz (5.7 dB deviation), TB16 at 1, 2, and 3 kHz (2.8 dB maximum deviation) and TB19 at 4 kHz (2.4 dB deviation).

3.2 Sound Pressures in Scala Vestibuli and Scala Tympani

To compare the measurement data across all TBs independent of stimulation level, the intracochlear sound pressures P_{SV} and P_{ST} were normalized to the outer ear canal SPL P_{OEC} (Fig. 3) and to the stapes footplate velocity V_{SFP} (Fig. 4).

In all specimens except TB05, intracochlear sound pressures were measurable in both scalae between 0.1 and 6.35 kHz with an SNR > 7 dB. When normalized to P_{OEC} the magnitudes of P_{SV} (Fig. 3a) were similar across all experiments, as well as P_{ST} (Fig. 3c) at frequencies ≥ 3 kHz. At lower frequencies the magnitudes of P_{ST}/P_{OEC} varied up to 42 dB across experiments. In particular in TB19 the magnitudes were at ≤ 0.4 kHz up to 27 dB smaller than in all other experiments.

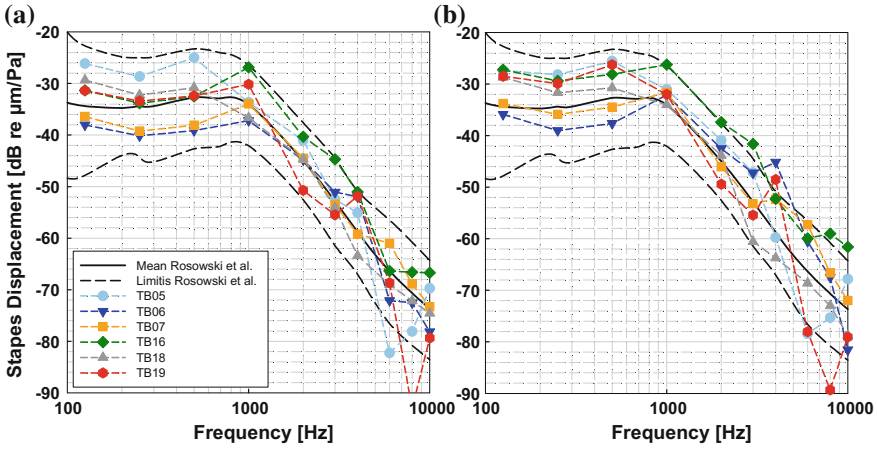

Fig. 2 SFP displacement in response to sound stimulation of the tympanic membrane. **a** Before pressure sensor insertion. **b** After cochleostomy and pressure sensor insertion. The black dashed lines depict the limits given by Rosowski et al. [5]. Modified from [1]

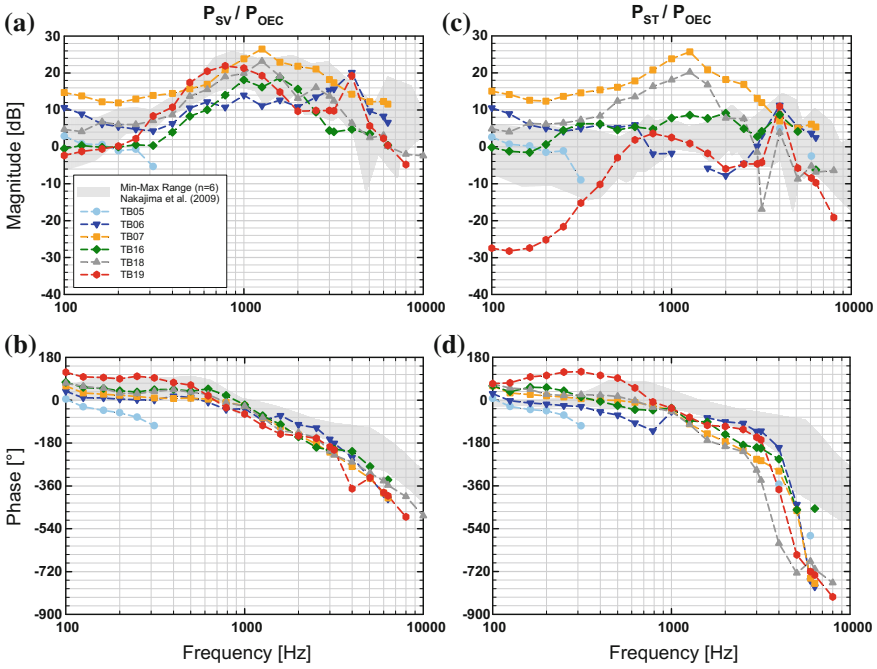

Fig. 3 Sound pressures in scala vestibuli (P_{SV}, **a** & **b**) and scala tympani (P_{ST}, **c** & **d**) normalized to the outer ear canal sound pressure level (P_{OEC}). For comparison the range of results obtained with a custom made pressure sensor by Nakajima et al. [22] is given (*grey shaded area*). Modified from [1]

The phases of P_{SV} (Fig. 3b) and P_{ST} (Fig. 3d) were similar across all TBs showing an increasing lag to P_{OEC} with increasing frequency. At frequencies >4 kHz the phases of P_{ST} decreased significantly, resulting in approx. two cycles shift at $\geq$5.5 kHz.

The magnitudes of P_{SV} normalized to V_{SFP} (Fig. 4a) were similar across all experiments, only TB07 showed a prominent peak at 2.525 kHz. In contrast, the magnitudes of P_{ST}/V_{SFP} (Fig. 4c) varied at frequencies below 3 kHz significantly by up to 49 dB. Again, at frequencies $\leq$0.4 kHz the magnitudes in TB19 were distinctly smaller compared to the other experiments. At frequencies $\leq$2 kHz the P_{SV}/V_{SFP} and P_{ST}/V_{SFP} phases were mainly constant for each TB whereas at higher frequencies the phases showed a higher variation.

In each experiment the normalized magnitude of P_{SV} was higher than the normalized magnitude of P_{ST} at frequencies above 400 Hz whereas the pressure magnitudes in both scalae were similar at lower frequencies. Only in TB07 the magnitudes of P_{SV} and P_{ST} were similar (differences $\leq$2 dB) up to 1.6 kHz and in TB19 the magnitude of P_{SV} was distinctly higher than P_{ST} at all frequencies.

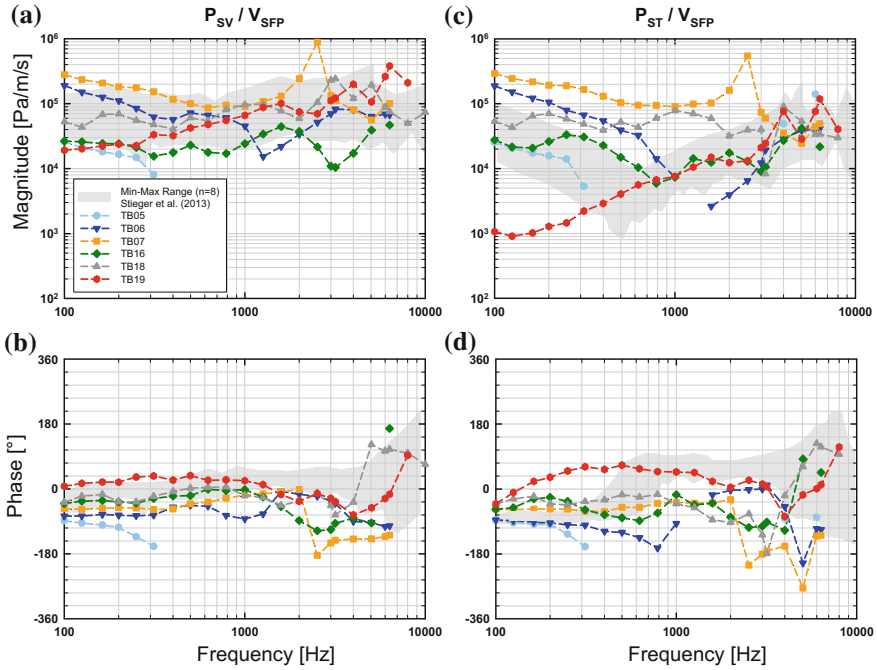

Fig. 4 Sound pressures in scala vestibuli (P_{SV}, **a** & **b**) and scala tympani (P_{ST}, **c** & **d**) normalized to the stapes footplate velocity (V_{SFP}). For comparison the range of results obtained with a custom made pressure sensor by Stieger et al. [7] is given (*grey shaded area*). Data with an SNR < 7 dB were omitted. Modified from [1]

3.3 *Intracochlear Pressure Differences*

The magnitudes and phases of the complex pressure differences ($\Delta P = P_{SV} - P_{ST}$) between SV and ST are plotted in Fig. 5 normalized to the SPL in the OEC (P_{OEC}). Apart from TB16, showing a sharp notch at 2525–3175 Hz, the magnitudes (Fig. 5a) were similar across all TBs with differences $\leq$20 dB. The phases (Fig. 5b) were also similar in all TBs showing a 1/8–2/3 cycle lead at frequencies below 1 kHz that decreased with increasing frequency to a lag of up to 1 1/3 cycle. Since in TB05 pressure differences were only measurable at $\leq$312.5 Hz and up to 20 dB lower than in the other experiments, it was assumed that the preparation in this TB failed and the TB was not further considered in the analysis. The magnitudes and phases of the differential pressure ($\Delta P = P_{SV} - P_{ST}$) normalized to the velocity of the SFP (V_{SFP}) (Fig. 6) were almost frequency independent. Across all TBs the magnitudes varied $\leq$21 dB, except in TB16 at 2525–3175 Hz where a notch was present. The phases were near 0° at frequencies $\leq$2 kHz and varied between −180° and +180° at higher frequencies.

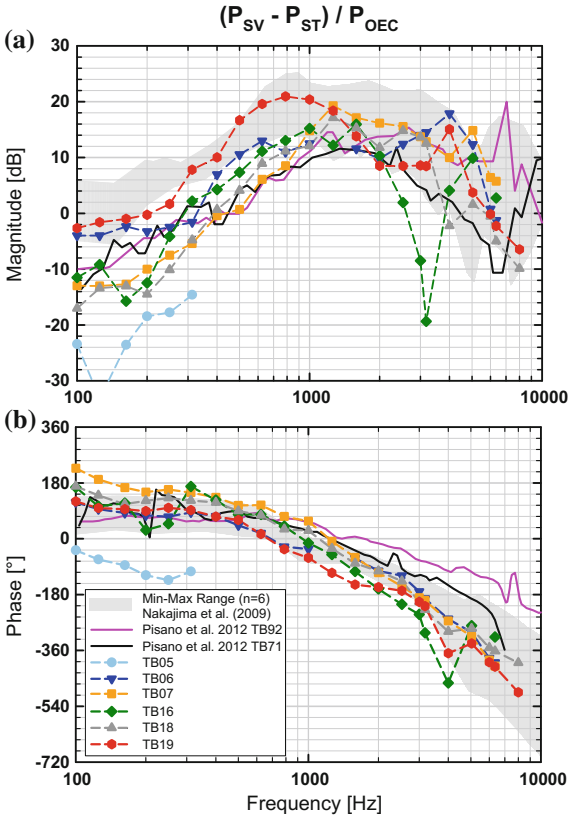

Fig. 5 Pressure differences ($P_{SV} - P_{ST}$,) normalized to the outer ear canal sound pressure level (P_{OEC}). For comparison the range of results (Nakajima et al. [22], *grey shaded area*) and two exemplary measurements (Pisano et al. [23], *solid lines*) obtained with a custom made pressure sensor are given. Data with an SNR < 7 dB were omitted. Modified from [1]

4 Discussion

4.1 Effect of Transducer Insertion on SFP Vibration Responses

After pressure transducer insertion most SFP vibration responses to sound (Fig. 2) were not significantly changed and fulfilled the modified ASTM criteria [5]. The difference between SFP vibration displacement before and after insertion of transducers ($\Delta d = d_{\text{post}} - d_{\text{pre}}$) was generally within 5 dB below 3 kHz and within 7 dB at higher frequencies. These results indicate that the opening and re-closure of the cochlea by insertion of the pressure transducers has no pronounced effect on cochlear mechanics and confirms the assumption that the inserted sensor has a much higher acoustic impedance than the round window membrane and does not lead to major changes in natural cochlea acoustics.

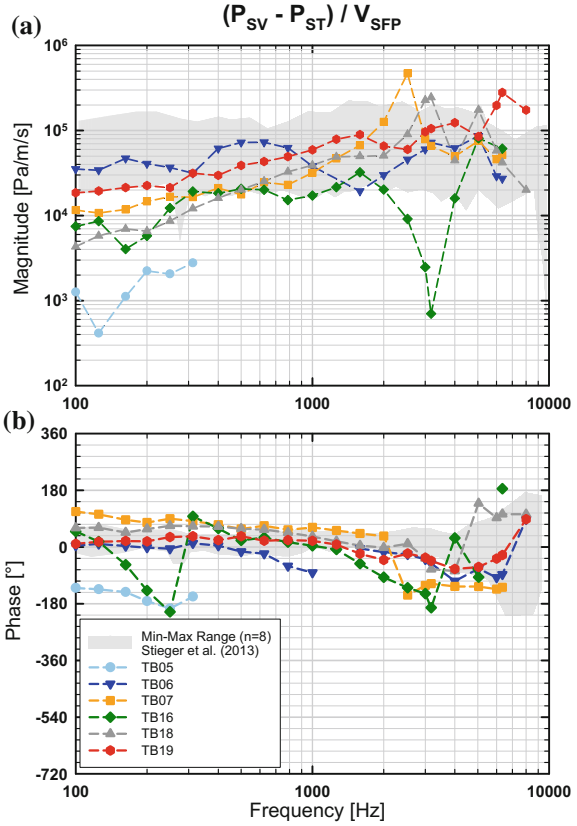

Fig. 6 Pressure differences ($P_{SV} - P_{ST}$,) normalized to the SFP velocity (V_{SFP}). For comparison the range of results obtained with a custom made pressure sensor by Stieger et al. [7] is given (*grey shaded area*). Data with an SNR < 7 dB were omitted. Modified from [1]

4.2 *Comparison to Previous Work with Custom-Made Pressure Sensors*

In the past it has been already demonstrated that the measurement of intracochlear pressure differences across the cochlear partition can be used to characterize the response levels from forward and reverse stimulation in human cadaveric TBs [7, 21–23]. The objective of this study was to investigate if intracochlear differential pressures are measurable in a similar manner with the off-the-shelf pressure transducer Samba Preclin 420 LP. Thus, the intracochlear sound pressures P_{SV}, P_{ST} and differential sound pressures ΔP measured here were compared (Figs. 3, 4, 5, 6) to earlier measurements [7, 22, 23] performed with custom-made sensors [24] that has proven to provide reliable results in the past.

Normalized to P_{OEC} or by V_{SFP}, our P_{SV} magnitudes (Figs. 3a and 4a) were largely within the minimum-maximum range of Stieger et al. [7] and Nakajima et al. [22] in the investigated frequency range. At frequencies ≥ 2 kHz the P_{ST} magnitudes (Figs. 3c and 4c) were also mostly comparable to these studies but differed up to approx. 20 dB at lower frequencies. Whereas we observed a

maximum variation of up to 42 dB in the magnitudes of P_{ST}/P_{OEC} and up to 49 dB in the magnitudes of P_{ST}/V_{SFP}, the magnitudes of P_{ST}/P_{OEC} in Nakajima et al. [22] and the magnitudes of P_{ST}/V_{SFP} in Stieger et al. [7] varied maximally approx. 25 dB. One potential reason for the difference between the P_{ST} magnitudes found here might have been the 6.3 times (approx. 16 dB) bigger sound sensitive integration area of the Samba Preclin 420 LP pressure transducer (0.1385 mm^2) compared to the custom-made sensor (0.0219 mm^2). Another reason for the higher variation of our P_{ST} magnitudes study might have been differences in sealing. This would also explain why in our study the magnitudes of P_{SV}/P_{OEC} and P_{SV}/V_{SFP} were more similar (maximum variation: 20 and 30 dB) across the TBs than the P_{ST} magnitudes.

In the experiments TB06, TB07 and TB16 where the magnitudes of P_{SV} and P_{ST} dropped at 8 and 10 kHz below 7 dB SNR the acoustic stimulation dropped to 70–90 dB SPL. This finding is in line with the theoretical resolution limit of the samba sensor system of 88–95 dB SPL at $\geq$7 kHz at the TM.

The phases of P_{SV} (Fig. 3b) and P_{ST} (Fig. 3d) relative to P_{OEC} were mostly within the range of Nakajima et al. [22]. Only at frequencies >4 kHz our P_{ST} phases differed significantly showing an up to 1 cycle longer delay which probably might be due to different unwrapping of the phase. Relative to V_{SFP} the P_{SV} and P_{ST} phases (Fig. 4b, d) were at frequencies <2 kHz comparable to Stieger et al. [7] but mostly lower at higher frequencies. A 1/2 cycle shift in P_{ST} phases at approx. 0.5 kHz determined by Stieger et al. [7] was not observable here. One potential reason for the lower similarity to Stieger et al. [7] might be that in their study the vibration response of the stapes was measured at the posterior crus whereas we measured it at the footplate leading to a different impact of rocking motions. However, to determine the input to the cochlea the relevant parameter is the pressure difference between SV and ST correlated to cochlear microphonics [20]. When normalized to P_{OEC} (Fig. 5a), at $\geq$1 kHz, the magnitude of the complex pressure difference $\Delta P = (P_{SV} - P_{ST})$ was within the minimum-maximum range of measurements by Nakajima et al. [22], but up to 16 dB less at lower frequencies. As mentioned before a probable reason for this discrepancy at low frequencies might have been the sealing between pressure transducer and bone. On the other hand our data was comparable in the whole frequency range (Fig. 5) to two exemplary measurements of a later study [23] performed by the same researchers. This variance demonstrates that more reference data of differential intracochlear pressure measurements would be useful but is currently not available. The phases of ΔP relative to P_{OEC} were similar to Nakajima et al. [22]. When normalized to the stapes velocity, almost all magnitudes of $\Delta P/V_{SFP}$ (Fig. 6a) were within the minimum-maximum range of Stieger et al. [7], except at frequencies <0.3 kHz where our results were maximally 15 dB less. Almost all phases of ΔP relative to V_{SFP} were within the range of Stieger et al. [7].

Between 2525 and 3175 Hz where the normalized ΔP magnitude decreased extraordinarily in TB16 (Figs. 5a and 6a), the absolute values of P_{SV} and P_{ST} were close in magnitude and phase in this experiment. Usually this might be an indication for placement of both pressure transducers accidently into the same scala.

However, in this experiment the differential intracochlear pressure at all other frequencies was normal and a defect of the preparation could be excluded based on the visual inspection during dissection.

In consideration of nonlinear effects on the normalized intracochlear pressure magnitudes, the range of acoustical stimulation levels has to be taken into account. In our study sounds were presented at 105–130 dB SPL, whereas in Stieger et al. [7] stimulation levels between 50 and 115 dB SPL and in Nakajima et al. [22] levels between 70 and 130 dB SPL. It is known that the vibration response of the stapes in human cadaveric TBs is linear with the level of acoustic stimulation up to 124 dB SPL at 0.4–6 kHz [28] and up to 130 dB SPL at 0.1–4 kHz [29]. Therefore it can be assumed that the normalized intracochlear pressures and pressure differences measured by Stieger et al., Nakajima et al. and Pisano et al. [7, 22, 23] and our results are not subject to significant middle ear non-linearities although our minimum stimulation levels were higher. In one experiment we stimulated acoustically first with sound pressure levels of 110–130 dB SPL and second with levels of 90–120 dB SPL. When normalized to P_{OEC} the magnitudes of P_{SV} and P_{ST} were similar within 3 dB except at 3175 Hz where a decrease in P_{ST} by 12 dB was found for the lower simulation level.

5 Conclusion

With the commercial off-the-shelf pressure transducer Samba Preclin 420 LP intracochlear pressure differences with acoustic stimulation were comparable to results obtained with custom-made sensors [24] at frequencies of 1–8 kHz and differed up to 16 dB below 1 kHz. The insertion of the pressure transducers only had a minor effect of <5 dB on the stapes vibration response to sound. Our results demonstrate that the Samba Preclin 420 LP is usable for simultaneous measurements of intracochlear sound pressures in SV and ST with sufficient SNR and sensitivity.

References

1. M. Grossöhmichen, R. Salcher, K. Püschel, T. Lenarz, H. Maier, Differential Intracochlear sound pressure measurements in human temporal bones with an off-the-shelf sensor. Biomed Res. Int. **2016**, 1–10 (2016), Article ID 6059479
2. J.F. Kasic, J.M. Fredrickson, The otologics MET ossicular stimulator. Otolaryngol. Clin. North Am. **34**(2), 501–513 (2001)
3. R. Mlynski, E. Dalhoff, A. Heyd, D. Wildenstein, K. Rak, A. Radeloff, R. Hagen, A.W. Gummer, S.P. Schraven, Standardized active middle-ear implant coupling to the short incus process. Otol. Neurotol. **36**(8), 1390–1398 (2015)
4. ASTM, F 2504 – 05 Standard Practice for Describing System Output of Implantable Middle Ear Hearing Devices (2005)

5. J.J. Rosowski, W. Chien, M.E. Ravicz, S.N. Merchant, Testing a method for quantifying the output of implantable middle ear hearing devices. Audiol. Neurotol. **12**(4), 265–276 (2007)
6. A. Devèze, K. Koka, S. Tringali, Ha Jenkins, D.J. Tollin, Techniques to improve the efficiency of a middle ear implant: effect of different methods of coupling to the ossicular chain. Otol. Neurotol. **34**(1), 158–166 (2013)
7. C. Stieger, J.J. Rosowski, H.H. Nakajima, Comparison of forward (ear-canal) and reverse (round-window) sound stimulation of the cochlea. Hear. Res. **301**, 105–114 (2013)
8. L. Bruschini, F. Forli, S. Passetti, P. Bruschini, S. Berrettini, Fully implantable Otologics MET Carina(^{TM}) device for the treatment of sensorineural and mixed hearing loss: Audio-otological results. Acta Otolaryngol. **130**(10), 1147–1153 (2010)
9. C. Martin, A. Deveze, C. Richard, P.P. Lefebvre, M. Decat, L.G. Ibañez, E. Truy, T. Mom, J.-P. Lavieille, J. Magnan, C. Dubreuil, S. Tringali, European results with totally implantable carina placed on the round window. Otol. Neurotol. **30**(8), 1196–1203 (2009)
10. V. Colletti, S.D. Soli, M. Carner, Treatment of mixed hearing losses via implantation of a vibratory transducer on the round window. Int. J. Audiol. **45**(10), 600–608 (2006)
11. T. Lenarz, J.W. Zwartenkot, C. Stieger, B. Schwab, E.A.M. Mylanus, M. Caversaccio, M. Kompis, A.F.M. Snik, C. D'hondt, H. Mojallal, Multicenter study with a direct acoustic cochlear implant. Otol. Neurotol. **34**(7), 1215–1225 (2013)
12. S. Busch, S. Kruck, D. Spickers, R. Leuwer, S. Hoth, M. Praetorius, P.K. Plinkert, H. Mojallal, B. Schwab, H. Maier, T. Lenarz, First clinical experiences with a direct acoustic cochlear stimulator in comparison to preoperative fitted conventional hearing aids. Otol. Neurotol. **34**(9), 1711–1718 (2013)
13. M. Grossöhmichen, R. Salcher, H.-H. Kreipe, T. Lenarz, H. Maier, The Codacs^{TM} direct acoustic cochlear implant actuator: exploring alternative stimulation sites and their stimulation efficiency. PLoS ONE **10**(3), e0119601 (2015)
14. A. Devèze, K. Koka, S. Tringali, H.A. Jenkins, D.J. Tollin, Active middle ear implant application in case of stapes fixation: a temporal bone study. Otol. Neurotol. **31**(7), 1027–1034 (2010)
15. S. Stenfelt, N. Hato, R.L. Goode, Fluid volume displacement at the oval and round windows with air and bone conduction stimulation. J. Acoust. Soc. Am. **115**(2), 797 (2004)
16. S. Stenfelt, N. Hato, R.L. Goode, Round window membrane motion with air conduction and bone conduction stimulation. Hear. Res. **198**(1–2), 10–24 (2004)
17. S. Tringali, K. Koka, A. Deveze, N.J. Holland, H.A. Jenkins, D.J. Tollin, Round window membrane implantation with an active middle ear implant: a study of the effects on the performance of round window exposure and transducer tip diameter in human cadaveric temporal bones. Audiol. Neurotol. **15**(5), 291–302 (2010)
18. H. Maier, R. Salcher, B. Schwab, T. Lenarz, The effect of static force on round window stimulation with the direct acoustic cochlea stimulator. Hear. Res. **301**, 115–124 (2013)
19. R. Salcher, B. Schwab, T. Lenarz, H. Maier, Round window stimulation with the floating mass transducer at constant pretension. Hear. Res. **314**, 1–9 (2014)
20. A. Dancer, R. Franke, Intracochlear sound pressure measurements in guinea pigs. Hear. Res. **2** (3–4), 191–205 (1980)
21. H.H. Nakajima, W. Dong, E.S. Olson, J.J. Rosowski, M.E. Ravicz, S.N. Merchant, Evaluation of round window stimulation using the floating mass transducer by intracochlear sound pressure measurements in human temporal bones. Otol. Neurotol. **31**(3), 506–511 (2010)
22. H.H. Nakajima, W. Dong, E.S. Olson, S.N. Merchant, M.E. Ravicz, J.J. Rosowski, Differential intracochlear sound pressure measurements in normal human temporal bones. J. Assoc. Res. Otolaryngol. **10**(1), 23–36 (2009)
23. D.V. Pisano, M.E.F. Niesten, S.N. Merchant, H.H. Nakajima, The effect of superior semicircular canal dehiscence on intracochlear sound pressures. Audiol. Neurotol. **17**(5), 338–348 (2012)
24. E.S. Olson, Observing middle and inner ear mechanics with novel intracochlear pressure sensors. J. Acoust. Soc. Am. **103**(6), 3445 (1998)
25. K. Püschel, Teaching and research on corpses. Rechtsmedizin **26**(2), 115–119 (2016)

26. Samba 201/202 User Manual. Samba Sensors AB (2011)
27. Samba Preclin Datasheet. Samba Sensors AB (2007)
28. R.L. Goode, M. Killion, K. Nakamura, S. Nishihara: New knowledge about the function of the human middle ear: development of an improved analog model (1994)
29. S.E. Voss, J.J. Rosowski, S.N. Merchant, W.T. Peake, Acoustic responses of the human middle ear. Hear. Res. **150**(1–2), 43–69 (2000)

Development of a Parametric Model of the Electrically Stimulated Auditory Nerve

Waldo Nogueira and Go Ashida

Abstract Cochlear implants (CIs) are used to restore the sense of hearing in people with profound hearing loss. Some CI users can communicate over the phone and even understand speech with some background noise, whereas some other CI users do not obtain the same benefit from the device. Due to differences in the interface between the electrodes and the auditory nerves, the best settings of the CI may be different for each user. In order to improve the fitting of CIs and to understand the electrode-nerve interface, a user-specific model of the auditory nerve activity has been developed. The model is based on a combination of existing models found in the literature. This chapter presents the basic components of the model: A three-dimensional finite element method to estimate the voltage distribution in the cochlea; and an auditory nerve model based on multi-compartment Hodgkin-Huxley-type equations fitted to known electrophysiological measurements. Using the above described model, intracochlear voltage distributions are reproduced. Additionally, amplitude growth functions of the evoked compound action potential (ECAP) were simulated using an artifact rejection forward masking paradigm. The model has been parameterized such that it can be personalized to each CI user by fitting its parameters to predict the individual voltage distributions and amplitude growth functions. The modeling results show that different amounts of nerve density and nerve degeneration lead to different shapes in the amplitude growth function. The future goal of the model is to create a tool to predict the most comfortable level of each CI user and to fit CI parameters in a personalized clinical situation.

W. Nogueira (✉)
Cluster of Excellence "Hearing4all", Department of Otolaryngology,
Hannover Medical School, 30625 Hannover, Germany
e-mail: nogueiravazquez.waldo@mh-hannover.de

G. Ashida
Cluster of Excellence "Hearing4all", Department of Neuroscience,
University of Oldenburg, 26129 Oldenburg, Germany
e-mail: go.ashida@uni-oldenburg.de

P. Wriggers and T. Lenarz (eds.), *Biomedical Technology*, Lecture Notes in Applied and Computational Mechanics 84, DOI 10.1007/978-3-319-59548-1_19

1 Introduction

The cochlear implant (CI) is an auditory prosthesis that converts acoustic waveforms into electrical pulses that are delivered to auditory nerves (ANs) via implanted electrodes [34]. The spectro-temporal information of the sound is first pre-processed and analyzed by the CI processor; then corresponding electrical pulses are generated to stimulate ANs through the array of electrodes that are inserted in the cochlea; and finally sequences of action potentials of the AN fibers are sent to higher brain areas to form an auditory perception [30].

While CIs are generally successful in restoring hearing to a reasonable degree in people with profound hearing loss, their performances show considerable variations between individual subjects [32]. Some CI users can communicate over the phone or even understand speech in a noisy environment, whereas other CI users do not obtain the same degree of benefits. A number of reasons may exist for the observed variations [9]. For example, the exact positions of the electrodes in the cochlea, and the amount of functional auditory neurons might differ significantly between individual CI users. Individualization of the CI strategy (location, stimulation protocol, etc.) thus seems to be necessary to achieve an optimal outcome of implanted CIs.

In order to improve the fitting of CIs and to understand how CI stimuli interact with AN fibers, we construct a user-specific model of the cochlea and ANs. The model is composed of two parts: A 3D-reconstructed finite element method (FEM) model of the cochlea (reviewed in [9, 14]), in combination with multi-compartment conductance-based model of ANs (reviewed in [24]). The goal of the study is to simulate and assess evoked compound action potentials (ECAPs). Since the parameters of the model can be adjusted to reproduce individual ECAPs of each CI user, it may be used as a tool to explore the optimal CI strategy tailored for individual CI users.

2 Methods

2.1 3D Cochlear Geometry and Finite Element Model

A general cochlea geometry was constructed based on a histological dataset of a single human cochlea (Fig. 1a). The shapes of the compartments (scala vestibuli, scala media, scala tympani, Reissener membrane and basilar membrane) were approximated by polygons with a relative low number of points as done by Rattay et al. [26]. At every 30° around the vertical axis, a new plane containing all the compartments was repeated. The new plane was extruded and joined to the previous plane. In total, 2.5 turns of the cochlea were modeled. Figure 1a, b present an example of the geometry and the triangulation for a cochlea. The resulting geometry can be easily modified and adapted to clinical computer tomography (CT) data of each individual [20–23]. The geometry of the electrode array was based on the nucleus contour advance electrode array. This electrode is composed by 22 electrodes inserted in the scala tympani.

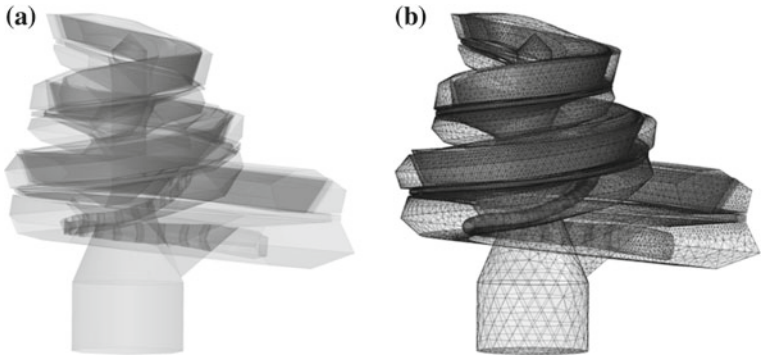

Fig. 1 3D reconstruction of the cochlea. **a** Geometry of a general cochlea with different compartments and a nucleus contour advance electrode array inserted in the scala tympani. **b** Corresponding mesh required for FEM

FEM was used to model the electric field in the cochlea. The geometry was classified into domains (bone, nerve tissue, perilymph, endolymph, Reissner membrane and basilar membrane), and each domain was assigned a material property in the form of resistivity. The relevant resistivity values can be found in [2]. Based on the reconstructed 3D cochlea, each AN fiber was modeled as a one-dimensional curve with estimated positions of 10 nodes of Ranvier (Fig. 2, left). All AN fibers run along the spiral ganglion over the two and half turns of the cochlea (Fig. 2, right). In total, 7000 AN fibers were modeled.

2.2 Auditory Nerve Model

In order to model neural activity, it is necessary to couple the 3D voltage distribution model with an appropriate AN model that can reliably reproduce known biophysical properties of human AN axons. The model is based on measured anatomical parameters and tuned to fit previous physiological recording results.

2.2.1 Anatomy

Based on previous anatomical results of human Type 1 auditory nerves, we constructed a one-dimensional nerve model (Fig. 3). The human AN has a bipolar shape with a peripheral axon receiving synaptic inputs from cochlear hair cells, a large unmyelinated cell body (soma), and a central axon innervating its target neurons in the central auditory system [19]. The diameter of the central axon is roughly as twice as that of the peripheral axon (peripheral: $1.32 \pm 0.15\,\mu m$, central: $2.65 \pm 0.30\,\mu m$, unmyelinated segments, measured by Rattay et al. [28]). Type 1 human ANs have

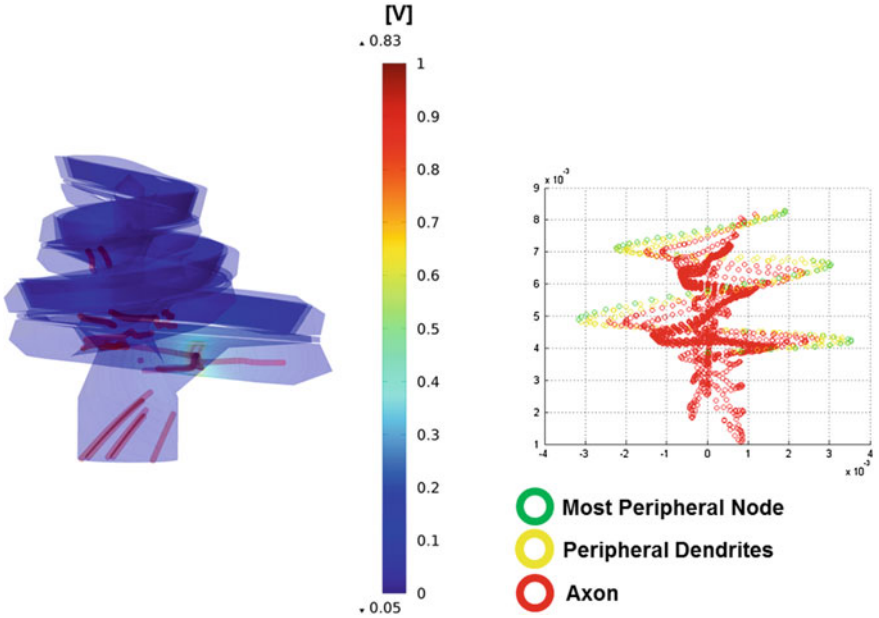

Fig. 2 3D reconstruction of AN fibers. *Left* FEM 3D voltage distribution simulation. The voltage distribution is sampled at AN node positions. *Right* Distribution of AN nodes, the different color indicates nodes corresponding to the most peripheral node (*green*), the peripheral dendrites (*yellow*) and the axon (*red*). In total 7000 nerve fibers were created

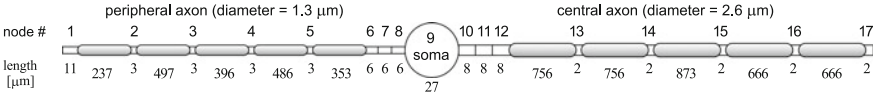

Fig. 3 Modeled anatomy of an AN fiber. Unmyelinated nodes and the soma are shown in *white*. Myelinated internodal segments are *gray-shaded*. Nodal and somatic compartments are sequentially numbered from the peripheral end. Presomatic (#6–8) and postsomatic axonal nodes (#10–12) are respectively subdivided into three compartments. Each compartment is assumed to be a uniform cylinder. The diameter and length of each compartment (shown below the drawing) were determined from previous anatomical results and our 3D reconstruction (see Sect. 2.2.1). In contrast to other mammals, the soma of a human AN is generally not myelinated [19]

myelinated axons: myelination starts at 5–26 μm from the cell body in the peripheral axon and at 4–38 μm in the central axon [25]. The diameter of the human AN soma is 22–34 μm [25], corresponding to the cross-sectional area of the soma (measured at the maximum diameter) of 400–900 μm^2 [18]. Since there are no systematic measurements available for the internodal length of human AN, we will use estimated values from our 3D reconstruction of the human cochlea (see Sect. 2.1 and Fig. 2).

Note that the presomatic compartment (unmyelinated peripheral axonal compartment next to the soma) of our model is significantly shorter than those of earlier references [3, 27, 28, 33]. These previous studies used an unrealistically long (100 μm)

presomatic compartment to ensure spike conduction across the large cell body. We used a shorter value in our model, and spike conduction was instead ensured by adjusting physiological parameters (see Sect. 2.2.3).

2.2.2 Physiology

A number of models have been used for simulating spiking activity of AN fibers (reviewed in [24]). In this study, we adopted the modified Hodgkin-Huxley model introduced by Smit et al. [33], which were tuned to reproduce known physiological data of human nerves. Equations and parameters of the Smit model are summarized in Tables 1 and 2, respectively. In short, each model compartment (axonal node or soma) is charged with its intrinsic sodium, potassium, and leak currents as well as axonal currents from the neighboring compartments and external stimuli. The dynamics of each ionic current is described by a first-order differential equation.

Actual capacitance (C) and conductances ($g_L, \bar{g}_{Na}, \bar{g}_K$) of each compartment (Table 1) were obtained by multiplying the values in Table 2 with the surface area calculated from the length and diameter of the compartment (Fig. 3). The Na and K conductance densities were the same for all compartments, while the leak conductance density of the soma and perisomatic compartments was set 10 times lower than

Table 1 Equations of the AN physiology model. The membrane potential V is measured from the resting potential $V_{\text{rest}} = -88.24$ mV. All the factors were adjusted for a body temperature of 37°. An apparent typo in the equation for α_n in [33] was corrected. For the sake of simplicity, the subscript k indicating the k-th compartment is dropped, except for the axonal current equation. I_{ext} denotes external stimulus current

Variable	Equation
Membrane potential V	$C\frac{dV}{dt} = I_L + I_{Na} + I_K + I_{\text{axon}} + I_{\text{ext}}$
Leak current	$I_L = g_L(E_L - V)$
Sodium current	$I_{Na} = \bar{g}_{Na} m^3 h (E_{Na} - V)$
Potassium current	$I_K = \bar{g}_K n^4 (E_K - V)$
Channel kinetics	$\frac{dx}{dt} = \alpha_x(V)\cdot(1-x) - \beta_x(V) \quad (x = m, h, n)$
Na activation	$\alpha_m(V) = 2.23^{(37-20)/10} \frac{4.42\cdot(2.5-0.1V)}{\exp(2.5-0.1V)-1}$
Na deactivation	$\beta_m(V) = 2.23^{(37-20)/10} \cdot 4.42 \cdot 4.0\exp(-V/18)$
Na inactivation	$\alpha_h(V) = 1.5^{(37-20)/10} \cdot 1.47 \cdot 0.07\exp(-V/20)$
Na deinactivation	$\beta_h(V) = 1.5^{(37-20)/10} \cdot 1.47 \,/\, (1+\exp(3.0-0.1V))$
K activation	$\alpha_n(V) = 1.5^{(37-20)/10} \frac{0.2\cdot(1.0-0.1V)}{10(1-\exp(1-0.1V))}$
K deactivation	$\beta_n(V) = 1.5^{(37-20)/10} \cdot 0.2 \cdot 0.125\exp(-V/80)$
Axonal current	$I_{\text{axon},k} = (V_{k-1} - V_k)/R_{k-1} + (V_{k+1} - V_k)/R_k$

Table 2 Parameters of the AN physiology model. Reversal potentials are measured from the resting potential. All the parameters were adjusted for a body temperature of 37° [33]

Parameter	Value
Leak reversal potential E_L	141.0 mV
Na reversal potential E_{Na}	−0.60 mV
K reversal potential E_K	−0.086 mV
Membrane capacitance density C_m	0.028×10^{-3} nF/μm^2
Leak conductance density G_L	0.905×10^{-3} uS/μm^2
Na conductance density G_{Na}	6.567×10^{-3} uS/μm^2
K conductance density G_K	0.728×10^{-3} uS/μm^2
Intracellular axial resistivity ρ_{axon}	0.25 MΩ μm

the value in the table (see Sect. 2.2.3). The axonal resistances R_k were also calculated from axial resitivity ρ_{axon} and the geometry of the model (Fig. 3).

Several models have been suggested to model the myelinated human AN fibers [24]. In this study, we simply assumed that the internodal segments are perfectly insulated and purely resistive. Therefore the axonal current at each compartment is determined by the voltage difference between the two neighboring compartments (Table 1).

2.2.3 Parameter Fitting

Before we used our AN model to predict ECAPs, we tested its biological plausibility and made additional modifications to the original model [33]. First, we calculated simulated conduction velocities for an axon with a diameter of 2.6 μm [28]. Assuming an internodal length of 500 μm and a nodal length of 2 μm, we obtained a conduction velocity of 27.5 m/s, which was within the range of estimated human AN conduction velocities (15–31 m/s) [17].

Next, we optimized the conductance of the soma. Initially, the modeled ionic conductances (leak, Na and K) of the soma were the same as those of the node. By running a number of preliminary simulations, however, we found that the static leak currents of the somatic and perisomatic compartments were the major cause of spike conduction failure (Fig. 4). Therefore we reduced the leak conductance of these compartments by a factor of 10 to allow action potentials to travel across the soma. Rattay et al. [27, 28] similarly assumed ten-fold higher conductance densities in the nodes than in the soma. We consider this modification as biologically relevant, since densities of ion channels are generally higher in nodes of Ranvier than in the soma [7, 15]. As conductances of other nodal compartments remained unchanged, conduction velocity and other biophysical factors of the central axon were not affected with this modification.

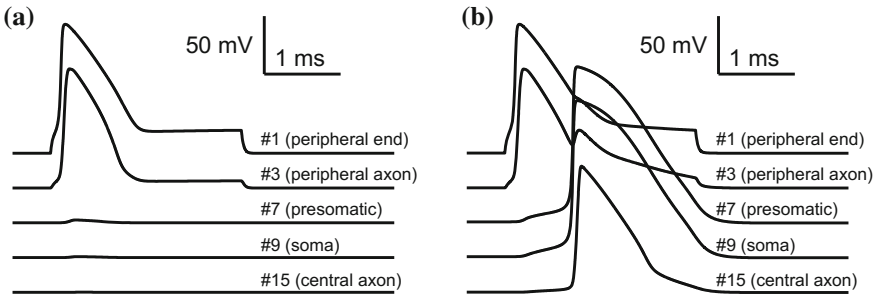

Fig. 4 Spike conduction failure and modification of the AN model. **a** Without the reduction of the leak conductances in somatic and perisomatic compartments, action potentials cannot go beyond the soma. **b** With the reduction of the leak conductances, the large unmyelinated somatic compartment allows a spike to transmit with some delay [27, 28]. An external step current (1.0 nA, 2.5 ms) was injected to the peripheral end of the model AN (compartment #1). Compartment numbers in the correspond to the numbering in Fig. 3

2.3 Evoked Compound Action Potentials (ECAPs)

The electrode-nerve interface of a CI user can be characterized with the recording capabilities of the device. Current commercial CIs can record small physiological potentials generated by stimulated AN fibers. This objective measure is known as evoked compound action potential (ECAP). The main goal of this chapter is to develop a model of the AN fiber activity to simulate ECAP responses for different electrode positions, stimulation modes and degrees of auditory nerve survival, and therefore allowing for a better understanding of the electrode-nerve interface.

2.3.1 Modeled ECAPs

The extracellular potential created by the j-th AN fiber measured by the m-th electrode is modeled as the sum of the contributions of all nodes along the fiber:

$$\mathbf{ECAP}_j^m(t) = \sum_{k=1}^{K} H_{j,k}^m \frac{dV_{j,k}(t)}{dt},$$

where K is the number of nodes (see Fig. 3), $V_{j,k}$ is the membrane potential of the k-th node of the j-th fiber, and $H_{j,k}^m$ is the transfer function between this node and the m-th electrode. We assumed that the measured ECAP is recorded at the center of each electrode, and the transfer function describes electrical coupling between the electrodes and the centers of AN nodes. The FEM model, in combination with known resistivity [2], was used to estimate the transfer function.

We obtain the final ECAP at the m-th electrode by simply summing up the contributions of all AN fibers:

$$\mathbf{ECAP}^m(t) = \sum_{j=1}^{J} \mathbf{ECAP}_j^m(t),$$

where J is the number of simulated AN fibers and set to 7000 in our simulations.

2.4 Parameterization of the Auditory Nerve Model

The auditory nerve model has been parameterized to simulate different amount of degeneration of each AN fiber at different locations. Figure 5 shows the parameterization graphically. The aim of the model is to fit the parameters to clinical measures on CI users. The clinical measures are described in the following section.

2.4.1 Recorded ECAPs

ECAPs from the AN represent the neural activity at the first encoding stage in the auditory pathway. These potentials do not require the subject to be attentive and can

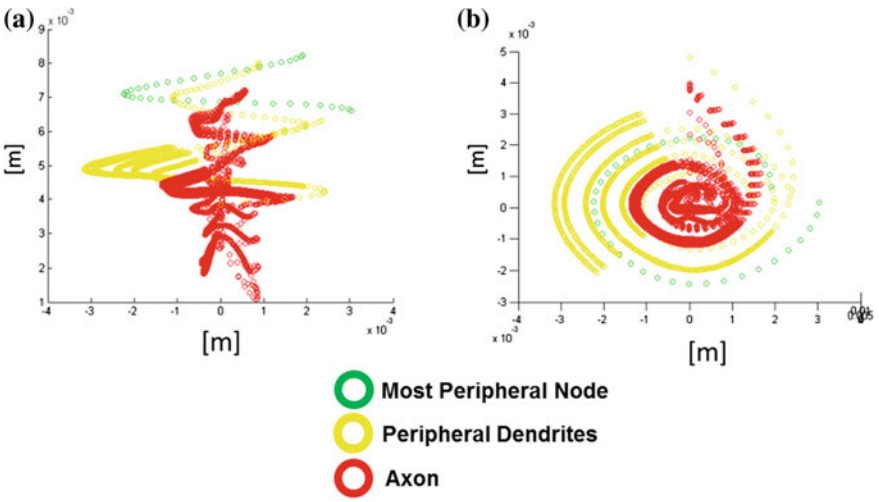

Fig. 5 Parametrized model of AN degeneration. **a** Modeled AN degeneration. Different amount of degeneration of the AN is shown. *Green* denotes the peripheral node, *yellow* the peripheral dendrites and *red* the axon nodes. The apical part is less degenerated (the dendrite peripheral node is still functional) than the basal part, where only the axons are modeled. **b** Higher density of dendrites existing on the basal part there than on the apical part of the cochlea

be recorded even when the listener is sleeping or under anesthesia. Moreover, these potentials are not affected by muscle activity and can therefore be recorded when the subject is moving. The ECAP consists of a negative (N1) and a positive (P2) peak, which occur approximately 0.2−0.4 and 0.6−0.8 ms following the stimulus onset, respectively [5]. CI manufacturers have simplified and automated ECAP recording methods using the intracochlear CI electrodes [8]. ECAP responses can be used to estimate the CI fitting parameters such as the comfort and threshold levels of electrical stimulation. However, the applicability of ECAPs to estimate behavioral levels has been limited by intra- and inter-subject variability [12]. It has been shown that the ECAP can potentially give information regarding cochlear health. For example, the N1 latency, the amplitude of the response (voltage difference of N1-P2 peaks), and the slope of the amplitude-growth function (AGF), which is defined as the input stimulation level versus the output recorded ECAP level curve, might all be influenced by the amount and density of auditory nerve fibers. Note that these parameters have been included in the parametric model.

The main difficulty in recording ECAPs is that the auditory nerve response occurs within 1 ms of onset of electrical stimulation. This means that an ECAP overlaps in time with the stimulus artifact. For this reason, artifact removal techniques are required to obtain reliable ECAP measurements in CIs. The two most common techniques used are the forward masking and the alternating polarity technique. The basic principal of the forward masking technique [4] is to record the response to a probe stimulus alone that contains both the neural response and the stimulus artifact. Next the response to probe stimulus preceded by a masker stimulus is recorded. This recording contains only the stimulus artifact and no neural response to the probe that is forward-masked by the masker. The artifact-only response is subtracted from the neural response plus the stimulus artifact, which leaves only the neural response. The alternating polarity artifact rejection technique consists of sending a biphasic pulse (e.g. cathodic-anodic) and recording the response. The stimulus polarity can be reversed in polarity so that the anodic pulse comes first. Assuming that the same neural response is generated using both polarities and that the stimulus artifact simply reverses in polarity, the sum of the response to the two pulse polarities should cancel the artifact and result in the neural response multiplied by two.

ECAPs can be recorded with the Advanced Bionics Volta 1.0 software. The software was configured to cancel the artifact using the forward-masking artifact rejection technique. Biphasic pulses (cathodic first) were generated having a pulse length of 60 μs. The inter pulse interval between the masker and the probe was set to 398.712 μs. Electrode 11 was used for probe and masker. Figure 6 shows the individually recorded ECAPs (after artifact removal) and the resulting AGF on the left. A linear fitting was used to obtain the stimulation level at which the first ECAP occurs. This stimulation value is termed threshold NRI and is typically used as en estimation of the behavioral most comfortable level with a CI.

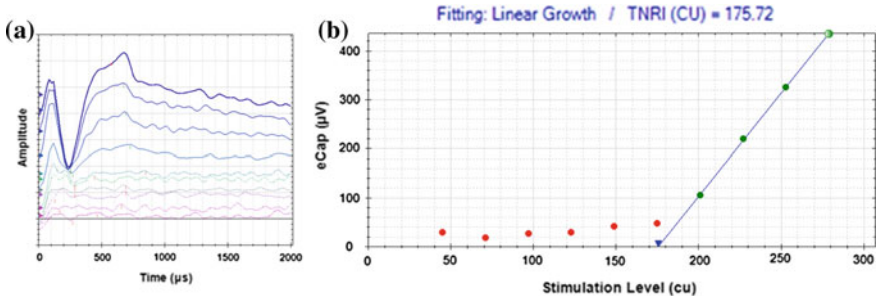

Fig. 6 Recorded ECAPs. **a** Raw ECAP recordings at different stimulation levels over time. **b** Recorded AGF on a CI user

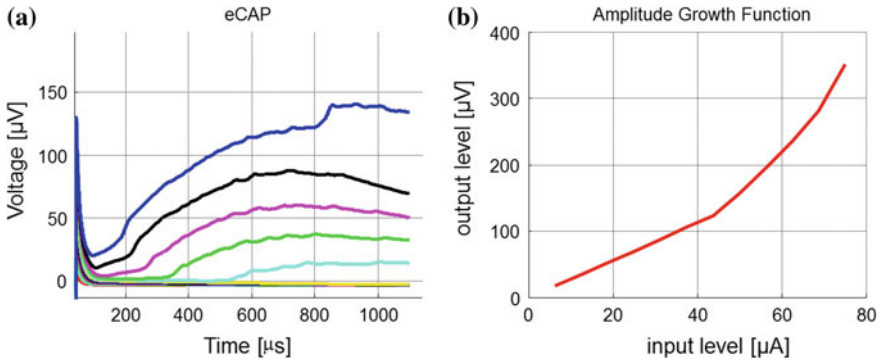

Fig. 7 Simulated ECAPs **a** Simulated single ECAP responses at different stimulation levels. **b** Simulated AGF

It can be observed that the waveform of the measured ECAP (Fig. 6) differs from the simulated ECAP (Fig. 7). The idea of the parametric model is to adapt the amount of neural degeneration and nerve density such that the measured and simulated AGF become as similar as possible.

3 Results

3.1 Simulation of the ECAP Using the Forward Masking Technique

ECAP responses were simulated using a generalized version of the 3D voltage distribution model and the AN model. Figure 7 presents the simulated ECAP responses and the corresponding AGF.

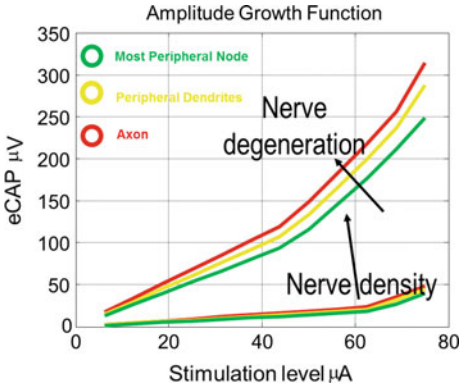

Fig. 8 Effects of different values for the parameters neural density and neural degeneration in the AGF predicted by the CI auditory nerve model

3.2 Effects of Different Amounts of Nerve Degeneration and Nerve Density on AGF

Using the parameterization presented above (density of nerve fibers and amount of degeneration of each nerve fiber) it is possible to model different morphologies for the AGF. Figure 8 presents an example of the effects observed in the AGF for an increased amount of nerve degeneration or nerve density. The nerve degeneration was simulated by selecting less apical peripheral node to initiate the action potential. The simulations show the estimated AGF when the action potential was generated at nodes 1 (most peripheral), 2 and 3. The same initial node was used in all the 7000 nerve fibers along the cochlea. Figure 8 shows that increasing the amount of nerve degeneration from 1 until 3 causes an increase in steepness of the AGF.

The change in nerve density was simulated by decreasing the amount of nerve fibers. Three versions of the model were run with different amounts of nerve density. The standard configuration used 7000 nerve fibers, while the degraded auditory configuration used 700 nerve fibers. The nerve fibers were equally spaced to cover the 2.5 turns of the cochlea. Figure 8 shows that the change in the nerve density causes not only a decrease in the level of each ECAP, but also an increase in the steepness of the AGF.

4 Discussion

Based on available anatomical and physiological results, we created an AN model that was combined with the 3D cochlea reconstruction data to predict ECAPs. We used an AN geometry similar to the model of Rattay et al. [27] but with shortening the presomatic unmyelinated compartment and with internodal lengths to fit anatomical measurements [25]. We adopted the modified HH equations proposed by Smit et al. [33] with optimization of the ionic conductances of the soma to allow stable spike conduction. Based on these formulations, we calculated ECAPs and compared

our model predictions with empirical human data. Our modeling results generally matched the shape and growth function of a general recorded ECAP from CI users. Next steps consist of extending our modeling framework to predict ECAPs in individual CI users. In the framework proposed we used two parameters to model the AN population; i.e., these parameters consist on the amount of nerve degeneration of each nerve fiber and the nerve density. Preliminary results show that these two factors have a large impact in the morphology of the ECAP. Fitting the model to recorded data might be useful to make hypotheses about the state of the AN for each CI user, and therefore it might be useful to optimize the fitting or the sound coding strategy individually.

The AN physiology model used in this study comprises only leak, fast sodium and delayed rectifier potassium conductances [33]. In human axons, however, more variations of ion channels are identified [29, 31]. Since nonlinear dynamics of active conductances may affect physiological properties of the model AN, such as adaptation [1], finer tuning of these additional ion channels would be necessary for more precise model predictions.

For the sake of simplicity, all the modeled AN fibers in this study were assumed to be identical morphologically and physiologically. Namely, we used the same anatomical (Fig. 3) and electrical (Tables 1 and 2) properties for the AN fibers. Actual ANs in vivo, however, show considerable variations in spontaneous and driven activities [10]. Sizes of AN fibers also vary along the cochlea, presumably reflecting tonotopic specializations [6]. In addition, channel noise may further affect the AN response patterns (e.g., [13]). Performance of our model may be improved by the inclusion of these sources of variations.

The relationship between the intracellular membrane potential and the extracellular field potential has long been a subject of both theoretical and experimental studies. Previous recording results in the rat hippocampus showed that the first time derivative of the membrane potential usually agrees well with the extracellular potential for the initial depolarizing phase of an action potential but not for the succeeding depolarizing and repolarizing phases [11]. In the mouse brainstem neurons, a weighed sum of the membrane potential (resistive current) and its first derivative (capacitive current) predicts well the extracellular potential [16]. Similarly in the model of AN fibers, a combination of resistive and capacitive currents might produce more precise and realistic ECAPs.

Acknowledgements This work was supported by the DFG Cluster of Excellence EXC 1077/1 “Hearing4all”.

References

1. J. Boulet, M. White, I.C. Bruce, Temporal considerations for stimulating spiral ganglion neurons with cochlear implants. J. Assoc. Res. Otolaryngol. **17**, 1–17 (2016)
2. J.J. Briaire, J.H.M. Frijns, Field patterns in a 3D tapered spiral model of the electrically stimulated cochlea. Hear. Res. **148**, 18–30 (2000)

3. J.J. Briaire, J.H.M. Frijns, Unraveling the electrically evoked compound action potential. Hear. Res. **205**, 143–156 (2005)
4. C.J. Brown, P.J. Abbas, B. Gantz, Electrically evoked whole nerve action potentials: data from human cochlear implant users. J. Acoust. Soc. Am. **88**(3), 138–591 (1990)
5. C.J. Brown, C. Etler, S. He et al., The electrically evoked auditory change complex: preliminary results from nucleus cochlear implant users. Ear Hear. **29**(5), 704–717 (2008)
6. R.L. Davis, Q. Liu, Complex primary afferents: what the distribution of electrophysiologically-relevant phenotypes within the spiral ganglion tells us about peripheral neural coding. Hear. Res. **276**, 34–43 (2011)
7. D. Debanne, E. Campanac, A. Bialowas, E. Carlier, G. Alcaraz, Axon physiology. Physiol. Rev. **91**, 555–602 (2011)
8. L. Gärtner, T. Lenarz, G. Joseph, A. Büchner, Clinical use of a system for the automated recording and analysis of electrically evoked compound action potentials (ECAPs) in cochlear implant patients. Acta Otolaryngol. **130**(6), 724–732 (2010)
9. T. Hanekom, J.J. Hanekom, Three-dimensional models of cochlear implants: a review of their development and how they could support management and maintenance of cochlear implant performance. Netw. Comput. Neural Syst. (2016)
10. P. Heil, A.J. Peterson, Basic response properties of auditory nerve fibers: a review. Cell Tissue Res. **361**, 129–158 (2015)
11. D.A. Henze, Z. Borhegyi, J. Csicsvari, A. Mamiya, K.D. Harris, G. Buzsáki, Intracellular features predicted by extracellular recordings in the hippocampus in vivo. J. Neurophysiol. **84**, 390–400 (2000)
12. M.L. Hughes, C.J. Brown, P.J. Abbas, A.A. Wolaver, J.P. Gervais, Comparison of EAP thresholds with MAP levels in the nucleus 24 cochlear implant: data from children. Ear Hear. **21**(2), 164–174 (2000)
13. N.S. Imennov, J.T. Rubinstein, Stochastic population model for electrical stimulation of the auditory nerve. IEEE Trans. Biomed. Eng. **56**, 2493–2501 (2009)
14. R.K. Kalkman, J.J. Briaire, J.H.M. Frijns, Stimulation strategies and electrode design in computational models of the electrically stimulated cochlea: an overview of existing literature. Netw. Comput. Neural Syst. (2016)
15. M.H.P. Kole, G.J. Stuart, Signal processing in the axon initial segment. Neuron **73**, 235–247 (2012)
16. J.A.M. Lorteije, S.I. Rusu, C. Kushmerick, J.G.G. Borst, Reliability and precision of the mouse calyx of held synapse. J. Neurosci. **29**, 13770–13784 (2009)
17. A.R. Møller, V. Colletti, F.G. Fiorino, Neural conduction velocity of the human auditory nerve: bipolar recordings from the exposed intracranial portion of the eighth nerve during vestibular nerve section. Electroencephalogr. Clin. Neurophysiol. **92**, 316–320 (1994)
18. J.B. Nadol Jr., Comparative anatomy of the cochlea and auditory nerve in mammals. Hear. Res. **34**, 253–266 (1988)
19. B.A. Nayagam, M.A. Muniak, D.K. Ryugo, The spiral ganglion: connecting the peripheral and central auditory systems. Hear. Res. **278**, 2–20 (2011)
20. W. Nogueira, W. Würfel, A. Büchner, Development of a model of the electrically stimulated auditory nerve. Biomed. Eng. Biomed. Tech. **1**(59), 786–789 (2014)
21. W. Nogueira, W. Würfel, R.T. Penninger, A. Büchner, Development of a model of the electrically stimulated cochlea, in *Biomedical Technology* ed. by T. Lenarz, P. Wriggers. Lecture Notes in Applied and Computational Mechanics, vol. 74 (2015), pp. 145–161
22. W. Nogueira, D. Schurzig, R. Penninger, A. Büchner, Validation of a Cochlear implant patient specific model of the voltage distribution in a clinical setting. Front. Bioeng. Biotechnol. **2016**(4), 84 (2016)
23. W. Nogueira, L. Litvak, D.M. Landsberger, A. Büchner, Loudness and pitch perception using dynamically compensated virtual channels. Hear. Res. **334**, 223–234 (2017)
24. G.E. O'Brien, J.T. Rubinstein, The development of biophysical models of the electrically stimulated auditory nerve: single-node and cable models. Netw. Comput. Neural Syst. (2016)

25. C.Y. Ota, R.S. Kimura, Ultrastructural study of the human spiral ganglion. Acta Otolaryngol. **89**, 53–62 (1980)
26. F. Rattay, R.N. Leao, H. Felix, A model of the electrically excited human cochlear neuron II. Influence of the three-dimensional cochlear structure on neural excitability. Hear. Res. **153**, 64–79 (2001)
27. F. Rattay, P. Lutter, H. Felix, A model of the electrically excited human cochlear neuron I. Contribution of neural substructures to the generation and propagation of spikes. Hear. Res. **153**, 43–63 (2001)
28. F. Rattay, T. Potrusil, C. Wenger, A.K. Wise, R. Glueckert, Schrott-Fischer, Impact of morphometry, myelinization and synaptic current strength on spike conduction in human and cat spiral ganglion neurons. PLoS ONE **8**(11), e79256 (2013)
29. G. Reid, A. Scholz, H. Bosstock, W. Vogel, Human axons contain at least five types of voltage-dependent potassium channel. J. Physiol. **518**(3), 681–696 (1999)
30. J.T. Rubinstein, How cochlear implants encode speech. Curr. Opin. Otolaryngol. Head Neck Surg. **12**, 444–448 (2004)
31. A. Scholz, G. Reid, W. Vogel, H. Bostock, Ion channels in human axons. J. Neurophysiol. **70**, 1274–1279 (1993)
32. D.P. Sladen, A. Zappler, Older and younger adult cochlear implant users: speech recognition in quiet and noise, quality of life, and music perception. Am. J. Audiol. **24**, 31–39 (2015)
33. J.E. Smit, T. Hanekom, J.J. Hanekom, Predicting action potential characteristics of human auditory nerve fibres through modification of the HodgkinHuxley equations. South Afr. J. Sci. **104**, 284–292 (2008)
34. B.S. Wilson, M.F. Dorman, Cochlear implants: A remarkable past and a brilliant future. Hear. Res. **242**, 3–21 (2008)